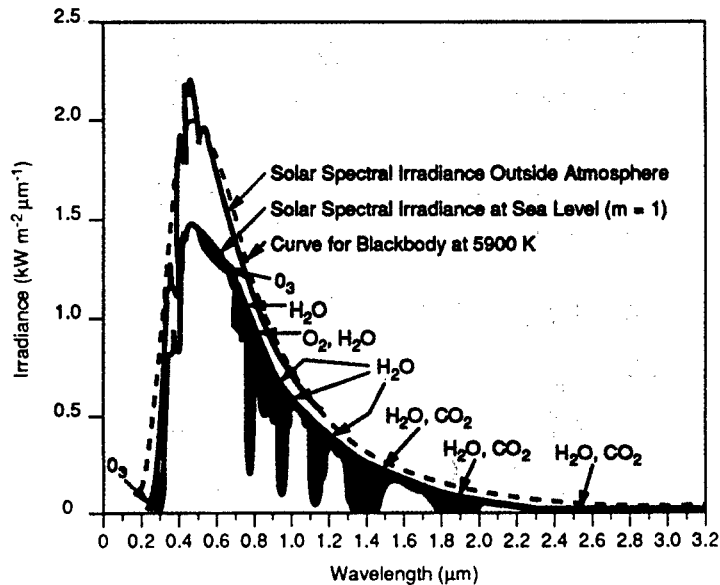


The Infrared &
Electro-Optical
Systems Handbook

VOLUME 2

Atmospheric Propagation of Radiation

Frederick G. Smith, Editor



DISTRIBUTION STATEMENT A
Approved for Public Release
Distribution Unlimited

Atmospheric Propagation of Radiation

540 70906661

VOLUME
2

**The Infrared and Electro-Optical
Systems Handbook**

The Infrared and Electro-Optical Systems Handbook

Joseph S. Accetta, David L. Shumaker, *Executive Editors*

■ VOLUME 1. **Sources of Radiation**, George J. Zissis, *Editor*

- Chapter 1. Radiation Theory, William L. Wolfe
- Chapter 2. Artificial Sources, Anthony J. LaRocca
- Chapter 3. Natural Sources, David Kryskowski, Gwynn H. Suits
- Chapter 4. Radiometry, George J. Zissis

■ VOLUME 2. **Atmospheric Propagation of Radiation**,

Fred G. Smith, *Editor*

- Chapter 1. Atmospheric Transmission, Michael E. Thomas, Donald D. Duncan
- Chapter 2. Propagation through Atmospheric Optical Turbulence, Robert R. Beland
- Chapter 3. Aerodynamic Effects, Keith G. Gilbert, L. John Otten III, William C. Rose
- Chapter 4. Nonlinear Propagation: Thermal Blooming, Frederick G. Gebhardt

■ VOLUME 3. **Electro-Optical Components**, William D. Rogatto, *Editor*

- Chapter 1. Optical Materials, William L. Wolfe
- Chapter 2. Optical Design, Warren J. Smith
- Chapter 3. Optomechanical Scanning Applications, Techniques, and Devices, Jean Montagu, Herman DeWeerd
- Chapter 4. Detectors, Devon G. Crowe, Paul R. Norton, Thomas Limperis, Joseph Mudar
- Chapter 5. Readout Electronics for Infrared Sensors, John L. Vampola
- Chapter 6. Thermal and Mechanical Design of Cryogenic Cooling Systems, P. Thomas Blotter, J. Clair Batty
- Chapter 7. Image Display Technology and Problems with Emphasis on Airborne Systems, Lucien M. Biberman, Brian H. Tsou
- Chapter 8. Photographic Film, H. Lou Gibson
- Chapter 9. Reticles, Richard Legault
- Chapter 10. Lasers, Hugo Weichel

■ VOLUME 4. **Electro-Optical Systems Design, Analysis, and Testing**,

Michael C. Dudzik, *Editor*

- Chapter 1. Fundamentals of Electro-Optical Imaging Systems Analysis, J. M. Lloyd
- Chapter 2. Electro-Optical Imaging System Performance Prediction, James D. Howe

-
- Chapter 3. Optomechanical System Design, Daniel Vukobratovich
Chapter 4. Infrared Imaging System Testing, Gerald C. Holst
Chapter 5. Tracking and Control Systems, Robert E. Nasburg
Chapter 6. Signature Prediction and Modeling, John A. Conant,
Malcolm A. LeCompte

■ **VOLUME 5. Passive Electro-Optical Systems,**

Stephen B. Campana, *Editor*

- Chapter 1. Infrared Line Scanning Systems, William L. McCracken
Chapter 2. Forward-Looking Infrared Systems, George S. Hopper
Chapter 3. Staring-Sensor Systems, Michael J. Cantella
Chapter 4. Infrared Search and Track Systems, Joseph S. Accetta

■ **VOLUME 6. Active Electro-Optical Systems,** Clifton S. Fox, *Editor*

- Chapter 1. Laser Radar, Gary W. Kamerman
Chapter 2. Laser Rangefinders, Robert W. Byren
Chapter 3. Millimeter-Wave Radar, Elmer L. Johansen
Chapter 4. Fiber Optic Systems, Norris E. Lewis, Michael B. Miller

■ **VOLUME 7. Countermeasure Systems,** David Pollock, *Editor*

- Chapter 1. Warning Systems, Donald W. Wilmot, William R. Owens, Robert J. Shelton
Chapter 2. Camouflage, Suppression, and Screening Systems, David E. Schmieder, Grayson W. Walker
Chapter 3. Active Infrared Countermeasures, Charles J. Tranchita, Kazimieras Jakstas, Robert G. Palazzo, Joseph C. O'Connell
Chapter 4. Expendable Decoys, Neal Brune
Chapter 5. Optical and Sensor Protection, Michael C. Dudzik
Chapter 6. Obscuration Countermeasures, Donald W. Hoock, Jr., Robert A. Sutherland

■ **VOLUME 8. Emerging Systems and Technologies,**

Stanley R. Robinson, *Editor*

- Chapter 1. Unconventional Imaging Systems, Carl C. Aleksoff, J. Christopher Dainty, James R. Fienup, Robert Q. Fugate, Jean-Marie Mariotti, Peter Nisenson, Francois Roddier
Chapter 2. Adaptive Optics, Robert K. Tyson, Peter B. Ulrich
Chapter 3. Sensor and Data Fusion, Alan N. Steinberg
Chapter 4. Automatic Target Recognition Systems, James W. Sherman, David N. Spector, C. W. "Ron" Swonger, Lloyd G. Clark, Edmund G. Zelnio, Terry L. Jones, Martin J. Lahart
Chapter 5. Directed Energy Systems, Gary Golnik
Chapter 6. Holography, Emmett N. Leith
Chapter 7. System Design Considerations for a Visually-Coupled System, Brian H. Tsou

Copublished by



Infrared Information Analysis Center
Environmental Research Institute of Michigan
Ann Arbor, Michigan USA

and



S P I E O P T I C A L E N G I N E E R I N G P R E S S
Bellingham, Washington USA

Sponsored by

Defense Technical Information Center, DTIC-DF
Cameron Station, Alexandria, Virginia 22304-6145

Atmospheric Propagation of Radiation

Frederick G. Smith, *Editor*
OptiMetrics Incorporated

VOLUME
2

The Infrared and Electro-Optical Systems Handbook

Joseph S. Accetta, David L. Shumaker, *Executive Editors*
Environmental Research Institute of Michigan

Library of Congress Cataloging-in-Publication Data

The Infrared and electro-optical systems handbook / Joseph S. Accetta,
David L. Shumaker, executive editors.
p. cm.
Spine title: IR/EO systems handbook.
Cover title: The Infrared & electro-optical systems handbook.
Completely rev. ed. of: Infrared handbook. 1978
Includes bibliographical references and indexes.
Contents: v. 1. Sources of radiation / George J. Zissis, editor —
v. 2. Atmospheric propagation of radiation / Fred G. Smith, editor —
v. 3. Electro-optical components / William D. Rogatto, editor —
v. 4. Electro-optical systems design, analysis, and testing /
Michael C. Dudzik, editor — v. 5. Passive electro-optical systems /
Stephen B. Campana, editor — v. 6. Active electro-optical systems /
Clifton S. Fox, editor — v. 7. Countermeasure systems / David Pollock, editor —
v. 8. Emerging systems and technologies / Stanley R. Robinson, editor.

ISBN 0-8194-1072-1
1. Infrared technology—Handbooks, manuals, etc.
2. Electrooptical devices—Handbooks, manuals, etc. I. Accetta, J.
S. II. Shumaker, David L. III. Infrared handbook. IV. Title:
IR/EO systems handbook. V. Title: Infrared & electro-optical
systems handbook.

TA1570.I5 1993

621.36'2—dc20

92-38055
CIP

Copublished by

Infrared Information Analysis Center
Environmental Research Institute of Michigan
P.O. Box 134001
Ann Arbor, Michigan 48113-4001

and

SPIE Optical Engineering Press
P.O. Box 10
Bellingham, Washington 98227-0010

Copyright © 1993 The Society of Photo-Optical Instrumentation Engineers

All rights reserved. No part of this publication may be reproduced or distributed in any form or by any means without written permission of one of the publishers. However, the U.S. Government retains an irrevocable, royalty-free license to reproduce, for U.S. Government purposes, any portion of this publication not otherwise subject to third-party copyright protection.

Preface

The Infrared and Electro-Optical Systems Handbook is a joint product of the Infrared Information Analysis Center (IRIA) and the International Society for Optical Engineering (SPIE). Sponsored by the Defense Technical Information Center (DTIC), this work is an outgrowth of its predecessor, *The Infrared Handbook*, published in 1978. The circulation of nearly 20,000 copies is adequate testimony to its wide acceptance in the electro-optics and infrared communities. *The Infrared Handbook* was itself preceded by *The Handbook of Military Infrared Technology*. Since its original inception, new topics and technologies have emerged for which little or no reference material exists. This work is intended to update and complement the current *Infrared Handbook* by revision, addition of new materials, and reformatting to increase its utility. Of necessity, some material from the current book was reproduced as is, having been adjudged as being current and adequate. The 45 chapters represent most subject areas of current activity in the military, aerospace, and civilian communities and contain material that has rarely appeared so extensively in the open literature.

Because the contents are in part derivatives of advanced military technology, it seemed reasonable to categorize those chapters dealing with systems in analogy to the specialty groups comprising the annual Infrared Information Symposia (IRIS), a Department of Defense (DoD) sponsored forum administered by the Infrared Information Analysis Center of the Environmental Research Institute of Michigan (ERIM); thus, the presence of chapters on active, passive, and countermeasure systems.

There appears to be no general agreement on what format constitutes a "handbook." The term has been applied to a number of reference works with markedly different presentation styles ranging from data compendiums to tutorials. In the process of organizing this book, we were obliged to embrace a style of our choosing that best seemed to satisfy the objectives of the book: to provide derivational material data, descriptions, equations, procedures, and examples that will enable an investigator with a basic engineering and science education, but not necessarily an extensive background in the specific technology, to solve the types of problems he or she will encounter in design and analysis of electro-optical systems. Usability was the prime consideration. In addition, we wanted each chapter to be largely self-contained to avoid time-consuming and tedious referrals to other chapters. Although best addressed by example, the essence of our handbook style embodies four essential ingredients: a brief but well-referenced tutorial, a practical formulary, pertinent data, and, finally, example problems illustrating the use of the formulary and data.

The final product represents varying degrees of success in achieving this structure, with some chapters being quite successful in meeting our objectives and others following a somewhat different organization. Suffice it to say that the practical exigencies of organizing and producing a compendium of this magnitude necessitated some compromises and latitude. Its ultimate success will be judged by the community that it serves. Although largely oriented toward system applications, a good measure of this book concentrates on topics endemic and fundamental to systems performance. It is organized into eight volumes:

Volume 1, edited by George Zissis of ERIM, treats sources of radiation, including both artificial and natural sources, the latter of which in most military applications is generally regarded as background radiation.

Volume 2, edited by Fred Smith of OptiMetrics, Inc., treats the propagation of radiation. It features significant amounts of new material and data on absorption, scattering, and turbulence, including nonlinear propagation relevant to high-energy laser systems and propagation through aerodynamically induced flow relevant to systems mounted on high-performance aircraft.

Volume 3, edited by William Rogatto of Santa Barbara Research Center, treats traditional system components and devices and includes recent material on focal plane array read-out electronics.

Volume 4, edited by Michael Dudzik of ERIM, treats system design, analysis, and testing, including adjunct technology and methods such as trackers, mechanical design considerations, and signature modeling.

Volume 5, edited by Stephen Campana of the Naval Air Warfare Center, treats contemporary infrared passive systems such as FLIRs,IRSTs, IR line scanners, and staring array configurations.

Volume 6, edited by Clifton Fox of the Night Vision and Electronic Sensors Directorate, treats active systems and includes mostly new material on laser radar, laser rangefinders, millimeter-wave systems, and fiber optic systems.

Volume 7, edited by David Pollock, consultant, treats a number of countermeasure topics rarely appearing in the open literature.

Volume 8, edited by Stanley Robinson of ERIM, treats emerging technologies such as unconventional imaging, synthetic arrays, sensor and data fusion, adaptive optics, and automatic target recognition.

Acknowledgments

It is extremely difficult to give credit to all the people and organizations that contributed to this project in diverse ways. A significant amount of material in this book was generated by the sheer dedication and professionalism of many esteemed members of the IR and EO community who unselfishly contributed extensive amounts of precious personal time to this effort and to whom the modest honorarium extended was scarcely an inducement. Their contributions speak elegantly of their skills.

Directly involved were some 85 authors and editors from numerous organizations, as well as scores of technical reviewers, copyeditors, graphic artists, and photographers whose skill contributed immeasurably to the final product.

We acknowledge the extensive material and moral support given to this project by various members of the managements of all the sponsoring and supporting organizations. In many cases, organizations donated staff time and internal resources to the preparation of this book. Specifically, we would like to acknowledge J. MacCallum of DoD, W. Brown and J. Walker of ERIM, and J. Yaver of SPIE, who had the foresight and confidence to invest significant resources in the preparation of this book. We also extend our appreciation to P. Klinefelter, B. McCabe, and F. Frank of DTIC for their administrative support during the course of this program.

Supporting ERIM staff included Ivan Clemons, Jenni Cook, Tim Kellman, Lisa Lyons, Judy Steeh, Barbara Wood, and the members of their respective organizations that contributed to this project.

We acknowledge Lorretta Palagi and the publications staff at SPIE for a professional approach to the truly monumental task of transforming the manuscripts into presentable copy and the patience required to interact effectively with the authors.

We would like to pay special tribute to Nancy Hall of the IRIA Center at ERIM who administrated this at times chaotic project with considerable interpersonal skill, marshaling the numerous manuscripts and coordinating the myriad details characteristic of a work of this magnitude.

We properly dedicate this book to the people who created it and trust it will stand as a monument to their skills, experience, and dedication. It is, in the final analysis, a product of the community it is intended to serve.

Joseph S. Accetta
David L. Shumaker
Ann Arbor, Michigan

January 1993

Notices and Disclaimer

This handbook was prepared by the Infrared Information Analysis Center (IRIA) in cooperation with the International Society for Optical Engineering (SPIE). The IRIA Center, Environmental Research Institute of Michigan, is a Defense Technical Information Center-sponsored activity under contract DLA-800-C-393 and administrated by the Defense Electronics Supply Center, Defense Logistics Agency.

This work relates to the aforementioned ERIM contract and is in part sponsored by the Department of Defense; however, the contents do not necessarily reflect the position or the policy of the Department of Defense or the United States government and no official endorsement should be inferred.

The use of product names does not in any way constitute an endorsement of the product by the authors, editors, Department of Defense or any of its agencies, the Environmental Research Institute of Michigan, or the International Society for Optical Engineering.

The information in this handbook is judged to be from the best available sources; however, the authors, editors, Department of Defense or any of its agencies, the Environmental Research Institute of Michigan, or the International Society for Optical Engineering do not assume any liability for the validity of the information contained herein or for any consequence of its use.

Contents

Introduction	xiii	
CHAPTER 1	Atmospheric Transmission, Michael E. Thomas, Donald D. Duncan	
1.1	Introduction	3
1.2	The Atmosphere of the Earth	7
1.3	Atmospheric Absorption and Refraction	13
1.4	Atmospheric Scattering	92
1.5	Computer Codes on Atmospheric Propagation	127
CHAPTER 2	Propagation through Atmospheric Optical Turbulence, Robert R. Beland	
2.1	Introduction	159
2.2	Theory of Optical Turbulence in the Atmosphere	161
2.3	Optical/IR Propagation through Turbulence	176
2.4	Measurements of Optical Turbulence in the Atmosphere	201
2.5	Models of Optical Turbulence	211
2.6	Sample Problems	224
CHAPTER 3	Aerodynamic Effects, Keith G. Gilbert, L. John Otten III, William C. Rose	
3.1	Introduction	235
3.2	Aerodynamic Considerations	237
3.3	Optical Considerations	246
3.4	Aero-Optical Design and Analysis Examples	264
3.5	Aero-Optics: Visions and Opportunities	278
CHAPTER 4	Nonlinear Propagation: Thermal Blooming, Frederick G. Gebhardt	
4.1	Introduction	289
4.2	Historical Overview	289
4.3	Blooming Basics	291
4.4	Steady-State Blooming with Wind/Beam Motion	294
4.5	Conclusions	311
Index	314	

Introduction

In the 14 years since the previous version of the *Infrared Handbook* was published, there has been tremendous progress in our understanding of atmospheric phenomena and in the application of atmospheric physics to predict the performance of infrared and electro-optical systems. This progress has been motivated by the increased reliance of military systems on electro-optical and infrared sensors and the recognition that often the performance of such sensors is severely limited by atmospheric conditions. A second motivation has been the development of high-energy and high-power laser systems and the need to understand the extreme sensitivity of laser propagation to small uncertainties in atmospheric parameters.

In general, the progress has not so much been in the development of new physics, but rather in working out details and applying existing physics to practical problems. Improvements in molecular atmospheric modeling have been fostered by vast increases in computing power over the last decade. The 1978 handbook included many tables and graphs that could be used for engineering estimates of atmospheric transmission. Those are largely absent from the present volume because virtually every electro-optical systems engineer now has access to atmospheric effects computer models. However, it is important for the engineer to understand the limits and assumptions of the physics represented in the models. He or she can gain that knowledge from Chapter 1 of the present volume.

Fourteen years ago, the physics of aerosol absorption and scattering was well understood; however, the data necessary to apply that knowledge to real-world weather and environmental conditions were limited. During this period, hundreds of field tests of electro-optical systems have been performed to relate their performance to propagation variables and environmental conditions. Much of this knowledge base is captured in computer models such as LOWTRAN and EO-SAEL maintained by government laboratories. This knowledge was also used by the field commanders during the Gulf War where the importance of atmospheric effects was clearly demonstrated by the decisive performance of U.S. infrared systems in adverse visibility conditions.

The most challenging area for atmospheric propagation research during the last 14 years has been in modeling of laser propagation. Turbulence and linear propagation effects on laser beams have been extensively studied during this period and are now quite well understood. Many of these factors are discussed in the first two chapters of this volume. Chapter 3 discusses how aerodynamic factors influence laser and sensing systems that must operate through the boundary layers of in-flight aircraft. A full treatment of the nonlinear interactions of high-energy or high-power laser beams with the atmosphere is

beyond the scope of this handbook. However, Chapter 4 provides a good introduction to the subject and provides references for further study.

Acknowledgments

I would like to thank the authors of this volume, in particular the authors of the original material in the first three chapters. They put in much more effort on their sections than their modest compensation could justify. The support of the IRIA staff in development of this volume is also greatly appreciated.

Frederick G. Smith
Ann Arbor, Michigan

January 1993

CHAPTER 1

Atmospheric Transmission

Michael E. Thomas

Donald D. Duncan

The Johns Hopkins University

Applied Physics Laboratory

Laurel, Maryland

CONTENTS

1.1	Introduction	3
1.1.1	Symbols and Units	3
1.1.2	Radiative Transfer in the Atmosphere	3
1.2	The Atmosphere of the Earth	7
1.2.1	Atmospheric Structure	7
1.2.2	Gas Composition	9
1.2.3	Particle Composition	11
1.2.4	Density Variation	12
1.3	Atmospheric Absorption and Refraction	13
1.3.1	Background	13
1.3.2	Absorption by Atmospheric Gases	39
1.3.3	HITRAN Database	65
1.3.4	Band Models	69
1.3.5	Refractive Effects of the Atmosphere	86
1.4	Atmospheric Scattering	92
1.4.1	Aerosol Scatter	92
1.4.2	Molecular (Rayleigh) Scatter	109
1.4.3	Example Applications	110
1.4.4	Propagation through a Highly Scattering Medium	115
1.4.5	Imaging through a Scattering Medium	123
1.5	Computer Codes on Atmospheric Propagation	127
1.5.1	LOWTRAN	127
1.5.2	MODTRAN	128
1.5.3	FASCODE	128
1.5.4	Algorithms for Calculation of Scatter Parameters	133
	References	147
	Bibliography	155

1.1 INTRODUCTION

The atmosphere is always an important consideration in the performance of many electro-optical systems. An electro-optical system can be described as containing three basic components: source, detector, and propagation medium. Because of the quality of source and detection systems today, the limiting factor in overall system performance often is the propagation medium. Thus, a thorough discussion of the atmosphere and various mechanisms of attenuation is required. Absorption, scattering, and turbulence are the dominant mechanisms of loss. This chapter addresses absorption and scattering. Turbulence is covered in Chap. 2 of this volume.

1.1.1 Symbols and Units

Table 1.1 lists symbols with the corresponding meaning and units used in this chapter. An attempt is made to consistently use mks units, but convention does not always allow this. Also, the defined symbols are used consistently throughout the chapter. However, absorption and scattering theory were developed separately and different symbols are often used for the same quantity. An attempt is made to use the most common symbols with both sets of literature and to otherwise select symbols in the most unambiguous way. When the usage should clearly indicate the meaning, the same symbol is sometimes used for two different quantities.

1.1.2 Radiative Transfer in the Atmosphere

The extinction of radiation that traverses a medium (Fig. 1.1) is proportional to the initial radiance, to the density of the attenuating medium, to thermally emitted radiation along the path, and to the incremental distance traversed, dr , so that¹

$$dL_\lambda(r) = - \left[\sum_i C_{ei}(\lambda, r) \rho_i(r) \right] L_\lambda(r) dr + J_\lambda(r) dr , \quad (1.1)$$

where

- $L_\lambda(r)$ = spectral radiance at a point r with coordinates (x, y, z)
- $J_\lambda(r)$ = source term accounting for path emission and scattering
- ρ_i = number density of the i 'th gas or particle (cm^{-3})
- $C_{ei}(\lambda, s)$ = spectral extinction cross section of the i 'th gas or particle (cm^2)
 - = $C_{ai}(\lambda, s) + C_{si}(\lambda, s)$
- $C_{ai}(\lambda, s)$ = spectral absorption cross section
- $C_{si}(\lambda, s)$ = spectral scattering cross section.

It is convenient at this point to introduce the extinction coefficient, which is related to the extinction cross section

$$\beta_{\text{ext}} = \sum_i C_{ei}(\lambda) \rho_i = \sum_i \beta_{\text{ext}i} , \quad (1.2)$$

where $\beta_{\text{ext}} = \beta_{\text{abs}} + \beta_{\text{sca}}$, when $\beta_{\text{sca}}r < 0.1$ (single-scatter limit). The usual assumption is made that the atmosphere is structured in plane-parallel, ho-

Table 1.1 Symbols, Nomenclature, and Units

Symbol	Meaning	Units*
a	Absolute humidity	g m^{-3}
$a = C_{\text{sca}}/C_{\text{ext}}$	Single-scatter albedo	—
a_n and b_n	Complex Mie coefficients	—
B_e	Rotational constant	cm^{-1}
C_{ext}	Extinction cross section	m^2
C_{abs}	Absorption cross section	m^2
C_{sca}	Scatter cross section	m^2
c	Speed of light (2.99792458×10^8)	m s^{-1}
$C(\tau)$	Autocorrelation function	$\text{s}^{-1} \text{ cm}$
E	Energy	J
$E_s(T)$	Saturation vapor pressure	kPa
E_ν	Spectral irradiance	W cm^{-2}
E	Intensity	W m^{-2}
F	Flux density	$\text{W m}^{-2} \text{ Hz}^{-1}$
g	Asymmetry parameter	—
g	Gravitational acceleration	m s^{-2}
$g(\nu)$	Line-shape function	cm
h	Planck's constant ($6.6260755 \times 10^{-34}$)	J s
I	Specific intensity	$\text{W m}^{-2} \text{ sr}^{-1} \text{ Hz}^{-1}$
I_s	Scattered intensity	W m^{-2}
I_i	Incident intensity	W m^{-2}
I_ν	Spectral radiant intensity	W sr^{-1}
$[I \ Q \ U \ V]$	Stokes vector	—
j	$\sqrt{-1}$	—
J	Source function	$\text{W m}^{-2} \text{ sr}^{-1} \text{ Hz}^{-1}$
$j(\nu)$	Spectral density function	cm
k	Imaginary part of index of refraction	—
k_B	Boltzmann's constant (1.380658×10^{-23})	W s K^{-1}
$k = 2\pi/\lambda$	Wave number (angular wave number)	m^{-1}
m	Mass	kg
$n,m = n - jk$	Complex refractive index	—
$M(\nu)$	Optical transfer function (OTF)	—
N	Number density	m^{-3}
$n(r)$	Size distribution function	$\text{cm}^{-3} \mu\text{m}^{-1}$
n	Index of refraction real part	—
n	Complex index of refraction	—
P,p	Pressure	Pa
$P(\theta), P_i(\theta)$	Phase functions	—
$p(\mu,\phi;\mu',\phi')$	Phase function—integral over 4π sr is a , the single-scatter albedo	—
Q_{ext}	Extinction efficiency	—
Q_{abs}	Absorption efficiency	—
Q_{sca}	Scatter efficiency	—
Q_{back}	Backscatter efficiency	—

Table 1.1 (continued)

Symbol	Meaning	Units*
Q	Partition function	—
R, r	Distance	m
rh	Relative humidity	—
r	Particle radius	m
R_v	Visibility range	km
R_m	Meteorological range	km
S_1 and S_2	Dimensionless complex amplitudes	—
S_i	Line strength of i 'th line	$\text{cm}^{-1} \text{ km}^{-1}$
T	Temperature	K
V	Volume	m^3
$x = kr$	Dimensionless size parameter	—
x, y, z	Cartesian coordinates (z directed upward)	m
α_{ext}	Extinctance (absorptance plus scatterance)	—
α_{abs}	Absorptance, absorptivity	—
α_{sca}	Scatterance	—
α_e	Electronic polarizability	—
α_i	Half-width at half maximum of i 'th line	cm^{-1}
β_{ext}	Extinction coefficient or extinction cross section per unit volume	km^{-1}
β_{abs}	Absorption coefficient or absorption cross section per unit volume	km^{-1}
β_{sca}	Scattering coefficient or scatter cross section per unit volume	km^{-1}
$\Gamma(\rho)$	Mutual coherence function (MCF)	—
δ	Depolarization factor	—
ϵ_0	Permittivity of free space (8.854188×10^{-12})	F m^{-1}
ϵ_r	Relative permittivity	—
ϵ	Emittance, emissivity	—
ζ	Zenith angle	rad
Θ, ϕ	Polar, azimuthal angles	rad or deg
κ	Spatial frequency	m^{-1}
λ	Wavelength	μm
$\mu = \cos\theta$		—
μ_0	Permeability of free space ($4\pi \times 10^{-7}$)	H m^{-1}
v	Wave number ($1/\lambda$)	cm^{-1}
π_n and τ_n	Angle-dependent functions	—
π	Pi (3.14159)	—
ρ_i	Number density of species i	cm^{-3}
ρ_m	Mass density	g cm^{-3}
ρ	Reflectance, reflectivity	—
σ_b	Backscatter cross section	m^2
τ, T	Transmittance, transmissivity	—
τ_{OD}	Optical distance or depth	—
ω	Angular frequency	rad s^{-1}
Ω	Solid angle	sr

*— indicates a dimensionless quantity.

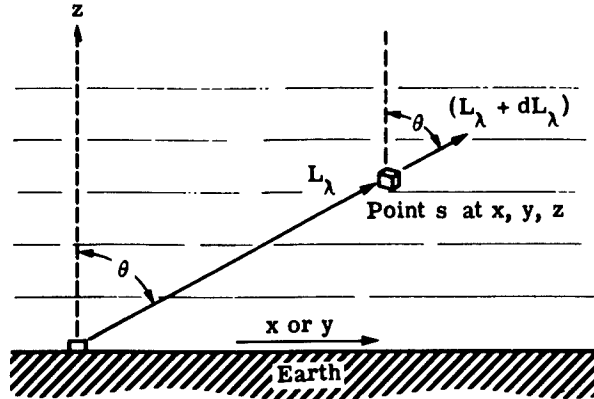


Fig. 1.1 Radiance extinction in a vertically stratified medium.

mogeneous layers, so that the only spatial variations in k and ρ_i are vertical, in the z direction. The radiative-transfer-equation solution following from Eq. (1.1) is

$$L_\lambda(r) = L_\lambda(0) \exp[-\tau_{OD}(r)] + \int_0^r J_\lambda(r') \exp[\tau_{OD}(r') - \tau_{OD}(r)] dr' , \quad (1.3)$$

where the optical depth is defined as

$$\tau_{OD}(r) = \int_0^r \beta_{ext}(r') dr' . \quad (1.4)$$

The source term represents the emitted radiation by the molecules and particles along the path and the scattered radiation by molecules and particles along the path that is received by the detector. When the transmission is high, this signal is very small and can be dropped. This leads to a simplified definition of transmittance:

$$\tau(r) = \frac{L_\lambda(r)}{L_\lambda(0)} = \exp[-\tau_{OD}(r)] . \quad (1.5)$$

For a homogeneous path,

$$\tau_{OD} = \beta_{ext} r . \quad (1.6)$$

The extintance α_{ext} is defined as (when boundaries are ignored, the reflectance ρ is zero)

$$\alpha_{ext} = 1 - \tau . \quad (1.7)$$

For the case of single scattering, the extintance becomes the sum of absorptance α_{abs} and scatterance α_{sca} ($\alpha_{ext} = \alpha_{abs} + \alpha_{sca}$).

At this point it is also useful to introduce the relationship between extinction coefficient and index of extinction (imaginary part of the complex index of

refraction, $m = n - jk$), when the single-scatter approximation is valid ($\beta_{\text{sca}}r < 0.1$):

$$k = \frac{\beta_{\text{ext}}}{4\pi\nu} . \quad (1.8)$$

This equation is obtained by comparing the radiation-transfer solution to the plane-wave solution of Maxwell's equations in an unbounded homogeneous medium. These definitions, parameters, and formulas are fundamental to the description of optical propagation in the atmosphere.

1.2 THE ATMOSPHERE OF THE EARTH

The atmosphere surrounds and protects the earth in the form of a gaseous blanket forming the transition between the solid surface of the earth and the near vacuum of the outer solar atmosphere. It acts as a shield against harmful radiation and meteors. The dynamics of the atmosphere drive the weather on the surface. It provides for life itself as part of the earth's biosphere. Optical propagation in this medium has many important characteristics and consequences. These include meteorological remote sensing, infrared and visible astronomy, remote sensing in general, and electro-optical systems performance. Therefore, it is appropriate to include in this chapter an introduction to the nature of the atmosphere.

1.2.1 Atmospheric Structure

The atmosphere is composed of gases and suspended particles at various temperatures and pressures as a function of altitude and azimuth. The variations in altitude show a marked structure. Six main horizontal layers form the stratified structure of the atmosphere, as shown in Fig. 1.2. The lowest is the troposphere, which extends from the ground to approximately 11 km (36,000 ft or 7 miles). The temperature in this layer generally decreases with increasing altitude at the rate of 6.5 K km^{-1} . However, variations on this rate can exist, which creates interesting refractive effects. The pressure varies from one atmosphere at sea level to a few tenths of an atmosphere at the top of this layer. Most of the important atmospheric attenuators exist in the troposphere (i.e., H_2O , CO_2 , clouds, fog, aerosols in general). Water is most important at lower altitudes, in particular over the ocean as part of the marine boundary layer. Also, this is the region of highest pressure or density and therefore has the highest molecular scatter. The next layer is the stratosphere, which extends up to 50 km (30 miles). In this layer, ozone (O_3), which protects life on the surface from ultraviolet radiation, is found. Ozone starts to absorb at and below $0.3 \mu\text{m}$, thus extending protection from these high-energy photons relative to molecular oxygen (which begins to strongly absorb below $0.185 \mu\text{m}$). Particles in this layer can remain for a long time. Above the stratosphere is the mesosphere. This layer begins at 50 km and extends to 90 km. Most models concerning optical propagation in the atmosphere end with this layer. Above the mesosphere is the ionosphere, which is important for radio-wave propagation. However, the plasma resonances that give it reflective properties at radio

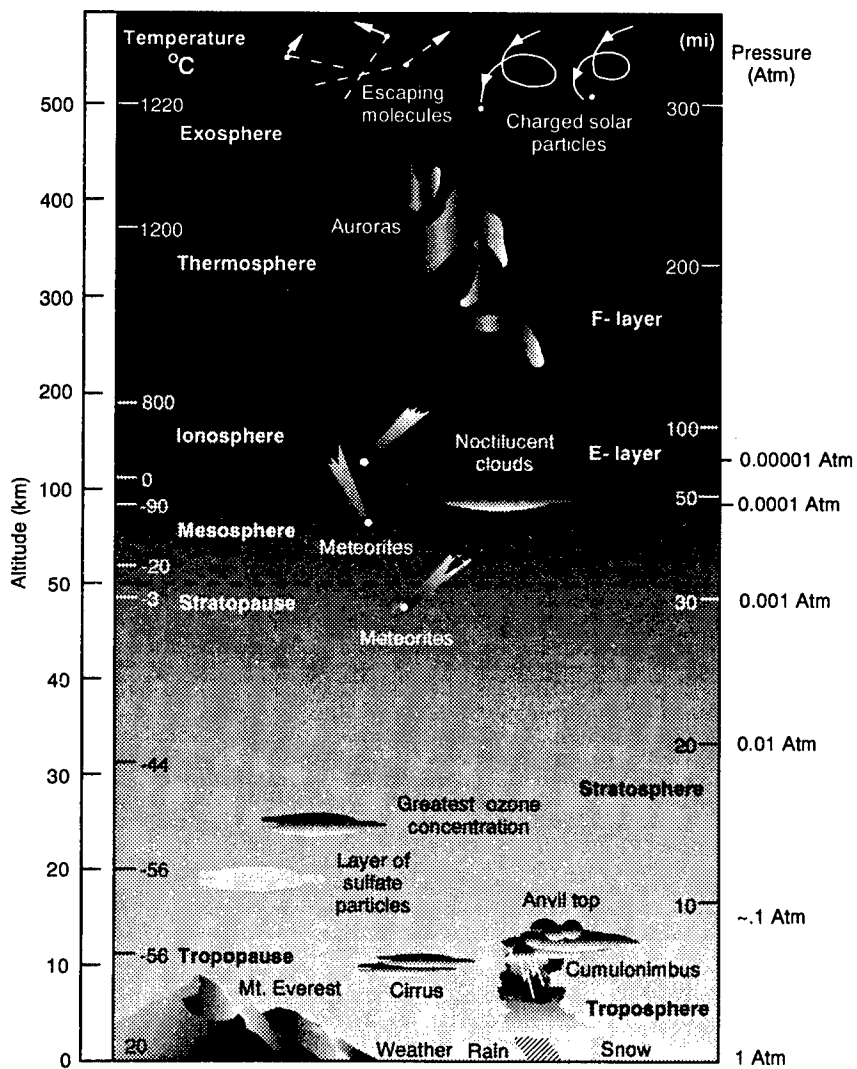


Fig. 1.2 Structure of the atmosphere with altitude.

frequencies are too slow for optical frequencies and this layer is optically transparent. Also, molecules in the ionosphere undergo photochemical dissociation. Thus, the chemical composition changes significantly at this altitude. The ionosphere extends up to nearly 300 km. Above the ionosphere are the thermosphere and the exosphere, which are influenced by solar radiation and the joining of the atmosphere of the earth to the solar atmosphere. The outermost altitude is approximately 500 km (300 miles).

1.2.2 Gas Composition

Table 1.2 lists uniformly mixed atmospheric gases (up to 100 km altitude) and their abundances. These molecules do not vary significantly in concentration with time. Nitrogen and oxygen are by far the most abundant. Oxygen has relatively narrow absorption bands at 60 GHz (2 cm^{-1}) because of a magnetic dipole moment, at 760 nm ($13,158\text{ cm}^{-1}$), and has strong absorption in the ultraviolet (the Schumann-Runge bands). Otherwise, neither gas has dipole-allowed infrared spectra. Only weak collision-induced-absorption (CIA) bands in N_2 and O_2 can be observed for very long tropospheric propagation paths. However, these molecules are very important for Rayleigh-scattering (see Sec. 1.4.2) and refractive-index (see Sec. 1.3.5) calculations. The inert gases contribute very little to optical-propagation phenomena.

The other molecules such as CH_4 , N_2O , and CO have pronounced spectral features (see Sec. 1.3.2) in the atmosphere even though they have very minor concentrations. Their importance is localized to these spectral features however. Some seasonal variation is observed in these gases as well, owing to fuel burning and other effects.

The molecules listed in Table 1.2 have basically fixed relative concentrations as a function of altitude in the earth's atmosphere. Some of the most important molecules impacting propagation have a variable concentration. This list is given in Table 1.3 and includes H_2O , CO_2 , and O_3 .

Water vapor exists primarily in the troposphere and is highly variable from day to day, from season to season, with altitude, and for different geographical locations. Carbon dioxide varies seasonally with a maximum during the early spring and a minimum during the late summer to early fall, and is uniformly mixed with altitude up to 80 km. These points are illustrated in Figs. 1.3 and 1.4.³⁻⁶ The variable nature of these important atmospheric gases makes the prediction of atmospheric propagation at infrared frequencies a challenge. The concentration of water vapor also influences particle scattering.

Table 1.2 Gases Present in Standard Amounts in a Dry Atmosphere (from Ref. 2)

Constituent	Volume Ratio (%)	Parts per Million
Nitrogen, N_2	78.084 ± 0.004	—
Oxygen, O_2	20.946 ± 0.002	—
Argon, Ar	0.934 ± 0.001	—
Neon, Ne	0.001818	18.18 ± 0.04
Helium, He	5.24×10^{-4}	5.24 ± 0.004
Krypton, Kr	1.14×10^{-4}	1.14 ± 0.01
Xenon, Xe	—	0.087 ± 0.001
Hydrogen, H_2	—	0.5
Methane, CH_4	—	1.6
Nitrous oxide, N_2O^*	—	0.5 ± 0.1

*Has varying concentration in polluted air.

Table 1.3 Atmospheric Gases Present in Variable Amounts (from Ref. 2)

Constituent	Volume ratio (%)	Parts per Million
Ozone, O ₃	—	0–0.3 (tropospheric*) 1–7 (20 to 30 km)
Water vapor, H ₂ O	0–2	—
Carbon dioxide, CO ₂	0.035	351 ± 4
Carbon monoxide, CO*	—	0.19
Nitric acid vapor, HNO ₃	—	(0 to 10) × 10 ⁻³
Ammonia, NH ₃	—	Trace
Hydrogen sulfide, H ₂ S	—	(2 to 20) × 10 ⁻³
Sulfur dioxide, SO ₂ *	—	(0 to 20) × 10 ⁻³
Nitrogen dioxide, NO ₂	—	Trace
Nitric oxide, NO	—	Trace

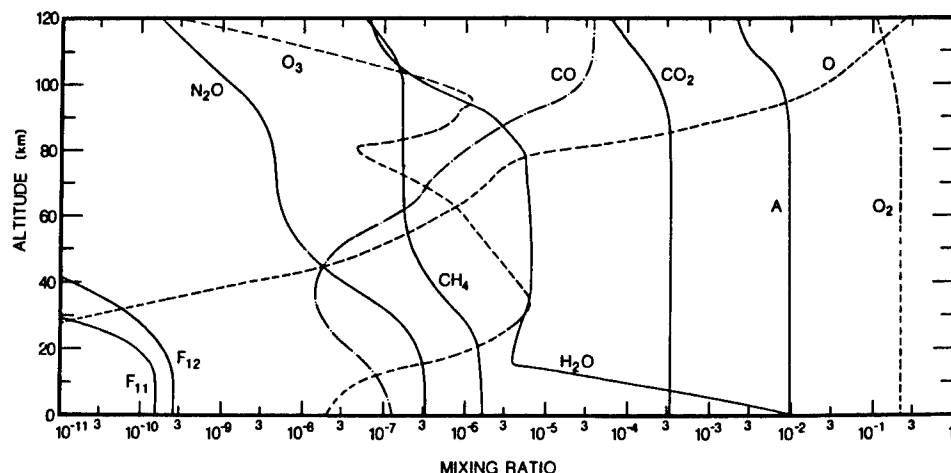
*Has varying concentration in polluted air.

At this point it is useful to review the different units used to quantify the amount of H₂O in the air.

1. Water-vapor partial pressure $p_{\text{H}_2\text{O}}$ is commonly given in units of kilopascals (kPa), millibars (mbar), torr (mm Hg), and atmospheres (atm), where 101.3 kPa = 760 Torr = 1013 mbar = 1 atm.
2. Relative humidity rh is the ratio of $p_{\text{H}_2\text{O}}$ to the saturation vapor pressure $E_s(T)$:

$$rh = \left[\frac{p_{\text{H}_2\text{O}}}{E_s(T)} \right] \times 100\% , \quad (1.9)$$

where

**Fig. 1.3** Vertical profiles of the mixing ratio of selected species at equinox.^{3–5}

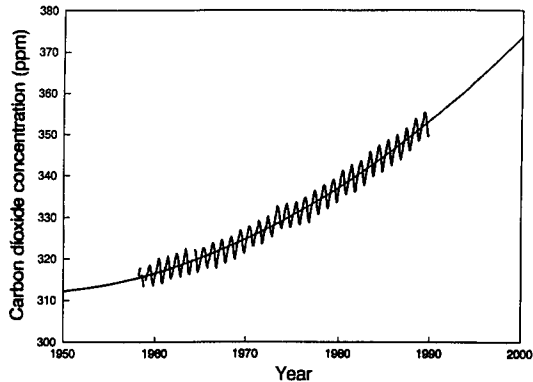


Fig. 1.4 Molecular concentration of CO₂ at Mauna Loa Observatory, Hawaii, as a function of year. Both long-term mean (smooth curve given by CO₂ concentration = 312.15 + 0.24 (year—1950) + 0.01943 (year—1950)⁴ and seasonal changes (oscillatory curve) are shown.^{2,6}

$E_s(T)$ in units of kPa is computed by the following formula with an accuracy of 0.1%⁷:

$$E_s(T) = 2.4096 \left(\frac{300}{T} \right)^5 10^{(10 - 2950.2/T)} \text{ (kPa)} , \quad (1.10)$$

where T is temperature in kelvin. Table 1.4 lists values of $E_s(T)$ based on the above formula.

3. Absolute humidity a (g m⁻³) is defined as

$$a = 2170 \frac{p_{\text{H}_2\text{O}}}{T} , \quad (1.11)$$

where the following units are used: $p_{\text{H}_2\text{O}}$ (kPa) and T (K). This formula can be obtained from the ideal gas law, $P_i V = \rho_i k_B T$.

1.2.3 Particle Composition

Particles vary not only in chemical composition but also in size (from about 0.01 to 10 μm) and shape (spheres, ellipsoids, rods, etc.). Therefore, the description of atmospheric particles is far more difficult than the description of atmospheric molecules. The range of sizes varies for different types of particles as Table 1.5 indicates. Size-distribution functions specify the concentration of a particle as a function of particle radius, and height-distribution functions specify the concentration as a function of altitude. Generally, simple shapes are assumed for model calculations; however, shape-distribution functions are needed also. Two basic classes of particles determine the majority of scattering attenuation in the atmosphere: aerosols and hydrometers.

Table 1.4 Saturation Vapor Pressure of H₂O (from Ref. 2)*

T (K)	<i>E_s</i> (kPa)	T (K)	<i>E_s</i> kPa)
250	0.0760	300	3.535
260	0.1958	305	4.75
270	0.4701	310	6.228
280	0.991	320	10.540
290	1.919	330	17.202
295	2.64		

*The following polynomial fit represents E_s with a standard deviation of ± 0.024 kPa, $\ln(E_s) = 16.323 - 3.7496 \times 10^3 T^{-1} - 2.3061 \times 10^5 T^{-2}$.

Table 1.5 Radius Range for Various Types of Particles

Type	Radius (μm)	Concentration (cm^{-3})
Air molecules	10^{-4}	10^{19}
Aiken nucleus	10^{-3} to 10^{-2}	10^4 to 10^2
Aerosol	10^{-2} to 1	10^3 to 10
Fog	1 to 10	100 to 10
Cloud	1 to 10	300 to 10
Raindrops	10^2 to 10^4	10^{-2} to 10^{-5}

The first class of particles has radii of less than 1 μm . Because these particles are very small, they are suspended in the atmosphere. This mixture is called an aerosol. Scattering by aerosols greatly increases optical attenuation over molecular scattering and is called haze. The particles have the highest concentration levels near the surface of the earth and therefore the highest levels of haze are also near the surface of the earth. This point is readily verified by observing the color of the sky as a function of zenith angle. Overhead the sky is a distinctive blue, because of molecular Rayleigh scattering, but toward the horizon the color becomes whitish. This is because of the increased path length in the particle-rich lower atmosphere. Examples are smog, smoke, fine soil particles, cosmic dust, clouds, fog, etc. Particles that contain moisture add another dimension to the description, as the humidity is also a factor.

The second class of particles, called hydrometers, consists of water-dominated particles in the liquid or solid state. Examples are many types of clouds, mist, fog, rain, freezing rain, hail, snow, ocean spray, etc. These particles are typically larger than 1 μm radius and exist for shorter periods of time than the smaller particles.

The discussion of the details of particle distribution functions is more appropriately contained in Sec. 1.4.

1.2.4 Density Variation

As the altitude increases, the density (pressure) decreases exponentially. To see this, consider a column of gas. The incremental pressure dP from an incremental altitude dz caused by its weight in a gravitational field is

$$dP = -\rho_m g dz , \quad (1.12)$$

where ρ_m is the mass density and g is the gravitational acceleration. However, ρ_m must vary with altitude z [i.e., $\rho_m = \rho_m(z)$]. Now let us use the ideal gas law,

$$\rho_m = m\rho = \frac{mP(z)}{k_B T(z)} , \quad (1.13)$$

where ρ is the number density and m is the average mass per molecule. Thus,

$$\frac{dP}{P(z)} = -\frac{mg}{k_B T(z)} dz . \quad (1.14)$$

Now let us assume $T(z) = T_0 + az$. (Note: $a = -6.5$ K/km, which is valid for the lower 10 km of the 1976 U.S. standard atmosphere.) Then it follows that

$$P(z) = P(0) \left(\frac{T(z)}{T_0} \right)^{-mg/ak_B} . \quad (1.15)$$

[Note: For the value of a given above, the numerical value of the exponent, $-mg/ak_B$, in Eq. (1.15) is 5.256.] In the isothermal limit [i.e., $T(z) = T_0$] Eq. (1.14) becomes

$$P(z) = P(0) \exp \left(-\frac{mgz}{k_B T_0} \right) . \quad (1.16)$$

These formulas can be used to form a piecewise continuous representation of the pressure variation of the real atmosphere with altitude given the temperature profile.

1.3 ATMOSPHERIC ABSORPTION AND REFRACTION

Absorption and refraction by atmospheric molecules are the topics of this section. The atmospheric window regions are defined by molecular absorption (primarily water vapor and carbon dioxide). Local-line and continuum absorption are of concern within the window regions. A basic understanding of the spectroscopy of these molecules is necessary for the understanding of the location and nature of the window regions. Also, dispersion and temperature dependence of the index of refraction are based on the spectroscopy of the atmospheric molecules. Thus, the discussion of absorption and refraction will begin with a background section on atmospheric spectroscopy.

1.3.1 Background

This section will lay the foundation concerning the description of atmospheric absorption and refraction. The formal development will be briefly outlined, resulting in formulas that are used in atmospheric modeling.

1.3.1.1 Basic Concepts

The energy structure of a molecule is composed of discrete energy levels. At optical frequencies, the quantum nature of molecules is important. This concept is illustrated in Fig. 1.5 for a two-level system. A photon with a frequency such that $E_1 - E_0 = hf_0$ (h is Planck's constant) is absorbed by this system. All other frequencies do not interact (to first order; e.g., scattering is excluded). Energy is removed from the photon field at precisely the frequency f_0 . Thus, a spectral line is observed at f_0 because of the absence of energy relative to the incident photon field.

1.3.1.1.1 Definitions

A real spectral line has an integrated amplitude (or strength S_i) and a half-width α_i because the energy levels are not single valued, but instead have a distribution of energies caused by the Heisenberg uncertainty principle, collisions from other molecules, electric fields, magnetic fields, and thermal motion. The resulting absorption feature is illustrated in Fig. 1.6. The strength of the i 'th absorption line is defined as the entire area under the absorption curve, $\beta_i(\nu)$. Thus,

$$S_i = \int_0^{\infty} \beta_{\text{abs},i}(\nu) d\nu . \quad (1.17)$$

The profile, or line-shape function, of the transition is defined as

$$g(\nu, \nu_0; \alpha_i) , \quad (1.18)$$

where α_i is the half-width at half maximum and ν_0 is the line center wave number (frequency). Thus, the absorption coefficient of a single line can be broken down into two factors, the line strength and the line-shape profile:

$$\beta_{\text{abs},i}(\nu) = S_i g(\nu, \nu_0; \alpha_i) . \quad (1.19)$$

The definition of S_i requires the line-shape profile to be normalized as

$$1 = \int_0^{\infty} g(\nu, \nu_0; \alpha_i) d\nu . \quad (1.20)$$

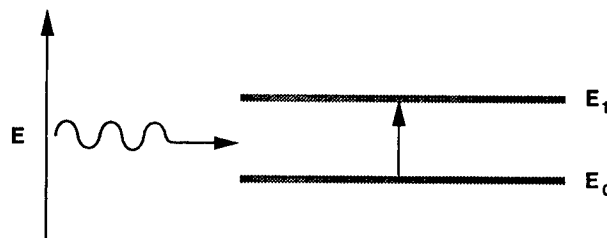


Fig. 1.5 Photon absorption in a two-level system.

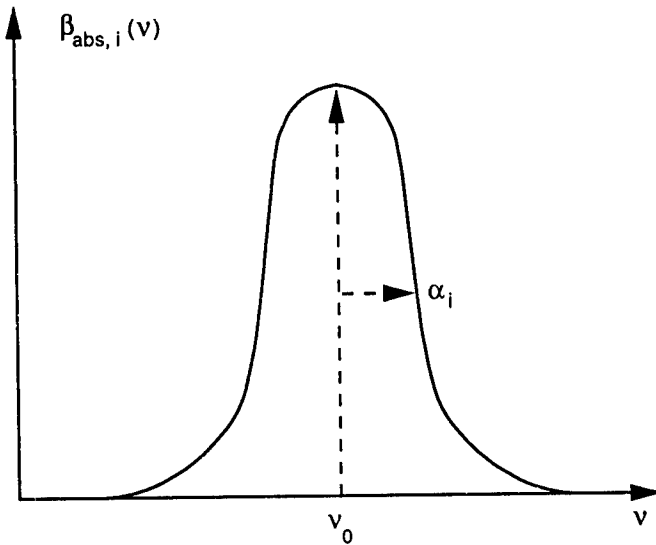


Fig. 1.6 Absorption coefficient of a spectral line, where $\nu_0 = (E_1 - E_0)/hc = f_0/c$, where c is the speed of light.

Also, detailed balance requires symmetry between absorption (positive frequencies) and emission (negative frequencies) profiles of the form $g(\nu) = g(-\nu)$.⁸

The next section is concerned with determining the position ν_0 of an absorption line. In the following sections the nature of the strength S_i and profile function $g(\nu)$ are developed more completely. At infrared frequencies only molecules and not atoms can strongly couple to the electromagnetic field. Atoms do not have rotational and vibrational spectra. Of course, no molecule has only one spectral line, and a sum over all spectral lines must be made to compute the total absorption as a function of frequency. Therefore,

$$\beta_{\text{abs}}(\nu) = \sum_i \beta_{\text{abs}, i}(\nu) = \sum_i S_i g(\nu, \nu_i) . \quad (1.21)$$

1.3.1.1.2 Dipole Moments, Intramolecular Potentials, and Selection Rules

Strength and line position of a molecule are influenced by the nature of the intramolecular bond and by the configuration and mass of the atoms forming the molecule. A molecule with a dipole moment can couple to the photon field. The strength of the dipole moment determines partially the strength of the transition. The masses of the atoms, the relative positions, and the bond strengths determine the line positions of the transitions (for rotational and vibration-rotation spectra). The dipole moment is defined as

$$\mu = qr . \quad (1.22)$$

An example of this is HCl. Figure 1.7 is a simplistic diagram for diatomic molecules. A more detailed analysis of the charge distribution produces not only a dipole moment but also a quadrupole moment, and so on. In molecules with proper symmetry $\mu = 0$ (e.g., N₂, O₂, CO₂, and CH₄); thus, quadrupole moments are the most important. However, only molecules with dipole-moment interactions will be considered because they are, by far, the strongest and therefore the most important in atmospheric absorption spectroscopy. Infrared-active rotational spectra require molecules with permanent dipole moments (e.g., H₂O, O₃, and CO). Such molecules are called polar. Spherically and symmetrically arranged molecules have zero dipole moment, have no rotational spectra, and are called nonpolar. Infrared-active vibrational spectra require molecules with only a change in the dipole moment caused by the asymmetric relative positions of the atoms within the molecule. Therefore, if the relative vibrational motion of the atoms within a nonpolar molecule is asymmetrical, then a dipole moment may be produced and vibrational spectra can exist. This point can be stated mathematically by considering a Taylor series expansion of the dipole-moment matrix element about the equilibrium position r_e of a molecule; thus,

$$\begin{aligned} \langle J_f v_f | \mu | J_i v_i \rangle &= \langle J_f v_f | \mu_0 | J_i v_i \rangle \\ &+ \langle J_f v_f | \left(\frac{\partial \mu}{\partial r} \right)_{r=r_e} (r - r_e) | J_i v_i \rangle + \dots , \end{aligned} \quad (1.23)$$

where $\langle r | Jv \rangle = \psi_{Jv}(r)$ represents the wave function of the molecule with the rotational quantum number J and the vibrational quantum numbers v (there are $3N - 5$ vibrational modes for linear molecules and $3N - 6$ otherwise; N is the number of atoms in the molecule). For $\mu_0 = 0$ the molecule is called nonpolar.

In the case of pure rotational transitions the first term must exist for a molecule to be infrared active. The second term is unimportant. In the case of vibrational transitions the second term must exist for a molecule to be infrared active. Examples of vibrational motions of important atmospheric molecules are illustrated in Fig. 1.8. Polar molecules are typically strong absorbers of infrared radiation and have spectra from the far-infrared (pure rotational) to throughout the mid-infrared (vibration-rotation bands). Water vapor, for example, is the most important absorber of IR in the troposphere.

Based on Eq. (1.23) the selection rules are determined. For pure rotational transitions, $J_f - J_i = \Delta J = 1$. For vibration-rotation transitions, $v_f - v_i = \Delta v = 1$ and $\Delta J = \pm 1, 0$. The different rotational selection rules form distinct

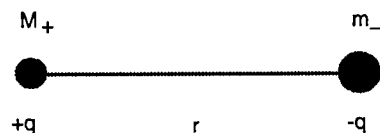


Fig. 1.7 Illustration of dipole moment for an ionic bond, where M_+ = mass of positive ion, m_- = mass of negative ion, and q is the charge magnitude.

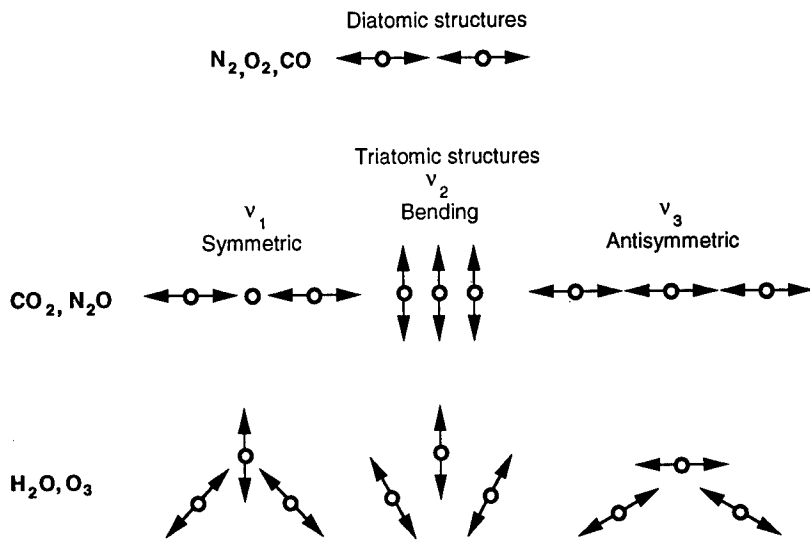


Fig. 1.8 Configurations and vibrational modes of diatomic and triatomic atmospheric molecules.

groups of lines, or branches. $\Delta J = -1$ corresponds to the P-branch, $\Delta J = 0$ is the Q-branch, and $\Delta J = 1$ is the R-branch. The consequences of these selection rules are discussed in the next section on line position.

A dipole moment can also be induced in molecules by an external electric field. Dipole-moment strength is proportional to the external field frequency and electronic polarizability α_e , which results from electronic cloud distortion by the incident light field. This mechanism is important for Rayleigh and Raman scattering. Rayleigh scatter is elastic; thus, the incident-field frequency equals the scattered-field frequency. Raman scatter is inelastic; the scattered-field frequency is shifted relative to the incident field, revealing internal rotational and vibrational structure. The selection rules change to $\Delta J = \pm 2, 0$, where $\Delta J = -2$ is called the O-branch and $\Delta J = 2$ is the S-branch, and with $\Delta v = \pm 1$ forming the Stokes ($\Delta v = -1$) and anti-Stokes ($\Delta v = 1$) vibrational bands.

A special case of interest to tropospheric propagation is collision-induced absorption (CIA) of N_2 and O_2 . Strong collisions by neighboring molecules induce a dipole moment that exists only during the duration of the collision. Because the collisions are very brief, the linewidths are very broad and individual transitions merge into a broadband structure. This type of absorption in the atmosphere is called continuum absorption.

Models of atmospheric absorption can be categorized into two groups: band and line-by-line models. Band models are discussed in Sec. 1.3.4. Line-by-line models require knowledge of line position, strength, and shape for each significant transition. These topics are covered in the remainder of this background section. It is important to understand the details of molecular spectra to appreciate the approximations used in band models.

1.3.1.2 Line Position

Fortunately, nature has greatly simplified the study of spectroscopy by sufficiently separating the fundamental energies of rotational, vibrational, and electronic transitions: $E_{\text{El}} > E_{\text{vib}} > E_{\text{rot}}$. The energy structure of each dynamics problem can be solved separately and then treated as a perturbation to the higher-energy term. Rotational spectra typically occur in the far-infrared (0.1 to 100 cm⁻¹). Vibrational spectra typically occur in the mid-infrared and near-infrared (100 to 10,000 cm⁻¹). Electronic spectra typically occur in the visible (weak bands) and ultraviolet (strong absorption bands, which determine the end of atmospheric transparency). Since the topics in this handbook are concerned with infrared and visible phenomena, electronic structure will not be covered in detail.

The development begins with rotation spectra, then vibration-rotation spectra. We close with a brief description of electronic spectra.

1.3.1.2.1 Rotational Spectra

Pure rotational bands typically exist from millimeter waves to the far-infrared. The formulas for rotational spectral line positions vary for different types of molecules. Molecules are classified as linear (e.g., N₂, O₂, H₂, CO, OH, CO₂, N₂O, OCS, HCN, etc.), spherical top (e.g., CH₄), symmetric top (e.g., NH₃, CH₃D, CH₃Cl, C₂H₆, etc.), and asymmetric top (e.g., H₂O, O₃, SO₂, NO₂, H₂O₂, H₂S, etc.). Energy-level structure is specified by the rotational term value $F(J)$ ($=E/hc$) and the rotational constants (A , B , and C), both in units of cm⁻¹. In general, there are three rotational degrees of freedom and three corresponding quantum numbers; however, symmetry reduces the degrees of freedom. The following lists the term-value functions with the degeneracy factor g_J for the various types of molecules.

Linear molecules

$$F(J) = BJ(J + 1) \text{ and } g_J = 2J + 1 . \quad (1.24)$$

Spherical-top molecules (A = B = C)

$$F(J) = BJ(J + 1) \text{ and } g_J = (2J + 1)^2 . \quad (1.25)$$

Symmetric-top molecules

Prolate (A > B = C)

$$F(J,K) = BJ(J + 1) + (A - B)K^2 \text{ and} \quad (1.26)$$

$$g_J = \begin{cases} 2J + 1, & K = 0 \\ 2(2J + 1), & K \neq 0 \end{cases} .$$

Oblate (A = B > C)

$$F(J,K) = BJ(J + 1) + (C - B)K^2 \text{ and} \quad (1.27)$$

$$g_J = \begin{cases} 2J + 1, & K = 0 \\ 2(2J + 1), & K \neq 0 \end{cases} .$$

Asymmetric-top molecules ($A > B > C$)

$F(J, K_a, K_c)$ is treated as an intermediate state between oblate and prolate symmetric tops. Thus, a precise statement depends on the molecule and the degree of asymmetry. For more information on this class of molecules see Herzberg.⁹

The rotational constants are defined as

$$A = \frac{h}{8\pi^2 c I_a}, \quad B = \frac{h}{8\pi^2 c I_b}, \quad C = \frac{h}{8\pi^2 c I_c}, \quad (1.28)$$

where I_a , I_b , and I_c are the molecular moments of inertia. Values of rotational constants of atmospheric molecules are listed in Table 1.6. Line positions are calculated by using the selection rule $\Delta J = J_f - J_i = 1$ and Eqs. (1.24) to (1.27). For linear and symmetric-top molecules the result is

$$\nu_{\text{Rot}} = F(J_f) - F(J_i) = 2BJ_f \quad (\text{cm}^{-1}). \quad (1.29)$$

Details of molecular structure are not important to the design engineer and this information is contained on the HITRAN database maintained by AFGL (Air Force Geophysical Laboratory; now called Phillips Laboratory). The purpose of this section is to develop insight into the nature of molecular rotational structure. For example, the rotational constants of water vapor are much larger than those of any other molecule listed of importance to atmospheric propagation. This means the rotational band structure of water vapor covers a much larger spectral range than the rotational structure of other molecules. Because

Table 1.6 Rotational Constants of Atmospheric Gases (from Refs. 9, 10, and 11)

Molecule	A (cm ⁻¹)	B (cm ⁻¹)	C (cm ⁻¹)
H ₂	—	60.853	—
OH	—	18.871	—
NO	—	1.7046	—
CO	—	1.9314	—
CO ₂	—	0.3902	—
N ₂ O	—	0.4190	—
H ₂ O	27.877	14.512	9.285
O ₃	3.553	0.445	0.395
CH ₄	—	5.249	—
N ₂	—	2.010	—
O ₂	—	1.44566	—
NH ₃	6.196	9.9444	—
SO ₂	2.0274	0.3442	0.2935
NO ₂	8.0012	0.4336	0.4104
H ₂ S	10.374	8.991	4.732

of this (and other properties), water vapor plays an important role in every infrared spectral region.

1.3.1.2.2 Vibration-Rotation Bands

Vibration bands of atmospheric gases typically exist in the mid-infrared. Atmospheric infrared windows are defined by the locations of these vibrational frequencies.

As mentioned previously, there are $3N - 6$ normal modes of vibration ($3N - 5$ for linear molecules), where N is the number of atoms in the molecule. Not all the modes are necessarily infrared active, as determined by group theory. The vibrational term value function $G(v)$ for a polyatomic molecule with no degeneracy is

$$G(v_1, v_2, v_3, \dots) = \sum_i \nu_i \left(v_i + \frac{1}{2} \right) + \sum_i \sum_{k \geq i} x_{ik} \left(v_i + \frac{1}{2} \right) \left(v_k + \frac{1}{2} \right) , \quad (1.30)$$

where v_i is the vibrational quantum number of the i 'th mode, ν_i is the i 'th harmonic vibrational mode frequency, and x_{ik} accounts for anharmonic correction. Most vibrational bands observed in the atmosphere originate from the vibrational ground state (where $0 = v_1 = v_2 = \dots$). The centers of such bands are calculated to be

$$\begin{aligned} G_0(v_1, v_2, v_3, \dots) &= G(v_1, v_2, v_3, \dots) - G(0, 0, 0, \dots) \\ &= \sum_i \nu_{0i} v_i + \sum_i \sum_{k \geq i} x_{0ik} v_i v_k , \end{aligned} \quad (1.31)$$

where

$$\nu_{0i} = \nu_i + x_{ii} + \frac{1}{2} \sum_{k \neq i} x_{ik} , \quad (1.32)$$

$$x_{0ik} = x_{ik} \text{ (ignoring higher powers)} . \quad (1.33)$$

If for the i 'th mode $v_i = 1$, then the transition is called fundamental. Fundamental normal mode vibrational frequencies of atmospheric molecules are listed in Table 1.7. When $v_i \geq 1$, overtone bands result that are harmonics of the fundamental. Combination bands involve transitions employing different vibrational modes. When the initial state of the molecule is not the ground state, hot bands result with the following term-value formula:

$$G(v_f, v_i) = G_0(v_{f1}, v_{f2}, v_{f3}, \dots) - G_0(v_{i1}, v_{i2}, v_{i3}, \dots) , \quad (1.34)$$

where $v_{f,i}$ are the vibrational quantum numbers of the final and initial states, respectively. Values of vibrational frequencies squared depend inversely on the reduced mass of the vibrating system and directly on the bond strength. Thus, molecules with light atoms will have the highest vibration frequencies. Again, water vapor is such a molecule.

**Table 1.7 Fundamental Vibrational Frequencies of Atmospheric Molecules
(from Refs. 9, 10, and 11)**

Molecule	ν_1 (cm $^{-1}$)	ν_2 (cm $^{-1}$)	ν_3 (cm $^{-1}$)	ν_4 (cm $^{-1}$)	Degeneracy			
					g_{ν_1}	g_{ν_2}	g_{ν_3}	g_{ν_4}
CO	2143				1			
H ₂	4401.21*				1			
OH	3735.21				1			
NO	1904.0				1			
N ₂	2359.6*				1			
O ₂	1580.4*				1			
CO ₂	1388.2*	667.4	2349.2		1	2	1	
N ₂ O	2223.8	588.8	1284.9		1	2	1	
H ₂ O	3657	1594.7	3755.7		1	1	1	
H ₂ S	2614.6	1182.7	2627.5		1	1	1	
NO ₂	1319.7	749.8	1617.7		1	1	1	
O ₃	1110	705	1042.1		1	1	1	
SO ₂	1151.3	517.6	1361.7		1	1	1	
NH ₃	3336.2	932.5	3443.6	1626.1	1	1	2	2
CH ₄	2916.5*	1533.6	3019.5	1310.8	1	2	3	3

*Infrared inactive

Rotational-vibrational spectra include the perturbation rotational motion has on the vibrational energies. The allowed rotational transitions become $\Delta J = \pm 1, 0$, which results in P-, Q-, and R-branch structures (see Herzberg). Net term-value energies of the vibrating rotor become

$$T(v, J) = G(v) + F(J) . \quad (1.35)$$

Applying the selection rules leads to formulas predicting line position (see Refs. 9–11). A comprehensive listing of atmospheric absorption line positions is contained on the HITRAN database maintained by AFGL (Phillips Laboratory). The reader is encouraged to use this source when detailed models are required (see Sec. 1.3.3).

1.3.1.2.3 Electronic Bands

Electronic bands typically exist in the ultraviolet for atmospheric molecules and involve transitions of outermost orbital electrons within the molecule. These transitions mark the end of optical transparency in the atmosphere. Thus, it is not necessary to present a detailed description of the entire band structure but rather the beginning absorption edge. The most important molecules in this case are O₂ and O₃ since these molecules begin absorbing at lowest ultraviolet frequencies of the atmospheric gases. Also, electronic transitions of N₂ and O₂ contribute significantly to the real part of index of refraction throughout the infrared and visible.

Figure 1.9 illustrates a ground-state electronic level and an excited-state electronic level. Within these electronic states is vibrational energy structure

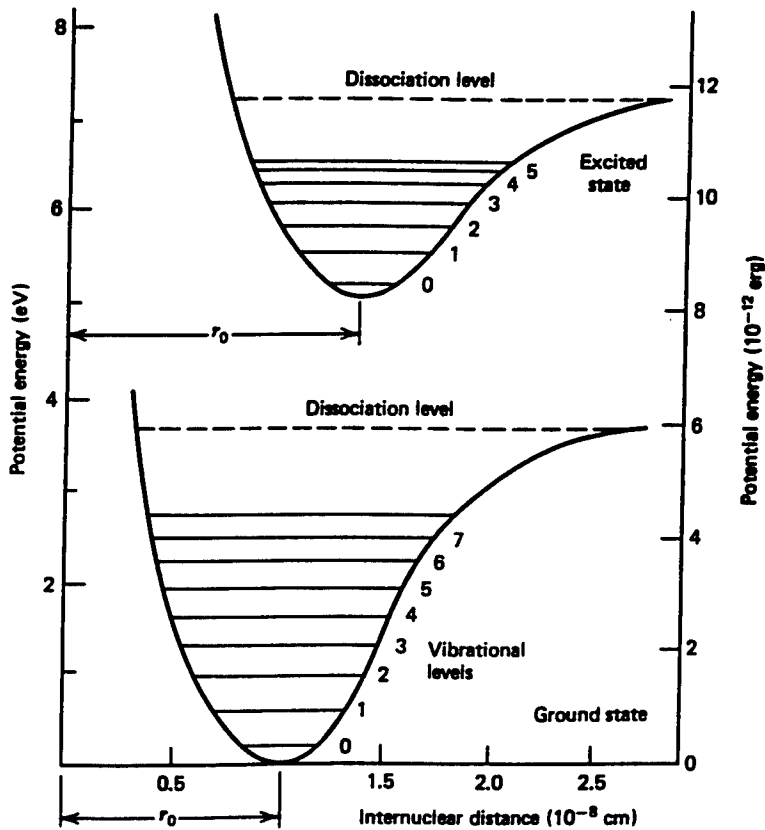


Fig. 1.9 Potential energy curves for two electronic states of a diatomic molecule.¹²

and within the vibrational structure is rotational structure. The transition between these electronic energies contains many possible vibration-rotation bands, as shown in the figure. A series of absorption bands results, which characterizes the beginning of electronic-band absorption. Oxygen begins strong absorption at 195 nm with the Schumann-Runge bands. Ozone, found primarily in the stratosphere, begins absorbing at 300 nm.

1.3.1.3 Interaction of Light with Matter

It is instructive to consider the interaction of light and matter from both a classical and a quantum perspective. Simple classical models are developed that are practical and demonstrate basic concepts. Detailed quantum and statistical mechanics models are stated and not developed here.

1.3.1.3.1 Classical Oscillator Model

Assuming the medium is at low density (e.g., a gas), the equation of motion for an electron bound by a harmonic force and acted upon by an electric field $\mathbf{e}(x,t)$ is

$$m\ddot{\mathbf{X}} + m\gamma\dot{\mathbf{X}} + m\omega_0^2\mathbf{X} = q\mathbf{e}(x,t) , \quad (1.36)$$

where m = mass, γ = phenomenological damping force, q = charge of the mass, and ω_0 = oscillation frequency. Magnetic-field effects will be ignored and the strength of the electric field will not distort the molecule to reveal anharmonic effects in the potential. Then, assume a time harmonic behavior as $\mathbf{x}(t) = \mathbf{X}(\omega)e^{j\omega t}$. The above equation becomes

$$-m\omega^2\mathbf{X} + jm\gamma\omega\mathbf{X} + m\omega_0^2\mathbf{X} = q\mathbf{E}(\omega,t) . \quad (1.37)$$

This is an algebraic equation with the following solution for $\mathbf{X}(\omega)$:

$$\mathbf{X}(\omega) = \frac{q}{m}(\omega_0^2 - \omega^2 + j\omega\gamma)^{-1}\mathbf{E}(\omega) . \quad (1.38)$$

Now, the dipole-moment vector \mathbf{p} (μ is scalar dipole moment) contributed by one bound electron becomes

$$\mathbf{p} = qX\hat{x} = \frac{q^2}{m}(\omega_0^2 - \omega^2 + j\omega\gamma)^{-1}\mathbf{E} . \quad (1.39)$$

If there are N_a absorbing molecules per unit volume V with a number density $\rho_a = N/V$, then summing over the different rotational, vibrational, and electronic transitions gives

$$\mathbf{P} = \chi\epsilon_0\mathbf{E} , \quad (1.40)$$

$$\epsilon(\omega) = \epsilon_r(\omega)\epsilon_0 = \epsilon_0 + \frac{|\mathbf{P}|}{|\mathbf{E}|} = [1 + \chi(\omega)]\epsilon_0 ,$$

where \mathbf{P} is the polarization vector, ϵ_0 is the free-space permittivity, ϵ_r is the relative permittivity, and χ is the electric susceptibility. Further, recall from electromagnetic theory that

$$\mathbf{P} = \rho_a \sum_i \mathbf{p}_i = \sum_i \frac{\rho_a(q^2/m)_i \mathbf{E}}{\omega_i^2 - \omega^2 + j\omega\gamma_i} . \quad (1.41)$$

Using Eqs. (1.40) and (1.41), the relative permittivity becomes

$$\epsilon_r(\omega) = 1 + \sum_i \frac{\rho_a(q^2/\epsilon_0 m)_i}{\omega_i^2 - \omega^2 + j\omega\gamma_i} . \quad (1.42)$$

Again, the sum on i is over all allowed rotational, vibrational, and electronic transitions. Let

$$\Delta\epsilon_i = \rho_a \frac{q_i^2}{m_i\omega_i^2\epsilon_0} \quad (1.43)$$

be the oscillator strength; then

$$\epsilon'_r(\omega) - j\epsilon''_r(\omega) = 1 + \sum_i \frac{\omega_i^2 \Delta \epsilon_i}{\omega_i^2 - \omega^2 + j\omega\gamma_i} . \quad (1.44)$$

Solving for the real and imaginary parts of the permittivity gives

$$\begin{aligned} \epsilon'_r(\omega) &= 1 + \sum_i \frac{\omega_i^2 \Delta \epsilon_i (\omega_i^2 - \omega^2)}{(\omega_i^2 - \omega^2)^2 + (\omega\gamma_i)^2} , \\ \epsilon''_r(\omega) &= \sum_i \frac{\omega_i^2 \Delta \epsilon_i \omega \gamma_i}{(\omega_i^2 - \omega^2)^2 + (\omega\gamma_i)^2} . \end{aligned} \quad (1.45)$$

Further, the absorption coefficient is defined as

$$\beta_{\text{abs}}(\omega) = 4\pi\nu k(\omega) = 2\frac{\omega}{c}k(\omega) = \frac{\omega}{nc}\epsilon''_r(\omega) . \quad (1.46)$$

Substituting Eq. (1.45) for ϵ'' leads to (assuming n is constant)

$$\beta_{\text{abs}}(\omega) = \frac{\omega^2}{nc} \sum_i \frac{\omega_i^2 \Delta \epsilon_i \gamma_i}{(\omega_i^2 - \omega^2)^2 + (\omega\gamma_i)^2} . \quad (1.47)$$

Near line center ($\omega \approx \omega_i$) the expression reduces to

$$\beta_{\text{abs}}(\omega) = \frac{\omega^2}{nc} \sum_i \frac{2\omega_i^2 \Delta \epsilon_i (\gamma_i/2)}{(\omega_i + \omega_i)^2 (\omega_i - \omega)^2 + 4[\omega_i(\gamma_i/2)]^2} . \quad (1.48)$$

Then,

$$\beta_{\text{abs}}(\omega) = \sum_i \frac{\pi \omega_i^2 \Delta \epsilon_i}{2nc} \left(\frac{\omega}{\omega_i} \right)^2 j_L(\omega) , \quad (1.49)$$

where the dimension of β_{abs} is reciprocal length and

$$j_L(\omega) = \frac{1}{\pi} \frac{\sigma_i}{(\omega_i - \omega)^2 + \sigma_i^2} \quad (1.50)$$

is the Lorentz line shape with $\sigma_i = \gamma_i/2$ representing the half-width at half maximum. Let

$$g(\omega) = \left(\frac{\omega}{\omega_i} \right)^2 j_L(\omega) \quad \text{and} \quad S_i = \frac{\pi \omega_i^2 \Delta \epsilon_i}{2nc} ; \quad (1.51)$$

then,

$$\beta_{\text{abs}}(\omega) = \sum_i S_i g(\omega, \omega_i) \quad \text{near line center} . \quad (1.52)$$

This equation agrees with the form stipulated in the introduction of this section [Eq. (1.21)]. Notice that $g(\omega, \omega_i)$ is the Van Vleck-Weisskopf line-shape function,¹³ is valid only near line center, and cannot satisfy the normalization condition as given by Eq. (1.20). A complete line-profile description is presented in the next section.

The real part of the permittivity ϵ'_r is related to the complex index of refraction by the expression

$$\epsilon'_r = n^2 - k_a^2 . \quad (1.53)$$

In the region of transparency (i.e., $n \gg k_a$) a simple expression for the real part of the index of refraction is obtained:

$$n^2(\omega) = 1 + \sum_i \frac{\omega_i^2 \Delta \epsilon_i}{\omega_i^2 - \omega^2} . \quad (1.54)$$

This formula is known as Sellmeier's equation and is a convenient way of representing the index of refraction of gases, liquids, and solids in spectral regions of transparency.

1.3.1.3.2 Quantum-Mechanical Model

The following expressions for line-profile function and line strength are based on statistical and quantum mechanics¹⁴⁻¹⁷ as applied to the interaction of light and matter. They can be applied quite generally to a wide class of problems: atmospheric propagation and molecular absorption (the AFGL codes FASCODE, MODTRAN, and LOWTRAN are based on these equations); small-signal laser gain calculations; and remote sensing.

The line-profile function is

$$g(\nu) = \frac{\nu}{\nu_0} \frac{\tanh(hc\nu/2k_B T)}{\tanh(hc\nu_0/2k_B T)} [j(\nu) + j(-\nu)] , \quad (1.55)$$

where k_B is Boltzmann's constant and $j(\nu)$ is the power spectral density function. The first factor states that the ability of the electromagnetic field to couple to a molecule increases with frequency. The second factor requires that Maxwell-Boltzmann statistics be satisfied across the entire line shape and fulfills detailed balance conditions.^{17,18} Here, $j(\nu)$ is the power spectral density function or the Fourier transform of the time-dependent autocorrelation function $C(\tau)$, which describes the time evolution of the state of the absorbing molecule, and is expressed by

$$j(\nu) = \frac{1}{2\pi} \int_{-\infty}^{\infty} d\tau \exp(-j2\pi c\nu\tau) \exp(j2\pi c\nu_0\tau) C(\tau) , \quad (1.56)$$

where

$$\begin{aligned} C(\tau) &= C_a(\tau)C_b(\tau)\dots C_m(\tau) , \\ g(\nu) &= g(-\nu) , \\ \int_0^\infty d\nu j(\nu) &= 1 \text{ for } C(0) = 1 , \end{aligned} \quad (1.57)$$

where the subscripts designate the different types of molecules in the medium and different broadening mechanisms and $C(\tau) = C^*(-\tau)$. Note that $j(\nu)$ is a real and even function. More details on the autocorrelation function will be given in the section on line shapes (Sec. 1.3.1.5).

The line strength is expressed as

$$S_{lu} = \rho_a \frac{8\pi^3 \nu_0}{3hn} \frac{\exp(-E_l/k_B T)}{Q(T)} \tanh\left(\frac{hc\nu_0}{2k_B T}\right) \sum |\mathbf{M}|^2 , \quad (1.58)$$

where ρ_a is the absorbing gas density (molecules per volume), n is the index of refraction (real part), E_l is the lower energy level of the transition, k_B is Boltzmann's constant, Q is the partition function (defined below), and $|\mathbf{M}|^2$ is the dipole matrix element.

1.3.1.4 Line Strength

To complete the line-strength expression requires specifying the partition function Q , the lower energy level E_l , and the matrix elements $\sum |\mathbf{M}|^2$. The matrix elements and the lower energy level are provided by the HITRAN database (see Sec. 1.3.3). The index of refraction of the atmosphere is approximately one. The partition functions must be determined for each class of molecule and this is discussed in the following.

1.3.1.4.1 Partition Functions

The partition function is a normalization factor in the Maxwell-Boltzmann distribution function. It is the sum over all energy levels (quantum numbers) of the molecule, as given by

$$Q = \sum_i g_i \exp\left(\frac{-E_i}{k_B T}\right) , \quad (1.59)$$

where g_i is the degeneracy factor for the i 'th energy level. However, because of the large differences between the different types of energies in molecules, the partition function can be approximately expressed by the following product:

$$\begin{aligned} Q &\approx Q_{El} Q_{Vib} Q_{Rot} \\ &= - \sum_n g_n \exp\left(\frac{-E_{El}}{k_B T}\right) \sum_v g_v \exp\left(\frac{-E_{Vib}}{k_B T}\right) \sum_J g_J \exp\left(\frac{-E_{Rot}}{k_B T}\right) . \end{aligned} \quad (1.60)$$

Over the range of atmospheric temperatures, $Q_{\text{El}} = 1$ and $Q_{\text{Vib}} \approx 1$ are good approximations. Knowledge of the rotational partition function is important and a listing is given, according to the class of molecule, in the following.

Diatom molecules

Because the rotational energy levels are closely spaced, the sum is converted to an integral. The rotational partition function becomes

$$Q_{\text{Rot}} = \frac{8\pi^2 I_e k_B T}{\sigma h^2} = \frac{1}{\sigma} \frac{T}{1.4388 B_e} \quad \left(\frac{hc}{k_B} = 1.4388 \right) , \quad (1.61)$$

where σ is a symmetry number with

$$\sigma = 2 \text{ for } A=B \quad (\text{i.e., N}_2, \text{O}_2...) ,$$

$$\sigma = 1 \text{ for } A \neq B \quad (\text{i.e., CO, NO...}) ,$$

and B_e can be found in Table 1.6.

The vibrational partition function for a purely harmonic potential becomes

$$Q_{\text{Vib}} = \left[1 - \exp\left(-\frac{hc\nu_0}{k_B T}\right) \right]^{-1} = \sum_{v=0}^{\infty} \exp\left(-\frac{hc\nu v_0}{k_B T}\right) . \quad (1.62)$$

Polyatomic molecules

a. Linear molecules

Since the same energy eigenvalues are obtained for linear polyatomic molecules as for diatomic molecules, the partition functions are also the same.

b. Symmetric top molecules

For symmetric top molecules,

$$Q_{\text{Rot}} = \frac{1}{\sigma} \sum_{K=-\infty}^{K=\infty} \left[-\frac{hc(A-B)K^2}{k_B T} \right] \sum_{J=|K|}^{\infty} (2J+1) \exp\left[-\frac{hcBJ(J+1)}{k_B T}\right] . \quad (1.63)$$

As before, the sums can be replaced by integrals; thus, for prolate symmetric top,

$$\begin{aligned} Q_{\text{Rot}} &= \frac{\sqrt{\pi}}{\sigma} \left(\frac{8\pi^2 I_a k_B T}{h^2} \right)^{1/2} \left(\frac{8\pi^2 I_b k_B T}{h^2} \right) \\ &= \frac{\sqrt{\pi}}{\sigma} \left(\frac{T}{1.4388 A} \right)^{1/2} \left(\frac{T}{1.4388 B} \right) . \end{aligned} \quad (1.64)$$

Spherical-top molecules are a special case of the prolate symmetric top where $A = B$ or $I_a = I_b$. This substitution into the above formulas produces the rotational partition function for the spherical top.

Similarly, for the oblate case (σ is a symmetry number),

$$Q_{\text{Rot}} = \frac{\sqrt{\pi}}{\sigma} \left(\frac{T}{1.4388C} \right)^{1/2} \left(\frac{T}{1.4388B} \right) . \quad (1.65)$$

c. Asymmetric top molecules

For asymmetric top molecules,

$$Q_{\text{Rot}} = \frac{\sqrt{\pi}}{\sigma} \left(\frac{T}{1.4388A} \right)^{1/2} \left(\frac{T}{1.4388B} \right)^{1/2} \left(\frac{T}{1.4388C} \right)^{1/2} . \quad (1.66)$$

The vibrational partition function for polyatomic molecules becomes

$$\begin{aligned} Q_{\text{Vib}} &= \sum_{v_1, v_2, \dots, v_n}^{\infty} \exp \left[-\frac{hc(v_1 v_1 + v_2 v_2 + \dots + v_n v_n)}{k_B T} \right] \\ &= \left[1 - \exp \left(-\frac{hcv_1}{k_B T} \right) \right]^{-1} \\ &\quad \times \left[1 - \exp \left(-\frac{hcv_2}{k_B T} \right) \right]^{-1} \dots \left[1 - \exp \left(\frac{hcv_n}{k_B T} \right) \right]^{-1}, \end{aligned} \quad (1.67)$$

where n is the number of normal modes.

1.3.1.5 Line-Shape Profiles

Homogeneous and inhomogeneous broadening are the most general classification of line shapes. Homogeneous broadening means that all molecules have the same basic line-shape characteristics. That is, if a line shape is observed for a collection of molecules, the same line shape will be observed for each molecule. Examples are natural broadening (radiation damping) and collision broadening. Inhomogeneously broadened lines represent a collection of shifted homogeneously broadened lines. Thus, each molecule's line shape may be completely different from the total line shape of a collection of molecules. Examples are Doppler broadening, nonuniform electric and magnetic fields in Stark and Zeeman effects, and inhomogeneities in a medium (such as crystalline strains and defects in solids). These concepts should become more clear when Doppler broadening is thoroughly treated.

1.3.1.5.1 Homogeneous Line Shapes

Two related cases will be considered, radiation damping (natural broadening) and collision broadening. Consider a perturbation to a quantum system, whether it be a photon or a neighboring molecule that will change the energy-level

structure with a certain probability. Owing to this probabilistic nature, an uncertainty results in observing the effects of the perturbation. This is manifested by the Heisenberg uncertainty principle:

$$\Delta x \Delta p = \Delta t \Delta E \approx h . \quad (1.68)$$

Using $\Delta E = h \Delta f$, where Δf is the change in frequency,

$$\Delta t \Delta f \approx \frac{1}{2\pi} \rightarrow \Delta f = \frac{1}{\Delta t 2\pi} = \frac{\gamma}{2\pi} , \quad (1.69)$$

where γ is the reciprocal lifetime. A transition between two energy levels of a quantum system that results in the emission or absorption of a photon will have an uncertainty in the separation of the levels and therefore an uncertainty in the emitted photon frequency. Therefore,

$$\Delta f_{ul} = \Delta f_{lu} = \frac{1}{h} (\Delta E_u + \Delta E_l) - \frac{1}{2\pi} (\gamma_u + \gamma_l) . \quad (1.70)$$

These concepts are illustrated in Fig. 1.10. A spread in frequency about line center of the transition results, which is the same for every molecule. The amount of spreading depends on the nature of the interaction, small shifts for radiation damping and large shifts for the molecular-collisions-driven condi-

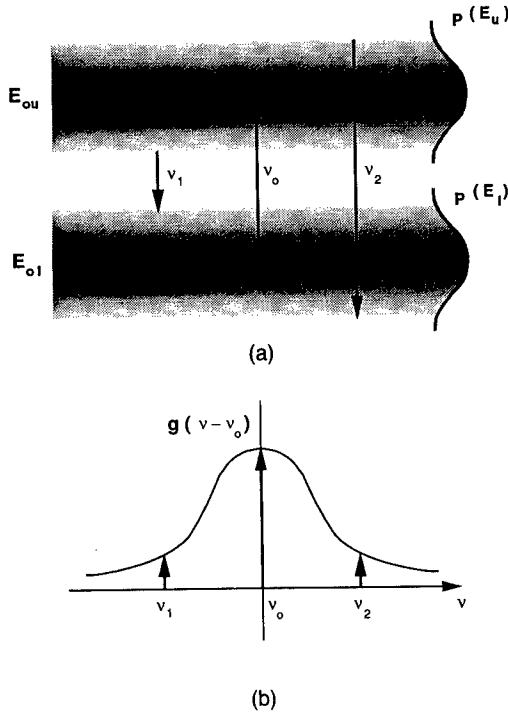


Fig. 1.10 (a) Smearing of energy levels caused by external perturbations and (b) the resulting line shape.

tions of the lower troposphere. A brief discussion of these different mechanisms follows.

Natural line shape

The natural line shape $g_N(\nu - \nu_0)$ is caused by the perturbations an incident photon has on a molecule. The effect is small but is important in determining lifetimes of energy levels and astrophysical problems.

The line-shape function $j_N(\nu)$ is based on an exponential autocorrelation function [i.e., $C_N(\tau) = \exp(-\alpha_N \tau)$] and is a Lorentzian function:

$$j_N(\nu - \nu_0) = \frac{1}{\pi} \left[\frac{\alpha_N}{(\nu - \nu_0)^2 + \alpha_N^2} \right], \quad (1.71)$$

where α_N is the half-width at half-intensity and is related to the Einstein spontaneous emission coefficient by¹⁸

$$\alpha_N = \frac{A_{ul}}{2\pi c} = \frac{1}{2\pi c t_{\text{spontaneous}}} , \quad (1.72)$$

with $t_{\text{spontaneous}}$ being the lifetime of the upper level and A_{ul} being the Einstein A-coefficient. Further, the line-profile function becomes

$$g_N(\nu; \nu_0) = \frac{\nu}{\nu_0} \frac{\tanh(hcv/2k_B T)}{\tanh(hcv_0/2k_B T)} [j_N(\nu) + j_N(-\nu)]. \quad (1.73)$$

For near line center ($\nu \approx \nu_0$) and $\nu_0 \gg \alpha_N$,

$$g_N(\nu; \nu_0) = j_N(\nu \approx \nu_0). \quad (1.74)$$

Natural linewidths are very narrow, making this an excellent approximation. Further, the line-profile function $g(\nu)$ is normalized as required by Eq. (1.20) within this approximation.

Collision-broadened line shape

The collision-broadened line shape is essential for accurate atmospheric propagation models. Long-path propagation simulations require characterization of the line profiles far from line center, and the commonly used Lorentz line-profile function is not adequate. This point is readily made by observing that the normalization condition of Eq. (1.20) cannot be satisfied by the simple Lorentz formula. Thus, a more complete theory must be applied and the work of Birnbaum^{19,20} will be followed because it leads to a simple, practical, and versatile line-shape function. Other formalisms are also possible²¹⁻²³ but lead to complicated numerical techniques for a complete line-profile representation. The autocorrelation function for a binary mixture is empirically chosen to be

$$\begin{aligned}
C(\tau) &= C_a(\tau)C_b(\tau) \\
&= \exp\left\{\frac{[\tau_{a2} - (\tau_{a2}^2 + \tau^2 + i2\tau_0)^{1/2}]}{\tau_{a1}}\right\} \exp\left\{\frac{[\tau_{b2} - (\tau_{b2}^2 + \tau^2 + i2\tau_0)^{1/2}]}{\tau_{b1}}\right\} ,
\end{aligned} \tag{1.75}$$

where $C_a(\tau)$ is the autocorrelation function for absorber-absorber interactions and $C_b(\tau)$ is the autocorrelation function for absorber-broadener interactions. The relaxation times τ_1 and τ_2 represent the long-time and short-time behavior of the autocorrelation function. The term τ_0 is a thermal time defined by

$$\tau_0 = \frac{h}{4\pi k_B T} . \tag{1.76}$$

(Note: for $T = 298$ K, $\tau_0 = 1.29 \times 10^{-14}$ s.) The long-time behavior of the autocorrelation function becomes

$$C(\tau \rightarrow \infty) = \exp\left(-\frac{|\tau|}{\tau_1}\right) , \tag{1.77}$$

where

$$\tau_1^{-1} = \tau_{a1}^{-1} + \tau_{b1}^{-1} = \sigma_c = \sigma_{ca} + \sigma_{cb} \tag{1.78}$$

for a binary mixture and σ_c is the usual collision-broadened half-width at half-intensity. Based on the kinetic theory of gases,

$$\begin{aligned}
\sigma_c &= \sigma_{cb0} \left[\rho_b + \left(\frac{\sigma_{ca0}}{\sigma_{cb0}} \right) \rho_a \right] \sqrt{T} \\
&= \sigma_{cb0} \frac{(p_b + B p_a)}{T^{1/2}} ,
\end{aligned} \tag{1.79}$$

where $\rho = p/k_B T$ and the ratio $\sigma_{ca0}/\sigma_{cb0}$ is the dimensionless-self-broadening coefficient B . Table 1.8 lists B values for various atmospheric absorbing gases relative to nitrogen. The exponent of the temperature can vary between 0.5 and 1.0, based on experimental results and more complete theories.

The long-time autocorrelation function results in the near-line-center line-shape function. Substituting Eq. (1.77) into Eqs. (1.56) and (1.55) results in the following near-line-center profile:

$$g_{NLC}(\nu; \nu_j) = \frac{\nu}{\nu_j} \frac{\tanh(-hcv/2k_B T)}{\tanh(-hcv_j/2k_B T)} [j_{NLC}(\nu) + j_{NLC}(-\nu)] , \tag{1.80}$$

$$j_{NLC}(\nu) = \frac{1}{\pi} \frac{\alpha_c}{(\nu - \nu_j + \alpha_{c,i})^2 + \alpha_c^2} , \tag{1.81}$$

Table 1.8 Dimensionless-Self-Broadening Coefficient Relative to Nitrogen and Near Line Center

Molecule	B
H ₂ O	5
CH ₄	1.3
N ₂ O	1.24
CO	1.02
CO ₂	1.3
O ₃	1.0

where $\sigma_c = 2\pi c \alpha_c$. This result is consistent with the FASCODE model (see Sec. 1.5.3) and, for $hcv/k_B T$ small, the millimeter-wave propagation model (MPM) (Sec. 1.3.2, Refs. 55 and 58). Equation (1.81) includes a pressure-shift term $\alpha_{c,i}$, which occurs in more general theories producing a complex α_c ($\alpha_{c,i} = \text{Im}[\alpha_c]$). Pressure-shift contributions are roughly one hundred times smaller than $\text{Re}[\alpha_c]$ and for this reason are usually ignored. It can be important for laser or narrow-band system propagation (e.g., lidar) when operating near a spectral absorption line. Many of the other popular line shapes can be obtained from these formulas by using various approximations. It should be noted that most of these approximations are not always appropriate for the rf-millimeter region.

One important shortcoming of this near-line-center model is that it does not include line-mixing effects. This is important for O₂ absorption of the 60 GHz band^{24,25} and for CO₂,^{26,27} but greatly complicates absorption-line modeling. A relatively simple modified Lorentz line shape, as given by Rosenkranz and applied to O₂,²⁴ is

$$j_{\text{NLC}}(\nu) = \frac{1}{\pi} \frac{\alpha_c + (\nu - \nu_j)y_j}{(\nu - \nu_j + \alpha_{c,i})^2 + \alpha_c^2}, \quad (1.82)$$

where y_j is the coupling constant, representing the effects of neighboring energy levels on the levels involved in the transition. Birnbaum has recently improved this line-shape formalism and now includes line-mixing effects²⁸; however, this complicates the model.

The leading factor in the line-shape profile,

$$\frac{\nu}{\nu_0} \frac{\tanh(hcv/2k_B T)}{\tanh(hcv_0/2k_B T)} = H(\nu, T; \nu_0), \quad (1.83)$$

is an important part of this model and makes $g(\nu)$ more general. The term $g(\nu)$ reduces to other models in appropriate limits. The following illustrates this point.

Classical limit ($h \rightarrow 0$)

$$g_{\text{NLC}}(\nu; \nu_0) \xrightarrow[h \rightarrow 0]{} \left(\frac{\nu}{\nu_0} \right)^2 [j_{\text{NLC}}(\nu) + j_{\text{NLC}}(-\nu)]. \quad (1.84)$$

This result is consistent with the classical oscillator model of Eq. (1.52).

$$\nu \rightarrow 0$$

$$g_{\text{NLC}}(\nu; \nu_0) \xrightarrow[\nu \rightarrow 0]{b\nu^2/T} \frac{b\nu^2/T}{\tanh(b\nu_0/T)} [j_{\text{NLC}}(\nu) + j_{\text{NLC}}(-\nu)] , \quad (1.85)$$

where $b = hc/2k_B$. The frequency-squared dependence is commonly observed at microwave and millimeter-wave frequencies.

$$\nu = \nu_0$$

$$g_{\text{NLC}}(\nu; \nu_0) = j_{\text{NLC}}(\nu) + j_{\text{NLC}}(-\nu) . \quad (1.86)$$

Thus, at line center the profile is Lorentzian.

$$\underline{b\nu \gg T \text{ and } b\nu_0 \gg T \text{ (infrared approximation)}}$$

$$g_{\text{NLC}}(\nu; \nu_0) \xrightarrow[b\nu \gg T]{b\nu_0 \gg T} \frac{\nu}{\nu_0} [j_{\text{NLC}}(\nu) + j_{\text{NLC}}(-\nu)] . \quad (1.87)$$

A plot of $H(\nu; \nu_0)$ is given in Fig. 1.11 as a function of ν for $T = 300$ K and a variety of line-center frequencies.

The short-time behavior of the autocorrelation function leads to the far-wing character of the profile. The short-time behavior ($\tau \rightarrow 0$) of Eq. (1.75) becomes

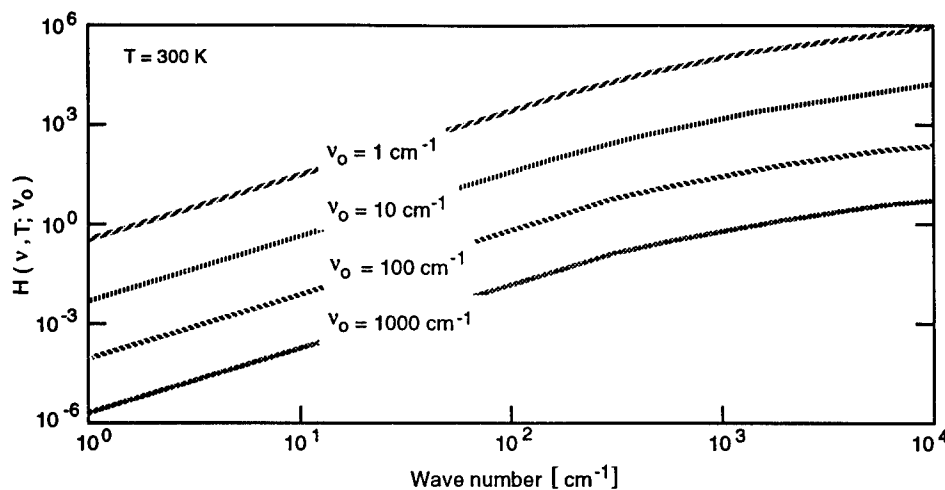


Fig. 1.11 H-function versus wave number for a variety of line-center positions and $T = 300$ K.

$$C(\tau) \xrightarrow[\tau \rightarrow 0]{} \exp\left(-\frac{\tau^2}{2\tau_1\tau_2}\right). \quad (1.88)$$

The Gaussian form is consistent with theoretical models of the autocorrelation function.²⁹ Thus, a complete line shape is specified from line center to the far wing. The far-wing result has been obtained for the case of a single absorbing molecule [i.e., $C(\tau) = C_a(\tau)$] and is given by²⁰

$$g_{FW}(\nu; \nu_j) = \frac{\nu}{\nu_j} \frac{\tanh(hcv/2k_B T)}{\tanh(hcv_j/2k_B T)} j_{FW}(\nu), \quad (1.89)$$

$$j_{FW}(\nu) = \left(\frac{\tau_{a2}}{2\pi}\right)^{1/2} \frac{1}{\tau_{a1}} \frac{\exp(-2\pi c|\nu - \nu_j|\tau_{a2})}{4\pi^2|\nu - \nu_j|^{1.5}} \exp[2\pi c(\nu - \nu_j)\tau_0]. \quad (1.90)$$

The exponential wing is consistent with experimental observation.^{20,30} The general far-wing result for a binary mixture can be obtained by solving a convolution integral of the individual line-shape functions (j_a and j_b) in the far-wing limit. Thus, given

$$\begin{aligned} j_a(\nu) &= \frac{1}{2\pi} \int_{-\infty}^{\infty} d\tau \exp(-i2\pi c\nu) C_a(\tau), \\ j_b(\nu) &= \frac{1}{2\pi} \int_{-\infty}^{\infty} d\tau \exp(-i2\pi c\nu) C_b(\tau), \\ j(\nu) &= \int_{-\infty}^{\infty} j_a(x) j_b(\nu - \nu_j - x) dx, \end{aligned} \quad (1.91)$$

then using contour integration and in the far-wing limit,

$$\begin{aligned} j_{FW}(\nu) &= \left(\frac{\tau_{a2}}{2\pi}\right)^{1/2} \frac{1}{\tau_{a1}} \frac{\exp(-2\pi c|\nu - \nu_j|\tau_{a2})}{4\pi^2|\nu - \nu_j|^{1.5}} \exp[2\pi c(\nu - \nu_j)\tau_0] \\ &\quad + \left(\frac{\tau_{b2}}{2\pi}\right)^{1/2} \frac{1}{\tau_{b1}} \frac{\exp(-2\pi c|\nu - \nu_j|\tau_{b2})}{4\pi^2|\nu - \nu_j|^{1.5}} \exp[2\pi c(\nu - \nu_j)\tau_0]. \end{aligned} \quad (1.92)$$

The formula for the autocorrelation function given by Eq. (1.75) agrees with theoretical and experimental results concerning near-line-center and far-wing phenomena. Because the function is continuous in time, a complete line-shape function is specified. The closed-form expression for the line shape has been obtained for a pure gas; the result is

$$j(\nu) = \frac{\tau_1}{\pi} \exp\left(\frac{\tau_2}{\tau_1}\right) \frac{\exp(2\pi c\nu - \tau_0) Z_- K_1(Z_-)}{1 + (2\pi c\nu - \tau_1)^2} + \frac{\exp(2\pi c\nu + \tau_0) Z_+ K_1(Z_+)}{1 + (2\pi c\nu + \tau_1)^2}, \quad (1.93)$$

where

$$\begin{aligned} \nu_{\pm} &= \nu \pm \nu_0 , \\ Z_{\pm} &= (\tau_1^{-2} + \nu_{\pm}^2)^{1/2}(\tau_2^2 + \tau_0^2)^{1/2} , \end{aligned} \quad (1.94)$$

and $K_1(Z_{\pm})$ is the modified Bessel function of the second kind. This line shape is consistent with the near-line-center results obtained earlier and in addition provides insight into the nature of the far wing as previously shown. Most important, a complete line shape allows proper normalization according to Eq. (1.20). The following result is obtained:

$$\int_0^{\infty} d\nu g(\nu, \nu_0) = \left(1 + \frac{\alpha_1 \alpha_2}{\alpha_0 \nu_0}\right) \coth(hc\nu_0/k_B T) . \quad (1.95)$$

For practical values of the parameters this line-profile function is normalized to one.

A line-shape formula for homogeneous collision-broadened lines has been developed that is compatible with the AFGL HITRAN database. The line shape has validity from line center to the far wing. Local line absorption and far-wing continuum absorption can now be modeled in greater detail. The present formalism, however, lacks line overlap or coupling effects.

1.3.1.5.2 Inhomogeneous Line Shapes

Doppler line shape

The random kinetic motion of the atoms causes a Doppler shift of the narrow homogeneously broadened atoms. Atoms with different velocities will be shifted by different amounts so that a new line shape results in the inhomogeneous Doppler profile.

Derivation of this effect begins with Doppler's equation

$$\nu = (c - v)\nu_0 , \quad v = \frac{c(\nu_0 - \nu)}{\nu_0} \quad (1.96)$$

and Maxwell-Boltzmann's distribution

$$f(E) = \exp\left(\frac{-E}{k_B T}\right) . \quad (1.97)$$

Using the kinetic energy $E = \frac{1}{2}mv^2$ and the previous equations, it follows that

$$f(v) = j_D(\nu - \nu_0) = \exp\left\{\left[\frac{c(\nu - \nu_0)}{\nu_0}\right]^2 \frac{m}{2k_B T}\right\} , \quad (1.98)$$

which represents the probability distribution of the shifted frequencies due to the velocity components of the atoms parallel to the incident photon field. Since Doppler lines are very narrow, it is valid to enforce normalization on the spectral density function, accounting for absorption as well as emission; thus,

$$\int_0^{\infty} [j_D(\nu - \nu_0) + j_D(\nu + \nu_0)]d\nu = 1 . \quad (1.99)$$

The Doppler spectral density function is commonly expressed as

$$j_D(\nu - \nu_0) = \frac{(\ln 2)^{1/2}}{\alpha_D \sqrt{\pi}} \exp\left[-\frac{(\nu - \nu_0)^2 \ln 2}{\alpha_D^2}\right] , \quad (1.100)$$

where

$$\alpha_D = \left[\frac{k_B T \ln 2}{mc^2} \right]^{1/2} \nu = 3.578 \times 10^{-7} \left(\frac{T}{m} \right)^{1/2} \nu_0 \quad (1.101)$$

is the half-width at half-intensity, T is the temperature in kelvin, m is the reduced mass in amu, and ν_0 is the line-center frequency in cm^{-1} . Because Doppler lines are narrow, a good approximation is

$$g_D(\nu - \nu_0) \approx j_D(\nu - \nu_0) . \quad (1.102)$$

Voigt line shape

The Doppler line shape assumes the shifted homogeneous line shapes are delta functions, which is usually a good approximation at very low pressures. However, the natural line shape is always present in any experiment and, in problems of atmospheric importance, collision broadening is present.

Figure 1.12 illustrates the shifted homogeneous line shape weighted by a Gaussian (Doppler) distribution. This process can be thought of as a convolution of a homogeneous shape, $g_H(\nu)$, through a Doppler profile. Thus,

$$g_v(\nu, \nu_0) = \int_0^{\infty} g_H(\nu, \nu_0) [j_D(\nu - \nu' - \nu_0) + j_D(\nu - \nu' + \nu_0)] d\nu' . \quad (1.103)$$

The resulting line shape is called the Voigt line shape $g_v(\nu)$. From the definition of the above equation, the normalization condition can be seen to be satisfied; i.e.,

$$\int_0^{\infty} g_v(\nu, \nu_0) d\nu = 1 . \quad (1.104)$$

The homogeneous line shape most often used is the Lorentz profile (but it may not always apply). Substituting in the Lorentz and Doppler line shapes and ignoring the emission term,

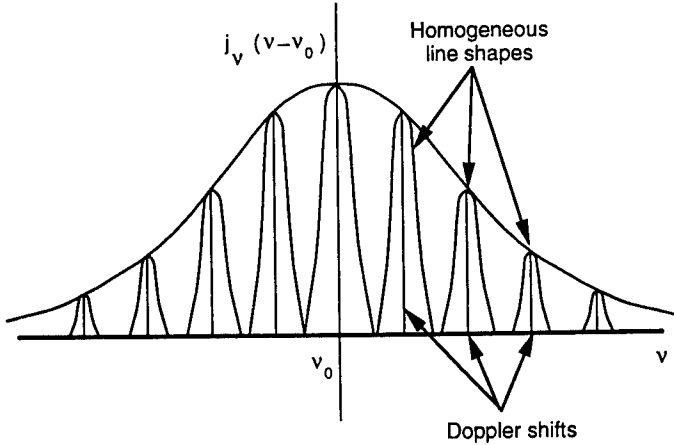


Fig. 1.12 Voigt-line-shape illustration.

$$g_v(v, v_0) = \frac{\alpha_H}{\pi^{3/2} \alpha_D} (\ln 2)^{1/2} \int_0^\infty \frac{\exp[-(v_0 - v')^2 \ln 2 / \alpha_D^2]}{[(v - v_0) - (v' - v_0)]^2 + \alpha_H^2} dv' . \quad (1.105)$$

Letting

$$y = \frac{v' - v_0}{\alpha_D} (\ln 2)^{1/2} ,$$

$$\xi = \frac{v - v_0}{\alpha_D} (\ln 2)^{1/2} , \quad (1.106)$$

$$a = \frac{\alpha_H}{\alpha_D} (\ln 2)^{1/2} ,$$

then

$$g_v(v, v_0) = \frac{\alpha_H}{\pi^{3/2} \alpha_D} \ln 2 \int_0^\infty \frac{\exp(-y^2)}{(\xi - y)^2 + a^2} dy . \quad (1.107)$$

[Note: $g_v(\Delta\nu) \approx j_{NLC}(\Delta\nu)$ for $\alpha_c/\alpha_D > 4$.] No closed-form representation exists for the Voigt profile and numerical techniques are commonly used.³¹

1.3.1.6 Refractivity Model

The index of refraction is the Hilbert transform of the index of absorption. Thus,

$$n(v, T) = 1 + \frac{2}{\pi} P \int_0^\infty \frac{v' k(v', T)}{v'^2 - v^2} dv' . \quad (1.108)$$

Substituting Eqs. (1.7) and (1.21) into the above expression gives

$$n(\nu, T) = 1 + \frac{1}{2\pi^2} \sum_i S_i P \int_0^\infty \frac{g(\nu_i, \nu')}{\nu'^2 - \nu^2} d\nu' . \quad (1.109)$$

The index of refraction (real part) comes from local line absorption phenomena based on the Hilbert transform. In the window regions of the atmosphere where weak absorption lines contribute very little to the index of refraction, the refractive index is determined by distant line-center contributions of absorption lines within the strong main bands of atmospheric gases. Thus, the following approximation can be made:

$$g(\nu, \nu_i) = \delta(\nu - \nu_i) + \delta(\nu + \nu_i) . \quad (1.110)$$

Substituting this expression into Eq. (1.109) results in a Sellmeier formula [recall Eq. (1.54)], as given by

$$\begin{aligned} n^2(\nu, T) = 1 &+ \frac{\langle \nu_{\text{Rot}} \rangle^2 \Delta \varepsilon_{\text{Rot}}(T)}{\langle \nu_{\text{Rot}} \rangle^2 - \nu^2} \\ &+ \sum_i \frac{\langle \nu_{\text{Vib}} \rangle_i^2 \Delta \varepsilon_{\text{Vib}_i}(T)}{\langle \nu_{\text{Vib}} \rangle_i^2 - \nu^2} \\ &+ \sum_k \frac{\langle \nu_{\text{El}} \rangle_k^2 \Delta \varepsilon_{\text{El}_k}(T)}{\langle \nu_{\text{El}} \rangle_k^2 - \nu^2} , \end{aligned} \quad (1.111)$$

where $\langle \nu \rangle$ is the average band position for rotational, vibrational, and electronic bands;

$$\Delta \varepsilon_{\text{Rot}} = \frac{8\pi}{3h} \rho_a \frac{\langle \sum |\mathbf{M}|_{\text{Rot}}^2 \rangle}{\langle \nu_{\text{Rot}} \rangle} \tanh\left(\frac{hc\langle \nu_{\text{Rot}} \rangle}{2k_B T}\right) \quad (1.112)$$

for the rotational band;

$$\Delta \varepsilon = \frac{8\pi}{3h} \rho_a \frac{\langle \sum |\mathbf{M}|^2 \rangle}{\langle \nu \rangle} \quad (1.113)$$

for vibrational and electronic bands [where the approximation $\tanh(hc\langle \nu \rangle / 2k_B T) \approx 1$ is used]; and the other parameters come from Eq. (1.58), the line-strength formula. Equation (1.111) is identical to the classical formula of Eq. (1.54) except more details are represented by the model parameters.

When weak local-line or anomalous dispersion is important, the complete near-line-center profile must be used. A closed-form expression based on Eq. (1.109) cannot be obtained in general. However, closed-form solutions in various limits within the collision-broadened regime are tractable.³² The results are summarized below for frequencies below 200 cm⁻¹ where $\tanh(hcv/2k_B T) \approx hcv/2k_B T$ and above 500 cm⁻¹ where $\tanh(hcv/2k_B T) \approx 1$ and T is in the range of typical atmospheric temperatures.

For $\nu < 200 \text{ cm}^{-1}$:

$$n^2 = 1 + \frac{2\pi hc}{k_B T} \sum_i S_i \nu_i \left\{ \left[\frac{\alpha_i}{\nu_i} j_{\text{NLC}}(\nu) - f(\nu) \right] + \left[\frac{\alpha_i}{\nu_i} j_{\text{NLC}}(-\nu) - f(-\nu) \right] \right\}. \quad (1.114)$$

For $\nu > 500 \text{ cm}^{-1}$:

$$n^2 = 1 - 4\pi \sum_i S_i [f(\nu) + f(-\nu)], \quad (1.115)$$

where

$$f(\nu) = \frac{1}{\pi} \frac{\nu - \nu_i}{(\nu - \nu_i)^2 + \alpha_i^2}. \quad (1.116)$$

The above formulas do not include line-mixing contributions.³²

1.3.2 Absorption by Atmospheric Gases

Absorption by molecules defines the atmospheric windows and is an important mechanism of tropospheric attenuation at millimeter and infrared wavelengths, especially in the marine or relatively humid environments. Therefore, the understanding and accurate modeling of absorption by atmospheric molecules are important to atmospheric remote sensing, infrared imaging systems, long-path laser propagation, electro-optical systems, radar, and atmospheric meteorology. The greenhouse effect of the atmosphere of the earth is caused by absorption of blackbody radiation in the 10- μm region from the surface. The absorbed energy heats the atmosphere, causing an increase in global temperature. Figure 1.13(a) shows low-resolution infrared transmittance of the atmosphere and demonstrates the importance of water vapor over other atmospheric constituents.³³ The H₂O absorption bands, along with those of CO₂, define the atmospheric window regions in the infrared. At millimeter and microwave wavelengths, O₂ and H₂O determine the window regions.

The main rotational and vibrational bands have been extensively characterized by many investigators.^{34–36} This work has resulted in a compendium of absorption-line parameters, maintained by the Geophysics Directorate at Hanscom Air (formerly Air Force Geophysics Laboratory),^{37,38} which represents a significant contribution to absorption calculations. Details of this database are discussed in Sec. 1.3.3. The database also contains parameters for weak absorption lines in the window regions. However, this information is, in general, not as accurate as that of the main bands.

The comparatively weak absorption that does occur in the window regions can be described as arising from two distinct sources, local-line and continuum absorption, as illustrated in the high-resolution computed spectrum of Fig. 1.13(b) for the 10- μm window region. Weak absorption bands of CO₂ and HDO, along with other H₂O absorption lines in the window regions, comprise the local-line contribution. The continuum contributes an additional, gradually varying, frequency-dependent background to the total absorption. A general

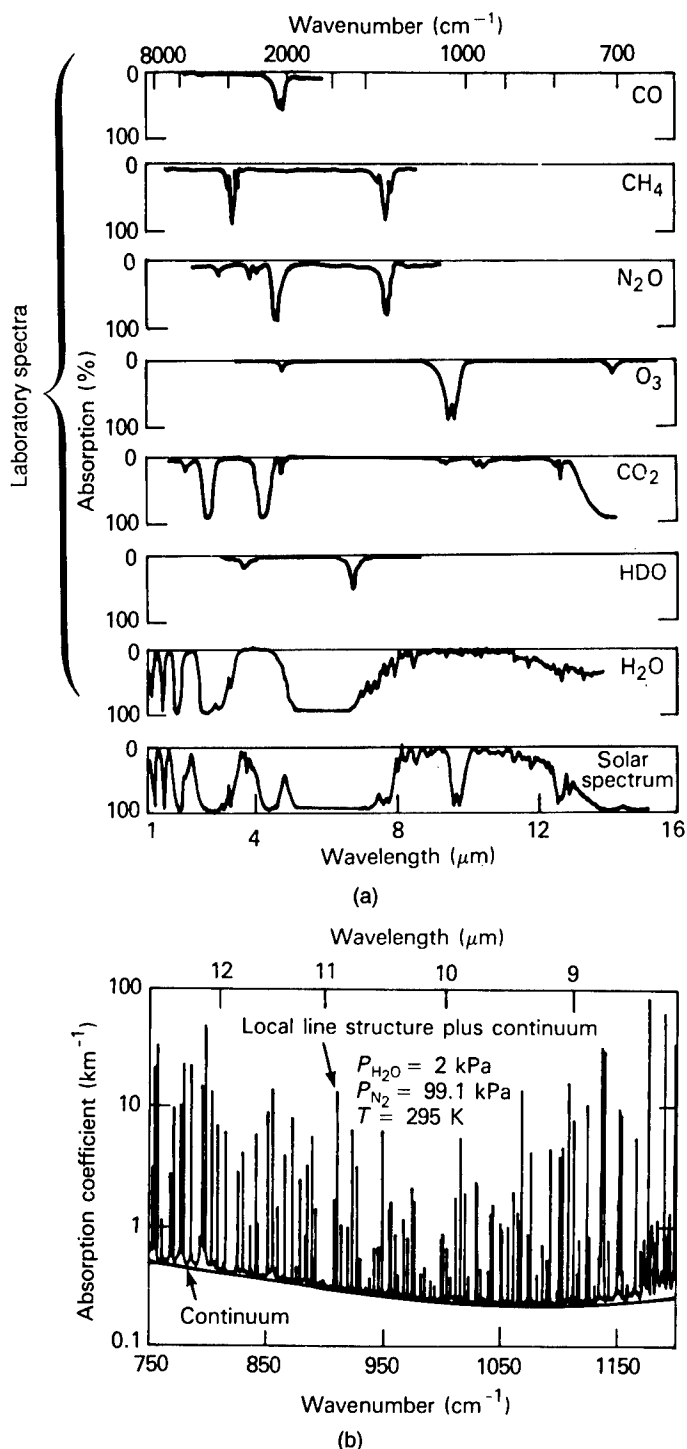


Fig. 1.13 (a) Low-resolution solar spectrum compared with laboratory spectra of atmospheric gases.³³ (b) Local-line structure plus continuum in the 10- μm region for a homogeneous path.

empirical form for the continuum absorption coefficient used to represent the data³⁷ is

$$\beta_{\text{cont}}(\nu, T, P_{f1} \dots P_{fi}, P_a) = \frac{P_a}{RT} \sum_i [C_{Fi}(\nu, T) P_{fi} + C_s(\nu, T) P_a] , \quad (1.117)$$

where C_s is the self-broadening coefficient of the absorbing gas, C_{Fi} is the foreign broadening coefficient due to the i 'th type foreign gas, $P_{a,fi}$ are the absorber and foreign gas partial pressures, respectively, and R is the ideal-gas constant. The above formula is consistent in form with a far-wing expansion of the collision-broadened absorption coefficient given in the previous section. This point will be used later to obtain a simple mathematical representation of continuum absorption. The equation can be conveniently rewritten for $i = 2$ to obtain

$$\beta_{\text{cont}}(\nu, T) = \frac{C_{F1}(\nu, T)}{RT} P_a [P_{f1} + F(\nu, T) P_{f2} + B(\nu, T) P_a] , \quad (1.118)$$

where $F = C_{F2}/C_{F1}$ and $B = C_s/C_{F1}$ are the dimensionless broadening coefficients. Near line center, B has the value of 5 for water vapor relative to nitrogen (see Table 1.8). In the real atmosphere, the effects of oxygen broadening must also be included. The dimensionless broadening coefficient F accounts for oxygen. However, many laboratory experiments ignore the effects of oxygen and use only nitrogen as the broadening gas along with the absorbing gas.

1.3.2.1 Water-Vapor Absorption

The strong dipole moment and the light hydrogen atoms composing water vapor result in strong and broad absorption bands. Also, water vapor is an asymmetric top that results in rich irregular spectra, as illustrated in Fig. 1.14 for the rotational band of water vapor. Thus, water-vapor absorption is important in every spectral window region of the atmosphere.

1.3.2.1.1 Fundamental Bands

To determine atmospheric-window locations and index-of-refraction contributions, knowledge of band strength and position is important. Table 1.9 lists band origins and integrated intensities $S_n(T)$, defined as

$$S_n(T) = \frac{1}{\rho_a} \int d\nu \beta_{\text{abs}}(\nu, T) \text{ (cm)} , \quad (1.119)$$

for several important water-vapor absorption bands. All bands listed originate from the ground state.

1.3.2.1.2 Window Regions

As previously mentioned, molecular absorption in the window regions manifests itself as local-line and continuum-type absorption. Narrow-band systems

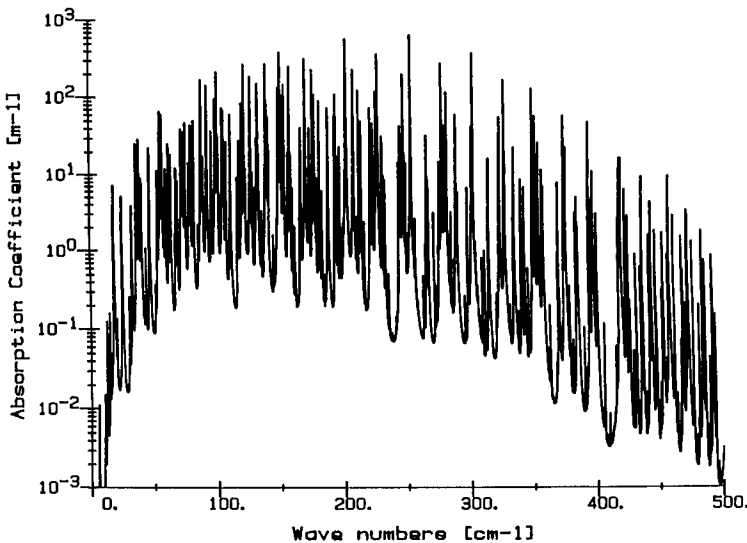


Fig. 1.14 Homogeneous-path pure rotational spectrum of water vapor for $p_{\text{H}_2\text{O}} = 0.02 \text{ atm}$, $p_{\text{N}_2} = 0.98 \text{ atm}$ at 296 K. Calculated based on HITRAN database.

can avoid local-line effects but not continuum absorption. Broadband systems must account for both.

1.3.2.1.2.1 Local Lines

Local-line structure of the 10- and 4- μm water-vapor window regions has been experimentally characterized by Thomas⁴⁰ and by Long and Damon⁴¹ using long-path laboratory measurements. Field measurements of local-line structure in the 10- μm region have been reported by Rinsland et al.⁴² The 1- to 1.1- μm local-line structure based on experimental data has been reported by Gallery et al.⁴³ The data demonstrate the importance of local-line structure in the case of water vapor and the need for experimental data to validate the HITRAN database. The HITRAN database also represents local-line structure based on experimental data and/or theoretical calculations. This database is described in more detail in Sec. 1.3.3.

1.3.2.1.2.2 Continuum

In 1942, Elsasser⁴⁴ recognized a continuum in the 13- to 8- μm window region, which he attributed to the far wings of the strong, nearby rotational and ν_2 vibrational rotational bands of H_2O . Further verification of this nonlocal line-absorption feature was provided by Yates and Taylor,⁴⁵ who studied infrared attenuation along horizontal paths at sea level. Solar spectra studies also indicated continuum absorption in the 13- to 8- μm window.^{46–48} The nature of the continuum, judged by those measurements, was uncertain. It could be due to far wings (far from the band center) of strong absorption bands or to scattering and absorption by particulates.

Table 1.9 Integrated Intensities of Water-Vapor Bands* (from Refs. 38 and 39)

Band Origin (cm ⁻¹)	Isotope	Upper Vibrational State ($\nu_1 \nu_2 \nu_3$)	$S_n(295\text{ K}) \times 10^{21}$ (cm)
0.0	H ¹⁶ OH	000	52,700.0
0.0	H ¹⁷ OH	000	19.4
0.0	H ¹⁸ OH	000	107.0
1588.28	H ¹⁸ OH	010	21.0
1591.33	H ¹⁷ OH	010	3.82
1594.75	H ¹⁶ OH	010	10,400.0
3151.63	H ¹⁶ OH	020	75.4
3657.05	H ¹⁶ OH	100	486.0
3707.47	H ¹⁶ OD	001	1.42
3741.57	H ¹⁸ OH	001	13.9
3748.32	H ¹⁷ OH	001	2.52
3755.93	H ¹⁶ OH	001	6,930.0
5234.98	H ¹⁶ OH	110	37.2
5331.27	H ¹⁶ OH	011	804.0
6871.51	H ¹⁶ OH	021	56.4
7201.48	H ¹⁶ OH	200	52.9
7249.93	H ¹⁶ OH	101	747.0
8807.0	H ¹⁶ OH	111	49.8
9000.0	H ¹⁶ OH	012	1.6
10,238.72	H ¹⁶ OH	121	2.1
10,613	H ¹⁶ OH	201	10.0
11,032	H ¹⁶ OH	003	2.4
12,151.26	H ¹⁶ OH	211	0.93
13,820.92	H ¹⁶ OH	301	1.08
14,318.80	H ¹⁶ OH	103	0.2

*The lower state is the ground state 000. S_n for isotopes is calculated on the basis of the total number of molecules of all isotopic species.

In an effort to determine the cause of continuum absorption in the 13- to 8- μm window, Bignell et al.,⁴⁹ in 1963, examined solar spectra while monitoring the atmosphere for aerosol concentrations and studying CO₂ far-wing contributions. They concluded that the amount of continuum absorption observed could not be explained by aerosol attenuation or far-wing absorption by CO₂. An attempt was then made to model the continuum by far wings of the bordering H₂O bands. The important contribution from this initial work was the realization of major water-vapor contributions to the continuum. A second paper by Bignell,⁵⁰ in 1970, described a careful examination of water-vapor absorption in the window regions by use of a multiple-traversal absorption cell and grating spectrometer. Two important characteristics of the 13- to 8- μm window were noted: (1) a large ratio of water-vapor self-to-foreign-gas broadening ability [see Eq. (1.118)] and (2) a strong negative temperature dependence. Neither of these findings was anticipated on the basis of the far-wing approaches of Bignell et al.'s 1963 paper.⁴⁹ Also reported by Bignell⁵⁰ was a similar, but much weaker, continuum absorption in the 4- μm region. (The 4- μm region also features a collision-induced absorption band of nitrogen.^{51,52} The band is of comparable strength to the water-vapor continuum in the earth's atmosphere. It is a smooth absorption band showing no structure; thus, it is often referred to as the nitrogen continuum. Also, a far-wing con-

tinuum of CO₂ beyond the ν_3 bandhead is observed between 4.1 and 4.0 μm .⁵³ These other continua are discussed later (see Secs. 1.3.2.4 and 1.3.2.2).

Since those initial experimental efforts to characterize water-vapor continuum absorption, many measurements have been made. They fall into three categories: (1) measurements within the earth's atmosphere or field measurements, (2) laboratory measurements using a long-path cell and a spectrometer, and (3) laboratory measurements using a long-path cell or a photoacoustic cell and a laser. Although continuum absorption was first observed through long-path field measurements, its precise characterization requires control and knowledge of the propagation path. The effects of turbulence, particulate scattering, temperature variations, and partial-pressure variations are difficult to determine in a field measurement. Thus, laboratory measurements are needed to characterize the pressure and temperature dependence of each atmospheric constituent. Spectrometer measurements determine the frequency dependence of the window regions, i.e., local lines and continuum absorption. Laser measurements are limited to discrete frequencies, but because of the laser's higher power and stability, greater accuracy can be obtained; this is particularly true for photoacoustic techniques. Laboratory transmission measurements require very long path lengths ($\approx 1 \text{ km}$ or longer) and thus are difficult to obtain. The photoacoustic cell, on the other hand, is compact (about 30 cm) but still maintains considerable sensitivity. Of course, field measurements will have the final say in the validation of atmospheric propagation computer codes.

As a result of these experiments, a good characterization of the commonly used window regions exists today. An excellent review of the field is given in the recent work of Hinderling et al.⁵⁴ and Grant.⁵⁵ They emphasize the 8- to 14- μm window region, which, along with the millimeter-wave window, is the most extensively measured. A review of the current experimental data for all the window regions is given in the next section, followed by a brief review of the theoretical and empirical models used to explain the experimental data.

Millimeter-wave window

Figure 1.15^{56–60} shows continuum absorption from 10 to 1000 GHz (total absorption minus local lines). The solid line represents an empirical formula given by Gaut and Reifenstein⁵⁷:

$$\beta_{\text{cont}} = (1.08 \times 10^{-6}) \rho_a \left(\frac{300}{T} \right)^{1/2} \left(\frac{P_T}{101} \right) f^2 \quad (\text{km}^{-1}), \quad (1.120)$$

where ρ_a is the water-vapor density (g/m^3), P_T is the total pressure (kPa), and f is the frequency (GHz). The plotted points indicate experimental data. The formula correctly demonstrates the frequency dependence of the continuum but not the temperature and pressure dependence. More recent work by Liebe⁶¹ uses a continuum formula, fitted to experimental data at 138 GHz, of the form

$$\beta_{\text{cont}} = (4.73 \times 10^{-8}) f^2 \left(\frac{300}{T} \right)^3 P_a \left[P_f + 31.6 \left(\frac{300}{T} \right)^{7.5} P_a \right] \quad (\text{km}^{-1}), \quad (1.121)$$

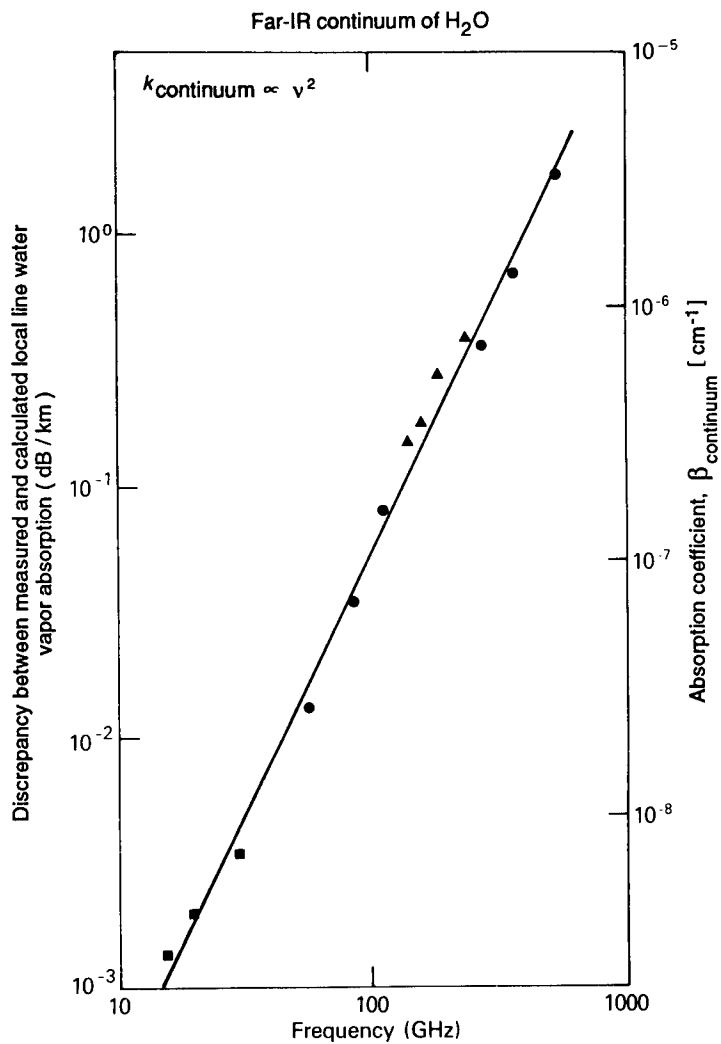


Fig. 1.15 Water-vapor-continuum absorption coefficient as a function of frequency. The solid line is an empirical fit to the experimental data points as given by Eq. (1.120). The plotted points are (▲),⁵⁸ (●),⁵⁹ and (■)⁶⁰ for $T = 300\text{ K}$, $P_T = 101\text{ kPa}$, and $\rho_a = 10^{-3}\text{ kg m}^{-3}$.

where f is in GHz, T is in K, and P_a and P_f ($P_f = P_T - P_a$) are in kPa. A strong dependence on the water-vapor partial pressure is shown ($B \gg 5$). The continuum calculated using Eq. (1.121) is smaller than that calculated using Eq. (1.120) because of improved local-line modeling. On the basis of the work by Liebe and Layton,^{62,63} the parameter B grows as the frequency decreases from 833 to 110 GHz (see Table 1.10). This dependence is expected based on the far-wing model of Birnbaum (see previous section) and leads to the following empirical model (for $f < 1000$ GHz and in units of km^{-1})⁶⁴:

$$\beta_{\text{cont}}(f) = (4.73 \times 10^{-8}) f^2 \theta^4 P_a (P_f + 40.9 e^{-0.0025f} \theta^{6.5} P_a) , \quad (1.122)$$

Table 1.10 Experimental Frequency Dependence of $B(\nu, 300)$
(from Ref. 62)

f (GHz)	ν (cm $^{-1}$)	$B(\nu, 300)$
110	3.7	32
138	4.6	31.6
213	7.1	20
833	27.8	7.4

where $\theta = (300/T)$ and the other variables have the same units as above.

As Eq. (1.121) indicates, B is not only a function of frequency but a strong function of temperature as well. Although Liebe^{61–63} chooses to represent his data in a power-law form, a comprehensive study at 213 GHz by Llewellyn-Jones⁶⁵ shows that the data fit an Arrhenius plot with the functional form

$$C_s(\nu, T) \propto e^{b/T}, \quad (1.123)$$

where $b = 5 \times 10^4$ K. Again, a strong negative temperature dependence is observed at this frequency as well. Figure 1.16 illustrates the experimental results of Llewellyn-Jones.⁶⁵

In summary, the millimeter-wave water-vapor continuum falls off as frequency squared, has an enhanced self-broadening contribution that grows with decreasing frequency, and has a strong negative temperature dependence.

The 8- to 12- μm window

Figure 1.17⁶⁶ shows the self-broadening water-vapor-continuum coefficient C_s as a function of frequency between 9 and 14 μm at 296 K. The coefficient decreases exponentially as the frequency increases. The same functional dependence is exhibited by the nitrogen-broadening coefficient C_N , as shown in Fig. 1.18,⁶⁶ but the rate of decrease is more rapid. Thus, $B (=C_s/C_N)$ increases as the frequency increases away from the rotational band. Long-path White cell and photoacoustic laser measurements indicate that B can be quite large. Values ranging from 100 to 600 have been measured in the 10- μm region with CO₂ lasers.^{53,67,68} Figure 1.19 illustrates a laser measurement at 940.548 cm $^{-1}$ as a function of the water-vapor partial pressure. The total pressure is maintained at 101 kPa (1 atm) with nitrogen.

The observed temperature dependence at 10.6 μm features a rapid decrease with increasing temperature (Fig. 1.20), just as in the millimeter-window region.^{69–72} The temperature dependence has the following functional form over a wide temperature range:

$$C_s(\nu, T) = C_s(\nu, T_0) \exp \left[b \left(\frac{1}{T} - \frac{1}{T_0} \right) \right], \quad (1.124)$$

where C_s (940 cm $^{-1}$, 296 K) = 1.83×10^{-22} cm $^{-2}$ molecule $^{-1}$ atm $^{-1}$ and $b = 1680$ K. This result at 10 μm is also consistent with other measurements in the 10- μm region and at 14.3 μm .^{53,66}

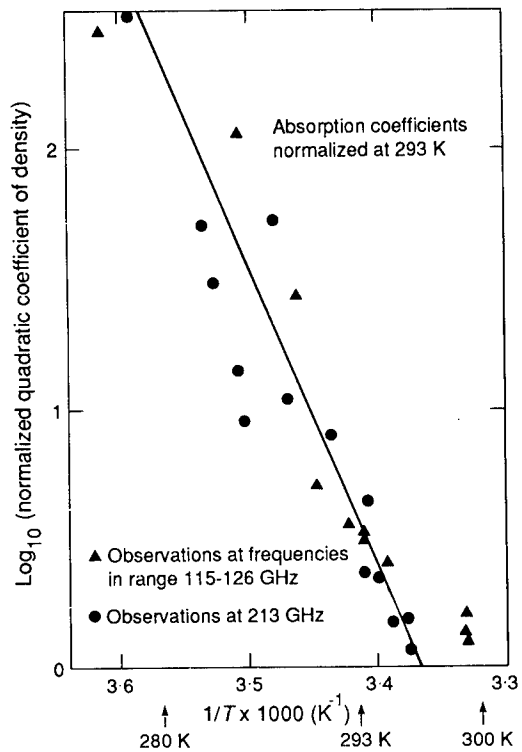


Fig. 1.16 Temperature dependence of millimeter-wave water-vapor continuum. Solid curve represents empirical fit to data as given by Eq. (1.123).

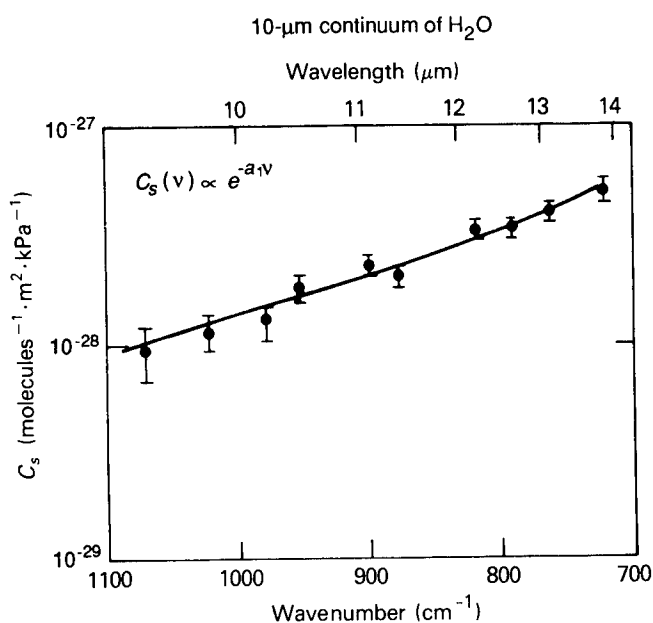


Fig. 1.17 Self-broadening coefficient as a function of wave number from 700 to 1100 cm^{-1} at 296 K.

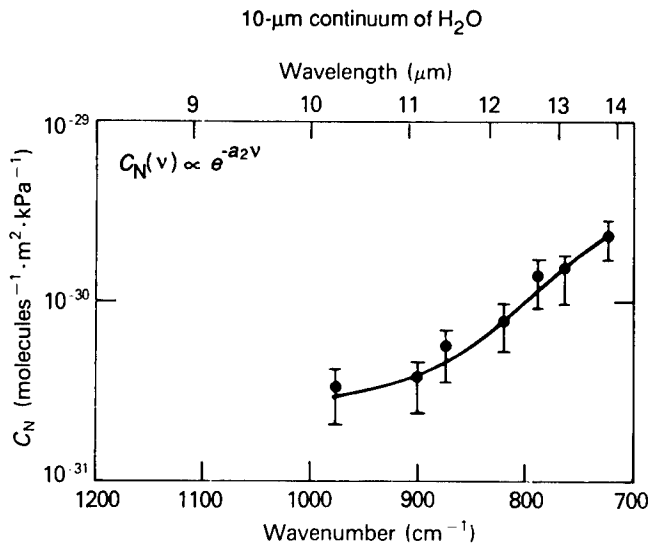


Fig. 1.18 Nitrogen-broadening coefficient as a function of wave number from 700 to 1200 \$\text{cm}^{-1}\$ at 296 K.

Based on the data presented and Birnbaum's line-shape formula, a simple formula for the nitrogen-broadened water-vapor-continuum absorption coefficient from 700 to 1100 \$\text{cm}^{-1}\$ and for typical atmospheric temperatures is given by⁷³

$$\beta_{\text{cont}} = 6.4 \times 10^5 \exp(-0.00839\nu) \left\{ \left(\frac{T_0}{T} \right)^3 p_{\text{N}_2} + 16.96 \exp \left[(0.00374\nu + 1680 \left(\frac{1}{T} - \frac{1}{T_0} \right) \right] p_{\text{H}_2\text{O}} \right\} \frac{p_{\text{H}_2\text{O}}}{T} \quad (\text{km}^{-1}), \quad (1.125)$$

where \$p\$ is in atm, \$\nu\$ is in wave numbers, and \$T_0 = 296\$ K.

An excellent review of experimental measurements in the 10-\$\mu\text{m}\$ region by Grant⁵⁵ makes the following additional points:

1. Oxygen does not broaden as effectively as nitrogen and must be included in a realistic model of the earth's atmosphere. A broadening coefficient of \$F = 0.75 \pm 0.1\$ for oxygen relative to nitrogen was measured by Nordstrom et al.⁷⁴ Using Eq. (1.118), this means air has an effective broadening of 0.95.
2. Understanding the local-line structure is critical in determining the true continuum. Line positions are known reasonably well; however, line strength and half-width are not known with enough accuracy.

Long-path field measurements by Devir et al.⁷⁵ are in excellent agreement with the laboratory measurements of Burch and Alt⁶⁶ and Peterson et al.⁶⁷ in this window region concerning the water-vapor continuum. The measured

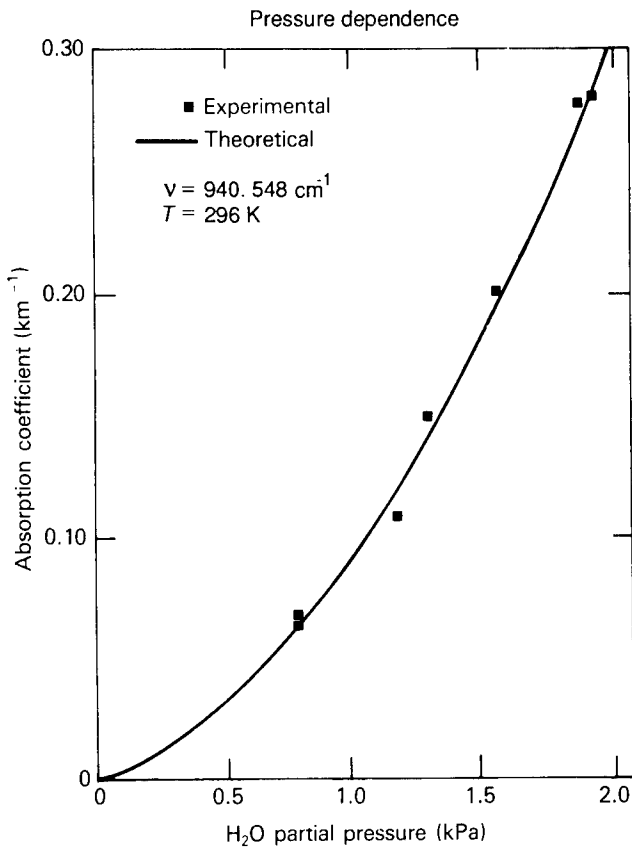


Fig. 1.19 Water-vapor partial-pressure dependence in the 10-μm region.

spectral range of Devir et al. extends the range covered by Burch and Alt and shows the water-vapor continuum increasing with increasing frequency. The minimum occurs at 9.0 μm (1100 cm⁻¹). The nature of 8- to 12-μm continuum absorption appears to be understood on the basis of the agreement between laboratory and field measurements.

The 3- to 5-μm window

The 3- to 5-μm continuum region has a different frequency dependence compared to the millimeter and 8- to 12-μm regions. Figure 1.21(b) displays a nearly parabolic dependence with a minimum at a wave number of 2600 cm⁻¹.^{66,76,77} As shown by the spectrometer measurements of Burch and Alt⁶⁶ [Fig. 1.21(a)], the self-broadening coefficient has an exponential falloff at wave numbers up to 2550 cm⁻¹, then the falloff rate decreases as the frequency increases. Figure 1.21(b) shows long-path White cell DF laser measurements⁷⁶ taken under atmospheric conditions, which indicate continuum absorption levels roughly 50% higher than those indicated by Burch and Alt. The level of

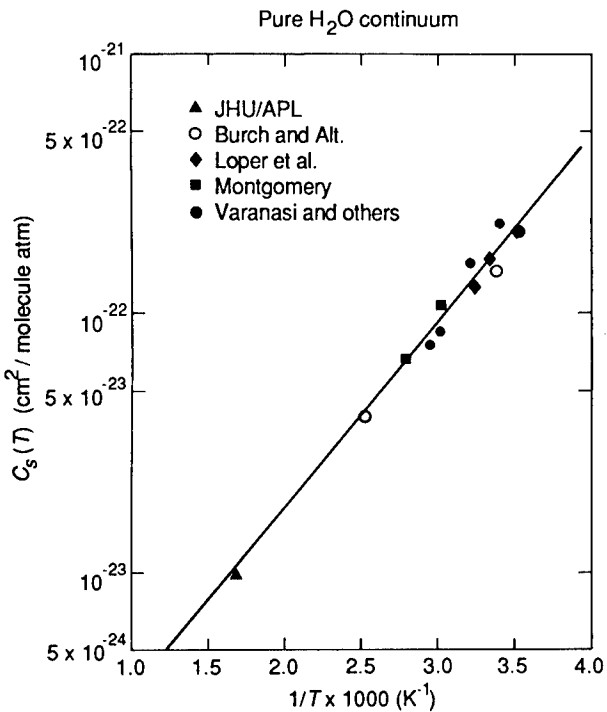


Fig. 1.20 Temperature dependence of self-broadening coefficient in the 10-μm region.

absorption in the 4-μm region is roughly an order of magnitude less than that in the 10-μm region. Long-path CO, DF, and HF laser measurements near room temperature again indicate large values for B in the continuum region, ranging from 10 to 20 at 5 μm⁴⁰ to approximately 50 to 60 at 4 μm⁷⁶ and back down to 10 at 3 μm.⁷⁸

A strong negative temperature dependence is again observed for the self-broadening coefficient. Figure 1.22 shows the results of laboratory long-path spectrometer measurements by Burch and Alt.⁶⁶ The temperature dependence at 2400 cm⁻¹ exhibits exponential falloff similar to that in the 10-μm and millimeter regions. However, the curves at 2500 and 2600 cm⁻¹ show double exponential trends. The nature of the water-vapor continuum in this window region is more complicated than the other windows discussed previously.

More experimental data are needed to generate a meaningful empirical model of the continuum absorption coefficient. An attempt at representing the existing data is given by the following formula for the nitrogen-broadened water-vapor continuum absorption coefficient valid from 2400 to 2800 cm⁻¹⁷³:

$$\beta_{\text{cont}} = 7.34 \times 10^{26} \frac{p_{\text{H}_2\text{O}}}{T} [C_s(\nu, T)p_{\text{H}_2\text{O}} + C_N(\nu, T)p_{\text{N}_2}] \quad (\text{km}^{-1}), \quad (1.126)$$

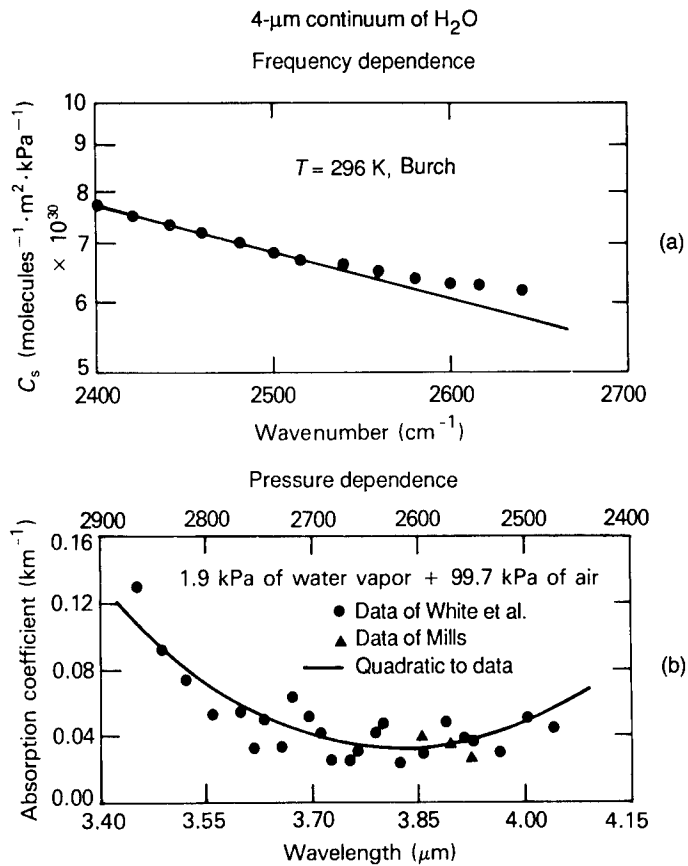


Fig. 1.21 4-μm water-vapor-continuum region at $T = 296 \text{ K}$. (a) C_s versus wave number⁶⁶ and (b) absorption coefficient versus wavelength.^{76,77}

where

$$\begin{aligned}
 C_s(\nu, T) &= 1.77 \times 10^{-20} \exp(-3.32 \times 10^{-3}\nu) \\
 &\times \exp\left[1234\left(\frac{1}{T} - \frac{1}{T_0}\right)\right] + 3.91 \times 10^{-28} \\
 &\times \exp(3.46 \times 10^{-3}\nu) \exp\left[2626\left(\frac{1}{T} - \frac{1}{T_0}\right)\right], \quad (1.127)
 \end{aligned}$$

$$\begin{aligned}
 C_N(\nu, T) &= \left(\frac{296}{T}\right)^3 [7.16 \times 10^{-19} \exp(-6.45 \times 10^{-3}\nu) \\
 &+ 2.73 \times 10^{-33} \exp(6.45 \times 10^{-3}\nu)]. \quad (1.128)
 \end{aligned}$$

Again, long-path field measurements by Devir et al.⁷⁵ are in good agreement with Burch and Alt⁶⁶ in this window region concerning the water-vapor con-

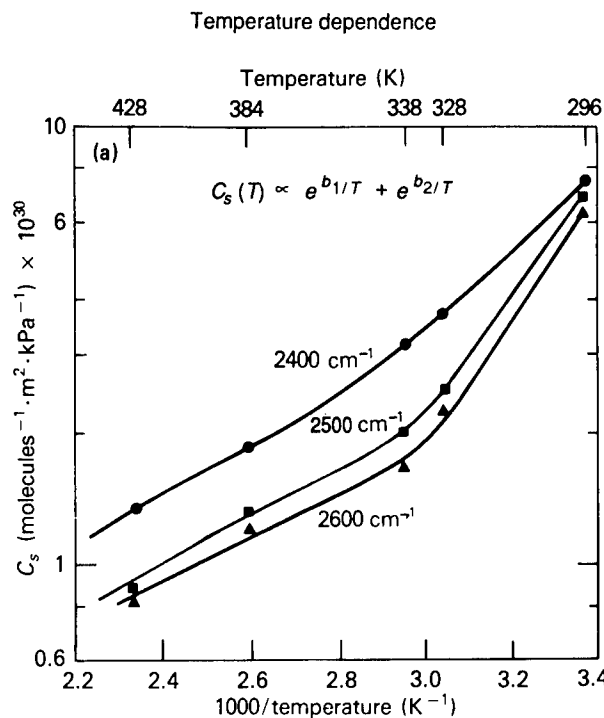


Fig. 1.22 Plots of the water-vapor self-broadening coefficients at 2400, 2500, and 2600 cm^{-1} versus reciprocal temperature.⁶⁶ The symbols •, ▀, and ▲ represent the experimental data points.

tinuum. The results of Devir et al. also point out the importance of the water-vapor continuum between 4.5 and 5.0 μm . In this region, local-line contributions can be significant as well, thus masking to some extent water-vapor-continuum absorption. CO laser transmission measurements as a function of water-vapor partial pressure show an increase in the dimensionless self-broadening coefficient B over the near-line-center value.⁴⁰ As observed in the previous window regions, this observation is indicative of continuum absorption. Another interesting observation based on the field measurements of Devir et al. is an absorption feature in the water-vapor continuum at 4.8 μm . The water-vapor-continuum frequency dependence is approximately exponential in this region except for the absorption band, which adds to the exponential background. Liquid water is known to have an association band at 4.8 μm , thus suggesting that the anomalous feature is caused by water vapor. More work is needed on this problem to fully appreciate this observation.

Field measurements between 4.1 and 3.8 μm reveal that other continuum sources exist. The far blue wing beyond the bandhead of the fundamental v_3 band of CO_2 ⁷⁹ and the collision-induced absorption band of nitrogen^{80–84} also contribute to continuum-type absorption in this window region and are discussed later (see Secs. 1.3.2.2 and 1.3.2.4).

The 2.0- to 2.5- μm window

This window region has not received the same attention as the longer-wavelength windows; as a result, no experimental continuum absorption has been previously reported. Recent measurements,⁸⁵ however, indirectly suggest that continuum absorption does exist. Transmission measurements on hot ($T = 685 \text{ K}$), high-pressure (up to 4.8 MPa) water vapor show the continuum absorption in the 2.1- and 4- μm regions (Fig. 1.23). Absorption levels at 4 μm are consistent with the extrapolated values from the curves in Fig. 1.22. The point to be made is that a similar continuum absorption process occurs in the 2.1- μm region, as shown in Fig. 1.23. If we assume that an extrapolation to lower temperature follows the same trend as at 4 μm , then a continuum exists in the 2.0- to 2.5- μm window that is very similar to the 3- to 5- μm window under normal atmospheric conditions.

The 1.7- to 1.5- μm window and beyond

Figure 1.22 shows the beginning of the continuum centered at 1.6 μm . Again, this suggests a water-vapor continuum in this window region at a weaker level than at 4 and 2 μm . Based on this observation, it is expected that every window in the infrared has a water-vapor continuum at some absorption level. This level should become weaker as the frequency increases.

The 1- μm window water-vapor continuum has been measured by a novel interferometric calorimeter technique.⁸⁶ A pulsed Nd-glass laser is used to

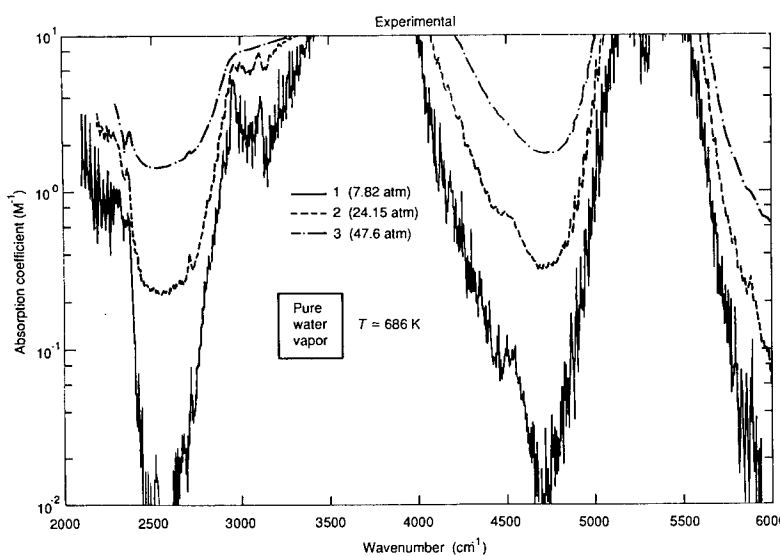


Fig. 1.23 Pure water-vapor absorption coefficient at $T \approx 685 \text{ K}$ and three different pressures as indicated.

heat a nitrogen-buffered water-vapor sample placed in the arm of a He-Ne Mach-Zehnder interferometer. Variations in the index of refraction due to the heating cause measurable fringe shifts proportional to the absorption coefficient. The resulting continuum absorption coefficient measured at 9466 cm^{-1} is $6 \times 10^{-10}\text{ cm}^{-1}$ for a water-vapor partial pressure of 16.5 Torr buffered by nitrogen to a total pressure of 1 atm at 30°C. Thus, the water-vapor continuum is roughly two orders of magnitude weaker near 1 μm than at 4 or 2 μm . Further measurements to determine the water-vapor partial pressure dependence and temperature dependence are needed.

The tragedy of experimental water-vapor-continuum characterization is that unlike nitrogen and CO₂ experiments, it presently cannot be done at high pressure. High-pressure water-vapor measurements also require high temperature and thus a theoretical understanding of the continuum-absorption temperature dependence to extrapolate back to atmospheric temperatures.

Concepts and models

No universal interpretation of continuum absorption by water vapor presently exists. Clearly, far wings must play a role in continuum absorption because of the observed frequency dependence observed in every window, and work is continuing to find a line-shape theory valid in the far wing.^{19–23,87–90} The major shortcoming of most current line-shape theories is in their failure to predict the observed strong negative temperature dependence characteristic of all the window regions, except for the work of Ma and Tipping in the millimeter wave and infrared windows. But this weakness is the very strength of an alternative hypothesis to explain the water-vapor continuum: the water dimer. The formation of water-vapor dimers has a strong negative temperature dependence that closely matches the temperature dependence of the continuum absorption in the 10- μm region.^{72,91} However, this near match does not occur in the microwave window or in the 4- μm window. This approach also requires dimer absorption bands to account for the continuum. However, the hypothesis would require a dimer absorption band in every water-vapor window, a condition that has not been experimentally found or theoretically shown.^{54,92} Furthermore, measurements on supersaturated water vapor indicate that dimer absorption is an order of magnitude too small to account for the water-vapor continuum at 10 μm .⁵⁴ In spite of these shortcomings, the dimer hypothesis demonstrates the importance of understanding water-vapor/water-vapor interactions to explain the continuum absorption temperature dependence.⁵⁴

Because of the lack of closed-form line-shape models or fast numerical techniques for water-vapor-continuum absorption calculations, it is commonly characterized by empirical models. One such model, developed at Johns Hopkins University/Applied Physics Laboratory (JHU/APL) and Ohio State University, uses a far-wing model with a semiempirical line shape and the Air Force Geophysics Laboratory's absorption-line data.^{93–95} The model has been applied to the 10- and 4- μm window regions and reproduces the experimental data quite well as a function of frequency, pressure, and temperature. An example is the curve in Fig. 1.19. The water-vapor-broadened far wing falls off less rapidly than the nitrogen-broadened far wing; thus, the self-broadening

coefficient grows as the line shape extends from line center. This is the trend observed in the data. The line shape is normalized, and the line-center function has been experimentally verified.⁹⁶ The far wings ($>100 \text{ cm}^{-1}$ from line center) of a line shape represent a very small percentage of the total area under an absorption line contour. Nonetheless, it is interesting to note that the magnitude of the continuum absorption can be correctly calculated from the far-wing contributions by this model. Contributions to the 10- μm region are dominated by far wings of the very strong rotational band of water vapor on the long-wavelength side of that window, whereas the 4- μm continuum absorption arises from the bordering strong vibrational bands of almost equal strength. That difference between sources explains the difference between the frequency dependence of the 10- μm continuum region and that of the 4- μm continuum region (see Figs. 1.17, 1.18, and 1.21). Unfortunately, the model is not valid in the millimeter region and does not fully represent the recent progress in line-shape theories as discussed in the background section (1.3.1). The success of this model, therefore, is by no means a statement of the validity of a far-wing interpretation of continuum absorption, but rather a statement of its feasibility.

The continuum models for the popular Air Force Geophysics Laboratory codes FASCODE and LOWTRAN are based on the efforts of Clough et al.,^{87,88} who used far-wing concepts to represent the water-vapor continuum throughout the entire infrared region. The experimental data previously described are reasonably represented by these codes. The strength of this approach and the previously mentioned approach over the APL model is accounting for the fluctuation dissipation theorem in enforcing detailed balance across the entire line shape. This results in a more physically meaningful far wing and a more versatile line shape overall.

On the basis of these far-wing models, the water-vapor continuum is extrapolated to higher frequencies beyond 4 μm in LOWTRAN-7 and FASCODE-2. As the previous section indicates, except for the limited data in the 1- μm region, no direct experimental evidence exists beyond 4 μm . Thus, the extrapolated continuum values must be applied with great care. Figure 1.24 illustrates this point by comparing the water-vapor-continuum models of LOWTRAN-6 and the APL model from 500 to 5000 cm^{-1} . The figure also shows another continuum loss mechanism, molecular Rayleigh scattering, based on the LOWTRAN-7 model. The conditions used in the calculation are for a horizontal path with $p_{\text{H}_2\text{O}} = 2.0 \text{ kPa}$, $p_{\text{N}_2} = 99.0 \text{ kPa}$, and $T = 295 \text{ K}$. The APL model has been extended beyond 4 μm by using the same empirical far-wing parameters of the ν_1 and ν_3 vibrational bands for all vibrational bands to higher frequencies. The fundamental vibrational band far-wing parameters do not vary greatly; thus, this is a reasonable approximation. Surprisingly, this extrapolation predicts closely the 1- μm laser measurements of the water-vapor continuum. Fair agreement between the two models exists in the region of the 10- μm window. Good agreement is obtained in the 4- and 2- μm windows as well. The water-vapor-continuum model in LOWTRAN-6 and -7 is also extrapolated beyond 5000 cm^{-1} . The LOWTRAN-6 model extrapolation is incorrect and is 100 times too large at 1 μm . The latest version of LOWTRAN-7 has corrected this error and now agrees reasonably well with the APL model.

Figure 1.24 illustrates another interesting point. Continuum absorption decreases with increasing frequency, and scattering loss increases with in-

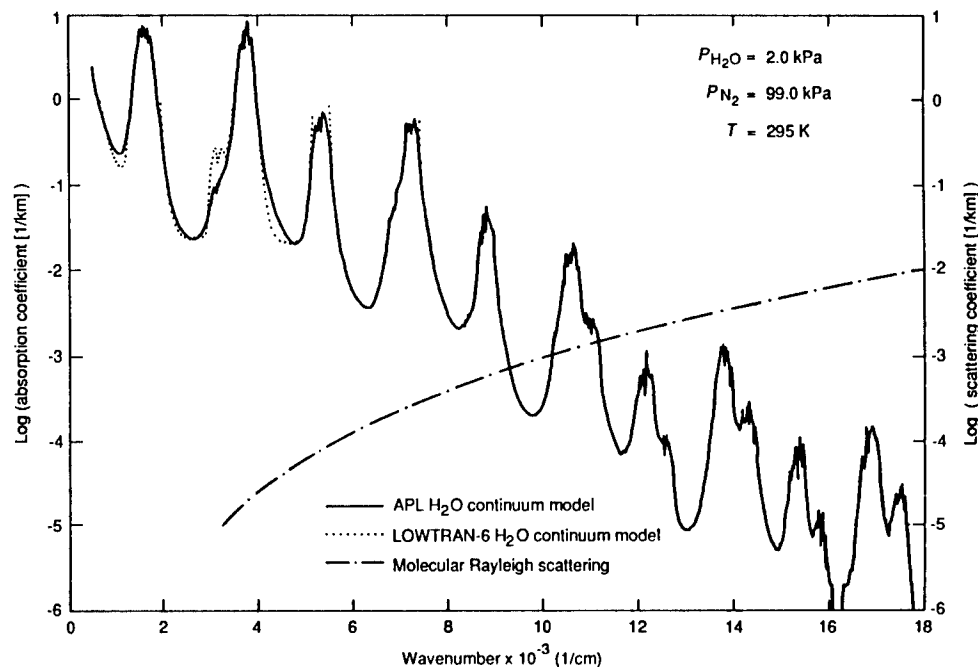


Fig. 1.24 A comparison of water-vapor-continuum absorption models and molecular Rayleigh scattering in a homogeneous path.

creasing frequency. Thus, for a particular set of atmospheric conditions, an optimal atmospheric window can be selected. Of course, local-line effects must be included in a broadband system, but a narrow-band system can avoid local-line attenuation.

Although no definitive interpretation of the water-vapor continuum exists, the experimental and theoretical evidence indicates that far-wing absorption contributions by the bordering strong water-vapor bands play a dominant role. The evidence is based largely on the frequency dependence of the continuum in all spectral windows reviewed (i.e., the shape of the continuum as a function of frequency and growth of the dimensionless broadening coefficient B away from a band as a function of frequency). The shortcoming of the far-wing approach is predicting the temperature dependence, but the character of a far wing must be driven by close binary interactions much like the creation of a dimer, which does exhibit the observed temperature dependence in the 10- μm window region.

1.3.2.2 Carbon-Dioxide Absorption

Carbon dioxide is a symmetric (e.g., nonpolar) linear molecule. It has a small B value (see Table 1.6) and thus dense compact spectra. Fundamental vibrational frequencies of the main isotope are listed in Table 1.7; only the bending (ν_2) and the asymmetric stretch (ν_3) are infrared active.

1.3.2.2.1 Vibrational Bands

The location of CO₂ and H₂O absorption bands determines the location of atmospheric windows. Table 1.11 lists the location and integrated band strength (see Sec. 1.3.2.1.1 for definition) of the most important vibrational bands. Because CO₂ does not have a permanent dipole moment the rotational band is not infrared active. The absorption bands near 667 cm⁻¹ are important contributors to the atmospheric greenhouse effect because of the proximity to the peak of the room-temperature blackbody curve. The 4.3 μm (ν_2 band) divides the 3- to 5-μm window region into two parts. Otherwise, the other CO₂ bands coincide with water-vapor absorption bands.

Table 1.11 Band Locations and Integrated Intensities of Carbon Dioxide*
(from Ref. 38)

Band Origin (cm ⁻¹)	Isotope	Upper State ($\nu_1\nu_2\nu_3$)	Lower State ($\nu_1\nu_2\nu_3$)	$S_n(295\text{ K}) \times 10^{20}$ (cm)
618.03	¹⁶ O ¹² C ¹⁶ O	10 ⁰ 0	01 ¹ 0	14.4
647.06	¹⁶ O ¹² C ¹⁶ O	11 ¹ 0	10 ⁰ 0	2.22
648.48	¹⁶ O ¹³ C ¹⁶ O	01 ¹ 0	00 ⁰ 0	8.6
662.37	¹⁶ O ¹² C ¹⁸ O	01 ¹ 0	00 ⁰ 0	3.3
667.38	¹⁶ O ¹² C ¹⁶ O	01 ¹ 0	00 ⁰ 0	826.0
667.75	¹⁶ O ¹² C ¹⁶ O	02 ² 0	01 ¹ 0	64.9
668.11	¹⁶ O ¹² C ¹⁶ O	03 ³ 0	02 ² 0	3.82
688.68	¹⁶ O ¹² C ¹⁶ O	11 ¹ 0	10 ⁰ 0	1.49
720.81	¹⁶ O ¹² C ¹⁶ O	10 ⁰ 0	01 ¹ 0	18.5
2271.76	¹⁶ O ¹³ C ¹⁶ O	01 ¹ 1	01 ¹ 0	8.18
2283.49	¹⁶ O ¹³ C ¹⁶ O	00 ⁰ 1	00 ⁰ 0	96.0
2311.68	¹⁶ O ¹² C ¹⁶ O	03 ³ 1	03 ³ 0	1.23
2319.74	¹⁶ O ¹² C ¹⁸ O	01 ¹ 1	01 ¹ 0	2.58
2324.15	¹⁶ O ¹² C ¹⁶ O	02 ² 1	02 ² 0	30.8
2326.59	¹⁶ O ¹² C ¹⁶ O	10 ⁰ 1	10 ⁰ 0	11.8
2327.43	¹⁶ O ¹² C ¹⁶ O	10 ⁰ 1	10 ⁰ 0	19.3
2332.11	¹⁶ O ¹² C ¹⁸ O	00 ⁰ 1	00 ⁰ 0	33.3
2336.64	¹⁶ O ¹² C ¹⁶ O	01 ¹ 1	01 ¹ 0	766.0
2349.15	¹⁶ O ¹² C ¹⁶ O	00 ⁰ 1	00 ⁰ 0	9600.0
3580.33	¹⁶ O ¹² C ¹⁶ O	11 ¹ 1	01 ¹ 0	8.04
3612.84	¹⁶ O ¹² C ¹⁶ O	10 ⁰ 1	00 ⁰ 0	104.0
3632.92	¹⁶ O ¹³ C ¹⁶ O	10 ⁰ 1	00 ⁰ 0	1.60
3714.78	¹⁶ O ¹² C ¹⁶ O	10 ⁰ 1	00 ⁰ 0	150.0
3723.25	¹⁶ O ¹² C ¹⁶ O	11 ¹ 1	01 ¹ 0	11.4
4977.83	¹⁶ O ¹² C ¹⁶ O	20 ⁰ 1	00 ⁰ 0	3.50
5099.66	¹⁶ O ¹² C ¹⁶ O	20 ⁰ 1	00 ⁰ 0	1.09
6972.58	¹⁶ O ¹² C ¹⁶ O	00 ⁰ 3	00 ⁰ 0	0.15

* S_n for isotopes is calculated on the basis of the total number of molecules of all isotopic species.

1.3.2.2 Window Regions

In the window regions of the atmosphere, local-line absorption by weak absorption bands of CO₂ is most important. The only continuum-type absorption of concern is the blue wing of the ν_3 fundamental band.

Local-line absorption

Weak vibrational bands in the 10- and 5-μm regions have significant local-line effects for long-path propagation. In particular, the same vibrational transitions used in the CO₂ laser occur in the atmosphere also. Laser radiation is at line center of the atmospheric CO₂ absorption lines. For this reason isotopic CO₂ (because of the different masses the vibrational frequencies are slightly shifted) is preferred for optimal atmospheric propagation. Again, it is recommended to consult the HITRAN database for details of the band structure.

Continuum absorption

Carbon-dioxide continuum-type absorption occurs near 4.1 μm. It is the blue wing of the 4.3-μm absorption band, as illustrated in Fig. 1.25 for pure and

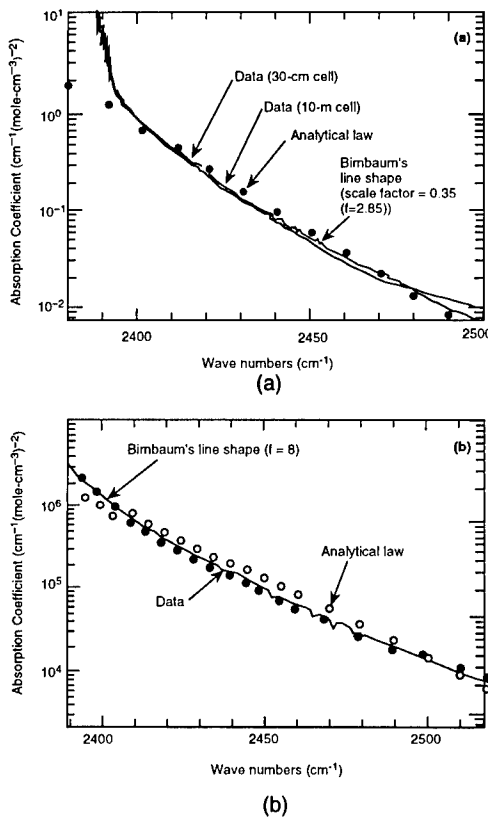


Fig. 1.25 Experimental absorption coefficient divided by the density squared for (a) pure CO₂ at $T = 296$ K and (b) N₂-broadened CO₂ at 296 K. Also shown are calculations based on Eq. (1.129) and a line-by-line calculation based on Birnbaum's line shape.⁷³

N_2 -broadened CO_2 . The figure also shows a line-by-line calculation based on Birnbaum's line shape. The shape of the wing is duplicated but the magnitude is not because line mixing is not included in the model; however, a simple scaling factor allows good agreement with experimental data.⁷³ The wing is exponential in nature, as Birnbaum's model predicts, and covers the spectral region from 2400 to 2500 cm^{-1} .

Based on the data in Fig. 1.25 and the theories discussed in Sec. 1.3.1, a simple empirical formula for the carbon-dioxide continuum (far blue wing of the v_3 band) absorption coefficient β_{cont} that is valid for typical atmospheric conditions is given by

$$\begin{aligned}\beta_{\text{cont}} = & 9.0 \times 10^3 \left(\frac{T_s}{T} \right)^{2.5} p_{\text{CO}_2}^2 \exp[-5.0 \times 10^{-2}(\nu - 2350)] \\ & + 1.623 \times 10^3 \left(\frac{T_s}{T} \right)^{2.5} p_{\text{CO}_2} p_{\text{N}_2} \exp[-4.47 \times 10^{-2}(\nu - 2350)],\end{aligned}\quad (1.129)$$

where p_{CO_2} and p_{N_2} are in atm, β_{cont} is in km^{-1} , and $T_s = 296$ K. The first term is the pure CO_2 contribution and the second term is the $\text{CO}_2\text{-N}_2$ contribution. The temperature dependence $n = 2.5$ comes from the partition function ($n = 1$), the half-width temperature dependence ($n \approx 0.5$), and the absorber density ($n = 1$). A similar model, empirically derived, has been proposed by Roney et al.⁹⁷ and validated against field measurements over the temperature range 252 to 303 K.

1.3.2.3 Absorption by Other Gases

Other absorbing gases in the atmosphere are important in limited spectral regions. Only band or local-line absorption need be considered.

Methane

Methane is a spherical-top nonpolar molecule with nine fundamental vibrational modes. Degeneracies reduce the number of observable vibrational bands to four, with three bands infrared active (see Table 1.7). Methane absorption bands are discussed by Brown.⁹⁸ Table 1.12 lists the location and integrated intensity of the most important vibrational bands.

Ozone

Ozone is an asymmetric-top polar molecule with three fundamental vibrational bands and a rotational band. Table 1.13 lists the band locations and the integrated intensities for the most important bands of concern to propagation in the atmosphere. Also, ozone has important electronic transitions that limit the amount of ultraviolet radiation reaching the surface of the earth.⁹⁹ These electronic bands are illustrated in Fig. 1.26. Ozone strongly absorbs out to 300 nm, but continues to absorb more weakly out to 350 nm.

Nitrous oxide

Nitrous oxide is a linear polar molecule with a rotational and three vibrational modes (one is degenerate). Table 1.14 lists band locations and integrated intensities of absorption bands important to atmospheric propagation.

Oxygen

Oxygen is a nonpolar diatomic molecule. Thus, first-order dipole rotational and vibrational bands do not exist; however, because of the high concentration of oxygen in the atmosphere higher-order effects are important. It does have a rotational absorption band through magnetic dipole transitions at 60 GHz and a nonresonant band near 10 kHz. The fundamental vibration band at 1556.379 cm^{-1} exists as a collision-induced-absorption band and is discussed in Sec. 1.3.2.4. Oxygen has near-infrared and ultraviolet electronic transitions. Table 1.15 lists the locations and integrated intensities of the near-infrared bands. Figure 1.27 plots the oxygen absorption cross section versus wavelength in the ultraviolet region, which determines the end of atmospheric transparency in the troposphere.

Table 1.12 Vibrational Bands of Methane* (from Ref. 38)

Band Origin (cm^{-1})	Isotope	Upper State ($v_1 v_2 v_3 v_4$)	$S_n(295) \times 10^{20}$ (cm)
1302.77	$^{13}\text{CH}_4$	0001	5.7
1310.76	$^{12}\text{CH}_4$	0001	504.1
1533.37	$^{12}\text{CH}_4$	0100	5.5
3009.53	$^{13}\text{CH}_4$	0010	29.3
3018.92	$^{12}\text{CH}_4$	0010	1022.0
2612	$^{12}\text{CH}_4$	0002	5.4
2822	$^{13}\text{CH}_4$	0101	4.3
2830	$^{12}\text{CH}_4$	0101	38.0
3062	$^{12}\text{CH}_4$	0201	16.4
4223	$^{12}\text{CH}_4$	1001	24.0
4340	$^{12}\text{CH}_4$	0011	40.8
4540	$^{12}\text{CH}_4$	0110	6.2

*The lower state is the ground state 000. S_n for isotopes is calculated on the basis of the total number of molecules of all isotopic species.

Table 1.13 Infrared Bands of Ozone* (from Ref. 38)

Band Origin (cm^{-1})	Upper State ($v_1 v_2 v_3$)	Lower State ($v_1 v_2 v_3$)	$S_n(295) \times 10^{20}$ (cm)
0.00	000	000	41.3
700.93	010	000	62.8
1015.81	002	001	17.4
1025.60	011	010	45.0
1042.08	001	000	1394.0
1103.14	100	000	67.1
2057.89	002	000	11.1
2110.79	101	000	113.4
3041.20	003	000	11.0

* S_n for isotopes is calculated on the basis of the total number of molecules of all isotopic species.

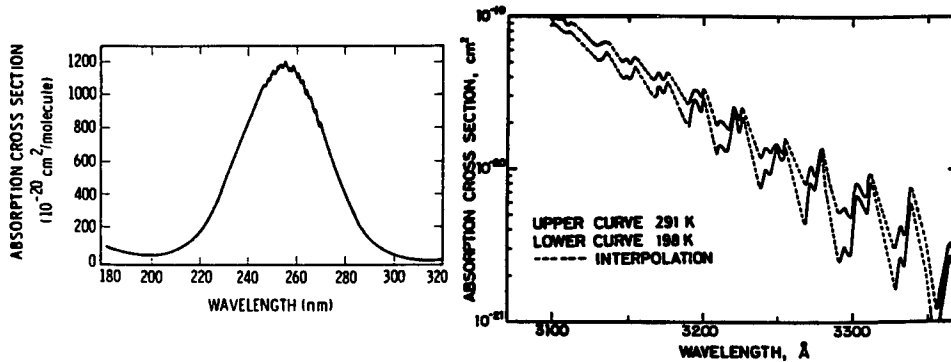
Fig. 1.26 Electronic absorption bands of ozone.^{39,99}

Table 1.14 Infrared Bands of Nitrous Oxide* (from Ref. 38)

Band Origin (cm ⁻¹)	Upper State ($\nu_1 \nu_2 \nu_3$)	$S_n(295) \times 10^{20}$ (cm)
0.00	00 ⁰ 0	Not listed
588.77	01 ¹ 0	118
1168.13	02 ⁰ 0	39
1284.91	10 ⁰ 0	996
2223.76	00 ⁰ 1	5710
2462.00	12 ⁰ 0	33
2563.34	20 ⁰ 0	135
3363.97	02 ⁰ 1	11
3480.82	10 ⁰ 1	197

*The lower state is the ground state 000. S_n for isotopes is calculated on the basis of the total number of molecules of all isotopic species.

Table 1.15 Near-Infrared Band of Oxygen (from Refs. 38 and 39)

Band Origin (cm ⁻¹)	Electronic Transition	Vibrational Transition	Band Intensity (cm)
		Infrared bands	
6326.033	a \leftarrow X	0 \leftarrow 1	1.13×10^{-28}
	a \leftarrow X	0 \leftarrow 0	1.82×10^{-24}
	a \leftarrow X	1 \leftarrow 0	8.63×10^{-27}
Red bands			
11,564.516	b \leftarrow X	0 \leftarrow 1	7.80×10^{-27}
	b \leftarrow X	1 \leftarrow 1	9.42×10^{-26}
	b \leftarrow X	0 \leftarrow 0	1.95×10^{-22}
	b \leftarrow X	1 \leftarrow 0	1.22×10^{-23}
	b \leftarrow X	2 \leftarrow 0	3.78×10^{-25}

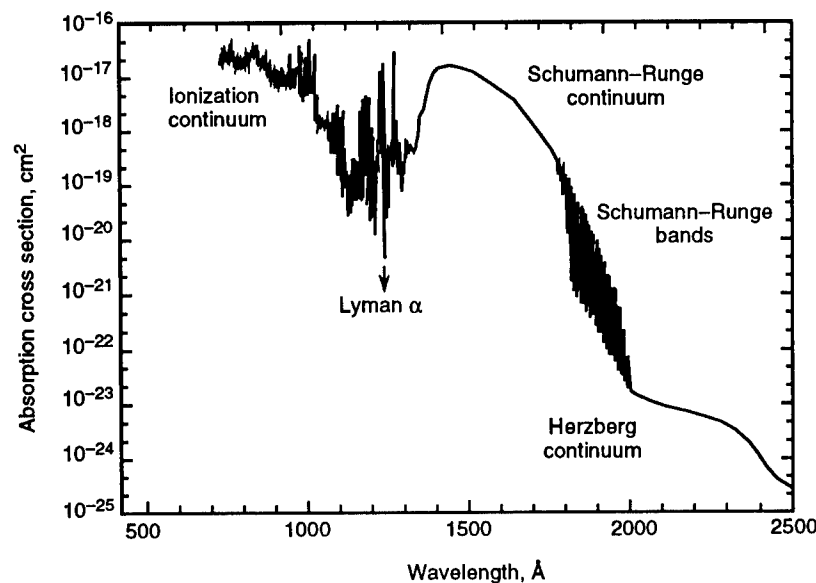


Fig. 1.27 Electronic transitions of oxygen in the ultraviolet.³⁹

Carbon monoxide

Carbon monoxide is a diatomic polar molecule. The fundamental vibration frequency is at 2143.27 cm^{-1} with an integrated band intensity of $9.81 \times 10^{-18}\text{ cm}$. Figure 1.28 plots the low-pressure absorption coefficient of pure CO versus wave number. The formation of the P- and R-branch structure is clear.

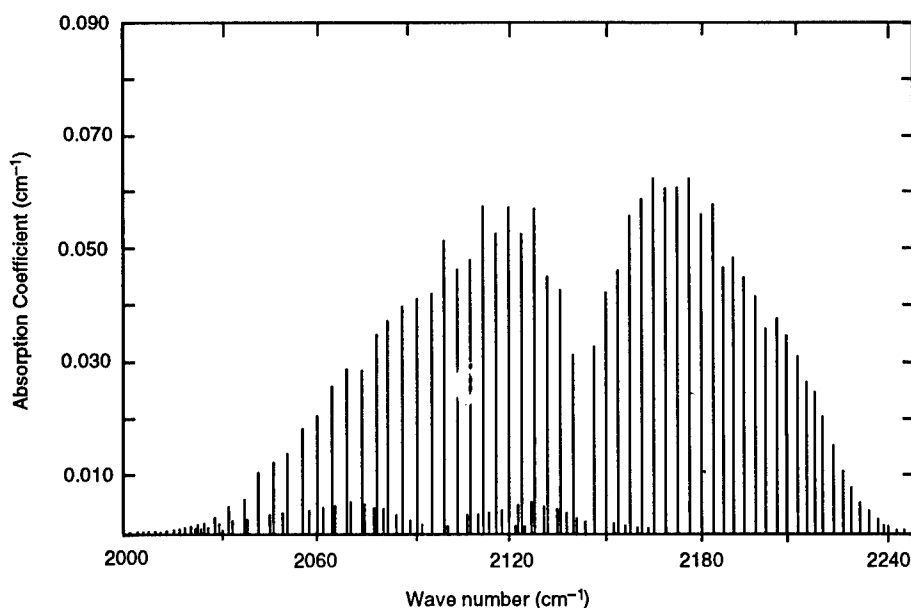


Fig. 1.28 Carbon-monoxide absorption spectrum for $p_{\text{CO}} = 3\text{ Torr}$ and $T = 295\text{ K}$.

Also, a weak isotopic band ($^{13}\text{C}^{16}\text{O}$) is observed. The line positions of CO are well known and CO can be used as a frequency standard.¹⁰⁰

Trace gases

The previous gases significantly contribute to attenuation of radiation in the atmosphere. Trace gases make only minor contributions and represent pollutants and gases formed naturally in the upper atmosphere. The list includes the freons, NO, SO₂, NO₂, NH₃, HNO₃, OH, HF, HCl, HBr, HI, ClO, OCS, HCN, H₂O₂, C₂H₂, C₂H₆, and so on. Molecular constants for some of these gases can be found in Tables 1.6 and 1.7. Details of the spectroscopic properties of these gases are contained on the HITRAN database (see Sec. 1.3.3). Table 1.16 summarizes some basic information on the main isotope of a few trace molecules.³⁸

1.3.2.4 Oxygen and Nitrogen Continua

The nitrogen continuum, due to collision-induced absorption in the fundamental vibration band, occurs between 4.7 and 3.8 μm ; thus, in the earth's atmosphere, it is masked by CO₂ absorption down to 4.1 μm . Figure 1.29(a)

Table 1.16 Trace Gas Properties (from Ref. 38)

Molecule	Classification	Quantum Numbers	Band Locations (cm^{-1})	Integrated Intensity (cm)
NO ₂	Asymmetric top	000-000	0.0	2.16×10^{-19}
		010-000	749.65	5.38×10^{-19}
		001-000	1616.85	6.11×10^{-17}
		111-010	2898.19	1.06×10^{-19}
		101-000	2906.07	2.88×10^{-18}
SO ₂	Asymmetric top	000-000	0.0	2.58×10^{-18}
		010-000	517.75	3.90×10^{-18}
		100-000	1151.71	3.52×10^{-18}
		001-000	1362.03	3.08×10^{-17}
		101-000	2499.87	3.95×10^{-19}
NH ₃	Symmetric top	0000-0000	0.0	1.77×10^{-17}
		0100-0000a	931.64	1.08×10^{-17}
		0100-0000s	968.12	1.12×10^{-17}
		0001-0000s	1630.00	2.05×10^{-18}
		0001-0000a	1630.34	2.05×10^{-18}
HCl	Linear	0-0	0.0	8.07×10^{-18}
		1-0	2885.98	4.52×10^{-18}
		2-0	5667.98	1.07×10^{-19}
HF	Linear	0-0	0.0	5.17×10^{-17}
		1-0	3961.44	1.55×10^{-17}
		2-0	7750.79	4.96×10^{-19}
HNO ₃	Asymmetric top	Rotational	0.0	5.81×10^{-19}
			ν_5	1.26×10^{-17}
			$2\nu_9$	9.84×10^{-18}
			ν_2	2.01×10^{-17}

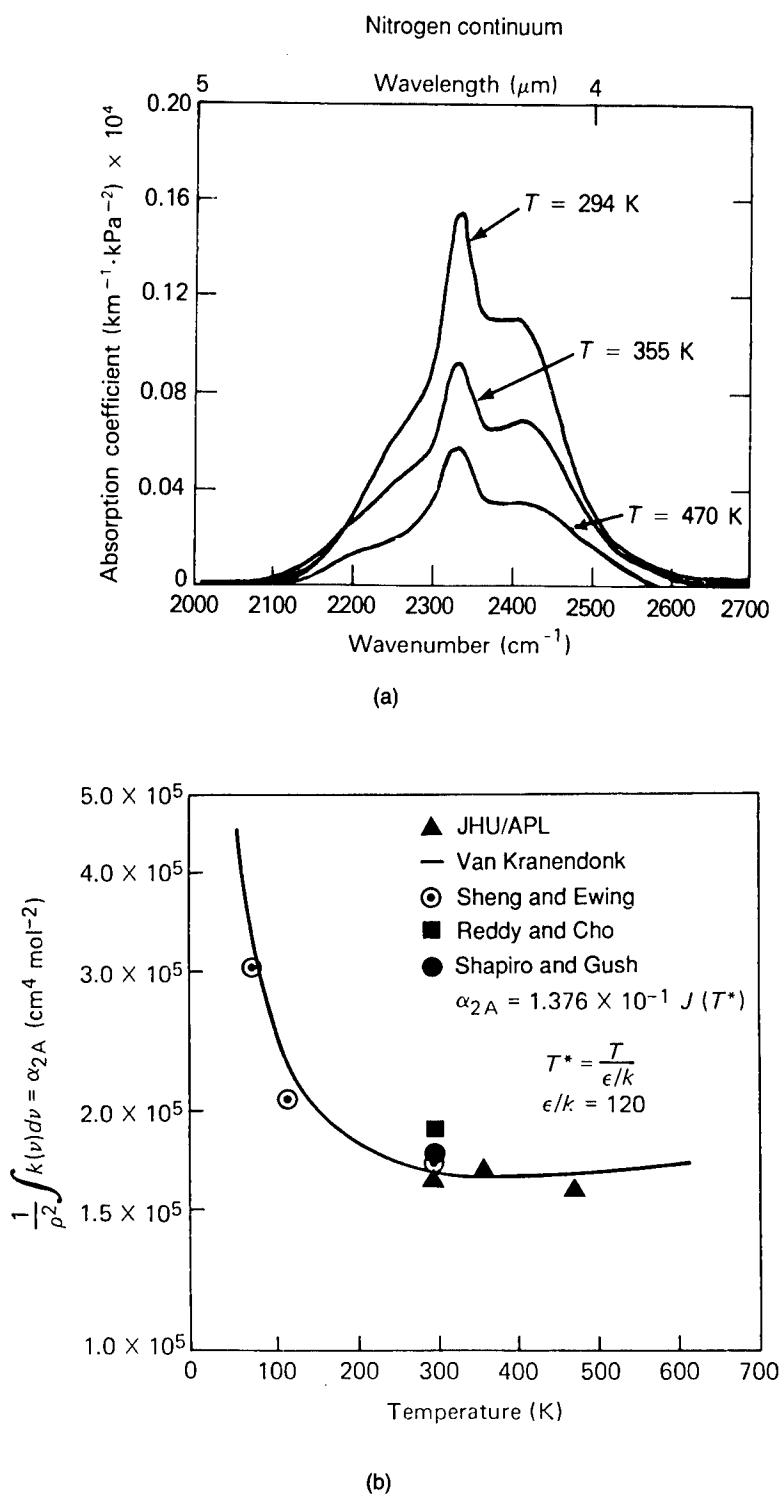


Fig. 1.29 Collision-induced absorption in N_2 : (a) band shape and (b) integrated intensity versus temperature.⁸⁵

illustrates pure nitrogen spectra at a variety of temperatures based on FTS measurements at JHU/APL.⁸⁵ In this case, the entire optical path was under vacuum to avoid CO₂ contamination. The temperature dependence of the integrated intensity divided by the density squared is shown in Fig. 1.29(b). A minor temperature dependence is observed over the range of atmospheric temperatures, and this dependence is modeled by the theory of Van Kranendonk.⁸⁰ Following the work of Sheng and Ewing,⁸¹ we obtain

$$\frac{1}{\rho_a^2} \int k(\nu) d\nu = 1.376 \times 10^{-1} J(T^*) \text{ (cm}^4 \text{ mol}^{-2}\text{)} , \quad (1.130)$$

where

$$J(T^*) = 12\pi \int_0^\infty x^{-8} \left\{ \exp \left[-\left(\frac{4}{T^*} \right) (x^{-12} - x^{-6}) \right] \right\} x^2 dx, \quad (1.131)$$

$$T^* = \frac{T}{100} .$$

The solid curve in Fig. 1.29(b) is Eq. (1.130). The coefficient in front of $J(T^*)$ is obtained by scaling to the experimental data.

In the earth's atmosphere, the effects of oxygen collisions on nitrogen continuum absorption must also be considered. A dimensionless broadening coefficient B of 1.28 was measured by Moskalenko et al.⁸⁴ relative to oxygen (B is 0.78 when relative to nitrogen). Another gas that may be important to nitrogen continuum models is water vapor. Because of the strong dipole moment of water vapor over the quadrupole moment of nitrogen, collisions between water vapor and nitrogen could be very effective in inducing a dipole moment in nitrogen. Thus, the much smaller concentration of water vapor over nitrogen could be neutralized by a large broadening coefficient. To the best of our knowledge, the value of B relative to water vapor has not been determined. Field measurements suggest this may be important and capable of explaining observed discrepancies between atmospheric measurements and laboratory measurements on pure nitrogen.⁷⁵ An analysis of the nitrogen continuum is given by Roney et al.⁹⁷

The collision-induced rotation band of nitrogen also exists and is important for microwave propagation modeling in the atmosphere.⁶³

The oxygen collision-induced-absorption vibration band or continuum occurs at 1556 cm⁻¹ and is masked by the ν_2 vibration band of water vapor in the troposphere. The oxygen continuum is important for long-path attenuation in the upper troposphere and stratosphere. Figure 1.30 illustrates this collision-induced-absorption band as a function of frequency.⁸³

1.3.3 HITRAN Database

High-resolution calculations require a detailed database of spectral-line parameters needed to complete the formulas given in Sec. 1.3.1. With projected computer capabilities of the future, computationally intensive atmospheric transmission codes will become more standard. Thus, the endeavor to create

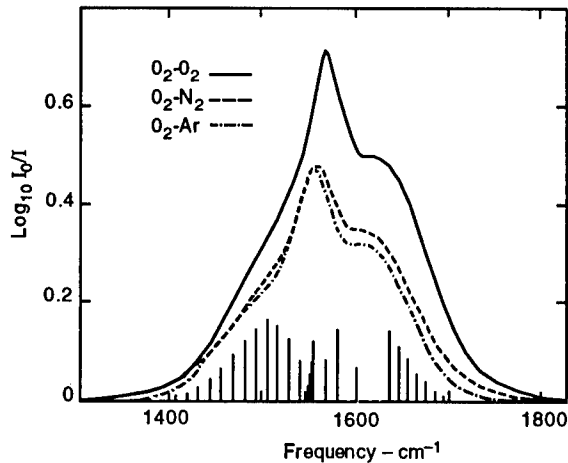


Fig. 1.30 The fundamental absorption band of oxygen for a path length of 40 m. The densities are as follows: pure oxygen 9.59 amagats; oxygen-nitrogen mixture, $\rho_{O_2} = 1.09$ amagats, $\rho_{N_2} = 56$ amagats; oxygen-argon mixture, $\rho_{O_2} = 1.12$ amagats, $\rho_{Ar} = 56.9$ amagats.⁸³ (Note: 1 amagat is the STP ratio of pressure in atm to temperature in K.)

and maintain such a database is vital to improved modeling capabilities. The Phillips Laboratory Geophysics Directorate [formerly Air Force Geophysics Laboratory (AFGL)] has been the United States center for this activity since the late 1960s.¹⁰¹ The latest version of the database became available in 1991. The most recent documentation of the HITRAN database (describing the 1986 database) is available in Ref. 102 and a recent review is given by Rothman.¹⁰³

The HITRAN database is a line-by-line compilation of 348,043 (1986 database) spectral-line parameters (e.g., line position, strength, half-width, lower energy level, etc.) representing 28 different molecules of atmospheric importance. Table 1.17 lists the various molecules and their relative isotopic abundance.¹⁰¹ Table 1.18 shows the parameter format used to organize the data on the tape.¹⁰¹ Each molecule is identified by the number in Table 1.17 along with an indication of the relative isotopic abundance (denoted by 1 for most abundant, 2 for second most abundant, etc.). Line position v_i is given in wave numbers (cm^{-1}). Line strength S' is given in units of $\text{cm}^{-1}/(\text{molecules cm}^{-2})$ (or cm) at $T = 296 \text{ K}$ and $p_a = 1 \text{ atm}$. To convert S of Eq. (1.58) from the AFGL definition of line strength S' , use

$$S \quad (\text{cm}^{-2}) = 7.33882 \times 10^{21} \frac{p_a}{T} [S' \quad (\text{cm})] . \quad (1.132)$$

The transition probability $R [= 3 \times 10^{36} \Sigma |M| I_{ab} g_l]$, where I_{ab} is the isotopic abundance, and see Eqs. (1.58) and (1.59)] is listed next in units of debyes². Air-broadened (collision) half-widths α_c are given in $\text{cm}^{-1}/\text{atm}$ for $T = 296 \text{ K}$. Self-broadened half-widths α_{ca} are given in the same units where available. (Otherwise, Table 1.8 must be used.) The lower-state energy $E'' (=E_l)$ is given

**Table 1.17 Molecular Species on HITRAN Database with Isotopic Abundance
(from Ref. 102)**

Molecule (#)	Isotope	Relative Natural Abundance	Molecule (#)	Isotope	Relative Natural Abundance	
H ₂ O (1)	161	0.9973	HNO ₃ (12)	146	0.9891	
	181	0.0020		61	0.9975	
	171	0.0004		81	0.0020	
	162	0.0003		62	0.00015	
CO ₂ (2)	626	0.9842	HF (14)	19	0.99985	
	636	0.0111		15	0.7576	
	628	0.0040	HCl (15)	17	0.2423	
	627	0.0008		19	0.5068	
	638	0.00044	HBr (16)	11	0.4930	
	637	0.000009		HI (17)	0.99985	
	828	0.000004	ClO (18)	56	0.7559	
	728	0.000002		76	0.2417	
O ₃ (3)	666	0.9928	OCS (19)	622	0.937	
	668	0.0040		624	0.0416	
	686	0.0020		632	0.0105	
N ₂ O (4)	446	0.9904	H ₂ CO (20)	822	0.0019	
	456	0.0036		126	0.9862	
	546	0.0036		136	0.0111	
	448	0.0020		128	0.0020	
CO (5)	447	0.0004	HOCl (21)	165	0.7558	
	26	0.9904		167	0.2417	
	36	0.011		N ₂ (22)	44	0.9928
	28	0.0020		HCN (23)	124	0.9852
CH ₄ (6)	27	0.0004	CH ₃ Cl (24)	215	0.7490	
	211	0.9952		217	0.2395	
	311	0.0111		H ₂ O ₂ (25)	1661	0.9949
O ₂ (7)	212	0.00059		C ₂ H ₂ (26)	1221	0.9776
	66	0.9952		C ₂ H ₆ (27)	1221	0.9770
	68	0.0040		PH ₃ (28)	1111	0.99955
NO (8)	67	0.0008				
	46	0.9940				
SO ₂ (9)	626	0.9454				
	646	0.0420				
NO ₂ (10)	646	0.9916				
	4111	0.9960				
NH ₃ (11)	5111	0.0036				

in units of cm⁻¹. The temperature dependence of the collision half-width follows a power law of the form

$$\alpha_c = \alpha_{c0} \left(\frac{T_0}{T} \right)^n . \quad (1.133)$$

As indicated by Eq. (1.79), *n* is 0.5 and is based on the kinetic theory of gases. Experimental data and more complete theories have shown that this is not always obeyed. For this reason the database also lists *n*, the coefficient of temperature dependence of the air-broadened half-width. Collisions with the absorbing molecule also produce shifts of line position. This is called pressure

**Table 1.18 Example of Direct Image of Parameters on 1986 HITRAN Database
(from Ref. 102)**

Mo	iso	Frequency	Intensity	S'	R	γ	γ_s	E''	n	δ or y	v'	v''	Q'	Q''	IER	IREF
31	800.276500	4.316E-25	3.777E-07	0.0599.0000	1162.00600.76	0.00000	2	12418.6	2517.9	382	0					
281	800.287000	2.270E-23	4.717E-05	0.0750.0000	1483.94700.50	0.00000	2	117.7	18.7	381	0					
101	800.301900	4.680E-23	2.421E-07	0.0630.0000	105.93600.50	0.00000	2	1.84.4	-9.3.7	-84	0					
31	800.304700	1.286E-24	1.131E-05	0.0618.0000	1636.93510.76	0.00000	2	159.951	58.850	382	0					
31	800.322500	1.243E-23	1.274E-06	0.0610.0000	720.65800.76	0.00000	2	11615.1	1614.2	382	0					
101	800.322700	1.840E-22	2.195E-06	0.0630.0000	277.86000.50	0.00000	2	126.224	-25.125	-84	0					
23	800.326900	5.380E-26	2.668E-05	0.0793.1103	1326.41920.75	0.00000	8	3	R 13	186	0					
271	800.332030	1.100E-22	3.212E-02	1.000.0000	2354.24000.50	0.00000	19	14	4.8	382	0					
101	800.361600	1.910E-22	2.278E-06	0.0630.0000	277.80700.50	0.00000	2	126.224	+25.125	+84	0					
31	800.379600	6.380E-24	6.554E-07	0.0602.0000	707.21200.76	0.00000	2	11515.1	1514.2	382	0					
101	800.416400	5.300E-23	1.025E-05	0.0630.0000	851.01800.50	0.00000	2	145.244	+44.143	+84	0					
271	800.416750	1.330E-22	2.035E-02	1.0000.0000	2221.36110.50	0.00000	19	14	3.8	382	0					
31	800.434100	4.273E-25	2.225E-05	0.0618.0000	1982.04700.76	0.00000	3	2501040	49.941	382	0					
22	800.444000	6.390E-26	1.396E-04	0.0652.0846	1844.81880.75	0.00000	8	3	R 38	186	0					
101	800.447000	5.180E-23	1.002E-05	0.0630.0000	851.04100.50	0.00000	2	145.244	-44.143	-84	0					
21	800.451200	3.210E-26	1.731E-05	0.0661.0872	2481.56150.75	0.00000	14	6	P 37	186	0					

FORMAT (I2, I1, F12, 1P2E10.3, 0P2F5.4, F10.4, F4.2, F8.5, 2I3, 2A9, 3I1, 3I2)
= 100 characters per transition

This format corresponds as follows:

- Mo — I2 — Molecule number
- iso — I1 — Isotope number (1—most abundant, 2—second, etc.)
- v — F12.6 — Frequency in cm^{-1}
- S' — E10.3 — Intensity in $\text{cm}^{-1}/(\text{molecules cm}^{-2})$ @ 296 K
- R — E10.3 — Transition probability in debyes² (presently lacking internal partition sum)
- γ — F5.4 — Air-broadened half-width (HWHM) in $\text{cm}^{-1}/\text{atm}^{-1}$ @ 296 K
- γ_s — F5.4 — Self-broadened half-width (HWHM) in $\text{cm}^{-1}/\text{atm}^{-1}$ @ 296 K
- E'' — F10.4 — Lower-state energy in cm^{-1}
- n — F4.2 — Coefficient of temperature dependence of air-broadened half-width
- y — F8.5 — Shift of transition due to pressure (presently empty; some coupling coefficients inserted)
- v' — I3 — Upper-state global quanta index
- v'' — I3 — Lower-state global quanta index
- Q' — A9 — Upper-state local quanta
- Q'' — A9 — Lower-state local quanta
- IER — 3I1 — Accuracy indices for frequency,* intensity, and half-width
- IRef — 3I2 — Indices for lookup of references for frequency, intensity, and half-width (not presently used)

*IER code for frequency when used:

IER	estimated error in wave numbers
0	$\geq 1.$
1	≥ 0.1 and < 1.0
2	≥ 0.01 and < 0.1
3	≥ 0.001 and < 0.01
4	≥ 0.0001 and < 0.001
5	≥ 0.00001 and < 0.0001
6	< 0.00001

shift $\alpha_{c,i}$ [see Eq. (1.81)] and is generally a weak effect. A location for this parameter is included in the database; however, it is generally not available. Coupling coefficients y_i are given, accounting for line mixing [see Sec. 1.3.1.5, Eq. (1.82)] for a few gases (e.g., O₂)¹⁰² in this position as well. The quantum numbers of the upper and lower levels are listed next.

The HITRAN database is available on nine-track magnetic tape from National Climatic Data Center, NOAA, Federal Building, Asheville, North Carolina 28801, telephone (704)259-0682. Other media, used for data storage and

retrieval, containing the HITRAN database will most likely be available in the future.

Other databases exist and one is worth mentioning briefly. The GEISA database is maintained by a French group and is very similar to the HITRAN database.¹⁰⁴ It includes molecules of importance to other planetary atmospheres and therefore may be a useful source for molecules not included on HITRAN.

1.3.4 Band Models

The most practical approach to computing atmospheric broadband absorption (transmittance) is to use an approximate, mathematically workable model of the band structure. This assumes that line positions and strengths are distributed in a way that can be represented by a simple mathematical formula. Band models compute transmittance averaged over a spectral band as defined by

$$\bar{\tau}(\nu) = \frac{1}{\Delta\nu} \int_{\nu - \frac{\Delta\nu}{2}}^{\nu + \frac{\Delta\nu}{2}} \tau(\nu') d\nu' . \quad (1.134)$$

The most commonly used band models are listed below:

1. The Elsasser, or regular model,^{105,106} assumes spectral lines of equal strength, equal spacing, and identical half-widths. The transmission function is averaged over an interval equal to the spacing between the line centers.
2. The statistical, or random model, originally developed for water vapor, assumes that the positions and strengths of the lines are given by a probability function. The statistical model was worked out by Mayer¹⁰⁷ and (independently) Goody.¹⁰⁸
3. The random-Elsasser model¹⁰⁹ is a generalization of the Elsasser and the statistical models. It assumes a random superposition of any number of Elsasser bands of different strengths, spacings, and half-widths.
4. The most accurate, presently available model is the quasi-random model,¹¹⁰ provided the averaging interval can be made sufficiently small. It requires the greatest amount of computation of all the models.

Assuming that the shape of a single spectral line for a homogeneous path in a single absorbing gas is represented by the Lorentz formula, the absorbance is given by

$$(1 - \bar{\tau})\Delta\nu = \overline{\alpha_{abs}}\Delta\nu = \int_{\Delta\nu} \left\{ 1 - \exp \left[-\frac{1}{\pi} \int_{\text{path}} \frac{S' \alpha \rho_a}{(\nu - \nu_0)^2 + \alpha^2} dz \right] \right\} d\nu . \quad (1.135)$$

For a homogeneous path, S' , α , and ρ_a are constant; Eq. (1.135) then further reduces to

$$\overline{\alpha_{\text{abs}}}\Delta\nu = \int_{\Delta\nu} \left\{ 1 - \exp \left[-\frac{S'}{\pi} \frac{\alpha w}{(\nu - \nu_0)^2 + \alpha^2} \right] \right\} d\nu , \quad (1.136)$$

where

$$w = \int_{\text{path}} \rho_a dz \quad (= \rho_a z \text{ for a homogeneous path}) \quad (1.137)$$

and is defined as the absorber amount in g cm^{-2} .^a

A plot of absorbance versus frequency is shown in Fig. 1.31 for different path lengths, or for different values of w . For an optical path of length z_1 , the absorption is small even at the line center. For a path of length z_3 , the center of the line is completely absorbed and any further increase in path length would only change the absorption in the wings of the line. Absorption by paths of length equal to or greater than z_2 are considered strong-line absorption.

If, in Eq. (1.136), one assumes that the interval $\Delta\nu$ is such that substantially the entire line is included, then the limits of integration can be taken from $-\infty$ to ∞ without introducing significant error. When these limits are used, Eq. (1.136) can be solved exactly for the total absorbance. Ladenburg and Reiche¹¹¹ have solved the integral to obtain

$$\overline{\alpha_{\text{abs}}}\Delta\nu = 2\pi\alpha\psi e^{-\psi}[I_0(\psi) + I_1(\psi)] , \quad (1.138)$$

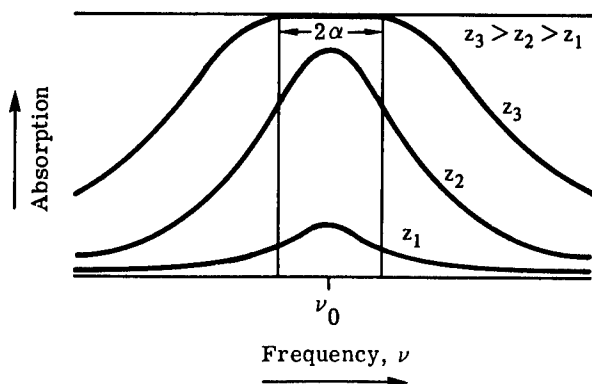


Fig. 1.31 Absorption versus frequency for a single line and for different absorber amounts.

^aThe basic unit for the absorber amount is g cm^{-2} , or alternatively, molecules cm^{-2} . These units refer to the amount of absorber in a transmission path confined within an imaginary cylindrical volume, 1 cm^2 in cross section. Other units are used in the case of water vapor, where one considers the resulting depth of water if the vapor in the cylinder were all condensed. The units are "precipitable centimeters" (pr cm). In the case of the atmospheric compressible gases, the amount of absorber is treated as if it were compressed within the cylinder until sea-level atmospheric pressure is reached. The length of the resulting gas volume would then be designated "atmospheric centimeters," (atm cm).

where $\psi = S'w/2\pi\alpha$ and I_0 and I_1 are modified Bessel functions. For weak-line absorption ($\psi \ll 1$), Eq. (1.138) reduces to

$$\overline{\alpha_{\text{abs}}}\Delta\nu = 2\pi\alpha\psi = S'w \quad (1.139)$$

and absorption is linear with the amount of absorber w . Under conditions of strong-line absorption, ψ is large and Eq. (1.138) reduces to

$$\overline{\alpha_{\text{abs}}}\Delta\nu = \sqrt{S'\alpha w} , \quad (1.140)$$

which is known as the square-root approximation. The above formulations for a single spectral line are also valid for absorption when many spectral lines are present but do not overlap.

1.3.4.1 Elsasser, Statistical, and Other Models

1.3.4.1.1 Elsasser Model

The Elsasser model of an absorption band is formed by repeating a single Lorentz line periodically throughout the interval $\Delta\nu$. This gives rise to a series of lines that are equally spaced and that have a constant strength and half-width throughout the interval. This arrangement of spectral lines was first proposed by Elsasser in 1938.¹⁰⁶

The general expression for absorption by an Elsasser band is

$$\overline{\alpha_{\text{abs}}} = (\sinh\beta) \int_0^Y I_0(Y) \exp(-Y \cosh\beta) dY , \quad (1.141)$$

where

$$\beta = 2\pi\alpha/d$$

$$Y = \beta\psi/\sinh\beta$$

$$\psi = S'w/2\pi\alpha$$

d = mean spacing between spectral lines

I_0 = Bessel function of imaginary argument.

A plot of this function for various values of β is given in Fig. 1.32. Because the function in its present form is difficult to evaluate, considerable effort has been expended comparing approximate formulas and evaluating the integral. Kaplan¹¹² has expanded the integral into a series that is convergent only for values of β less than 1.76. An algorithm for the Elsasser integral that is convergent for all values of β and ψ is written in a computer program used in the calculation of spectral transmittance with the aggregate method (described later). However, it is frequently desirable to work with approximations to the function that are valid for certain conditions.

Weak-line approximation

In Fig. 1.33, the absorption given by Eq. (1.135) is plotted as a function of the product $\beta\psi = S'w/d$ for four values of β . For $\beta \geq 1$, the absorption curves

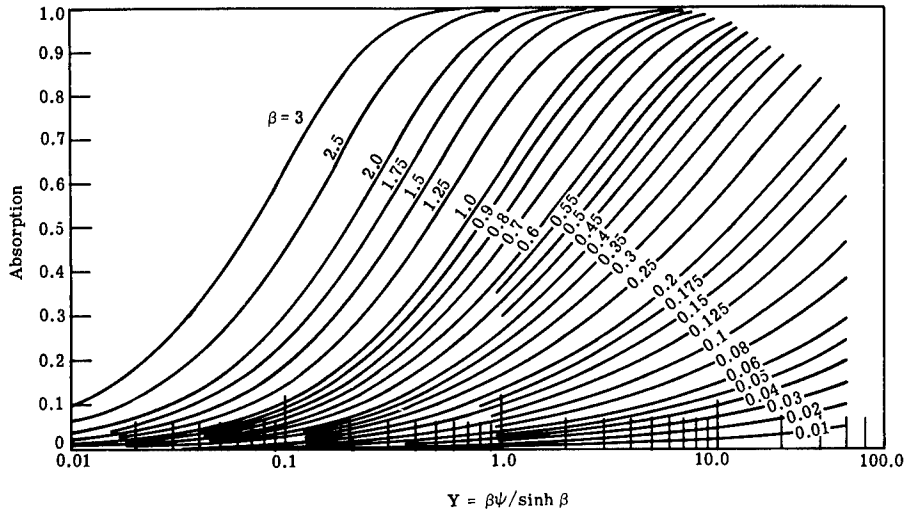


Fig. 1.32 Absorption by a single Elsasser band.

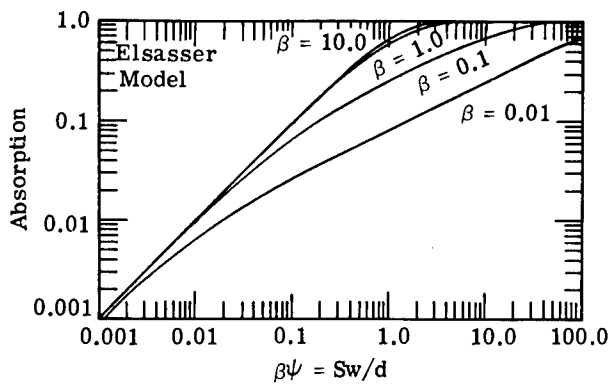


Fig. 1.33 Absorption as a function of $\beta\psi = S'w/d$ for the Elsasser model. The weak-line approximation is the uppermost curve.¹¹²

become nearly superimposed for all values of ψ . Since the parameter β measures the ratio of linewidth to the distance between neighboring lines, $\beta \geq 1$ implies that the spectral lines are strongly overlapping and spectral-line structure is not observable. This condition corresponds to large pressures, which would be realistic for atmospheric paths at low altitudes. For $\beta \geq 1$, Eq. (1.142) can be approximated by

$$\overline{\alpha_{abs}} = 1 - e^{\beta\psi} . \quad (1.142)$$

Equation (1.142) is also a good approximation to Eq. (1.141) whenever the absorption is small at the line centers (small ψ), regardless of the value of β . This approximation is referred to as the weak-line approximation and is independent of the position of the spectral lines within the band. Table 1.19

Table 1.19 Regions of Validity of Various Approximations for Band Absorption*

Approximation	$\beta = 2\pi\alpha/d$	Elsasser Model	Statistical Model; All Lines Equally Intense	Statistical Model; Exponential Line Intensity Distribution
Strong-line approximation	0.001	$\psi > 1.63$	$\psi > 1.63$	$\psi_0 > 2.40$
	0.01	$\psi > 1.63$	$\psi > 1.63$	$\psi_0 > 2.40$
	0.1	$\psi > 1.63$	$\psi > 1.63$	$\psi_0 > 2.30$
	1.0	$\psi > 1.35$	$\psi > 1.10$	$\psi_0 > 1.40$
	10.0	$\psi > 0.24$	$\psi > 0.24$	$\psi_0 > 0.27$
	100.00	$\psi > 0.024$	$\psi > 0.024$	$\psi_0 > 0.24$
Weak-line approximation	0.001	$\psi < 0.20$	$\psi < 0.20$	$\psi_0 < 0.10$
	0.01	$\psi < 0.20$	$\psi < 0.20$	$\psi_0 < 0.10$
	0.1	$\psi < 0.20$	$\psi < 0.20$	$\psi_0 < 0.10$
	1.0	$\psi < \infty$	$\psi < 0.23$	$\psi_0 < 0.11$
	10.0	$\psi < \infty$	$\psi < \infty$	$\psi_0 < \infty$
	100.0	$\psi < \infty$	$\psi < \infty$	$\psi_0 < \infty$
Nonoverlapping-line approximation	0.001	$\psi < 600000$	$\psi < 63000$	$\psi_0 < 80000$
	0.01	$\psi < 6000$	$\psi < 630$	$\psi_0 < 800$
	0.1	$\psi < 60$	$\psi < 6.30$	$\psi_0 < 8.00$
	1.0	$\psi < 0.7$	$\psi < 0.22$	$\psi_0 < 0.23$
	10.0	$\psi < 0.02$	$\psi < 0.020$	$\psi_0 < 0.020$
	100.00	$\psi < 0.002$	$\psi < 0.0020$	$\psi_0 < 0.0020$

*When $\psi = S'w/2\pi\alpha$ satisfies the given inequalities, the indicated approximation for the absorption is valid with an error of less than 10%. For the exponential line intensity distribution, $\psi_0 = S'_0 w/2\pi\alpha$, where S'_0 is defined by $P(S') = S'_0^{-1} \exp(-S'/S'_0)$.

summarizes the regions of β and ψ for which the weak-line approximation is valid with an error of less than 10%. This approximation is particularly useful in extrapolating the absorption to small values of ψ and to large values of pressure. The weak-line approximation reduces to the linear approximation when the absorption is small, even if the lines overlap; i.e., when $\beta\psi$ is small, all terms in the expansion of the exponential of Eq. (1.142) are neglected except the linear one.

Strong-line approximation

Long atmospheric paths at high altitudes have large values of w and small values of pressure. Under these conditions, the absorption at the line centers is usually complete (large ψ), the half-widths are narrow, and the lines do not overlap strongly (small β). For large ψ and small β , Eq. (1.135) may be approximated by an error function:

$$\overline{\alpha_{\text{abs}}} = \text{erf}\left(\frac{1}{2}\beta^2\psi\right)^{1/2}, \quad (1.143)$$

where

$$\text{erf}(a) = \frac{2}{\sqrt{\pi}} \int_0^a e^{-t^2} dt. \quad (1.144)$$

This is known as the strong-line approximation to the Elsasser band model.

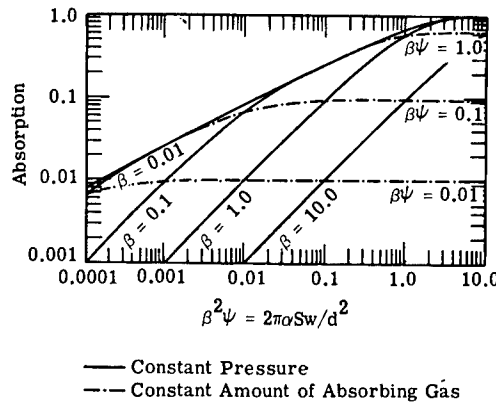


Fig. 1.34 Absorption of a function of $\beta^2\psi = 2\pi\alpha(S'w/d^2)$ for the Elsasser model. The curves are shown for constant pressure ($\beta = \text{constant}$) and the constant amount of the absorbing gas ($\beta\psi = \text{constant}$). The strong-line approximation is the uppermost curve.¹¹³

Figure 1.34 is a plot of Eq. (1.141) with absorption as a function of $\beta^2\psi$. For $\beta \leq 0.01$, Eqs. (1.141) and (1.143) are nearly equal when $\beta^2\psi > 0.0003$. If $\beta \leq 0.1$, then Eq. (1.143) is valid whenever $0.1 \leq \alpha_{\text{abs}} \leq 1.0$. This includes most values of absorption that are usually of interest. This case differs from the square-root approximation in that it does not require nonoverlapping. For overlapping spectral lines (larger β), the values of ψ for which the approximation is valid is simply restricted to large values of ψ . Specific regions of validity are given in Table 1.19.

Nonoverlapping approximation

The third approximation to the Elsasser band model is known as the non-overlapping approximation. It is particularly useful for extrapolating the absorption to small values of w and small values of pressure, which correspond to short paths at high altitudes. Under these conditions, Eq. (1.141) reduces to

$$\overline{\alpha_{\text{abs}}} = \beta\psi e^{-\psi}[I_0(\psi) + I_1(\psi)] . \quad (1.145)$$

This is exactly the same expression as that obtained for the absorption by a single spectral line.

In Fig. 1.35, $\alpha_{\text{abs}}/\beta$ is given as a function of ψ . The uppermost curve is the nonoverlapping approximation. For $\psi \ll 1$, the curve has a slope of 1 (i.e., a region where the weak-line approximation is valid) and for $\psi \gg 1$ the curve has a slope of one-half (i.e., a region where the strong-line approximation is valid). The regions of validity for various values of β and ψ are given in Table 1.19.

The general expression for absorption by an Elsasser band given by Eq. (1.141) and the strong-line approximation given by Eq. (1.143) are useful for determining absorption by CO₂, since the bands consist of fairly regularly spaced lines. However, the bands of H₂O and O₃ have a highly irregular, fine structure and cannot be well described by Eq. (1.141). Statistical methods must

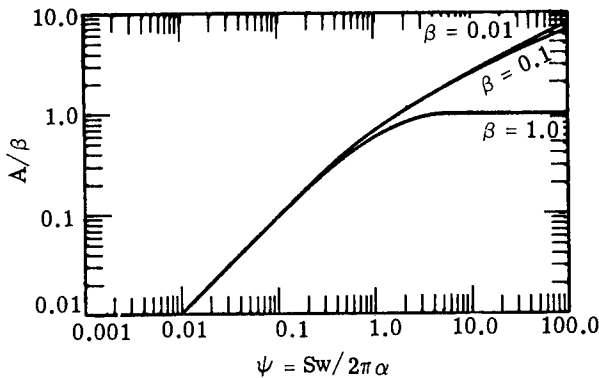


Fig. 1.35 Absorption divided by β as a function of $\psi = S'w/2\pi\alpha$ for the Elsasser model.¹¹³ The nonoverlapping-line approximation is the uppermost curve.

be used to develop an analytical expression for the transmittance function for H₂O and O₃.

Golden¹¹⁴ has described an Elsasser-like model using the Doppler shape instead of a Lorentz line shape, and Goody and Yung discuss the Voigt shape.¹¹⁵

1.3.4.1.2 Statistical Band Model

With a spectral interval

$$\Delta\nu = nd , \quad (1.146)$$

where there are n lines of mean wave-number spacing d , and with $P(S')dS'$ the normalized probability that a line will have a strength between S' and $S' + dS'$, with the requirement that

$$\int_0^\infty P(S') dS' = 1 . \quad (1.147)$$

The expression for transmittance is

$$\bar{\tau} = \exp \left[- \frac{1}{d} \int_0^\infty (\bar{\alpha}_{s1}\Delta\nu) P(S') dS' \right] , \quad (1.148)$$

where

$$\bar{\alpha}_{s1}\Delta\nu = \int_{\Delta\nu} 1 - e^{-k_a w} d\nu \quad (1.149)$$

and α_{s1} is the absorbance of a single line integrated over the interval $\Delta\nu$.

Equal-intensity lines

Equation (1.148) can be evaluated for two special cases. When all the lines have equal intensities, $P(S) = \delta(S - S_0)$, in which $\delta(x)$ is the Dirac delta function, and Eq. (1.148) reduces to

$$\bar{\tau} = \exp\left(\frac{\overline{\alpha_{s1}}\Delta\nu}{d}\right) = \exp\{-\beta\psi e^{-\psi}[I_0(\psi) + I_1(\psi)]\} . \quad (1.150)$$

In terms of absorption,

$$\overline{\alpha_{abs}} = 1 - \exp\{-\beta\psi e^{-\psi}[I_0(\psi) + I_1(\psi)]\} . \quad (1.151)$$

If each of the lines absorbs weakly, so that ψ is small, then Eq. (1.142) reduces to

$$\overline{\alpha_{abs}} = 1 - e^{-\beta\psi} . \quad (1.152)$$

If the lines absorb strongly, then Eq. (1.151) reduces to

$$\overline{\alpha_{abs}} = 1 - \exp\left[-2\left(\frac{S'\alpha w}{d}\right)^{1/2}\right] . \quad (1.153)$$

In terms of β and ψ ,

$$\overline{\alpha_{abs}} = 1 - \exp\left[-\left(\frac{2}{\pi}\beta^2\psi\right)^{1/2}\right] . \quad (1.154)$$

The nonoverlapping approximation to Eq. (1.151) is obtained from the first term in the expansion of the exponential, so that

$$\overline{\alpha_{abs}} = \beta\psi e^{-\psi}[I_0(\psi) + I_1(\psi)] . \quad (1.155)$$

This is the same expression as that obtained for the nonoverlapping approximation to the Elsasser model [Eq. (1.145)].

Line strength with an exponential probability distribution

When lines are of different strength and the distribution for the probability of their strength is an exponential distribution, namely,

$$P(S') = \frac{1}{S'_0} \exp\left(-\frac{S'}{S'_0}\right) , \quad (1.156)$$

where S'_0 is a mean line strength, then

$$\bar{\tau} = \exp \left[-\frac{wS'_0\alpha}{d \left(\alpha^2 + \frac{wS'_0\alpha}{\pi} \right)^{1/2}} \right]. \quad (1.157)$$

In terms of absorption, and β and ψ ,

$$\overline{\alpha_{\text{abs}}} = 1 - \exp \left[\frac{-\beta\psi_0}{(1 + 2\psi_0)^{1/2}} \right], \quad (1.158)$$

where $\psi_0 = S'_0 w / 2\pi\alpha$. This is the formula developed by Goody¹⁰⁸ and is therefore referred to as the Goody band model.

The weak-line approximation to Eq. (1.158) is obtained when $\psi_0 \ll 1$. Under these conditions,

$$\overline{\alpha_{\text{abs}}} = 1 - e^{-\beta\psi_0}. \quad (1.159)$$

The strong-line approximation to the statistical model with an exponential distribution of line strengths is obtained when $\psi_0 \gg 1$. Under these conditions, Eq. (1.158) becomes

$$\overline{\alpha_{\text{abs}}} = 1 - \exp \left[-\left(\frac{1}{2} \beta^2 \psi_0 \right)^{1/2} \right]. \quad (1.160)$$

The nonoverlapping approximation is obtained from Eq. (1.158) when the exponent is small and is therefore given by the first two terms of the expansion, or

$$\overline{\alpha_{\text{abs}}} = \frac{\beta\psi_0}{(1 + 2\psi_0)^{1/2}}. \quad (1.161)$$

Strong-line, weak-line, and nonoverlapping approximations

These three approximations to the statistical models are discussed concurrently because they are so closely related. For the weak-line approximation, absorption is given by $\alpha_{\text{abs}} = 1 - \exp(-\beta\psi)$, similar to that for the Elsasser model. When an exponential distribution of line strengths is assumed, ψ is replaced by ψ_0 . This confirms that weak-line absorption is independent of the arrangement of the spectral lines within the band. Absorption versus $\beta\psi$ is plotted for Eq. (1.151) in Fig. 1.36. The solid curves give the absorption for the statistical model for the case in which all lines are equally strong. The dashed curves give the absorption for the statistical model with an exponential distribution of line strengths. The uppermost solid and dashed curves represent the weak-line approximations for those strength distributions. The regions of validity are given in Table 1.19. When all lines are equally strong, the weak-line approximation is always valid within 10% when $\psi < 0.2$. It is valid for the exponential strength distribution when $\psi < 0.1$.

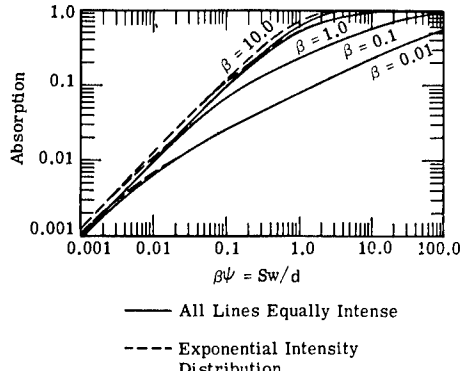


Fig. 1.36 Absorption as a function of $\beta\psi = S'w/d$ for the statistical model. The absorption for a model in which the spectral lines are all of equal intensity is compared to that for a model in which the spectral lines have an exponential intensity-distribution function. The weak-line approximation is the uppermost curve.¹¹³

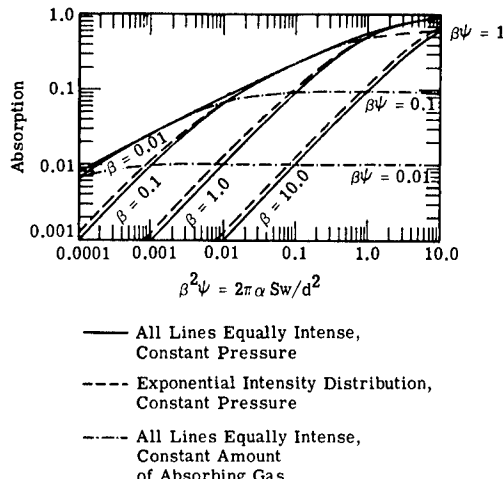


Fig. 1.37 Absorption as a function of $\beta^2\psi = 2\pi\alpha S'w/d^2$ for the statistical model. Curves are shown for constant pressure ($\beta = \text{constant}$) and for the constant amount of the absorbing gas ($\beta\psi = \text{constant}$). The absorption is shown when all the spectral lines have equal intensity and when there is an exponential intensity-distribution function. The strong-line approximation is the uppermost curve.¹¹³

The strong-line approximations to the statistical model for all lines of equal strength and for an exponential distribution of line strengths are given by Eqs. (1.154) and (1.60), respectively. The absorption for these models as a function of $\beta^2\psi$ is shown in Fig. 1.37. The strong-line approximation is the uppermost curve in the figure. The distribution of the line strengths in a band only slightly influences the shape of the absorption curve. As with the strong-line approximation to the Elsasser model, the strong-line approximation to the statistical model for either distribution of the line strengths is always valid where $\beta \leq 0.1$ and $0.1 \leq \alpha_{\text{abs}} \leq 1$. The complete regions of validity are given in Table 1.19.

For all lines of equal strength, the absorption is given by the expression used for the nonoverlapping approximation to the Elsasser model; namely,

$$\overline{\alpha_{\text{abs}}} = \beta\psi e^{-\psi} [I_0(\psi) + I_1(\psi)] . \quad (1.162)$$

For an exponential distribution of line strengths, the absorption is given by Eq. (1.161). Therefore, the strength distribution, but not the spacing of the spectral lines, influences the absorption curve in this approximation. In Fig. 1.38, $\alpha_{\text{abs}}/\beta$ is plotted as a function of ψ for the statistical model. The nonoverlapping approximation to the Elsasser model has a considerably larger region of validity because the spectral lines begin to overlap at considerably larger path lengths for the Elsasser model than for the statistical model (Table 1.19).

These three approximations to the band models of Elsasser and Goody provide a reliable means for the extrapolation of laboratory absorption data to

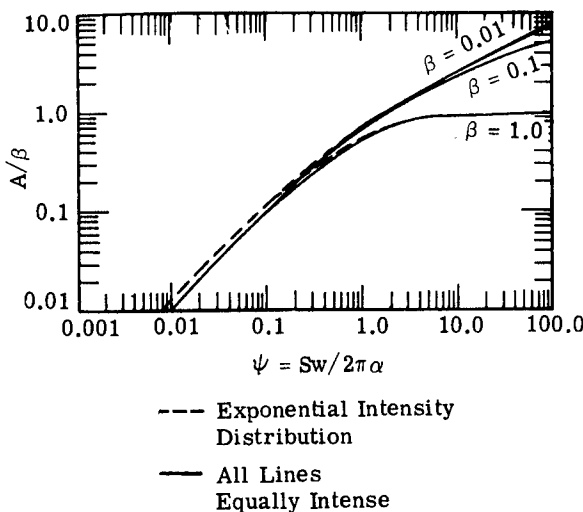


Fig. 1.38 Absorption divided by β as a function of $\psi = S'w/2\pi\alpha$ for the statistical model. The absorption for a model in which the spectral lines are all of equal intensity is compared to that for a model in which the spectral lines have an exponential intensity-distribution function. The nonoverlapping-line approximation is the uppermost curve.¹¹³

values of the pressure and path length. For example, the absorption for large values of pressure can be obtained from the strong- and weak-line approximations, depending on whether w is relatively large or small. For extrapolation to small values of pressure, one may use all three approximations in their respective region of validity; however, the nonoverlapping-line approximation is valid over the largest range of values of w . For extrapolation to large values of w , one may use either the strong- or weak-line approximation, but the former is valid over a much wider range of pressure than the latter. For extrapolation to small values of w , one may use all three approximations in their respective regions of validity; however, the nonoverlapping-line approximation is valid over a wider range of pressure. In general, atmospheric slant paths of interest to the systems engineer contain relatively large amounts of absorber, and the range of pressures is such that the strong-line approximation to any of the models is applicable.

Exponential-tailed S^{-1} random-band model

Malkmus¹¹⁶ described a model comprising a line strength distribution that is defined by

$$P(S') \propto S'^{-1} \exp\left(-\frac{1}{\pi} \frac{S'}{S'_E}\right), \quad (1.163)$$

where S'_E is fixed in the expressions

$$\lim_{w \rightarrow 0} \left(\frac{\bar{W}/d}{w} \right) = \frac{S'_E}{d_E} \quad (1.164)$$

and

$$\lim_{w \rightarrow \infty} \left(\frac{\bar{W}/d}{w^{1/2}} \right) = \frac{2(S'_E \alpha)^{1/2}}{d_E}, \quad (1.165)$$

with $W/d = -\ln(\tau_{\Delta\nu})$, an experimentally determined value. The resultant calculated transmittance is given by

$$\bar{\tau}_{\Delta\nu} = \exp \left\{ -\frac{2\alpha}{d_E} \left[\left(1 + \frac{S'_E w}{\alpha} \right)^{1/2} - 1 \right] \right\} \quad (1.166)$$

$$= \exp \left\{ -\frac{\beta_E}{\pi} [(1 + 2\pi\psi_E)^{1/2} - 1] \right\}. \quad (1.167)$$

1.3.4.1.3 Random Elsasser Band Model

For some gases and spectral regions, absorption can be represented more accurately by the random Elsasser band model than by either the statistical or Elsasser model alone. This is a natural generalization of the original models that assumes that the absorption can be represented by the random superposition of Elsasser bands. The individual bands may have different line spacings, half-widths, and strengths. As the number of superposed Elsasser bands becomes large, the predicted absorption approaches that of the usual statistical model.

The absorption for N randomly superposed Elsasser bands with arbitrary strengths, half-widths, and line spacings is given by

$$\overline{\alpha_{\text{abs}}} = 1 - \prod_{i=1}^N [1 - \alpha_{E,i}(\psi_i, \beta_i)], \quad (1.168)$$

where

$$\begin{aligned} \psi &= S'_i w / 2\pi\alpha_i \\ \beta_i &= 2\pi\alpha_i / d_i \\ S'_i \text{ and } \alpha_i &= \text{the line strength and half-width of the } i\text{'th Elsasser band} \\ d_i &= \text{the line spacing of the } i\text{'th band.} \end{aligned}$$

The derivation of this general equation for different strengths, half-widths, and line spacings is discussed in detail by Plass.¹⁰⁹

1.3.4.1.4 Quasi-Random Model

The quasi-random model is the most accurate and, necessarily, the most complicated of the band models. It is especially useful when the absorbance is required over a wide range of path lengths and pressures.

The spectral lines in an actual band are arranged neither as regularly as required by the Elsasser band model nor in as random a fashion as in the

statistical model, but there is some order in their arrangement. In the quasi-random model, the absorptance is calculated first for a frequency interval that is much smaller than the interval size of interest. This localizes the stronger lines to a narrow interval around their actual positions and prevents the introduction of spurious overlapping effects. The absorptance of this narrow interval is calculated from the equation for the single-line absorptance over a finite interval. The absorptance for each of the N spectral lines in the interval is calculated separately and the results combined by assuming a random placing of the spectral lines within the small interval. The absorption from the wings of lines in neighboring intervals is included in the calculation. The results are averaged for at least two different arrangements of the mesh that divides the spectrum into frequency intervals. Finally, the absorbance values for all of the small intervals that fill the larger interval of interest are averaged to obtain the final value for the absorbance. A computer is commonly used to calculate results for this model when many spectral lines are involved. The many weak spectral lines and their relative spacing are accurately taken into account by this model.

The absorbance for the quasi-random model is given by

$$\overline{\alpha_{\text{abs}}} = \frac{1}{n_j} \sum_{j=1}^n \alpha_{\text{abs}_j}, \quad (1.169)$$

where α_{abs_j} is the absorbance of each of the n smaller wave-number intervals of width D into which the original interval $\Delta\nu$ is subdivided. The absorptance is calculated from

$$\overline{\alpha_{\text{abs}}_j} = 1 - \prod_{i=1}^M [1 - \alpha_{\text{sl}}(\psi_{i,j}; \beta_{i,j})], \quad (1.170)$$

where α_{sl} is the single-line absorbance of the i 'th line over the j 'th finite interval D and M is the number of lines in the j 'th frequency interval D .¹¹⁰

References 117 and 118 give absorptance tables for H₂O and CO₂ based on the quasi-random-model calculations. In these calculations, the lines in the small frequency interval were grouped by line-strength decades. The average strength and number of lines in each of these decades were calculated and used in Eq. (1.170). All lines (from all isotopic species) having strengths greater than 10⁻⁸ of the strongest line in an absorption region were included in the calculation.

1.3.4.1.5 Temperature and Frequency Dependence of Band-Model Parameters

Table 1.20 is a summary of the band models that yield closed-form expressions for spectral-band absorption. All of these expressions are functions of two parameters, β and ψ , which in turn are functions of temperature, pressure, absorber concentration, and wave number of wavelength (or frequency).

Since the variation of line strength with temperature is different for each spectral line, it would be impossible to include the effect of temperature on line strength and still retain the band-model expressions in closed form. For

Table 1.20 Summary of Closed-Form Expressions for Spectral Absorbance*

Band Model	Approximation	Equation
Single Lorentz line	None	$\bar{\alpha}_{\text{abs}} = \frac{1}{\Delta\nu} 2\pi\alpha\psi e^{-\psi} [I_0(\psi) + I_1(\psi)]$
Single Lorentz line	Linear	$\bar{\alpha}_{\text{abs}} = S'w/\Delta\nu$
Single Lorentz line	Square Root	$\bar{\alpha}_{\text{abs}} = 2\left(\frac{S'\alpha w}{\Delta\nu}\right)^{1/2}$
Elsasser band	None	$\bar{\alpha}_{\text{abs}} = \sinh\beta \int_0^Y I_0(Y) \exp(-Y\cosh\beta) dY$
Elsasser band	Weak	$\bar{\alpha}_{\text{abs}} = 1 - e^{-\beta\psi}$
Elsasser band	Strong	$\bar{\alpha}_{\text{abs}} = \text{erf}\left(\frac{1}{2}\beta^2\psi\right)^{1/2}$
Statistical band (exponential)	None	$\bar{\alpha}_{\text{abs}} = 1 - \exp\left[\frac{-\beta\psi_0}{(1 + 2\psi_0)^{1/2}}\right]$
Statistical band	None	$\bar{\alpha}_{\text{abs}} = 1 - \exp\{-\beta\psi e^{-\psi}[I_0(\psi) + I_1(\psi)]\}$
Statistical band (exponential and equal)	Weak	$\bar{\alpha}_{\text{abs}} = 1 - e^{-\beta\psi}$
Statistical band (exponential)	Strong	$\bar{\alpha}_{\text{abs}} = 1 - \exp\left[-\left(\frac{1}{2}\beta^2\psi_0\right)^{1/2}\right]$
Statistical band (equal)	Strong	$\bar{\alpha}_{\text{abs}} = 1 - \exp\left[-\left(\frac{2}{\pi}\beta^2\psi\right)^{1/2}\right]$
Exponential-tailed S^{-1} statistical band	Strong	$\bar{\alpha}_{\text{abs}} = 1 - \exp\left\{-\frac{\beta_E}{\pi}[(1 + 2\pi\psi_E)^{1/2} - 1]\right\}$
Random Elsasser band (equal line strengths, half-widths, and spacings)	Strong	$\bar{\alpha}_{\text{abs}} = 1 - \left[1 - \text{erf}\left(\frac{1}{2}\frac{\beta^2\psi}{N^2}\right)^{1/2}\right]^N$

* $\beta = 2\pi\alpha/d$, $\psi = S'w/2\pi\alpha$, where S' is the line strength (S'_0 is mean strength), α is the Lorentz-line half-width, d is the (mean) line spacing, and w is the absorber amount.

this reason, the band-model expressions in their present form can be used only to predict absorption for homogeneous paths at standard temperature. Since Drayson¹¹⁹ has shown that the effect of temperature on line half-width has a secondary effect on absorption, this dependence is neglected also. Therefore, if $T = T_0$, the expressions for β and ψ become

$$\beta = \left(\frac{2\pi\alpha_0}{d} \frac{P}{P_0}\right) = \frac{2\pi\alpha_0}{d} P , \quad (1.171)$$

$$\psi = \left(\frac{Sw}{2\pi\alpha_0} \frac{P_0}{P}\right) = \frac{S}{2\pi\alpha_0} \frac{w}{P} , \quad (1.172)$$

where α_0 is the half-width at standard conditions, per unit pressure.

The expressions listed in Table 1.20 are of the following general form:

1. $\alpha_{\text{abs}} = \alpha_{\text{abs}}(\beta, \psi)$ when no approximation of the model is assumed.
2. $\alpha_{\text{abs}} = \alpha_{\text{abs}}(\beta^2 \psi)$ for the strong-line approximation.
3. $\alpha_{\text{abs}} = \alpha_{\text{abs}}(\beta \psi)$ for the weak-line approximation.

The first expression is a function of two frequency-dependent parameters, $2\pi\alpha_0$, and two path parameters, w and P . The second expression gives absorption as a function of one frequency-dependent parameter, $2\pi\alpha_0 S'/d^2$, and two path parameters, w and P . The last is a function of S'/d and w , being independent of pressure.

The next problem in completely specifying the absorption expressions is that of evaluating the frequency-dependent parameters by empirically fitting the respective equations to laboratory, homogeneous-absorption spectra. The empirical procedure is most involved when no approximations to the model are assumed, since in this case two parameters must be evaluated. After the frequency-dependent parameters have been specified and the values of w and P have been determined for a given slant path, it becomes a simple matter to generate absorption spectra.

There are two practical methods for calculating spectral transmittance, the aggregate and LOWTRAN methods.¹²⁰ The aggregate method, so-called because it uses a selected collection of the conventional two-parameter models described earlier in this chapter, is perhaps more adaptable to a wide variety of different atmospheric conditions than LOWTRAN, which is strictly empirical and depends essentially on a single adjustable parameter. However, for transmittances between roughly 10 and 90%, the values calculated using either method are not greatly different, and the simplicity of using LOWTRAN makes it much more attractive for routine computations. Neither method perfectly reproduces the results of field measurements. Direct line-by-line calculations are required to achieve accuracies consistent with that of the basic data.

1.3.4.1.6 Aggregate Method

Table 1.21 shows which models are used for different spectral regions for the various atmospheric molecules. Details of the aggregate method are contained in Chapter 5 of *The Infrared Handbook* (see Bibliography).

1.3.4.2 LOWTRAN Method

This method is empirical, yielding a form for the transmittance given by (wave-number resolution = 20 cm^{-1})

$$\bar{\tau}(\lambda) = f[G_v, w, P^n] = f[G(\lambda), w^*], \quad (1.173)$$

where

G_v = spectral coefficients, independent of temperature and pressure,
empirically derived from the HITRAN database with data points
every 5 cm^{-1}

Table 1.21 Summary of Band Models for the Aggregate Method (from Ref. 121)

Gas	Spectral Region (μm)	Approximate Resolution (μm)	Model	Coefficient Acquisition Procedure	Source of Data
H ₂ O	1 to 2	0.10	Strong-line Goody*	Empirical fit to lab data	Howard et al. ¹²²
	2. to 4.3	0.05	Goody*	Empirical fit to lab data	Burch et al. ¹²³
	4.3 to 15	0.50	Strong-line Goody*	Empirical fit to lab data	Howard et al. ¹²²
	7.0 to 30	—	H ₂ O continuum	Empirical fit to lab data	Burch ¹²⁴ and Bignell ¹²⁵
	15 to 30	1.00	Goody*	Direct from line parameters	McClatchey et al. ¹²⁶
CO ₂	1.37 to 2.64	0.20	Empirical	Empirical fit to lab data	Howard et al. ¹²²
	2.64 to 2.88	0.01	Classical Elsasser	Empirical fit to lab data	Burch et al. ¹²³
	4.184 to 4.454	0.02	Classical Elsasser	Empirical fit to lab data	Bradford et al. ¹²⁷
	4.465 to 5.355				
	9.13 to 11.67	0.50	Empirical	Empirical fit to lab data	Howard et al. ¹²²
	11.67 to 19.92	0.10	Temperature-dependent classical Elsasser	Empirical fit to line-by-line spectra	Drayson and Young ¹²⁸
O ₃	9.398 to 10.19	0.10	Modified classical Elsasser	Empirical fit to lab data	Walshaw ¹²⁹
	11.7 to 15.4	0.50	Goody*	Empirical fit to lab data	McCaa and Shaw ¹³⁰
	4.228 to 4.73	0.50	Strong-line Elsasser	Empirical fit to lab data	Plyler and Barker ¹³¹
N ₂ O	7.53 to 8.91	0.50	Classical Elsasser	Empirical fit to lab data	Burch et al. ¹²³
	15.4 to 19.3	0.50	Goody*	Empirical fit to lab data	Burch et al. ¹²³
CH ₄	5.91 to 9.1	0.10	Classical Elsasser	Empirical fit to lab data	Burch et al. ¹²³

*The Goody model is the statistical model with an exponential line-strength distribution.

$$w = \text{quantity of absorber} = \int_z^\infty \rho_a(z') dz'$$

P = quantity of pressure

$$w^* = \text{equivalent absorber amount} = w [P/P_0(T_0/T)^{1/2}]^n,$$

where $P_0 = 1$ atm and $T_0 = 273$ K. This is a single-parameter band model depending only on $w^*(P, T)$, a density-path-length variable times pressure divided by the square root of temperature raised to an empirical exponent n , and does not fully represent the correct temperature dependence. For this reason LOWTRAN calculations should be checked against more complete models (such as FASCODE) before a series of similar calculations are made. The pressure and temperature factor in w^* represents contributions from absorption-line half-widths.

The functional form of τ is determined empirically for three classes of atmospheric gases, water vapor, ozone, and uniformly mixed gases (e.g., CO₂, CH₄, N₂O, etc.). Figure 1.39 illustrates these different curves.^{126,132} The details of the band structure are represented empirically by τ , which greatly simplifies the previously described band-model approach. Setting n in Eq. (1.173) to zero or unity will lead to the weak-line or the strong-line approximation, respectively. The mean values of n are determined to be 0.9 for H₂O, 0.75 for the uniformly mixed gases, and 0.4 for ozone. The fact that such simple curves can be generated by a diverse database is the strength of the LOWTRAN method. Figures 1.40 to 1.42 present the G_ν functions for ozone, water vapor, and the uniformly mixed gases, respectively, from 0 to 5000 cm⁻¹. G_ν is determined from the HITRAN database degraded to 20 cm⁻¹ resolution.

The equivalent absorber amount is

$$w^* = \int_0^\infty \rho_a(z') \left(\frac{P}{P_0} \sqrt{\frac{T_0}{T}} \right)^n dz' . \quad (1.174)$$

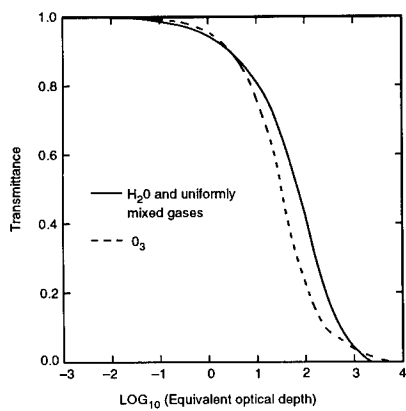


Fig. 1.39 LOWTRAN empirical transmittance functions versus \log_{10} of the effective optical depth ($G_\nu w^*$).¹³²

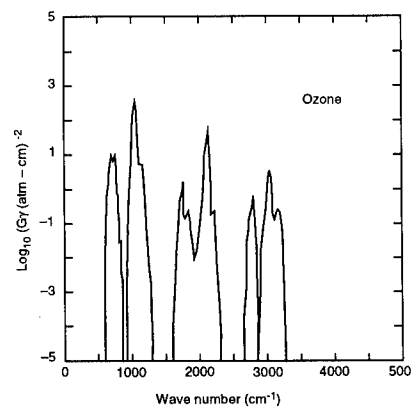


Fig. 1.40 Absorption coefficient G_ν for ozone from 350 to 5000 cm⁻¹.¹³²

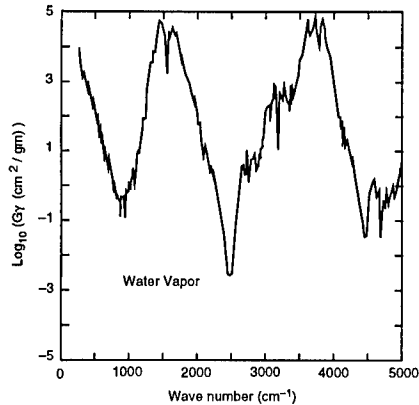


Fig. 1.41 Absorption coefficient G_v for water vapor from 350 to 5000 cm^{-1} .¹³²

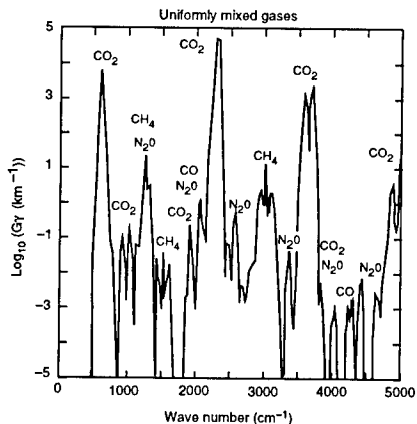


Fig. 1.42 Absorption coefficient G_v for the uniformly mixed gases from 350 to 5000 cm^{-1} .¹³²

The absorber density must be known as a function of altitude. Standard curves are used for specific latitudes and time of year.¹²⁶ An example for water vapor is given in Fig. 1.43.

1.3.4.3 MODTRAN Method

The single-parameter LOWTRAN approach is upgraded by a two-parameter MODTRAN^{133,134} model that features 2- cm^{-1} resolution. MODTRAN is also supported by AFGL. The main goal of MODTRAN is to improve temperature-dependent calculations. Significant improvements are listed below:

1. 2- cm^{-1} resolution (FWHM) band model is used, and thus spectral parameters are calculated every wave number.
2. More realistic temperature-dependent model is implemented. This is accomplished by using Eq. (1.58) for the temperature dependence of the line strength, which is now included in the spectral parameter.
3. The number of molecules represented is expanded to include water vapor, carbon dioxide, ozone, nitrous oxide, carbon monoxide, methane, oxygen, nitric oxide, sulfur dioxide, ammonia, and nitric acid.
4. High-altitude transmittance/radiance calculations are allowed, up to 60 km where local thermal equilibrium (LTE) is satisfied. This is made possible by including the Voigt line shape (see Sec. 1.3.1.3.2) in the band-model formalism. The Voigt line shape also represents the pressure dependence of the band more accurately.
5. Curtis-Godson approximation is used, which replaces an inhomogeneous path with a homogeneous one by using average values for the various band-model parameters.

Examples of the MODTRAN band-model improvements are given in Sec. 1.5.2.

1.3.5 Refractive Effects of the Atmosphere

The real part of the atmospheric index of refraction is a function of pressure, temperature, and frequency. Many interesting refractive effects exist because

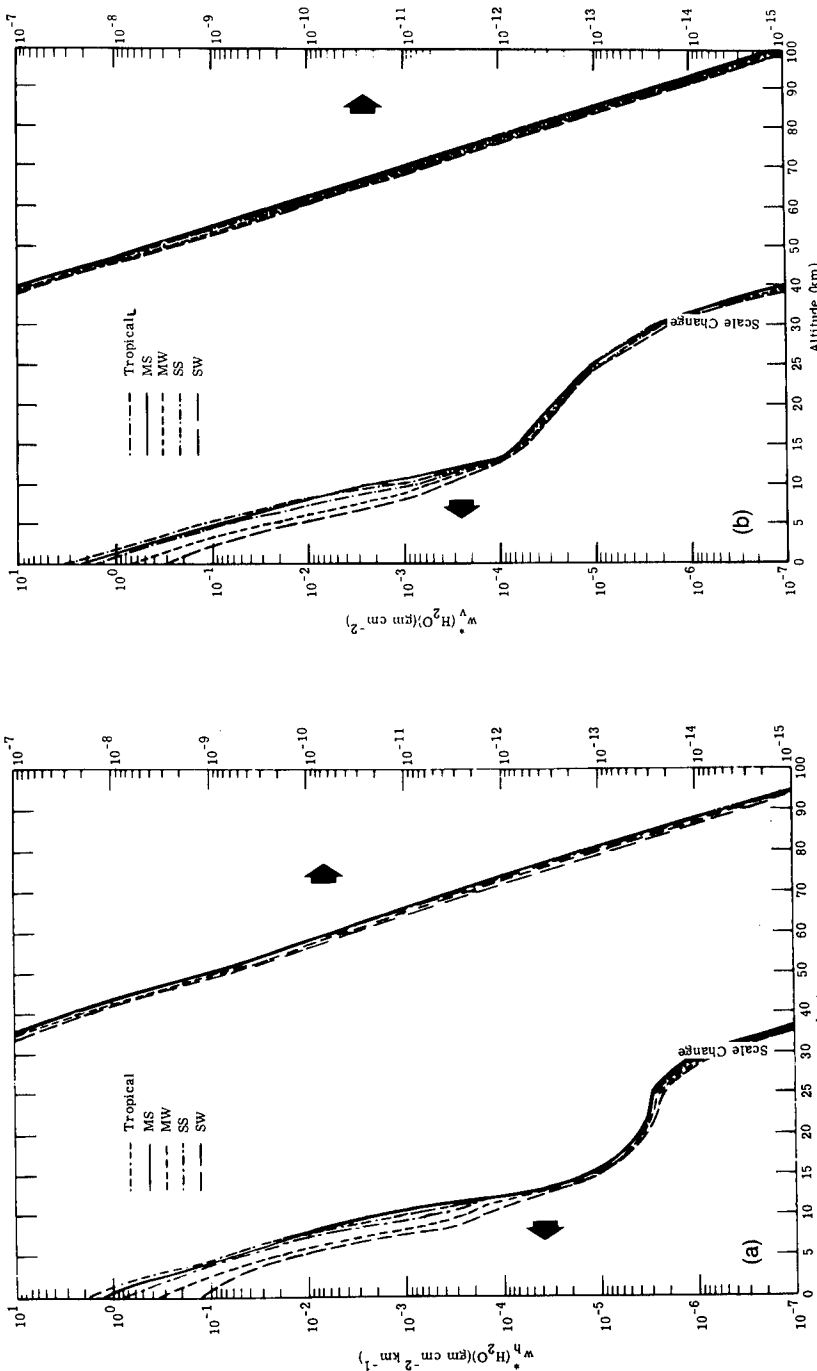


Fig. 1.43 Values obtained for model atmospheres tabulated for the so-called standard seasonal conditions. (a) Equivalent sea-level path length of water vapor as a function of altitude for horizontal atmospheric paths. (b) Equivalent sea-level path length of water vapor as a function of altitude for vertical atmospheric paths. For slant paths multiply by $\sec\theta$, for $\theta < 80^\circ$.

of tropospheric variations in density and water-vapor partial pressure as a function of position. This section begins with a discussion of atmospheric index-of-refraction models at optical frequencies and then examines different effects caused by refractive variations. Also of importance is the refractive index of particles in the atmosphere.

1.3.5.1 Index of Refraction of the Atmosphere

Because of their abundance, nitrogen and oxygen make significant contributions to the refractivity of the earth's atmosphere. These molecules have no infrared bands of importance to the refractive index and thus only electronic bands need to be considered for a model valid from low frequency to the ultraviolet. Based on the work of Edlen,¹³⁵ a simple Sellmeier-type model (see Sec. 1.3.1.3.1) for the dry atmospheric index can be obtained¹³⁶:

$$N_{\text{dry}} = (n - 1) \times 10^6 = \left(237.2 + \frac{526.3\nu_1^2}{\nu_1^2 - \nu^2} + \frac{11.69\nu_2^2}{\nu_2^2 - \nu^2} \right) \frac{P_{\text{dry}}}{T}, \quad (1.175)$$

where N is refractivity, ν is wave number in cm^{-1} , $\nu_1 = 114,000.0 \text{ cm}^{-1}$, $\nu_2 = 62,400.0 \text{ cm}^{-1}$, P_{dry} is dry-air pressure in kPa, and T is temperature in kelvin. This model is valid from 0.2 to $\infty \mu\text{m}$ (near dc) and compares well with other models.^{137,138} Moist air requires an additional term accounting for water vapor. Based on the work of Hill and Lawrence,¹³⁹ a Sellmeier-type term is obtained, representing the electronic transition contributions of pure water vapor:

$$N_{\text{H}_2\text{O}} = \frac{651.7\nu_3^2}{\nu_3^2 - \nu^2} \frac{P_{\text{H}_2\text{O}}}{T}, \quad (1.176)$$

where $\nu_3 = 111,575.0 \text{ cm}^{-1}$. The net refractivity is the sum of N_{dry} plus $N_{\text{H}_2\text{O}}$.

The model becomes more complicated at infrared wavelengths because the strong infrared vibrational and rotational absorption bands of water vapor must be considered. The importance of water vapor is demonstrated by the refractivity model at radar frequencies, which is the sum of all oscillator strengths, as given by^{140,141}

$$N_{\text{rf}} = \frac{776.4P_{\text{dry}}}{T} + \frac{717P_{\text{H}_2\text{O}}}{T} + \frac{3.744 \times 10^6 P_{\text{H}_2\text{O}}}{T^2}. \quad (1.177)$$

The rf refractivity can vary from 250 to 500 over the range of atmospheric temperatures and water-vapor partial pressures.¹⁴² Most of this variation is caused by the presence of water vapor. In particular, the last term in Eq. (1.177) represents the rotational band of water vapor. A model can be constructed, however, based on Eqs. (1.111), (1.112), (1.113), and Table 1.9 that allows reasonable prediction of refractivity at infrared wavelengths. Table 1.22 lists parameters for a refractivity Sellmeier model that includes the effect of

Table 1.22 Oscillator Parameters for Atmospheric Refractivity

Mode Number	ν_i (cm ⁻¹)	$\Delta\epsilon_i^*$
1	∞	$4.744 \times 10^{-4} P_{\text{dry}}/T$
2	114,000.0	$1.053 \times 10^{-3} P_{\text{dry}}/T$
3	63,400.0	$2.338 \times 10^{-5} P_{\text{dry}}/T$
4	111,575.0	$1.303 \times 10^{-3} P_{\text{H}_2\text{O}}/T$
5	3740.0	$1.48 \times 10^{-5} P_{\text{H}_2\text{O}}/T$
6	1595.0	$1.158 \times 10^{-4} P_{\text{H}_2\text{O}}/T$
7	125.0	$7.488 P_{\text{H}_2\text{O}}/T^2$

* P_{dry} and $P_{\text{H}_2\text{O}}$ are in units of kPa; T is in units of kelvin.

water vapor. Temperature and pressure dependence of the band strength are determined by the gas number density. The exception is the rotational band, for which, because of the low-band-center frequency, the population difference factor in Eq. (1.82) contributes another factor of $1/T$ to the band strength. This Sellmeier model reproduces available experimental data at visible and microwave frequencies^{143,144} and allows reasonable predictions ($\pm 0.5 N$ units) at infrared frequencies for a humid atmosphere. More accurate approaches are possible but will be more complicated.¹³⁹ A small discrepancy also exists between $N_{\text{dry}}(\nu = 0)$ and N_{rf} , which can be explained by the neglected contributions of the 60 GHz O₂ band and other minor contributions from CO₂, N₂O, and CH₄ infrared absorption bands.

1.3.5.2 Earth-Atmosphere Geometry

Given that the index of refraction depends on density and the density of the atmosphere depends on altitude (see Sec. 1.2.4), then light propagating in the atmosphere will be bent (typically toward lower altitudes or regions of higher density). To account for this geometrically, a suitable coordinate system must be used such as that illustrated in Fig. 1.44.¹⁴⁵ An observer at altitude s (in units of feet) can see beyond the geometrical horizon. A formula for calculating the optical horizon oh (in units of nautical miles) in a standard atmosphere is given by

$$oh = 1.14s^{1/2}. \quad (1.178)$$

The accuracy of Eq. (1.178) depends on deviations of atmospheric density from standards that are almost always present. This point is discussed further in the next two sections. The angle between OH" and OH is the refraction correction angle and is listed in Table 1.23 for altitudes near sea level. It is interesting to note that the angular extent of the sun is 32 arc min and the maximum refraction correction is 34.5 arc min; thus, even though the setting sun is below the geometrical horizon it can still be observed. Note also from

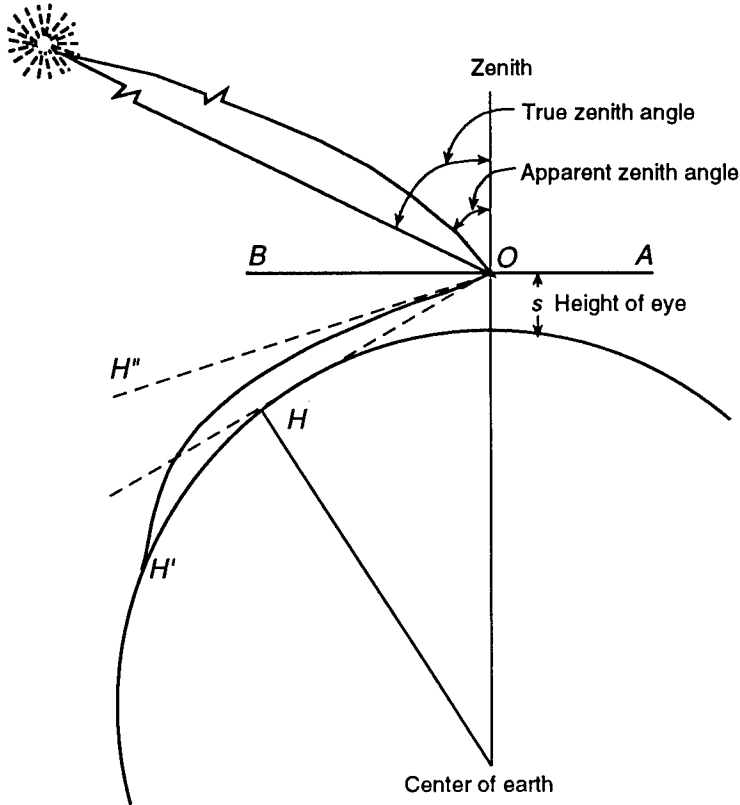


Fig. 1.44 Earth-atmosphere geometry and the effects of refraction.

Table 1.23 that the refraction correction angle varies across the angular extent of the sun near the horizon; thus, the sun appears flattened in this case. Also, dispersion of the refractive index causes the refraction correction angle to vary slightly for different colors. Thus, the setting sun disappears one color at a time, red first blue last. This explains the observance of the "green spot."¹⁴⁶ (Note: the "green flash" requires ducting phenomena and this is presented in Sec. 1.3.5.4.) Typical variations in the atmospheric index of refraction cause an uncertainty in refraction correction angles listed in Table 1.23 with a rms deviation of 0.16 arc sec.¹⁴⁷

1.3.5.3 Subrefractive and Superrefractive Effects

As mentioned previously, the standard refractive profile of the atmosphere hardly ever exists and corrections must be made if high accuracy is required. Either the atmospheric index of refraction increases less rapidly (or even decreases) with altitude than standard, which produces subrefractive conditions, or the atmospheric index increases more rapidly with altitude, which produces superrefractive conditions. Such conditions produce nonnormal images or mi-

Table 1.23 Sea-Level Refraction Correction Angles for Elevation Angles of Astronomical Lines of Sight

(deg)	Observed Altitude (min)	Refraction Correction (min)	Observed Altitude (deg)	Refraction Correction (min)
0	00	34.5	11	4.9
	15	31.4	12	4.5
	30	28.7	13	4.1
	45	26.4	14	3.8
1	00	24.3	15	3.6
	15	22.5	16	3.3
	30	20.9	17	3.1
	45	19.5	18	2.9
2	00	18.3	19	2.8
	15	17.2	20	2.6
	30	16.1	25	2.1
	45	15.2	30	1.7
3	00	14.4	35	1.4
4	30	10.7	50	0.8
5	00	9.9	55	0.7
6	00	8.5	60	0.6
7	00	7.4	65	0.5
8	00	6.6	70	0.4
9	00	5.9	80	0.2
10	00	5.3	90	0.0

ranges. Subrefractive effects are also called inferior mirages, and superrefractive effects are also called superior mirages.¹⁴⁸ Because these are non-standard processes, detailed knowledge of the temperature and pressure as a function of position is required to calculate such effects along an optical path. Subrefractive effects typically occur over a hot surface such as a road in the summer time. A reflective surface is observed because the rays are bent upward toward the cooler, denser air. Superrefractive effects typically occur over cold surfaces, such as snow or ice. A good example is the Fata Morgana, which can produce amplified images of rough snow and make them appear as pillars or walls in the horizon.¹⁴⁷

1.3.5.4 Ducting Effects

A duct is an atmospheric dielectric waveguide that allows light rays to maintain intensity for long distances. This requires a layered atmosphere with a high-index layer surrounded by low-index layers (this can occur during a temperature inversion). Good examples are the rarely observed “green flash” and the more common serrated edge of the setting sun.^{146–149}

1.4 ATMOSPHERIC SCATTERING

1.4.1 Aerosol Scatter

The theme of this section is the characterization of the physical propagation medium. This characterization is in terms of models and data on the atmosphere-borne particulates—dust, water, ice, salt, etc. These aerosols are further characterized in terms of size distributions, spatial constituent distributions, spatial size distributions, humidity effects, temporal effects, etc. Throughout this section, to keep notation tractable, explicit wavelength dependence is suppressed.

1.4.1.1 Single Scatter (Mie Theory)

In the calculation of scatter from aerosols, it is usually assumed that the particles are spherical. The method of analysis uses the Mie theory. It remains a fact, however, that many atmosphere-borne particles are not spherical. Nevertheless, the assumption is made that because of random orientation of the particles, one can assume some “average” particle size. In many cases, this is a reasonable assumption. There are cases in which it is not. One particular case is the one in which polarization properties are of interest. Another is in measuring backscatter. It can be shown¹⁵⁰ that the sphere produces the highest backscatter for a given particle radius. For other than a perfect sphere, the backscatter will be less (for an equal “average” radius). Further discussion of scatter from nonspherical particles is beyond the scope of this work. For such scatter, see Refs. 151–154.

Another qualification of the Mie theory is that each particle is treated as being isolated from all its neighbors. That is, it is assumed that the particles are in the far field of the scatter from each other. With this assumption it becomes possible to calculate the scatter and absorption properties of an ensemble of particles as the linear superposition of the scatter from each. That this may not be justified is almost always ignored.

The Mie solution for scatter from a spherical particle is a lengthy but straightforward process that results in infinite series expressions for the field components polarized perpendicular and parallel to the scattering plane (see Fig. 1.45). Although the formal solution is lengthy, the series solutions for the field components are computed easily on a personal computer (see Sec. 1.5.4). The procedure begins by solving the vector wave equation in a spherical coordinate system, and obtaining a formal solution in terms of infinite series of spherical Bessel functions. Next, the incident plane wave, the scattered field, and the internal field are all expanded in vector spherical harmonics. Matching of the boundary conditions at the surface of the sphere finally results in the infinite series solutions for the field components. Deirmendjian¹⁵⁵ also gives a very succinct description of this procedure.

The solution for the scattered electric field is given in terms of two scalar components S_1 and S_2 perpendicular and parallel to the scatter plane (the plane in which θ is measured):

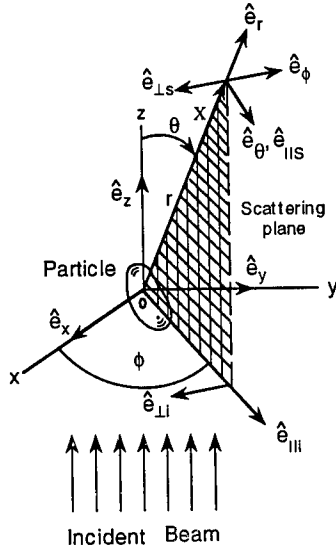


Fig. 1.45 Illustration of geometry for calculation of Mie scatter.

$$S_1 = \sum_{n=0}^{\infty} \frac{2n+1}{n(n+1)} (a_n \pi_n + b_n \tau_n) , \quad (1.179)$$

$$S_2 = \sum_{n=0}^{\infty} \frac{2n+1}{n(n+1)} (b_n \pi_n + a_n \tau_n) , \quad (1.180)$$

where S_1 and S_2 are dimensionless complex amplitudes, the π_n and τ_n are the angle-dependent functions, and the a_n and b_n are the complex Mie coefficients. These coefficients are functions of the complex refractive index of the particle, $m = n + in'$, and of Riccati-Bessel functions of the size parameter x , given by

$$x = kr , \quad (1.181)$$

where r is the particle radius.

We assume that the infinite series above are uniformly convergent so that for kR sufficiently large (where R is the distance between the particle center and the field point), they may with negligible error be truncated at n_c terms. If, in addition, we assume that $kR \gg n_c^2$ (basically a far-field requirement), then Bohren and Huffman¹⁵⁰ have shown that the solution may be expressed as

$$\begin{bmatrix} E_{\parallel s} \\ E_{\perp s} \end{bmatrix} = \frac{\exp[ik(R-z)]}{-ikR} \begin{bmatrix} S_2 & 0 \\ 0 & S_1 \end{bmatrix} \begin{bmatrix} E_{\parallel i} \\ E_{\perp i} \end{bmatrix} . \quad (1.182)$$

That is, under the above conditions, the scattered field appears as an outward-traveling spherical wave. Note that the incident and scattered field components

are expressed in terms of different basis vectors (see Fig. 1.44), and that the assumption of a spherical particle results in a scatter that does not depolarize the incident radiation; i.e., the S_3 element [upper right in Eq. (1.182)] and the S_4 element (lower left) are zero. See the following discussion of polarization effects.

These field components are often expressed in terms of the Stokes vector $[I, Q, U, V]$, whose components are given by

$$\begin{aligned} I &= \langle |E_{\parallel}|^2 + |E_{\perp}|^2 \rangle , \\ Q &= \langle |E_{\parallel}|^2 - |E_{\perp}|^2 \rangle , \\ U &= \langle E_{\parallel}E_{\perp}^* + E_{\perp}E_{\parallel}^* \rangle , \\ V &= \langle E_{\parallel}E_{\perp}^* - E_{\perp}E_{\parallel}^* \rangle . \end{aligned} \quad (1.183)$$

With this notation, the relationship between the Stokes vectors of the incident and scattered fields becomes

$$\begin{bmatrix} I_s \\ Q_s \\ U_s \\ V_s \end{bmatrix} = \frac{1}{k^2 R^2} \begin{bmatrix} S_{11} & S_{12} & 0 & 0 \\ S_{12} & S_{11} & 0 & 0 \\ 0 & 0 & S_{33} & S_{34} \\ 0 & 0 & -S_{34} & S_{33} \end{bmatrix} \begin{bmatrix} I_i \\ Q_i \\ U_i \\ V_i \end{bmatrix}, \quad (1.184)$$

where the (Mueller) matrix elements¹⁵⁶ are defined as

$$\begin{aligned} S_{11} &= \frac{1}{2}(|S_2|^2 + |S_1|^2) , \\ S_{12} &= \frac{1}{2}(|S_2|^2 - |S_1|^2) , \\ S_{33} &= \frac{1}{2}(S_2^*S_1 + S_2S_1^*) , \\ S_{34} &= \frac{1}{2}i(S_1S_2^* - S_2S_1^*) . \end{aligned} \quad (1.185)$$

The utility of the Stokes formulation is that the Stokes parameters of the light scattered by a collection of randomly separated particles are the sum of the Stokes parameters of the light scattered by the individual particles. The random positions of the particles ensure that (except in the exact forward direction¹⁵⁰) the relative phases of the scattered fields are uniformly distributed over the interval $(0, 2\pi)$, thus allowing addition of intensities rather than of fields.

On the basis of the above formulation, it is easily seen that for incident radiation polarized parallel to the scattering plane, the resulting scattered radiation is fully polarized parallel to the scattering plane. This same result holds for incident radiation polarized perpendicular to the scattering plane. On the other hand, if the incident radiation is unpolarized, the differential

scatter of the two field components parallel and perpendicular to the scattering plane results in a degree of polarization P given by

$$P = \frac{-S_{12}(\theta)}{S_{11}(\theta)} . \quad (1.186)$$

For $P > 0$, we have partial polarization perpendicular to the scattering plane; for $P < 0$, we have partial polarization parallel to the scattering plane. In general, $|P| \leq 1$. If a collection of scatterers is heterogeneous by virtue of variations in either size or optical properties, or both, the polarization is strictly less than unity.

The energy removed from the incident beam by scatter on the particle is proportional to the extinction cross section C_{ext} :

$$C_{\text{ext}} = C_{\text{abs}} + C_{\text{sca}} , \quad (1.187)$$

which is the sum of the absorption and scatter cross sections. The extinction cross section is expressed as

$$C_{\text{ext}}(r) = \frac{4\pi}{k^2} \text{Re}\{S_i(0,r)\} , \quad (1.188)$$

where $i = 1$ or 2 . [Note: $S_1(0,r) = S_2(0,r)$.] The scatter cross section is expressed as

$$C_{\text{sca}}(r) = \frac{1}{k^2} \int_{4\pi} S_{11}(\theta,r) d\omega , \quad (1.189)$$

where the integration is over the entire solid angle. In these last two equations, the dependence on the particle radius has been explicitly denoted.

A very useful parameter, the significance of which will be discussed later, is the single-scatter albedo. This is defined as the ratio of the scatter and extinction cross sections:

$$\alpha = \frac{C_{\text{sca}}}{C_{\text{ext}}} . \quad (1.190)$$

This notation is used, for example, by van de Hulst.^{157,158} Others, Deirmendjian,¹⁵⁵ for example, use the notation $\tilde{\omega}$ or simply ω .

By normalizing the above scatter and extinction cross sections to the geometrical cross sections, one may define the corresponding efficiencies:

$$Q_{\text{sca}} = \frac{C_{\text{sca}}}{\pi r^2} , \quad (1.191)$$

$$Q_{\text{ext}} = \frac{C_{\text{ext}}}{\pi r^2} . \quad (1.192)$$

In addition, the backscatter efficiency is often useful:

$$Q_{\text{back}} = \frac{\sigma_b}{\pi r^2}, \quad (1.193)$$

where the backscatter cross section is given by

$$\sigma_b = \frac{4\pi}{k^2} S_{11}(180 \text{ deg}). \quad (1.194)$$

Note that for historical reasons, the backscatter cross section is *defined* as 4π times that which should be expected on geometrical grounds. The reason is that in radar parlance, the radar backscatter cross section is defined with respect to an isotropic scatterer. It is clear that the backscatter intensity received by a detector due to scatter from a single particle is given by

$$I_s = \frac{I_i}{R^2 k^2} S_{11}(180 \text{ deg}) = \frac{I_i \sigma_b}{4\pi R^2}. \quad (1.195)$$

In any case, the definition of the backscatter cross section is consistent with the traditional definition of the phase function (see following sections).

Shown in Fig. 1.46 is an example of the scatter and extinction efficiencies calculated for $10.591 \mu\text{m}$ radiation as a function of the "x" parameter ($x = kr$).

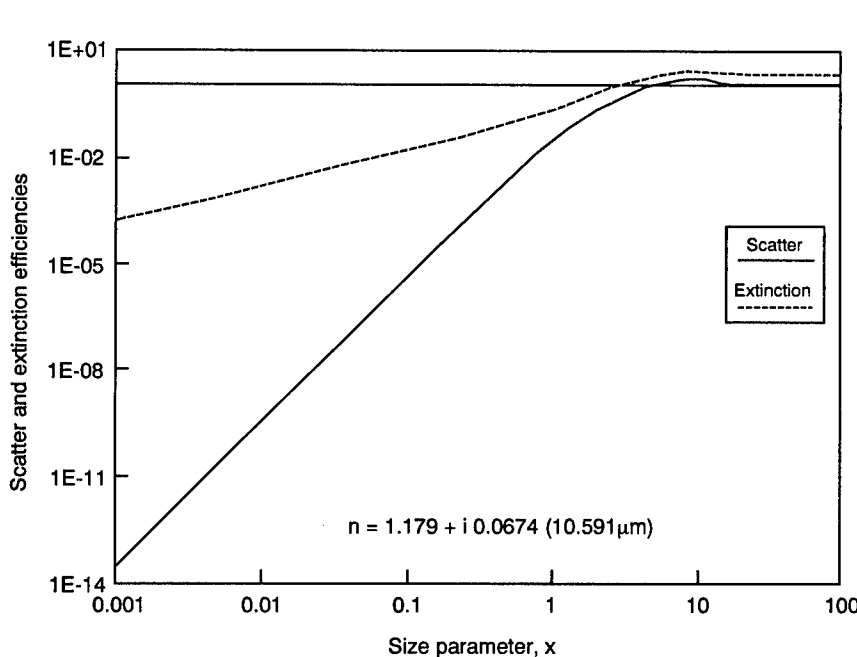


Fig. 1.46 Scatter and extinction efficiencies.

1.4.1.2 Various Limiting Forms

Figure 1.47, taken from van de Hulst,¹⁵⁷ is a plot of the "m-x" domain for nonabsorbing particles ($\Rightarrow Q_{\text{ext}} = Q_{\text{sca}}$). Shown in Table 1.24 is the corresponding listing of the various regions of the "m-x" domain, i.e., regions that have distinct names associated with them and those for which limiting forms are available.

In the Rayleigh regime, the first term a_1 in the Mie solution dominates. This corresponds to electric dipole scattering. Similarly, in the resonance region there is a sharply defined value of x for which a single term in the Mie series dominates. Within the geometrical optics regime, the phase function is given by contributions due to diffraction and reflection plus refraction. For the anomalous diffraction domain the transmitted and diffracted light interferes; light is scattered in diffraction rings with anomalous sizes and brightness distributions. Finally, in the Rayleigh-Gans approximation, there is simultaneous Rayleigh scattering from all elements of the volume, and purely geometrical interference effects produce phase functions with successive light and dark rings.

The following are explicit formulas for the efficiencies and phase functions under various approximations.

In the Rayleigh limit:

$$Q_{\text{sca}} = \frac{8}{3}x^4 \left| \frac{m^2 - 1}{m^2 + 2} \right|^2, \quad (1.196)$$

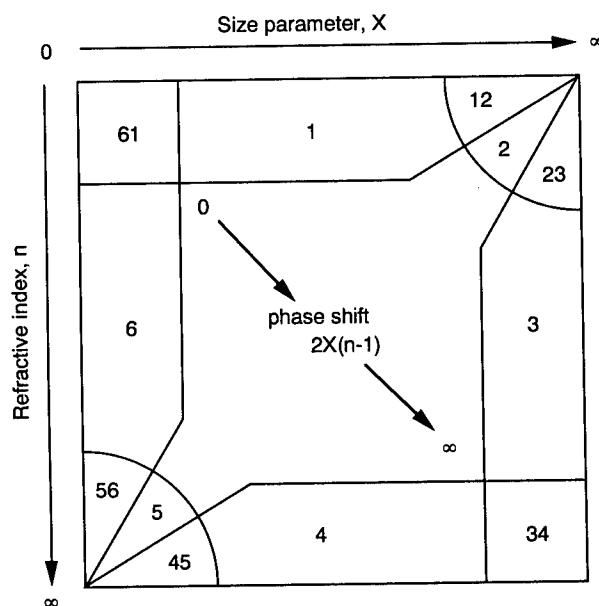


Fig. 1.47 The "m-x" domain.

Table 1.24 Boundary Values for the m - x Domain

Region	x	$m - 1$	$x(m - 1)$	Name	Extinction Formula
61	s	s	s		$Q_{\text{ext}} = (32/27) m - 1 ^2 x^4$
1	arb	s	s	Rayleigh-Gans	$Q_{\text{ext}} = 2 m - 1 ^2 x^2$
12	l	s	s		
2	l	s	arb	Anomalous diffraction	
23	l	s	l		$Q_{\text{ext}} = 2$
3	l	arb	l	Large spheres	
34	l	l	l		$Q_{\text{ext}} = 2$
4	arb	l	l	Total reflector	
45	s	l	l		$Q_{\text{ext}} = (10/3)x^4$
5	s	l	arb	Optical resonance	
56	s	l	s		$Q_{\text{ext}} = (8/3)x^4$
6	s	arb	s	Rayleigh	

$$Q_{\text{back}} = 4x^4 \left| \frac{m^2 - 1}{m^2 + 2} \right|^2 , \quad (1.197)$$

$$Q_{\text{abs}} = 4x \operatorname{Im} \left\{ \frac{m^2 - 1}{m^2 + 2} \right\} \left[1 + \frac{4x^3}{3} \operatorname{Im} \left\{ \frac{m^2 - 1}{m^2 + 2} \right\} \right] , \quad (1.198)$$

$$P(\theta) = \frac{3}{4}(1 + \cos^2 \theta) . \quad (1.199)$$

In the geometrical limit; i.e., $r \gg \lambda$:

$$Q_{\text{sca}} P(\theta) = x^2 \left[\frac{2J_1(x \sin \theta)}{(x \sin \theta)} \right]^2 , \quad (1.200)$$

where J_1 is the Bessel function of the first kind and order unity. This formula follows from Babinet's principle¹⁵⁹ and arises from consideration of the scatterer as a flat opaque disk. The backscatter and absorption efficiencies, respectively, are given by

$$Q_{\text{back}} = \left| \frac{m - 1}{m + 1} \right|^2 , \quad (1.201)$$

$$Q_{\text{abs}} = \frac{8n'}{3n} x [n^2 - (n^2 - 1)^{3/2}] , \quad (1.202)$$

where n' is the imaginary portion of the refractive index. Equation (1.201) for the backscatter efficiency will be recognized as the Fresnel reflection coefficient for a planar surface. This formula is valid only for absorbing spheres, so that

the internally reflected rays do not contribute to the backscatter. Further, Eq. (1.202) for the absorption cross section is valid only for weakly absorbing spheres, so that the total absorption is proportional to volume as it is for small particles [see Eq. (1.198)]. For strongly absorbing particles, such that $4n'x \gg 1$, the absorption takes place only in the surface layer of the particle, and the absorption efficiency becomes equal to the geometrical cross section (as does the scatter efficiency for $r \gg \lambda$).

1.4.1.3 Polydispersions

We next generalize the above results to scattering on many particles of various sizes. To this end, we define a scatter cross section per unit volume β_{sca} , expressed as

$$\beta_{\text{sca}} = \int_0^{\infty} C_{\text{sca}}(r) n(r) dr , \quad (1.203)$$

where the function $n(r)$ is the particle size distribution function defined as the number of particles per unit volume with radii between r and $r + dr$. These distribution functions are usually expressed in units of $\text{cm}^{-3} \mu\text{m}^{-1}$. For more on these distribution models, see Sec. 1.4.1.4.3. Also note that the scatter cross section per unit volume has units of inverse length. It is often called the scatter "coefficient." The extinction cross section per unit volume is defined analogously to that for scatter, and the corresponding single-scatter albedo is defined as $\alpha = \beta_{\text{sca}}/\beta_{\text{ext}}$.

The corresponding generalization of the Mueller matrix elements is the following:

$$S_{ij}(\theta) = \int_0^{\infty} S_{ij}(\theta, r) n(r) dr . \quad (1.204)$$

Note that this element is now defined per unit scatter volume. The implications for the interpretation and use of this redefined variable are discussed in Sec. 1.4.3.

Before proceeding with examples of the use of these concepts in calculating the power due to scatter that is received by a sensor, we connect the above notation with that used by other authors, notably Deirmendjian.¹⁵⁵ Let us assume that the incident radiation is unpolarized and that the receiver is insensitive to the polarization of the scattered radiation. In this case, the relevant Mueller matrix element is S_{11} . Deirmendjian and others define a "phase function" $P(\theta)$ that can be considered a three-dimensional probability density function (unnormalized) for the scatter direction. In the notation established above, this phase function is given by

$$P(\theta) = \frac{4\pi S_{11}(\theta, r)}{k^2 C_{\text{sca}}(r)} . \quad (1.205)$$

The normalization of this phase function is such that its integral over the entire solid angle is equal to 4π sr; the phase function $P(\theta)$ is thus dimensionless. For a polydispersion, the corresponding relationship is

$$P(\theta) = \frac{4\pi S_{11}(\theta)}{k^2 \beta_{\text{sca}}} . \quad (1.206)$$

The specific connection between Deirmendjian's Mueller matrix components and those discussed herein is the following:

$$P_1(\theta) = \frac{4\pi [S_{11}(\theta) - S_{12}(\theta)]}{k^2 \beta_{\text{sca}}} , \quad (1.207)$$

$$P_2(\theta) = \frac{4\pi [S_{11}(\theta) + S_{12}(\theta)]}{k^2 \beta_{\text{sca}}} , \quad (1.208)$$

$$P_3(\theta) = \frac{4\pi S_{33}(\theta)}{k^2 \beta_{\text{sca}}} , \quad (1.209)$$

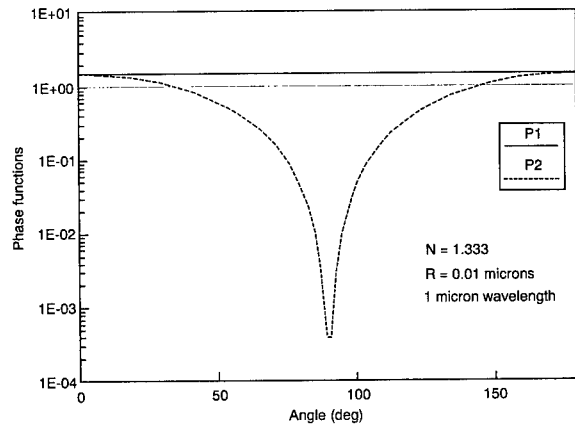
$$P_4(\theta) = \frac{4\pi S_{34}(\theta)}{k^2 \beta_{\text{sca}}} . \quad (1.210)$$

Note that in each of the above equations, the $P_j(\theta)$ are dimensionless. Other authors, for example, Fenn et al.,¹⁶⁰ define the phase function such that the integral over the entire solid angle is unity. In this case, therefore, the phase function has the formal interpretation as a (three-dimensional) probability density function with the units of inverse steradians. Shown in Fig. 1.48 are example phase functions for $x \ll 1$, a 0.55 μm wavelength, and a 0.6328 μm wavelength, respectively. Note the shift in features between the latter two figures for this small wavelength change.

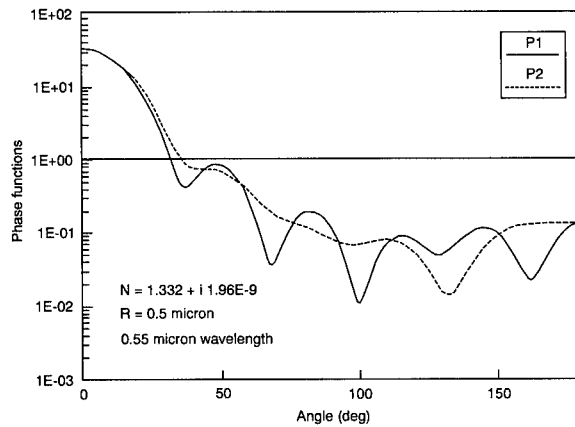
1.4.1.4 Terrestrial Aerosols

One can perform a number of categorizations of terrestrial aerosol particles. Here, we use the general classifications of dust and hygroscopic particles. Dust particles are a rather passive constituent of atmospheric haze. On the other hand, hygroscopic particles display a strong dependence on relative humidity and are thus more highly variable.

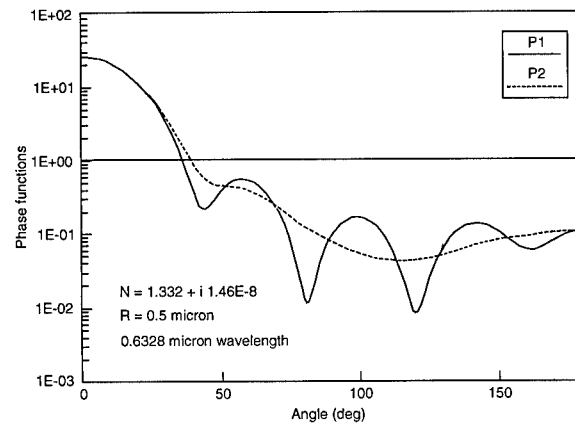
Dust particles are derived from a number of terrestrial and extraterrestrial sources. Extraterrestrial sources include planetary accretion (due to interplanetary debris within the volume swept by the earth's passage through space) and meteoroids. Particles due to these two sources are the predominant haze components in the outermost atmosphere. Volcanos generate a huge volume of fine ash and gases. These particles are injected high into the stratosphere, where they remain for extended periods of time. In the lowest levels of the atmosphere, surface winds play an important role in sweeping up soil-based dusts. Finally, industry and construction are important sources of dust particles.



(a)



(b)



(c)

Fig. 1.48 (a) Typical phase function for $x \gg 1$. (b) Phase function for water at $0.55 \mu\text{m}$ wavelength. (c) Phase function for water at $0.6328 \mu\text{m}$ wavelength.

Hygroscopic particles, the much more dynamic of the two aerosol categories, are derived from a number of sources, primarily vegetation and the sea. Vegetation exudes aromatic hydrocarbons that under the influence of ozone and sunlight oxidize and condense or nucleate into tiny droplets of complex tars and resins. These particles have an average radius of approximately 0.15 μm . Sea salt is injected into the air by bursting bubbles that are created by cresting waves at ocean surfaces. The concentration of these particles, which range in size from 0.3 μm to 3 μm , is therefore highly dependent on local wind velocity.^{161,162} Many of the by-products of combustion undergo photochemical reactions that produce small hygroscopic particles. For all of the above condensation nuclei sizes are categorized as Aitken ($r < 0.1 \mu\text{m}$), large ($0.1 \mu\text{m} < r < 1 \mu\text{m}$), and giant ($r > 1 \mu\text{m}$).

1.4.1.4.1 Vertical Density Variations

Models for the vertical variability of atmospheric aerosols are generally broken into a number of distinct layers. In each of these layers a dominant physical mechanism determines the type, number density, and size distribution of particles. Figure 1.49¹⁶³ is an example of such a description. Generally accepted layer models consist of the following: a boundary layer that goes from 0 to 2 km, a region running from 2 to 6 km in which the number density displays an exponential decay with altitude, a stratospheric layer from 6 to 30 km, and layers above 30 km composed mainly of particles that are extraterrestrial in origin.

The average thickness of the aerosol-mixing region is approximately 2 km. Within this region, one would expect the aerosol concentration to be influenced strongly by conditions at ground level. Consequently, aerosols in this region display the highest variability with meteorological condition, climate, etc. In this layer particles are either transported from their point of origin into the atmosphere or are formed by gas-to-particle conversion or photochemical processes. In the maritime environment they are composed largely of sea-salt solutions and sulfates. Wind-blown dust from desert regions is an important constituent of continental aerosols. Extant models describe environments for rural, urban, maritime, and desert areas and for fogs.

In the layer that extends from 2 to 6 km, an exponential decay is observed. Specifically, one often sees total number densities vary as follows:

$$N(z) = N(0) \exp\left(-\frac{z}{z_s}\right), \quad (1.211)$$

where the scale height z_s ranges from 1 to 1.4 km.¹⁶⁴

Within the stratospheric layers, the aerosol constituents are largely photochemically derived sulfuric acid solutions that display a variability that is highly dependent on volcanic activity.

Above the stratospheric layer, particles are mainly meteoric in origin.

The growth and decay of hygroscopic particles is governed by two opposing forces: reduced vapor pressure required for saturation (due to the presence of the solute) and surface tension effects that require supersaturation for con-

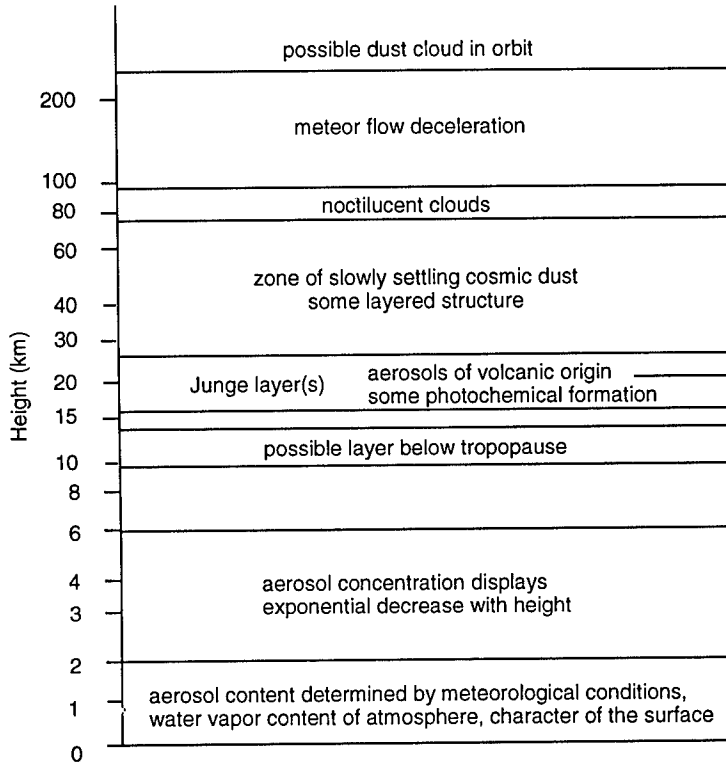


Fig. 1.49 Character of atmospheric aerosols.

densation to occur. In the absence of a hygroscopic species, it is highly unlikely that water droplets smaller than approximately $0.3 \mu\text{m}$ will be observed.

An example of the temporal variation of a haze composed of condensation nuclei is the radiation fog. A haze composed of such nuclei appears blue-gray. At sundown, as the ground loses heat through radiation, the air above it cools and the air becomes supersaturated. Water therefore condenses onto the nuclei, producing a white fog. At sunrise, when the air begins to be heated, the vapor pressure is reduced and water evaporates from the nuclei, aided by the surface-tension effects. Under these conditions, one observes a strong correlation between relative humidity and visibility range (see discussion in Sec. 1.4.5.1).

Particle-removal processes include coagulation, fallout, and washout. Coagulation occurs when particles collide and coalesce, forming fewer but larger particles. (Collision of Aitken particles is due to Brownian motion.) Collision for larger particles is caused by small-scale turbulence. Collisions affect the large population of small particles more strongly than the small population of large particles.¹⁶⁴ Fallout is due to effects of gravity. This effect is offset by wind and convective currents. A particle's terminal velocity is an equilibrium between acceleration due to gravity and viscous drag due to the air. Because of the vertical variability of atmospheric pressure, there is a large altitude dependence on the terminal velocity.¹⁶⁴ In any case, however, particles larger than approximately $20 \mu\text{m}$ are rare. Washout is the removal of particles by

rain and snow. Snow, which has smaller terminal velocity and rougher surfaces, may be more effective at this purging effect.

On the basis of the foregoing, it is observed that the two items required for determining propagation effects due to terrestrial aerosols are the aerosol constituent material, specifically its refractive index, and a description of the particle-size distribution. In the discussion that follows we present a number of models and techniques for specifying each of these components.

1.4.1.4.2 Refractive Indices

One can take two approaches to specifying the complex refractive index for typical aerosol constituents. One is simply to use tabulated data, as for water.¹⁶⁵ In this case, data for wavelengths not tabulated may be obtained by interpolation. For further data on pure water, water solubles, dust, soot, and sea salt¹⁶⁶ see the program listing in Sec. 1.5.4 (subroutine INTRP).

*The Infrared Handbook*¹⁶⁷ contains extensive listings of refractive indices. These are tabulated in Table 1.25.

Another approach to obtaining the complex refractive index is based on a parametric model. Specifically, we demonstrate the use of a Sellmeir model for NaCl. Recall the relationship between the complex permittivity and the refractive index:

$$[\epsilon(\nu)]^{1/2} = n(\nu) + i n'(\nu) . \quad (1.212)$$

We express the complex permittivity in terms of a pole model of the form

$$\epsilon(\nu) = \epsilon_{\infty} + \sum_j \frac{\Delta\epsilon_j \nu_j^2}{\nu_j^2 - \nu^2 + i\gamma_j \nu f(\nu)} , \quad (1.213)$$

where the function f is given by

$$f(\nu) = \begin{cases} 1 & , \nu \leq \bar{\nu} , \\ \exp\left\{-a\left[\left(\frac{\nu}{\bar{\nu}}\right)^2 - 1\right]\right\} & , \nu > \bar{\nu} , \end{cases} \quad (1.214)$$

Table 1.25 Refractive Indices Tabulated in *The Infrared Handbook* (from Ref. 167)

Species	Wavelength Region	Source
Water	0.4–14.0 μm	Ref. 165
Sulfuric-acid solutions (25%, 38%, 50%, 75%, 84.5%, 95.65%)	0.36–25 μm	Ref. 168
Dust	0.4–14.0 μm	Refs. 169–171
Quartz	0.768–13.6 μm	Ref. 172
Ammonium sulfate 21%, 30%, 41% humidities 39% humidity	7.7–10.3 μm 4.4–13.4 μm	Ref. 173 Ref. 173
NaCl	0.2–100 μm	Ref. 174

Table 1.26 Optical Mode Constants of NaCl

ν_{TO} (cm $^{-1}$)	$\Delta\epsilon$	γ/ν_{TO}	ν_{LO} (cm $^{-1}$)	ϵ_∞
83.1	0.05	0.165		1.00055
163.6	3.20	0.052		
232.0	0.038	0.078		
253.0	0.05	0.088	268.	
63,291.*	0.26	0.0001		
78,125.*	0.387	0.0001		
100,000.*	0.484	0.0001		
200,000.*	0.198	0.0001		

*Electronic transitions.

where a is generally chosen as equal to 4 and $\bar{\nu} = 1.1$ times the highest infrared allowed transverse optical mode frequency.¹⁷⁵ As an example of the use of this technique, the parameters of this model for NaCl are displayed in Table 1.26.

The real portion of the refractive index as given by this model is good over the spectral range 0.2 to 120 μm . The imaginary portion is valid over the range of frequencies running from the first (infrared) transverse mode (83.1 cm^{-1}) to the highest-order longitudinal mode (268 cm^{-1}). This is the single-phonon regime. Within the multiphonon region, an exponential model can be used¹⁷⁶:

$$n_i = \frac{A}{4\pi\nu} \exp\left(-\nu \frac{\gamma}{\nu_0}\right), \quad (1.215)$$

where $A = 24,273 \text{ cm}^{-1}$ and $\nu_0/\gamma = 56 \text{ cm}^{-1}$. This model is valid over the region 356 to 945 cm^{-1} . With these two models, the complex refractive index is specified over much of the spectral range from 0.2 to 120 μm . Results of these calculations are shown in Fig. 1.50; these results compare very well with the data tabulated in Ref. 167.

Additionally, optical mode constants for fused silica, quartz, and $\alpha\text{-Fe}_2\text{O}_3$ are shown in Tables 1.27, 1.28, and 1.29, respectively.

1.4.1.4.3 Aerosol Size Distribution Models

There are a number of analytic models of aerosol size distributions in current use. These include power laws, exponentials, and log-normals. One that incorporates power law and exponentials is Deirmendjian's¹⁵⁵ "modified gamma" distribution described by the following:

$$n(r) = ar^\alpha \exp(-br^\gamma), \quad 0 \leq r < \infty. \quad (1.216)$$

The total particle density, given by the integral over all particle radii, for this distribution, is

$$N = a\gamma^{-1}b^{-(\alpha+1)/\gamma} \Gamma\left(\frac{\alpha+1}{\gamma}\right). \quad (1.217)$$

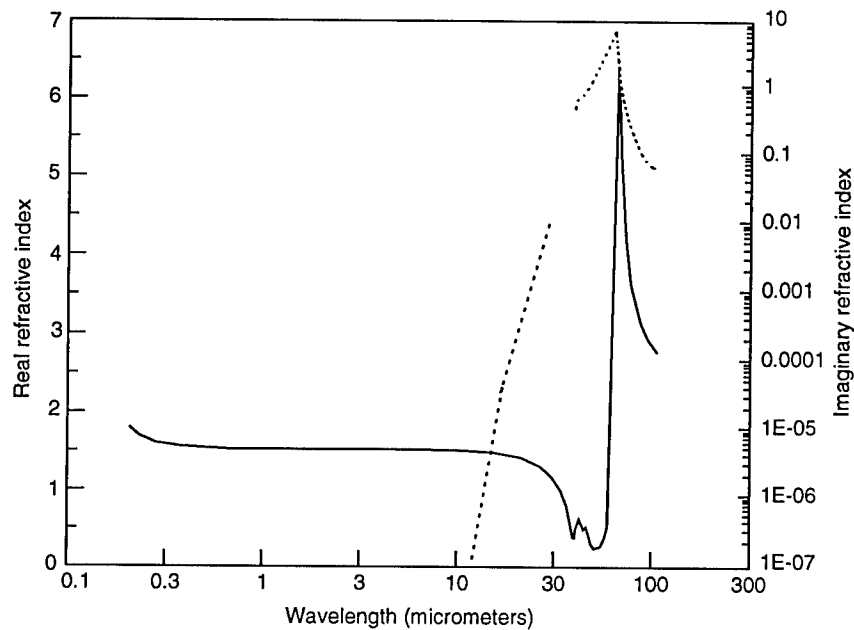


Fig. 1.50 Results of pole-fit refractive-index model for NaCl.

By differentiating the expression for the particle size distribution, the modal radius may be found:

$$r_c^\gamma = \frac{\alpha}{b\gamma} . \quad (1.218)$$

Finally, from Eqs. (1.216) and (1.218), the value of the distribution function at the modal radius is

$$n(r_c) = ar_c^\alpha e^{-\alpha/\gamma} . \quad (1.219)$$

Table 1.27 Optical Mode Constants of Fused Silica

ν_{TO} (cm $^{-1}$)	$\Delta\epsilon$	γ/ν_{TO}	ν_{LO} (cm $^{-1}$)	ϵ_∞
460	0.74	0.045		1.0
797	0.08	0.06		
1046	0.2	0.045		
1070	0.45	0.05		
1105	0.12	0.08		
1193	0.06	0.082	1263	
86,028*	0.4079	—		
146,190*	0.6962	—		

*Electronic transitions.

Table 1.28 Optical Mode Constants of Quartz (from Ref. 177)

ν_{TO} (cm $^{-1}$)	$\Delta\epsilon$	γ/ν_{TO}	ν_{LO} (cm $^{-1}$)	ϵ_∞
o-ray				
128	0.0006	0.039		
394	0.33	0.007		
450	0.82	0.009		
697	0.02	0.012		
797	0.11	0.009		
1072	0.67	0.0071		
1163	0.01	0.006		
1227	0.0094	0.110	1235	
e-ray				
364	0.68	0.014		
495	0.66	0.009		
509	0.05	0.014		
539	0.01	0.040		
778	0.10	0.010		
1080	0.67	0.0069		
1220	0.011	0.150	1235	

Table 1.29 Optical Mode Constants of α -Fe₂O₃ (from Ref. 178)

ν_{TO} (cm $^{-1}$)	$\Delta\epsilon$	γ/ν_{TO}	ν_{LO} (cm $^{-1}$)	$\epsilon(0)$	ϵ_∞
o-ray					
227	1.1	0.005	230	24.1	7.0
286	12.0	0.042	368		
437	2.9	0.007	494		
524	1.1	0.002	662		
e-ray					
299	11.5	0.050	414	20.6	6.7
526	2.2	0.004	662		

In using this model for aerosol distributions, care must be taken because the dimensional units of the parameters a and b depend on the choice of the powers α and γ .

Another commonly used distribution function is the Junge,¹⁶⁷ or power law, described as

$$n(r) = cr^{-(\beta + 1)}, \quad r \geq r_{min}, \quad (1.220)$$

where c is a normalizing constant that sets the total particle density and β is the shaping parameter. Note that this distribution is a special case of Deirmendjian's "modified gamma" distribution. Generally, one finds measured

values of β in the range of $2 \leq \beta \leq 4$ for aerosols whose radii lie between 0.1 and 10 μm , and that aerosol densities drop off rapidly below some radius less than 0.1 μm ¹⁶⁷ (Deirmendjian's distribution model accounts for this drop-off analytically). Typical hazes conform to $3 < \beta < 4$, while many fogs are characterized by $\beta \approx 2$.¹⁶⁴ Finally, note that here also the dimensional units of the constant c depend on the parameter β .

Still another commonly used distribution is the log-normal¹⁷⁹:

$$n(r) = \frac{1}{(2\pi)^{1/2} \sigma_g r} \exp\left[-\frac{(\ln r - \ln r_m)^2}{2\sigma_g^2}\right]. \quad (1.221)$$

In this distribution, it is the natural logarithm of the particle radius rather than the particle radius itself that is normally distributed. The mean of $\ln r$ and the variance, respectively, are given by

$$\ln r_m = \int_0^\infty \ln r n(r) dr, \quad (1.222)$$

$$\sigma_g^2 = \int_0^\infty (\ln r - \ln r_m)^2 n(r) dr. \quad (1.223)$$

An alternative expression for the log-normal distribution¹⁶³ is given in terms of the base 10 logarithm of the particle radius:

$$n(r) = \frac{1}{\ln(10)(2\pi)^{1/2} \sigma_g r} \exp\left[-\frac{(\log r - \log r_m)^2}{2\sigma_g^2}\right]. \quad (1.224)$$

Another less commonly used distribution is the zero-order logarithmic distribution (ZOLD). However, as Kerker¹⁷⁹ points out, the log-normal and ZOLD distributions are special cases of a family of logarithmically skewed distributions.

Tables 1.30 and 1.31 give examples of the values of the adjustable parameters of the above models for various hazes, fogs, and clouds.

Table 1.30 Parameters of the "Modified Gamma" Distribution (from Ref. 155)

Distribution Type	N (cm^{-3})	a	r_c (μm)	α	γ	b	$n(r_c)$
Haze M	100	5.3333×10^4	0.05	1	0.5	8.94433	$60.9 \text{ cm}^{-3} \mu\text{m}^{-1}$
Haze L	100	4.9757×10^6	0.07	2	0.5	15.1186	$446.6 \text{ cm}^{-3} \mu\text{m}^{-1}$
Haze H	100	4.0000×10^5	0.10	2	1	20.	$541.4 \text{ cm}^{-3} \mu\text{m}^{-1}$
Rain M	10^{-3}	5.3333×10^5	50.	1	0.5	8.94433	$609.0 \text{ m}^{-3} \text{ mm}^{-1}$
Rain L	10^{-3}	4.9757×10^7	70.	2	0.5	15.11864	$466.0 \text{ m}^{-3} \text{ mm}^{-1}$
Hail H	10^{-5}	4.0000×10^4	100.	2	1	20.	$54.14 \text{ m}^{-3} \text{ mm}^{-1}$
Cumulus C.1	100	2.3730	4.	6	1	1.5	$24.09 \text{ cm}^{-3} \mu\text{m}^{-1}$
Corona C.2	100	1.0851×10^{-2}	4.	8	3	0.041666	$49.41 \text{ cm}^{-3} \mu\text{m}^{-1}$
MOP cloud C.3	100	5.5556	2.	8	3	0.333333	$98.82 \text{ cm}^{-3} \mu\text{m}^{-1}$

Table 1.31 Parameters for Fog and Cloud Distributions Used in LOWTRAN and FASCODE (from Ref. 163)

Distribution Type	α	a	b	N (cm $^{-3}$)	W (g m $^{-3}$)	R_N (μm)	R_M (μm)	ext (km $^{-1}$)
Heavy fog, advective	3	0.027	0.3	20	0.37	10.	20.	28.74
Moderate fog, radiative	6	607.5	3.	20	0.02	2.	3.	8.672
Cumulus	3	2.604	0.5	250	1.	6.	12.	130.8
Stratus	2	27.0	0.6	250	0.29	3.33	8.33	55.18
Stratus/strato-cumulus	2	52.734	0.75	250	0.15	2.67	6.67	35.65
Alto-stratus	5	6.268	1.111	400	0.41	4.5	7.2	91.04
Nimbo-stratus	2	7.676	0.425	200	0.65	4.7	11.76	87.08
Cirrus	6	2.21×10^{-12}	0.09375	0.025	0.06405	64.	96.	1.011
Thin cirrus	6	0.011865	1.5	0.5	3.128×10^{-4}	4.	6.	0.0831

Notes:

 R_N and R_M are the modal radii for number density and mass, respectively.Extinction (ext) is specified at 0.55 μm .The parameter γ is unity for all models.**Table 1.32 Common Military Aerosols**

Type	Composition	Median Particle Diameter (μm)
WP, PWP, RP	$\text{H}_3\text{PO}_4 \cdot n\text{H}_2\text{O}$	1.1
HC (Hexachlorethane, ZnO, Al)	$\text{ZnCl}_2 \cdot n\text{H}_2\text{O}$	1.3
FS	$\text{H}_2\text{SO}_4 \cdot n\text{H}_2\text{O}$	0.85
SGF2 (Petroleum oil fog)	Oil droplets	0.6–3.4*

*Oil fog produced by pyrotechnic means = 0.6; oil fog produced by dripping oil on hot plate = 3.4.

1.4.1.5 Other Aerosols

Aside from naturally occurring aerosols and those arising from industry are those created intentionally for purposes of obscuring vision or sensors. An important application here is obscurant fogs or hazes for battlefields. Listed in Table 1.32 are some of the more commonly used obscurants.^{180,181}

1.4.2 Molecular (Rayleigh) Scatter

Rayleigh scattering by molecules is a result of the dipole moment that is synchronously induced by the incident radiation. This is an elastic scatter phenomenon that is responsible for the blue appearance of the clear sky and the linear polarization of the sky at a 90-deg scatter angle. McCartney¹⁶⁴ shows the molecular scatter cross section per unit volume (also called the volume scatter coefficient, or simply the scatter coefficient) to be given by

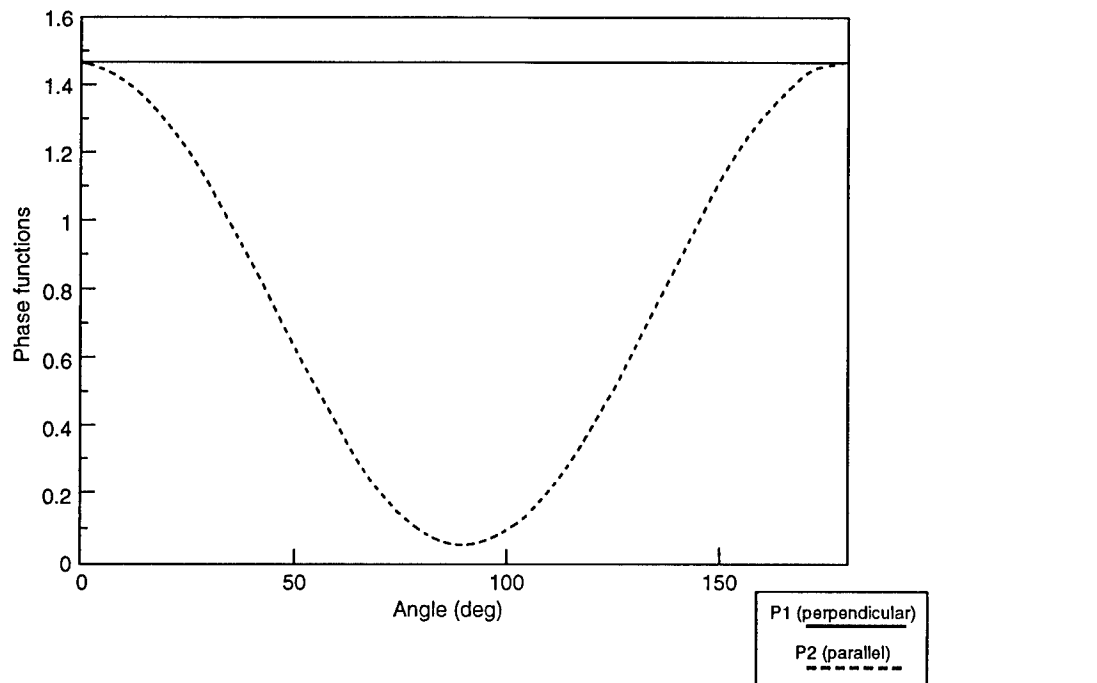


Fig. 1.51 Rayleigh phase function for molecular atmosphere.

$$\sigma_{\text{sca}}(z) = \frac{8\pi^3(n^2 - 1)^2 N(z)}{3N^2(0)\lambda^4} \frac{(6 + 3\delta)}{(6 - 7\delta)}, \quad (1.225)$$

where δ is the depolarization factor arising from the anisotropy of the gas molecule. For air, a commonly accepted value is 0.035.¹⁶⁴ As a result of this molecular anisotropy, the molecular scatter viewed at a scatter angle of 90 deg is not completely linearly polarized. The factor $N(z)$ is the number density of gas molecules at altitude z .

As a result of the molecular anisotropy, the phase function is modified¹⁸² as follows:

$$P(\theta) = \frac{3}{4} \left(\frac{1 + \delta}{1 + \delta/2} \right) \left[1 + \left(\frac{1 + \delta}{1 - \delta} \right) \cos^2 \theta \right]. \quad (1.226)$$

Shown in Fig. 1.51 are plots of these two phase functions.

1.4.3 Example Applications

We now present some applications of the foregoing theory. Implicit in these examples is the assumption that the medium is tenuous, i.e., that there is no multiple scattering. Further, we consider aerosol effects only, not molecular effects.

1.4.3.1 Electro-Optic Sensors

Consider a single scattering particle within the field of view of a sensor (see Fig. 1.52). The power due to scatter from the particle that is received by the sensor is given by

$$P_d = I_i C_{\text{sca}}(r) \frac{P(\theta)}{4\pi} \Omega_d , \quad (1.227)$$

where I_i is the incident intensity and Ω_d is the solid angle subtended at the scatterer by the input aperture of the detector. Approximating the solid angle as $\Omega_d \approx A_d/R^2$, where A_d is the area of the input aperture, yields the following:

$$\frac{P_d}{A_d} = I_d = I_i \frac{P(\theta)C_{\text{sca}}(r)}{4\pi R^2} . \quad (1.228)$$

Using the relationship between the Mueller matrix element and the phase function [see Eq. (1.205)], we have

$$I_d = I_i \frac{S_{11}(\theta, r)}{k^2 R^2} , \quad (1.229)$$

which is the result directly from Eq. (1.184).

Next, consider the problem shown in Fig. 1.53. Here we have illustrated a sensor viewing a portion of an unpolarized laser beam that is traversing an aerosol-laden medium. In this case, the power received by the sensor is given by

$$P_d = I_i A_b \beta_{\text{sca}} L \frac{P(\theta)}{4\pi} \Omega_d , \quad (1.230)$$

where A_b is the cross-sectional area of the laser beam and L is the length of the beam within the field of view of the sensor. Using the relationship between

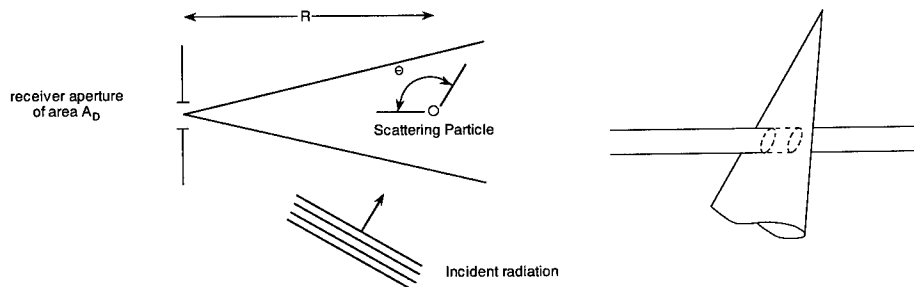


Fig. 1.52 Illustration of scatter from a single particle.

Fig. 1.53 Scatter from laser beam propagating through an aerosol-laden medium.

the phase function and the Mueller matrix element, Eq. (1.205), this equation can be expressed as

$$I_d = I_i \frac{VS_{11}(\theta)}{k^2 R^2} , \quad (1.231)$$

where $V = A_b L$ is the volume of the beam viewed by the sensor.

1.4.3.2 Transmission along a Slant Path

The change in the intensity for propagating a differential distance dz is proportional to the product of the intensity and a constant. This constant is given by the "extinction coefficient":

$$\frac{dE}{dz} = -\beta_{\text{ext}} E . \quad (1.232)$$

This differential equation is solved easily to yield an exponential damping of the intensity known as Bouguer's law (sometimes called Beer-Lambert's law):

$$E(z) = E(0) \exp(-\beta_{\text{ext}} z) . \quad (1.233)$$

We define the transmission as the quotient of the observed intensity and the incident intensity;

$$T \equiv \frac{E(z)}{E(0)} = \exp(-\beta_{\text{ext}} z) . \quad (1.234)$$

This is the solution for the case of propagation through a homogeneous medium. For the case in which the scatter properties of the medium vary along the path length, the exponent is the path integral along the propagation path:

$$T = \exp \left[- \int_0^z \beta_{\text{ext}}(s) ds \right] . \quad (1.235)$$

Finally, if we consider molecular absorption, the total transmission is simply the product of that due to aerosol extinction and that due to molecular absorption.

On the basis of the previous development, we see that the transmission from ground level to a point R along a slant path is given by the following formula:

$$T(0, R) = \exp \left[- \int_0^R \beta_{\text{ext}}(r) dr \right] . \quad (1.236)$$

By dividing and multiplying the exponent by the path integral along the vertical path, we can write this expression in the following form:

$$T(0,R) = \exp\left(-\frac{S}{V}V\right) , \quad (1.237)$$

where we have defined the slant path and vertical line integrals, respectively, as

$$\begin{aligned} S &= \int_0^R \beta_{\text{ext}}(r) dr , \\ V &= \int_0^z \beta_{\text{ext}}(s) ds . \end{aligned} \quad (1.238)$$

Finally, we observe that the slant path transmission is simply the vertical transmission raised to the secant of the angle of the slant path with respect to vertical:

$$T(0,R) = \exp(-V)^{S/V} , \quad (1.239)$$

or, finally,

$$T(0,R) = T(0,z)^{\sec\zeta} , \quad (1.240)$$

where ζ is the zenith angle. Note that implicit in this development is the assumption that the earth is flat, i.e., that the medium is plane-stratified. This approximation is generally adequate if the zenith angle is less than 75 deg. Beyond this point, however, earth-curvature effects come into play.

A convenient means of accounting for earth-curvature effects is to use the Chapman function¹⁸³ in place of the term $\sec\zeta$. This function is expressed as

$$\text{Ch}(\chi, \zeta) = \chi \sin\zeta \int_0^\zeta \exp(\chi - \chi \sin\zeta \csc\psi) \csc^2\psi d\psi , \quad (1.241)$$

where

$$\chi = \frac{(Z_p + r_e)}{H_\rho} , \quad (1.242)$$

where, as illustrated in Fig. 1.54, Z_p is the altitude of the receiver, r_e is the radius of the earth, and H_ρ is the density scale height appropriate for the altitude Z_p .

This function is based on an isothermal atmosphere, and ignores refractive bending. The sea-level density scale height is given by the expression

$$H_\rho = \frac{RT}{g} , \quad (1.243)$$

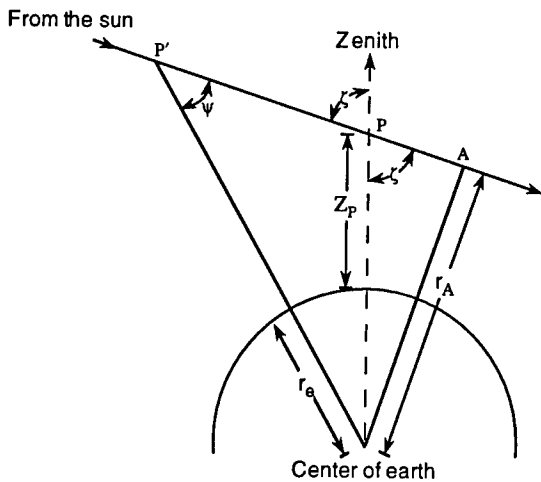


Fig. 1.54 Illustration of geometry for Chapman function. The altitude of P above the earth's surface relative to the earth's radius has been exaggerated somewhat for illustrative purposes.

where R is the gas constant, T is temperature, and g is the acceleration of gravity. For $T = 0^\circ\text{C}$, the scale height is 8 km; for the U.S. Standard Atmosphere—1962, the scale height is 9.3 km. Listed in Table 1.33 are computed values of the Chapman function for representative values of the parameter χ . Also shown for comparison are values of $\sec \zeta$.

The data in Table 1.33 may be extended by making use of the identity

Table 1.33 Values of the Chapman Function

ζ	$\sec \zeta$	$\chi = 600$	$\chi = 700$	$\chi = 800$	$\chi = 900$	$\chi = 1000$
70	2.924	2.889	2.893	2.897	2.900	2.902
71	3.072	3.030	3.036	3.040	3.044	3.046
72	3.236	3.188	3.194	3.199	3.203	3.206
73	3.420	3.363	3.370	3.376	3.381	3.385
74	3.628	3.559	3.568	3.575	3.581	3.586
75	3.864	3.780	3.791	3.800	3.807	3.812
76	4.143	4.031	4.045	4.055	4.064	4.070
77	4.445	4.318	4.335	4.348	4.358	4.366
78	4.810	4.650	4.671	4.687	4.700	4.710
79	5.241	5.036	5.062	5.083	5.099	5.112
80	5.759	5.491	5.525	5.551	5.572	5.590
81	6.392	6.034	6.079	6.113	6.141	6.164
82	7.185	6.692	6.572	6.799	6.836	6.867
83	8.206	7.503	7.585	7.650	7.702	7.745
84	9.567	8.523	8.639	8.732	8.807	8.870
85	11.474	9.838	10.008	10.144	10.257	10.352
86	14.336	11.580	11.839	12.051	12.228	12.378
87	19.107	13.970	14.384	14.730	15.024	15.277
88	28.654	17.388	18.087	18.686	19.209	19.670
89	57.299	22.523	23.784	24.905	25.914	26.830
90	∞	30.719	33.177	35.466	37.615	39.648
91	—	44.789	50.030	55.211	60.362	65.505
92	—	71.132	83.522	96.753	—	—

$$\text{Ch}(\chi, \zeta) + \text{Ch}(\chi, \pi - \zeta) = 2 \exp(\chi - \chi \sin \zeta) \text{Ch}\left(\chi \sin \zeta, \frac{\pi}{2}\right), \quad (1.244)$$

and by making use of the fact that $\text{Ch}(\chi, \pi/2) = \chi e^\chi K_1(\chi)$, where K_1 is the modified Bessel function of the first kind and order unity.

1.4.4 Propagation through a Highly Scattering Medium

Next, we take up the problem of propagation through a highly scattering medium. The general context is that of multiple scatter. After first stating some definitions we derive the "transport" equation, also known as the equation of transfer. Finally, we indicate how this equation can be solved. One concept integral to these solutions is the approximation of the phase function. Actually, this approximation finds use in single-scatter calculations also.

1.4.4.1 Energy Propagation and the Transport Equation

Illustrated in Fig. 1.55 is the phenomenology of propagation through a highly scattering medium. We want to consider the case in which the photons are multiply scattered within the aerosol medium. As a result of this multiple-scatter effect, the original radiance distribution undergoes angular spreading, spatial spreading, multipath temporal spreading, and, for a nonconservative medium, reduced total transmission. Table 1.34 lists the general approaches to solving the problem of propagation through a multiple-scattering medium.

In the material that follows, we confine our attention to the transport-theory approach. This approach is common to many scatter problems, not just those involving scatter of photons. We therefore can freely borrow theory and algorithms developed, for instance, to describe neutron scatter in reactor shielding.¹⁸⁴

Of central importance to the transport theory is the concept of specific intensity $I(\bar{r}, \hat{s})$, also known in other contexts as spectral brightness, or spectral

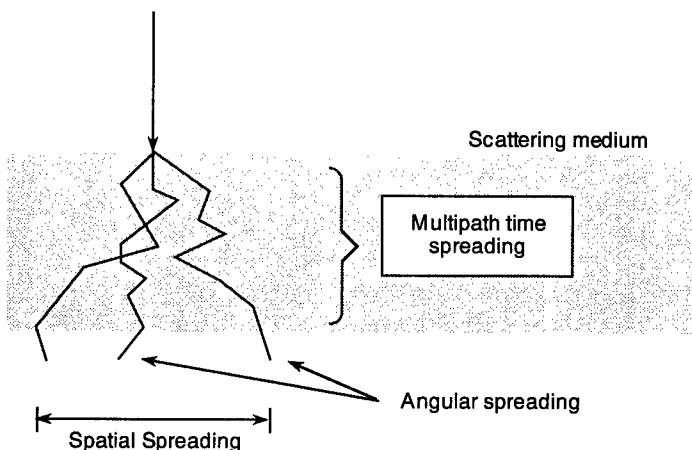


Fig. 1.55 Phenomenology of propagation through a highly scattering medium.

Table 1.34 General Approaches to the Multiple-Scatter Problem

Analytic Theory
Start with Maxwell's equations
Introduce scattering and absorption characteristics of particles
Obtain integro-differential equations for statistical quantities—variances, correlations (Mathematically rigorous)
Transport Theory (aka Radiative Transport Theory)
(Deals with transport of energy through medium containing particles)
Development of theory is heuristic
Diffraction effects not included explicitly*
Assume no correlation between fields \Rightarrow intensities are additive

*Diffraction effects are accounted for through the use of the formal solution to the single-scatter problem.

radiance. The units of specific intensity, which unfortunately is often called simply "intensity," are $\text{W m}^{-2} \text{ sr}^{-1} \text{ Hz}^{-1}$. As an application of this concept (see Fig. 1.56), the power flowing through a differential surface element da (oriented \perp to \hat{s}_0) within the solid angle $d\omega$, in the direction \hat{s} , and in the frequency interval $(\nu, \nu + d\nu)$, is given by

$$dP = I(\bar{r}, \hat{s}) \cos\theta da d\omega d\nu \quad (\text{W}) \quad (1.245)$$

The variables *surface* and *field* intensity describe the radiation characteristic of flux (power) emitted from a real surface or through a hypothetical surface. As illustrated in Fig. 1.57, the *surface intensity* is denoted by I_+ , and the *field*

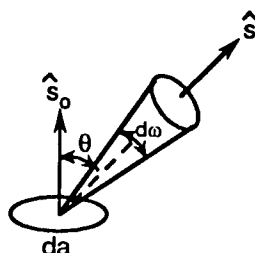
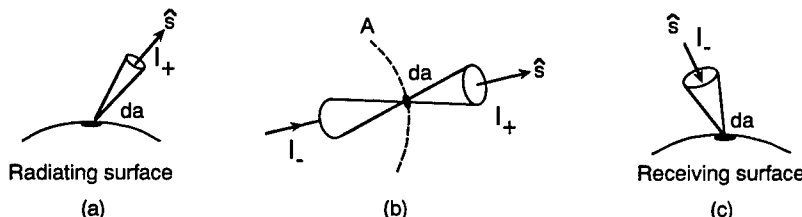


Fig. 1.56 Illustration of the concept of specific intensity.

Fig. 1.57 Surface intensity I_+ and field intensity I_- .

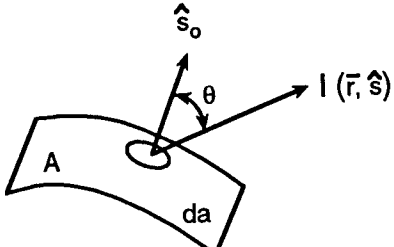


Fig. 1.58 Illustration of the concept of flux density.

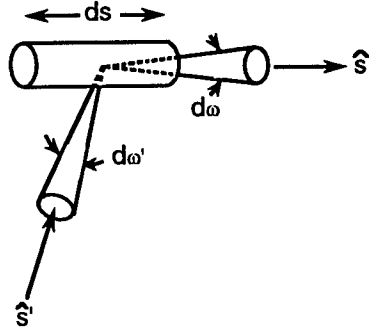


Fig. 1.59 Illustration for derivation of equation of transport.

intensity is denoted by I_- . These are different, but numerically equal, concepts. In the field of radiometry, this equality is referred to as the conservation of brightness.

The concept of *flux density* is illustrated in Fig. 1.58. The forward flux density is given by

$$F_+(\bar{r}, \hat{s}_0) = \int_{\text{forward}}_{2\pi} I(\bar{r}, \hat{s}) \hat{s} \cdot \hat{s}_0 d\omega , \quad (1.246)$$

where $\hat{s} \cdot \hat{s}_0 = \cos\theta$. For a radiating surface, F_+ is the *radiant emittance*. The backward flux density is given by

$$F_-(\bar{r}, \hat{s}_0) = \int_{\text{backward}}_{2\pi} I(\bar{r}, \hat{s}) \hat{s} \cdot \hat{s}_0 d\omega . \quad (1.247)$$

For energy incident on a surface, F_- is the *irradiance*.

With these basic definitions, we proceed with a brief derivation of the equation of transport. With reference to Fig. 1.59, we see that the decrease in specific intensity for propagating a distance ds is given by

$$dI(\bar{r}, \hat{s}) = -\sigma_{\text{ext}} I(\bar{r}, \hat{s}) ds . \quad (1.248)$$

But the specific intensity *increases* because of energy incident on this volume being scattered in the direction \hat{s} . The incident flux density is given by

$$F_i = I(\bar{r}, \hat{s}') d\omega' \quad (1.249)$$

and the scattered flux density at a distance R is given by

$$F_s = \frac{\beta_{\text{ext}} ds p(\hat{s}, \hat{s}')}{4\pi R^2} F_i , \quad (1.250)$$

where $p(\hat{s}, \hat{s}')$ is the phase function such that

$$\frac{1}{4\pi} \int_{4\pi} p(\hat{s}, \hat{s}) d\omega = a \text{ (albedo)} . \quad (1.251)$$

Integrating over the solid angle, the contribution to the specific intensity is

$$\frac{\beta_{\text{ext}} ds}{4\pi} \int_{4\pi} p(\hat{s}, \hat{s}') I(\bar{r}, \hat{s}') d\omega' . \quad (1.252)$$

Including the possibility of emission within the volume, the specific intensity is *increased* by

$$\varepsilon(\bar{r}, \hat{s}) ds , \quad (1.253)$$

where $\varepsilon(\bar{r}, \hat{s})$ is the power radiated per unit volume and per solid angle in the direction \hat{s} . The equation of transport thus becomes

$$\frac{dI(\bar{r}, \hat{s})}{ds} = -\beta_{\text{ext}} I(\bar{r}, \hat{s}) + \frac{\beta_{\text{ext}}}{4\pi} \int_{4\pi} p(\hat{s}, \hat{s}') I(\bar{r}, \hat{s}') d\omega' + \varepsilon(\bar{r}, \hat{s}) . \quad (1.254)$$

In this equation, the left-hand side represents the change in specific intensity. Terms on the right-hand side represent the extinction, the increase due to scatter, and the increase due to sources within the scattering medium, respectively.

By defining the "optical distance" τ as the path integral of the extinction cross section per unit volume,

$$\tau = \int \beta_{\text{ext}} ds , \quad (1.255)$$

the transport equation can be written as

$$\frac{dI(\bar{r}, \hat{s})}{d\tau} = -I(\bar{r}, \hat{s}) + \frac{1}{4\pi} \int_{4\pi} p(\hat{s}, \hat{s}') I(\bar{r}, \hat{s}') d\omega' + J(\bar{r}, \hat{s}) , \quad (1.256)$$

where

$$J(\bar{r}, \hat{s}) = \frac{\varepsilon(\bar{r}, \hat{s})}{\beta_{\text{ext}}} \quad (1.257)$$

is commonly called the *source function*.

There are myriad approaches to solution of the transport equation. Chapter 4 of Ref. 167 discusses various exact (normal-mode expansion, Wiener-Hopf) and approximate (spherical harmonics, discrete ordinates, doubling, Monte Carlo, etc.) techniques. Here we show one example of each of the exact and approximate techniques. We restrict our attention to the plane-parallel ge-

ometry. This geometry is appropriate, for example, to planetary atmospheres, clouds, ocean waters illuminated by the sun, etc. The basic assumption is that of a plane wave incident on a plane-parallel medium. For discussion of other geometries and solution approaches, see Refs. 158, 182, and 185.

1.4.4.1.1 Two- and Four-Flux Theory

The (Kubelka-Munk) two-flux theory is an approximate solution that adequately describes the case in which the illumination is diffused and the medium is "dull" so that light is diffusely scattered. It does not adequately describe the case of collimated incident radiation; for this case, the four-flux theory is required.

In the two-flux theory the flux is envisioned as being composed of a positive-flowing flux F_+ and a negative-flowing flux F_- . Conceptually, it is equivalent to approximating the phase function as a weighted sum of delta functions in the forward and backward directions.

In propagating a differential distance dz , the positive-flowing flux is decreased due to absorption within dz and scattering into the backward direction:

$$dF_+ = -(K + S)F_+ \beta_{\text{ext}} dz = -(K + S)F_+ d\tau , \quad (1.258)$$

where K and S are dimensionless absorption and scatter coefficients. On the other hand, the positive-flowing flux is increased due to backward scattering from F_- :

$$dF_+ = SF_- \beta_{\text{ext}} dz = SF_- d\tau . \quad (1.259)$$

With similar behavior for the backward-flowing flux, we arrive at a coupled set of differential equations:

$$\begin{aligned} \frac{dF_+}{d\tau} &= -(K + S)F_+ + SF_- , \\ \frac{dF_-}{d\tau} &= (K + S)F_- - SF_+ . \end{aligned} \quad (1.260)$$

By assuming an exponential behavior for F_+ and F_- , $\exp(\alpha z)$ so that $d/d\tau = \alpha$, we obtain a pair of algebraic equations whose solution is given by

$$\alpha_{\pm} = [K(K + 2S)]^{1/2} \equiv \pm \alpha_0 . \quad (1.261)$$

The complete solutions for F_+ and F_- are then given by

$$\begin{aligned} F_+(\tau) &= C_1 e^{\alpha_0 \tau} + C_2 e^{-\alpha_0 \tau} , \\ F_-(\tau) &= C_3 e^{\alpha_0 \tau} + C_4 e^{-\alpha_0 \tau} , \end{aligned} \quad (1.262)$$

where the C 's are determined by application of the boundary conditions. As Ishimaru¹⁸⁵ points out, the coefficients K and S are not clearly related to the physical properties of the scattering particles. However, they can be determined empirically, with the following result¹⁸⁶:

$$\begin{aligned} K\beta_{\text{ext}} &\approx 2\beta_{\text{abs}}, \\ S &\approx \frac{3}{4}\alpha(1 - g), \end{aligned} \quad (1.263)$$

where α is the single-scatter albedo and g is the asymmetry parameter (see Sec. 1.4.4.2).

As noted previously, the four-flux theory is required for describing the propagation, for example, of a laser beam in a highly scattering medium. In this theory, the power flow is represented in terms of forward- and backward-flowing collimated fluxes and forward- and backward-flowing diffuse fluxes. The collimated fluxes, i.e., the reduced intensities, decrease due to scattering and absorption; they are continuously being converted into diffuse intensities by scattering. This approach is similar to that of the two-flux method, with the addition of parameters that represent the scatter and absorption from collimated beams.

1.4.4.1.2 Discrete Ordinates Method

This is an example of an exact method. We restrict our attention to a source-free region, so the transport equation becomes

$$\frac{dI(\bar{r},\hat{s})}{ds} = -\beta_{\text{ext}}I(\bar{r},\hat{s}) + \frac{\beta_{\text{ext}}}{4\pi} \int_{4\pi} p(\hat{s},\hat{s}') I(\bar{r},\hat{s}') d\omega'. \quad (1.264)$$

We decompose the intensity into the sum of the reduced incident intensity and the diffuse intensity, and use for the incident (plane-wave) flux

$$I_{ri}(\bar{r},\hat{s}) = F_0 \exp(-\tau)\delta(\mu - 1)\delta(\phi), \quad (1.265)$$

where $\mu = \cos\theta$. Using this decomposition of the specific intensity and Eq. (1.265) for the reduced incident intensity in the transport equation and integrating over the azimuthal variable ϕ , we obtain the following equation for the diffuse intensity:

$$\begin{aligned} \mu \frac{dI_d(\tau,\mu)}{d\tau} + I_d(\tau,\mu) &= \frac{1}{2} \int_{-1}^1 p_0(\mu,\mu') I_d(\tau,\mu') d\mu' \\ &+ \frac{1}{4\pi} p_0(\mu,1) F_0 e^{-\tau}, \end{aligned} \quad (1.266)$$

where

$$p_0(\mu,\mu') = \frac{1}{2\pi} \int_0^{2\pi} d\phi \frac{1}{2\pi} \int_0^{2\pi} d\phi' p(\mu,\phi;\mu',\phi'). \quad (1.267)$$

As an example, for the Rayleigh phase function,

$$p(\mu, \phi; \mu', \phi') = \frac{3}{4}a(1 + \cos^2\gamma) , \quad (1.268)$$

where γ is the angle between (μ, ϕ) and (μ', ϕ') , given by

$$\cos\gamma = \cos\theta \cos\theta' + \sin\theta \sin\theta' \cos(\phi - \phi') . \quad (1.269)$$

Integrating this phase function over ϕ and ϕ' , one obtains

$$p_0(\mu, \mu') = \frac{3}{4}a \left[1 + \mu^2\mu'^2 + \frac{1}{2}(1 - \mu^2)(1 - \mu'^2) \right] . \quad (1.270)$$

Equation (1.266) plus the boundary conditions constitute the complete statement of the problem. One commonly used solution of this integro-differential equation is to approximate the integral with a quadrature technique; the integration is replaced by a summation. In effect, the integrand is sampled at a number of discrete angles μ_i . As a result, one obtains a matrix linear first-order differential equation. Upon assuming exponential variations for the homogeneous and particular solutions, the problem reduces to a matrix eigenvalue problem. See Ishimaru¹⁸⁵ for details.

1.4.4.2 Phase Function Approximation

A very useful computational expedient, especially within the context of multiple-scatter calculations, is the approximate representation of the single-scatter phase function. The traditional expansion is the following:

$$aP(\cos\theta) = \sum_{n=0}^N \omega_n P_n(\cos\theta) , \quad (1.271)$$

where the single-scatter albedo is denoted by a and P_n is the Legendre polynomial of order n . Making use of the orthogonality of these polynomials results in the expression for the expansion coefficients:

$$\omega_n = \frac{(2n+1)a}{2} \int_{-1}^1 P(\cos\theta) P_n(\cos\theta) d(\cos\theta) . \quad (1.272)$$

From this equation, one finds that $\omega_0 = a$ and $\omega_1 = 3ag$, where g is the asymmetry parameter defined as

$$g = \frac{1}{2} \int_{-1}^1 P(\cos\theta) \cos\theta d(\cos\theta) . \quad (1.273)$$

This asymmetry parameter finds use as a parameter in many other phase-function approximations, notably the Henyey-Greenstein approximation¹⁸⁷:

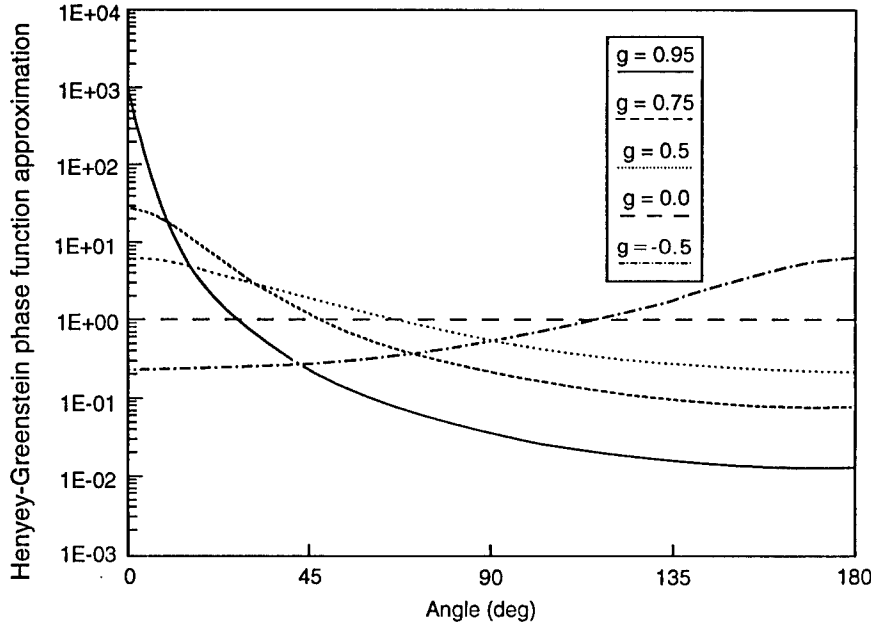


Fig. 1.60 Example Henyey-Greenstein phase function.

$$P(\cos\theta) = \frac{1 - g^2}{(1 + g^2 - 2g \cos\theta)^{3/2}}. \quad (1.274)$$

For this phase-function approximation, the expansion coefficients as in Eq. (1.272) are given by $\omega_n = (2n + 1)g^n$. For an asymmetry parameter of +1 (-1), the phase function is completely in the forward (backward) direction. For $g = 0$, the scatter is isotropic. Example Henyey-Greenstein phase functions are shown in Fig. 1.60.

1.4.4.3 Temporal Effects—Pulse Stretching

So far, we have considered only steady-state conditions, ignoring the fact that in the process of scattering from particulate media, the "time of flight" of the individual photons is increased. This effect is of importance, for example, when the source of radiation, e.g., a laser, is being temporally modulated. An analysis of this effect is usually accomplished through the use of Monte Carlo techniques, e.g., see Bucher.¹⁸⁸ There are, however, analytic formulas for this effect. One, due to Stott,¹⁸⁹ is the following:

$$\Delta t = \frac{z}{c} \left[\frac{0.30}{a\tau\theta_{\text{rms}}^2} (1 + 2.25a\tau\theta_{\text{rms}}^2)^{1.5} - 1 \right], \quad (1.275)$$

where z is the propagation distance in medium, c is the propagation velocity in medium, θ_{rms} is the rms scatter angle, a is the single-scatter albedo, and $\tau = \beta_{\text{sca}}z$.

This formula for pulse stretching (Δt) is based purely on geometrical arguments. Implicit in the derivation is that we are in the geometrical optics regime; i.e., the phase function is highly peaked in the forward direction.

1.4.5 Imaging through a Scattering Medium

In this section we draw a link between the characterization of the aerosol-scattering medium and its effect on imaging. As examples we discuss “visibility range” and the mutual coherence function (MCF) for multiple-forward-scatter media.^{190,191}

1.4.5.1 Visibility Range

Estimates of the visual range usually are made from the appearance of buildings and special targets at differing distances against the skyline. The formula for the visual range R_v is

$$R_v = \frac{1}{\beta_{\text{sca}}} \ln \frac{C}{\varepsilon} , \quad (1.276)$$

where C is the inherent contrast of the target and ε is the threshold contrast of the observer. The use of the scatter cross section rather than the extinction cross section in this definition implies that absorption by atmospheric particles at visual wavelengths is small enough to ignore. This view probably is justified except in cases of polluted air. Meteorological range is defined in terms of a black target (inherent contrast against sky is unity, $C = 1$) and for a 2% contrast threshold:

$$R_m = \frac{3.912}{\beta_{\text{sca}}} . \quad (1.277)$$

Unfortunately, sometimes reference is made to a “visibility range” at a wavelength other than the visible. From the above discussion, however, it is obvious that at wavelengths for which absorption cannot be ignored, β_{sca} in Eq. (1.277) must be replaced by β_{ext} . See the earlier discussion of the wavelength variation of scatter cross section (and extinction cross section) and also McCartney’s¹⁶⁴ discussion.

1.4.5.2 MCF for Aerosol Scatter

We here derive an expression for the point-spread function for propagation through aerosol-laden media. We do this first by deriving an expression for the (spatial) Fourier transform of the PSF, i.e., the optical transfer function (OTF).

Goodman¹⁹² has shown that the OTF for propagation through a random inhomogeneous medium can be written as

$$M(\nu) = \left. \frac{\Gamma(\rho)}{\Gamma(0)} \right|_{\rho = \bar{\lambda}f\nu} , \quad (1.278)$$

where ν is a spatial frequency in units of inverse length, $\bar{\lambda}$ is the mean wavelength, and f is the focal length of the imaging optics. In this equation, the function Γ is the mutual coherence function of the fields in the transverse plane, given by

$$\Gamma(\rho) = \langle u(\bar{r} + \bar{\rho}) u^*(\bar{r}) \rangle , \quad (1.279)$$

and we have assumed rotational symmetry; i.e., $\rho = (\rho_x^2 + \rho_y^2)^{1/2}$. A number of assumptions are implicit in Eq. (1.278). Specifically, we have made the quasimonochromatic assumption

$$\frac{\Delta\lambda}{\bar{\lambda}} \ll 1 , \quad (1.280)$$

and have assumed that the path length differences for the possible photon trajectories through the medium are small with respect to the coherence length of the source:

$$\Delta R \ll l_c \approx \frac{\bar{\lambda}^2}{\Delta\lambda} . \quad (1.281)$$

The situation we are interested in is illustrated in Fig. 1.61. We calculate the MCF for a point source whose field has propagated a distance z through a homogeneous, aerosol-laden medium. We therefore write explicitly

$$\Gamma(\rho, z) = \langle u(\bar{r} + \bar{\rho}, z) u^*(\bar{r}, z) \rangle . \quad (1.282)$$

For the case in which the separation between the field points is zero, we have

$$\Gamma(0) = \langle u(\bar{r}, z) u^*(\bar{r}, z) \rangle = \exp(-\beta_{\text{abs}} z) , \quad (1.283)$$

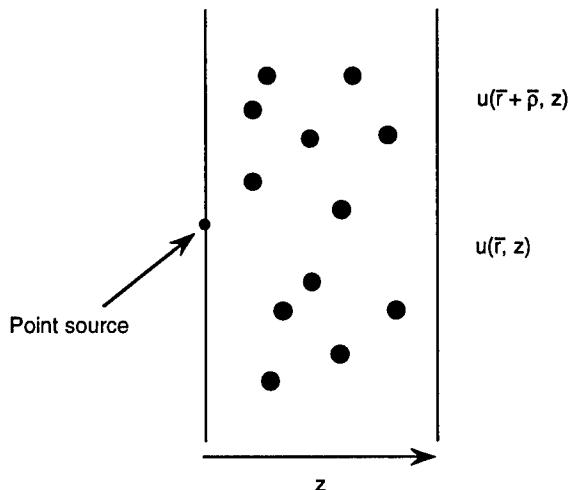


Fig. 1.61 Illustration for derivation of the MCF for scatter.

where β_{abs} is the aerosol absorption cross section per unit volume. We now consider separations so large that no radiation scattered from any single aerosol particle can reach both points $\bar{r} + \bar{p}$ and \bar{r} . In this case, any coherence that exists between the fields at the two points must be due to radiation that has not been scattered; i.e.,

$$\Gamma(\infty) = \exp(-\beta_{\text{ext}}z) , \quad (1.284)$$

where the extinction cross section per unit volume β_{ext} is given by the sum of the absorption and scatter cross sections per unit volume:

$$\beta_{\text{ext}} = \beta_{\text{abs}} + \beta_{\text{sca}} . \quad (1.285)$$

Between these two limits the MCF decreases more or less monotonically from a maximum at $\rho = 0$ to a minimum as $\rho \rightarrow \infty$. Based on the assumption of multiple independent small-angle scatterings, Wells¹⁹³ has shown that the MCF can be expressed as

$$\Gamma(\rho) = \exp\{-\beta_{\text{abs}}z - \beta_{\text{sca}}z[1 - f(\rho)]\} , \quad (1.286)$$

where the function $f(\rho)$ is given by

$$f(\rho) = \frac{1}{4\pi} \int_{4\pi} P(\theta) d\Omega \int_0^1 J_0(k\rho u \sin\theta) du , \quad (1.287)$$

where $P(\theta)$ is the average of the two scatter polarization components perpendicular and parallel to the scattering plane:

$$P(\theta) = \frac{[P_1(\theta) + P_2(\theta)]}{2} , \quad (1.288)$$

and J_0 is the Bessel function of the first kind and order zero.

With the preceding, we can write the OTF as the linear superposition:

$$M(\rho) = \exp(-\beta_{\text{sca}}z) + [1 - \exp(-\beta_{\text{sca}}z)]M_{\text{sca}}(\rho) . \quad (1.289)$$

The first term on the right-hand side of Eq. (1.289) represents the contribution to the OTF that is due to light not scattered within the medium; it represents the asymptote to which the OTF falls for large separation ρ . The second term is due to that portion of the radiation that is scattered. From Eqs. (1.278), (1.286), and (1.289), we can write this portion as

$$M_{\text{sca}}(\rho) = \left(\frac{\exp\{-\beta_{\text{sca}}z[1 - f(\rho)]\} - \exp(-\beta_{\text{sca}}z)}{1 - \exp(-\beta_{\text{sca}}z)} \right) . \quad (1.290)$$

We formally regard this as the OTF due to scatter. These two components of the OTF [Eqs. (1.289) and (1.290)] are illustrated in Fig. 1.62.

We now derive an expression for the OTF due to scatter in the multiple-scatter regime. In this case $\beta_{\text{sca}}z \gg 1$, and Eq. (1.290) becomes $M_{\text{sca}}(\rho) \approx$

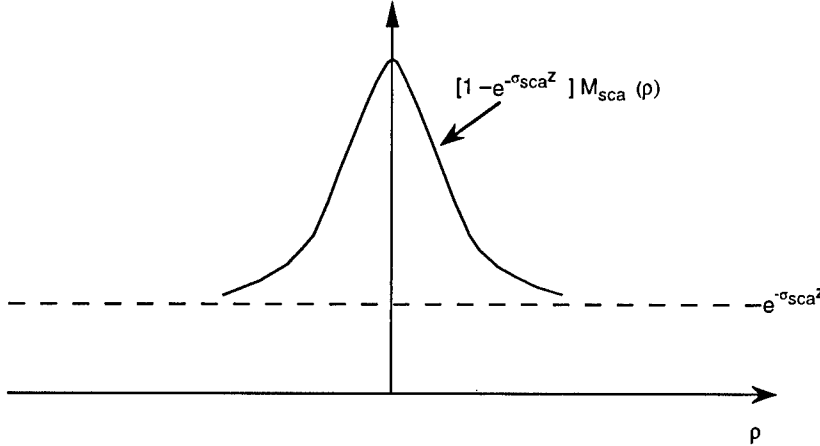


Fig. 1.62 Conceptual form of the OTF for scatter.

$\exp\{-\beta_{sca}z[1 - f(\rho)]\}$. To obtain an expression for f in the case of small-angle scatter, we use the ascending series expression for the Bessel function:

$$\begin{aligned} \int_0^1 J_0(au) du &= \int_0^1 \left[1 - \frac{(au)^2}{4} + \frac{(au)^4}{64} - O(au)^6 \right] du \\ &= 1 - \frac{a^2}{12} + \frac{a^4}{320} + O(a^6) . \end{aligned} \quad (1.291)$$

If the scattering is predominately in the forward direction, we can make the paraxial approximation $\sin\theta \approx \theta$, with the result that

$$f(\rho) \approx 1 - \frac{\langle \theta^2 \rangle}{12} (k\rho)^2 , \quad k\rho\theta_{rms} \ll 1 , \quad (1.292)$$

where $\theta_{rms}^2 = \langle \theta^2 \rangle$ is the mean-squared scattering angle. Substituting these results into Eq. (1.290) we have, for the OTF for scatter,

$$M_{sca}(\rho) = \exp\left[-\left(\frac{\rho}{\rho_a}\right)^2\right] , \quad (1.293)$$

where ρ_a is the (transverse) coherence length for propagation through the aerosol medium, given by

$$\rho_a = \frac{\lambda}{\pi\theta_{rms}} \left(\frac{3}{\beta_{sca}z} \right)^{1/2} . \quad (1.294)$$

From Eq. (1.278), we have the results in terms of spatial frequency:

$$M_{sca}(\nu) = \exp\left[-\left(\frac{\bar{\lambda}f\nu}{\rho_a}\right)^2\right] . \quad (1.295)$$

Recall that the point-spread function is the inverse Fourier transform of the OTF. It therefore can be shown easily that the PSF for scatter $s_{\text{sca}}(r)$ is given by

$$s_{\text{sca}}(r) = \frac{\pi \rho_a^2}{(\lambda f)^2} \exp\left[-\frac{\pi^2 r^2}{(\lambda f/\rho_a)^2}\right]. \quad (1.296)$$

We note that the $1/e$ point of this PSF is given by

$$r = \frac{\lambda f}{\pi \rho_a}, \quad (1.297)$$

or, expressed in terms of the angle at the focal plane,

$$\frac{r}{f} = \frac{\lambda}{\pi \rho_a}. \quad (1.298)$$

These results state that in the focal plane, the image of a point source will appear as a bright spot at the geometrical image position, surrounded by a diffuse halo. The bright spot is due to light that has not undergone scatter [the first term on the right-hand side of Eq. (1.289)] and a portion that has been scattered [the second term in Eq. (1.289)]. The angular half-width of the halo surrounding the geometrical point image is given by Eq. (1.298).

1.5 COMPUTER CODES ON ATMOSPHERIC PROPAGATION

Many of the models discussed previously are contained in atmospheric transmission codes, which provide a powerful tool for quantifying atmospheric effects. The most commonly used codes are maintained by the Geophysics Directorate at Hanscom Air Force Base, Massachusetts (formerly Air Force Geophysics Laboratory and Air Force Cambridge Research Laboratory). They are LOWTRAN, MODTRAN, and FASCODE and are briefly described in this section. These codes allow for complex atmospheric transmittance and radiance calculations based on absorption and scattering phenomena for a variety of path geometries. LOWTRAN is a low-resolution (20-cm^{-1}) code, MODTRAN is a moderate resolution (2-cm^{-1}) code, and FASCODE is a high-resolution code. FASCODE uses the HITRAN database directly and LOWTRAN and MODTRAN use the HITRAN database indirectly to determine band-model parameters. The widespread availability and use of these codes is why this chapter foregoes extensive figures and tables of limited value on transmittance and radiance.

1.5.1 LOWTRAN

LOWTRAN is the name of a series of computer codes beginning with LOWTRAN 2 (first available in 1972) and ending with the most recent version LOWTRAN 7 (first available in 1989).^{194–200} LOWTRAN calculates the transmittance and/or radiance for a specified path through the atmosphere based on the LOWTRAN band model discussed previously, molecular continuum absorption, molecular scattering, and aerosol absorption and scattering models. Ra-

diance calculations include atmospheric self-emission, solar and/or lunar radiance single scattered into the path, direct solar irradiance through a slant path to space, and multiple scattered solar and/or self-emission radiance into the path. The model covers the spectral range from 0 to 50,000 cm^{-1} at a resolution of 20 cm^{-1} . The band model spectral parameters exist every 5 cm^{-1} .

The atmosphere is represented as 32 layers from 0 to 100,000 km altitude. Layer thickness varies from 1 km up to 25 km, 5 km from 25 to 50 km (the top of the stratosphere), and the last two layers are 20 and 30 km thick, respectively. Detailed structure just above the land or sea is not represented by this model and thus model predictions can be inaccurate if nonstandard conditions exist. Attenuation and refractive effects are calculated for each layer and summed along the path. The physical characteristics of each layer are determined by inputs and predetermined standard models of various regions and seasons (see Table 1.35).^{194–200} The option to specify a particular atmosphere also exists. The atmosphere is assumed to be in thermal equilibrium; the code should not be used above 100 km or at and above the ionosphere.

Figures 1.63 to 1.67 illustrate typical LOWTRAN outputs for various types of atmospheres, spectral regions, mechanisms of attenuation, path emission, and path geometries.

LOWTRAN has been validated against field measurements^{75,201} and is widely used for many broadband system performance studies. However, the single-parameter band model used in LOWTRAN has limited validity with respect to temperature dependence. Calculations above and below room temperature should be checked against more physically complete codes such as FASCODE (see Sec. 1.5.3). In particular, LOWTRAN works best at low altitudes with moderate temperatures. High-altitude calculations (> 40 km) will have the least accurate results. Because of the limited resolution of LOWTRAN it should not be applied to laser propagation modeling when local line absorption is important.

1.5.2 MODTRAN

MODTRAN is identical to LOWTRAN except it contains the MODTRAN band model as described in Sec. 1.3.4.3. MODTRAN offers moderate-resolution (2 cm^{-1}) calculations with improved temperature and pressure dependence over LOWTRAN. Thus, high-altitude (< 60 km) calculations are more valid compared to LOWTRAN calculations. Figure 1.68 compares a MODTRAN output to a LOWTRAN output and clearly demonstrates the improved representation when resolution is an issue. Figure 1.69 compares a high-altitude radiance calculation from LOWTRAN and MODTRAN. In this case LOWTRAN 7 does not correctly model the radiance at low temperature.

1.5.3 FASCODE

For studies involving the propagation of very narrow optical bandwidth radiation, for example, lasers, the high resolution afforded by FASCODE is required. Characterization of the aerosol and molecular medium in FASCODE is much the same as that for LOWTRAN. In fact, FASCODE contains a version of LOWTRAN. Here, we present an example of typical results to be obtained with FASCODE. This test case was run on a 386 PC using ONTAR's version

Table 1.35 LOWTRAN Inputs

Input	Options
Model atmosphere	Midlatitude summer model Midlatitude winter Tropical Subarctic summer Subarctic winter Meteorological data input 1962 standard atmosphere
Type of atmospheric path	Slant path to space Horizontal path Slant path
Mode of execution	Transmittance Radiance Radiance with scattering Trans. solar irradiance
Temperature and pressure altitude profile	Midlatitude summer, etc.
Water-vapor altitude profile	Midlatitude summer, etc.
Ozone altitude profile	Midlatitude summer, etc.
Radiosonde data are to be input	Yes/No
Suppress profile output	Yes/No
Temperature at boundary (0.0-T at first level)	Surface temperature
Surface albedo (0.0-blackbody)	0-1
Extinction type and default range	Rural—VIS = 23 km Rural—VIS = 5 km Navy maritime Maritime—VIS = 23 km Urban—VIS = 5 km Tropospheric—VIS = 50 km User-defined—VIS = 23 km Fog advection—VIS = 0.2 km Fog radiation—VIS = 0.5 km No aerosol attenuation
Seasonal aerosol profile	Determined by model Spring-summer Fall-winter
Aerosol profile and extinction type	Background stratospheric Moderate/aged volcanic High/fresh volcanic High/aged volcanic Moderate/fresh volcanic
Air mass character	0
Inclusion of cirrus attenuation	Yes/No
Use of Army (VSA) for aerosols	Yes/No
Surface range (0.0-default)	-
Current wind speed (m/s)	-
24-h average wind speed (m/s)	-
Rain rate	-

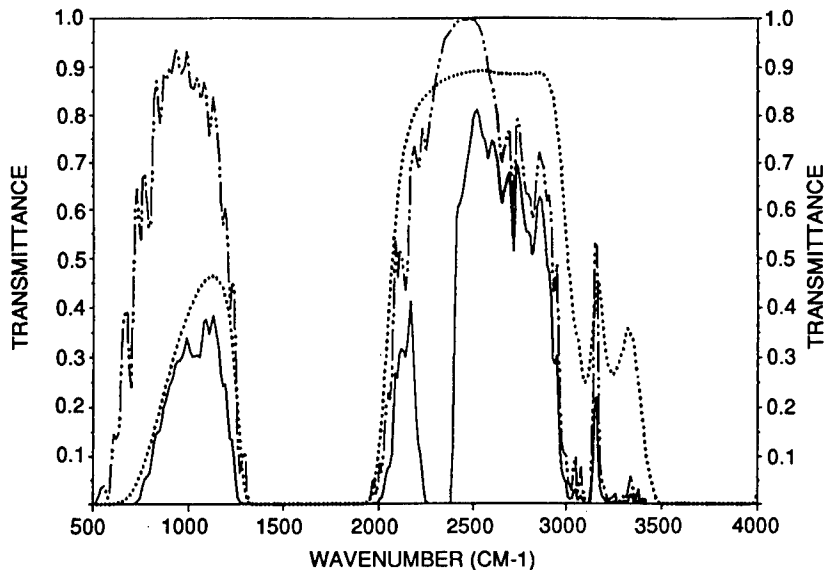


Fig. 1.63 LOWTRAN calculation of the 10- and 4-μm window regions for the midlatitude summer model and horizontal sea-level path of 5 km. The solid curve represents the total transmittance, the dot-dash curve the water-vapor local-line contributions, and the dotted curve the water-vapor continuum.

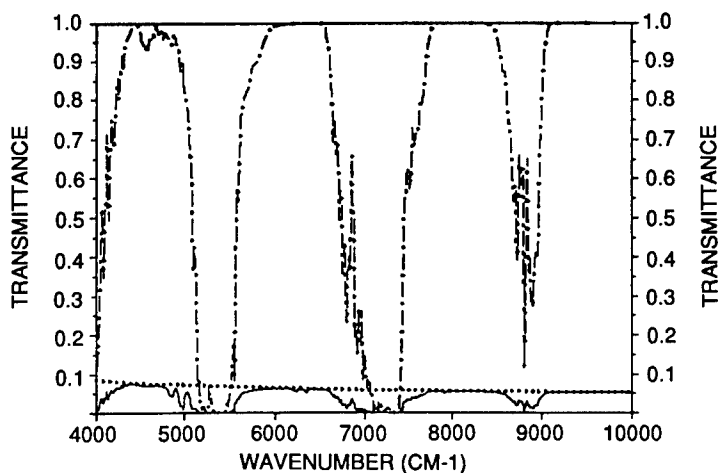


Fig. 1.64 LOWTRAN calculation for the subarctic winter model with the Navy maritime aerosol model at sea level and a 10-km path. Solid curve is the total transmittance, the dot-dash curve represents water-vapor absorption-band contributions, and the dotted curve represents aerosol contributions.

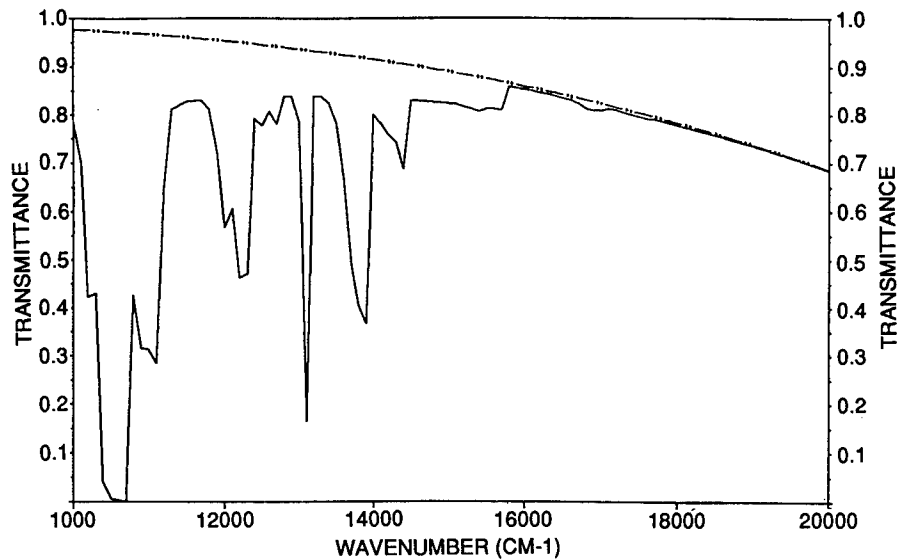


Fig. 1.65 LOWTRAN calculation of the near-IR and visible regions for the tropical model and a horizontal path at 1-km altitude with a path length of 25 km. The solid curve represents the total transmittance and the dot-dash curve represents molecular scattering.

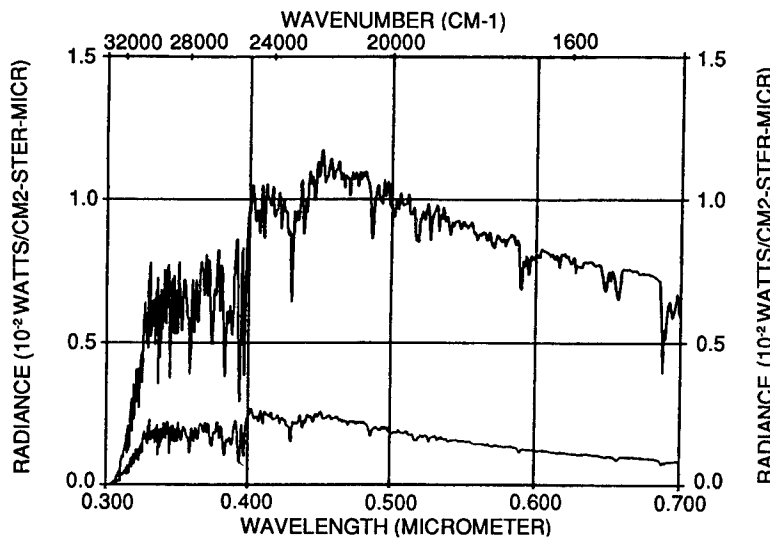


Fig. 1.66 Slant-path radiance calculation for an observer at 20-km altitude looking straight down. The solar zenith angle is 60 deg. The 1976 U.S. Standard Atmosphere is used with the rural aerosol model. The lower curve is the radiance due to single scatter and the upper curve includes multiple scatter, thus emphasizing its importance.

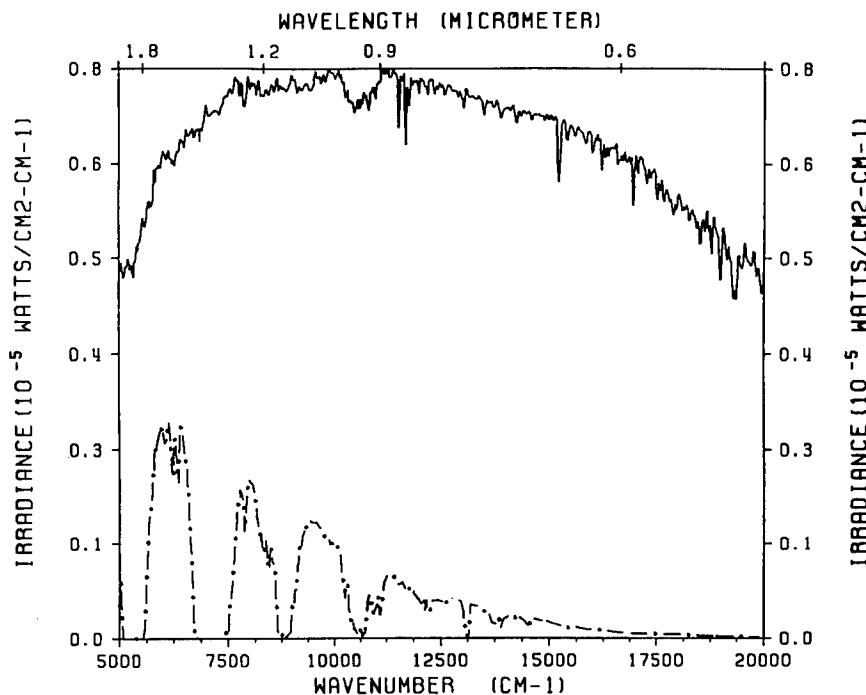


Fig. 1.67 Solar irradiance LOWTRAN 7 calculation using the 1976 U.S. Standard Atmosphere, rural aerosol model (23-km visibility), a solar angle of 85 deg from the zenith, on March 15. The upper curve is the incident solar irradiance at the top of the atmosphere and the lower curve is the transmitted solar irradiance through the atmosphere to an observer on earth. The calculation predicts a reddened sun for this geometry, caused mostly by scatter.

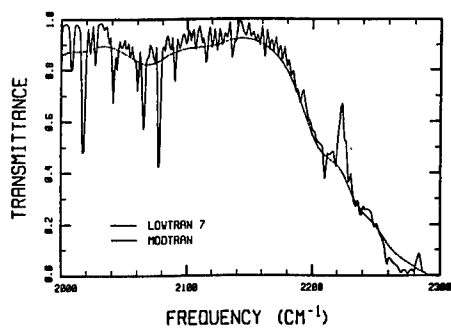


Fig. 1.68 Comparison between a MODTRAN calculation (solid curve) and LOWTRAN calculation (dotted curve) for the same atmospheric conditions and path geometry (Sec. 1.3.4, Ref. 134).

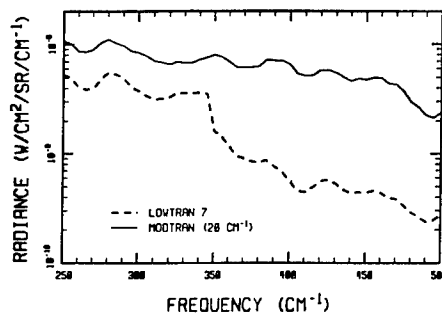


Fig. 1.69 Comparison between LOWTRAN 7 and MODTRAN predictions of radiance of the pure rotational band of water vapor for a 60-km limb path.

Table 1.36 Input for Example FASCODE Run

Wave-number range	850–1100 cm ⁻¹
Molecular profile	Midlatitude summer
Path description	6.096 km—ground
Path length	100 km
Path type	Short
Aerosol profile	Maritime, 23-km visibility
No clouds or rain	

of FASCOD2. This is a menu-driven package that allows line file generation, creation of the input file for FASCODE, execution of the transmission calculations, and subsequent plotting of results. Input for this test case is given in Table 1.36.

Results are shown in a series of four figures, beginning with Fig. 1.70, which shows the transmission over the entire range of 850 to 1100 cm⁻¹. Figure 1.71 shows the transmission in the vicinity of the P(20) (10.591 μm for the ¹²C and ¹⁶O isotopes) line of the CO₂ laser. Figure 1.72 shows the transmission around the ¹³C-isotope-based CO₂, P(20) line at 11.15 μm. Note that the lack of this isotopic form of CO₂ in the atmosphere leads to a markedly better transmission. Finally, Fig. 1.73 shows the transmission in the vicinity of the R(20) line (9.115 μm) of the ¹⁸O isotopic form of CO₂.

1.5.4 Algorithms for Calculation of Scatter Parameters

Herein are presented two algorithms for calculation of scatter from homogeneous spheres. The first is given essentially verbatim from Bohren and Huffman.²⁰² For a given wavelength, particle radius, and refractive index (as well as the specified refractive index of the surrounding medium), it generates estimates of the efficiencies (scatter, extinction, backscatter) and the scatter matrix components (S₁₁, S₁₂, S₃₃, and S₃₄) for the specified number of angles between 0 and 90 deg. The second program is an adaptation of BHMIE to the calculation of these scatter parameters for polydispersions. This program is configured to call a subroutine function that specifies the aerosol size distribution. This function can be an analytic one, such as Deirmendjian's modified gamma (see Sec. 1.4.1.4.3), or one that interpolates from tabulated data. Examples of each of these two distributions are provided as well as example results of the code execution. All of these program components are coded in Fortran 77 and run efficiently on a personal computer.

Shown in Table 1.37 is a listing of subroutine BHMIE with a typical calling program, or "driver." Typical results are shown in Table 1.38.

Also note that Bohren and Huffman²⁰² supply a subroutine for calculation of scatter from coated spheres.

A convenient way of obtaining refractive-index data is to interpolate from tabulated data. Table 1.39 illustrates a four-point Lagrange interpolation of

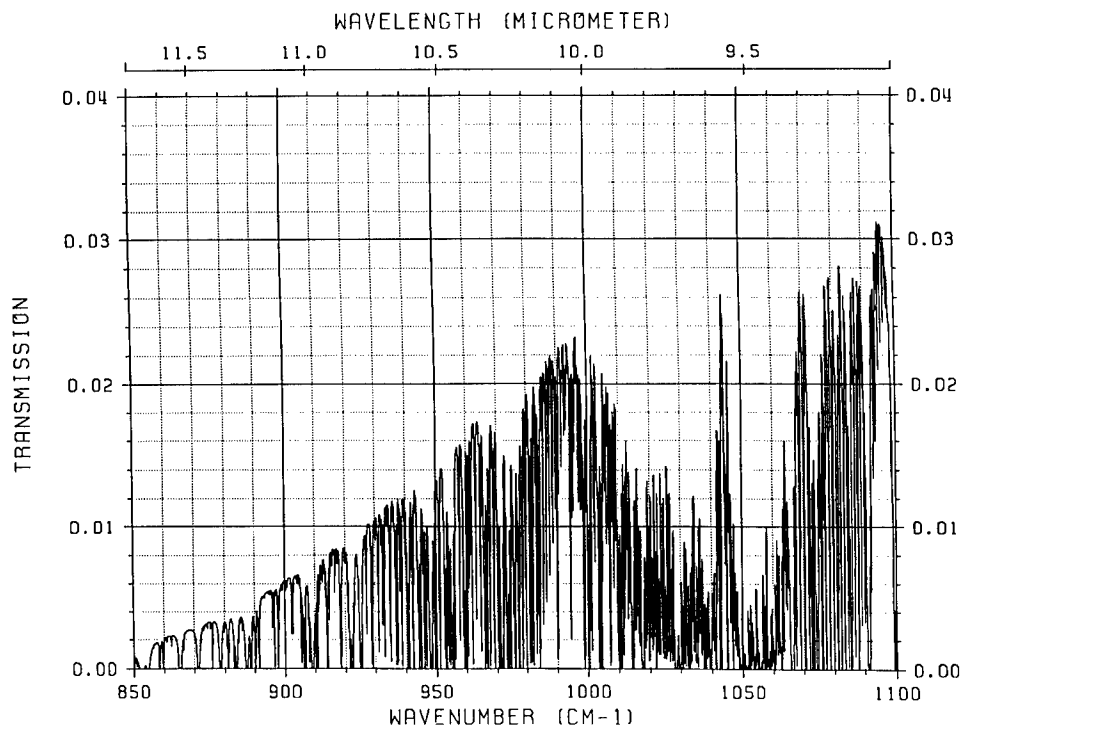


Fig. 1.70 FASCODE transmission estimates in the 850 to 1100 cm^{-1} range.

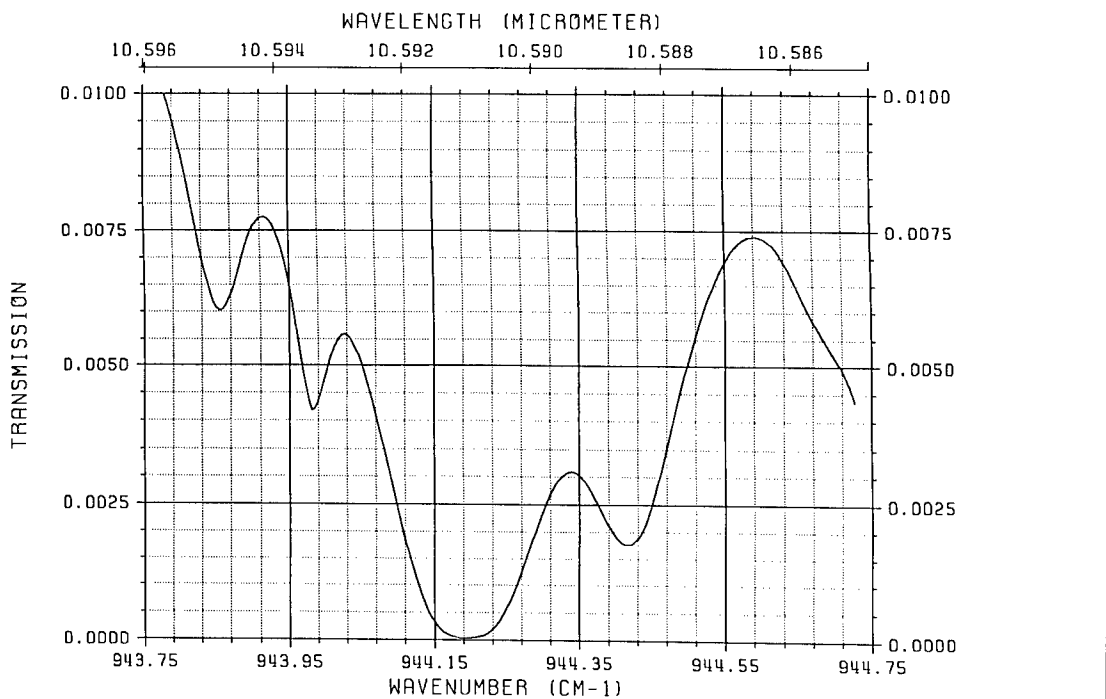


Fig. 1.71 FASCODE transmission estimates in the vicinity of 10.591 μm .

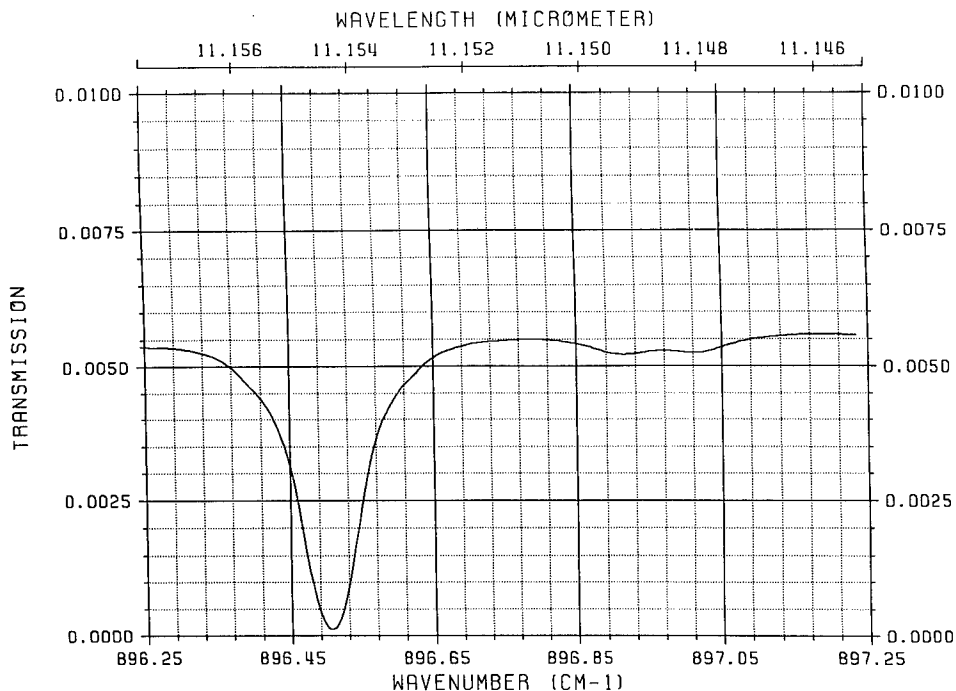


Fig. 1.72 FASCODE transmission estimates in the vicinity of 11.15 μm .

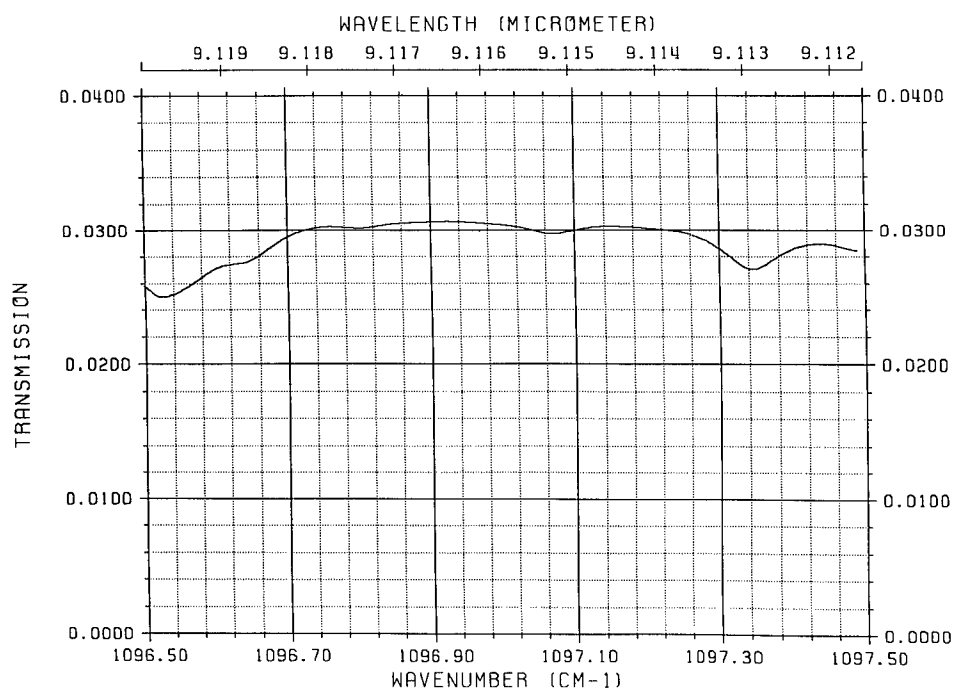


Fig. 1.73 FASCODE transmission estimates in the vicinity of 9.115 μm .

Table 1.37 Calling Program and Subroutine BHMIE

```

C*****
C THIS PROGRAM CALCULATES THE SIZE PARAMETER, X, AND RELATIVE REFRACTIVE
C INDEX, REFREL, FOR A GIVEN SPHERE REFRACTIVE INDEX, MEDIUM REFRACTIVE INDEX,
C RADIUS, AND FREE SPACE WAVELENGTH. IT THEN CALLS BHMIE, THE SUBROUTINE THAT
C COMPUTES AMPLITUDE SCATTERING MATRIX ELEMENTS AND EFFICIENCIES.
C*****
      COMPLEX REFREL,S1(200),S2(200)
      DATA PI/3.141592654/, PIO2/1.570796327/
      WRITE(6,10)
10   FORMAT(' SPHERE SCATTERING PROGRAM'//)
      REFMED = 1.
C
C REFMED IS THE (REAL) REFRACTIVE INDEX OF THE SURROUNDING MEDIUM
C
      REFRE = 1.55
      REFIM = 0.
C
C SPHERE (COMPLEX) RELATIVE REFRACTIVE INDEX, REFREL = CMPLX(REFRE,REFIM)
C
      REFREL = CMPLX(REFRE,REFIM)/REFMED
      WRITE(6,20) REFMED, REFRE, REFIM
20   FORMAT(5X,'REFMED = ',F8.4,' REFRE = ',E14.6,' REFIM = '
     1,E14.6)
      RAD = 0.525
      WAVEL = 0.6328
C
C SPHERE RADIUS, RAD, AND WAVELENGTH, WAVEL, ARE IN SAME UNITS
C
      X = 2.*PI*RAD*REFMED/WAVEL
      WRITE(6,30) RAD, WAVEL
30   FORMAT(' SPHERE RADIUS = ', F7.3,' WAVELENGTH = ',F7.4)
      WRITE(6,40) X
40   FORMAT(' SIZE PARAMETER = ',F8.3/)
C
C NANG IS THE NUMBER OF ANGLES BETWEEN 0 AND 90 DEGREES. MATRIX ELEMENTS
C ARE CALCULATED AT 2*NANG-1 ANGLES INCLUDING 0, 90, AND 180 DEGREES.
C
      NANG = 11
      DANG = PIO2/(NANG-1.)
      CALL BHMIE(X, REFREL, NANG, S1, S2, QEXT, QSCA, QBACK)
      WRITE(6,50) QSCA, QEXT, QBACK
50   FORMAT('' QSCA = ',E13.6,' QEXT = ',E13.6,' QBACK = ',E13.6)
      WRITE(6,60)
60   FORMAT('' ANGLE',7X,'S11',12X,'POL',12X,'S33',12X,'S34'//)
C
C S33 AND S34 MATRIX ELEMENTS ARE NORMALIZED BY S11. S11 ITSELF IS NORMALIZED
C TO UNITY IN THE FORWARD DIRECTION. THE DEGREE OF POLARIZATION IS GIVEN BY
C POL (INCIDENT LIGHT IS UNPOLARIZED).
C
      S11NOR = 0.5 * (CABS( S2(1) )**2 + CABS( S1(1) )**2)
      NAN = 2*NANG-1
      DO 70 J = 1, NAN
      AJ = J
      S11 = 0.5 * CABS( S2(J) )**2
      S11 = S11 + 0.5 * CABS( S1(J) )**2
      S12 = 0.5 * CABS( S2(J) )**2
      S12 = S12 - 0.5 * CABS( S1(J) )**2
      POL = -S12/S11
      S33 = REAL( S2(J)*CONJG(S1(J)) )
      S33 = S33/S11
      S34 = AIMAG( S2(J)*CONJG(S1(J)) )
      S34 = S34/S11
      S11 = S11/S11NOR

```

Table 1.37 (continued)

```

ANG = DANG*(AJ-1)*57.2958
70   WRITE(6,80) ANG, S11, POL, S33, S34
80   FORMAT(1X,F6.2,4(2X,E13.6))
      STOP
      END
*****
C SUBROUTINE BHMIE CALCULATES AMPLITUDE SCATTERING MATRIX ELEMENTS AND
C EFFICIENCIES FOR EXTINCTION, SCATTER, AND BACKSCATTER FOR A GIVEN SIZE
C PARAMETER AND RELATIVE REFRACTIVE INDEX.
*****
SUBROUTINE BHMIE(X, REFREL, NANG, S1, S2, QEXT, QSCA, QBACK)
DIMENSION AMU(100),THETA(100),PI(100),TAU(100),PIO(100),PI1(100)
COMPLEX D(3000),Y,REFREL,XI,XIO,XI1,AN,BN,S1(1),S2(1)
DOUBLE PRECISION PIO,PSI1,PSI,DN,DX
DATA PIO2/1.570796327/
DX = X
Y = X*REFREL
C
C SERIES TERMINATED AFTER NSTOP TERMS
C
      XSTOP = X + 2. + 4.*X**0.3333
      NSTOP = XSTOP
      YMOD = CABS(Y)
      NMX = AMAX1(XSTOP, YMOD) + 15
      DANG = PIO2/AMAX1(1., NANG-1.)
      DO 555 J = 1, NANG
         THETA(J) = (J-1.)*DANG
      555   AMU(J) = COS(THETA(J))
C
C LOGARITHMIC DERIVATIVE, D(J), CALCULATED BY DOWNWARD RECURRENCE BEGINNING
C WITH INITIAL VALUE CMPLX(0,0) AT J = NMX
C
      D(NMX) = CMPLX(0.,0.)
      NN = NMX - 1
      DO 120 N = 1, NN
         RN = NMX - N + 1
      120   D(NMX - N) = (RN/Y) - (1. / (D(NMX-N+1) + RN/Y))
      DO 666 J = 1, NANG
         PIO(J) = 0.
      666   PI1(J) = 1.
      NN = 2*NANG - 1
      DO 777 J = 1, NN
         S1(J) = CMPLX(0.,0.)
      777   S2(J) = CMPLX(0.,0.)
C
C RICCATI-BESSEL FUNCTIONS WITH REAL ARGUMENT X CALCULATED BY UPWARD RECURRENCE
C
      PSI0 = DCOS(DX)
      PSI1 = DSIN(DX)
      CHI0 = -SIN(X)
      CHI1 = COS(X)
      APSI0 = PSI0
      APSI1 = PSI1
      XIO = CMPLX(APSI0, -CHI0)
      XI1 = CMPLX(APSI1, -CHI1)
      QSCA = 0.
      N = 1
200   DN = N
      RN = N
      FN = (2.*RN + 1.) / (RN*(RN + 1.))
      PSI = (2.*DN - 1.)*PSI1/DX - PSI0
      APSI = PSI
      CHI = (2.*RN - 1.)*CHI1/X - CHI0
      XI = CMPLX(APSI, -CHI)

```

(continued)

Table 1.37 (*continued*)

```

AN = ( D(N)/REFREL + RN/X )*APSI - APSI1
AN = AN/( (D(N)/REFREL + RN/X)*XI - XI1 )
BN = ( REFREL*D(N)+RN/X )*APSI - APSI1
BN = BN/( (REFREL*D(N) + RN/X)*XI - XI1 )
QSCA = QSCA + (2.*RN + 1.)*(CABS(AN)**2+CABS(BN)**2)
P = (-1.)**(N-1)
DO 789 J = 1, NANG
JJ = 2*NANG - J
PI(J) = PI1(J)
TAU(J) = RN*AMU(J)*PI(J) - (RN+1.)*PIO(J)
S1(J) = S1(J)+FN*(AN*PI(J) + BN*TAU(J))
S2(J) = S2(J) + FN*(AN*TAU(J) + BN*PI(J))
IF(J. EQ. JJ) GOTO789
S1(JJ) = S1(JJ) + FN*(AN*PI(J) - BN*TAU(J))*P
S2(JJ) = S2(JJ) + FN*(BN*PI(J) - AN*TAU(J))*P
789 CONTINUE
PSIO = PSI1
PSI1 = PSI
APSI1 = PSI1
CHIO = CHI1
CHI1 = CHI
XI1 = CMPLX(APSI1,-CHI1)
N = N + 1
RN = N
DO 999 J = 1, NANG
PI1(J) = ( (2.*RN - 1.)/(RN - 1. ) )*AMU(J)*PI(J)
PI1(J) = PI1(J) - RN*PIO(J)/(RN-1.)
999 PIO(J) = PI(J)
IF(N-1-NSTOP) 200, 300, 300
300 QSCA = (2./(X*X))*QSCA
QEXT = (4./(X*X))*REAL(S1(1))
QBACK = (4./(X*X))*CABS( S1(2*NANG-1)**2 )
RETURN
END

```

data due to Shettle and Fenn.²⁰³ Typical results of this program are shown in Table 1.40.

The program and subroutine in Table 1.41 represent a generalization of the codes shown in Table 1.37. This code calculates the efficiencies and scatter matrix components for polydispersions. This particular example used Deirmendjian's Haze L distribution. Further, the Mueller matrix elements are for the Stokes vector as defined by Deirmendjian. Typical output is shown in Table 1.42.

Acknowledgments

The authors gratefully acknowledge support from the Applied Physics Laboratory/Johns Hopkins University during the preparation of this manuscript. Also, the following individuals are recognized for significant contributions to the overall quality and accuracy of the text by reviewing drafts at various stages: Robert Au, Corinne T. Delaye, Scott Gearhart, William B. Grant, Michael Hoke, Milton J. Linevsky, William J. Tropf, and Adam Zysnarski. The secretarial support of Mary Jo McCormick and Machele Wiley is also greatly appreciated.

Table 1.38 Typical Output of Program in Table 1.37

SPHERE SCATTERING PROGRAM

```

REFMED = 1.0000  REFRE = 0.155000E+01  REFIM = 0.000000E+00
SPHERE RADIUS = 0.525  WAVELENGTH = 0.6328
SIZE PARAMETER = 5.213

QSCA = 0.310543E+01  QEXT = 0.310543E+01  QBACK = 0.292534E+01

      ANGLE      S11      POL      S33      S34
      0.00  0.100000E+01  0.317543E-07  0.100000E+01  -0.387934E-07
      9.00  0.785390E+00  -0.459814E-02  0.999400E+00  0.343261E-01
     18.00  0.356897E+00  -0.458542E-01  0.986022E+00  0.160184E+00
     27.00  0.766119E-01  -0.364744E+00  0.843603E+00  0.394076E+00
     36.00  0.355355E-01  -0.534997E+00  0.686967E+00  -0.491787E+00
     45.00  0.701845E-01  0.959967E-02  0.959825E+00  -0.280434E+00
     54.00  0.574313E-01  0.477926E-01  0.985371E+00  0.163584E+00
     63.00  0.219659E-01  -0.440604E+00  0.648042E+00  0.621216E+00
     72.00  0.125959E-01  -0.831995E+00  0.203255E+00  -0.516208E+00
     81.00  0.173750E-01  0.341669E-01  0.795354E+00  -0.605182E+00
     90.00  0.124601E-01  0.230462E+00  0.937497E+00  0.260742E+00
     99.00  0.679092E-02  -0.713472E+00  -0.717361E-02  0.700647E+00
    108.00  0.954238E-02  -0.756256E+00  -0.394749E-01  -0.653084E+00
    117.00  0.863418E-02  -0.281216E+00  0.536250E+00  -0.795835E+00
    126.00  0.227421E-02  -0.239613E+00  0.967602E+00  0.795787E-01
    135.00  0.543997E-02  -0.850803E+00  0.187531E+00  -0.490883E+00
    144.00  0.160243E-01  -0.706334E+00  0.495255E+00  -0.505781E+00
    153.00  0.188852E-01  -0.891081E+00  0.453277E+00  -0.226816E-01
    162.00  0.195254E-01  -0.783319E+00  -0.391614E+00  0.482752E+00
    171.00  0.301676E-01  -0.196193E+00  -0.962069E+00  0.189555E+00
    180.00  0.383189E-01  0.903473E-08  -0.100000E+01  0.000000E+00

```

Table 1.39 Calling Program and Subroutine INTRP

```

C PROGRAM TO CALCULATE REFRACTIVE INDEX FOR SPECIFIED MATERIAL
DOUBLE PRECISION EN(2), WL
OPEN(UNIT=8,FILE='OUTPUT.TMP')
WRITE(6,10)
10 FORMAT(' ENTER CONSTITUENT, 1...5'')
READ(5,*)MODL
WRITE(8,15)MODL
15 FORMAT(/' MATERIAL MODEL = ',I3//)
N = 10
DELWL = (12.-0.5)/(N-1.)
WRITE(8,20)
20 FORMAT(2X,'WAVELENGTH',17X,'INDEX')
      DO 25 I = 1, N
      WL = 0.5 + (I-1.)*DELWL
      CALL INTRP(WL, EN, MODL)
      WRITE(8,30)WL, EN(1), EN(2)
      25 FORMAT(1X,E12.6,4X,2(2X,E12.6))
      STOP
      END

```

(continued)

Table 1.39 (continued)

```

C*****
C SUBROUTINE INTRP TO CALCULATE THE COMPLEX REFRACTIVE INDEX FOR VARIOUS
C AEROSOL CONSTITUENTS
C INPUT: WVLN, WAVELENGTH IN MICROMETERS
C MODL (-1,...,5), WHERE
C 1: PURE WATER
C 2: WATER SOLUBLES
C 3: DUST-LIKE
C 4: SOOT
C 5: SEA SALT
C OUTPUT: EN(1), EN(2), THE COMPLEX INDEX OF REFRACTION
C*****
```

SUBROUTINE INTRP(WVLN,EN,MODL)
IMPLICIT DOUBLE PRECISION(E,W-Z)
PARAMETER (NPTS=41,NMODS=5)
DIMENSION EN(2),ALAM(NPTS),TABR(NPTS,NMODS)
1,TABI(NPTS,NMODS)
DATA ALAM/.4,.488,.5145,.55,.6328,.6943,.86,1.06,1.3,1.536,1.8
1.,2.,2.25,2.5,2.7,3.,3.2,3.3923,3.5,3.75,4.,4.5,5.,5.5,6.,6.2,6.5
2,7.2,7.9,8.2,8.5,8.7,9.,9.2,9.5,9.8,10.,10.591,11.,11.5,12.5/

C
C TABULATED DATA FOR PURE WATER
C
DATA (TABR(K,1),K=1,NPTS)
1/1.339,1.335,1.334,1.333,1.332,1.331,1.329,1.326,1.323,1.318
2,1.312,1.306,1.292,1.261,1.18,1.371,1.47,1.422,1.4,1.369,1.351
3,1.332,1.325,1.298,1.265,1.363,1.339,1.312,1.294,1.286,1.278
4,1.272,1.262,1.255,1.243,1.229,1.218,1.179,1.153,1.126,1.123/
DATA (TABI(K,1),K=1,NPTS)
1/1.86E-9,9.69E-10,1.1E-9,1.96E-9,1.46E-8,3.35E-8,3.29E-7
2,4.18E-6,3.69E-5,9.97E-5,1.15E-4,1.1E-3,3.9E-4,1.74E-3,1.9E-2
3,.272,9.24E-2,2.04E-2,9.4E-3,3.5E-3,4.6E-3,1.34E-2,1.24E-2,1.16E-2
4.,107,8.8E-2,3.92E-2,3.21E-2,3.29E-2,3.51E-2,3.67E-2,3.79E-2
5,3.99E-2,4.15E-2,4.44E-2,4.79E-2,5.E-2,6.74E-2,9.68E-2,.142,.259/

C
C TABULATED DATA FOR WATER SOLUBLES
C
DATA (TABR(K,2),K=1,NPTS)
1/1.53,1.53,1.53,1.53,1.53,1.53,1.52,1.52,1.51,1.51,1.46,1.42,1.42
2,1.42,1.4,1.42,1.43,1.43,1.45,1.452,1.455,1.46,1.45,1.44,1.41,1.43
3,1.46,1.4,1.2,1.01,1.3,2.4,2.56,2.2,1.95,1.87,1.82,1.76,1.72,1.67
4,1.62/
DATA (TABI(K,2),K=1,NPTS)
1/.005,.005,.005,.006,.007,.012,.017,.02,.023,.017,.008,.01
2,.012,.055,.022,.008,.007,.005,.004,.005,.013,.012,.018,.023,.027
3,.033,.07,.065,.1,.215,.29,.37,.42,.16,.095,.09,.07,.05,.047,.053/

C
C TABULATED DATA FOR DUST
C
DATA (TABR(K,3),K=1,NPTS)
1/1.53,1.53,1.53,1.53,1.53,1.53,1.52,1.52,1.46,1.4,1.33,1.26,1.22
2,1.18,1.18,1.16,1.22,1.26,1.28,1.27,1.26,1.26,1.25,1.22,1.15,1.14
3,1.13,1.4,1.15,1.13,1.3,1.4,1.7,1.72,1.73,1.74,1.75,1.62,1.62,1.59
4,1.51/
DATA (TABI(K,3),K=1,NPTS)
1/.008,.008,.008,.008,.008,.008,.008,.008,.008,.008,.008,.009
2,.009,.013,.012,.01,.013,.011,.011,.012,.014,.016,.021,.037,.039
3,.042,.055,.04,.074,.09,.1,.14,.15,.162,.162,.162,.12,.105,.1,.09/

C
C TABULATED DATA FOR SOOT
C

Table 1.39 (continued)

```

DATA (TABR(K,4),K=1,NPTS)
1/1.75,1.75,1.75,1.75,1.75,1.75,1.75,1.75,1.76,1.77,1.79,1.8,1.81
2,1.82,1.83,1.84,1.86,1.87,1.88,1.9,1.92,1.94,1.97,1.99,2.02,2.03
3,2.04,2.06,2.12,2.13,2.15,2.16,2.17,2.18,2.19,2.2,2.21,2.22,2.23
4,2.24,2.27/
DATA (TABI(K,4),K=1,NPTS)
1/.46,.45,.45,.44,.43,.43,.44,.45,.46,.48,.49,.5,.51,.52,.54
2,.54,.55,.56,.57,.58,.59,.6,.61,.62,.625,.63,.65,.67,.68,.69,.69
3,.7,.7,.71,.713,.72,.73,.73,.74,.75/
C
C TABULATED DATA FOR SEA SALT
C
DATA (TABR(K,5),K=1,NPTS)
1/1.5,1.5,1.5,1.5,1.49,1.49,1.48,1.47,1.47,1.46,1.45,1.45,1.45,1.44
2,1.43,1.4,1.61,1.49,1.48,1.48,1.47,1.48,1.49,1.47,1.42,1.41,1.6
3,1.46,1.42,1.4,1.42,1.48,1.6,1.65,1.61,1.58,1.56,1.54,1.5,1.48
4,1.48,1.42/
DATA (TABI(K,5),K=1,NPTS)
1/3.E-8,2.E-8,1.E-8,2.E-8,1.E-7,3.E-6,2.E-4,4.E-4,6.E-4
2,8.E-4,1.E-3,2.E-3,4.E-3,7.E-3,1.E-2,3.E-3,2.E-3,1.6E-3,1.4E-3
3,1.4E-3,1.4E-3,2.5E-3,3.6E-3,1.1E-2,2.2E-2,5.E-3,7.E-3,1.3E-2
4,2.E-2,2.6E-2,3.E-2,2.8E-2,2.6E-2,1.8E-2,1.6E-2,1.5E-2,1.4E-2
5,1.4E-2,1.4E-2,1.6E-2/
IF(WVLN.LT.ALAM(1).OR.WVLN.GT.ALAM(NPTS))THEN
  WRITE(6,5)

5 FORMAT(' *** INDEX NOT TABULATED ***/
1,' *** FOR THIS WAVELENGTH ***')
RETURN
END IF
DO 10 I=1,NPTS
K=I
10 IF(ALAM(I).GE.WVLN)GOTO15
15 IF(K.GE.3.AND.K.LE.NPTS-1)THEN
X1=ALAM(K-2)
X2=ALAM(K-1)
X3=ALAM(K )
X4=ALAM(K+1)
Y1R=TABR(K-2,MODL)
Y1I=TABI(K-2,MODL)
Y2R=TABR(K-1,MODL)
Y2I=TABI(K-1,MODL)
Y3R=TABR(K ,MODL)
Y3I=TABI(K ,MODL)
Y4R=TABR(K+1,MODL)
Y4I=TABI(K+1,MODL)
ELSE IF(K.LT.3)THEN
X1=ALAM(1)
X2=ALAM(2)
X3=ALAM(3)
X4=ALAM(4)
Y1R=TABR(1,MODL)
Y1I=TABI(1,MODL)
Y2R=TABR(2,MODL)
Y2I=TABI(2,MODL)
Y3R=TABR(3,MODL)
Y3I=TABI(3,MODL)
Y4R=TABR(4,MODL)
Y4I=TABI(4,MODL)
ELSE
X1=ALAM(NPTS-3)
X2=ALAM(NPTS-2)

```

(continued)

Table 1.39 (continued)

```

X3=ALAM(NPTS-1)
X4=ALAM(NPTS )
Y1R=TABR(NPTS-3,MODL)
Y1I=TAJI(NPTS-3,MODL)
Y2R=TABR(NPTS-2,MODL)
Y2I=TAJI(NPTS-2,MODL)
Y3R=TABR(NPTS-1,MODL)
Y3I=TAJI(NPTS-1,MODL)
Y4R=TABR(NPTS ,MODL)
Y4I=TAJI(NPTS ,MODL)
END IF
W1=(WVLN-X2)*(WVLN-X3)*(WVLN-X4)/((X1-X2)*(X1-X3)*(X1-X4))
W2=(WVLN-X1)*(WVLN-X3)*(WVLN-X4)/((X2-X1)*(X2-X3)*(X2-X4))
W3=(WVLN-X1)*(WVLN-X2)*(WVLN-X4)/((X3-X1)*(X3-X2)*(X3-X4))
W4=(WVLN-X1)*(WVLN-X2)*(WVLN-X3)/((X4-X1)*(X4-X2)*(X4-X3))
EN(1)=EXP(W1*ALOG(Y1R)+W2*ALOG(Y2R)
1+W3*ALOG(Y3R)+W4*ALOG(Y4R))
EN(2)=EXP(W1*ALOG(Y1I)+W2*ALOG(Y2I)
1+W3*ALOG(Y3I)+W4*ALOG(Y4I))
RETURN
END

```

Table 1.40 Typical Output from Program in Table 1.39

MATERIAL MODEL = 1

WAVELENGTH	INDEX
0.500000E+00	0.133453E+01 - .998262E-09
0.177778E+01	0.131257E+01 -.105686E-03
0.305556E+01	0.140715E+01 -.231158E+00
0.433333E+01	0.133639E+01 -.955461E-02
0.561111E+01	0.127376E+01 -.204525E-01
0.688889E+01	0.132063E+01 -.291661E-01
0.816667E+01	0.128689E+01 -.348599E-01
0.944444E+01	0.124537E+01 -.438177E-01
0.107222E+02	0.117042E+01 -.753318E-01
0.120000E+02	0.111294E+01 -.196609E+00

Table 1.41 Calling Program and Subroutine MIEGEN

(continued)

Table 1.41 (continued)

```

C*****
C SUBROUTINE MIEGEN CALCULATES AMPLITUDE SCATTERING MATRIX ELEMENTS AND
C EFFICIENCIES FOR EXTINCTION, SCATTER, AND BACKSCATTER FOR A SIZE
C DISTRIBUTION SPECIFIED BY FUNCTION 'DIST', AND RELATIVE REFRACTIVE INDEX.
C*****
SUBROUTINE MIEGEN(WAVEL,REFREL,NANG,S11,S12,S33,S34,BEXT,BSCA)
DIMENSION AMU(100),THETA(100),PI(100),TAU(100),PIO(100),PI1(100)
COMPLEX D(3000),Y,REFREL,XI,XIO,XII,AN,BN,S1(200),S2(200)
REAL S11(1), S12(1), S33(1), S34(1)
DIMENSION G(4), W(4)
DOUBLE PRECISION PSI0,PSI1,PSI,DX,DN
DATA PIO2/1.570796327/
C
C THE FOLLOWING ARE RESPECTIVELY THE WEIGHTS AND ABSCISSAS OF THE 8-POINT
C GAUSS-LEGENDRE QUADRATURE:
C
DATA G/.362683783378361983D0, 0.313706645877887287D0
1, 0.222381034453374471D0, 0.101228536290376259D0/
DATA W/.183434642495649805D0, 0.525532409916328986D0
2, 0.796666477413626740D0, 0.960289856497536232D0/
C
BEXT = 0.
BSCA = 0.
NUMANG = 2*NANG-1
DO 2 J = 1, NUMANG
S11(J) = 0.
S12(J) = 0.
S33(J) = 0.
2 S34(J) = 0.
WAVEN = 4*PIO2/WAVEL
C
C DELTA IS THE LENGTH OF THE SUB-INTERVAL (XL,XU)...DIMENSIONSLESS
C
DELTA = 0.5/WAVEL
DANG = PIO2/AMAX1(1., NANG-1.)
DO 555 J = 1, NANG
THETA(J) = (J-1)*DANG
555 AMU(J) = COS(THETA(J))
C
C BEGINNING OF COMPOUND INTEGRATION LOOP
C
XL = 0.
9990 XU = XL + DELTA
XMEAN = 0.5*(XL+XU)
DBEXT = 0.
DBSCA = 0.
C
C BEGINNING OF GAUSS-LEGENDRE INTEGRATION ON SUB-INTERVAL (XL,XU)
C
DO 9994 JJJ = 1,3,2
DO 9994 III = 1,4
X = DELTA*(0.5*JJJ-1)*W(III) + XMEAN
DX = X
G1 = G(III)*DIST(DX/WAVEN)
Y = X*REFREL
C
C SERIES TERMINATED AFTER NSTOP TERMS
C

```

Table 1.41 (continued)

```

XSTOP = X + 4.*X**(0.3333) +2.
NSTOP = XSTOP
YMOD = CABS(Y)
NMX = AMAX1(XSTOP, YMOD) + 15
C
C LOGARITHMIC DERIVATIVE, D(J), CALCULATED BY DOWNWARD RECURRENCE BEGINNING
C WITH INITIAL VALUE CMPLX(0,0) AT J = NMX
C
D(NMX) = CMPLX(0.,0.)
NN = NMX - 1
DO 120 N = 1, NN
RN = NMX - N + 1
120 D(NMX-N) = (RN/Y)-(1./(D(NMX-N+1) + RN/Y))
DO 666 J = 1, NANG
PIO(J) = 0.
666 PI1(J) = 1.
DO 777 J = 1, NUMANG
S1(J) = CMPLX(0.,0.)
S2(J) = CMPLX(0.,0.)
C
C RICCATI-BESSEL FUNCTIONS WITH REAL ARGUMENT X CALCULATED BY UPWARD RECURRENCE
C
PSIO = DCOS(DX)
PSI1 = DSIN(DX)
CHIO = -SIN(X)
CHI1 = COS(X)
APSI0 = PSIO
APSI1 = PSI1
XIO = CMPLX(APSI0, -CHIO)
XI1 = CMPLX(APSI1, -CHI1)
QSCA = 0.
N = 1
200 DN = N
RN = N
FN = (2.*RN + 1.)/(RN*(RN + 1.))
PSI = (2.*DN - 1.)*PSI1/DX - PSIO
APSI = PSI
CHI = (2.*RN - 1.)*CHI1/X - CHIO
XI = CMPLX(APSI, -CHI)
RNOX = RN/X
AN = (D(N)/REFREL+RNOX)*APSI-APSI1
AN = AN/( (D(N)/REFREL + RNOX)*XI - XI1 )
BN = (REFREL*D(N)+RNOX)*APSI-APSI1
BN = BN/( (REFREL*D(N) + RNOX)*XI - XI1 )
QSCA = QSCA + (2.*RN + 1.)*(CABS(AN)**2+CABS(BN)**2)
P = (-1)**(N-1)
DO 789 J = 1, NANG
JJ = 2*NANG - J
PI(J) = PI1(J)
TAU(J) = RN*AMU(J)*PI(J) - (RN+1.)*PIO(J)
S1(J) = S1(J)+FN*(AN*PI(J) + BN*TAU(J))
S2(J) = S2(J)+FN*(AN*TAU(J) + BN*PI(J))
IF(J. EQ. JJ) GOTO789
S1(JJ) = S1(JJ)+FN*(AN*PI(J) - BN*TAU(J))*P
S2(JJ) = S2(JJ)+FN*(BN*PI(J) - AN*TAU(J))*P
789 CONTINUE
PSIO = PSI1
PSI1 = PSI
APSI1 = PSI1
CHIO = CHI1
CHI1 = CHI

```

(continued)

Table 1.41 (continued)

```

XII = CMPLX(APSII,-CHI1)
N = N + 1
RN = N
DO 999 J = 1, NANG
    PI1(J) = ( (2.*RN - 1.)/(RN - 1.) )*AMU(J)*PI(J)
    PI1(J) = PI1(J) - RN*PIO(J)/(RN-1.)
999    PIO(J) = PI(J)
    IF(N-1-NSTOP) 200, 300, 300
300    QSCA = (2./(X*X))*QSCA
    QEXT = (4./(X*X))*REAL(S1(1))
    QBACK = (4./(X*X))*CABS( S1(2*NANG-1)**2 )
    DO 950 J = 1,NUMANG
        TEMP2 = REAL( S2(J)*CONJG(S2(J)) )
        TEMP1 = REAL( S1(J)*CONJG(S1(J)) )
        S11(J) = S11(J) + G1*( TEMP2 + TEMP1 )/2
        S12(J) = S12(J) + G1*( TEMP2 - TEMP1 )/2
        S33(J) = S33(J) + G1*REAL( S1(J)*CONJG(S2(J)) )
950    S34(J) = S34(J) + G1*AIMAG(S1(J)*CONJG(S2(J)) )
    DBEXT = DBEXT + QEXT*G1*(X*X)
    DBSCA = DBSCA + QSCA*G1*(X*X)
9994    CONTINUE
C
C END OF 8-POINT QUADRATURE ON SUB-INTERVAL (XL,XU)
C
    BEXT = BEXT + DBEXT
    BSCA = BSCA + DBSCA
C
C TEST FOR CONVERGENCE OF COMPOUND INTEGRATION
C
    IF((DBEXT*1.D4 .LT. BEXT) .AND. (DBSCA*1.D4 .LT. BSCA) )GOTO9995
C
C CONTINUE COMPOUND INTEGRATION
C
    XL = XU
    GOTO9990
C
C NORMALIZE EFFICIENCIES TO UNITS OF 1/M AND MATRIX ELEMENTS TO 1/M**3
C
9995    FACTOR = 1.E-6*PIO2*DELTA/(WAVEN**3)
    BEXT = BEXT*FACTOR
    BSCA = BSCA*FACTOR
    FACTOR = 0.5E6*DELTA/WAVEN
    DO 9996 J = 1,NUMANG
        S11(J) = S11(J)*FACTOR
        S12(J) = S12(J)*FACTOR
        S33(J) = S33(J)*FACTOR
9996    S34(J) = S34(J)*FACTOR
    RETURN
    END
*****
C FUNCTION DIST - TO CALCULATE THE AEROSOL SIZE DISTRIBUTION FOR HAZE L.
C THE PARTICLE RADIUS, R, IS IN MICROMETERS.
*****
FUNCTION DIST(R)
IMPLICIT DOUBLE PRECISION(A-H,O-Z)
DATA ALPH/2.D0/, A/4.9757D6/, GAMMA/5.D-1/, B/1.51186D1/
DIST=A*(R**ALPH)*EXP(-B*(R**GAMMA))

RETURN
END

```

Table 1.42 Typical Output from Program in Table 1.41

POLYDISPERSION SCATTERING PROGRAM

REFMED = 1.0000 REFRE = 0.117900E+01 REFIM = 0.718000E-01
 WAVELENGTH = 10.5910

BSCA = 0.255259E-07 BEXT = 0.970839E-06

ANGLE	P1	P2	P3	P4
0.00	0.207087E+01	0.207087E+01	0.207087E+01	0.000000E+00
10.00	0.205817E+01	0.199807E+01	0.202790E+01	-0.500164E-03
20.00	0.202121E+01	0.179187E+01	0.190308E+01	-0.188354E-02
30.00	0.196317E+01	0.148584E+01	0.170788E+01	-0.383600E-02
40.00	0.188874E+01	0.112707E+01	0.145892E+01	-0.594161E-02
50.00	0.180325E+01	0.766085E+00	0.117514E+01	-0.779705E-02
60.00	0.171205E+01	0.447637E+00	0.875012E+00	-0.910357E-02
70.00	0.161982E+01	0.204397E+00	0.574617E+00	-0.971197E-02
80.00	0.153037E+01	0.542824E-01	0.286547E+00	-0.961880E-02
90.00	0.144648E+01	0.895995E-03	0.197137E-01	-0.892964E-02
100.00	0.137003E+01	0.359734E-01	-0.220284E+00	-0.781031E-02
110.00	0.130214E+01	0.142764E+00	-0.430504E+00	-0.644282E-02
120.00	0.124339E+01	0.299496E+00	-0.609935E+00	-0.499442E-02
130.00	0.119398E+01	0.482446E+00	-0.758831E+00	-0.360147E-02
140.00	0.115390E+01	0.668398E+00	-0.878161E+00	-0.236479E-02
150.00	0.112299E+01	0.836477E+00	-0.969186E+00	-0.135267E-02
160.00	0.110108E+01	0.969430E+00	-0.103316E+01	-0.607389E-03
170.00	0.108801E+01	0.105444E+01	-0.107110E+01	-0.152677E-03
180.00	0.108367E+01	0.108367E+01	-0.108367E+01	0.000000E+00

References

1. B. Herman, A. J. LaRocca, and R. E. Turner, "Atmospheric scattering," Chap. 4 in *The Infrared Handbook*, 2nd ed., W. L. Wolfe and G. J. Zissis, Eds., Environmental Research Institute of Michigan, Ann Arbor, MI (1985).
2. *CRC Handbook of Chemistry and Physics*, 72nd ed., D. R. Lide, Ed., CRC Press, Boca Raton, FL (1991).
3. M. Allen, Y. L. Yung, and J. W. Waters, "Vertical transport and photochemistry in the terrestrial mesosphere and lower thermosphere 50–120 km," *J. Geophys. Res.* **86**, 3617 (1981).
4. M. Allen, J. I. Limine, and Y. L. Yung, "The vertical distribution of ozone in the mesosphere and lower thermosphere," *J. Geophys. Res.* **89**, 4841 (1984).
5. R. M. Goody and Y. L. Yung, *Atmospheric Radiation Theoretical Basis*, 2nd ed., Oxford University Press, Oxford (1989).
6. R. B. Bacastow, C. D. Keeling, and T. P. Whorf, "Seasonal amplitude increase in the atmospheric CO₂ concentration at Mauna Loa, Hawaii, 1959–1982," *J. Geophys. Res.* **90**, 10,529 (1985); see also *CRC Handbook of Chemistry and Physics*, 72nd ed., D. R. Lide, Ed., pp. 14–20, CRC Press, Boca Raton, FL (1991).
7. H. J. Liebe, "A contribution to modeling atmospheric millimeter-wave properties," *Frequenz* **41**, 31–36 (1987).
8. F. K. Kneubühl, "Review on the theory of dielectric dispersion of insulators," *Infrared Phys.* **29**, 925–942 (1989).
9. G. Herzberg, *Infrared and Raman Spectra of Polyatomic Molecules*, Van Nostrand Reinhold, New York (1945).
10. G. Herzberg, *Spectra of Diatomic Molecules*, 2nd ed., Van Nostrand Reinhold, New York (1950).

11. G. Herzberg, *Electronic Spectra and Electronic Structure of Polyatomic Molecules*, Van Nostrand Reinhold, New York (1966).
12. E. J. McCartney, *Absorption and Emission by Atmospheric Gases*, John Wiley & Sons, New York (1983).
13. J. H. Van Vleck and V. F. Weisskopf, "On the shape of collision-broadened lines," *Rev. Mod. Phys.* **17**, 227–236 (1945).
14. A. Einstein, *Phys. Z.* **18**, 121 (1917).
15. P. W. Anderson, "Pressure broadening in the microwave and infrared regions," *Phys. Rev.* **76**, 647 (1949).
16. C. J. Tsao and B. Curnutte, "Line widths of pressure broadened spectral lines," *J. Quant. Spectros. Radiat. Transfer* **2**, 41 (1962).
17. J. H. Van Vleck and D. L. Huber, "Absorption, emission and linebreadths: a semihistorical perspective," *Rev. Mod. Phys.* **49**, 939–959 (1977).
18. P. W. Milonni and J. H. Eberly, *Lasers*, John Wiley & Sons, New York (1988).
19. G. Birnbaum and E. R. Cohen, "Theory of line shape in pressure-induced absorption," *Can. J. Phys.* **54**, 593–602 (1976).
20. G. Birnbaum, "The shape of collision broadened lines from resonance to the far wing," *J. Quant. Spectros. Radiat. Transfer* **21**, 597–607 (1979).
21. C. Boulet and D. Robert, "Short time behavior of the dipole autocorrelation function and molecular gases absorption spectrum," *J. Chem. Phys.* **77**, 4288–4299 (1982).
22. Q. Ma and R. H. Tipping, "Water vapor continuum in the millimeter spectral region," *J. Chem. Phys.* **93**, 6127–6139 (1990); see also Q. Ma and R. H. Tipping, "The atmospheric water continuum in the infrared: extension of the statistical theory of Rosenkranz," *J. Chem. Phys.* **93**, 7066–7075 (1990).
23. P. W. Rosenkranz, "Pressure broadening of rotational band. II. Water vapor from 300 to 1100 cm^{-1} ," *J. Chem. Phys.* **83**, 6139 (1985); see also P. W. Rosenkranz, *J. Chem. Phys.* **87**, 163–170 (1987).
24. P. W. Rosenkranz, "Shape of the 5 mm oxygen band in the atmosphere," *IEEE Trans. Antennas Propag.* **23**(4), 498–506 (1975).
25. P. W. Rosenkranz, "Interference coefficients for overlapping oxygen lines in air," *J. Quant. Spectros. Radiat. Transfer* **39**(4), 287–297 (1988).
26. L. L. Strow, "Line mixing in infrared atmospheric spectra," in *Modeling of the Atmosphere*, L. S. Rothman, Ed., *Proc. SPIE* **928**, 194–212 (1988).
27. J. M. Hartman, "Line mixing and finite duration of collision effects in pure CO_2 infrared spectra: fitting and scaling analysis," *J. Chem. Phys.* **94**, 6406–6419 (1991).
28. G. Birnbaum, "A kinetic approach to the shape of pressure broadened molecular bands," in *Spectral Line Shapes AIP Conference Proceedings* (1990).
29. R. W. Davies, R. H. Tipping, and S. A. Clough, "Dipole autocorrelation function for molecular pressure broadening: a quantum theory which satisfies the fluctuation-dissipation theorem," *Phys. Rev.* **26**, 3378 (1982).
30. M. E. Thomas, "Infrared- and Millimeter-wavelength continuum absorption in the atmospheric windows: measurements and models," *Infrared Phys.* **30**, 161–174 (1990).
31. C. Young, "Calculation of the absorption coefficient for lines with combined Doppler and Lorentz broadening," *J. Quant. Spectros. Radiat. Transfer* **5**, 549 (1965).
32. K. Tomiyama, S. A. Clough, and F. K. Kneizys, "Unified real part of the susceptibility for collisional broadening," Report No. AFGL-TR-86-0181, Air Force Geophysics Laboratory, Hanscom AFB, MA (1986).
33. J. H. Shaw, *Ohio J. Sci.* **53**, 258 (1953).
34. W. S. Benedict and R. F. Calfee, "Line parameters for the 1.9 and 6.3 micron water vapor bands," ESSA Professional Paper 2, U.S. Government Printing Office, Washington, D.C. (1987).
35. D. M. Gates, R. F. Calfee, D. W. Hansen, and W. S. Benedict, "Line parameters and computed spectra for water vapor bands at 2.7 μm ," National Bureau of Standards Monograph 71, U.S. Government Printing Office, Washington, D.C. (1964).
36. C. Camy-Peyret and J.-M. Flaud, "Line positions and intensities in the band of H_2O ," *Mol. Phys.* **32**, 523 (1976).
37. R. A. McClatchey, W. S. Benedict, S. A. Clough, D. E. Burch, R. F. Calfee, K. Fox, L. S.

- Rothman, and J. S. Garing, "AFCRL atmospheric absorption line parameters compilation," AFCRL-TR-73-0096, Air Force Cambridge Research Laboratories, Bedford, MA (1973).
38. L. S. Rothman, R. R. Gamache, A. Goldman, L. R. Brown, R. A. Toth, H. M. Pickett, R. L. Poynter, J.-M. Flaud, C. Camy-Peyret, A. Barbe, N. Husson, C. P. Rinsland, and M. A. H. Smith, "The HITRAN database: 1986 edition," *Appl. Opt.* **26**, 4058–4097 (1987).
 39. R. M. Goody and Y. L. Yung, *Atmospheric Radiation Theoretical Basis*, 2nd ed., Oxford University Press, Oxford (1989).
 40. M. E. Thomas, "Tropospheric water vapor absorption in the infrared window regions," Dissertation, Ohio State University (1979).
 41. R. K. Long and E. K. Damon, "An atlas of pure water vapor spectra from 500 to 5000 cm^{-1} Vol. I and II," Ohio State University/ElectroScience Laboratory, Report No. 713774-3 (1984).
 42. C. P. Rinsland, A. Goldman, M. A. H. Smith, and V. Malathy Devi, "Measurements of Lorentz air-broadening coefficients and relative intensities in the H_2^{16}O pure rotational and ν_2 bands from long horizontal path atmospheric spectra," *Appl. Opt.* **30**, 1427–1438 (1991).
 43. R. E. Meredith, R. L. Spellacy, W. O. Gallery, S. G. O'Brien, and B. K. Matise, "Revised water vapor line parameters in the 1.0 to 1.1 μm region," in *Propagation Engineering: Third in a Series*, L. R. Bissonnette and W. B. Miller, Eds., *Proc. SPIE* **1312**, 364–366 (1990).
 44. W. M. Elsasser, *Heat Transfer by Infrared Radiation in the Atmosphere*, Harvard University Press, Cambridge, MA (1942).
 45. H. W. Yates and J. H. Taylor, "Infrared transmission of the atmosphere," NRL Report 5453 (1960).
 46. A. Adel, *Astrophys. J.* **89**, 1 (1939).
 47. R. Anthony, "Atmospheric absorption of solar infrared radiation," *Phys. Rev.* **85**, 674 (1952).
 48. W. T. Roach and R. W. Goody, *Q. J. R. Meteorol. Soc.* **84**, 319 (1958).
 49. K. Bignell, F. Saiedy, and P. A. Sheppard, "On the atmospheric infrared continuum," *J. Opt. Soc. Am.* **53**, 466 (1963).
 50. K. Bignell, "The water-vapour infra-red continuum," *Q. J. R. Meteorol. Soc.* **96**, 390–403 (1970).
 51. M. F. Crawford, H. L. Welsh, and J. L. Locke, "Infrared absorption of oxygen and nitrogen induced by intermolecular forces," *Phys. Rev.* **75**, 1607 (1949).
 52. J. Susskind and J. E. Searl, "Atmospheric absorption near 2400 cm^{-1} ," *J. Quant. Spectros. Radiat. Transfer* **18**, 581 (1977).
 53. B. H. Winters, S. Silverman, and W. S. Benedict, *J. Quant. Spectros. Radiat. Transfer* **4**, 527 (1964).
 54. J. Hinderling, M. W. Sigrist, and F. K. Kneubuhl, "Laser photoacoustic spectroscopy of water-vapor continuum and line-absorption in the 8- to 14- μm atmospheric window," *Infrared Phys.* **27**, 63 (1987).
 55. W. B. Grant, "A critical review of measurements of water vapor absorption in the 840 to 1100 cm^{-1} spectral region," *Appl. Opt.* **29**, 451–462 (1990).
 56. J. W. Waters, "Methods of experimental physics," in *Astrophysics Radio Telescopes*, M. L. Meeks, Ed., Vol. 12, Part B, Academic Press, New York (1976).
 57. N. E. Gaut and E. C. Reifenstein III, Environmental Research and Technical Report No. 13, Lexington, MA (1971).
 58. G. E. Becker and S. H. Autler, "Water vapor absorption of electromagnetic radiation in the centimeter wavelength range," *Phys. Rev.* **70**, 300 (1946).
 59. L. Frenkel and D. Woods, "The microwave absorption by H_2O vapor and its mixtures with other gases between 100 and 300 GHz," *Proc. IEEE* **54**, 498 (1966).
 60. D. E. Burch, "Absorption of infrared radiant energy by CO_2 and H_2O . III. Absorption by H_2O between 0.5 and 36 cm^{-1} ($278\mu\text{--}2 \text{ cm}$)," *J. Opt. Soc. Am.* **58**, 1383 (1968).
 61. H. J. Liebe, "A contribution to modeling atmospheric millimeter-wave properties," *Frequenz* **41**, 31 (1987).
 62. H. J. Liebe and D. H. Layton, "Experimental and analytical aspects of atmospheric EHF refractivity," in *Proc. URSI Commission F 1983 Symposium*, Louvain, Belgium (1983).
 63. H. J. Liebe, "An updated model for millimeter wave propagation in moist air," *Radio Sci.* **20**, 1069 (1985).
 64. M. E. Thomas, "Atmospheric absorption model from 0.01 to 10 wave numbers," in *Propagation*

- Engineering*, L. R. Bissonnette and W. B. Miller, Eds., *Proc. SPIE* **1312**, 355–363 (1990).
65. D. T. Llewellyn-Jones, "Laboratory measurements of absorption by water vapor in the frequency range 100 to 1000 GHz," in *Atmospheric Water Vapor*, A. Deepak, T. D. Wilkerson, and L. H. Ruhnke, Eds., p. 255, Academic Press, New York (1980).
 66. D. E. Burch and R. L. Alt, "Continuum absorption by H_2O in the 700–1200 cm^{-1} and 2400–2800 cm^{-1} windows," AFGL-TR84-0128, Ford Aerospace and Communications Corp., Aerotonutronic Div. (1984).
 67. J. C. Peterson, M. E. Thomas, R. J. Nordstrom, E. K. Damon, and R. K. Long, "Water vapor nitrogen absorption at CO_2 laser frequencies," *Appl. Opt.* **18**, 834 (1979).
 68. G. L. Loper, M. A. O'Neill, and J. A. Gelbwachs, "Water-vapor continuum CO_2 laser absorption spectra between 27°C and 10°C," *Appl. Opt.* **22**, 3701 (1983).
 69. J. C. Peterson, "A study of water vapor absorption at CO_2 laser frequencies using a differential spectrophotometer and white cell," Dissertation, Ohio State University (1978).
 70. V. N. Aref'ev and V. I. Dianov-Klokov, "Attenuation of 10.6- μm radiation by water vapor and the role of $(\text{H}_2\text{O})_2$ dimers," *Opt. Spectros. (USSR)* **42**, 488 (1977).
 71. G. P. Montgomery, Jr., "Temperature dependence of infrared absorption by the water vapor continuum near 1200 cm^{-1} ," *Appl. Opt.* **17**, 2299 (1979).
 72. P. S. Varanasi, S. Chou, and S. S. Penner, *J. Quant. Spectros. Radiat. Transfer* **8**, 1537 (1968); see also P. Varanasi and S. Chadamani, "Self- and N_2 -broadened spectra of water vapor between 7.5 and 14.5 μm ," *J. Quant. Spectros. Radiat. Transfer* **38**, 407 (1987); and P. Varanasi, "Infrared absorption by water vapor in the atmosphere," in *Modeling of the Atmosphere*, L. R. Rothman, Ed., *Proc. SPIE* **928**, 213 (1988).
 73. C. T. Delaye and M. E. Thomas, "Atmospheric continuum absorption models," in *Propagation Engineering: Fourth in a Series*, L. R. Bissonnette and W. B. Miller, Eds., *Proc. SPIE* **1487**, 291–298 (1991).
 74. R. J. Nordstrom, M. E. Thomas, J. C. Peterson, E. K. Damon, and R. K. Long, "Effects of oxygen addition on pressure-broadened water vapor absorption in the 10- μm region," *Appl. Opt.* **17**, 2724 (1978).
 75. A. D. Devir, A. Ben-Shalom, E. Trakhovsky, E. Raz, M. Engel, S. G. Lipson, and U. P. Oppenheim, "Experimental validation of atmospheric transmittance codes," in *Optical, Infrared, and Millimeter-Wave Propagation Engineering*, W. B. Miller and N. S. Kopeika, Eds., *Proc. SPIE* **926**, 54–64 (1988).
 76. K. O. White, W. R. Watkins, C. W. Bruce, R. E. Meredith, and F. G. Smith, "Water vapor continuum absorption in the 3.5 to 4.0 μm region," *Appl. Opt.* **17**, 2711 (1978).
 77. F. S. Mills, "Absorption of deuterium fluoride laser radiation by the atmosphere," Dissertation, Ohio State University (1975).
 78. W. R. Watkins, R. L. Spellacy, K. O. White, B. Z. Sojka, and L. R. Bower, "Water vapor absorption coefficients at HF laser wavelength (2.64 & 2.93 μm)," *Appl. Opt.* **18**, 1582 (1979).
 79. T. G. Kyle, D. G. Murcray, F. H. Murcray, and M. J. Williams, "Absorption of solar radiation by atmospheric carbon dioxide," *J. Opt. Soc. Am.* **55**, 1421 (1965).
 80. J. Van Kranendonk, "Induced infrared absorption in gases: calculation of the binary absorption coefficients of symmetrical diatomic molecules," *Physica* **24**, 347 (1958).
 81. D. T. Sheng and G. E. Ewing, "Collision-induced infrared absorption of gaseous nitrogen at low temperatures," *J. Chem. Phys.* **55**, 5425 (1971).
 82. S. P. Reddy and C. W. Cho, "Induced infrared absorption of nitrogen and nitrogen-foreign gas mixtures," *Can. J. Phys.* **43**, 2331 (1965).
 83. M. M. Shapiro and H. P. Gush, "The collision-induced fundamental and first overtone bands of oxygen and nitrogen," *Can. J. Phys.* **44**, 949 (1966).
 84. N. I. Moskalenko, Y. A. Ilin, S. N. Parzhin, and L. V. Rodionov, "Pressure-induced IR radiation absorption in atmospheres," *Izv. Acad. Sci. USSR Atmos. Oceanic Phys.* **15**, 632 (1979).
 85. M. E. Thomas, "Infrared and millimeter-wavelength absorption in the atmospheric windows by water vapor and nitrogen: measurements and models," *Infrared Phys.* **30**, 161 (1990).
 86. S. F. Fulghum and M. M. Tilleman, "Interferometric calorimeter for the measurement of water vapor absorption," *J. Opt. Soc. Am. B*, 2401–2413 (1991).
 87. S. A. Clough, F. X. Kneizys, R. Davies, R. Gamache, and R. H. Tipping, "Theoretical line shape for H_2O vapor; application to the continuum," in *Atmospheric Water Vapor*, A. Deepak, T. D. Wilkerson, and L. H. Ruhnke, Eds., p. 25, Academic Press, New York (1980).

88. S. A. Clough, F. X. Kneizys, and R. Davies, "Line shape and water vapor continuum," *Atmospheric Research* **23**, 229–241 (1989).
89. V. E. Zuev and V. V. Fomin, "Consideration of continuum absorption in the problems of sounding from outer space," Presentation at the Symposium on Remote Sensing of the Atmosphere from Space, Innsbruck, Austria (1978).
90. E. Hudis, Y. Ben-Aryeh, and Y. P. Oppenheim, "Third order linear absorption by pairs of molecules," *Phys. Rev. A* **43**, 3631–3639 (1991).
91. S. S. Penner, *J. Quant. Spectros. Radiat. Transfer* **13**, 383 (1973).
92. R. A. Bohlander, R. J. Emery, D. T. Llewellyn-Jones, G. G. Gimmestad, H. A. Gebbie, O. A. Simpson, J. J. Gallagher, and S. Perkowitz, "Excess absorption by water vapor and comparison with theoretical dimer absorption," in *Atmospheric Water Vapor*, A. Deepak, T. D. Wilkerson, and L. H. Ruhnke, Eds., p. 241, Academic Press, New York (1980).
93. M. E. Thomas and R. J. Nordstrom, "The N₂-broadened water vapor absorption line shape and infrared continuum absorption I. Theoretical development," *J. Quant. Spectros. Radiat. Transfer* **28**, 81 (1982).
94. M. E. Thomas and R. J. Nordstrom, "The N₂-broadened water vapor absorption line shape and infrared continuum absorption II. Implementation of the line shape," *J. Quant. Spectros. Radiat. Transfer* **28**, 103 (1982).
95. M. E. Thomas and R. J. Nordstrom, "Line shape model for describing infrared absorption by water vapor," *Appl. Opt.* **24**, 3526 (1985).
96. C. B. Farmer, "Extinction coefficients and computed spectra for the rotational band of water vapor between 0.7 and 1000 cm⁻¹," Contract No. KHG5828CB19(d)3, EMI Electronics, England (1967).
97. P. L. Roney, F. Reid, and J.-M. Theriault, "Transmission window near 2400 cm⁻¹: an experimental and modeling study," *Appl. Opt.* **30**, 1995–2004 (1991).
98. L. R. Brown, "Methane line parameters from 3700 to 4136 cm⁻¹," *Appl. Opt.* **27**, 3275–3279 (1988).
99. L. T. Molina and M. J. Molina, "Absolute absorption cross sections of ozone in the 185- to 350-nm wavelength range," *J. Geophys. Res.* **91**, 14,501–14,508 (1986).
100. G. Guelachvili and K. N. Rao, *Handbook of Infrared Standards: With Spectral Maps and Transition Assignments between 3 and 2600 μm*, Academic Press, London (1986).
101. R. A. McClatchey et al., "AFCRL atmospheric absorption line parameter compilation," AFCRL Technical Report 0096 (1973); see also L. S. Rothman and R. A. McClatchey, "Updating of the AFCRL atmospheric absorption line parameters compilation," *Appl. Opt.* **15**, 2616 (1976); L. S. Rothman et al., "AFGL trace compilation," *Appl. Opt.* **17**, 507 (1978); L. S. Rothman, "Update of the AFGL atmospheric absorption line parameters compilation," *Appl. Opt.* **17**, 3517–3518 (1978); L. S. Rothman, "AFGL atmospheric absorption line parameters compilation: 1980 version," *Appl. Opt.* **20**, 791–795 (1981); L. S. Rothman et al., "AFGL trace compilation: 1980 version," *Appl. Opt.* **20**, 1323–1328 (1981); L. S. Rothman et al., "AFGL atmospheric absorption line parameters compilation: 1982 version," *Appl. Opt.* **22**, 2247–2256 (1983); L. S. Rothman et al., "AFGL trace compilation: 1982 version," *Appl. Opt.* **22**, 1616–1627 (1983).
102. L. S. Rothman, R. R. Gamache, A. Goldman, L. R. Brown, R. A. Toth, H. M. Pickett, R. L. Poynter, J.-M. Flaud, C. Camy-Peyret, A. Barbe, N. Husson, C. P. Rinsland, and M. A. H. Smith, "The HITRAN database: 1986 edition," *Appl. Opt.* **26**, 4058–4097 (1987).
103. L. S. Rothman, "The spectroscopic database for high resolution atmospheric modeling," in *Modeling of the Atmosphere*, L. S. Rothman, Ed., *Proc. SPIE* **928**, 79–93 (1988).
104. N. Husson, A. Chedin, N. A. Scott, D. Bailey, et al., "The GEISA spectroscopic line parameter data bank in 1984," *Ann. Geophys.* **4 A2**, 185–190 (1986).
105. J. C. Gille and R. G. Ellingson, "Correction of random exponential band transmissions for Doppler effects," *Appl. Opt.* **7**(3), 471–474 (1968).
106. W. M. Elsasser, "Mean absorption and equivalent absorption coefficient of a band spectrum," *Phys. Rev.* **54**, 126 (1938).
107. H. Mayer, "Methods of opacity calculations, V. Effect of lines on opacity, methods for treating line contributions," Los Alamos Scientific Laboratory Report No. AECD-1870 (1947).
108. R. M. Goody, "A statistical model for water-vapour absorption," *Q. J. R. Meteorol. Soc.* **58**, 165–169 (1952).
109. G. N. Plass, "Models for spectral band absorption," *J. Opt. Soc. Am.* **48**, 690–703 (1958).

110. P. J. Wyatt, V. R. Stull, and G. N. Plass, "Quasi-random model of band absorption," *J. Opt. Soc. Am.* **52**, 1209 (1962).
111. R. Ladenburg and F. Reiche, "Über selektive absorption," *Ann. Phys. (Leipzig)* **42**, 181 (1913).
112. L. D. Kaplan, "Regions of validity of various absorption-coefficient approximations," *J. Meteorology* **10**, 100–104 (1953).
113. G. N. Plass, "Useful representations for measurements of spectral band absorption," *J. Opt. Soc. Am.* **50**, 868–875 (1960).
114. S. A. Golden, "The Doppler analog of the Elsasser band model," *J. Quant. Spectros. Radiat. Transfer* **7**, 483–494 (1967).
115. R. M. Goody and Y. L. Yung, *Atmospheric Radiation Theoretical Basis*, 2nd ed., Oxford University Press, Oxford (1989).
116. W. Malkmus, "Random Lorentz band model with exponential-tailed S^{-1} line intensity distribution function," *J. Opt. Soc. Am.* **57**(3), 323–329 (1967).
117. P. J. Wyatt, V. R. Stull, and G. N. Plass, "The infrared transmittance of water vapor," *Appl. Opt.* **3**(2) (1964); see also Aeronutronic Report U-1717, Aeronutronic Systems, Newport Beach, CA (1962).
118. V. R. Stull, P. J. Wyatt, and G. N. Plass, "The infrared transmittance of water vapor," *Appl. Opt.* **3**(2) (1964); Aeronutronic Report U-1718, Aeronutronic Systems, Newport Beach, CA (1962).
119. S. R. Drayson, "Atmospheric slant-path transmission in the 15μ CO₂ band," Report No. 05863–6T, The Institute of Science and Technology, University of Michigan, Ann Arbor, MI (1964).
120. A. J. LaRocca and R. E. Turner, "Atmospheric transmittance and radiance: methods of calculation," Report No. 107600–10-T, Environmental Research Institute of Michigan, Ann Arbor, MI.
121. J. N. Hamilton, J. A. Rowe, and D. Anding, "Atmospheric transmission and emission program," Report No. TOR-0073(3050-02)-3, Aerospace Corp., El Segundo, CA (1973).
122. J. N. Howard, D. Burch, and D. Williams, "Near-infrared transmission through synthetic atmospheres," Geophysics Research Paper No. 40, Report No. AFCRL-TR-55-213, Ohio State University Research Foundation, Columbus, OH (1955).
123. D. E. Burch, D. A. Gryvnak, and J. D. Pembrook, "Investigation of infrared absorption by nitrous oxide from 4000 to 6000 cm⁻¹ (2.5 to 1.5 μm)," Aeronutronics Report U-4393, AFCRL-71-0536, Philco-Ford Corp., Newport Beach, CA (1971); see also D. E. Burch, D. A. Gryvnak, and J. D. Pembrook, "760 to 2380 cm⁻¹ (13.2 to 4.2 μm)," Aeronutronics Report U-4995, AFCRL-71-0620, Philco-Ford Corp., Newport Beach, CA (1971).
124. D. E. Burch, "Investigation of the absorption of infrared radiation by atmospheric gases," Philco Report No. U-4784, Philco-Ford Corp., Newport Beach, CA (1970).
125. K. Bignell, "The water vapor infrared continuum," *Q. J. R. Meteorol. Soc.* **96**, 390–403 (1970).
126. R. A. McClatchey et al., "Optical properties of the atmosphere," AFCRL-72-0497, 3rd ed., Air Force Cambridge Research Lab, Bedford, MA (1972); see also R. A. McClatchey et al., "AFCRL atmospheric absorption line parameters compilation," Report No. AFCRL-TR-73-0096, Air Force Research Labs., Hanscom Field, Bedford, MA (1973).
127. W. R. Bradford, T. M. McCormick, and J. A. Selby, "Laboratory representation of atmospheric paths for infrared absorption," Report No. DMP 1431, EMI Electronics, Hayes, Middlesex, England (1963).
128. S. R. Drayson and C. Young, "The frequencies and intensities of carbon dioxide absorption lines between 12 to 18 microns," Report No. 08183-1-T, Institute of Science and Technology, University of Michigan, Ann Arbor, MI (1967).
129. C. Walshaw, "Integrated absorption by the 9.6 μm band of ozone," *Q. J. R. Meteorol. Soc.* **83**, 315–321 (1957).
130. D. J. McCaa and J. H. Shaw, "The infrared spectrum of ozone," *J. Mol. Spectrosc.* **25**(3), 374–397 (1968).
131. E. Plyler and E. Barker, "Infrared spectrum and molecular configuration on N₂O," *Phys. Rev.* **38**, 1827 (1931).
132. R. W. Fenn et al., "Optical and infrared properties of the atmosphere," Chap. 18 in *Handbook of Geophysics and Space Environment*, Adolph S. Jeursa, Ed., Air Force Geophysics Laboratory (1985).

133. D. C. Robertson, L. S. Bernstein, R. Haimes, J. Wunderlich, and L. Vega, "5-cm⁻¹ band model option to LOWTRAN 5," *Appl. Opt.* **20**, 3218–3226 (1981).
134. A. Berk, L. S. Bernstein, and D. C. Robertson, "MODTRAN: a moderate resolution model for LOWTRAN 7," Report No. GL-TR-89-0122, Geophysics Laboratory, Air Force Systems Command, Hanscom AFB, MA (1989).
135. B. Edlen, "The refractive index of air," *Metrologia* **2**, 12 (1966).
136. R. W. Fenn et al., "Optical and infrared properties of the atmosphere," Chap. 18 in *Air Force Handbook of Geophysics and Space Science* (1985).
137. L. D. Lorah and E. Rubin, "Aerodynamic influences on infrared system design," Chap. 24 in *The Infrared Handbook*, 2nd ed., W. L. Wolfe and C. J. Zissis, Eds., Environmental Research Institute of Michigan, Ann Arbor, MI (1985).
138. H. Barrell and J. E. Sears, "The refraction and dispersion of air for the visible spectrum," *Philos. Trans. R. Soc. London A* **238**, 1–64 (1939).
139. R. J. Hill and R. S. Lawrence, "Refractive index of water vapor in infrared windows," *Infrared Phys.* **26**, 371–376 (1986).
140. H. J. Leibe, "An updated model for millimeter wave propagation in moist air," *Radio Sci.* **20**, 1069–1089 (1985).
141. B. R. Bean and E. J. Dutton, *Radio Meteorology*, Dover, New York (1968).
142. H. W. Ko, J. W. Sari, and J. P. Skura, "Anomalous microwave propagation through atmospheric ducts," *Johns Hopkins APL Technical Digest* **4**(1), 12–26 (1983).
143. D. E. Gray, *American Institute of Physics Handbook*, 3rd ed., pp. 6–110, McGraw-Hill, New York (1972).
144. C. M. Crain, "The dielectric constant of several gases at a wavelength of 3.2 centimeters," *Phys. Rev.* **74**, 691–693 (1948).
145. E. J. McCartney, *Optics of the Atmosphere: Scattering by Molecules and Particles*, Wiley, New York (1976).
146. A. Aden and M. Meinel, "At sunset," *Optics News* **14**(11), 6 (1988).
147. B. E. Schaefer and W. Liller, "Refraction near the horizon," *Publ. Astron. Soc. Pac.* **102**, 796–805 (1990).
148. R. Greenler, *Rainbows, Halos, and Glories*, Cambridge University Press, Cambridge, England (1980).
149. D. J. K. O'Connell S. J., "The green flash and other low sun phenomena," North-Holland, Vatican Observatory (1958).
150. C. F. Bohren and D. R. Huffman, *Absorption and Scattering of Light by Small Particles*, Wiley-Interscience, New York (1983).
151. P. Barber and C. Yeh, "Scattering of electromagnetic waves by arbitrarily shaped dielectric bodies," *Appl. Opt.* **14**, 2864–2872 (1975).
152. P. W. Barber and S. C. Hill, *Optical Effects Associated with Small Particles*, World Scientific, Singapore (1990).
153. P. W. Barber and S. C. Hill, *Light Scattering by Particles: Computational Methods*, World Scientific, Singapore (1990).
154. D. W. Schuerman, Ed., *Light Scattering by Irregularly Shaped Particles*, Plenum Press, New York (1979).
155. D. Deirmendjian, *Electromagnetic Scattering on Spherical Polydispersions*, American Elsevier Publishing, New York (1969).
156. E. Hecht, *Optics*, 2nd ed., Addison-Wesley, Reading, MA (1987).
157. H. C. van de Hulst, *Light Scattering by Small Particles*, Dover, New York (1981).
158. H. C. van de Hulst, *Multiple Light Scattering: Tables, Formulas, and Applications*, Vols. 1 and 2, Academic Press, New York (1980).
159. M. Born and E. Wolf, *Principles of Optics: Electromagnetic Theory of Propagation, Interference and Diffraction of Light*, Pergamon Press, Elmsford, NY (1970).
160. R. W. Fenn, S. A. Clough, W. O. Gallery, R. E. Good, F. X. Kneizys, J. D. Mill, L. S. Rothman, E. P. Shettle, and F. E. Volz, "Optical and infrared properties of the atmosphere," Chap. 18 in *Handbook of Geophysics and Space Environment*, Adolph S. Jeursa, Ed., Air Force Geophysics Laboratory (1985).

161. G. de Leeuw, K. L. Davidson, S. G. Gathman, and R. V. Noonkester, "Modeling of aerosols in the marine mixed layer," in *Propagation Engineering*, N. S. Kopeika and W. B. Miller, Eds., *Proc. SPIE 1115*, 287–294 (1989).
162. M. H. Smith, P. M. Park, and I. E. Consterdine, "Wind speed dependence of North Atlantic aerosol spectra," in *Propagation Engineering*, N. S. Kopeika and W. B. Miller, Eds., *Proc. SPIE 1115*, 278–286 (1989).
163. E. P. Shettle, "Models of aerosols, clouds and precipitation for atmospheric propagation studies," in *AGARD Conference Proceedings No. 454 on Atmospheric Propagation in the UV, Visible, IR, and MM-Wave Region and Related Systems Aspects*, pp. 15-1 to 15-13 (1989).
164. E. J. McCartney, *Optics of the Atmosphere: Scattering by Molecules and Particles*, John Wiley & Sons, New York (1976).
165. G. M. Hale and M. R. Querry, "Optical constants of water in the 200-nm to 200- μm wavelength region," *Appl. Opt.* **12**, 555–563 (1973).
166. E. P. Shettle and R. W. Fenn, "Models for the aerosols of the lower atmosphere and the effects of humidity variations on their optical properties," Air Force Geophysics Laboratory Report AFGL-TR-79-0214, Environmental Research Papers, N0676 (1979).
167. W. L. Wolfe and G. J. Zissis, Eds., *The Infrared Handbook*, The Infrared Information and Analysis (IRIA) Center, Environmental Research Institute of Michigan, Ann Arbor, MI (1978).
168. K. F. Palmer and D. Williams, "Optical constants of sulphuric acid: applications to the clouds of Venus," *Appl. Opt.* **14**, 208–219 (1975).
169. L. S. Ivlev and S. I. Popova, "The complex index of refraction of the matter of the disperse phase of the atmospheric aerosol," *Izv. Acad. Sci. USSR Atmos. Oceanic Phys.* **9**, 587–591 (1973).
170. F. E. Volz, "Infrared optical properties of ammonium sulphate, volcanic pumice, and flyash," *Appl. Opt.* **12**, 564–568 (1973).
171. F. E. Volz, "Infrared refractive index of atmospheric aerosol substances," *Appl. Opt.* **11**, 755–759 (1972).
172. J. T. Peterson and J. A. Weinman, "Optical properties of quartz dust particles at IR wavelengths," *J. Geophys. Res.* **74**, 6947–6952 (1969).
173. E. E. Remsberg, "Radiative properties of several probable constituents of atmospheric aerosols," PhD Thesis, University of Wisconsin (1971).
174. O. B. Toon and J. P. Pollack, "A global average model of atmospheric aerosols for radiative transfer calculations," *J. Appl. Meteorol.* **15**(3), 225–246 (1976).
175. M. E. Thomas and R. I. Joseph, "A comprehensive model for the intrinsic transmission properties of optical windows," in *Infrared Optical Materials VI*, S. Musikant, Ed., *Proc. SPIE 929*, 87–92 (1988).
176. T. F. Deutsch, "Absorption coefficient of infrared laser window material," *J. Phys. Chem. Solids* **34**, 2091–2104 (1973).
177. W. G. Spitzer and D. A. Kleinman, "Infrared lattice bonds of quartz," *Phys. Rev.* **121**, 1324–1335 (1961).
178. S. Onari, T. Arai, and K. Kudo, "Infrared lattice vibrations and dielectric dispersion in Fe_2O_3 ," *Phys. Rev. B* **16**, 1717–1721 (1977).
179. M. Kerker, *The Scattering of Light and Other Electromagnetic Radiation*, Academic Press, New York (1969).
180. R. C. Harney, "Military applications of coherent infrared radar," in *Physics and Technology of Coherent Infrared Radar*, R. C. Harney, Ed., *Proc. SPIE 300*, 2–11 (1981).
181. M. Milham, "A catalog of optical extinction data for various aerosols/smokes," Special Publication ED-SP-77002, Edgewood Arsenal (1976).
182. S. Chandrasekhar, *Radiative Transfer*, Dover, New York (1960).
183. M. V. Wilkes, "A table of Chapman's grazing incidence integral, $\text{Ch}(x,\chi)$," *Proc. Phys. Soc. London B* **67**, 304–308 (1954).
184. "RSIC computer code & data collections: a capsule review of the computer code collection (CCC), peripheral shielding routines (PSR), and data library collection (DLC)"; see also "Personal computer codes/data availability," both documents available from Oak Ridge National Laboratory (Feb. 1990).

-
185. A. Ishimaru, *Wave Propagation and Scattering in Random Media, Volume 1: Single Scattering and Transport Theory, Volume 2: Multiple Scattering, Turbulence, Rough Surfaces, and Remote Sensing*, Academic Press, New York (1978).
186. P. S. Mudgett and L. W. Richards, "Multiple scattering calculations for technology," *Appl. Opt.* **10**, 1485–1502 (1971).
187. L. Henyey and J. Greenstein, "Diffuse radiation in the galaxy," *Astrophys. J.* **93**, 70–83 (1941).
188. E. A. Bucher, "Computer simulation of light pulse propagation for communication through thick clouds," *Appl. Opt.* **12**, 2391–2400 (1973).
189. L. B. Stotts, "Closed form expression for optical pulse broadening in multiple-scattering media," *Appl. Opt.* **17**, 504–505 (1978).
190. R. F. Lutomirski, "Atmospheric degradation of electro-optical system performance," *Appl. Opt.* **17**, 3915–3921 (1978).
191. R. F. Lutomirski, "The irradiance distribution in a scattering medium," PSR Note 73, Pacific-Sierra Research Corp. (1975).
192. J. W. Goodman, *Statistical Optics*, John Wiley & Sons, New York (1985).
193. W. H. Wells, "Loss of resolution in water as a result of multiple small-angle scattering," *J. Opt. Soc. Am.* **59**, 686–691 (1969).
194. J. E. A. Selby and R. A. McClatchey, "Atmospheric transmittance from 0.25–28.5 μm : computer code LOWTRAN 2," Report AFCRL-72-0745, Air Force Cambridge Research Laboratory (1972).
195. J. E. A. Selby and R. A. McClatchey, "Atmospheric transmittance from 0.25–28.5 μm : computer code LOWTRAN 3," Report AFCRL-75-0255, Air Force Cambridge Research Laboratory (1975).
196. J. E. A. Selby and R. A. McClatchey, "Atmospheric transmittance from 0.25–28.5 μm : computer code LOWTRAN 3B," Report AFCRL-TR-76-0258, Air Force Cambridge Research Laboratory (1976).
197. J. E. A. Selby, F. X. Kneizys, J. H. Chetwynd, and R. A. McClatchey, "Atmospheric transmittance/radiance: computer code LOWTRAN 4," Report AFGL-TR-78-0053, Air Force Cambridge Research Laboratory (1978).
198. F. X. Kneizys, E. P. Shettle, W. O. Gallery, J. H. Chetwynd, L. W. Abreu, J. E. A. Selby, R. W. Fenn, and R. A. McClatchey, "Atmospheric transmittance/radiance: computer code LOWTRAN 5," Report AFGL-TR-80-0067, Air Force Cambridge Research Laboratory (1980).
199. F. X. Kneizys, E. P. Shettle, W. O. Gallery, J. H. Chetwynd, L. W. Abreu, J. E. A. Selby, S. A. Clough, and R. W. Fenn, "Atmospheric transmittance/radiance: computer code LOWTRAN 6," Report AFGL-TR-83-0187, Air Force Cambridge Research Laboratory (1985).
200. F. X. Kneizys, E. P. Shettle, L. W. Abreu, G. P. Anderson, J. H. Chetwynd, W. O. Gallery, J. E. A. Selby, and S. A. Clough, "Atmospheric transmittance/radiance: the LOWTRAN 7 model," (in preparation).
201. A. D. Devir, A. Ben-Shalom, S. G. Lipson, U. P. Oppenheim, and E. Ribak, "Atmospheric transmittance measurements: comparison with LOWTRAN 6," Report RAA/99-85, Technion—Israel Institute of Technology (1985).
202. C. F. Bohren and D. R. Huffman, *Absorption and Scattering of Light by Small Particles*, Wiley-Interscience, New York (1983).
203. E. P. Shettle and R. W. Fenn, "Models for the aerosols of the lower atmosphere and the effects of humidity variations on their optical properties," Air Force Geophysics Laboratory Report AFGL-TR-79-0214, Environmental Research Papers, N0676 (1979).

Bibliography

Section 1.1

Goody, R. M., and Y. L. Yung, *Atmospheric Radiation Theoretical Basis*, 2nd ed., Oxford University Press, Oxford (1989).

Section 1.2

- McCartney, E. J., *Absorption and Emission by Atmospheric Gases: The Physical Processes*, John Wiley & Sons, New York (1983).
- McCartney, E. J., *Optics of the Atmosphere: Scattering by Molecules and Particles*, John Wiley & Sons, New York (1976).

Section 1.3.1

- Breene, R. G., Jr., *Theories of Spectral Line Shape*, John Wiley & Sons, New York (1981).
- Cohen-Tannoudji, C., J. Dupont-Roc, and G. Grynberg, *Photons and Atoms: Introduction to Quantum Electrodynamics*, John Wiley & Sons, New York (1989).
- Guelachvili, G., and K. N. Rao, *Handbook of Infrared Standards: With Spectral Maps and Transition Assignments between 3 and 2600 μm* , Academic Press, London (1986).
- Haken, H., *Light: Waves, Photons, Atoms*, Vol. I, North-Holland, Amsterdam (1986).
- Herzberg, G., *Atomic Spectra and Atomic Structure*, Dover, Mineola, NY (1944).
- Herzberg, G., *Electronic Spectra and Electronic Structure of Polyatomic Molecules*, Van Nostrand Reinhold, New York (1966).
- Herzberg, G., *Infrared and Raman Spectra of Polyatomic Molecules*, Van Nostrand Reinhold, New York (1945).
- Herzberg, G., *Spectra of Diatomic Molecules*, 2nd ed., Van Nostrand Reinhold, New York (1950).
- Jackson, J. D., *Classical Electrodynamics*, 2nd ed., John Wiley & Sons, New York (1975).
- Rothman, L. S., Ed., *Modeling of the Atmosphere*, Proc. SPIE 928 (1988).
- Webster, C. R., R. T. Menzies, and E. D. Hinkley, "Infrared laser absorption: theory and applications," Chap. 3 in *Laser Remote Chemical Analysis*, R. M. Measures, Ed., pp. 163–272, John Wiley & Sons, New York (1988).
- Weissbluth, M., *Photon-Atom Interactions*, Academic Press, Orlando, FL (1989).

Section 1.3.2

- Bojkov, R. D., and P. Fabian, Eds., *Ozone in the Atmosphere*, A. Deepak Publishing Co., Hampton, VA (1989).
- Deepak, A., T. D. Wilkerson, and L. H. Ruhnke, Eds., *Atmospheric Water Vapor*, Academic Press, New York (1980).
- Flaud, J.-M., C. Camy-Peyret, C. P. Rinsland, M. A. H. Smith, and V. Malathy Devi, *Atlas of Ozone Spectral Parameters from the Microwave to Medium Infrared*, Academic Press, San Diego, CA (1990).
- Goody, R. M., and Y. L. Yung, *Atmospheric Radiation Theoretical Basis*, 2nd ed., Oxford University Press, Oxford (1989).
- Grant, W. B., Ed., *Ozone Measuring Instruments for the Stratosphere*, Optical Society of America (1989).
- LaRocca, A. J., "Atmospheric absorption," Chap. 5 in *The Infrared Handbook*, 2nd ed., W. L. Wolfe and G. J. Zissis, Eds., Environmental Research Institute of Michigan, Ann Arbor, MI (1985).
- McCartney, E. J., *Absorption and Emission by Atmospheric Gases: The Physical Processes*, John Wiley & Sons, New York (1983).
- Zuev, V. E., *Laser Beams in the Atmosphere*, Plenum Press, New York (1982).
- Zuev, V. E., *Propagation of Visible and Infrared Radiation in the Atmosphere*, John Wiley & Sons, New York (1974).

Section 1.4

- Bohren, C. F., Ed., *Selected Papers on Scattering in the Atmosphere*, SPIE Milestone Series Vol. MS 7, SPIE Optical Engineering Press, Bellingham, WA (1989).
- Karp, S., R. M. Gagliardi, S. E. Moran, and L. B. Stotts, *Optical Channels: Fibers, Clouds, and the Atmosphere*, Plenum Press, New York (1988).

CHAPTER 2

Propagation through Atmospheric Optical Turbulence

Robert R. Beland
*Phillips Laboratory
Geophysics Directorate
Hanscom Air Force Base, Massachusetts*

CONTENTS

2.1	Introduction	159
2.2	Theory of Optical Turbulence in the Atmosphere	161
2.2.1	Introduction	161
2.2.2	Statistical Concepts	161
2.2.3	Structure Functions	165
2.2.4	Kolmogorov Theory of Turbulence	167
2.2.5	Conservative Passive Scalars	169
2.2.6	Index of Refraction	171
2.2.7	Atmospheric Temporal Statistics	174
2.3	Optical/IR Propagation through Turbulence	176
2.3.1	Introduction	176
2.3.2	Formal Solutions of the Wave Equation	177
2.3.3	Amplitude and Phase Statistics	179
2.3.4	Scintillation	184
2.3.5	Imaging Effects	190
2.3.6	Beam Effects	195
2.3.7	Isoplanatism	201
2.4	Measurements of Optical Turbulence in the Atmosphere	201
2.4.1	Introduction	201
2.4.2	Atmospheric Boundary Layer	202
2.4.3	Free Atmosphere	206
2.4.4	Issues of Measurement	209
2.4.5	Measurements of Moments	210

2.5	Models of Optical Turbulence	211
2.5.1	Introduction	211
2.5.2	Boundary-Layer Turbulence	212
2.5.3	Model Optical Turbulence Profiles.....	217
2.5.4	Parametric Models	221
2.6	Sample Problems	224
2.6.1	Scintillation	224
2.6.2	Image Resolution	226
2.6.3	Beam Wander and Broadening	227
	References	229

2.1 INTRODUCTION

All systems utilizing electromagnetic waves must take into account the characteristics of the medium in which propagation occurs. As more sophisticated electro-optic systems are developed, details of the propagation medium that had previously been ignored become important. Optical turbulence is such an important characteristic for propagation through the atmosphere. Optical turbulence can be defined as the fluctuations in the index of refraction resulting from atmospheric turbulence. It is responsible for a variety of effects, such as temporal intensity fluctuations, or scintillation; the twinkling of stars is the classic example. In laser beam propagation, the effects include beam wander and broadening. In imaging applications, turbulence effects include image dancing and blurring. It is turbulence that limits the resolution of astronomical telescopes and motivates the placement of telescopes in space to avoid the atmosphere's deleterious effect. There are other more sophisticated and subtle effects that arise in modern systems, particularly those that utilize adaptive optics elements.

Atmospheric turbulence produces small fluctuations in the index of refraction. Although the magnitude of the individual fluctuations is very small, the cumulative effect in propagation along an atmospheric path may be very significant. Their effect is easily described qualitatively. The turbulence-induced fluctuations in the refractive index produce a phase distortion of the wavefront as it passes through the turbulence, and it is this distorted wavefront that continues to propagate and is itself further distorted.

In this chapter, the theory of optical turbulence in the atmosphere is reviewed. The propagation through turbulence by optical and infrared radiation also is treated. The focus is on "small"-scale atmospheric turbulence, where "small" is used in the sense of micrometeorology. No consideration is given to the "large"-scale atmospheric turbulence that is associated with large-scale flow, such as the meridional flow from the equator to the poles or synoptic meteorology. Our interest is in the characterization of optical paths. As will be seen, the index of refraction structure parameter C_n^2 along the path emerges as the critical parameter in characterizing the effects of the atmosphere.

The propagation of electromagnetic radiation through random media is a large subject area. Only the optical/IR segment of the electromagnetic spectrum is discussed here. The approach to turbulence and its effects treats the atmosphere and the turbulence-induced refractive-index fluctuations as a continuum. Effects arising out of discrete scatterers, such as aerosols, are not treated, despite the fact that they may be considered as representing fluctuations in the index of refraction. The effects of absorption by atmospheric particulates or molecules also are excluded. This last exclusion includes the phenomenon of thermal blooming of high-power laser beams in the atmosphere, but the effect of optical turbulence on low-power laser beams is treated. The complex phenomena associated with high-energy laser propagation through the atmosphere, including stimulated Raman scattering, aerosol vaporization, thermal-blooming instability, and interactions with turbulence effects are an area of active research that warrants a more thorough and diverse treatment than could be given in the present chapter.

A listing of symbols and notation used in this chapter is given in Table 2.1.

Table 2.1 List of Symbols and Notation

B_x	Covariance function of quantity x
C_n^2	Refractive-index structure constant ($\text{m}^{-2/3}$)
C_6^2	Potential temperature structure constant
C_q^2	Specific humidity structure constant
C_T^2	Temperature structure constant
D	Aperture diameter
D_x	Structure function of quantity x
E	Magnitude of electric field or wave amplitude
f	Focal length
F_x	Two-dimensional spatial power spectrum of quantity x
h	Height or altitude above ground level (AGL)
I	Intensity
k	Wave number of light ($2\pi/\lambda$)
K	Spatial wave number (m^{-1})
\mathbf{K}	Vector spatial wave number (m^{-1})
l_0	Inner scale of turbulence (m)
L_0	Outer scale of turbulence (m)
L_*	Monin-Obhukov length (similarity theory)
L	Path length
MCF	Mutual coherence function
MTF	Modulation transfer function
n	Index of refraction
N^2	Brunt-Vaisala frequency (s^{-2})
P_x	One-dimensional spatial power spectrum of quantity x
q	Specific humidity (kg/kg)
r_0	Fried's coherence length diameter (m)
S	Phase
S_x	One-sided, one-dimensional spatial power spectrum ($0 \leq K \leq \infty$) of quantity x
T_*	Temperature scaling parameter (similarity theory)
V_{\perp}	Transverse wind speed (m/s)
W	Beamwidth
W_x	Temporal power spectrum of quantity x
$\langle x \rangle$	Ensemble average of scalar x
\bar{x}	Time average of x
\mathbf{x}	Vector x
z	Altitude above mean sea level (MSL)
χ	Log amplitude
δ	Image displacement in the focal plane
ε	Turbulence energy dissipation rate ($\text{m}^2 \text{s}^{-3}$)
ϕ	Angle of arrival
Φ_x	Three-dimensional spatial power spectrum of quantity x
φ	Zenith angle
λ	Wavelength of light
ν	Spatial wave number in focal plane (cy m^{-1})
θ	Potential temperature (K)
θ_0	Isoplanatic angle (μrad)
ρ_0	Transverse coherence length (m)
ρ_L	Long-time beam radius
ρ_s	Short-time beam radius
ρ_c	Short-time beam centroid position
ρ_b	Beam transverse coherence length (m)
σ_x^2	Variance of quantity x [$\sigma_x^2 = B_x(0)$]
ω	Temporal frequency (s^{-1})

2.2 THEORY OF OPTICAL TURBULENCE IN THE ATMOSPHERE

2.2.1 Introduction

When the flow of a viscous fluid, characterized by the Reynold's number, exceeds a critical value, the flow changes from laminar to a more chaotic regime. This regime is turbulence. It is fundamentally a state where the velocity of a parcel of the fluid fluctuates about the mean velocity of the flow and these fluctuations possess a continuous power spectrum. The fluctuations are usually conceptualized in the form of vortices or eddies. These eddies result in the transport or mixing of other characteristics of the fluid. In the case of the atmosphere, the turbulent fluctuations in wind speed result in the mixing of atmospheric quantities, such as temperature, aerosols, or water vapor. The quantity that is the focus here is the index of refraction, that is, optical turbulence. The theoretical framework of optical turbulence is based on the theory of the fundamental physical process, velocity turbulence.

Turbulence is fundamentally a nonlinear process. The governing equations, the Navier-Stokes equations, are nonlinear. As if this were not difficult enough, they also suffer from the closure problem; i.e., there are more variables than equations. This difficult subject matter has occupied some of the great minds of twentieth century science. Because of these difficulties, a statistical approach, relying heavily on dimensional analysis, was pursued by Kolmogorov. Kolmogorov's theory provides the cornerstone for the study of optical turbulence and is the subject of a subsequent section. It should be emphasized that turbulence theory is not rigorously derived from first principles. Furthermore, when one is considering a fluid as complex and varied as the atmosphere, additional simplifications and approximations enter.

2.2.2 Statistical Concepts

As mentioned earlier, a statistical approach has achieved considerable success in describing both atmospheric turbulence and its effects on optical/IR systems. In this section, the necessary tools and concepts are summarized, first for scalar random processes in one dimension and then for scalar processes in three dimensions. The generalization to vector processes is cumbersome but straightforward. Let $\xi(t)$ be a random variable at time t . This is a one-dimensional time series that is the subject of a vast literature.^{1,2} The ensemble average of an arbitrary function, say f , of ξ will be denoted by the bracketed quantity $\langle f(\xi) \rangle$. Most of our treatment is in terms of first- and second-order statistics. The covariance function of ξ is defined by

$$B_\xi(t_1, t_2) = \langle [\xi(t_1) - \langle \xi(t_1) \rangle][\xi(t_2) - \langle \xi(t_2) \rangle] \rangle . \quad (2.1)$$

In this general definition, the covariance represents the correlation between the fluctuations from the mean at t_1 with those at t_2 . If the process is stationary, then its moments are invariant under translations in time.^a For stationary

^aThe distinction between second order and strict stationarity is not important for this discussion. We shall assume strict stationarity so that all moments and all order probability distributions are invariant under translation of the time origin.

random processes, the mean is independent of time (that is, $\langle \xi(t) \rangle = \langle \xi \rangle$) and the covariance depends only on the difference $\tau = t_1 - t_2$ and can be written for any time t as

$$B_\xi(\tau) = \langle [\xi(t + \tau) - \langle \xi \rangle][\xi(t) - \langle \xi \rangle] \rangle = \langle \xi(t + \tau)\xi(t) \rangle - \langle \xi \rangle^2 . \quad (2.2)$$

For the class of stationary processes that are known as ergodic processes, the ensemble averages such as the mean and the covariance can be determined from time averages.³ In our notation, the time average over a time interval T of some quantity, say f , is denoted by an overbar, \bar{f}_T . For example, the covariance averaged over a time T is

$$\bar{B}_{\xi,T}(\tau) = \frac{1}{T} \int_0^T [\xi(t + \tau) - \bar{\xi}_T][\xi(t) - \bar{\xi}_T] dt . \quad (2.3)$$

The ergodic property assures us that

$$B_\xi(\tau) = \lim_{T \rightarrow \infty} \bar{B}_{\xi,T}(\tau) . \quad (2.4)$$

Thus, we have the equivalence between infinite time averages and ensemble averages. This presentation shows that for finite T , $\bar{B}_{\xi,T}$ is a statistical estimator of the infinite time average, denoted by B_ξ , or equivalently, of the ensemble average B_ξ . The accuracy of the statistical estimator for a stationary process is a central issue in the accuracy of measurements.

There is an alternative description of the correlations of fluctuations of stationary random processes that is heavily utilized. The Wiener-Kinchine theorem^{1,3} established a Fourier transform relationship between the autocovariance and the power spectrum of a stationary random process, denoted by $W_\xi(\omega)$; that is,

$$W_\xi(\omega) = \frac{1}{2\pi} \int_{-\infty}^{\infty} B_\xi(\tau) e^{i\omega\tau} d\tau . \quad (2.5)$$

The inverse relation is

$$B_\xi(\tau) = \int_{-\infty}^{\infty} W_\xi(\omega) e^{-i\omega\tau} d\omega . \quad (2.6)$$

Since the covariance is a real, even function, it can be shown that the spectrum is a real, even function. Therefore, these two Fourier integrals can be written as cosine transforms:

$$W_\xi(\omega) = \frac{1}{2\pi} \int_{-\infty}^{\infty} B_\xi(\tau) \cos(\omega\tau) d\tau , \quad (2.7)$$

$$B_\xi(\tau) = \int_{-\infty}^{\infty} W_\xi(\omega) \cos(\omega\tau) d\omega . \quad (2.8)$$

The power spectrum is a frequency-domain representation or spectral decomposition of the temporal correlations. By ergodicity, it can also be estimated by time averages and its estimation is the domain of the subject of spectral analysis.⁴

Next, consider scalar random processes in three dimensions, also called random fields. The spatial covariance of the field $\xi(\mathbf{r})$ is defined as

$$B_\xi(\mathbf{r}_1, \mathbf{r}_2) = \langle [\xi(\mathbf{r}_1) - \langle \xi(\mathbf{r}_1) \rangle][\xi(\mathbf{r}_2) - \langle \xi(\mathbf{r}_2) \rangle] \rangle .$$

The property of homogeneity is the spatial counterpart of stationarity in time. A homogeneous process is one that has moments that are invariant under a spatial translation. Thus, the mean is independent of \mathbf{r} (that is, $\langle \xi(\mathbf{r}) \rangle = \langle \xi \rangle$), and the covariance depends only on $\mathbf{r} = \mathbf{r}_2 - \mathbf{r}_1$ and can be written as

$$B_\xi(\mathbf{r}_1, \mathbf{r}_2) = B_\xi(\mathbf{r}) = \langle \xi(\mathbf{r}_1) \xi(\mathbf{r}_1 + \mathbf{r}) \rangle - \langle \xi \rangle^2 . \quad (2.10)$$

For homogeneous random processes, there is also an analogous property to ergodicity that allows ensemble properties to be measured by spatial averaging.⁵ Thus, the ensemble covariance for a separation \mathbf{r} can be measured by averaging measurements that are spatially separated by \mathbf{r} . There is still a further simplification that occurs for homogeneous processes that are also spatially isotropic, that is, have invariance properties under rotations. For such processes, the ensemble properties of the fluctuations do not depend on direction and thus the dependence is on r only, the magnitude of \mathbf{r} : $B_\xi(\mathbf{r}) = B_\xi(r)$. For this kind of process, the ensemble properties can be readily estimated by spatial averaging.

These assumptions of stationarity, homogeneity, and isotropism of course are not likely to be strictly true in the physical world, and this is especially true in turbulence modeling. They are utilized assuming they are approximately true. For example, the atmosphere could never be treated strictly as homogeneous and isotropic, but over some limited volume and time, these properties are reasonable. The key to the validity of these assumptions is in terms of local behavior.

There are spectral representations for the homogeneous and isotropic cases. For a homogeneous process, the power spectrum $\Phi(\mathbf{K})$ is simply a three-dimensional Fourier transform of the covariance:

$$\Phi_\xi(\mathbf{K}) = \left(\frac{1}{2\pi} \right)^3 \iiint_{-\infty}^{\infty} B_\xi(\mathbf{r}) e^{i\mathbf{K}\cdot\mathbf{r}} d\mathbf{r} . \quad (2.11)$$

where \mathbf{K} is the vector wavenumber. The inverse relation is thus

$$B_\xi(\mathbf{r}) = \iiint_{-\infty}^{\infty} \Phi_\xi(\mathbf{K}) e^{-i\mathbf{K}\cdot\mathbf{r}} d\mathbf{K} . \quad (2.12)$$

Since both the covariance and the spectrum are real, even functions, these can be written as cosine transforms:

$$\Phi_\xi(\mathbf{K}) = \left(\frac{1}{2\pi}\right)^3 \iiint_{-\infty}^{\infty} B_\xi(\mathbf{r}) \cos(\mathbf{K} \cdot \mathbf{r}) d\mathbf{r} , \quad (2.13)$$

$$B_\xi(\mathbf{r}) = \iiint_{-\infty}^{\infty} \Phi_\xi(\mathbf{K}) \cos(\mathbf{K} \cdot \mathbf{r}) d\mathbf{K} . \quad (2.14)$$

If the process is also isotropic, then Φ_ξ depends only on the magnitude of \mathbf{K} , and thus, by integrating out the angular spherical coordinates, we get

$$B_\xi(r) = (4\pi/r) \int_0^{\infty} K \Phi_\xi(K) \sin(Kr) dK , \quad (2.15)$$

$$\Phi_\xi(K) = \frac{1}{2\pi^2 K} \int_0^{\infty} B_\xi(r) \sin(Kr) r dr . \quad (2.16)$$

In some instances we are interested in the covariance of a spatial random process along a single axis. This situation often arises in measurements. Thus, we are sometimes interested in the one-dimensional spectrum, denoted by $P_\xi(K)$, of three-dimensional fluctuations. This relation is⁶

$$\Phi_\xi(K) = -\frac{1}{2\pi K} \frac{dP_\xi(K)}{dK} . \quad (2.17)$$

As an example of this relation, a one-dimensional spectrum that has a $K^{-5/3}$ dependence will behave as $K^{-11/3}$ in three dimensions.

It will often occur in the analysis of propagation problems that we are interested in the spectrum of the fluctuations in a plane perpendicular to the direction of propagation. Thus, we shall consider the two-dimensional spectrum in the x - y plane with propagation in the z direction. Let $F_\xi(K_1, K_2, z)$ be the spectrum of the homogeneous fluctuations between planes separated by z . Then F_ξ is readily obtained from Φ_ξ by integrating over the K_3 dependence:

$$F_\xi(K_1, K_2, z) = \int_{-\infty}^{\infty} \Phi_\xi(K_1, K_2, K_3) \cos(K_3 z) dK_3 . \quad (2.18)$$

If the fluctuations are homogeneous and isotropic in three dimensions, then they are also homogeneous and isotropic in the plane $z = \text{constant}$. Thus, we can convert to cylindrical spatial variables (ρ, θ, z) and the fluctuations in the $z = \text{constant}$ plane have a spectrum given by $F_\xi(K_1, K_2, 0)$ and a two-dimensional covariance that depends only on ρ , given by⁷

$$B_\xi(\rho) = 2\pi \int_{-\infty}^{\infty} J_0(\mathcal{K}\rho) F_\xi(\mathcal{K}, 0) \mathcal{K} d\mathcal{K} , \quad (2.19)$$

where $\mathcal{K} = [K_1^2 + K_2^2]^{1/2}$ and $J_0(\cdot)$ is a Bessel function of the first kind of zero order.

2.2.3 Structure Functions

The treatment of spatial (or temporal) fluctuations in terms of the covariance and the spectrum depends on the assumptions of homogeneity (or stationarity). Of particular importance is the assumption that the mean is the same over all space (time). This constancy of the mean is clearly not satisfied by atmospheric parameters, for example, wind or temperature. Nor is it always satisfied by optical parameters, such as the phase of a beam at a telescope aperture. In the case of wind, there is a mean that varies in space. In such cases, the fluctuations about the spatially (temporally) varying means may be a homogeneous/isotropic (stationary) process. Thus, the random variable $\xi(\mathbf{r})$ may be decomposed into a mean and a fluctuating part:

$$\xi(\mathbf{r}) = \langle \xi(\mathbf{r}) \rangle + \xi'(\mathbf{r}), \quad (2.20)$$

where the fluctuations ξ' satisfy $\langle \xi'(\mathbf{r}) \rangle = 0$ for all \mathbf{r} . Random processes that allow such a decomposition into a varying mean and stationary fluctuations are referred to as possessing stationary increments in the time domain and the analogous spatial property is referred to as local homogeneity. Of course, all homogeneous (stationary) random processes are locally homogeneous (have stationary increments). The theoretical framework of the previous section may be applied to the homogeneous fluctuations ξ' . However, it is not always advantageous to do so. Measurements and effects of such processes almost always include the spatially varying mean, and in some cases, mean square differences are the relevant and measurable quantity, such as the phase difference between two aperture points. The utilization of structure functions provides a framework for the treatment of random processes with slowly varying means. The structure function of ξ is defined as

$$D_\xi(\mathbf{r}_1, \mathbf{r}_2) = \langle [\xi(\mathbf{r}_1) - \xi(\mathbf{r}_2)]^2 \rangle. \quad (2.21)$$

If the decomposition into mean and fluctuations is substituted, we get

$$D_\xi(\mathbf{r}_1, \mathbf{r}_2) = [\langle \xi(\mathbf{r}_1) \rangle - \langle \xi(\mathbf{r}_2) \rangle]^2 + \langle [\xi'(\mathbf{r}_1) - \xi'(\mathbf{r}_2)]^2 \rangle, \quad (2.22)$$

which shows the utility of the structure-function approach: the structure function decomposes into a contribution from the difference in the means and a difference in the fluctuations. Since the means are by definition slowly varying, for separations between \mathbf{r}_1 and \mathbf{r}_2 that are not too large, the term in ξ' dominates the structure function. The extension of the structure function to locally homogeneous and isotropic random processes is straightforward. For any \mathbf{r}_1 , we have

$$D_\xi(r) = \langle [\xi(\mathbf{r}_1) - \xi(\mathbf{r}_1 + \mathbf{r})]^2 \rangle, \quad (2.23)$$

where r is the magnitude of \mathbf{r} . As with covariance functions, there is a generalization of the Wiener-Khinchine theorem giving the spectral representation of D_ξ . For a locally homogeneous random field, the spectrum is related to the structure function by

$$D_\xi(\mathbf{r}) = 2 \iint_{-\infty}^{\infty} \Phi(\mathbf{K}) [1 - \cos(\mathbf{K} \cdot \mathbf{r})] d\mathbf{K} . \quad (2.24)$$

If the fluctuations are also locally isotropic, this can be written as⁷

$$D_\xi(r) = 8\pi \int_0^{\infty} \Phi(K) \left[1 - \frac{\sin(Kr)}{Kr} \right] K^2 dK . \quad (2.25)$$

The value of the structure function approach is also apparent in this spectral representation. The term $\{1 - [\sin(Kr)/Kr]\}$ acts as a high-pass filter, removing the low spatial frequencies $K < r^{-1}$. In other words, the contribution from scale sizes much larger than the separation is removed in the structure function. Note also that the spectrum of the structure function is allowed to have a singularity at $K = 0$ (of type $K^{-\alpha}$, where $\alpha < 5$).⁶ Due to this singularity, the inverse relation is not as straightforward as for the covariance. For a locally homogeneous isotropic process, the inverse relation is⁷

$$\Phi_\xi(K) = \left(\frac{1}{4\pi^2 K^2} \right) \int_0^{\infty} \frac{\sin(Kr)}{Kr} \frac{d}{dr} \left[r^2 \frac{d}{dr} D_\xi(r) \right] dr . \quad (2.26)$$

For locally homogeneous, isotropic fields, the relation between the spectrum in three dimensions and the one-dimensional spectrum, $P_\xi(K)$, along any axis is exactly the same as for homogeneous fields:

$$\Phi_\xi(K) = -(1/2\pi K) dP_\xi(K)/dK . \quad (2.27)$$

Next, consider the two-dimensional spectrum in the x - y plane with propagation in the z direction. If $F_\xi(K_1, K_2, z)$ is the spectrum of the homogeneous fluctuations between planes separated by z , it is given by

$$F_\xi(K_1, K_2, z) = \int_{-\infty}^{\infty} \Phi_\xi(K_1, K_2, K_3) \cos(K_3 z) dK_3 . \quad (2.28)$$

This relation is again the same for homogeneous, isotropic fields as for those that also satisfy the local property. Using the local isotropy property, it can also be shown that the fluctuations in the $z = \text{constant}$ plane have a spectrum given by $F_\xi(K_1, K_2, 0)$ and a two-dimensional structure function in the cylindrical coordinate ρ that depends only on ρ , given by⁶

$$D_\xi(\rho) = 4\pi \int_0^{\infty} [1 - J_0(\mathcal{K}\rho)] F_\xi(\mathcal{K}, 0) \mathcal{K} d\mathcal{K} , \quad (2.29)$$

where $\mathcal{K} = [K_1^2 + K_2^2]^{1/2}$.

For random fields that are homogeneous and isotropic, we can derive expressions between the covariance and structure functions and their spectra. It is straightforward to show that for such a case

$$D_\xi(r) = 2[B_\xi(0) - B_\xi(r)] . \quad (2.30)$$

Substitution of the spectral expansions for B_ξ yields

$$D_\xi(r) = 2 \int \int_{-\infty}^{\infty} \Phi_\xi(K)[1 - \cos(\mathbf{K} \cdot \mathbf{r})] d\mathbf{r} , \quad (2.31)$$

which is identical to our earlier result. Thus, the spectrum of the covariance is the same as the spectrum corresponding to the structure function. In this case, the structure function spectrum represents only the fluctuations. In the more general case of a field that is homogeneous and isotropic only locally, the spectrum contains a contribution from the spatially varying mean. The spectrum in this case is not necessarily integrable, and thus there is no covariance that can be associated with it.

2.2.4 Kolmogorov Theory of Turbulence

It is significant that Kolmogorov's theory was presented in terms of a set of hypotheses,⁸ which embody considerable physical insight. His theory treated the velocity fluctuations. Kolmogorov assumed that the velocity fluctuations can be represented by a locally homogeneous and isotropic random field for scales less than the largest eddies or the energy source. The treatment in terms of structure functions follows. The central physical concept of Kolmogorov's theory is the description due to Richardson⁹ of a cascade of energy from large-scale sizes to the small. The source of the energy at the large-scale sizes may be convection or wind shear. The energy is dissipated by viscosity at the small-scale sizes. In between, there is a range where inertial forces dominate. Furthermore, in this range the fluctuations are assumed to be spatially homogeneous and isotropic. If ϵ is the energy dissipation rate (units of $\text{m}^2 \text{s}^{-3}$), Kolmogorov showed by dimensional arguments that in this inertial range, the longitudinal structure function of wind velocity satisfies the famous $2/3$ power law:

$$D_{rr}(r) = C_v^2 r^{2/3} , \quad l_0 < r < L_0 , \quad (2.32)$$

where the longitudinal velocity component is that parallel to the vector \mathbf{r} connecting the two observation points. The constant C_v^2 is known as the velocity structure constant, which Kolmogorov defined to be given by

$$C_v^2 = a \epsilon^{2/3} = 2 \epsilon^{2/3} , \quad (2.33)$$

where a is a dimensionless constant whose value has been determined from measurements.^{10,11} The domain of validity of the $2/3$ structure function law is the so-called inertial range, defined by the inner scale l_0 and the outer scale L_0 . The inner scale l_0 is the small-scale size at which viscosity effects become dominant and the energy is dissipated into heat. For velocity fluctuations, the inner scale is often equated to the Kolmogorov microscale, given by¹²

$$l_0 = (\nu^3/\epsilon)^{1/4} , \quad (2.34)$$

where ν is the kinematic viscosity (units of $\text{m}^2 \text{ s}^{-1}$). The inner scale ranges from a few millimeters near the surface to centimeters or more in the troposphere and stratosphere. Note that l_0 increases with kinematic viscosity, which increases with altitude. The inverse dependence on the energy dissipation rate shows that strong turbulence has small inner scales and weak turbulence larger inner scales.

The outer scale L_0 is regarded as (1) the largest scale size where local homogeneity and isotropy are reasonable, (2) the scale size of the energy source, or (3) the dimension of the flow as a whole. In the theory presented by Tatarski,^{6,13} this vagueness arises partly out of the heavy use of dimensional arguments, where factors of order unity are used throughout. It has become customary to define the outer scale by the limits of the $2/3$ power law. Representative values of L_0 are from tens to a few hundred meters. Near the surface, L_0 scales with height above ground according to⁶ $L_0 = 0.4h$. This can produce values of the order of hundreds of meters in the atmospheric or planetary boundary layer, that is, the region (typically the first kilometer) where frictional forces and heat exchange with the surface dominate. In the free atmosphere, the outer scale is typically of the order of tens of meters^{14,15} but can reach values of hundreds of meters in large, strong layers. L_0 can be shown to scale with $\epsilon^{1/2}$, so the outer scale increases with the strength of turbulence. Thus, the inertial range broadens at both ends in strong turbulence; l_0 decreases and L_0 increases.

The behavior of the structure function at small-scale sizes (i.e., $r < l_0$) can be easily inferred. From the definition of a structure function, we can show by a Taylor series expansion applied to small r that the structure function behaves as r^2 . The two domains and power laws are reconciled by choosing the constant such that the two power laws agree at l_0 . This gives⁶ the relation

$$D_{rr}(r) = C_b^2 l_0^{4/3} r^2 , \quad r < l_0 . \quad (2.35)$$

Tatarski⁶ uses this definition to consistently define l_0 so that the two power laws agree at $r = l_0$. He gives

$$l_0 = 12.8(\nu^3/\epsilon)^{1/4} . \quad (2.36)$$

In Fig. 2.1, the behavior of the structure function is shown. For values of separation r larger than L_0 , no general behavior can be predicted in most cases since the structure function depends on anisotropic eddies and the theory breaks down. Tatarski⁶ states that the growth of the structure function in general slows down in the region $r > L_0$. However, if the random field were strictly homogeneous and isotropic, then for large r the structure function would asymptotically approach the value of $2\sigma^2$, where σ^2 is the variance of the fluctuations. This latter case is schematically shown in the figure.

The $2/3$ structure function can be shown to be equivalent to the power spectrum in three dimensions:

$$\Phi_{rr}(K) = 0.033C_v^2 K^{-11/3} , \quad (2.37)$$

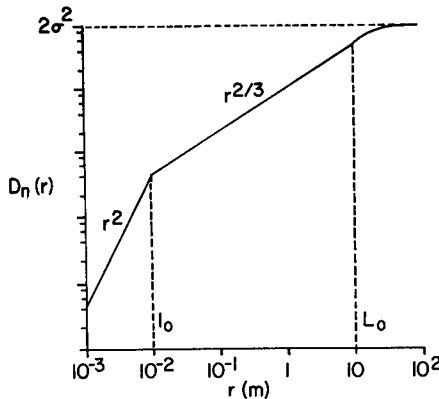


Fig. 2.1 Structure function showing r^2 and $r^{2/3}$ domains. For $r > L_0$, the solid line suggests the asymptotic approach to $2\sigma^2$ for strictly homogeneous and isotropic turbulence.

where the range of validity is limited by the inertial range wavenumbers, $2\pi/L_0$ to $2\pi/l_0$. The one-dimensional spectrum corresponding to the $\frac{2}{3}$ structure function is thus

$$P_{rr}(K) = 0.125C_v^2 K^{-5/3} . \quad (2.38)$$

The coefficient of 0.125 applies to the one-dimensional spectrum defined for K in the range $(-\infty, \infty)$. If the domain of K is restricted to only the positive frequencies, then we can define a different form, $S_{rr}(K)$. Since the spectrum is an even function, it is clear that $S_{rr}(K) = 2\Phi_{rr}(K)$ for $K > 0$. Then, we get the form and coefficient usually seen in the literature:

$$S_{rr}(K) = 0.25C_v^2 K^{-5/3} . \quad (2.39)$$

The validity of Kolmogorov's power laws for the structure function or the spectrum has been established in a wide range of experiments. Indeed, the Kolmogorov theory has achieved "an embarrassment of success,"¹⁶ in that spectra having a $-5/3$ power law have been found in turbulence fields where there is reason to question homogeneity or isotropy.

2.2.5 Conservative Passive Scalars

The fundamental characterization of turbulence is in terms of the velocity fluctuations. Turbulence effects arise because of the turbulent mixing of atmospheric parameters, such as temperature, water vapor, and the index of refraction. These quantities are passive since their dynamics do not affect the turbulence. The usual characterization of temperature and water vapor in terms of degrees Kelvin and relative humidity, respectively, is not in terms of conservative quantities. Thus, a parcel of air at temperature T when displaced vertically by an eddy assumes a new temperature T' . This is because the parcel expands and cools adiabatically as it rises. However, we may characterize the parcel by the potential temperature θ given by¹⁷

$$\theta(z) = T(z)[P_0/P(z)]^\alpha , \quad (2.40)$$

where the units of T are kelvins, the pressure P is in mb, P_0 is the reference pressure of 1000 mbar, and the exponent α is 0.286 for air. This is the definition in widespread use in the meteorological community, which defines the potential temperature as the temperature a parcel of air at temperature T and pressure P would have if it were expanded or compressed adiabatically to a pressure of 1000 mb. The potential temperature is a property of a parcel of air that is unchanged under adiabatic displacements and is a conservative quantity. Turbulence mixing of air is an adiabatic process¹⁸ in that the parcel of air being swirled about by an eddy does not have time to gain or lose heat. Another definition of potential temperature, used by Tatarski,⁶ is in widespread use in optical propagation studies:

$$\theta'(z) = T(z) + \Gamma z , \quad (2.41)$$

where Γ is the adiabatic lapse rate given by 9.8 K/km. In θ , the definition is made with regard to a fixed reference defined by pressure, whereas in θ' the definition is relative. The difference in the definitions for calculating changes in potential temperature is not significant for pressures near the reference of 1000 mbar. Note that θ is the appropriate definition for calculating profiles of potential temperature or Brunt-Vaisala frequency. In a similar manner, the specific humidity is the conservative passive representation of humidity used.

The Kolmogorov theory of structure functions was extended by Corrsin and Obhukov to conservative passive scalars. For concreteness, the potential temperature θ will be developed here; however, any conservative passive scalar can be substituted in the equations. Such a scalar can be treated as a locally homogeneous and isotropic random field, and the structure function for θ satisfies the relationships⁶

$$D_\theta(r) = \begin{cases} C_\theta^2 r^{2/3} , & l_0 \leq r < L_0 , \\ C_\theta^2 l_0^{-4/3} r^2 , & r \leq l_0 . \end{cases} \quad (2.42)$$

$$(2.43)$$

The three-dimensional spectrum is defined in the inertial subrange to be

$$\Phi_\theta(K) = 0.033 C_\theta^2 K^{-11/3} . \quad (2.44)$$

The one-dimensional spectrum is defined as

$$S_\theta(K) = 0.25 C_\theta^2 K^{-5/3} . \quad (2.45)$$

The parameter C_θ^2 is known as the potential temperature structure constant. The dissipation mechanism for potential temperature inhomogeneities is not viscosity, as in the case of velocity fluctuations. Temperature fluctuations are dissipated through molecular diffusion. Thus, the inner scale l_0 is again defined by the equality of the r^2 and $r^{2/3}$ forms of the structure function. The inner scale for temperature fluctuations has been shown¹⁹ to be

$$l_0 = 5.8(D^3/\epsilon)^{1/4} , \quad (2.46)$$

where D is the diffusivity of heat in air. Since the Prandtl number, ν/D , is approximately 0.72 for air, the diffusion scale is larger than the viscous scale. Hill and Clifford¹⁹ have shown that this gives rise to a bump in the spectrum at small scales that can be important in optical problems. They also point out that this problem arises not just for temperature, but also in a wide range of cases where structure functions and the inertial range are defined. However, this is a subtle distinction, and in this treatment we use the inner scale for velocity.

Despite the fact that it is not a conservative quantity, the temperature structure constant is used extensively in the literature. This arises because it is the straightforward quantity to measure.²⁰ In the usual experimental case, the structure function is measured over a horizontal distance. In such a situation, the distinction between temperature and potential temperature need not be made. In a horizontal plane, the temperature can be treated as locally homogeneous and isotropic and possesses a $\frac{2}{3}$ power-structure function and a $-\frac{5}{3}$ power spectrum (one dimensional). In three dimensions, temperature can still be treated as locally homogeneous and isotropic, but only over a smaller vertical scale than potential temperature. This can be readily seen from the Tatarski form of potential temperature.

2.2.6 Index of Refraction

The index of refraction n for the atmosphere can be written for optical and infrared wavelengths as²¹

$$n - 1 = a_d(\lambda)P_d/T + a_w(\lambda)P_w/T , \quad (2.47)$$

where $a_d(\lambda)$ and P_d are the wavelength-dependence function and partial pressure of the dry air (in mbar), $a_w(\lambda)$ and P_w are those for the water vapor, and the temperature is in kelvins. The wavelength dependence is, for λ in micrometers,

$$\begin{aligned} a_d(\lambda) = & [2371.34 + 68393.7/(130 - \lambda^{-2}) \\ & + 4547.3/(38.9 - \lambda^{-2})] \times 10^{-8} , \end{aligned} \quad (2.48)$$

$$a_w(\lambda) = (6487.31 + 58.08/\lambda^2 - 0.71150/\lambda^4 + 0.08851/\lambda^6) \times 10^{-8} . \quad (2.49)$$

The dry-air term applies in the range 0.23 to 20 μm , while the water-vapor term is limited to the visible, 0.36 to 0.64 μm . These are the two dominant terms; the contributions from other atmospheric constituents, such as CO_2 , are negligible in comparison. The refractive index can be written in terms of the conservative passive scalars, potential temperature θ , and specific humidity q , where q is defined by⁶

$$q = P_w/1.62P , \quad (2.50)$$

where $P = P_d + P_w$. Note that the form of the water-vapor contribution differs from that of Tatarski,⁶ who uses a form suitable for microwaves. Let $\Delta n =$

$n(\mathbf{r}_1) - n(\mathbf{r}_1 + \mathbf{r})$. For a fixed λ , the differential of n can be formally written in terms of conservative passive variables as

$$\Delta n = (\partial n / \partial \theta) \Delta \theta + (\partial n / \partial q) \Delta q . \quad (2.51)$$

The term in ΔP has been neglected; pressure fluctuations are not important in steady-state turbulence, as they damp out quickly. In this form, it is apparent that n is a passive scalar and is locally homogeneous and isotropic, since its fluctuations are a function of scalars satisfying these properties. However, it is not a conservative quantity, since a parcel of air assumes a different value of refractive index when displaced vertically, owing to the dependence on pressure. Squaring the fluctuation Δn and taking the ensemble average, we get the structure function:

$$D_n(r) = (\partial n / \partial \theta)^2 D_\theta(r) + (\partial n / \partial q)^2 D_q(r) + 2(\partial n / \partial \theta)(\partial n / \partial q) \times \langle [\theta(\mathbf{r}_1) - \theta(\mathbf{r}_1 + \mathbf{r})][q(\mathbf{r}_1) - q(\mathbf{r}_1 + \mathbf{r})] \rangle . \quad (2.52)$$

Here, θ and q have $2/3$ power-structure functions. Furthermore, since the fluctuations in θ and q are locally homogeneous and isotropic, so is their cross-covariance, and the term $\langle [\theta(\mathbf{r}_1) - \theta(\mathbf{r}_1 + \mathbf{r})][q(\mathbf{r}_1) - q(\mathbf{r}_1 + \mathbf{r})] \rangle$ can also be shown to satisfy an $r^{2/3}$ power law²² and this is used to define the structure coefficient $C_{\theta q}$. Thus, the fluctuations in the index of refraction are locally homogeneous and isotropic and the structure function satisfies the relationships

$$D_n(r) = \begin{cases} C_n^2 r^{2/3} , & l_0 \leq r < L_0 , \\ C_n^2 l_0^{-4/3} r^2 , & r \leq l_0 . \end{cases} \quad (2.53)$$

The three-dimensional spectrum is defined in the inertial subrange to be

$$\Phi_n(K) = 0.033 C_n^2 K^{-11/3} . \quad (2.54)$$

The one-dimensional spectrum is defined as

$$S_n(K) = 0.25 C_n^2 K^{-5/3} . \quad (2.55)$$

These equations define the refractive-index structure constant C_n^2 , which is the critical parameter for describing optical turbulence. Indeed, C_n^2 will be used synonymously with optical turbulence. In the above differential form, it is apparent that C_n^2 is a function of the structure constants of q and θ . Specifically,

$$C_n^2 = (\partial n / \partial \theta)^2 C_\theta^2 + (\partial n / \partial q)^2 C_q^2 + 2(\partial n / \partial \theta)(\partial n / \partial q) C_{\theta q} . \quad (2.56)$$

Differentiation of the expression for n in terms of θ and q will yield the specific functional form of the coefficients in this relation. For the vast majority of applications in the atmosphere, the dry-air term dominates. Contributions calculated using the complete expressions represent no more than a factor of two to C_n^2 at best. The humidity effects on C_n^2 through the index of refraction

can be ignored except near a marine surface or saturated soil where a maximum of 20% contribution to C_n^2 can occur. It is interesting to note that when humidity effects are important, it is through the contribution of $C_{\theta g}^2$.²³ Although humidity generally has a negligible direct contribution to C_n^2 , it does however have an important indirect effect on atmospheric C_n^2 through meteorological processes. Thus, for example, the convection and thermal pluming is reduced by the presence of ground moisture since part of the solar energy is diverted from thermal pluming into evaporation.

The dry-air wavelength-dependence function $a_d(\lambda)$ gives a range of values of 82.9×10^{-6} at $0.3 \mu\text{m}$ to 77.5×10^{-6} at $10 \mu\text{m}$. Since C_n^2 in the atmosphere varies by more than an order of magnitude, it is customary in the literature to ignore the wavelength dependence and to simply use the value at $0.5 \mu\text{m}$, which is 79×10^{-6} . Thus, we have

$$n - 1 = 79 \times 10^{-6} P/T , \quad (2.57)$$

and the structure constants are related by

$$C_n^2 = (\partial n / \partial \theta)^2 C_\theta^2 = [79 \times 10^{-6} (P/P_0)^\alpha P/\theta^2]^2 C_\theta^2 = [(n - 1)/\theta]^2 C_\theta^2 . \quad (2.58)$$

In situations where we have locally homogeneous and isotropic temperature fluctuations, it is also easily shown that we can write the relation involving C_T^2 :

$$C_n^2 = (\partial n / \partial T)^2 C_T^2 = (79 \times 10^{-6} P/T^2)^2 C_T^2 = [(n - 1)/T]^2 C_T^2 . \quad (2.59)$$

There are several more useful expressions involving C_n^2 . Tatarski⁶ showed a useful relationship between optical turbulence and the gradients of the means. The fluctuations in the index of refraction are not independent of the gradient of the mean index, but rather are determined by it. This is due to the mixing action of mechanical turbulence. Tatarski quantifies this relationship in the equation

$$C_n^2 = a L_0^{4/3} (\text{grad } n)^2 , \quad (2.60)$$

where a is a constant generally taken to be 2.8²⁴ and where n is the mean, nonfluctuating refractive index. Tatarski refers to this quantity L_0 as the outer scale of turbulence, although this equivalence has been questioned.²⁵ Since the mean gradient of n is primarily in the vertical direction, we can explicitly calculate it by

$$\text{grad } n \approx \partial n / \partial z = (\partial n / \partial \theta)(d\theta / dz) = (79 \times 10^{-6} P/gT) N^2 , \quad (2.61)$$

where $N^2 = (g/\theta)(d\theta/dz)$ is the Brunt-Vaisala frequency¹⁷ and g is the acceleration of gravity. This expression for grad n is sometimes referred to as the potential refractivity. The reason for this name can be seen by combining the results to show

$$C_n^2 = aL_0^{4/3} (79 \times 10^{-6} P/gT)^2 N^4 . \quad (2.62)$$

In this form, the refractive-index structure constant, which gives the strength of the turbulence, is related directly to the Brunt-Vaisala frequency, which gives the strength of the temperature gradients. Note that C_n^2 is nonzero only if there is incomplete mixing; that is, N^2 is nonzero. If the temperature lapse rate is zero, i.e., adiabatic, C_n^2 is also zero. This occurs in strong mechanical turbulence near the ground, where the turbulence produces perfect mixing. Furthermore, this equation also supports the experimental observations of the occurrence of strong optical turbulence at temperature inversions, that is, where the temperature gradients are large. Note that the dependence is on N^4 , so that positive and negative temperature inversions contribute equally.

There are additional forms of the spectrum for the refractive-index fluctuations that are very useful in calculations. The previous expressions, giving the $-11/3$ power law, apply only for wave numbers corresponding to the inertial range. Tatarski¹³ introduced a form of the spectrum that is a reasonable approximation for large wave numbers:

$$\Phi_n(K) = 0.033C_n^2 K^{-11/3} \exp(-K^2/K_m^2) , \quad (2.63)$$

where the constant K_m is related to the inner scale by $K_m = 5.92/l_0$. Note that this Gaussian cutoff is not strictly a transform of the behavior for $r < l_0$, but rather is a convenient form for computations. Since refractive-index fluctuations are essentially temperature fluctuations, the bump in the temperature spectrum¹⁹ also occurs in the refractive-index spectrum and this physical effect is also not modeled by this spectral form. The behavior of the fluctuations for large scales also is treated in an ad hoc manner by the addition of another form. The von Karman²⁶ form of the spectrum is given by

$$\Phi_n(K) = 0.033C_n^2(K^2 + K_0^2)^{-11/6} , \quad (2.64)$$

where K_0 is related to the outer scale by $K_0 = 2\pi/L_0$. This von Karman form is useful in some computations since it avoids the singularity at $K = 0$ that occurs with the $-11/3$ power law. If we combine both of these extensions to the inertial range spectrum, we get the modified von Karman spectrum:

$$\Phi_n(K) = 0.033C_n^2(K^2 + K_0^2)^{-11/6} \exp(-K^2/K_m^2) . \quad (2.65)$$

These different forms of the turbulence spectrum are shown in Fig. 2.2. All of the forms have the correct physical behavior in the inertial range. These forms of the spectrum, however, are used for computational reasons and are not based on physical models. They must be used with caution if the results of the calculations depend strongly on scales outside the inertial range.

2.2.7 Atmospheric Temporal Statistics

The theory presented so far has described turbulence in terms of spatial statistics. In many applications, it is the temporal statistics that are measured

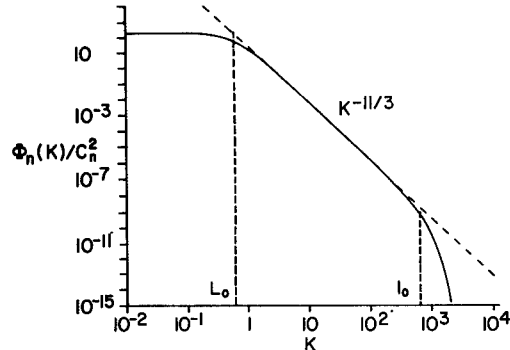


Fig. 2.2 Spectrum of turbulence fluctuations. The inner and outer scales use values of 1 cm and 10 m, respectively, and are shown on the graph. The solid lines denote the extension to the Kolmogorov spectrum given by the modified von Karman form. The dashed line shows the extension of the $K^{-11/3}$ form beyond the inertial range.

and are important. Indeed, the relation between the temporal and spatial statistics is a central issue in measurements of turbulence. It is also important in describing turbulence effects on systems and in specifying the required bandwidth for adaptive optics systems.

The theory presented has explicitly avoided a treatment of a random variable that depends both on spatial variables and temporal variables, that is, a random variable of the form $\xi(\mathbf{r}, t)$. In the case of atmospheric turbulence, there are two time scales of concern. The first time scale is that due to the motion of the atmosphere across the path of interest. This motion is the advection of the turbulence variables. In the framework of fluid dynamics, this motion results from the utilization of an Eulerian reference frame fixed in space. The second time scale results from the dynamics of the turbulence itself, that is, the dynamics of the individual eddies. These are the changes that would be observed in a reference frame moving at the mean flow rate along with the fluid. This is a Lagrangian reference frame.¹² Estimates of these two time scales can be readily made. The first scale, that due to advection, can be estimated as L_0/V_\perp , where L_0 is the outer scale of turbulence and V_\perp is the mean wind speed transverse to the direction of observation. Using nominal values of 10 m for L_0 and 10 m/s for V_\perp , the time scale is thus of the order of 1 s. The second time scale is that arising from the wind fluctuations. These are much smaller than the mean wind speed and can be estimated as 10% of the mean wind speed. This yields a time scale of 10 s. This second time scale is the eddy turnover time and is seen to be much slower than the time scale of the advection. By these arguments, the internal temporal dynamics of the turbulence may be neglected in comparison to the mean flow. This is the essence of the famous Taylor frozen turbulence hypothesis. To be explicit, the internal dynamics of the eddies are neglected and the turbulent eddies are simply treated as frozen in space and advected across the observation path by the mean wind.⁸ In the reference frame moving with the mean flow, a turbulence variable $\xi(\mathbf{r}, t)$ has no time dependence. Translated to a fixed reference frame of the observer, the time dependence is given by

$$\xi(\mathbf{r}, t + \tau) = \xi(\mathbf{r} - \mathbf{V}_\perp \tau, t) \quad (2.66)$$

for any time t . The reasonableness of this hypothesis has been established in a variety of measurements.⁶ The important limitation arises when the transverse wind flow is small, as occurs when the wind is parallel to the observation path. Lawrence and Strohbehn¹⁸ give as the condition for validity of the frozen turbulence assumption that

$$L_0 \gg (\lambda L)^{1/2}, \quad (2.67)$$

where L is the path length. This condition applies even to the case of very low wind speed. This condition implicitly assumes that the propagation is along a homogeneous path, so that L_0 is unambiguously defined. Substitution of nominal values for L_0 (10 m) and optical/IR wavelengths shows that the condition is nearly always satisfied for propagation along reasonable horizontal paths. For inhomogeneous paths such as vertical, the transverse wind speed varies in the vertical direction, as does the outer scale, and the applicability of this criterion is uncertain. Nonetheless, the frozen turbulence hypothesis is in common use. Its limitations must be recognized when interpreting data under conditions with small transverse wind speeds.

Equation (2.66) allows the relationship between spatial and temporal covariance, structure functions, and power spectra to be immediately written down. For the covariance and structure function, the important relation is that $x = V_\perp \tau$; for the power spectrum, the temporal and spatial frequencies are related by $\omega = KV_\perp$. In our notation, the relations for the structure functions and spectra are, for the one-dimensional spatial fluctuations of the parameter ξ ,

$$B_\xi(\tau) = B_\xi(V_\perp \tau), \quad (2.68)$$

$$D_\xi(\tau) = D_\xi(V_\perp \tau), \quad (2.69)$$

where the interpretation of the covariance or structure function as being spatial or temporal is to be understood from the argument. Using the definitions of the spectra [Eq. (2.8)], it is easy to show that the relation between the temporal and spatial one-dimensional spectra is

$$W_\xi(\omega) = (L/V_\perp) P_\xi(\omega/V_\perp). \quad (2.70)$$

The different notation for the spectra makes it clear whether it is the temporal or the spatial spectrum.

2.3 OPTICAL/IR PROPAGATION THROUGH TURBULENCE

2.3.1 Introduction

There are several detailed presentations on propagation through optical turbulence that should be consulted. In particular, the books by Tatarski,^{6,13} Chernov,²⁷ Strohbehn,²⁸ Ishimaru,²⁹ and Goodman³⁰ and the reviews by Law-

rence and Strohbehn,¹⁸ Fante,^{31,32} and Coulman³³ provide more detail than can be provided here. In this section, we sketch the methodology and formulation of the problems and their solution and focus on the presentation of formulas describing the major effects of optical turbulence on the propagation of optical/IR radiation.

2.3.2 Formal Solutions of the Wave Equation

The starting point for describing the propagation through turbulence is, of course, Maxwell's equations. For a monochromatic wave, the following wave equation for the vector electric field \mathbf{E} results:

$$\nabla^2\mathbf{E} + k^2n^2\mathbf{E} + 2\nabla[\mathbf{E} \cdot \nabla \log(n)] = 0 , \quad (2.71)$$

where k is the wave number of the radiation ($2\pi/\lambda$). In this equation, we have implicitly assumed that the time variations of the refractive index are slow compared to the frequency of the radiation. Since the wavelength for optical/IR radiation is much smaller than the smallest scale of turbulence (the inner scale, which ranges from the order of millimeters to centimeters), it can be shown that the third term in the wave equation can be neglected. This term represents polarization effects in the propagation, and thus the approximation implies that there is no depolarization in propagation through turbulence. The neglect of this term allows the above equation to be reduced to the wave equation for a scalar component of the electric field:

$$\nabla^2E + k^2n^2E = 0 . \quad (2.72)$$

Because of the term in n^2 , this is a stochastic equation that cannot be exactly solved, and various approaches have been applied. The most straightforward solution is a perturbation expansion. First, we acknowledge that refractive-index fluctuations n_1 are small and can be written as $n = n_0 + n_1$, where $n_1 \ll n_0$. Second, we assume that $E = E_0 + E_1 + \dots$, where E_0 is the incident field, E_1 is the first-order scattered field, and so on for higher-order terms. The higher-order terms represent multiple scattering. Our approach is to treat single or weak scattering only. Since n_1/n_0 is small, we have

$$\nabla^2E + k_0^2E = -2k_0^2(n_1/n_0)E , \quad (2.73)$$

where $k_0 = n_0k$. To simplify notation, we will drop the subscript on k and will simply write n_1 instead of n_1/n_0 . This equation, in conjunction with the observation that the wavelength is smaller than any of the scale sizes of the turbulence, implies that there is negligible backscattering and that small-angle forward scattering dominates the propagation. In contrast, radar wavelengths are of the same order as the turbulence eddies, and this enables their measurement from backscatter. The perturbation series solution is then straightforward. By grouping terms of zeroth-order and first-order perturbation, we arrive at the equation

$$\nabla^2E_1 + k^2E_1 = -2k^2n_1E_0 . \quad (2.74)$$

The solution of this is formally straightforward utilizing the Green's function for the wave equation. It is

$$E_1(\mathbf{r}) = 2k^2(4\pi)^{-1} \int \frac{\exp(ik|\mathbf{r} - \mathbf{r}'|)}{|\mathbf{r} - \mathbf{r}'|} n_1(r') E_0(\mathbf{r}') d\mathbf{r}' , \quad (2.75)$$

where the integration is over the scattering volume between the source and receiver. Since the turbulence scattering is very weak and in the forward direction, we can make the Fresnel or paraxial approximation to these equations. Specifically, let \mathbf{p} be a vector in the plane transverse to the direction of propagation. Then the term in the exponent can be approximated by

$$|\mathbf{r} - \mathbf{r}'| \approx |z - z'| \{1 + |\mathbf{p} - \mathbf{p}'|^2/[2(z - z')^2]\} , \quad (2.76)$$

and in the denominator we replace $|\mathbf{r} - \mathbf{r}'|$ by $|z - z'|$. Then the integral becomes

$$\begin{aligned} E_1(r) &= k^2(2\pi)^{-1} \int \left\{ \frac{\exp[ik|\mathbf{p} - \mathbf{p}'|^2/(2|z - z'|)]}{|z - z'|} \right\} n_1(r') \\ &\quad \times \exp(ik|z - z'|) E_0(\mathbf{r}') d\mathbf{r}' . \end{aligned} \quad (2.77)$$

The perturbation method presented so far is essentially the Born approximation. Its applicability is determined by the neglect of terms higher than E_1 in the perturbation expansion. Its domain of validity is restricted to very weak turbulence; that is, $E_1 \ll E_0$. Another perturbation method, applied by Tatarski, is the Rytov method, or the method of smooth perturbations. Its assumptions are less restrictive than the Born method and therefore it has a wider range of applicability, although it is still restricted to weak turbulence. The Rytov method begins by writing

$$E = \exp(\psi) = A \exp(iS) , \quad (2.78)$$

where $\psi = \chi + iS$ and so $\chi = \log(A)$. Here, χ is the so-called log amplitude and S is the phase. This approximation is closer to our objectives in determining amplitude and phase distortions due to the turbulence. In the Rytov method, the substitution $\exp(\psi)$ is made into the wave equation, which yields the Riccati equation in ψ :

$$\nabla^2\psi + \nabla\psi \cdot \nabla\psi + k^2n^2 = 0 . \quad (2.79)$$

The essence of the Rytov approximation is to perform a perturbation expansion in ψ . Tatarski⁶ should be consulted for the details. The solution is

$$\psi_1(\mathbf{r}) = k^2[2\pi E_0(\mathbf{r})]^{-1} \int \frac{\exp(ik|\mathbf{r} - \mathbf{r}'|)}{|\mathbf{r} - \mathbf{r}'|} n_1(r') E_0(\mathbf{r}') d\mathbf{r}' . \quad (2.80)$$

This solution can be shown to be equivalent to the Born method. The important result is that the Rytov method, since the perturbation is essentially multi-

plicative [since $E = \exp(\psi_0) \exp(\psi_1)$], is less restrictive than the Born method, requiring only that the changes in the perturbations be small over a scale of a wavelength, rather than simply that the perturbations themselves be small.

There is a third approach developed by Lutomirski and Yura.³⁴ This approach uses an extended Huygens-Fresnel theory. A diffraction-type integral results for the scattered field:

$$E(r) = -ik/(2\pi) \int \frac{\exp(ik|\mathbf{r} - \mathbf{r}'|)}{|\mathbf{r} - \mathbf{r}'|} E_0(\mathbf{r}') \exp[\psi(\mathbf{r}, \mathbf{r}')] d^2 r' . \quad (2.81)$$

Note that this expression gives the total field, which is the sum of incident and scattered fields. In contrast to the previous integrals, which were over volume, this integral is a diffraction-type integral that expresses the scattered field at \mathbf{r} in terms of an integral over a surface. However, the factor ψ has an implied integration along the z axis. If we use the geometric optics approximation, then ψ can be written as an integral along the path from z to z' :

$$\psi(\mathbf{r}, \mathbf{r}') = \psi(z, z') = k \int n_1(\zeta) d\zeta . \quad (2.82)$$

The utility and appeal of the extended Huygens-Fresnel approach is that it allows a linear systems type representation:

$$E(\mathbf{p}) = \int h(\mathbf{p}, \mathbf{p}') E_0(\mathbf{p}') d\mathbf{p}' , \quad (2.83)$$

where $h(\mathbf{p}, \mathbf{p}')$ is the atmospheric propagation impulse response function.

The Fresnel approximation could be utilized in the Lutomirski and Yura and the Rytov solutions as well. All these formal solutions apply to weak scattering. This case includes most of the applications involving propagation from the ground up to space. The specific limitations will be described later. However, when there is propagation through strong turbulence such as through long horizontal paths, other more sophisticated techniques must be applied. The reviews by Strohbehn³⁵ and Fante³² should be consulted for some of these approaches.

2.3.3 Amplitude and Phase Statistics

The key questions to be answered are the effects of the turbulence on amplitude and phase. From the definition of ψ , it is straightforward to show that the perturbation ψ_1 is given by

$$\psi_1 = \psi - \psi_0 \approx E_1/E_0 , \quad (2.84)$$

where the approximation of small perturbation has been used. This equation shows the equivalence of the Rytov and Born integral solutions. Using the Fresnel approximation to the Rytov solution, we get formal solutions for the log amplitude and phase from the real and imaginary parts:

$$\chi_1(r) = k^2 [2\pi E_0(\mathbf{r})]^{-1} \int \frac{\cos[k|\mathbf{p} - \mathbf{p}'|^2/(2|z - z'|)]}{|z - z'|} \\ \times n_1(\mathbf{r}') \exp(ik|z - z'|) E_0(\mathbf{r}') d\mathbf{r}' , \quad (2.85)$$

$$S_1(r) = k^2 [2\pi E_0(\mathbf{r})]^{-1} \int \frac{\sin[k|\mathbf{p} - \mathbf{p}'|^2/(2|z - z'|)]}{|z - z'|} \\ \times n_1(\mathbf{r}') \exp(-ik|z - z'|) E_0(\mathbf{r}') d\mathbf{r}' . \quad (2.86)$$

In the following, the subscript on χ and S will be dropped for simplicity. In this form, it is apparent that the statistics of log amplitude and phase are determined by those of the refractive-index fluctuations. In particular, it follows from the Rytov solution that the means of χ and S are zero since the mean of n_1 is zero. Furthermore, both S and χ are made up of the sum of a very large number of fluctuations in n along the propagation path. Since the fluctuations arising from different eddies are considered independent (as occurs in different layers), the central limit theorem can be invoked to predict that S and χ should be normally distributed. Since $A = \exp(\chi)$ and $I = \exp(2\chi)$, it follows that both amplitude A and intensity I are log-normally distributed. Note that the Born solution, on the other hand, implies that the field E is normally distributed, and as a consequence, the amplitude and intensity would each have Rice-Nakagami distributions.¹⁸ For very low levels of turbulence the distinction between these distributions is small, and for higher levels of turbulence (but still weak) the evidence supports the log normal. It is standard to assume the log-normal distribution applies in weak turbulence, not only because the Rytov solution is less restrictive than the Born, but also because measurements and strong scintillation theory applied to the weak regime support the conclusion.

In determining optical effects of turbulence, it is the second-order statistics that are of most concern. From Eqs. (2.85) and (2.86), it is clear that all statistics of χ and S are determined from those of n_1 in the volume between the source and the receiver. The statistics of χ and S are in a plane, and we are particularly interested in the receiver aperture plane. Even allowing for some variation in the statistics of the fluctuations along the propagation path, it still follows that the statistical homogeneity of the log amplitude and phase in the aperture plane is a consequence of the two-dimensional homogeneity of n_1 along the path.

The covariance, spectrum, and structure function of χ and S in the aperture plane are calculated from the Rytov solutions. These are dependent on the characteristics of the incident wave, for example, plane or spherical wave, or focused or collimated beam. The calculations are lengthy and involve difficult integration. In the general case, the turbulence is allowed to vary in strength along the path (e.g., layers) by parameterizing the spectrum. Thus, we write $\Phi_n(K, z)$ for the turbulence spectrum at position z along the path. In using the Kolmogorov spectrum, this simply allows C_n^2 to vary along the path. To simplify the formulas, let ξ be a parameter that can be either χ or S . For a plane wave given by $E_0(r) = E_0 \exp(ikz)$, the covariance and structure functions for propagation from $z = 0$ to L are

$$B_\zeta(\rho, L) = 4\pi^2 \int_0^L d\eta \int_0^\infty dK K J_0(K\rho) H_\zeta(L - \eta, K) \Phi_n(K, \eta) , \quad (2.87)$$

$$D_\zeta(\rho, L) = 8\pi^2 \int_0^L d\eta \int_0^\infty dK K [1 - J_0(K\rho)] H_\zeta(L - \eta, K) \Phi_n(K, \eta) . \quad (2.88)$$

Comparison of Eq. (2.88) with Eq. (2.29) yields the expression for the two-dimensional spectrum of the fluctuations in χ or S in the plane $z = L$:

$$F_\zeta(K, 0, L) = 2\pi \int_0^L d\eta H_\zeta(L - \eta, K) \Phi_n(K, \eta) . \quad (2.89)$$

The filter functions H_χ and H_S depend on the characteristics of the radiation and, for a plane wave, are given by

$$H_\chi(x, K) = \{k \sin[K^2 x/(2k)]\}^2 , \quad (2.90)$$

$$H_S(x, K) = \{k \cos[K^2 x/(2k)]\}^2 . \quad (2.91)$$

It is sometimes useful in calculations of optical effects to use the wave-structure function. This is defined by

$$D_w(\rho) = D_\chi(\rho) + D_S(\rho) . \quad (2.92)$$

From Eqs. (2.90) and (2.91) the computational advantages of D_w can be seen for a plane wave after substituting Eq. (2.88) into Eq. (2.92):

$$D_w(\rho, L) = 8\pi^2 k^2 \int_0^L d\eta \int_0^\infty dK K [1 - J_0(K\rho)] \Phi_n(K, \eta) . \quad (2.93)$$

This integral can be evaluated for a Kolmogorov spectrum given by $\Phi_n(K, \eta) = 0.033 C_n^2(\eta) K^{-11/3}$. The plane-wave structure function becomes

$$D_w(\rho, L) = 2.91 k^2 \rho^{5/3} \int_0^L C_n^2(\eta) d\eta , \quad \text{for } (\lambda L)^{1/2} < \rho < L_0 , \quad (2.94)$$

$$D_w(\rho, L) = 3.44 k^2 l_0^{-1/3} \rho^2 \int_0^L C_n^2(\eta) d\eta , \quad \text{for } \rho < l_0 .$$

It is instructive to express the covariance, structure function, and spectrum for constant turbulence along the propagation path; i.e., $C_n^2(z) = C_n^2$. The covariance, structure function, and spectrum for a plane wave become⁷

$$B_\chi(\rho, L) = 2\pi^2 k^2 L \int_0^\infty dK K J_0(K\rho) \{1 - [k/(K^2 L)] \sin(K^2 L/k)\} \Phi_n(K) , \quad (2.95)$$

$$B_S(\rho, L) = 2\pi^2 k^2 L \int_0^\infty dK K J_0(K\rho) \{1 + [k/(K^2 L)] \sin(K^2 L/k)\} \Phi_n(K) , \quad (2.96)$$

$$D_X(\rho, L) = 4\pi^2 k^2 L \int_0^\infty dK K [1 - J_0(K\rho)] \\ \times \{1 - [k/(K^2 L)] \sin(K^2 L/k)\} \Phi_n(K), \quad (2.97)$$

$$D_S(\rho, L) = 4\pi^2 k^2 L \int_0^\infty dK K [1 - J_0(K\rho)] \\ \times \{1 + [k/(K^2 L)] \sin(K^2 L/k)\} \Phi_n(K), \quad (2.98)$$

$$F_X(K, 0, L) = \pi k^2 L \{1 - [k/(K^2 L)] \sin(K^2 L/k)\} \Phi_n(K), \quad (2.99)$$

$$F_S(K, 0, L) = \pi k^2 L \{1 + [k/(K^2 L)] \sin(K^2 L/k)\} \Phi_n(K). \quad (2.100)$$

An examination of these equations allows physical insight into propagation through turbulence. In the spectra for log amplitude and phase, the turbulence spectrum is multiplied by a factor that represents the optical transfer function of the atmosphere for propagation from $z = 0$ to L . The difference between log amplitude and phase in the above expressions for covariance, structure function, and spectrum is solely in a sign. In Fig. 2.3, the spectra in Eqs. (2.99) and (2.100) are plotted for a von Karman turbulence spectrum. As can be seen, the phase fluctuations are dominated by the low spatial frequencies. It is these low-frequency components that are responsible for tilt effects, beam wander, and image dancing. Thus, phase fluctuations are very sensitive to large-scale sizes. This makes the measurement of the covariance difficult and motivates the measurement of the structure function instead. Furthermore, the phase covariance is sensitive to outer-scale effects and the form of the spectrum. If

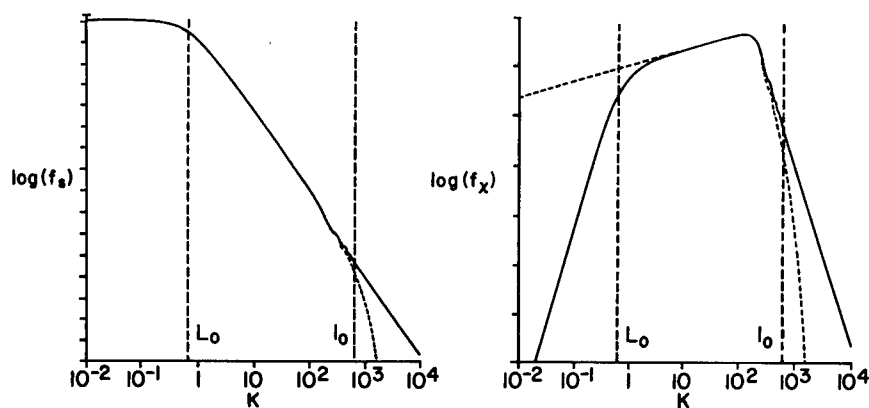


Fig. 2.3 Log amplitude and phase spectra for a plane wave ($\lambda = 0.5 \mu\text{m}$) in homogeneous turbulence ($L = 1 \text{ km}$). The values of inner and outer scale used are 1 cm and 10 m, respectively. The spectra are normalized by C_n^2 and other constants. The solid curves are calculated from the von Karman spectrum, with the dashed curve at large K showing the effect of using the modified von Karman spectrum. In the log-amplitude spectrum graph, the dashed line shows the behavior for $K < L_0$ that results from the use of the $K^{-1/3}$ turbulence spectrum.

the Kolmogorov spectrum is used with its implied infinite outer scale, the phase variance does not exist, as the integral of Eq. (2.96) is infinite. This further motivates the use of phase structure function.

The figure also shows the insensitivity of log-amplitude fluctuations to large-scale sizes. The log-amplitude spectrum goes to zero at $K = 0$. Further, it is seen to reach a peak, and it can be shown that this peak occurs for scale sizes approximately equal to the Fresnel zone scale, $(\lambda L)^{-1/2}$. The consequences of these log-amplitude statistics will be discussed in terms of scintillation. Finally, the different spectral characteristics of χ and S allow the approximation of D_ω to be used instead of D_S for computational simplicity. This approximation is reasonable in those effects that arise primarily from low-frequency phase.

The light from astronomical objects can be treated by the plane-wave case. However, another important case is that of a spherical wave. This applies to point objects within the atmosphere. The spherical wave originating at $z = 0$, $E(r) = r^{-1} \exp(ikr)$, gives

$$D_\omega(\rho, L) = 2.91k^2 \rho^{5/3} \int_0^L C_n^2(\eta) (\eta/L)^{5/3} d\eta . \quad (2.101)$$

The spherical-wave expressions for covariance and structure function are

$$B_\zeta(\rho, L) = 4\pi^2 \int_0^L d\eta \int_0^\infty dK K J_0(K\rho\eta/L) H_\zeta(L - \eta, K, L) \Phi_n(K, \eta) , \quad (2.102)$$

$$D_\zeta(\rho, L) = 8\pi^2 \int_0^L d\eta \int_0^\infty dK K [1 - J_0(K\rho\eta/L)] H_\zeta(L - \eta, K, L) \Phi_n(K, \eta) . \quad (2.103)$$

The spherical-wave filter functions H_χ and H_S are

$$H_\chi(L - x, K, L) = (k \sin\{K^2[x(L - x)]/(2kL)\})^2 , \quad (2.104)$$

$$H_S(L - x, K, L) = (k \cos\{K^2[x(L - x)]/(2kL)\})^2 . \quad (2.105)$$

For a collimated beam, the plane-wave formulas may be used to sufficient approximation in many applications. For a beam wave, starting at $z = 0$ and focused at L , Sasiela³⁶ states that the equations for a plane wave (2.87), (2.88), and (2.89) can be used with the filter functions defined as follows:

$$H_\chi(L - x, K, L) = [(L - x)/L]^{5/3} (k \sin\{K^2xL/[2k(L - x)]\})^2 , \quad (2.106)$$

$$H_S(L - x, K, L) = [(L - x)/L]^{5/3} (k \cos\{K^2xL/[2k(L - x)]\})^2 . \quad (2.107)$$

This representation, valid for a Kolmogorov spectrum, does not include the beam width. The same is true for the approximation of a collimated beam by a plane wave or a diverging beam by a spherical wave. However, the beam width is not important in many applications. The discussion of beam waves with finite widths will follow in a subsequent section.

2.3.4 Scintillation

The fluctuation in received intensity resulting from propagation through turbulence is described as scintillation. The term scintillation is applied to various phenomena, including the temporal variation in received intensity (such as the twinkling of a star) or the spatial variation in received intensity within a receiver aperture. From the definition of log amplitude, it is seen that the statistics of intensity are determined by those of log amplitude. Since there is experimental evidence supporting the log-normal distribution of intensity, it can be shown that if χ is a normal random variable, then

$$\langle I \rangle = \langle \exp(2\chi) \rangle = \exp(2\langle \chi \rangle + 2\sigma_\chi^2). \quad (2.108)$$

Note that in our notation, $\sigma_\chi^2 = B_\chi(0)$. The variance of intensity is a fourth-order moment. For log-normal variables, all statistics are specified in terms of the first- and second-order moments, and thus it can be shown that the normalized intensity variance σ_I^2 is defined by and satisfies

$$\begin{aligned} \sigma_I^2 &= \langle [I - \langle I \rangle]^2 \rangle / \langle I \rangle^2 \\ &= \exp(4\sigma_\chi^2) - 1. \end{aligned} \quad (2.109)$$

This relation is solely a consequence of the normality of χ and the relation between I and χ . For weak turbulence and hence small σ_χ^2 , this can be approximated by

$$\sigma_I^2 \approx 4\sigma_\chi^2. \quad (2.110)$$

Since turbulence does not attenuate the light, conservation of energy requires that the average intensity be the same with or without turbulence. From Eq. (2.108), this is true provided the average of log amplitude satisfies

$$\langle \chi \rangle = -\sigma_\chi^2. \quad (2.111)$$

This is a requirement on the overall fluctuations, that is, the exact solution that includes all order perturbations. As discussed earlier, the Rytov solution implies that $\langle \chi \rangle = 0$. The Rytov solution violates conservation of energy, but it is only a first-order perturbation solution. This contradiction is seldom manifest in weak fluctuation problems within the domain of the Rytov approximation.

The intensity variance is a readily observable quantity and is the important quantity in many applications. From the formulations for the covariance of χ in the previous section, the quantities necessary for the calculation of the intensity variance are at hand. For a plane wave, Eq. (2.87) can be evaluated at $\rho = 0$ and gives, for $l_0 \ll (\lambda L)^{1/2}$,

$$\sigma_\chi^2(L) = 0.56k^{7/6} \int_0^L C_n^2(\eta)(L - \eta)^{5/6} d\eta. \quad (2.112)$$

For a spherical wave, the equation becomes

$$\sigma_\chi^2(L) = 0.56k^{7/6} \int_0^L C_n^2(\eta)(\eta/L)^{5/6}(L - \eta)^{5/6} d\eta. \quad (2.113)$$

In these equations, the source is at $z = 0$ and the observation point is at $z = L$. It can be seen that the scintillation from a spherical wave is less than that from a plane wave, owing to the inclusion of the extra factor $(\eta/L)^{5/6}$ in the integrand. In these forms, it is apparent that the path weighting of C_n^2 for scintillation favors turbulence far from the receiver. Generally speaking, turbulence near the receiver does not contribute to scintillation. For the case of constant C_n^2 along the path, as might approximate a horizontal path, these equations become

$$\begin{aligned}\sigma_x^2(L) &= 0.307k^{7/6}L^{11/6}C_n^2, && \text{plane wave}, \\ \sigma_x^2(L) &= 0.124k^{7/6}L^{11/6}C_n^2, && \text{spherical wave}.\end{aligned}\quad (2.114)$$

The wavelength dependence of this scintillation variance exhibits a general feature of turbulence effects: turbulence effects are greater for shorter wavelengths.

These equations have limited applicability as they stand. The spherical-wave expressions of course assume a point source, but more important, both expressions assume a point receiver. Whether a receiver can be approximated by a point receiver depends on its lateral dimension relative to the lateral dimensions of the intensity fluctuations. The important scale size of scintillation is determined from the log-amplitude covariance. Unfortunately, even for a plane wave in homogeneous turbulence, the resulting expression is quite complex and will not be reproduced here. Lawrence and Strohbehn¹⁸ give a complete expression, and Ishimaru²⁹ gives a slightly different form. The importance of the Fresnel scale, $(\lambda L)^{1/2}$, emerges in these expressions, as does a slight dependence on the inner scale. Clifford⁷ discusses the important features of the covariance for constant C_n^2 . First, the covariance is small in magnitude for ρ greater than the Fresnel length, $(\lambda L)^{1/2}$, and second, the covariance goes to small negative values at greater lengths.

The general behavior of the log-amplitude fluctuations can be inferred from properties of the integrand in the plane-wave spectrum [Eq. (2.89)]. The \sin^2 term in the filter function dominates the shape of the spectrum. It is easy to see that the integrand, and hence the spectrum, has a peak approximately at the first maximum of the sine. Indeed, this peak is approximately given by the Fresnel scale. For scales smaller than the Fresnel scale, the \sin^2 term causes an attenuation of the turbulence spectrum, as seen in Fig. 2.3. For larger scales (or smaller wave numbers), the approach of the \sin^2 term to zero is according to K^4 , which dominates even the Kolmogorov $K^{-11/3}$ singularity. If the Fresnel scale is smaller than the inner scale, the log-amplitude spectrum in the inertial range is attenuated, but now has a maximum at the inner scale; in this case, it is the inner scale and not the Fresnel scale that is the dominant scale size of the fluctuations. However, in some such cases, the existence of the bump in the spectrum¹⁹ near the inner scale may be an important feature. The other extreme situation where the Fresnel scale is larger than the outer scale is analogous; the log-amplitude fluctuations are greatly attenuated since the \sin^2 term filters out fluctuations with scale sizes in the inertial range.

These properties of the log-amplitude covariance and spectrum covariance allow a qualitative explanation of the characteristics of scintillation in weak turbulence where C_n^2 varies along the path. Suppose there is only one narrow

layer of turbulence along the propagation path at a distance z from the source. As can be seen from Eq. (2.112), the intensity fluctuations will increase as the strength of the turbulence, C_n^2 , increases. Second, for constant C_n^2 , the magnitude of the intensity fluctuations will increase as the distance from the layer to the detector, $L - z$, increases. But there is a limit to this increase. From the discussion of the spectrum, it is shown that the eddies of the Fresnel scale size are the dominant contributors to the scintillation. However, note that the Fresnel scale is determined by the distance from the turbulence layer to the detector, $L - z$.^b At a far enough distance, the Fresnel scale is larger than the outer scale, and thus there is negligible contribution to intensity fluctuations from turbulence scales.

Observations of scintillation from stars show the fine-scale structure of the intensity distribution; that is, the intensity tends to get broken up into patches and, from the covariance function, these are also of the size of the Fresnel length. But since the covariance goes negative for separations greater than $[\lambda(L - z)]^{1/2}$, this implies that, on average, points in the observation plane separated by a Fresnel length will be alternately bright and dark. A final qualitative observation is that, from the frozen turbulence hypothesis, these patches move across the aperture according to the wind speed at the distance corresponding to the Fresnel length.

This discussion of the characteristics and scales of scintillation suggests a method for measuring path-resolved C_n^2 . Thus, the strength of the intensity fluctuation determines C_n^2 and the scale size of the fluctuation determines the height of the turbulence. This concept is the principle behind the stellar scintillometer³⁷ for profiling C_n^2 and the horizontal scintillometer³⁸ for measuring path-averaged C_n^2 . In addition, the technique also has been applied to the remote sensing of winds.³⁹

Equations (2.112) and (2.113) predict that the variance of log amplitude is a linear function of C_n^2 . This was derived under the Rytov approximation and is true only for weak turbulence. Figure 2.4 shows the experimental behavior of the intensity variance. In agreement with the Rytov theory, the variance increases linearly with C_n^2 only for low levels of turbulence. For higher levels, the experimental variance approaches a constant and indeed decreases slightly for still higher levels of turbulence. This behavior has been confirmed in many measurements⁴⁰ and is known as the saturation of scintillations. Physically, saturation occurs when the fluctuations in intensity become so large that the intensity fluctuates to zero much of the time.

As a result of saturation, the limits of applicability of the Rytov solution are usually stated in terms of a σ_x^2 criterion. The Rytov theory is regarded as applicable for log-amplitude fluctuations provided $\sigma_x^2 < 0.3$. However, experimental evidence suggests that the Rytov solution for phase fluctuations is applicable to higher levels of turbulence, so that the phase solution may still be accurate even though the log-amplitude solution is not. The failure of the Rytov solution is rooted in the fact that it does not accurately account for the multiple scattering effects that occur in strong turbulence, nor does it account for the progressive loss of coherence as the wave propagates through strong

^bThe turbulence layer is located at z . For a source at $z = 0$ and receiver at $z = L$, the relevant plane-wave Fresnel scale is given by $[\lambda(L - z)]^{1/2}$. For a source at $z = L$ and receiver at $z = 0$, it is given by $(\lambda z)^{1/2}$.

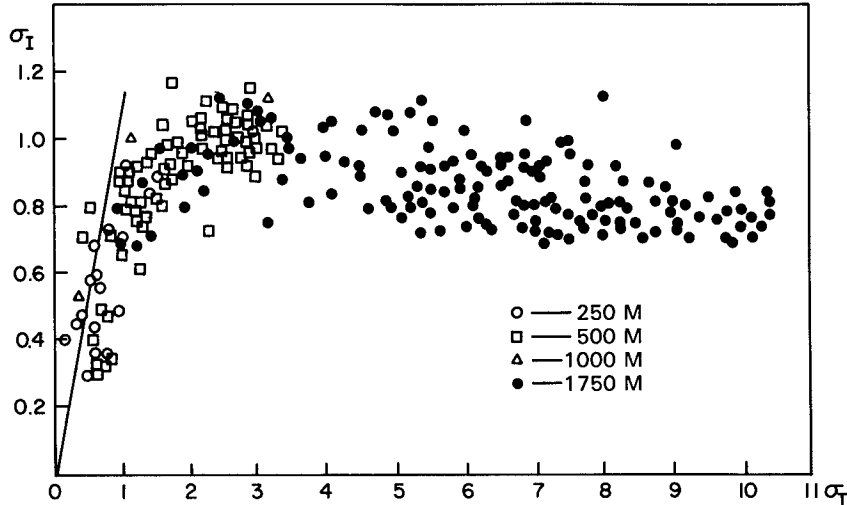


Fig. 2.4 Measurements showing the saturation of scintillations. The ordinate corresponds to the measured values of log-amplitude variance, while the abscissa corresponds to those calculated according to the Rytov theory. The measurements were performed for various path lengths. (Adapted from Ref. 93, © 1968 IEEE)

turbulence. This limitation has motivated the extension of the theory to the strong fluctuation regime.^{35,32} The formulation of intensity fluctuations in the strong-turbulence regime is also approached as a problem of a fourth-order moment. In addition, there are limitations that arise in the beam case, which will be discussed later. Note that the normality of the log amplitude and consequent log normality of intensity are clearly specified by the Rytov theory. Experimental data indicate the failure of log normality for fluctuations in moderate turbulence, and the family of K distributions has been the subject of much work.⁴¹

The description of scintillation effects in weak turbulence has been confined to point detectors. A detector can be treated as a point detector if its aperture is small relative to the Fresnel length for the dominant turbulence or relative to the inner scale. For larger apertures, an averaging of scintillations occurs and the intensity variance is reduced. Since the covariance scale of the fluctuations is the Fresnel scale, an aperture larger than the Fresnel scale will average over several intensity patches and thus the fluctuations will be reduced. In the discussion of the scintillation at an aperture, it is the total aperture intensity or log amplitude that is considered, defined as the integral over the aperture. Fried⁴² has shown that the intensity variance measured by an aperture of diameter D can be written as

$$\sigma_x^2(L) = 2\pi(\pi D^2/4)^{-2} \int_0^D \rho B_x(\rho, L) \text{MCF}(\rho) d\rho , \quad (2.115)$$

where $\text{MCF}(\rho)$ is the aperture mutual coherence function. For a circular aperture, this is

$$\text{MCF}(\rho) = (2/\pi) \{ \cos^{-1}(\rho/D) - (\rho/D)[1 - (\rho/D)^2]^{1/2} \}, \quad \text{for } \rho \leq D , \quad (2.116)$$

and where the MCF is 0 for $\rho > D$. It can be shown that this MCF has a transfer or filter function

$$H(K) = [2J_1(KD/2)/(KD/2)]^2 . \quad (2.117)$$

Simply stated, the effect of an aperture is to spatially filter the log-amplitude spectrum. The effect of aperture averaging can be included in our plane-wave formalism by making the following substitution for the filter function:

$$H_x(L - \eta, K) \rightarrow H_x(L - \eta, K)[2J_1(KD/2)/(KD/2)]^2 , \quad (2.118)$$

Substitution into Eq. (2.89) for a plane wave yields an expression that can be written as

$$\sigma_x^2(L) = 16\pi^2 \int_0^L d\eta \int_0^\infty dK K H_x(L - \eta, K) [J_1(KD/2)/(KD/2)]^2 \Phi_n(K, \eta) , \quad (2.119)$$

which yields the log-amplitude spectrum as

$$F_x(K, L) = 8\pi [J_1(KD/2)/(KD/2)]^2 \int_0^L d\eta H_x(L - \eta, K) \Phi_n(K, \eta) . \quad (2.120)$$

These expressions show that the aperture acts as a low-pass filter. The evaluation of this integral for the variance is difficult and has been done numerically for constant turbulence.⁴² The qualitative features of the aperture averaging can be understood from the scale characteristics of scintillation. This filtering in the frequency domain is equivalent to the filtering out of various small-scale sizes. Since small-scale scintillation comes from near the aperture, the aperture filters out the scintillation arising from turbulence nearer to the aperture and changes the path weighting of the variance from $(L - z)^{5/6}$. If the aperture is larger than the outer scale of the turbulent layers at all altitudes, the filtering will almost eliminate all scintillation.

There is a completely analogous procedure for a spherical wave. The receiver aperture averaging filter function for a point source at $z = 0$ is given by

$$H(K, L) = \{2J_1[KD\eta/(2L)]/[KD\eta/(2L)]\}^2 . \quad (2.121)$$

This filter function is then included in the formalism by making the analogous substitution as for the plane-wave case. The spherical-wave filter function becomes

$$H_x(L - \eta, K) \rightarrow H_x(L - \eta, K, L) \{2J_1[KD\eta/(2L)]/[KD\eta/(2L)]\}^2 . \quad (2.122)$$

A similar approach is used to treat the scintillation from an extended source, such as a planet. For an extended source that consists of multiple, independent radiators, it is expected that scintillation will be reduced, owing to an averaging of the scintillation from the independent sources. For a source of diameter a , located at $z = 0$ and observed at $z = L$, the appropriate filter function is

$$H(K) = \{2J_1[Ka(L - \eta)/2]/[Ka(L - \eta)/2]\}^2 . \quad (2.123)$$

We again make the substitution in our formalism, only this time the filter arising from the source has a path dependence

$$H_x(L - \eta, K) \rightarrow H_x(L - \eta, K)(2[J_1[Ka(L - \eta)/2]/[Ka(L - \eta)/2]]^2 . \quad (2.124)$$

Performing this substitution into Eq. (2.87) for the plane-wave covariance results in a useful form:

$$\begin{aligned} \sigma_x^2(L) &= 16\pi^2 \int_0^L d\eta \int_0^\infty dK KH_x(L - \eta, K) \\ &\times (\{J_1[Ka(L - \eta)/2]/[Ka(L - \eta)/2]\}^2 \Phi_n(K, \eta)) , \end{aligned} \quad (2.125)$$

which gives the log-amplitude spectrum including the finite-source effect:

$$\begin{aligned} F_x(K, 0, L) &= 8\pi \int_0^L d\eta H_x(L - \eta, K) \\ &\times (\{J_1[Ka(L - \eta)/2]/[Ka(L - \eta)/2]\}^2 \Phi_n(K, \eta)) . \end{aligned} \quad (2.126)$$

Again, this form shows the filtering performed by the spatial extent of the source. Note that the low-pass filtering is altitude dependent. This treatment of extended sources applies to the case where the size of the source is such that the anisoplanatic effects can be neglected.

The spherical-wave expression for the source averaging effect is given by the filter

$$H(K) = \{2J_1[Ka(L - \eta)/(2L)]/[Ka(L - \eta)/(2L)]\}^2 , \quad (2.127)$$

and the analogous filter substitution is made into the spherical-wave covariance, structure function, and spectrum.

If we have both aperture averaging and an extended source, the substitution of the filter function in the covariance equation can be extended. The substitution uses both filter functions. The emphasis has been on presenting a formalism³⁶ on how such problems are treated. Thus, the filter substitutions can readily be made for spherical waves or for apertures with another transfer function, such as those with central obscurations.

The equations that have been provided apply to those cases where either C_n^2 is known along the propagation path or the zenith angle is zero. For the case where we know or model the C_n^2 profile in the vertical direction, a correction with zenith angle must be applied. This correction simply scales the optical path. If ϕ is the angle from zenith, it is easy to show that the correct altitude scaling is achieved by multiplying the path variables by $\sec(\phi)$ in Eqs. (2.112) and (2.113), yielding a scaling of σ_x^2 according to $[\sec(\phi)]^{11/6}$ and the following expressions for a plane wave:

$$\sigma_x^2(L) = 0.56k^{7/6}[\sec(\phi)]^{11/6} \int_0^L C_n^2(\eta)(L - \eta)^{5/6} d\eta , \quad (2.128)$$

and for a spherical wave:

$$\sigma_x^2(L) = 0.56k^{7/6}[\sec(\phi)]^{11/6} \int_0^L C_n^2(\eta)(\eta/L)^{5/6}(L - \eta)^{5/6} d\eta . \quad (2.129)$$

For vertical propagation through the entire atmosphere, this scaling in zenith angle is appropriate only up to about 40 deg or less, dependent on the strength of the atmospheric turbulence. At larger angles, the variance of log amplitude becomes larger than the limit imposed by the Rytov approximation, owing to the greater turbulence in the optical path.

2.3.5 Imaging Effects

Turbulence effects on imaging arise primarily from the effects of turbulence on the phase, in contrast to scintillation, which arises from log-amplitude effects. The most common effects are those of image blurring and image dancing. These image-degradation effects are different manifestations of the phase distortions that result from propagation through turbulence.

The approach to image degradation involves the determination of the atmospheric transfer function or point-spread function. This is determined by the image of a point through the atmosphere. It is most convenient to utilize the Lutomirski and Yura solution to the wave equation [Eq. (2.81)]. The instantaneous intensity at a position vector \mathbf{r} in the aperture plane is

$$I(\mathbf{r}) = E(\mathbf{r})E^*(\mathbf{r}) . \quad (2.130)$$

The average of this is, using Eq. (2.81),

$$\begin{aligned} \langle I(\mathbf{r}) \rangle &= k^2/(2\pi)^2 \iint \frac{\exp(ik|\mathbf{r} - \mathbf{r}'|)}{|\mathbf{r} - \mathbf{r}'|} \frac{\exp(-ik|\mathbf{r} - \mathbf{r}''|)}{|\mathbf{r} - \mathbf{r}''|} E_0(\mathbf{r}')E_0^*(\mathbf{r}'') \\ &\times \langle \exp(\psi' + \psi''^*) \rangle d^2r' d^2r'' . \end{aligned} \quad (2.131)$$

This quantity is a form of the mutual coherence function, also known as the mutual intensity function. This function is determined by evaluating the ensemble average $\langle \exp(\psi' + \psi''^*) \rangle$. Indeed, this latter quantity is the atmospheric mutual coherence function in the aperture plane. By using the Fresnel approximation, this equation is simplified and some of the integration can be performed. Since the Rytov solution has justified the normality of ψ , it can be shown⁴³ from properties of log-normal variables that this can be evaluated to yield

$$\langle \exp(\psi' + \psi''^*) \rangle = \exp[-D_w(\rho)/2] , \quad (2.132)$$

where ρ is the radial position magnitude in the aperture plane and D_w is the wave-structure function, defined in Eq. (2.92). But D_w has previously been

evaluated in Eqs. (2.94) for a plane wave and Eq. (2.101) for a spherical wave. If this substitution is made, the result can be written as

$$\text{MCF}(\rho) = \langle \exp(\psi' + \psi''') \rangle = \exp[-(\rho/\rho_0)^{5/3}] . \quad (2.133)$$

In this expression, ρ_0 is called the transverse coherence length, given by

$$\rho_0 = \left[1.46k^2 \int_0^L C_n^2(\eta) d\eta \right]^{-3/5}, \quad \text{plane wave ,} \quad (2.134)$$

$$\rho_0 = \left[1.46k^2 \int_0^L C_n^2(\eta)(\eta/L)^{5/3} d\eta \right]^{-3/5}, \quad \text{spherical wave .} \quad (2.135)$$

In these expressions, the form of the wave structure function applicable to most problems is used. For those problems that require a smaller scale, as for example when $\rho < l_0$, a different form of the transverse coherence length must be used based on the second equation in (2.94).

This formulation of the propagation problem in terms of the atmospheric mutual coherence function has a very important interpretation that clearly shows one of the pronounced effects of propagation through turbulence. For a wave that starts out at a transmitter or other source with some very large spatial coherence, the spatial coherence of the wave front will have been degraded and reduced to ρ_0 after propagation through turbulence. Two points on the wave front separated by a distance greater than ρ_0 will be uncorrelated. This loss of coherence is important in a wide range of applications. Since a collimated laser beam can be approximated by a plane wave, a collimated beam with a spatial coherence length of D (transmitter aperture diameter) at the source will have its coherence length reduced to ρ_0 in its transit through the atmosphere. Since a typical value of ρ_0 is 5 cm for a vertical path at $\lambda = 0.5 \mu\text{m}$, it is clear that this is a very important effect. The variation in coherence length, as well as the result of measurements, is discussed in a subsequent section.

Several aspects of the expression for the coherence length should be emphasized. First, the plane-wave form shows a dependence simply on the integrated optical turbulence, with no path weighting. Since usually the largest values of C_n^2 occur near the ground, these are very important to coherence length. This is especially true for the turbulence at the receiving or transmitting apertures or associated dome structures. Second, the coherence length scales with wavelength according to $\lambda^{6/5}$; ρ_0 increases with wavelength, so the loss of coherence is less in the IR than at visible wavelengths.

The formulation of the mutual coherence function has been in the aperture plane. In most applications, it is more useful to translate these results into the focal plane of the imaging system. This involves the translation of the mutual coherence function in the spatial domain into the modulation transfer function in the spatial frequency domain. The modulation transfer function (MTF) is the magnitude of a system's optical transfer function.³⁰ The customary convention will be followed for spatial frequency; namely, in the focal plane

of a system with focal length f , the spatial frequency will be represented by ν (in units of cycles per unit length) instead of K , as has been our custom. The relation between the two is simply $K = 2\pi\nu$. Following Fried,⁴³ the MTF in the focal plane is given by

$$\text{MTF}(\nu) = \exp[-3.44(\lambda f \nu / r_0)^{5/3}] , \quad (2.136)$$

where r_0 is called the atmospheric coherence length and is related to ρ_0 by $r_0 = 2.1\rho_0$. As with scintillation, r_0 is a function of the zenith angle φ . The complete expressions for Fried's coherence length are

$$r_0 = 2.1 \left[1.46 \sec(\varphi) k^2 \int_0^L C_n^2(\eta) d\eta \right]^{-3/5} , \quad \text{plane wave} , \quad (2.137)$$

$$r_0 = 2.1 \left[1.46 \sec(\varphi) k^2 \int_0^L C_n^2(\eta) (\eta/L)^{5/3} d\eta \right]^{-3/5} , \quad \text{spherical wave} . \quad (2.138)$$

This coherence length r_0 is in more widespread use than ρ_0 . A typical value for r_0 at $\lambda = 0.5 \mu\text{m}$ is 10 cm for a vertical path. The atmospheric coherence length r_0 is one of the most important parameters for characterizing the effects of turbulence on an optical system, ranging from telescopes to lasers. The interpretation of the MTF formulation is straightforward. The net MTF of an optical system looking through the atmosphere is the product of the MTF of the system and the atmospheric turbulence MTF.⁴⁴ Optical turbulence behaves as a low-pass filter on an optical system by filtering out the high spatial frequencies. Thus, sharp edges are lost and even point sources become blurred objects. The $1/e$ point of the MTF can be found and gives, for a plane wave, a cutoff frequency ν_c due to turbulence:

$$\begin{aligned} \nu_c &= r_0/(2.1\lambda f) \\ &= 0.0878 f^{-1} \lambda^{1/5} \sec^{-3/5}(\varphi) \left[\int_0^L C_n^2(\eta) d\eta \right]^{-3/5} . \end{aligned} \quad (2.139)$$

This cutoff frequency has a direct interpretation in terms of resolution. Note that this cutoff frequency depends on wavelength to the $1/5$ power, a very weak dependence. Since the inverse of ν_c is a representation of resolution, this shows that the resolution degradation caused by atmospheric turbulence is only slightly improved at longer wavelengths.

The motivation for the use of r_0 can be seen from Fried's original work. The resolution R of a system can be defined as a volume associated with the transfer function:

$$R = \int \nu \text{MTF}_o(\nu) \text{MTF}(\nu) d\nu , \quad (2.140)$$

where $\text{MTF}_o(\nu)$ is the MTF associated with the system optics (i.e., the MTF without the atmosphere) and $\text{MTF}(\nu)$ is that of the atmosphere. For a circular aperture with diameter D , this integral becomes

$$R = (2D/\lambda)^2 \int_0^1 u[\cos^{-1}(u) - u(1-u^2)^{1/2}] \exp[-3.44(Du/r_0)^{5/3}] du . \quad (2.141)$$

Note the dependence on the ratio of the aperture diameter to r_0 . Fried evaluated this integral numerically and the results are shown in Fig. 2.5. The resolution is seen to increase initially with aperture diameter until the diameter equals the coherence length. For larger apertures, no increase in resolution results. The important deduction is that r_0 imposes a limit on the effective aperture size of a system, provided that no adaptive optics techniques are used to compensate for the turbulence.

The formulation in terms of mutual coherence function and modulation transfer function implicitly assumes long time averages, and hence, long time exposures. Eddies of all sizes are averaged over. Since the phase spectra is dominated by the largest eddies, it follows that the largest eddies are critical for determining the image degradation. The eddies of size comparable to the aperture move across the aperture at a nominal rate of D/V , where V is the wind speed transverse to the propagation. For a 10-cm aperture and 10-m/s wind, this gives a time scale of 0.01 s. Long time averaging is thus determined with respect to the time required to average over several of the largest eddies. The motion of the smallest eddies is estimated using the inner scale. Using a value of 1 cm for inner scale, this yields a time scale of 0.001 s. Times shorter than this value will not average over different eddies and will yield an image that is blurred by the aberrations in the path and not by any averaging over changes in the instantaneous path turbulence. This distinction between long and short time scales is not rigorously defined. It is generally accepted that exposures of the order of 0.01 s or less correspond to the short-exposure case.

A distinction is made when the averaging time is short so that the large eddies, primarily responsible for image motion, are not included in the average. This corresponds to short exposures. The effect of turbulence on images can be considered as two effects: image blurring and image dancing. Image dancing arises from the overall tilt imparted to the wave front primarily by the advection of large eddies, which causes the image to move, or "dance," as the large eddies move across the aperture. For a series of short exposures, a blurred image is seen that moves about the aperture; the blur arises from the small-scale eddies and the dancing from the changes in the tilt from the large eddies.

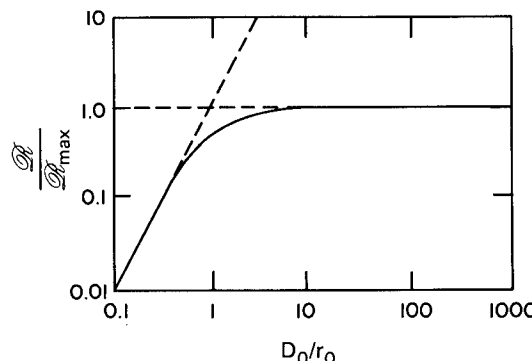


Fig. 2.5 Normalized resolution in long-exposure imaging versus normalized aperture diameter.⁴³ D_0 is the aperture diameter and r_0 is the coherence diameter of the turbulence.

For a long exposure, the resulting blur arises from the superposition of the dancing and the short-term blur and thus includes the effect of all scale sizes.

The approach to treatment of short exposures is to make this distinction in time scales. The formulation considers the "tilt-removed" phase of the wave front. Fried's approach⁴³ performs a least-squares fit of a plane to an incident wave front, defining this as the tilt and performing a subtraction to determine the short exposure MTF. From his analysis, the short-term MTF is

$$\text{MTF}_s(\nu) = \exp\{-3.44(\lambda f\nu/r_0)^{5/3}[1 - b(\lambda f\nu/D)^{1/3}]\}, \quad (2.142)$$

where b is a constant taking the value 1 for near-field propagation and 0.5 for far-field propagation. The distinction between near-field and far-field propagation is that the log-amplitude fluctuations are taken into effect in the far-field case but are negligible in the near-field case. The short-term MTF is given as a correction factor applied to the long-term MTF. Especially noteworthy is the fact that the correction factor depends on the aperture diameter. In this expression, it can be seen that as ν gets larger and approaches $D/f\lambda$, the correction term gets smaller. If $D > r_0$, this effect produces a higher value at large ν for the short-exposure MTF than for the long-term MTF. Thus, higher spatial frequencies are present in the short term than in the long term and superior resolution results.

Closely related conceptually to the short-term MTF are the effects of image dancing and angle of arrival fluctuations. These effects are the short-term manifestations of wave front tilt and the temporal dynamics of the large-scale eddies. Consider two points on the wave front, separated by ρ . A plane wave passing through these two points will be tilted from the normal to the aperture by an amount ϕ satisfying

$$(S_2 - S_1) = k\rho\phi, \quad (2.143)$$

where the approximation $\sin(\phi) \approx \phi$ has been used. The mean-square angle of arrival is therefore given by

$$\langle\phi^2\rangle = D_S(\rho)/(k\rho)^2. \quad (2.144)$$

Using the approximation of $D_S \approx D_w$ and using Eq. (2.94) for a plane wave, this becomes

$$\langle\phi^2\rangle = 2.91\rho^{-1/3}\int_0^L C_n^2(\eta) d\eta. \quad (2.145)$$

It is primarily the larger scales responsible for these angle-of-arrival fluctuations, since phase variations smaller than the aperture are averaged. It is therefore customary to replace ρ with the aperture size D , and this equation becomes

$$\langle\phi^2\rangle = 2.91D^{-1/3}\int_0^L C_n^2(\eta) d\eta. \quad (2.146)$$

The absence of a wavelength dependence in the angle of arrival warrants emphasis. An analogous expression can be written for the spherical-wave case by using Eq. (2.101) for D_w . This formulation of the angle of arrival is one dimensional, i.e., the angular fluctuations relative to a plane containing the axis of propagation. A more rigorous derivation can be made by including the aperture filter function, but at the expense of difficult integrations, and yields the same result. Measurements have verified this expression for angle-of-arrival fluctuations. Values of the order of tens of microradians were measured for path lengths of a few hundred meters. A noteworthy result of these measurements is that this formulation still holds even in the regime where the Rytov approximation breaks down. This is one example of the applicability of the Rytov phase results in a regime where the log-amplitude results are not applicable.

The calculation of image dancing is very similar, except this takes place in the focal plane of the system. Thus, the theoretical approach is the same except for the inclusion of the focal length. Hufnagel⁴⁵ performs a rigorous derivation of the image displacement in the focal plane. The mean-square displacement can be written from the angle-of-arrival result at the aperture by using the simple relation $\delta \approx f\phi$. The expression for the mean-square displacement in the focal plane then follows from Eq. (2.145) for a plane wave:

$$\langle \delta^2 \rangle = 2.91f^2 D^{-1/3} \int_0^L C_n^2(\eta) d\eta . \quad (2.147)$$

The effect of turbulence and its decomposition into short- and long-term effects is essential to the understanding of speckle imaging techniques. A short exposure of an object yields an image that possesses a speckle texture from the turbulence; that is, it is made up of many tiny spots, or speckles, similar to the result from laser scattering from a surface that is rough on the scale of the laser wavelength. The size of the speckles arising from propagation through turbulence can be as small as the diffraction limit of the imaging system. From the discussion of short exposures, it has been shown that short exposures still contain the high spatial frequency information filtered out in long exposures. Speckle imaging is an image reconstruction technique that uses the statistics of short exposures to correct for the turbulence distortion and thereby achieve a resolution in excess of the limitation imposed by the long-exposure MTF. The discussion of this technique, as well as other imaging methods for turbulence compensation, is beyond the scope of this chapter. There are many works in speckle imaging and speckle interferometry that should be consulted.^{30,46–49}

2.3.6 Beam Effects

Much of the treatment of the previous sections on scintillation and imaging can be carried over to laser beam propagation through the atmosphere. This is because a beam wave front, in general, falls somewhere between the plane-wave and spherical-wave cases. Indeed, a collimated beam can be treated as a plane wave in some problems, while a diverging beam may be treated as a spherical wave. The case of a focused beam, however, often requires special

treatment. At the focus, the beam can sometimes be treated as a spherical wave originating from the focal point. However, there are exceptions to this as well, since the turbulence phase distortions in a focused beam can in some cases be sufficient to overwhelm the focusing.

The general beam case can be formulated as follows.^{50,31,29} At the transmitter aperture, the beam is assumed for mathematical simplicity to have a Gaussian amplitude profile. Let W_0 be the beamwidth and f be the wave front radius of curvature at the aperture. Then, the wave is given by

$$E_0(\rho, 0) = \exp\{-\rho^2[W_0^{-2} + ik/(2f)]\}. \quad (2.148)$$

Note that the wave front is radially symmetric at the aperture. The radius of curvature f is positive for a converging beam and negative for a diverging, and f is, in fact, the focal length. A collimated beam corresponds to $f \rightarrow \infty$, and thus the imaginary part of Eq. (2.148) can be dropped. The beamwidth W_0 is the beam radius at the Gaussian $1/e$ points. Since a Gaussian beam has long tails and is an approximation of a beam truncated by an aperture of diameter D , the Gaussian width is related to the aperture diameter by $W_0 = D/\sqrt{2}$. Following Ishimaru,⁵⁰ another notation is convenient. If we define α by

$$\alpha = \alpha_1 + i\alpha_2 = 2/(kW_0^2) + if, \quad (2.149)$$

then we have the notationally simple form

$$E_0(\rho, 0) = \exp(-k\alpha\rho^2/2). \quad (2.150)$$

At an arbitrary point for propagation along z , the wave in free space is

$$E_0(\rho, z) = (1 + i\alpha z)^{-1} \exp[-ikz - \rho^2(k\alpha/2)/(1 + i\alpha z)]. \quad (2.151)$$

It is straightforward to show that the free-space beam size is given by

$$W = W_0[(1 - \alpha^2 z)^2 + (\alpha z)^2]^{1/2}. \quad (2.152)$$

Beam spreading and beam wander are the beam counterparts to image blurring and image dancing. As with imaging, it is customary to make the distinction between the short- and long-term effects. The discussion of the time and spatial scales in imaging carries over to beams. In particular, turbulence scales that are large with respect to the beam size cause tilt and thereby deflect the beam and result in beam wander. The turbulence scales that are small relative to the beam cause the beam broadening. A long-time exposure of a beam would show the superposition of the wander of the broadened beam. The wander is important for beam pointing and tracking considerations, while the short-time broadening is important for pulse propagation problems and high-energy laser systems. The long-term beam radius is denoted by ρ_L . The short-term beam radius is denoted by ρ_s , but the position of the short-term beam centroid is denoted by ρ_c . The variation in the centroid position is the beam wander. The long-term broadening is thus represented by $\langle \rho_L^2 \rangle$, the short-term

broadening by $\langle \rho_s^2 \rangle$, and the wander in the centroid by $\langle \rho_c^2 \rangle$. The relation between these is

$$\langle \rho_L^2 \rangle = \langle \rho_s^2 \rangle + \langle \rho_c^2 \rangle . \quad (2.153)$$

The long-term beamwidth is given by (note $W^2 = 2\langle \rho_L^2 \rangle$)

$$\langle \rho_L^2 \rangle = 4L^2/(kD)^2 + (D/2)^2(1 - L/f)^2 + 4L^2/(k\rho_0)^2 , \quad (2.154)$$

where ρ_0 is the transverse coherence length given by

$$\rho_0 = \left[1.46k^2 \sec(\varphi) \int_0^L C_n^2(\eta)(1 - \eta/L)^{5/3} d\eta \right]^{-3/5} . \quad (2.155)$$

Although the beam propagates from $z = 0$ to L , this is the expression for ρ_0 of a spherical wave propagated from $z = L$ to 0. The long-term beamwidth is given as the sum of the width for the vacuum-propagation case [Eq. (2.152)] and the turbulence broadening. The first term is due to diffraction, the second is due to focusing, and the third is the long-time average beam spreading due to turbulence. For a collimated beam, the second expression is constant. This expression applies to most cases of practical interest (within the domain of weak-fluctuation theory) except very long horizontal or slant paths.

For $\langle \rho_s^2 \rangle$ and $\langle \rho_c^2 \rangle$, there are different solution regimes. For $\rho_0 \ll D < L_0$, the useful expressions are

$$\begin{aligned} \langle \rho_s^2 \rangle &= 4L^2/(kD)^2 + (D/2)^2(1 - L/f)^2 \\ &\quad + 4L^2/(k\rho_0)^2[1 - 0.62(\rho_0/D)^{1/3}]^{6/5} , \end{aligned} \quad (2.156)$$

$$\langle \rho_c^2 \rangle = 2.97L^2/(k^2\rho_0^{5/3}D^{1/3}) . \quad (2.157)$$

It is seen that the beam wander, $\langle \rho_c^2 \rangle$, has no wavelength dependence since $\rho_0^{5/3}$ behaves as k^{-2} . For the case where $\rho_0 \gg D$, which corresponds to a very-small-diameter beam as is used for lidar or communications, $\langle \rho_c^2 \rangle$ is negligible in comparison to $\langle \rho_s^2 \rangle$ or $\langle \rho_L^2 \rangle$. Thus, there is negligible beam wander and the short- and long-term spreading are the same and can be calculated using the above expression for $\langle \rho_L^2 \rangle$. These expressions apply to the weak-turbulence case. For the strong-turbulence case, the beam will be broken up into multiple patches and strong-fluctuation theory must be resorted to.

As with the discussion of dancing, angle of arrival, and tilt in their application to imaging, the concept of beam tilt is closely related to beam wander. The tilt, or angle-of-arrival fluctuations, is in fact equal to $\langle \rho_c^2 \rangle/L$. Sasiela³⁶ has derived expressions for the collimated and focused cases:

$$\langle \rho_c^2 \rangle \approx 6.08L^2D^{-1/3} \int_0^L C_n^2(\eta) d\eta , \quad \text{collimated} , \quad (2.158)$$

$$\langle \rho_c^2 \rangle \approx 6.08L^2 D^{-1/3} \int_0^L C_n^2(\eta) (1 - \eta/L)^{11/3} d\eta , \quad \text{focused .} \quad (2.159)$$

The collimated expression agrees with our previous expression except for a slight disagreement with numerical coefficient and the use of a plane wave ρ_0 instead of Eq. (2.155). The focused form, however, is distinctly different and, because of the altitude weighting, shows a reduction in the wander for a focused beam relative to a collimated beam.

If we neglect the finite beam diameter, the beam waves can be treated as either plane or spherical waves for the calculation of scintillation on the beam axis. For a collimated beam, if the separation ρ is well within the beam so the edge of the beam can be neglected, the plane-wave expressions for spectra, covariance, and structure function can be used and the earlier equations can be directly applied. For a focused wave, the approximations by a plane wave or a spherical wave can be used, depending on the circumstances. Thus, for a beam focused at a point much further than the observation point, the focusing curvature of the beam wave front can be neglected and the beam treated as a collimated beam, and the plane-wave approximations can be used. For calculations near the focal point, the treatment is nearly a spherical wave, provided the width at the focus can also be neglected. The spherical-wave approximation to a focused beam wave involves an inversion of the spatial coordinates for the spherical-wave case, as we have previously seen for ρ_0 in Eq. (2.155).

With regard to scintillation effects, we can immediately write a useful approximation for the fluctuations in the on-axis intensity of a beam, neglecting the beamwidth. The expressions are

$$\sigma_x^2(L) = 0.56k^{7/6} \int_0^L C_n^2(\eta) (L - \eta)^{5/6} d\eta , \quad \text{collimated ,} \quad (2.160)$$

$$\sigma_x^2(L) = 0.56k^{7/6} \int_0^L C_n^2(\eta) (\eta)^{5/6} (1 - \eta/f)^{5/6} d\eta , \quad \text{focused .} \quad (2.161)$$

In the focused-beam case, the expression has been written in a general form where the beam is focused at a point f that may be beyond the observation point L . When $f \gg L$, the focused expression in fact reduces to a collimated expression. This approximation also applies if the focal point is much higher than the atmosphere (i.e., $C_n^2(z) = 0$ for $z > L$), as applies for a target in space.

In those applications where the finite beamwidth must be accounted for, the complexity increases considerably since the characteristics of the beam are not homogeneous in a plane transverse to the propagation direction. The statistics cannot be written in terms of the difference between the coordinates in the plane, but must include their position relative to the beam axis. Thus, the covariance and structure functions are in general written as functions of the two observation points in the plane. These expressions are complex integrals and can be found elsewhere.^{31,18,29} For the case of the variance in log amplitude, it can be written in terms of a single position relative to the beam axis,

$\sigma_x^2(\rho, L)$. This too is a complicated integral,²⁹ and only the results on the beam axis ($\rho = 0$) will be stated. For a general beam as defined previously, the expression is

$$\sigma_x^2(L) = 2.1755 k^{7/6} L^{5/6} \int_0^L C_n^2(\eta) G(\eta) d\eta , \quad (2.162)$$

where

$$G(\eta) = \text{Re}[\gamma(1 - \eta/L)]^{5/6} + [\gamma_i(1 - \eta/L)]^{5/6} , \quad (2.163)$$

$$\gamma = (1 + i\alpha\eta)/(1 + i\alpha L) = \gamma_r - i\gamma_i ,$$

where α is as defined earlier. This expression reduces to expressions similar to plane and spherical waves when the beam is collimated and diverging, respectively. Figure 2.6 shows the predictions of this theory by comparing the predictions to those of a spherical wave. For either long paths through turbulence or small apertures, the log-amplitude variances for both focused and collimated beams are closely approximated by the spherical-wave results. For short paths or large apertures, a collimated beam is approximated by the plane-wave results, while a focused beam is distinctly different. The focused beam is predicted to have significantly reduced scintillation. Ishimaru²⁹ reviewed experimental evidence of the behavior of scintillation by a focused beam and states that there is no experimental confirmation of this predicted scintillation reduction. Rather, data suggest that focused beams behave very similarly to collimated beams. Ishimaru also suggests that this inadequacy of the theory may result from the limitation of the Rytov approximation applied to the scintillation of focused beams, and that a much lower limit in σ_x^2 than 0.3 may be true for the focused case.

This theory has been reviewed for completeness. The best approach for the calculation of the on-axis log-amplitude variance for a focused beam is to use either the plane- or spherical-wave approximation. A further limitation of the approach to on-axis scintillation is that it does not apply to many actual mea-

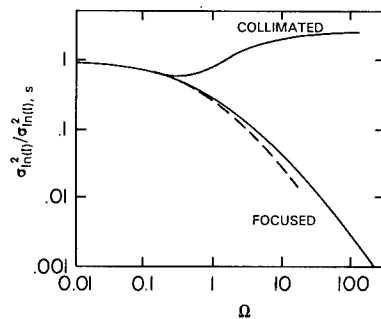


Fig. 2.6 Log-intensity variance for beam waves in homogeneous turbulence. The ordinate is the log-intensity variance normalized by that of a spherical wave. The abscissa is the normalized aperture size given by $\Omega = kW_0^2/(2L)$. (Adapted from Ref. 94)

surement scenarios. A measurement of intensity fluctuation will generally have a contribution from scintillation, but also from the beam motion since the tilt is not removed.

The coherence of a beam can be treated as an extension of the treatment of plane and spherical waves. It is expected that under certain conditions, the plane- and spherical-wave results may be used. The starting point is again the extended Huygens-Fresnel approach in Eq. (2.131). Substitution of the general Gaussian beam expression yields a modulation transfer function of the form³¹

$$\text{MCF}(\rho) = \exp[-(\rho/\rho_b)^{5/3}] , \quad (2.164)$$

where ρ_b is the beam transverse coherence length given by

$$\rho_b = \rho_0 \left\{ \frac{(1-L/f)^2 + [2L/(kD^2)]^2[1+(1/3)(D/\rho_0)^2]}{1-(1/3)L/f+(1/3)(L/f)^2+[4L^2/(3k^2D^4)][1+(D/2\rho_0)^2]} \right\} , \quad (2.165)$$

where ρ_0 is the plane-wave coherence length given in Eq. (2.134). The beam coherence length is written as a correction to the plane-wave coherence arising from diffraction, the finite beam size, and focusing. A limitation of this formulation of the coherence of laser beams is that it is the long-term coherence length. In many cases, it is the coherence over short-time scales, within the wandering beam, that is important. Fante³¹ gives an approximation that derives from the approach in Eq. (2.142) and thus uses the previous equation to define the short-term beam coherence ρ_{bs} by replacing the long-term plane-wave coherence ρ_0 in Eq. (2.165) with the short-time plane-wave coherence ρ_{0s} , defined by

$$\rho_{0s} = \rho_0[1 + 0.37(\rho_0/D)^{1/3}] . \quad (2.166)$$

The average beam intensity at a distance L can be estimated using previous results. Since there is no loss of energy due to propagation through optical turbulence, conservation of energy requires that the total energy in the beam is a constant. The total energy in the beam can be approximated using the on-axis intensity and the beamwidth [Eq. (2.154)], yielding the result

$$\langle I(0,L) \rangle \approx (\pi D^2/4)I_0/\langle \rho_L^2 \rangle . \quad (2.167)$$

This is the long-term average on-axis intensity. The analogous expression for the short term is, using Eq. (2.156),

$$\langle I(0,L) \rangle_s \approx (\pi D^2/4)I_0/\langle \rho_s^2 \rangle . \quad (2.168)$$

Substitution of the expressions for the long- or short-term beamwidth yields the desired expressions. As pointed out by Fante,³¹ these expressions can be used to determine the maximum intensity possible at the beam focus without the use of adaptive optics. For an aperture that is large with respect to ρ_0 , the maximum on-axis intensity can be written as

$$\langle I(0,L) \rangle_{\text{MAX}} \approx P_0 k^2 \rho_0^2 / (4L^2) , \quad (2.169)$$

where $L = f$ and $P_0 = (\pi D^2/4)I_0$ is the power output at the aperture. This equation shows that, for constant power and $D \gg r_0$, increasing the aperture size does not increase the on-axis intensity at the focal point.

2.3.7 Isoplanatism

The previous sections have shown that optical turbulence degrades and limits the performance of imaging and laser beams in the atmosphere. Adaptive techniques have arisen to overcome the turbulence effects and enhance performance. The principle behind one broad area of these methods is to sense the phase distortions from some known source or beacon and apply the conjugate of this phase to the outgoing laser beam or incoming image. A class of problems known as anisoplanatism arises from the difference in turbulence along the beacon path and along the outgoing laser or incoming image. The pioneering work in this area was performed by Fried.⁵¹ The foundation of his approach lies in the isoplanatic angle θ_0 , defined by

$$\theta_0 = [2.91k^2 \sec(\varphi)^{8/3} \int_0^L C_n^2(\eta) \eta^{5/3} d\eta]^{-3/5}, \quad (2.170)$$

where φ is the angle from zenith. Physically, θ_0 defines the maximum angle between the beacon optical path and the outgoing laser beam (or incoming image wave front) for which the two paths may be regarded to possess the same turbulence distortions. In this way, we speak of an isoplanatic patch. If this angle between the beacon and outgoing beam is larger than the isoplanatic angle, the application of the wave-front correction sensed along the beacon path will not completely correct for the turbulence on the outgoing path. A typical value for θ_0 at $\lambda = 0.5 \mu\text{m}$ is $10 \mu\text{rad}$ for a near-vertical ground-to-space path. This concept of isoplanatic angle also has implications for the imaging from extended sources. Thus, if an object being imaged subtends an angle greater than θ_0 at the aperture, the treatment of the propagation as passing through the same optical turbulence breaks down.

The effect of isoplanatism can be formulated in terms of an optical transfer function or modulation transfer function. For a system with perfect adaptive optics and satisfying $D \gg r_0$, the effect of isoplanatism is represented by

$$\text{MTF}_0(\nu, \theta) = \exp[-(\theta/\theta_0)^{5/3}], \quad (2.171)$$

where θ is the angle between the beacon and aim points. This function provides no filtering, just simply an overall reduction in system performance. The isoplanatic angle is seen to be defined as the $1/e$ point of the MTF. This approach has been extended⁵² to include the case where the adaptive optics compensation is bandlimited.

2.4 MEASUREMENTS OF OPTICAL TURBULENCE IN THE ATMOSPHERE

2.4.1 Introduction

In discussing measurements of optical turbulence in the atmosphere, it is convenient to make the distinction between the atmospheric boundary layer

(ABL) and the free atmosphere. The boundary layer is the region where the atmospheric dynamics are dominated by the interaction and heat exchange with the earth's surface. In the free atmosphere, the dynamics are more complicated and turbulence depends on synoptic meteorology, wind shear, and gravity waves.

2.4.2 Atmospheric Boundary Layer

In the daytime, the heating of the surface results in convective instability and gives rise to thermal plumes and strong optical turbulence. The daytime ABL extends to a capping inversion layer, typically 1 or 2 km above the surface.¹⁰ The boundary layer can be further partitioned, into the surface layer, the mixed layer, and the interfacial layer. The surface layer consists of the first few meters above the ground and its properties are determined by the air-to-ground differences in atmospheric parameters. The interfacial layer is the vicinity of the capping inversion that separates the boundary layer from the free atmosphere. The mixed layer consists of the region from the surface layer up to the interfacial layer.

There have been numerous measurements of C_n^2 , or, equivalently, C_T^2 , near the ground. Figure 2.7 shows a sample of such measurements.²⁴ The 15-min average values of C_n^2 are shown for a cloudless day over dry soil at a height of 9 m. The data show the well-established diurnal cycle of C_n^2 , with a well-behaved peak in the daytime, near constant on average at night, and minima near sunrise and sunset. The daytime behavior shows the dominance of convection, rising and falling along with the solar irradiance. The C_n^2 minima occur in association with the neutral events, that is, when the soil and air temperature are the same. This occurs approximately one-and-a-half hours after sunrise and one hour before sunset. During these neutral events, the

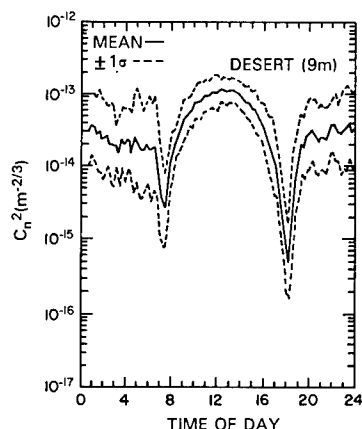


Fig. 2.7 Fifteen-minute average C_n^2 measurements and standard deviations plotted for a 24-h period. The data derive from C_T^2 measurements on a tower 9 m above the desert floor under cloudless conditions.²⁴

relationship between optical turbulence and temperature gradients qualitatively explains these minima in C_n^2 . There is some residual optical turbulence at the neutral events due to mechanical turbulence and incomplete mixing. The behavior of C_n^2 at night is seen from the figure to be much more variable, exhibiting fluctuations about a mean.

In the daytime, optical turbulence is strongest near the ground, typically with C_n^2 of the order of 10^{-13} (units of $m^{-2/3}$), and has been observed to fall from the surface layer with a $-4/3$ exponent altitude dependence. The capping inversion layer is expected to be a region of strong C_n^2 , since it is a region of strong temperature gradients. Figure 2.8 shows a sample daytime profile of C_n^2 along with the temperature profile. These data were measured by a balloon-borne C_T^2 instrument⁵³ during clear summer skies in a desert basin. This profile shows the classic behavior of C_n^2 in the daytime convective boundary layer, that is, an exponential falloff with a large peak in C_n^2 corresponding to the capping inversion. This classic behavior is observed during conditions when convection dominates the boundary layer dynamics. When there are strong winds or clouds or in early morning or late afternoon, optical turbulence profiles deviate from this pattern. Figure 2.9 shows a daytime C_n^2 profile from the same location but during the winter under clear skies and 10- to 20-m/s boundary-layer winds. Note that the profile does not exhibit the classic behavior of Fig. 2.8.

At night, the surface cools by radiation and is colder than the air, and this is usually denoted by the presence of a strong surface temperature inversion. This inversion can range from tens to hundreds of meters thick.⁵⁴ Figure 2.7 shows some of the variability of nighttime data near the surface. The relation of temperature gradients and C_n^2 is further emphasized by the analysis of tower C_n^2 data, which shows an increase of nighttime C_n^2 with wind speed until about 4 m/s where C_n^2 then decreases as wind speed increases further.⁵⁴ The interpretation of these data is in terms of mixing; in strong mechanical turbulence, the temperature gradients necessary for optical turbulence are minimized due to mixing.

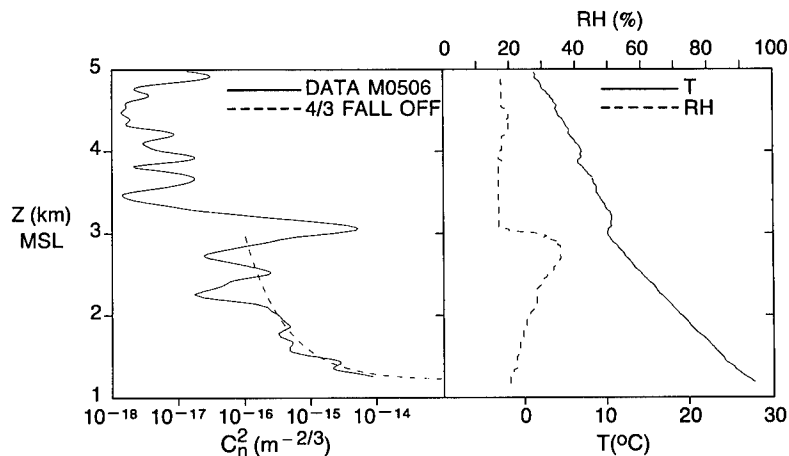


Fig. 2.8 Daytime profile of C_n^2 with concurrent measurements of temperature and relative humidity. Data measured by thermosonde⁵³ on a clear, calm, sunny summer day (1:19 p.m. Mountain Standard Time) in the New Mexico desert.

Although the nocturnal boundary layer is strictly defined by the surface inversion, the region above this to the first few kilometers is a region whose turbulence strength and characteristics are distinct from the free atmosphere. This may arise from orographic effects or from the vestigial daytime boundary layer. Owing to these effects, nocturnal C_n^2 profiles present a wide range of variability. Figure 2.10 shows sample C_n^2 and temperature profiles for nighttime conditions. The strongest values of C_n^2 again occur in conjunction with the sharp temperature gradients of the surface inversion. There is no discernible falloff rate and the most dominant characteristic above the surface is the stratification of the optical turbulence. The presence of a strong layer in association with the vestigial daytime boundary layer inversion warrants emphasis.

For flat terrain, the atmospheric boundary layer is reasonably well defined and identifiable. However, the height of the capping inversion is variable and

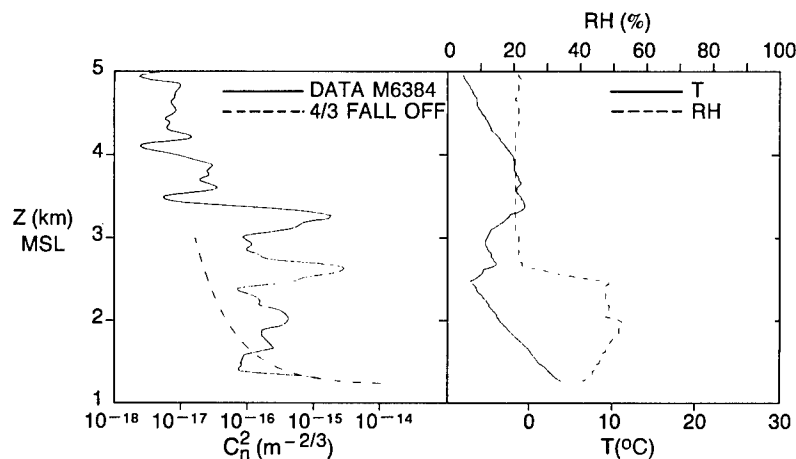


Fig. 2.9 Daytime profile of C_n^2 with concurrent measurements of temperature and relative humidity. Data measured by thermosonde⁵³ on a clear, sunny winter day (9:04 a.m. Mountain Standard Time) in the New Mexico desert.

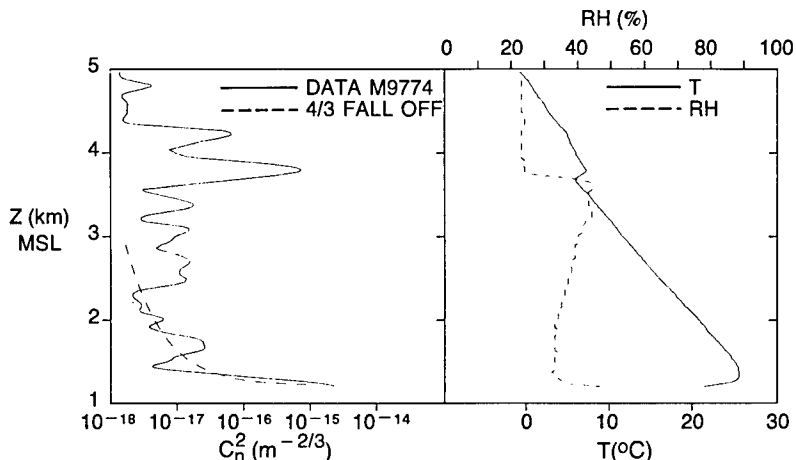


Fig. 2.10 Nighttime profile of C_n^2 with concurrent measurements of temperature and relative humidity. Data measured by thermosonde⁵³ on a clear, calm night (9:00 p.m. Mountain Standard Time) in the New Mexico desert.

depends on a variety of factors, including terrain, solar insolation, vegetation, winds, etc. At one extreme, we have the boundary layer above a desert extending to as much as 3 km above the ground. At the other extreme lies mountaintop locations that in some cases rise above the boundary layer of the surrounding terrain. Such a site is not expected to have a well-developed atmospheric boundary layer. Instead, a mountain location has its own surface layer or boundary layer, depending on whether it more closely resembles a sharp peak or a plateau. The existence of some form of mountaintop boundary layer is to be expected owing to daytime convection, but this convective layer does not extend vertically to kilometer distances. At night, the structure of the boundary layer depends strongly on the winds and local terrain.⁵⁵ On a sharp mountain peak,²⁴ the cool air at the ground rolls off the peak down the mountain, inhibiting the formation of the inversion and, hence, reducing C_n^2 . In Fig. 2.11, a sample optical turbulence profile of the first few kilometers is shown for a mountaintop location at night. The complicated structure of both the C_n^2 and temperature profiles in the first kilometer is evident, especially in comparison to the profile over flat terrain in Fig. 2.10. Since the atmosphere above a mountaintop is extremely variable in terms of winds and meteorology, this profile is to be treated as just a sample. It is shown to dramatize the difference with the flat-terrain case and to emphasize the importance of meteorology and local terrain on turbulence in the first few kilometers above the ground. In particular, the figure is not a sample of the very-low-turbulence conditions that sometimes occur at mountaintop astronomical sites.

The data presented so far have focused on the gross behavior of C_n^2 in the boundary layer, particularly on vertical profiles and on measurements of C_n^2 at a point. An important consideration is the horizontal structure of C_n^2 . This structure is important not only for horizontal propagation, but also for understanding the temporal characteristics of vertical propagation. From the

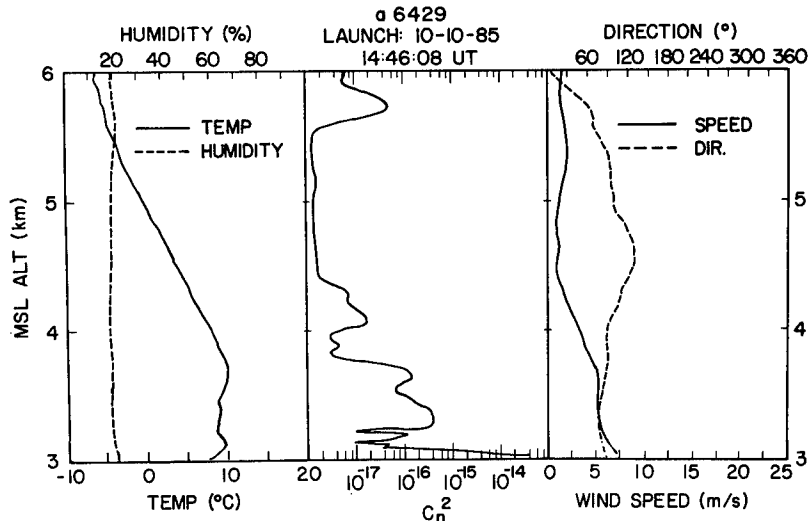


Fig. 2.11 Mountaintop nighttime profile of C_n^2 with concurrent measurements of temperature, relative humidity, and winds. Data measured by thermosonde⁵³ on a clear night on Mt. Haleakala, Maui, Hawaii (surface altitude of 3.030 km MSL).

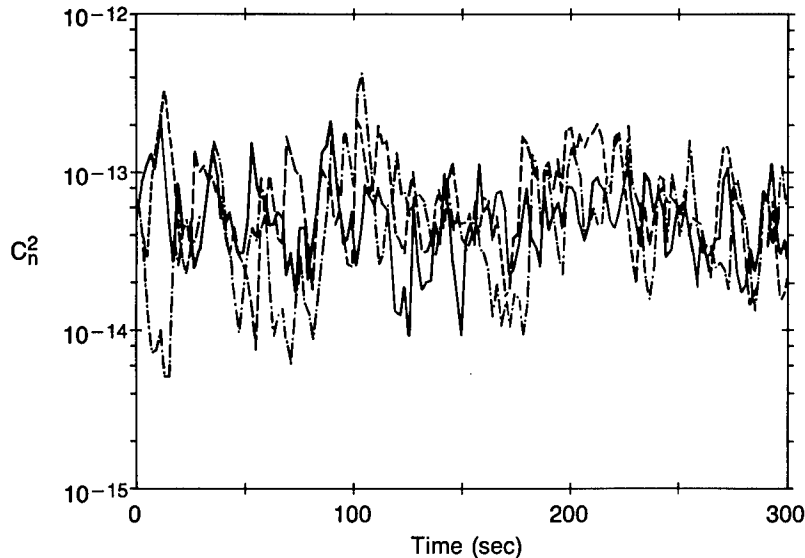


Fig. 2.12 Five-minute segment of C_n^2 measurements by three C_T^2 instruments.⁵⁶ The measurements were made 2 m above flat, grassy terrain on a clear, sunny day. The instruments were in a straight line and were separated by approximately 30 m.

frozen turbulence hypothesis, the relation is established between the temporal characteristics of C_n^2 at a point in space and its spatial distribution, at a point in time, along the axis defined by the mean wind. In Fig. 2.12, the fine-scale temporal and spatial behavior is shown for three C_T^2 instruments mounted at 2 m above the grass-covered ground on a clear, sunny day.⁵⁶ The instruments are spaced about 30 m apart. The fluctuations of nearly two orders of magnitude in time or space is typical of such measurements. Note that the data are seen to be fluctuating about a common mean. This structure is believed to be associated with the spatial structure of thermal plumes, which are dramatically shown in acoustic sounder profiles.^{7,24,57} In contrast, Fig. 2.7 shows 15-min averages and such fluctuations are removed in the averaging. At night, similar fluctuations are observed but are believed to be superimposed on longer-time-scale buoyancy oscillations that are vividly shown by acoustic sounders⁵⁷ as well as Raman lidar.⁵⁸

2.4.3 Free Atmosphere

The free atmosphere consists of the troposphere, tropopause region, and stratosphere. Optical turbulence in these regions is not well understood, especially the relation with synoptic meteorology. The general characteristic of C_n^2 in the free atmosphere is stratification superimposed on an exponential falloff. A sample profile of C_n^2 , along with the simultaneously measured meteorological data, is shown in Fig. 2.13. These data were measured by a balloon-borne C_T^2 instrument⁵³ in central Pennsylvania. The profile exhibits a fundamental characteristic of optical turbulence in the free atmosphere, namely, stratification. The large values of C_n^2 occur in narrow layers, of the order of hundreds of meters in thickness, and the magnitude of C_n^2 in these layers exceeds that of the "background" by more than an order of magnitude. The horizontal extent

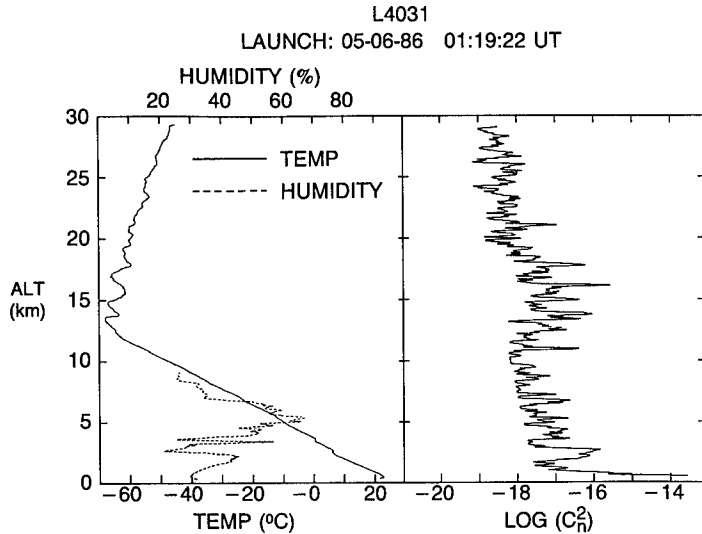


Fig. 2.13 Profiles of C_n^2 , temperature, and humidity from central Pennsylvania (night, clear skies, low upper-air winds). The data were measured by thermosonde.⁵³ The C_n^2 shown derives from applying a Gaussian averaging ($\sigma = 40$ m) to the raw data.

of these layers and their temporal duration are not well understood. However, these layers are responsible for variability of C_n^2 in the free atmosphere, since C_n^2 can vary by a factor of 100, depending on whether there is a strong layer present. Figure 2.14 shows another example of the stratification as measured by radar in New Mexico. Also shown in the figure is a balloon-borne C_n^2 profile for comparison. Although the radar and balloon data were concurrent in time, they are not concurrent in space. Thus, some layers are seen in both profiles, while others are not, which is indicative that the horizontal variability observed by Gossard *et al.*⁵⁷ in the lower atmosphere may also apply to the upper atmosphere.

Figures 2.13 and 2.14 both show vertical profiles of C_n^2 under low wind conditions. As an example of the relation between C_n^2 and synoptic meteorology, measurements have been performed during passage of the jet stream using radar⁵⁹ and balloon-borne instruments.^{60,61} In Fig. 2.15, a sample profile is shown that exhibits the classic enhancement of C_n^2 along the upper and lower edges of the jet. Furthermore, the enhancement occurs in layers of thickness of the order of a kilometer or more and with a magnitude that exceeds the background C_n^2 value by more than a factor of 10. The regions of enhancement are those with large vertical shear in the horizontal winds. This profile was measured during the passage of the polar-front jet stream. A series of jet-stream measurements have been analyzed,⁶⁰ and the classic enhancement shown in this figure is not a consistent feature. The measurements suggest that the jet-stream enhancement may occur in two forms: an overall increase in tropospheric C_n^2 or through the occurrence of thick layers of enhanced turbulence. Indeed, in some measurements of the jet stream, neither of these enhancements occurs. It also has been experimentally observed⁶¹ that there is a difference in the optical turbulence characteristics associated with the subtropical jet stream (as occurs in Hawaii) and the midlatitude, polar-front jet (which is prevalent in the continental U.S.). Owing to the different mete-

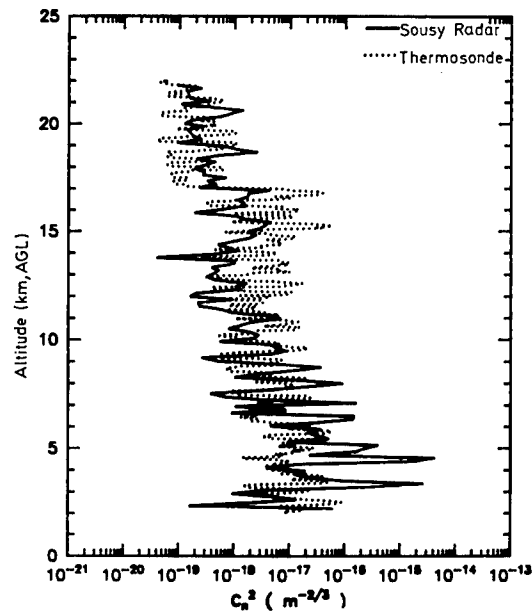


Fig. 2.14 Comparison of profiles of C_n^2 measured by the Sousy radar and thermosonde.⁷² The radar data were measured from 20:25 to 20:40 Mountain Standard Time and are corrected for humidity and correspond to optical wavelengths. The thermosonde data were smoothed with a 150-m running average, corresponding to the radar resolution.

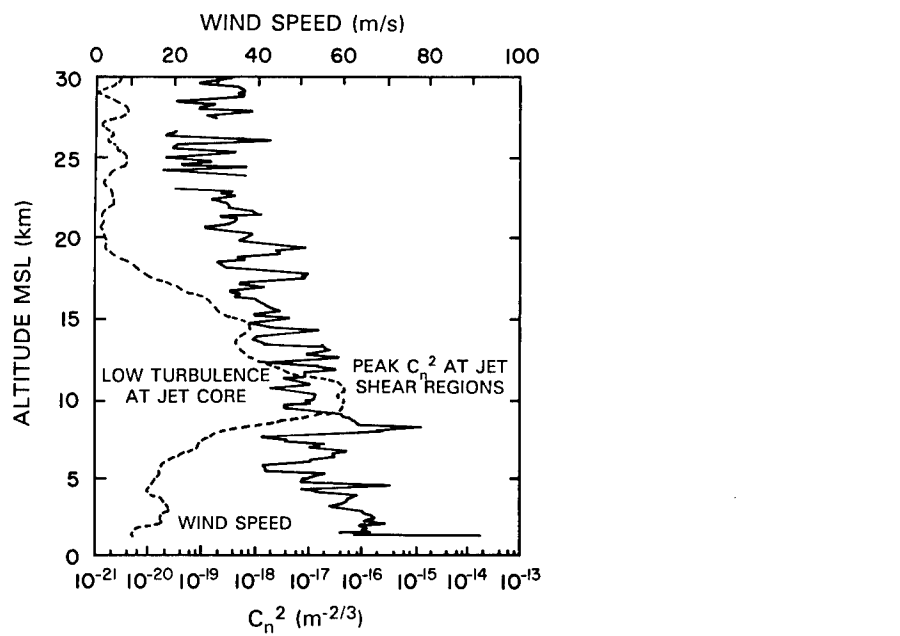


Fig. 2.15 Thermosonde profiles of C_n^2 and wind speed measured at night during a jet-stream passage in New Mexico.⁷⁵

orological origins and mechanisms of these jet streams,⁶² this is not surprising. The first-order model of C_n^2 in terms of the magnitude of the tropospheric wind cannot explain the variability of the measurements, nor the difference between the subtropical and polar-front jets.

From Eq. (2.62), it is seen that there is a dependence of C_n^2 on the temperature lapse rate and density. Analysis of the C_n^2 lapse rate in the stratosphere shows a general trend of a decrease according to the square of density for balloon data⁶³ and a great similarity in the stratospheric falloff trend of balloon measurements from different sites.⁶⁴ The troposphere, however, does not exhibit such a similarity or universality of behavior in C_n^2 from site to site, or between seasons, or with synoptic meteorology. The tropospheric C_n^2 is highly variable. A general exponential falloff in trend can be predicted according to the equation just cited. However, the layering of the turbulence dominates the falloff in trend in the troposphere.

Since the temperature lapse rate of the troposphere and stratosphere are different, this would predict an inflection point in trend at the tropopause. Closely related to this hypothesis is the widespread belief in a tropopause bulge in the C_n^2 profile, since the tropopause is a region of sharp temperature gradients. Of the three previous figures, only Fig. 2.13 unambiguously shows a bulge at the tropopause, and it could be argued that this feature results more from the relatively low C_n^2 in the troposphere compared to the other figures. Note that Fig. 2.14 shows a change in falloff rate at the tropopause (16 to 17 km), while there is no discernible bulge or change between troposphere and stratosphere in Fig. 2.15. In this latter case, this might be expected since in the polar-front jet stream, there is a break in the tropopause and it is thus not unambiguously defined.

2.4.4 Issues of Measurement

In performing and using measurements of atmospheric optical turbulence, several competing issues must be balanced. As has been shown, C_n^2 is an ensemble parameter, a second-order moment, and measurements must assume that the statistical ensemble possesses certain properties in order to be able to statistically estimate this moment. Since frozen turbulence is assumed, the spatial properties are translated into temporal properties. Almost all measurements are performed by averaging over time. Thus, we must assume that the atmosphere is statistically stationary and ergodic over some limited time and vertical dimension. Since these are ensemble properties, they depend on the definition of the ensemble, which in atmospheric turbulence theory is not well defined.

Closely related to this issue of stationarity are the issues of volume averaging and intermittency. If we consider a layer of homogeneous turbulence, the fluctuations are not evenly distributed in the layer. Rather, there are pockets of strong and weak turbulence and this intermittency is a fundamental characteristic of turbulence. This was recognized by Kolmogorov, who added a hypothesis to his original theory to account for intermittency.⁶⁵ From this perspective, the result of a measurement depends on the volume averaged. Clearly, these considerations lead into the statistical estimation problem,⁶⁶ namely, a large enough volume must be averaged to get a reliable estimator

of the ensemble parameter. However, since turbulence is a nonlinear phenomenon, the distribution of the pockets is not necessarily the same as a linear random process and thus the statistical estimation theory is very difficult.

These are far from solely academic issues, but have important applications in comparing measurements from different instruments or in using data or models to predict a system's performance. For example, suppose we wish to estimate the turbulence effects on the propagation of a collimated laser beam over a short time interval. A Doppler radar measurement of C_n^2 may measure the backscatter from a volume with a scale size of a kilometer and further may average over several minutes. Another instrument in routine use for C_n^2 profiling is the stellar scintillometer,³⁷ which typically measures along an optical path with a vertical resolution of kilometers and averages over minutes. Scintillometers and some low-resolution radars cannot resolve the narrow layers of turbulence. At the other extreme are balloon-borne instruments, which possess the highest resolution but measure along a vertical path determined by the wind. Clearly, as one measures a smaller and smaller volume, the structure in the C_n^2 profile increases. However, there is a limit to this resolution, namely, that imposed by statistical estimation requirements.

Both the tower data shown in Fig. 2.7 and the radar data in Fig. 2.14 are 15-min averages. Whether this averaging is too long depends on the application. The most prudent definition of the ensemble is not in terms of the atmosphere, with its layering and large- and small-scale dynamics, but rather in terms of the particular optical effect and the system. For example, if scintillation is the important effect, the important scale size has been shown to be the Fresnel scale. Furthermore, the volume of interest is determined by the source and the optical path. Similarly, if the dominant optical effect of interest arises from coherence length, the vertical volume averaging or vertical resolution are not important since coherence length is determined from integrated C_n^2 .

2.4.5 Measurements of Moments

Numerous measurements have been reported of the two most important moments of C_n^2 : the coherence length r_0 and the isoplanatic angle θ_0 . These have been reported in the open literature by direct measurements via optical means^{67–72} and by numerical integration of measured profiles.^{73,74} Table 2.2 lists some of these measurements at a variety of times and locations.

For coherence length, several features emerge from these data. First, in general, daytime values are smaller than nighttime values. This is due to the greater daytime turbulence arising from convection. Depending on season and location, this diurnal variation in r_0 can be weak, as during the desert winter data when winds dominated the boundary layer meteorology, or strong, as during the desert summer data when surface convection dominated. Second, in general, mountain locations have larger average values of coherence length at night than desert. Again, this can be explained in terms of the boundary layers. In the day, the difference between mountain and desert is not as clear and similar values have been reported. A third observation from the data is the much larger standard deviation associated with nighttime r_0 at mountain-tops. This indicates the existence of very good (as well as very poor) seeing conditions on some nights, which are conditions that do not occur in deserts.

Table 2.2 Comparison of r_0 and θ_0 ($\lambda = 0.3 \mu\text{m}$)

Balloon Data	r_0 (cm)		θ_0 (μrad)		Comments
	Night	Day	Night	Day	
AMOS 1985 ⁶¹	7.2 ± 3.5	4.4 ± 1.3	7.0 ± 3.0		Mountain
AMOS 1982 ⁷³	4.5 ± 0.5		5.5 ± 0.7		Mountain
MASS 1981 ⁷⁴	4.1 ± 1.3	3.6 ± 0.7	2.8 ± 0.6		Massachusetts
BOUL 1983	3.1 ± 0.5	2.8 ± 0.1	2.0 ± 0.2		Colorado
NM 1984	5.7	2.6	4.5 ± 1.3	3.5 ± 0.9	Desert-summer
NM 1985	4.7 ± 0.9	4.2 ± 0.9	4.2 ± 0.5	2.9 ± 0.5	Desert-winter
NM 1985	5.6	4.3	4.2	3.9	Desert-rainy
Optical Data					
AMOS 1977 ⁶⁷	5.2 ± 1.2				Mountain
NM 1981 ⁶⁹	2.5	1.8			Mountain/Desert
NM 1981 ⁶⁹	4.4				Desert
NM 1981 ⁶⁹					Mountain

The r_0 data also suggest that the optical data yield smaller average values than the balloon data. This is consistent with other observations.⁷² The optical measurements are made from domes that may have their own temperature structure and perturb the airflow, and these effects can result in dome-related turbulence. In contrast, the balloon-derived data are regarded as representative of the atmosphere without such surface effects.

The comparison of isoplanatic angle data yields similar results. Although the integral of C_n^2 in calculating θ_0 provides an increasing altitude weighting of optical turbulence, there may still be a contribution from the upper boundary layer and this effect is believed to be responsible for the smaller daytime values in the table. The superiority of nighttime θ_0 from mountain locations also emerges from the data. Again, the large standard deviation for nighttime θ_0 indicates the occurrence of conditions of very high isoplanatic angles, consistent with the selection of astronomical sites.

2.5 MODELS OF OPTICAL TURBULENCE

2.5.1 Introduction

In applications involving propagation through the atmosphere, calculations of optical turbulence effects need to be made. Such calculations are made for experiment or system modeling and usually rely on models of optical turbulence. As with the previous discussion of data, the models will be considered according to the different dynamic regimes of the atmosphere, the boundary layer, and the free atmosphere.

Optical turbulence models are developed with particular goals in mind and can create problems when applied without knowing the limitations. Most models attempt to represent either a mean or median value of C_n^2 . This is an important distinction that arises from the representation of C_n^2 , at a fixed altitude, by a random variable with a log-normal distribution. This distribution is intended

to model the stratification and variation on different days and meteorological conditions. Many models are therefore developed by log averaging of data. The difficulty arises because the mean of the log of C_n^2 is of course the median for a Gaussian distribution, but this is distinct from, and smaller than, the mean of C_n^2 . As the data have shown, a fundamental characteristic of atmospheric turbulence is stratification, which is responsible in part for the order of magnitude variation in C_n^2 at a fixed altitude. With respect to a sample profile such as those in Fig. 2.13 or Fig. 2.14, the eye draws a median curve (that is, averaging the logarithm of C_n^2) through the fluctuations to generate a model profile. However, most applications are concerned with average or mean values of C_n^2 , not the median value, and moments involve linear averaging of C_n^2 with some appropriate weighting. Because of the log-normal distribution, the relationship between the median and mean can be estimated and is typically a factor of 2. A more thorough discussion of the assumptions and limitations of the individual models will be provided in the following.

There have come into existence a variety of models of C_n^2 profiles.⁷⁵ These arrange themselves into a hierarchy. There are no-parameter models, which are assumed to provide representative average profiles. A slight improvement on this are the site-dependent models. The parametric models have been developed in an attempt to incorporate the dependency on site and meteorology. However, these still tend to provide models only for average conditions. These models will be discussed in terms of their hierarchy of increasing complexity. It is not the intent of this presentation to perform a historical and all-inclusive review of models. Rather, the most useful and representative models, as well as those in the most widespread use, are the focus.

It will become apparent that the current state of C_n^2 modeling has several deficiencies. For example, one category of models simply represents average conditions and shows no stratification. A significant omission of this category is the absence of error bars about the averages, which could be used to determine confidence levels. Such error bars would be of limited use because of the layering of C_n^2 and the subsequent vertical correlation, that is, the multiparametric statistical nature of an optical turbulence profile. Thus, a profile constructed of 2σ values would represent an integrated level of turbulence far in excess of any real profile and additionally, a real profile would also likely exceed the 2σ value at several layers. The second broad category of models introduces stratification by incorporating a dependence on meteorological parameters. A limitation of these models tends to be the restricted altitude domain; none of these models extends to the boundary layer. In particular, the nocturnal boundary layer remains a key problem in C_n^2 modeling. Nonetheless, these models show considerable promise, not only in terms of providing more realistic models for system designers, but also in terms of providing insight into the relation between meteorological conditions and atmospheric turbulence.

2.5.2 Boundary-Layer Turbulence

The cornerstone of models of boundary-layer turbulence is similarity theory.^{10,76} Similarity theory utilizes a dimensional analysis and physical modeling to determine dominant length scales. The Monin-Obhukov length is the scaling length parameter in the surface layer to describe the heat and mo-

mentum transfer between the surface and the atmosphere. Similarity theory is very detailed and the key results pertain to the altitude dependence. They can be summarized as follows: for unstable, free convection, C_n^2 scales with a $-4/3$ exponent in altitude dependence; for neutral conditions (near sunrise and sunset), the altitude exponent is $-2/3$; for stable conditions (night), the altitude exponent also is $-2/3$. It should be pointed out that the stable condition also applies to some daytime conditions when there is warm air over cold ground, as occurs over snow-covered terrain. The criterion that defines stability is the Brunt-Vaisala frequency or potential temperature lapse rate. The Wyngaard⁷⁶ similarity theory can be summarized in the following equations:

$$C_T^2(h) = 4.9T_*^2 h^{-2/3} (1 - 7h/L_*)^{-2/3}, \quad \text{unstable conditions ,} \quad (2.172)$$

$$C_T^2(h) = 4.9T_*^2 h^{-2/3} [1 + 2.4(h/L_*)^{2/3}], \quad \text{stable conditions ,} \quad (2.173)$$

where h is height above ground, L_* is the Monin-Obhukov length, and T_* is a temperature scaling parameter. Various momentum and heat fluxes as well as wind speed and surface parameters go into determining L_* and T_* .

Although the similarity theory of Wyngaard provides models of C_T^2 , these are difficult to use since they involve fluxes and parameters that are difficult to estimate or measure. Kunkel and Walters⁷⁷ have extended this theory in a practical fashion by providing models and estimates of the fluxes, based on energy balance considerations. The model requires latitude, time of day, time of year, wind speed, soil parameters, and soil moisture. However, the model is limited to cloud-free skies. Owing to the numerous equations involved in the model, the original paper should be consulted. Figure 2.16 shows a representative comparison of the modeled C_n^2 and data at a fixed height. The agreement, especially in the daytime, is very good. At night, the average C_n^2 data are modeled well, but the model does not quantitatively agree with the fluctuations in the data. The model can provide altitude profiles, with a daytime exponential altitude falloff of $-4/3$ and at night with a $-2/3$ exponent. The range of modeling in the daytime extends to approximately one-half the height of the boundary-layer inversion, which is another parameter that can be estimated.⁷⁸⁻⁸⁰ At night, the applicable altitude range is much smaller and Kunkel and Walters give a limit of the order of tens of meters. Another aspect of this model worth emphasis is that, in principle, the model may also be used for horizontal structure in C_n^2 , that is, of course, if the various fluxes are known over the horizontal range.

Ryzner and Bartlo⁵⁴ have investigated the dependence of C_n^2 on solar flux, soil moisture, and surface wind speed. For the smooth, grass-covered fields they studied, C_n^2 increased with solar flux. However, there was less C_n^2 for the same solar-flux levels in the afternoon than in the morning. This solar-flux dependence supports observations of a near-instantaneous drop in tower measurements of C_n^2 as a cloud shaded the tower. As mentioned earlier, their analysis of tower data also showed C_n^2 to increase with wind speed up to 4 to 5 m/s with C_n^2 decreasing with further increasing wind. These last observations are consistent with the earlier claims about the relationship of mixing and C_n^2 .

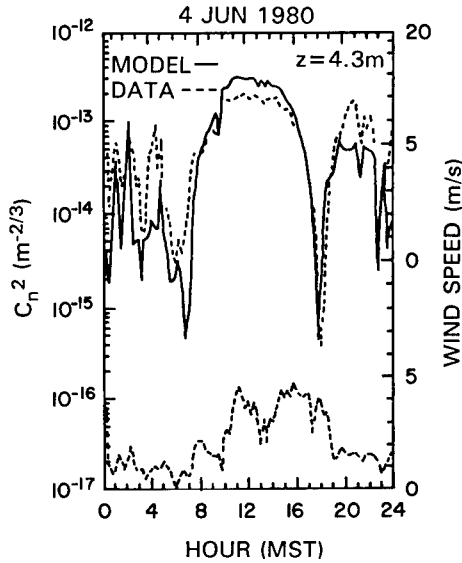


Fig. 2.16 Comparison of the Kunkel-Walters model and data for C_n^2 at 4.3 m above the ground. The measurements represent 15-min averages. The wind speed at 2.7 m is also shown.⁷⁷

Owing to the difficulty in measuring, estimating, or modeling the fluxes and other parameters, Walters and Kunkel²⁴ modified the similarity model of Kaimal *et al.*¹⁰ for the daytime convective boundary layer. By using a reference height h_0 and reference C_n^2 , $C_n^2(h_0)$, the model for a height h above ground can be simplified and is given by

$$\frac{C_n^2(h)}{C_n^2(h_0)} = \begin{cases} (h/h_0)^{-4/3}, & h_0, h \leq 0.5h_i, \\ (0.5h_i/h_0), & 0.5h_i \leq h \leq 0.7h_i, \\ 2.9(0.5h_i/h_0)^{-4/3}(h/h_i)^3, & 0.7h_i \leq h \leq h_i, \end{cases} \quad (2.174)$$

where h_i is the height of the inversion layer above ground and h_0 is the reference altitude, usually taken to be a tower level above the surface layer. It should be emphasized that this model is a modification of the full similarity theory model for the unstable free-convection case. Thus, this model applies only in the daytime, in convection-dominated conditions. The three segments of this model correspond to the mixed layer, a transition layer, and the interfacial layer. The transition layer, where C_n^2 is a constant, is the region of transition from the mixed layer to the interfacial layer, which itself is the transition between the boundary layer and the troposphere. Note that the surface layer, which is the first few meters above the ground, is not included. Figure 2.17 shows a comparison of a measured profile with the Kaimal/Walters-Kunkel model. Since the data were taken under convection-dominated conditions, the agreement up to the inversion height is very reasonable. Especially noteworthy is the agreement with the $-4/3$ falloff.

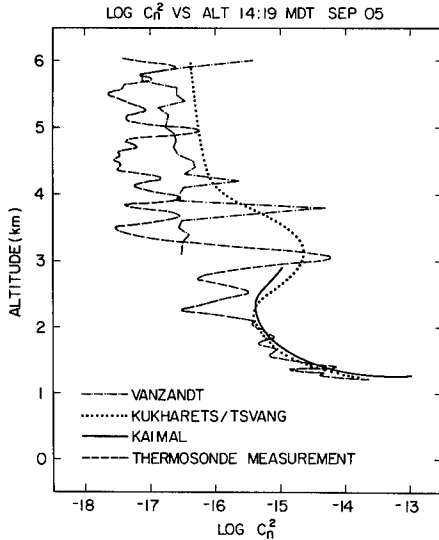


Fig. 2.17 Comparison of measured and modeled profiles of C_n^2 in the daytime convective boundary layer.⁸² The solid curve is the Kaimal/Walters-Kunkel model.

Kukharets and Tsvang⁸¹ have introduced an exponential version of the Kaimal model that models the peak in C_n^2 that usually accompanies the inversion layer. This is given by

$$\frac{C_n^2(h/h_i)}{C_n^2(0.1)} = 0.046(h/h_i)^{-4/3} + 0.6 \exp\{-12[(h/h_i) - 1.1]^2\}. \quad (2.175)$$

This model is simply an exponential with a Gaussian peak centered at $1.1h_i$ and a fixed width. Murphy *et al.*⁸² modified the Kukharets-Tsvang model to allow the use of any reference height measurement of C_n^2 near the surface:

$$\frac{C_n^2(h)}{C_n^2(h_0)} = \frac{0.046(h/h_i)^{-4/3} + 0.6 \exp\{-12[(h/h_i) - 1.1]^2\}}{0.046(h_0/h_i)^{-4/3}}. \quad (2.176)$$

Note that these Kaimal-family models extend down to near the surface but do not represent the thin, surface-layer turbulence. It is assumed that the user is interested in turbulence at and above some observing station. It should also be remembered that these models of convective conditions represent average turbulence conditions. If an observation is being made as a thermal plume passes by, the optical turbulence will be much higher. Outside a plume, the turbulence will be lower than the model predicts. If there are sufficient winds, the plumes become tilted and the altitude dependence is no longer $h^{-4/3}$. The proper use of the models is specifically as a representation of average daytime conditions when convection dominates the boundary-layer dynamics. Comparisons to data under moderate to strong winds or with passing clouds do not

support these models, especially the $- \frac{1}{3}$ falloff. The models, however, have been compared to data at mountain sites and, for clear, low-wind conditions, can represent the average daytime profile. However, orographic and topographic effects are very important in modeling turbulence above mountain sites.²⁴ In particular, the tilting of the convective plumes by the wind results in an anisotropy of turbulence around a mountain peak.

When there is a well-developed boundary layer, the models for C_n^2 can be applied to coherence length. Murphy *et al.*⁸² applied the Kukharets-Tsvang model to the calculation of coherence length in the fully developed convective boundary layer. Figure 2.18 shows the favorable comparison of the model and optical measurements of r_0 . In particular, the form of the model used required a reference C_n^2 and height as input, and horizontal scintillometer measurements provided these data. A fairly simple model for daytime r_0 resulted, requiring only a near-ground measurement.

There are no models analogous to these Kaimal-family models applicable to either the neutral or stable boundary layers, that is, for sunrise/sunset or nighttime. The similarity theory predicts a $- \frac{1}{3}$ altitude exponent. However, the predicted falloff has not been confirmed with measurements.^{83,24,54} Walters and Kunkel²⁴ concluded that, if such a falloff rate existed, it was below 8 m. Ryzner and Bartlo⁵⁴ analyzed a wide range of nighttime data from tower measurements and balloon profiles and also could not substantiate the $z^{-\frac{2}{3}}$ falloff. They found a general decrease with altitude, regardless of wind speed. For the range 10 to 300 m, they found the altitude dependence fell within the

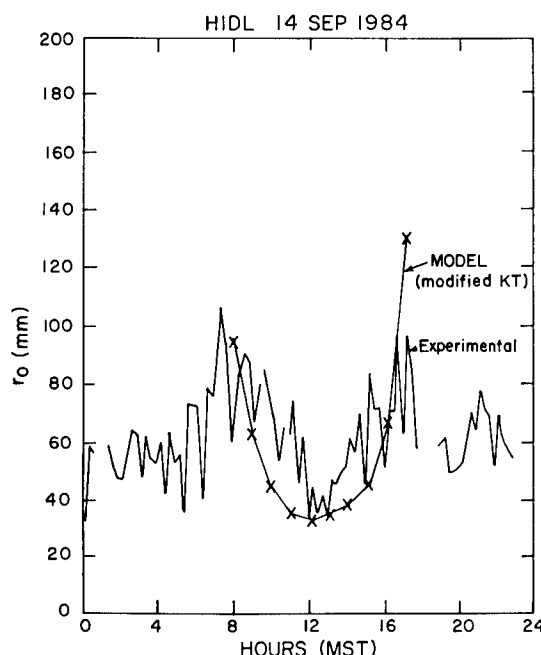


Fig. 2.18 Comparison of measured coherence length and modeled values derived by integrating the Kukharets-Tsvang model.⁸² The measurements were made optically by an MTF device. The modeled values used a tower measurement as the C_n^2 reference for the model.

range $z^{-0.5}$ and z^{-2} , depending on the strength of the winds. They also found the interesting result that C_n^2 fell as $z^{-4/3}$ for winds in the 4 to 6 m/s range and stated that this exponent was the most reasonable approximation. However, in contrast to the daytime convective boundary layer where the $-4/3$ exponent applies up to a kilometer or so, stable nighttime conditions allow this exponent to apply only through the surface inversion, that is, to a height of the order of a few hundred meters. Above this height, the stratification of optical turbulence is the dominant characteristic and no simple exponential behavior can be predicted. This nighttime model of Ryzner and Bartlo requires further validation. In particular, much of their analysis was based on slopes computed from averages at different heights. Thus, although the slope of the averages may be satisfactorily modeled by $z^{-4/3}$, it is not clear that this slope is an effective model of an individual profile.

Ryzner and Bartlo⁵⁴ also performed a similar analysis on C_n^2 data from the transition period of sunrise and sunset. Again, a $-4/3$ slope was determined as the best fit. Their results should be treated cautiously, since the data sets were very limited.

The class of empirical models provides alternatives for boundary-layer modeling. These fall into two categories. The first corresponds to model profiles derived from averaging measured profiles. These are discussed in more detail in the following section, since such averages include the free atmosphere as well. A caveat in the use of these models is that they tend to vary from site to site, with season and meteorology. Furthermore, in averaging boundary-layer data, any variation in the height of the boundary-layer inversion in the daytime, or the nocturnal surface inversion, tends to distort the resulting average. Such average profiles do not correspond to any boundary-layer profile and correlations with meteorology and winds are lost in the averaging. The second alternative for modeling is to use an actual representative profile. Thus, the daytime desert could be represented by the profile in Fig. 2.8, the nighttime desert by Fig. 2.10, and the nighttime mountaintop by Fig. 2.11. The advantage of such profiles is that they correspond to actual measurements and have correlations with winds and meteorology. The disadvantage is that they are dependent on time of day, site, season, and meteorology.

The issue of horizontal models arises in propagation over horizontal or slant paths through the atmosphere. The customary approach for a horizontal path over flat terrain is to use the value determined for the proper height from one of the previous boundary-layer models or even data such as Fig. 2.16 and assume that C_n^2 is a constant over the path. Although this assumption conflicts with point measurements, the variation along the path is less important for the calculation of many of the standard optical effects because of volume averaging. This is analogous to the issues that arise in comparing a point measurement of C_n^2 with data from a path-averaging instrument.

2.5.3 Model Optical Turbulence Profiles

The first class of model profiles is empirically derived from averaged data. The most widely used of these are the so-called SLC models, from Miller and Zieske⁶⁸ (the acronym derives from submarine laser communications studies). These models were derived by curve-fitting a piecewise-continuous polynomial to a

variety of measurements (e.g., scintillometer data, acoustic sounder, aircraft, and others). The SLC model represents median values of C_n^2 above the AMOS observatory on Mt. Haleakala, Maui, Hawaii. There are no parametric dependencies other than altitude. The AMOS site is unusual, situated on top of a dormant volcano 3 km above the surrounding land and ocean. Further, the SLC model is derived for a subtropical atmosphere, with a high (17 km MSL) tropopause. The original SLC model was a nighttime model and a daytime model extension was subsequently developed. The coefficients of the models are listed in Table 2.3. Note that the models agree above 1.5 km.

There is an important flaw in the SLC nighttime model: the segment of constant C_n^2 from 110 to 1500 m arises because of the lack of measurements in this region. This altitude regime is one of significant variability in C_n^2 and meteorology, as has been seen in other measurements at this site.⁷³ Figure 2.19 shows a plot of the SLC nighttime profile.

A primary caveat associated with the use of the SLC model is its site dependency. It is derived from a high, mountaintop location. Thus, there is an absence of a well-defined boundary layer, even in the daytime. It is noteworthy that the daytime model does not exhibit the classic $-4/3$ falloff. Furthermore, the models arise from data gathered in a marine subtropical atmosphere. These site-specific issues make the application of these models to another location questionable, especially continental locations. Another limitation of the model is that it was derived by the logarithmic averaging of data, and thus more suitably represents the median and not the mean. It is, however, a popular model in widespread use.

Based on a series of high-resolution balloon measurements from the top of Mt. Haleakala, a refinement of the nighttime SLC model was developed^{61,75} for the AMOS Observatory. The model was developed by piecewise fitting the arithmetic average of a large number of measurements under a wide range of meteorological conditions. The fit models the arithmetic average C_n^2 and not the logarithmic average. The AFGL AMOS model is shown in Fig. 2.19 and its coefficients are listed in Table 2.4. Note that the coefficients are given for

Table 2.3 SLC Models

SLC Nighttime Model	
Altitude (above ground)	C_n^2
$h \leq 18.5$ m	8.40×10^{-15}
$18.5 < h \leq 110$ m	$2.87 \times 10^{-12} h^{-2}$
$110 < h \leq 1500$ m	2.5×10^{-16}
$1500 < h \leq 7200$ m	$8.87 \times 10^{-7} h^{-3}$
$7200 < h \leq 20,000$ m	$2.00 \times 10^{-16} h^{-0.5}$
SLC Daytime Model	
$h \leq 18.5$ m	1.70×10^{-14}
$18.5 < h \leq 240$ m	$3.13 \times 10^{-13} h^{-1}$
$240 < h \leq 880$ m	1.30×10^{-15}
$880 < h \leq 7200$ m	$8.87 \times 10^{-7} h^{-3}$
$7200 < h \leq 20,000$ m	$2.00 \times 10^{-16} h^{-0.5}$

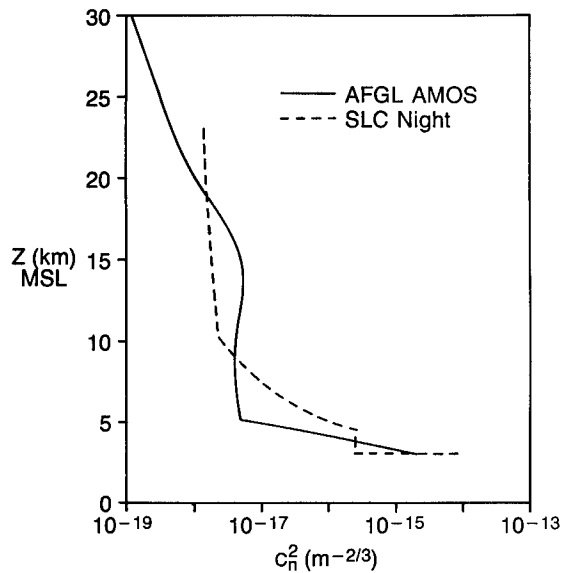


Fig. 2.19 Comparison of the SLC night and the AFGL AMOS model. Both are displayed relative to the mountaintop surface (3.038 km).

altitude above mean sea level. Since the surface of the mountain is at 3.038 km, the model begins at 14 m above ground.

The comparison of the SLC model with the AFGL AMOS night model is shown in Fig. 2.19. Given that both sets of data were gathered at AMOS under a range of meteorological conditions, the disagreement is surprising. In particular, the SLC model does not show the region of relatively low optical turbulence in the troposphere repeatedly measured by the AFGL instruments. The AFGL AMOS model profile shows the rapid falloff of C_n^2 from the surface to the relatively quiet troposphere. The other striking aspects of the disagreement between these two models is their contrasting behavior in the stratosphere and at the tropopause. It should be noted that the upper atmospheric SLC data were derived from scintillometers, whose vertical resolution is of the order of kilometers, far less than the high-resolution data used for the AFGL AMOS model.

Despite the difference in the distribution of C_n^2 between the AFGL AMOS and SLC models, the two models produce very similar values of coherence length r_0 and isoplanatic angle θ_0 . For $\lambda = 0.5 \mu\text{m}$, the SLC model gives values of r_0 and θ_0 of 10 cm and $12.7 \mu\text{rad}$, respectively, while the AFGL AMOS model gives values of 8.9 cm and $12.4 \mu\text{rad}$.

Table 2.4 AFGL AMOS Night Model C_n^2 Profile (z in km MSL)

$3.052 < z \leq 5.2$ $\log_{10}(C_n^2) = A + Bz + Cz^2$ $A = -12.412 \quad B = -0.4713 \quad C = -0.0906$
$5.2 < z \leq 30$ $\log_{10}(C_n^2) = A + Bz + Cz^2 + D \exp\{-0.5[(z - E)/F]^2\}$ $A = -17.1273 \quad B = -0.0301 \quad C = -0.0010$ $D = 0.5061 \quad E = 15.0866 \quad F = 3.2977$

Table 2.5 CLEAR I Night Model (z in km MSL)

$1.23 < z \leq 2.13$
$\log_{10}(C_n^2) = A + Bz + Cz^2$
$A = -10.7025 \quad B = -4.3507 \quad C = +0.8141$
$2.13 < z \leq 10.34$
$\log_{10}(C_n^2) = A + Bz + Cz^2$
$A = -16.2897 \quad B = +0.0335 \quad C = -0.0134$
$10.34 < z \leq 30.$
$\log_{10}(C_n^2) = A + Bz + Cz^2 + D \exp\{-0.5[(z - E)/F]^2\}$
$A = -17.0577 \quad B = -0.0449 \quad C = -0.0005$
$D = 0.6181 \quad E = 15.5617 \quad F = 3.4666$

Similar models were developed by AFGL for the New Mexico desert in the summer. The same procedure was followed as for the AMOS model, but a smaller number of measurements were made under fairly homogeneous meteorological conditions. The forms and coefficients of this model, known as CLEAR I, are listed in Table 2.5. In this table, z is altitude, in kilometers, above mean sea level (MSL). Station height for the desert site is 1.216 km (MSL). Note that the lowest altitude point of the models is 14 m above ground.

The CLEAR I summer model is shown in comparison to the AFGL AMOS model in Fig. 2.20. The agreement is excellent between the two models above 10 km. This is significant since, in the summer, a subtropical atmosphere with a high tropopause occurs in New Mexico. The major difference is in the boundary layer and the lower troposphere where the CLEAR I model shows significantly more average turbulence. This CLEAR I model gives values of 5.8 cm for r_0 and 6.7 μ rad for θ_0 ($\lambda = 0.5 \mu\text{m}$). This significantly smaller value for θ_0 is indicative of the greater tropospheric turbulence than in the AFGL AMOS model.

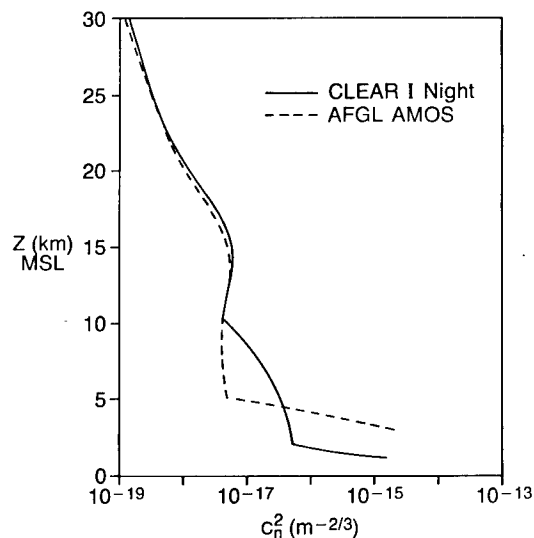


Fig. 2.20 Comparison of the AFGL AMOS and the AFGL CLEAR I night model. The AMOS model is displayed relative to the mountaintop surface (3.038 km), while the CLEAR I model is shown relative to the desert floor (1.216 km).

The similarity shown between the previous models in the stratosphere has also been substantiated by other analysis⁶³ and data.^{64,25} Battles *et al.*⁶³ have shown that the drop-off rate of C_n^2 in the stratosphere is consistent with assuming the decrease in C_n^2 results from the decreasing atmospheric density. This implies that C_T^2 should be essentially constant with altitude, leading to a universal profile of C_T^2 .

2.5.4 Parametric Models

The next class of models includes parameters in an attempt to incorporate some dependencies on winds and meteorology and to model the complexity of actual C_n^2 measurements. The first such model historically is the well-known Hufnagel model,⁴⁵ which was developed on the basis of stellar scintillations and balloon measurements. This model replaced earlier empirical models developed on less data (Hufnagel⁸⁴ and Hufnagel and Stanley⁸⁵). The model, developed for altitudes from 3 to 24 km above the surface, is represented as

$$C_n^2(h) = 8.2 \times 10^{-16} W^2 (h/10)^{10} e^{-h} + 2.7 \times 10^{-16} e^{-h/1.5}, \quad (2.177)$$

where the height h is in km and the parameter W is in m/s. The parameter W is defined as the rms wind speed in the range 5 to 20 km above ground, specifically,

$$W^2 = (1/15) \int_5^{20} V^2(h) dh, \quad (2.178)$$

where $V(h)$ is the wind speed in m/s and the height h is in km. The initial version of this model included a random modulation factor in order to introduce stratification and structure. This random model has not seen much use since the statistical parameters of the random factor are difficult to estimate or validate experimentally. The form given above is the mean of Hufnagel's original statistical model.

The Hufnagel model is a one-parameter model that is determined from the upper-air winds. Since it provides C_n^2 beginning at 3 km above ground, there is no attempt to include the boundary layer and thus it is intended for use either day or night. As can be seen, Eq. (2.177) models C_n^2 in terms of two exponential trends. The second exponential dominates at the lower altitudes while the first dominates in the upper troposphere and into the stratosphere. The first term also provides an inflection point, that is, a bulge in C_n^2 , which occurs at 10 km above ground. The Hufnagel model is a mid-latitude model, since it assumes a low tropopause and was developed from mid-latitude data. Its applicability to modeling C_n^2 in subtropical atmospheres with a high tropopause is questionable. Its performance was found to be poor for a subtropical atmosphere, specifically, the AFGL AMOS data set.⁶¹ The comparison to New Mexico data showed that the model performed poorly under conditions of low tropospheric winds. However, the Hufnagel model performed reasonably well in modeling the variation and trend in isoplanatic angle, but not the specific values, under high winds aloft in New Mexico. Data taken at Penn State⁶⁰ showed that the Hufnagel model did not model effectively the variation in

C_n^2 , isoplanatic angle, or scintillation moment that occurs during a jet-stream passage. A further shortcoming of the Hufnagel model is that it incorporates a dependence of the stratospheric falloff in C_n^2 on tropospheric wind speed, a dependence that is not in agreement with the data discussed previously.

Ulrich⁸⁶ extended the Hufnagel model from the lower 3-km altitude down to the ground following the suggestion of Valley⁸⁷ to include a boundary-layer term. This new model, referred to as the Hufnagel-Valley model, adds an additional exponential term for the boundary layer. Furthermore, the model includes two parameters that can be adjusted. The specific form of the model in most widespread use is

$$\begin{aligned} C_n^2(h) = & 8.2 \times 10^{-26} W^2 h^{10} e^{-h} + 2.7 \\ & \times 10^{-16} e^{-h/1.5} + A e^{-h/0.1}, \end{aligned} \quad (2.179)$$

where the height h is specified in kilometers. The two parameters can be chosen so as to yield specific values of coherence length and isoplanatic angle.³⁶ The most popular use of this model is termed the Hufnagel-Valley 5/7 model; that is, the parameters are selected such that the C_n^2 profile yields a value of coherence length of 5 cm and isoplanatic angle of 7 μrad ($\lambda = 0.5 \mu\text{m}$). For the 5/7 model, the parameters assume values of $A = 1.7 \times 10^{-4}$ and $W = 21$. This extension of the Hufnagel model is in widespread use and a plot of the profile is shown in Fig. 2.21. Of course, it suffers from some of the same limitations as the original Hufnagel model. In addition, its exponential falloff in the first 3 km is unrealistic in light of boundary-layer modeling. The virtue and appeal of the Hufnagel-Valley model is that it provides a model consistent with moderate values of r_0 and θ_0 . In many applications, the distribution of C_n^2 is of less importance than the integrated values. It should be noted that other authors have used the Hufnagel-Valley model with slightly different coefficients,⁸⁶ but

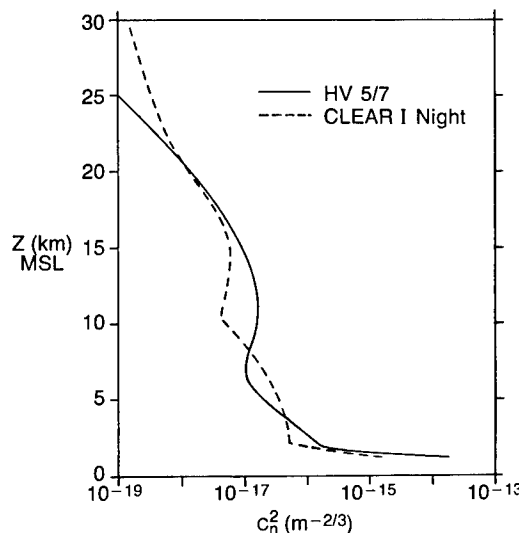


Fig. 2.21 The C_n^2 profile calculated from the Hufnagel-Valley 5/7 model. The CLEAR I night model is shown for comparison.

these differences are minor and arise largely from the fact that Valley suggested this extension but did not actually implement it.

The Hufnagel model was the first attempt to explicitly incorporate some dependence of C_n^2 on atmospheric quantities. A whole category of models has arisen that carries this further. The starting point for these models is the Tatarski expression [Eq. (2.60)], which is rewritten here as

$$C_n^2 = 2.8L_0^{4/3}M^2 . \quad (2.180)$$

The explicit dependence on meteorology enters via the term M (the gradient of the refractive index) and to a lesser extent through L_0 . The inclusion of these terms results in models of individual profiles that exhibit the characteristic stratification of data. Because of the relation between temperature gradients and optical turbulence, these models produce profiles in which there is a correlation between C_n^2 layers and temperature gradients. The models are, however, limited to the free atmosphere.

The first such model historically, as well as the most complex, is the NOAA model, also known as the VanZandt model. VanZandt et al.⁵⁹ developed a two-parameter C_n^2 model based on a statistical treatment of the fine structure of the vertical wind shear. VanZandt et al. developed this model in order to derive C_n^2 profiles from meteorological data available from standard radiosonde observations. An important aspect of the NOAA model is that it was developed from radar data, i.e., from measurements with low vertical resolution and averaged over large volumes, and lacked simultaneous measurement of meteorological data in the same volume. An improved model was developed several years later⁸⁸ that incorporated statistically both the fine structure of wind shears, the fine structure of the potential temperature defined in terms of the Brunt-Vaisala frequency N^2 , and the statistics of encountering a turbulent layer of thickness L . The C_n^2 value at a particular altitude is expressed as a triple integral over these probabilities as

$$C_n^2 = 2.8M_0^2 \int_{L_{\min}}^{L_{\max}} L^{4/3}P_L dL \int_0^\infty P_s dS \int_{-\infty}^\infty N^4P_N dN^2 , \quad (2.181)$$

where $M_0 = -79 \times 10^{-6}P/Tg$, where P is pressure in mbar, T is temperature in K, and g is the gravitational acceleration. The probability densities P_L , P_s , and P_N are those for the outer scale of the layer, shear, and Brunt-Vaisala frequency, respectively, and these utilize the radiosonde data. For specific details on implementation, the cited works should be consulted as well as more recent refinements.⁸⁹ Improvements in the model have continued, and now the NOAA model provides reasonable profiles of C_n^2 from above the boundary layer to well into the stratosphere. Comparison of the NOAA model with measurements⁹⁰ is shown in Fig. 2.22. As can be seen, there is excellent agreement between the balloon C_n^2 measurement and the model.

The NOAA model incorporates the most physics of any of the existing models. There are, however, drawbacks. It is the most complex model and requires expertise. In its original form, it was developed in mountainous terrain and utilized the nonsimultaneous radiosonde data to predict C_n^2 for comparison

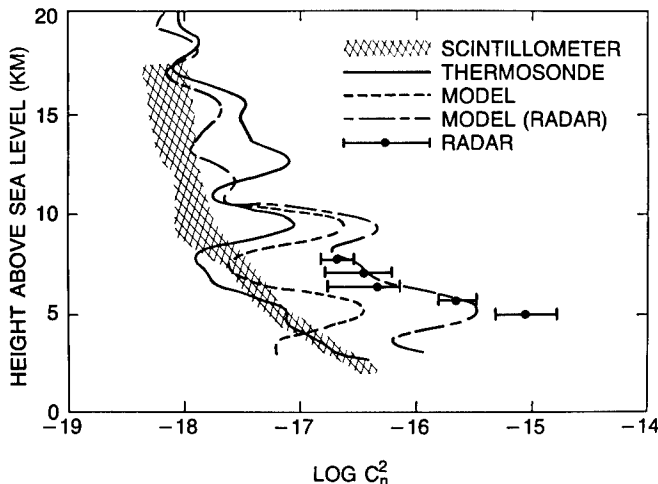


Fig. 2.22 Comparison of NOAA model and measurements for the period 02 to 03 hours Universal Time, 8 June 1988. The solid line is the thermosonde profile, while the hatched area gives the range of scintillometer measurements over the hour. (Adapted from Ref. 91)

with radar measurements of C_n^2 . The model has parameters in the shear probability distribution that must be adjusted for the site.^{90,91} The model is still being refined and validated for other sites and meteorology.

There are several, simplified models that are based on the Tatarski equation. Good et al.⁷⁵ proposed a simplified version of and variant of the NOAA model. This AFGL model is also intended to use meteorological data derived from standard radiosondes and is computationally much simpler than the NOAA model. Beland and Brown²⁵ developed a simple Tatarski-type model that relates C_n^2 to the meteorological data from a radiosonde in a deterministic fashion. This model is limited to the stratosphere where a universal behavior was found. This model approach was not extended to the troposphere, since a universal behavior is not observed owing to the large variability of tropospheric turbulence. Coulman et al.⁹² used a similar technique to devise a deterministic model also applicable to the troposphere. This model uses different fits for different sites. These models have been only recently developed and their validation and further development is continuing.

2.6 SAMPLE PROBLEMS

2.6.1 Scintillation

The calculation of the scintillation from a star will exhibit the technique of performing calculations of scintillation as well as the statistics of intensity. In particular, we will calculate the 95% confidence interval for intensity from a plane-wave source (or equivalently, for a spherical wave at a very large distance, such as a star). The source will be assumed to be at zenith, or directly overhead. The receiver will be assumed to be a point receiver. The formulation of the problem applies to the observation of stellar scintillation as by the human eye. The calculation could be readily extended to determine scintillation effects in applications pertaining to eye safety.

Equation (2.128) could be used directly to calculate the log-amplitude variance. This assumes that the source is located at $\eta = 0$ and the receiver at $\eta = L$. However, it is more useful to translate from the path variable η to altitude z . The source is then at $z = L$ and the receiver at $z = 0$ and Eq. (2.128) becomes

$$\sigma_\chi^2 = 0.56k^{7/6} \int_0^L C_n^2(z) z^{5/6} dz . \quad (2.182)$$

The calculation will be performed for a wavelength of 0.5 μm . The C_n^2 profile will be provided by the Hufnagel-Valley $5/7$ model [Eq. (2.179)]. The use of the Hufnagel-Valley $5/7$ model allows the variance to be evaluated analytically. The result is $\sigma_\chi^2 = 0.059$. This value shows that we are well within the limits of the Rytov theory, which is generally the case for vertical propagation.

Statements about the range of variation in intensity can be immediately made. Since the fluctuations are weak, we have from Eq. (2.109) that the normalized intensity variance is

$$\sigma_I^2 = \langle (I - \langle I \rangle)^2 \rangle / \langle I \rangle^2 \approx 4\sigma_\chi^2 = 0.236 . \quad (2.183)$$

Thus, an estimate of the fluctuations in normalized intensity can be given by σ_I . This gives a value of approximately 0.5, that is, 50% fluctuations. This value is typical of stellar scintillation and quantifies the familiar observations of twinkling.

The estimate of the fluctuations must take into account the relevant statistical distributions to be precise. From the Rytov theory, it has been established that log amplitude satisfies a normal distribution. Therefore, it follows that 95% of the fluctuations in χ will fall in the range of $\pm 2\sigma$ about the mean $\langle \chi \rangle$. Specifically, the confidence interval is

$$(\langle \chi \rangle - 2\sigma_\chi, \langle \chi \rangle + 2\sigma_\chi) . \quad (2.184)$$

Since the intensity is given by $I = \exp(2\chi)$, this immediately yields the 95% confidence interval for intensity:

$$[\exp(2\langle \chi \rangle - 4\sigma_\chi), \exp(2\langle \chi \rangle + 4\sigma_\chi)] . \quad (2.185)$$

Note that the normality of χ and the resulting log normality of I produces a confidence interval for intensity that is determined by multiplication and division by the factor $\exp(4\sigma_\chi)$. The intensity confidence interval is also written in terms of the median intensity I_m , and not the mean (where $I_m = \exp(2\langle \chi \rangle)$). This can be translated into the mean intensity by using Eq. (2.108), which can be written as

$$\langle I \rangle = I_m \exp(2\sigma_\chi^2) . \quad (2.186)$$

Since conservation of energy requires that $\langle I \rangle = 1$, the confidence interval for normalized intensity is given by

$$[\exp(-2\sigma_\chi^2) \exp(-4\sigma_\chi), \exp(-2\sigma_\chi^2) \exp(+4\sigma_\chi)] . \quad (2.187)$$

Substitution yields the values of [0.34, 2.35]. Especially noteworthy is the upper limit, where even in this weak scintillation case, the normalized intensity fluctuates by more than a factor of 2. If we had instead used the less precise Rytov approximation of $\langle \chi \rangle = 0$, the interval would have been calculated as [0.38, 2.64], which is a small correction.

An alternative approach to this problem is to formulate it in terms of the probability distribution of the intensity. Our approach followed the easier route, since normal distributions have statistically desirable properties. Nonetheless, in some problems the intensity distribution itself must be resorted to. For a unit intensity source and requiring that $\langle I \rangle = 1$ (and consequently $\langle \chi \rangle = -\sigma_\chi^2$), it can be shown³⁰ that the probability distribution of the intensity is given by

$$P_I(I) = [2I\sigma_\chi(2\pi)^{1/2}]^{-1} \exp\{-[\ln(I) + 2\sigma_\chi^2]^2/(8\sigma_\chi^2)\} . \quad (2.188)$$

This can be written in terms of only intensity variables without reference to log amplitude. Equation (2.110) can be solved to give

$$\sigma_\chi^2 = (1/4) \ln(\sigma_I^2 + 1) . \quad (2.189)$$

Substitution into Eq. (2.188) gives the form of the distribution

$$P_I(I) = \{[2\pi \ln(\sigma_I^2 + 1)]\}^{-1/2}(1/I) \\ \times \exp\{-[\ln(I) + (1/2) \ln(\sigma_I^2 + 1)]^2/[2 \ln(\sigma_I^2 + 1)]\} . \quad (2.190)$$

Since the normalized intensity and its variance are the directly measurable quantities, this form is useful in some applications.

2.6.2 Image Resolution

As an example of turbulence in imaging problems, the long-exposure resolution of an imaging system will be calculated. The specifications of the system are similar to those of a small telescope: aperture diameter D of 8 in. and focal length f of 2.032 m. The object to be imaged will be assumed to be at a distance L of 300 m. The light of interest will be assumed to be monochromatic and of wavelength $\lambda = 0.5 \mu\text{m}$.

For comparison to the turbulence-induced limitation in resolution, the resolution limit due to diffraction can be readily estimated from

$$R_d \approx \lambda L/D \approx 0.74 \text{ mm} . \quad (2.191)$$

This spatial resolution is readily given in terms of a range-independent angular resolution λ/D , which yields 2.5 μrad .

From Eq. (2.139), the minimum resolvable scale size in the system's focal plane is given by

$$R_f = 1/\nu_c = 2.1\lambda f/r_0 . \quad (2.192)$$

For line-of-sight propagation a few meters above the ground, Fig. 2.7 shows that a C_n^2 value of 1.0×10^{-13} is a reasonable approximation. The turbulence will be assumed to be homogeneous along the horizontal path. This assumption is not critical, since the coherence length has no path weighting and is determined by the integrated C_n^2 along the path. The illumination from the object will be assumed to be a plane wave. From Eq. (2.137), the coherence diameter for homogeneous turbulence is

$$r_0 = 2.1(1.46k^2C_n^2L)^{-3/5} = 1.04 \text{ cm} . \quad (2.193)$$

Comparison of this value to data in Table 2.2 or Fig. 2.18 shows that this 300-m horizontal path has smaller r_0 and hence more integrated turbulence than a ground-to-space path. Substitution of this value into Eq. (2.192) yields

$$R_f = 2.05 \times 10^{-4} \text{ m} . \quad (2.194)$$

This is the minimum resolvable scale in the focal plane. The resolution is sought in the object plane for comparison to the diffraction limit. These two are simply related by the magnification of the system, so that

$$R_t = R_f L/f = 3.0 \text{ cm} . \quad (2.195)$$

Dividing by L , this spatial resolution can be stated as an angular resolution and yields the value of $101 \mu\text{rad}$. This limit is more than 40 times larger than the diffraction limit. Objects smaller than 3 cm will be blurred in long-exposure images. Since the object-plane resolution limit scales with path length as $L^{8/5}$, longer paths will produce significantly worse degradation.

In this calculation of the resolution degradation, the resolution has been calculated in both the focal and object planes. This same result could have been derived starting from the mutual coherence function formulation in the aperture plane and using Yura's transverse coherence length ρ_0 . In particular, it is easy to show that our calculation of R_t in the object plane is equivalent to

$$R_t = \lambda L / \rho_0 . \quad (2.196)$$

In this form, the resolution degradation in the object plane induced by turbulence is seen to be independent of aperture diameter D and focal length f . Greater magnification or a larger aperture will not alleviate the problem. The angular resolution, given by λ/ρ_0 , is range dependent owing to the dependence of ρ_0 .

2.6.3 Beam Wander and Broadening

As an example of the calculation of the turbulence effects on a laser beam, the problem of the beam broadening and wander will be treated. The specific case is the propagation of a collimated beam from the ground to an object in space. This general problem has many applications. The object will be assumed to be at a distance of 200 km and at zenith. The laser beam will have a

transmitter diameter of 1 m and will be assumed to have a Gaussian intensity profile at the aperture. The laser wavelength is assumed to be 0.5 μm . The model for C_n^2 will be that of the CLEAR I night model (Table 2.5).

The diffraction-limited beam radius will be calculated and compared to the case of propagation through turbulence. For the turbulence case, the long-term radius, short-term radius, and beam-wander radius will all be calculated. From Eq. (2.154), the long-term beam radius for a collimated beam is given by

$$\langle \rho_L^2 \rangle = 4L^2/(kD)^2 + (D/2)^2 + 4L^2/(k\rho_0)^2 , \quad (2.197)$$

where ρ_0 is the transverse coherence length given by

$$\rho_0 = [1.46k^2 \sec(\varphi) \int_0^L C_n^2(\eta)(1 - \eta/L)^{5/3} d\eta]^{-3/5} . \quad (2.198)$$

We can write this equation as

$$\langle \rho_L^2 \rangle = \rho_d^2 + 4L^2/(k\rho_0)^2 , \quad (2.199)$$

where

$$\rho_d = [4L^2/(kD)^2 + (D/2)^2]^{1/2} . \quad (2.200)$$

Clearly, ρ_d is the beam radius that results in the absence of turbulence ($\rho_0 \rightarrow \infty$), that is, the diffraction limit. Substitution of the numerical values of the parameters yields a value of ρ_d of 0.501 m. Thus, diffraction is negligible in this problem, as the diffraction broadens the beam by only 1 mm.

To calculate the turbulence effects, the value of the coherence length must be specified. It will be assumed that C_n^2 is zero for altitudes greater than 30 km. This is a reasonable assumption, since as has been shown, there is evidence that C_n^2 falls off with the square of density in the stratosphere and is therefore small compared to tropospheric turbulence. The weighting factor of $(1 - \eta/L)$ in the integrand is negligible since $\eta \ll L$, where C_n^2 is nonzero and the coherence length expression reduces to that of a plane wave [Eq. (2.134)]. The value of the coherence diameter ρ_0 can be calculated from the CLEAR I model and yields a value of 2.76 cm at $\lambda = 0.5 \mu\text{m}$. The mean-square beam radius for long exposure can then be calculated from Eq. (2.199) and gives a value of 1.58 m². Of more importance is the rms radius, which is 1.257 m. Thus, turbulence more than doubles the beam radius.

This is the long-exposure value that would be seen at the target. Of more practical importance is the short-term broadening and the beam wander. Equation (2.153) gives the relation between these as

$$\langle \rho_L^2 \rangle = \langle \rho_s^2 \rangle + \langle \rho_c^2 \rangle . \quad (2.201)$$

Since $\rho_0 \ll D < L_0$, the expressions for broadening and wander are given by Eqs. (2.156) and (2.157), which are written here as

$$\langle \rho_s^2 \rangle = \rho_d^2 + 4L^2/(k\rho_0)^2[1 - 0.62(\rho_0/D)^{1/3}]^{6/5} , \quad (2.202)$$

$$\langle \rho_c^2 \rangle = 2.97L^2/(k^2\rho_0^{5/3}D^{1/3}) . \quad (2.203)$$

Substitution results in the values of $\langle \rho_s^2 \rangle = 1.28 \text{ m}^2$ and $\langle \rho_c^2 \rangle = 0.30 \text{ m}^2$. In terms of the rms quantities, the rms short-term beam radius is 1.13 m and the rms wander is 0.55 m. Even in the short-time case, turbulence broadens the beam by more than a factor of 2 compared to the vacuum radius. The long-term beam radius comprises a broadened beam of rms radius 1.13 m that wanders about with an rms radius of 0.55 m. The beam wander is especially significant in applications where the object is smaller than or of the same order as the wander radius. In such cases, the turbulence will cause the laser illumination to wander on and off the object.

References

1. E. Parzen, *Stochastic Processes*, Holden-Day, San Francisco (1962).
2. G. E. P. Box and G. M. Jenkins, *Time Series Analysis: Forecasting and Control*, Holden-Day, San Francisco (1976).
3. J. L. Doob, *Stochastic Processes*, Wiley, New York (1953).
4. R. B. Blackman and J. W. Tukey, *The Measurement of Power Spectra*, Dover, New York (1958).
5. A. S. Monin and A. M. Yaglom, *Statistical Fluid Mechanics: Mechanics of Turbulence*, Vol. 1, MIT Press, Cambridge, MA (1971).
6. V. I. Tatarski, *Wave Propagation in a Turbulent Medium*, McGraw-Hill, New York (1961).
7. S. F. Clifford, "The classical theory of wave propagation in a turbulent medium," Chap. 2, in *Laser Beam Propagation in the Atmosphere*, J. W. Strohbehn, Ed., Springer-Verlag, New York (1978).
8. A. S. Monin and A. M. Yaglom, *Statistical Fluid Mechanics: Mechanics of Turbulence*, Vol. 2, MIT Press, Cambridge, MA (1975).
9. L. F. Richardson, *Weather Prediction by Numerical Process*, Cambridge Univ. Press, Cambridge, U.K. (1922).
10. J. C. Kaimal, J. C. Wyngaard, D. A. Haugen, O. R. Cote, and Y. Izumi, "Turbulence structure in the convective boundary layer," *J. Atmos. Sci.* **33**, 2152–2169 (1976).
11. F. H. Champagne, C. A. Friehe, J. C. Larue, and J. C. Wyngaard, "Flux measurements, flux estimation techniques and fine scale turbulence measurements in the unstable surface layer over land," *J. Atmos. Sci.* **34**, 515–530 (1977).
12. H. Tennekes and J. L. Lumley, *A First Course in Turbulence*, MIT Press, Cambridge, MA (1972).
13. V. I. Tatarski, "The effects of the turbulent atmosphere on wave propagation," NOAA Report No. TT 68–50464, U.S. Dept. of Commerce, Springfield, VA (1971).
14. J. Barat, "Some characteristics of clear-air turbulence in the middle stratosphere," *J. Atmos. Sci.* **39**, 2553–2564 (1982).
15. W. K. Hocking, "Measurement of turbulent energy dissipation rates in the middle atmosphere by radar techniques: A review," *Radio Sci.* **20**, 1403–1422 (1985).
16. R. H. Kraichnan, "On Kolmogorov's inertial-range theories," *J. Fluid Mech.* **62**, 305–330 (1974).
17. J. R. Holton, *An Introduction to Dynamic Meteorology*, Academic Press, New York (1972).
18. R. S. Lawrence and J. W. Strohbehn, "A survey of clear-air propagation effects relevant to optical communications," *Proc. IEEE* **58**, 1523–1545 (1970).
19. R. J. Hill and S. F. Clifford, "Modified spectrum of atmospheric temperature fluctuations and its application to optical propagation," *J. Opt. Soc. Am.* **68**, 892–899 (1978).
20. R. S. Lawrence, G. R. Ochs, and S. F. Clifford, "Measurements of atmospheric optical turbulence relevant to optical propagation," *J. Opt. Soc. Am.* **60**, 826–830 (1970).
21. J. C. Owens, "Optical refractive index of air: Dependence on pressure, temperature and compositions," *Appl. Opt.* **6**, 51–59 (1967).

22. J. C. Wyngaard and M. A. LeMone, "Behavior of the refractive index structure parameter in the entraining convective boundary layer," *J. Atmos. Sci.* **37**, 1573–1585 (1980).
23. C. A. Friehe, J. C. La Rue, F. H. Champagne, C. H. Gibson, and G. F. Dreyer, "Effects of temperature and humidity fluctuations on the optical refractive index in the marine boundary layer," *J. Opt. Soc. Am.* **65**, 1502–1511 (1975).
24. D. L. Walters and K. E. Kunkel, "Atmospheric modulation transfer function for desert and mountain locations: the atmospheric effects on r_0 ," *J. Opt. Soc. Am.* **71**, 397–405 (1981).
25. R. R. Beland and J. H. Brown, "A deterministic temperature model for stratospheric optical turbulence," *Physica Scripta* **37**, 419–423 (1988).
26. V. A. Banakh and V. L. Mironov, *Lidar in a Turbulent Atmosphere*, Artech House, Boston (1987).
27. L. A. Chernov, *Wave Propagation in a Random Medium*, McGraw-Hill, New York (1960).
28. J. W. Strohbehn, Ed., *Laser Beam Propagation in the Atmosphere*, Springer-Verlag, New York (1978).
29. A. Ishimaru, *Wave Propagation and Scattering in Random Media*, Vol. 2, Academic Press, New York (1978).
30. J. W. Goodman, *Statistical Optics*, Wiley, New York (1985).
31. R. L. Fante, "Electromagnetic beam propagation in a turbulent media," *Proc. IEEE* **63**, 1669–1692 (1975).
32. R. L. Fante, "Electromagnetic beam propagation in a turbulent media: An update," *Proc. IEEE* **68**, 1424–1443 (1980).
33. C. E. Coulman, "Fundamental and applied aspects of astronomical seeing," *Ann. Rev. Astron. Astrophys.* **23**, 19–57 (1985).
34. R. F. Lutomirski and H. T. Yura, "Wave structure function and mutual coherence function of an optical wave in a turbulent atmosphere," *J. Opt. Soc. Am.* **61**, 482–487 (1971).
35. J. W. Strohbehn, "Modern theories in the propagation of optical waves in a turbulent medium," in *Laser Beam Propagation in the Atmosphere*, J. W. Strohbehn, Ed., Springer-Verlag, New York (1978).
36. R. J. Sasiela, "A unified approach to electromagnetic wave propagation in turbulence and the evaluation of multiparameter integrals," Technical Report No. 807, MIT/Lincoln Laboratory (1988).
37. T. Wang, G. R. Ochs, and S. F. Clifford, "A saturation-resistant optical scintillometer to measure C_n^2 ," *J. Opt. Soc. Am.* **68**, 334–338 (1978).
38. G. R. Ochs, D. S. Reynolds, and R. L. Zurawski, "Folded-Path Optical C_n^2 Instrument," NOAA Technical Memorandum ERL WPL-123, Boulder, CO (1985).
39. G. R. Ochs and T. Wang, "Finite aperture scintillometer for profiling wind and C_n^2 ," *Appl. Opt.* **17**, 3774–3778 (1978).
40. S. F. Clifford, G. R. Ochs, and R. S. Lawrence, "Saturation of optical scintillations by strong turbulence," *J. Opt. Soc. Am.* **64**, 148 (1974).
41. L. C. Andrews, R. L. Phillips, and B. K. Shivamoggi, "Relations of the parameters of the I-K distribution for irradiance fluctuations to physical parameters of the turbulence," *Appl. Opt.* **27**, 2150–2156 (1988).
42. D. L. Fried, "Aperture averaging of scintillation," *J. Opt. Soc. Am.* **57**, 169–175 (1967).
43. D. L. Fried, "Optical resolution through a randomly inhomogeneous medium," *J. Opt. Soc. Am.* **56**, 1372–1379 (1966).
44. R. F. Lutomirski, "Atmospheric degradation of electrooptical system performance," *Appl. Opt.* **17**, 3915–3921 (1978).
45. R. E. Hufnagel, "Propagation through atmospheric turbulence," in *The Infrared Handbook*, Chap. 6, USGPO, Washington, D.C. (1974).
46. D. Y. Gezari, A. Labeyrie, and R. V. Stachnik, "Speckle interferometry: Diffraction-limited measurements of nine stars with the 200 inch telescope," *Astrophys. J.* **173**, L1–L5 (1972).
47. A. Labeyrie, "Speckle interferometry observations at Mount Palomar," *Nouvelle Revue D'Optique* **5**, 141–151 (1974).
48. D. Korff, "Analysis of a method for obtaining near-diffraction-limited information in the presence of atmospheric turbulence," *J. Opt. Soc. Am.* **63**, 971–980 (1973).
49. K. T. Knox and B. J. Thompson, "Recovery of images from atmospherically degraded short-exposure photographs," *Astrophys. J.* **193**, L45–L48 (1973).

-
50. A. Ishimaru, "The beam wave case and remote sensing," in *Laser Beam Propagation in the Atmosphere*, J. W. Strohbehn, Ed., Springer-Verlag, New York (1978).
51. D. L. Fried, "Anisoplanatism in adaptive optics," *J. Opt. Soc. Am.* **72**, 52–61 (1982).
52. G. A. Tyler, "Turbulence induced adaptive optics performance degradation: evaluation in the time domain," in *Laser Beam Propagation in the Atmosphere*, Proc. SPIE **410**, 179–188 (1983).
53. J. H. Brown, R. E. Good, P. M. Bench, and G. Faucher, "Sonde measurements for comparative measurements of optical turbulence," Air Force Geophysics Laboratory, AFGL-TR-82-0079, ADA118740, NTIS (1982).
54. E. Ryzner and J. A. Bartlo, "Dependence of C_n^2 (C_T^2) in the atmospheric boundary layer on conventional meteorological parameters," Air Force Geophysics Laboratory, AFGL-TR-86-0013 (1986).
55. R. Lynds and J. W. Goad, "Observatory-site reconnaissance," *Pub. of the Astron. Soc. of the Pacific* **96**, 750–766 (1984).
56. R. R. Beland, E. A. Murphy, G. G. Koenig, and P. C. Thomas, "Comparison of horizontal scintillation measurements and models," in *Optical, Infrared, and Millimeter Wave Propagation Engineering*, Proc. SPIE **926**, 44–51 (1988).
57. E. E. Gossard, W. D. Neff, R. J. Zamora, and J. E. Gaynor, "The fine structure of elevated refractive layers: Implications for over-the-horizon propagation and radar sounding systems," *Radio Sci.* **19**, 1523–1533 (1984).
58. S. H. Melfi and D. Whiteman, "Observation of lower atmospheric moisture structure and its evolution using a Raman lidar," *Bull. Am. Meteor. Soc.* **66**, 1288–1292 (1985).
59. T. E. Van Zandt, J. L. Green, K. S. Gage, and W. L. Clark, "Vertical profiles of refractivity turbulence structure constant: Comparison of observations by the Sunset Radar with a new theoretical model," *Radio Sci.* **13**, 819–829 (1978).
60. R. R. Beland and J. H. Brown, "Optical turbulence measurements in jet streams," *Annual Review Conf. on Atmospheric Transmission Models*, June 2–3, 1987, Hanscom AFB, MA (1987).
61. R. R. Beland, J. H. Brown, R. E. Good, and E. A. Murphy, "Optical turbulence characterization of AMOS, 1985," AFGL-TR-88-0153, Air Force Geophysics Laboratory (1988).
62. E. R. Reiter, *Jet Stream Meteorology*, Univ. of Chicago Press, Chicago (1963).
63. F. P. Battles, E. A. Murphy, and J. P. Noonan, "The contribution of atmospheric density to the drop-off rate of C_n^2 ," *Physica Scripta* **37**, 151–153 (1988).
64. J. H. Brown and R. R. Beland, "A site comparison of optical turbulence in the lower stratosphere at night using thermosonde data," *Physica Scripta* **37**, 424–426 (1988).
65. A. N. Kolmogorov, "A refinement of previous hypotheses concerning the local structure of turbulence in a viscous incompressible fluid at high Reynolds number," *J. Fluid Mech.* **13**, 82–85 (1962).
66. E. L. Andreas, "Estimating averaging times for point and path-averaged measurements of turbulence spectra," *J. Appl. Meteor.* **27**, 295–304 (1988).
67. M. G. Miller and P. L. Zieske, "Measurements of the atmospheric correlation scale," *J. Opt. Soc. Am.* **67**, 1680–1685 (1977).
68. M. G. Miller and P. L. Zieske, "Turbulence environment characterization," RADC-79-131, ADA072379, Rome Air Development Center (1979).
69. D. L. Walters, "Atmospheric modulation transfer function for desert and mountain locations: r_0 measurements," *J. Opt. Soc. Am.* **71**, 406–409 (1981).
70. F. D. Eaton, D. M. Garvey, E. Dewan, and R. Beland, "Transverse coherence length (r_0) observations," in *Adaptive Optics*, Proc. SPIE **551**, 42–51 (1985).
71. F. D. Eaton, W. A. Peterson, J. R. Hines, and G. Fernandez, "Isoplanatic angle direct measurements and associated atmospheric conditions," *Appl. Opt.* **24**, 3264–3273 (1985).
72. F. D. Eaton, W. A. Peterson, J. R. Hines, K. R. Peterman, R. E. Good, R. R. Beland, and J. H. Brown, "Comparisons of VHF radar, optical, and temperature fluctuation measurements of C_n^2 , r_0 and θ_0 ," *Theor. Appl. Climatol.* **39**, 17–29 (1988).
73. J. H. Brown and R. E. Good, "Thermosonde C_n^2 measurements in Hawaii—August 1982," AFGL-TR-84-0110, ADA148016, Air Force Geophysics Laboratory (1984).
74. J. H. Brown and R. E. Good, "Thermosonde and UHF radar measurements at Westford, Massachusetts—July 1981," AFGL-TR-84-0109, ADA145398, Air Force Geophysics Laboratory (1984).
75. R. E. Good, R. R. Beland, E. A. Murphy, J. H. Brown, and E. M. Dewan, "Atmospheric models

- of optical turbulence," in *Modeling of the Atmosphere, Proc. SPIE* **928**, 165–186 (1988).
76. J. C. Wyngaard, "On surface layer turbulence," in *Workshop of Micrometeorology*, Chap. 3, pp. 101–149, American Meteorological Society, Boston (1973).
 77. K. E. Kunkel and D. L. Walters, "Modeling the diurnal dependence of the optical refractive index structure parameter," *J. Geophys. Res.* **88**, 10,999–11,004 (1983).
 78. G. C. Holzworth, "Estimates of the mean maximum mixing boundary layer," *Atmos. Environ.* **3**, 519–536 (1969).
 79. G. C. Holzworth, "Mixing depths, wind speeds and air pollution potential for selected locations in the United States," *J. Appl. Meteor.* **6**, 1039–1044 (1967).
 80. C. L. Norton and G. B. Hoidale, "The diurnal variation of mixing height by season over White Sands Missile Range, New Mexico," *Monthly Weather Review*, **104**, 1317–1320 (1976).
 81. V. P. Kukharets and L. R. Tsvang, "Structure parameter of the refractive index in the atmospheric boundary layer," *Izv. Atmos. Oceanic Phys.* **16**, 73–77 (1980).
 82. E. A. Murphy, E. M. Dewan, and S. M. Sheldon, "Daytime comparison of C_n^2 models to measurements in a desert location," in *Adaptive Optics, Proc. SPIE* **551**, 156–162 (1985).
 83. K. E. Kunkel, D. L. Walters, and G. A. Ely, "Behavior of the temperature structure parameter in a desert basin," *J. Appl. Meteor.* **20**, 130–136 (1981).
 84. R. Hufnagel, "Restoration of atmospherically degraded images," Vol. 2 (Woods Hole Summer Study, July 1966), National Academy of Sciences, 806879 (1966).
 85. R. Hufnagel and N. R. Stanley, "Modulation transfer function associated with image transmission through turbulent media," *J. Opt. Soc. Am.* **54**, 52–61 (1964).
 86. P. B. Ulrich, "Hufnagel-Valley profiles for specified values of the coherence length and isoplanatic angle," MA-TN-88-013, W. J. Schafer Associates (1988).
 87. G. C. Valley, "Isoplanatic degradation of tilt correction and short-term imaging systems," *Appl. Opt.* **19**, 574–577 (1980).
 88. T. W. VanZandt, K. S. Gage, and J. M. Warnock, "An improved model for the calculation of profiles of C_n^2 and ϵ in the free atmosphere from background profiles of wind, temperature and humidity," *Proc. 20th Conf. on Radar Meteorology*, Am. Meteor. Soc. (1981).
 89. J. M. Warnock and T. E. VanZandt, "A statistical model to estimate the refractivity turbulence structure constant C_n^2 in the free atmosphere," NOAA Tech. Memo. ERL AL-10, Boulder, CO (1985).
 90. J. M. Warnock, R. R. Beland, J. H. Brown, W. L. Clark, F. D. Eaton, L. D. Favier, K. S. Gage, J. L. Green, W. H. Hatch, J. R. Hines, E. A. Murphy, G. D. Nastrom, W. A. Peterson, and T. E. VanZandt, "Comparison among clear air radar, thermosonde and optical measurements and model estimates of C_n^2 made in very flat terrain over Illinois," *MAP Handbook for Fourth MST Radar Workshop* (1989).
 91. J. L. Green, R. R. Beland, J. H. Brown, W. L. Clark, F. D. Eaton, L. D. Favier, K. S. Gage, W. H. Hatch, J. R. Hines, E. A. Murphy, G. D. Nastrom, W. A. Peterson, T. E. VanZandt, and J. M. Warnock, "Comparisons of refractivity measurements from the flatlands VHF radar with other measurement techniques," *24th Conf. on Radar Meteorology*, Tallahassee, FL, March 27–31, 1989.
 92. C. E. Coulman, J. Vernin, Y. Coqueugnoit, and J. L. Caccia, "Outer scale of turbulence appropriate to modeling refractive-index profiles," *Appl. Opt.* **27**, 155–160 (1988).
 93. J. W. Strohbehn, "Line-of-sight wave propagation through the turbulent atmosphere," *Proc. IEEE* **56**, 1301–1318 (1968).
 94. D. L. Fried and J. B. Seidman, "Laser beam scintillation in the atmosphere," *J. Opt. Soc. Am.* **57**, 181–185 (1967).

CHAPTER 3

Aerodynamic Effects

Keith G. Gilbert*

*BDM International, Inc.
Albuquerque, New Mexico*

L. John Otten III

*Phillips Laboratory
Kirtland Air Force Base, New Mexico*

William C. Rose

*Rose Engineering, Inc.
Incline Village, Nevada*

CONTENTS

3.1	Introduction	235
3.2	Aerodynamic Considerations	237
3.2.1	Boundary Layers	241
3.2.2	Open Cavities and Shear Layers	243
3.3	Optical Considerations	246
3.3.1	Inviscid Flows	247
3.3.2	Shock Waves	249
3.3.3	Random Flows	253
3.4	Aero-Optical Design and Analysis Examples	264
3.4.1	Example 1—Subsonic Imaging Platform: Boundary-Layer Aberrations	264
3.4.2	Example 2—Supersonic Imaging Platform: Boundary-Layer Aberrations	268
3.4.3	Example 3—Optical Degradation Resulting from Open Cavity	269
3.4.4	Example 4—Visible Imager: Selecting the Optimal Wavelength	270
3.4.5	Example 5—Aperture Optimization	271
3.4.6	Example 6—Thermal Noise Resulting from an IR Window	272
3.4.7	Example 7—Supersonic Vehicle Optical Aberrations	274

*Presently with Logicon RDA, Albuquerque, New Mexico.

3.4.8 Example 8—Supersonic Vehicle Flow-Field-Induced Thermal-Radiation Effects	277
3.5 Aero-Optics: Visions and Opportunities	278
References	284

3.1 INTRODUCTION

This chapter discusses the aberrating influences of aerodynamics on optical systems. While the focus is on airborne platforms, the discussions are relevant to all manner of moving transmitting media. Two classes of optical systems will be discussed, those that gather optical information and those that emit photons (optical energy). The physics of interaction with an airflow is the same (for a particular wavelength) whether the beam is incoming or outgoing, coherent or incoherent (in the absence of nonlinear effects). However, the impact of the resulting degradation depends markedly on the application.

Two central issues influence the overall performance of optical systems located in aerodynamic environments. The first is aeromechanical effects. These arise from interactions of the external flow field with the airborne platform. This base motion, in concert with intrinsic platform sources of vibration (e.g., engines, pumps, fluid flow, etc.), defines the overall mechanical jitter environment in which the optical system must operate. Jitter can result in spurious laser beam motion on target and image blurring as well as general misalignments of optical elements. The second major issue influencing airborne optical systems is aero-optical (AO) effects. These are caused by index-of-refraction variations induced by the platform moving through the flow field. This results in reduced far-field peak intensity as well as beam spread and wander for outgoing wave fronts. For imaging systems, these several effects manifest themselves as loss of contrast and resolution. In designing an airborne optical system one seeks first to mitigate mechanical effects, and then addresses aero-optical phenomena.

Optical aberrations resulting from aerodynamic flow fields can be placed in two categories: First, viscous flow phenomena include laminar and turbulent boundary layers, shear layers, and wake turbulence. The second category, inviscid or potential flow, arises from the acceleration of (compressible) fluid, generally along fuselage contours or around protuberances.

For wavelengths ranging from the visible to the mid-IR, flush-mounted material windows generally can be employed to shield the optical components from the external aerodynamic flow field. An exception may occur if a high-power laser is to be transmitted through the window; in this case, thermal-induced distortions or potential damage may preclude its use. If such installations are feasible, then the aeromechanical issue is only associated with the aircraft motion. The resulting aero-optical performance is driven by the aerodynamic flow field that exists over the external portion of the aircraft and window itself. These aerodynamic flow fields, if laminar, tend to be relatively benign and are influenced by the mean flow fields that exist over the aerodynamic contours. However, if the surface boundary layer over the window is turbulent, as is more likely in operational settings, the resulting unsteady air density variations (resulting in unsteady index-of-refraction fields) can yield significant optical aberrations. These platform-induced aero-optical effects are discussed in this chapter.

For long-wavelength IR transmission and reception ($\lambda \geq 10 \mu\text{m}$), a material window becomes much less attractive owing to optical transmission losses and window radiative effects. For such applications, cavities that are open to the surrounding aerodynamic flow field may be used. These cavities may take on

various configurations; however, all are basically openings in the nominal mold line of the aircraft surrounded by bulkheads, floors, or other walls creating the cavity. The aeromechanical environment of such a cavity flow field is potentially debilitating. In addition, the AO flow field can cause a whole range of optical aberrations. The net result is degraded system performance. These aberrations can be severe enough to stifle the mission of interest; effective control of these aberrations is a prerequisite to any optical application.

Our approach offers classes of solutions via three steps:

1. What are the requirements? An optical instrument on an airborne platform either collects or projects optical information. As mentioned earlier, the physics of interaction with an airflow is generally the same (for a particular wavelength) whether the beam is incoming or outgoing, coherent or incoherent. However, the impact of the degradation depends markedly on the application.

In general, the objective for an outgoing laser wave front is to maximize peak irradiance at the target. This is often referred to as "power in the bucket." Applications include lidar, optical meteorology, and weaponry. The net effect of the AO field in all cases is a reduction of intensity at the target.

An incoming wave front is also scattered, absorbed, refracted, and reflected by the AO interface. If the optical system is an imager, an important parameter is the pixel field of view (FOV). In general, rays will be deflected from the intended (unaberrated) focus to adjacent areas on the array. The result is an image that suffers both resolution and contrast losses.

2. Once the requirements are defined, scaling relations will be developed that allow the planner to size and prioritize these several optical aberrations.
3. Finally, we offer several options for ameliorating these AO aberrations. These options include changing optics beam diameter or wavelength, tailoring the flow field, introducing advanced beam control techniques, or postexperiment processing. Sometimes several approaches must be combined.

Random flow fields include turbulent boundary layers and shear layers, the latter being developed at a flow discontinuity (e.g., fuselage protuberance or recession). The optical aberrations impressed on a beam transiting these random flows are determined by three aerodynamic parameters: the field's fluctuating density ρ' , the correlation length along the optical axis ℓ_z , and the total path length through the disturbance L . The predicted wave-front variance σ^2 is given by¹

$$\sigma^2 = 2G^2 \int_0^L \langle \rho'^2 \rangle \ell_z dz, \quad \ell_z \ll L , \quad (3.1)$$

with G being the Gladstone-Dale parameter,² relating medium index of refraction to density fluctuations. Note that the above equation assumes isotropic turbulence. If the condition $\ell_z \ll L$ is not fulfilled, for example, generally in

the case of shear layers,^{1,3} then the above expression overestimates the actual optical aberrations.

Table 3.1 depicts broad AO characteristics of the several germane flow fields. The examples that follow deal with several important elements of this table. Wind tunnels are valuable simulation tools for some facets of an airborne-platform optical system. For example, high-fidelity aeromechanical simulations of turrets and open ports have been accomplished. Less success has been achieved simulating platform-induced optical turbulence effects. This is because wind tunnels tend to have considerable intrinsic turbulence, caused by the flow-generation system, as well as wall boundary layers. This background "noise" can mask model-induced flow fields. Reference 4 details a variety of wind-tunnel experiments. Recently, tunnels have been developed to be "optically quiet." In general, however, tunnels as a simulator of airborne-platform optical turbulence must be approached with considerable caution. In many cases, actual flight testing is more cost-effective.

A variety of AO instrumentation has been developed for both wind-tunnel and airborne-platform testing. Rugged thin-film sensors have been fielded that yield the above three primary aerodynamic parameters of interest. Bandwidths of order 10 to 50 kHz are achievable; however, signal to noise is frequently the dominant design dimension. Standard techniques such as interferometry or holography have been used to infer the integrated-path wave-front variance σ^2 . Careful AO experiments have shown good correlations between the aerodynamic predictions of σ^2 and the actual optical measurements.¹

Section 3.2 discusses the range of aerodynamic phenomena that can affect airborne optical systems. Section 3.3 highlights the optical physics of interaction with these flow fields, including germane scaling relationships. Section 3.4 is a collection of examples that serve as guidelines to the AO analyst or experimentalist. The final section looks to the future; advanced AO beam-control techniques are emerging that may offer a path to near-pristine optical platforms for both outgoing and incoming wave-front systems.

Table 3.2 gives the symbols, nomenclature, and units used in this chapter.

3.2 AERODYNAMIC CONSIDERATIONS

This section discusses the nature of aerodynamic flows that one encounters in an aero-optical situation.

The motion of a simple (Newtonian) flow is characterized by two dimensionless parameters, the Reynolds number Re and the Mach number M , defined by

$$Re = \frac{VW}{v} , \quad (3.2)$$

$$M = \frac{V}{a} ,$$

where

V = fluid velocity

W = size of flow pattern

v = kinematic viscosity

a = velocity of sound.

Table 3.1 Aero-Optical Effects in Three Mach Number Regimes*

AO Phenomena	$M < 0.3$	$0.3 < M < 8$	$M > 8$
Boundary layers/ shear layers Mixing layers (e.g., open cavities)	<ul style="list-style-type: none"> Incompressible flow regime Natural AO effects negligible (injection of thermal energy can yield strong optical aberrations) Calculate properties via classical fluid mechanics 	<ul style="list-style-type: none"> Compressibility flow regime Perfect gas law valid Random flow phase variance $\sigma^2 = 2G^2 \int_0^L \langle \rho'^2 \rangle \ell_z dz,$ $(\ell_z \ll L)$ <p>G = Gladstone-Dale parameter $\langle \rho'^2 \rangle$ = fluctuating density variance ℓ_z = flow correlation length along optical axis L = path length through flow field</p> <ul style="list-style-type: none"> In weak-aberration regime ($\sigma/\lambda < 1/\pi$) Strehl $S \propto \exp^{-(K\sigma)^2}$, $K \equiv 2\pi/\lambda$ Resolution loss $\theta_B \propto \theta_D/S^{1/2}$ In strong-aberration regime ($\sigma/\lambda \gg 1/\pi$) Strehl $S \propto (\ell_z/\sigma)^2$ Resolution loss $\theta_B \propto \sigma/\ell_z$ Nominal aberration compensation bandwidth requirements > 10 kHz Thermal control of windows may be essential 	<ul style="list-style-type: none"> Perfect gas law invalid Chemistry of air important Ionization/plasma causes beam reflection/refraction/absorption and radiation effects; longer wavelength degraded more Radiated sound intensity scales strongly with velocity, probably effects turbulent field Thermal control of optical windows essential Flow reradiation effects can contribute significantly to sensor background noise
Inviscid flow/ shocks	<ul style="list-style-type: none"> Negligible effects 	<ul style="list-style-type: none"> Boresite error, defocus Correctable via low-order adaptive optics unless angle of attack varying rapidly Phase error scales as $\Delta\phi \propto KG \int_0^L \rho' dz$ <ul style="list-style-type: none"> Shock strength is function of adiabatic index, Mach number, and shock angle Flow reradiation energy can cause sensor thermal noise 	<ul style="list-style-type: none"> Inviscid field strength scales as $\phi \propto \rho'/R$ (R = flow-field radius curvature) Shock-induced ionization/plasma formation degrades wave front

*AO effects can be partitioned into three Mach-number regimes. Below Mach 0.3 the (incompressible) flow generally yields small optical distortion. Between Mach 0.3 and ~ 8 a host of flow fields impress optical aberrations on both incoming and outgoing wave fronts. Additional aberrations arise beyond Mach 8 owing to ionization and acoustical radiation effects. Optical degradations in these latter two regimes may stifle mission objectives if mitigation procedures are not implemented.

Table 3.2 Symbols, Nomenclature, and Units

Symbol	Nomenclature	Units
a	Velocity of sound	cm/s
A_c	Area collector	cm ²
A_d	Area detector	cm ²
C_w	Heat capacity window	J g ⁻¹ K ⁻¹
C_ϕ	Phase correlation function	—
C_{1,C_2}	Thermal-radiation constants	—
D	Exit aperture diameter	cm
f	MTF shear frequency	—
F	Focal length	cm
F^*, F_M	Performance figures of merit	—
G	Gladstone-Dale parameter	cm ³ /g
h	Heat-transfer coefficient	W cm ⁻² K ⁻²
H	Cavity depth . . . edge to first optical surface	cm
I_0	Peak far-field intensity in absence of AO aberration (aka irradiance)	W/cm ²
I	Peak far-field intensity in presence of AO aberration	W/cm ²
K	Wave number	cm ⁻¹
K_w	Thermal-conductivity window	W cm ⁻¹ K ⁻¹
L	Optical path length through disturbance	cm
L^*	Radiance	W cm ⁻² sr ⁻¹
ℓ_z	Correlation length along optical axis	cm
ℓ_x, ℓ_y	Correlation lengths along orthogonal axes in beam plane	cm
ℓ	General flow correlation length	cm
M^*, M^*	MTF	—
M, M_0, M_a, M_b	Mach number	—
M_λ	Spectral exitance	W cm ⁻² μm ⁻¹
n^*	Intrinsic quality of system optics	—
n'	Fluctuating index of refraction	—
n	Optical index of refraction in disturbance	—
n_0	Optical index of refraction in ambient medium	—
P^*	Power	W
p	Percentage energy within blur circle	—
PSF	Point spread function	—
Q	Thermal-radiance figure of merit (FOM)	cm
Q_w, Q_s, Q_r	Thermal-radiance FOM for window, shock, random flow	cm
q	Aerodynamic heat transfer	W/cm ²
R_0	Ratio of window radiances for two temperatures	W/cm ²
R_T	Ratio of total airflow radiation to window radiation	—
R^*	Radius curvature of protuberance or flow field	cm
R^+	Image plane spatial frequency	cm ⁻¹
R	Optical reflectivity, also radius	—, cm
Re	Reynolds number	—
r	Recovery factor, radius of focal-plane spot	—, cm
RSS	Root sum square	—
R_p	Reflectivity parallel to plane of incidence	—
R_s	Reflectivity perpendicular to plane of incidence	—
S	System Strehl ($S = I/I_0$)	—
s	Spot-size diameter	cm
T_0	Free-stream temperature	K
T'	Fluctuating temperature	K
T	Temperature at point within flow, mean temperature	K
ΔT	Temperature difference	K
T_R	Random flow radiation temperature	K
T_w, T_0	Window temperature, wall adiabatic temperature	K
T_s	Shock temperature	K
t	time	s
T_i	Initial window temperature	K
T_c	Coolant temperature	K
V	Fluid velocity	cm/s
W	Size of flow pattern	cm
X	Distance along flow from platform leading edge	m
Y	Distance across flow	cm

(continued)

Table 3.2 (continued)

Symbol	Nomenclature	Units
Z	Distance along optical axis	cm
ΔZ	Thickness of aberrating element	cm
β_0, β	Angles of incidence, refraction of light rays at AO interface	deg
γ	Adiabatic index ~ 1.4 (air)	—
γ^*	Strehl for particular AO component	—
ϵ	Emissivity	—
$\epsilon_w, \epsilon_s, \epsilon_R$	Window, shock, random flow emissivities	—
θ	Shock angle, also angular station	deg
θ_T	Total system jitter	μrad
θ_L	Laser optical jitter	μrad
θ_P	Platform mechanical jitter	μrad
θ_{AO}	Aero-optical jitter	μrad
θ_A	Natural atmospheric jitter	μrad
θ_D	Diffraction angle for optical system for 84% circular energy distribution circular aperture $\theta_D \sim 2.4 \lambda/D$	μrad
θ_B	Blur angle in presence of AO aberration (84% energy)	μrad
θ_s	Characteristic random flow scattering angle	μrad
λ	Wavelength	$\mu\text{m}(10^{-4} \text{ cm})$
λ^*	Optimal wavelength: best performance for given random flow field	μm
\bar{z}	Mean wavelength	μm
ν	Kinematic viscosity	cm^2/s
ξ	Characteristic width of PSF	cm
ρ_0	Free-stream density	g/cm^3
ρ_a, ρ_b	Flow-field density at particular point, mean flow density, window density	g/cm^3
$\langle \rho'^2 \rangle$	Variance of fluctuating density	$(\text{g}/\text{cm}^3)^2$
ρ'	Fluctuating density ($\rho' = \langle \rho'^2 \rangle^{1/2}$)	g/cm^3 or kg/m^3
ρ_w	Airflow density at wall	g/cm^3
σ^2	Optical phase variance	cm^2
σ_{SB}	Stefan-Boltzmann constant	$\text{W cm}^{-2} \text{ K}^{-4}$
τ	Transmission efficiency of optical system	—
τ_w	Window heating time constant	s
Φ	Phase aberration ($\Phi = 2\pi\sigma/\lambda$)	—
ϕ_0^2	Phase variance of optics	—
ϕ'	Optical waves of distortion across an aperture	—
Ω	Sensor FOV half-angle	rad

The complexity of the AO field for an airborne optical system increases with both M and Re . For very low flow velocities, compressibility effects are negligible; unless thermal energy is artificially introduced there is little optical aberration. As M increases beyond about 0.3, compressibility effects become important. The flow velocity must, of course, be zero at the wall (airborne-platform surface), and increase away from the wall to the free-stream velocity. The ensuing acceleration yields rotational flow near the surface, leading to either steady or unsteady density variations.

The flow is heated as it is compressed and accelerated from free-stream velocity to stagnation at the wall. Assuming an adiabatic process, we can approximate this heating by⁵

$$T_w = bT_0 \left[1 + r \frac{(\gamma - 1)}{2} M_0^2 \right], \quad (3.3)$$

where

T_w = adiabatic wall temperature

T_0 = free-stream temperature

M_0 = free-stream Mach number

r = recovery parameter ($r = 0.85$ laminar, 0.89 turbulent)

γ = adiabatic index, the ratio of the specific heat at constant pressure to that at constant volume; for most AO conditions of interest, $\gamma \approx 1.4$ (air)

b = a constant reflecting real gas effects; for Mach numbers below about 6, $b \approx 1.0$; for $M_0 > 8$, $b \approx 0.5$.

As M_0 continues to increase, the fluid temperature and velocity changes induce increasing density changes. From Eq. (3.1) we note this yields even greater optical aberrations. Further increases to transonic flow lead to local supersonic-flow regimes in which shocks appear, causing additional reflection and refraction effects. In the supersonic regime (Mach 1 to 8) the high stagnation temperatures can cause thermo-optical window distortions. In some cases a window coolant is essential. Above Mach 8, dissociation and ionization result from the heating of the gas. These plasmas introduce another level of optical distortion, with particularly strong vibrational absorption bands. In this hypersonic regime, strong coupling between acoustical and turbulence fields occurs. Because the radiated acoustical power scales very strongly with M , it may even dominate above some critical Mach number. We next examine the several platform-induced aerodynamic flow fields of interest to airborne optical systems.

3.2.1 Boundary Layers

Boundary layer flows are described here as attached-wall viscous layers that naturally occur over aerodynamic surfaces due to the nonslip velocity condition at the wall. These boundary layers can be either laminar or turbulent.

Laminar Boundary Layers. Laminar boundary layers exhibit well-behaved, steady flow in which fluid particles in the boundary layer slide smoothly past one another. As a result of accelerating the gas from the flight velocity to zero at the surface of the aircraft, the mean temperature varies throughout the boundary layer. For most boundary-layer flows the static pressure remains constant throughout the layer, thus giving rise to a variation in density throughout the boundary layer. For laminar boundary layers, the density variation is smooth; these idealized flow fields usually cause little optical degradation. Exceptions exist if there is external heating or cooling of the flow; both situations can result in significant system optical aberrations.

Also, in the presence of accelerating flows (such as those occurring on platform external protuberances) inviscid lensing effects occur. These generally result in weak optical aberrations of low order (e.g., focus, tilt, astigmatism). Only limited subsonic experimental investigations of such effects have been described.⁴ Computational fluid dynamics is the best tool today for estimating the strength of these inviscid flow fields.

Turbulent Boundary Layers. Turbulent boundary layers differ from laminar boundary layers in that the orderly sliding of the fluid layers past one another exhibited in laminar flow breaks down and the process becomes chaotic, although the chaos is known to be statistically definite. Scaling relations have been developed for turbulent boundary-layer flow [e.g., Eq. (3.1)] that estimate

their adverse effects on optical performance. In general, a boundary layer becomes turbulent under actual flight conditions for Reynolds numbers Re in the range 10^5 to 5×10^5 (Ref. 6).

The physics of turbulent boundary layers are extremely complicated and poorly understood considering that research has been ongoing for nearly a hundred years. Turbulent boundary layers exist adjacent to aerodynamic surfaces at nominal operating altitudes and Mach numbers in the atmosphere.^{4,7–10} Turbulence can be visualized as a collection of "turbules" of varying scale sizes and differing indices of refraction. These random flows impress wave-front aberrations on transiting optical radiation. The turbulence consists of scale sizes that span a spectrum from several times the local thickness of the boundary layer to less than $\frac{1}{10}$ of 1% of the local thickness. Scale lengths vary in magnitude throughout the layer, but are generally assumed to be characterized by ℓ_z , a representative correlation length of the density fluctuation (optical disturbance). For attached, fully developed subsonic turbulent boundary layers the scale size is of order 10% of the local boundary-layer thickness. In terms of Eq. (3.1), the boundary layer thickness is L and $\ell_z \approx 0.10L$ (Ref. 4). The turbulent boundary-layer thickness itself grows as the distance along the body (streamwise) to the 0.8 power.¹² A sketch of an attached boundary layer is shown in Fig. 3.1. Here, L is approximately equal to $0.015X$, where X is the flow distance from the platform leading edge to the optical station. For optical installations located near the nose of an aerodynamic configuration, X is relatively small, while for installations near the aft portion of the installation, X can be fairly large. For transport-class aircraft the boundary-layer thickness can vary from about 10 to 50 cm at useful optical locations. As a general rule, to reduce the total boundary-layer path length one should be further forward on the aerodynamic installation. The remaining aerodynamic parameter that is required to yield an estimate of optical phase variance through the random flow [Eq. (3.1)] is the unsteady density ρ' .

Extensive aerodynamic research reveals that the magnitude of the density fluctuations in a turbulent boundary layer is driven by the difference between the density at the wall ρ_w and the free-stream density ρ_0 (Ref. 4). Again, this density difference is due to the increased temperature and velocity fluctuations resulting from flow acceleration within the boundary layer. The density at the

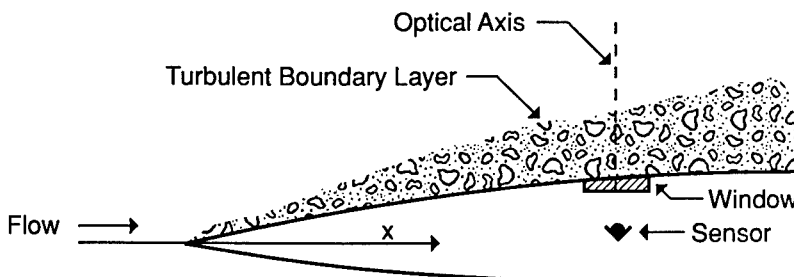


Fig. 3.1 An airborne-platform attached turbulent boundary layer forms near the leading edge and grows in this region as $L \approx X^{0.8}$, where X is the distance from the leading edge. Density fluctuation scale sizes along the optical axis vary from the viscosity limit (approx. a few mm) to the TBL thickness; typical values are 10% of the thickness. (In the examples we will make the conservative assumption that $L \propto X$.)

wall in the regime of no shock waves and assuming zero pressure gradient across the boundary layer is

$$\rho_w = \rho_0 \left[1 + r \left(\frac{\gamma - 1}{2} \right) M_0^2 \right]^{-1}. \quad (3.4)$$

For purposes of making fluctuating density estimates, the density variation for a turbulent boundary layer may be assumed to occur in a fashion such that a peak density fluctuation occurs halfway through the turbulent boundary layer and has an average magnitude of about 10% of the difference between the wall and free-stream densities. This produces a triangular-like fluctuating density profile; generally, a weighted mean value is used to estimate the optical losses. Herein we adopt the conservative approach of selecting as this characteristic fluctuating density the peak value in the flow.

3.2.2 Open Cavities and Shear Layers

Shear layers develop when the wall beneath the boundary layer is removed, whether via an open cavity or a fuselage recession. Shear layers also can occur on the downstream side of a turret or cylindrical protuberance from an aircraft. Shear layers are inherently more optically degrading than attached boundary layers. Moreover, they can drive severe acoustical effects within open cavity geometries.

Material windows can serve two important functions on an optical airborne platform: First, they insulate the optical train from the relatively hostile external aero-optical environment. Second, if the window is fuselage-flush mounted, it provides a more predictable flow over the optical aperture. However, windows can have considerable disadvantages, particularly for IR optical systems, including (1) poor transmission properties, particularly for wavelengths beyond 10 μm , (2) optical aberrations, either intrinsic or environmentally induced (e.g., pressure or thermally driven), and (3) strong thermal radiation (IR emissions) within the instrument bandpass.

An alternative to a material window is an open cavity, which interacts with external flow around the aircraft. The most profound aerodynamic phenomenon that exists over an open cavity at moderate and transonic flow speeds is known as cavity resonance. This is usually defined as the presence of ordered, single-frequency pressure variations within the confines of the cavity. If uncontrolled, these pressure fluctuations can cause unwanted vibrations of the optical components located within the cavity. Both this and the resulting cavity turbulence cause degradation of the overall optical performance. In addition, the structural implications of an uncontrolled cavity resonance are potentially harmful and must be avoided at all costs.

A sequence of events occurs in an uncontrolled cavity that produces resonance (Fig. 3.2). Flow is assumed to exist from left to right over a cross section of a cavity. In general, a shear layer forms at the leading edge of the cavity. This shear layer expands and interacts with the superimposed natural fuselage boundary layer as well as the cavity flow field. Wind-tunnel and airborne-platform experiments^{4,8} suggest the thickness L of a free shear layer is approximately $L = 0.25X$, with X being the distance downstream from the for-

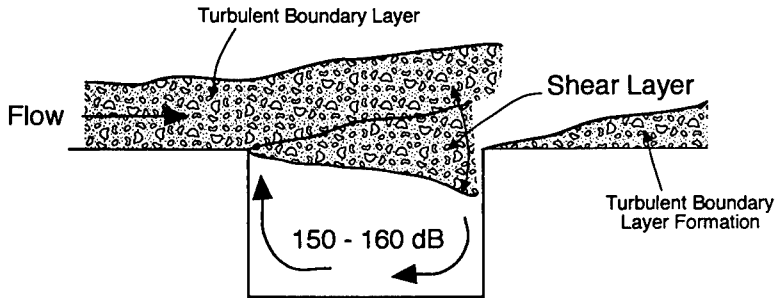


Fig. 3.2 A shear layer (SL) forms at the leading edge of an airborne-platform cavity. The Bernoulli effect results in air being drawn from the cavity into the SL, with an attendant cavity pressure drop. This pulls the SL inward, increasing cavity pressure, which then pushes the SL outward, etc. The resulting cavity sound level can be very high (~160 dB) for large subsonic aircraft at nominal operating conditions. If not attenuated, these can cause severe airframe and optical-train vibrations. Mitigation procedures seek to "feed" the SL smoothly.

mation point. Correlation lengths along the optical axis ℓ_z are about 20% of L (Ref. 8). The corresponding unsteady density ρ' is now about 20% of the difference between cavity and free-stream density.⁸ The resulting optical degradation through this composite of random flow fields is usually greater than that due to the natural boundary layer. Without any forward treatment, such as a porous fence, historically used to eliminate cavity resonance, the shear layer has an entrainment requirement that "pumps" the cavity, reducing its pressure relative to the pressure outside of the cavity. The pressure drop that results produces an imbalance in the pressure and the shear layer is deflected into the cavity, as shown in the central region of the sketch. Because of the higher pressures contained in the shear layer, the pressure increases within the cavity, eventually becoming higher than that which exists outside of the shear layer. This forces the shear layer back outside the cavity. The resulting fluttering of the shear layer results from a strong coupling between the external flow field, the shear layer, and the intracavity aerothermal flow fields. If not mitigated, it can cause severe degradation to both the airborne platform and the onboard optical systems.

Resonance is controlled by feeding the shear layer smoothly. This can be done in many ways. Details of the cavity and flow, such as cavity volume relative to the area of the aperture, the velocities at which the gases are flowing, and so forth, are important but not particularly critical to the general concept of cavity resonance suppression.

The classical suppression technique is the placement of a porous fence upstream of the aperture on the cavity, as shown in Fig. 3.3 (Ref. 11). This porous fence has two primary functions that control cavity resonance. First, the positioning of the fence displaces the shear layer away from the surface such that the reattachment point of the shear layer exists well downstream of the aft bulkhead (or junction of the bulkhead and the fuselage). The second function of the fence is to provide air (through the openings in the fence) at relatively low velocities to feed the shear layer from below, thus reducing the requirement of entraining cavity air.

Two aerodynamic and one optical difficulty are associated with porous fences. First, the shear layer has no fixed attachment point on the downstream fu-

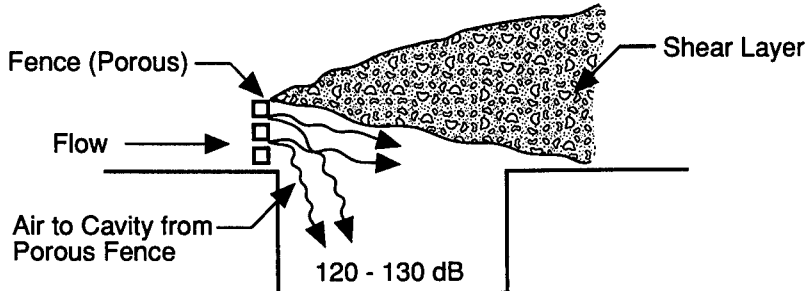


Fig. 3.3 Insertion of a porous fence near the leading edge of an airborne-platform cavity acts to quiesce acoustical resonance by both moving the shear layer away from the cavity and providing air to feed the SL. However, this SL has no fixed downstream attachment point. The resulting cavity sound levels are typically 30 dB below no-fence configurations (e.g., 130 dB versus 160 dB for large subsonic aircraft). A porous fence is the classical cavity acoustical suppression technique.

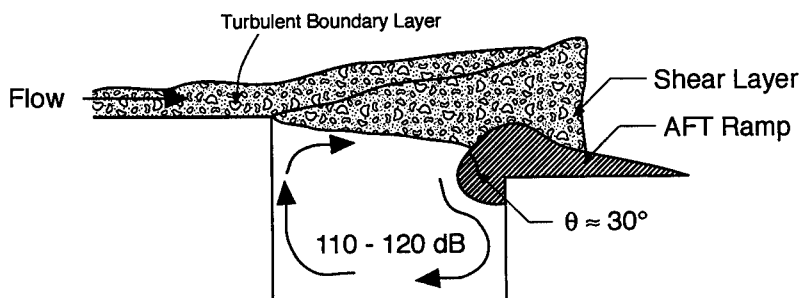


Fig. 3.4 A passive aft ramp provides the best-known solution for attenuating airborne-platform-cavity acoustical resonances. No forward fence is required. The ramp fixes the shear-layer attachment as well as balancing the cavity-entrained air flow. Resulting cavity sound-pressure levels are usually in the range 110 to 120 dB for large subsonic aircraft. These levels are generally lower than (natural) attached random flow-field pressure fluctuations, and form a low-noise environment for optical-train components. Recent wind-tunnel tests confirm these results.

selage, and thus wanders about, producing random, unwanted pressure fluctuations, even though they are of much lower magnitudes than the resonating cavity. Second, some entrainment does occur near the aft edge of the aperture. Both of these lead to overall (unwanted) pressure fluctuations. Optically, the fence does work on the flow, resulting in higher fluctuating densities, with attendant stronger optical aberrations.

More recently, passive designs involving little or no upstream treatment have been demonstrated. One such device is a passive aft ramp developed by the Boeing Aerospace Corporation for use in the Airborne Optical Adjunct (AOA) aircraft.¹³ A sketch of a passive aft ramp appears in Fig. 3.4, showing the two primary constituents of a successful aft ramp. The first is a forward sloping (approximately 30 deg) section that fixes the attachment point of the shear layer. The second is a relatively large bullnose located below and tangent to the aft ramp. This latter feature allows the required entrainment to occur smoothly.

Whether or not treatment to eliminate resonance is required depends strongly on the ratio of the upstream boundary-layer thickness to the streamwise length

of the aperture. For a boundary layer with thickness greater than or equal to the aperture streamwise length, no cavity resonance suppression methodology is usually employed since these cavities are isolated from the external stream owing to the very thick boundary layer. On the other hand, when the streamwise length of the cavity begins to increase, some control is necessary. The passive aft ramp concept has been demonstrated for cases where the streamwise opening is up to 20 times that of the initial boundary-layer thickness. Usually these aft ramps are intrusive to some extent, so that the clear aperture may be slightly limited; however, design methodology for the passive aft ramp system is well understood.^{14–16}

The measures of aerodynamic goodness for cavity resonance suppression can be expressed in terms of the overall sound-pressure level. At operating altitudes for large subsonic transport aircraft, cavity resonance can produce overall levels as high as 160 dB. A fence is capable of controlling the resonance and reducing the background random-pressure fluctuation to around 120 to 130 dB. For the case of the passive aft ramp, pressure levels can further be reduced to the range of around 110 to 120 dB. These levels are generally very acceptable for the placement of optical components within open cavities. Quieted cavity sound levels can be (and in fact are typically) lower than the turbulent boundary-layer pressure fluctuations that exist on the fuselage of a normal, attached turbulent boundary layer in flight.

As always, once the aeromechanical issues of cavity resonance have been addressed and an acceptable antiresonance system has been put in place, the optical performance of any observation or projection system located within the open port is of interest. The general nature of these optical aberrations is discussed in the following section.

3.3 OPTICAL CONSIDERATIONS

Airborne-platform flow fields can induce a variety of AO effects. Figure 3.5 depicts the several flow-field components that an airborne platform can generate. These can result in three classes of optical aberrations at the sensor: Strehl loss, beam spread, and beam tilt (Fig. 3.6). The Strehl ratio is an important measure of beam quality at a focal plane. This is defined as the ratio of peak intensity of the aberrated beam to that of the unaberrated beam. A general focal-plane image can be described by a composite of these effects.

The physics of optical interaction with platform-induced flow field is identical for incoming and outgoing wave fronts. However, the effects of the resulting aberrations on these two classes of optical systems generally differ. The principal figure of merit for an outgoing focused wave front is usually Strehl or power-in-the-bucket, the latter being the amount of power concentrated within a given target area. Interaction of the beam with the platform random flow in the near field can result in scattering outside the “bucket.” This energy is lost to the system.

Next, consider an incoming wave front interacting with the same flow field and then focused on an imaging sensor. Because the turbulence is close to the sensor, energy can be scattered within the detector field of view. Photons are thus deflected to pixels peripheral to those that would capture a diffraction-limited image. The resulting blurred image has both contrast and resolution loss.

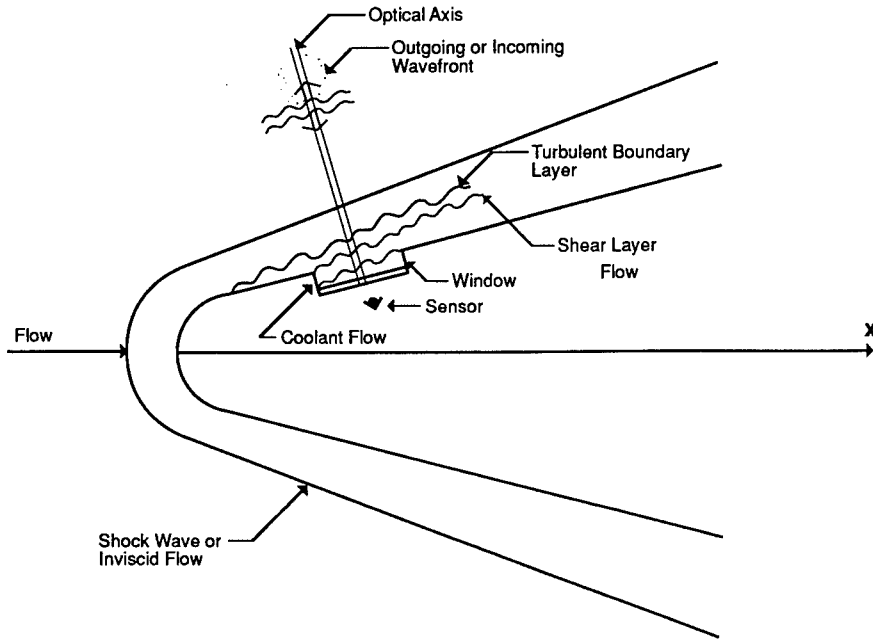


Fig. 3.5 General flow-field components induced by an airborne platform. Each results in a unique aberration impressed on both outgoing and incoming wave fronts. Major components include inviscid flow and shock waves as well as random phenomena such as shear layers and turbulent boundary layers. In addition, thermal control of the sensor window may yield significant optical aberrations if a layer of liquid or cooled gas is flowed over this window. In the hypersonic domain ($>$ Mach 8), ionization and plasma effects can cause further wave-front distortions.

3.3.1 Inviscid Flows

The density variations arising from inviscid flow fields result when compressible fluid is accelerated. An example is an airborne-platform optical turret. Streamlines of smoothly varying density establish an index-of-refraction field via the Gladstone-Dale relationship:

$$n' = G\rho', \quad (3.5)$$

where n' is the index of refraction (fluctuation) variation, ρ' is the density fluctuation, and G is the Gladstone-Dale parameter. The density ratio from one streamline to another in the absence of shock waves is given by

$$\frac{\rho_b}{\rho_a} = \left\{ \frac{1 + [(\gamma - 1)/2]M_a^2}{1 + [(\gamma - 1)/2]M_b^2} \right\}^{\frac{1}{\gamma-1}}. \quad (3.6)$$

The corresponding optical phase $\Delta\phi$ is found by integrating $\rho' \equiv |\rho_a - \rho_b|$ through the disturbance in the z (optical axis) direction:

$$\Delta\phi = KG \int_0^L \rho' dz, \quad (3.7)$$

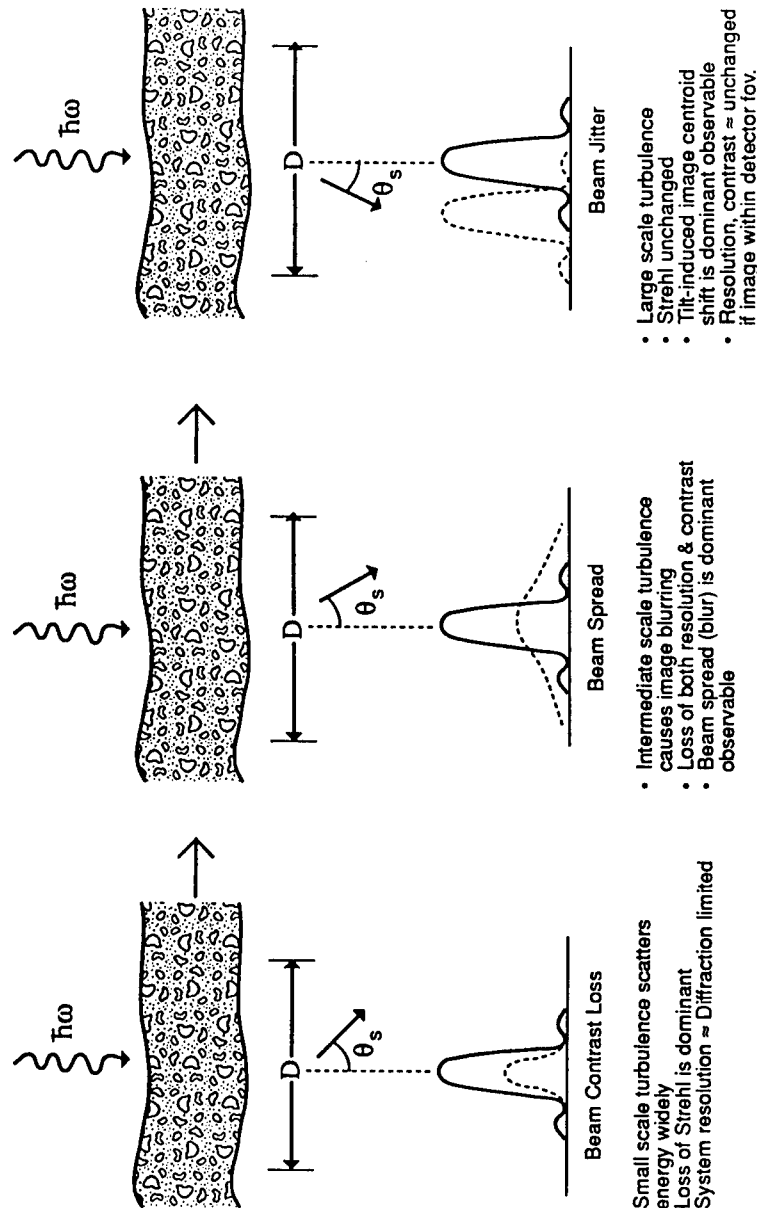


Fig. 3.6 The three principal optical distortions due to airborne-platform flow fields are Strehl loss, beam spread, and jitter. The general far-field pattern is a composite of these aero-optical effects.

- Small scale turbulence scatters energy widely
- Loss of Strehl is dominant
- System resolution \approx Diffraction limited
- Intermediate scale turbulence causes image blurring
- Loss of both resolution & contrast
- Beam spread (blur) is dominant observable
- Large scale turbulence
 - Strehl unchanged
 - Tilt-induced image centroid shift is dominant observable
 - Resolution, contrast \approx unchanged if image within detector fov.

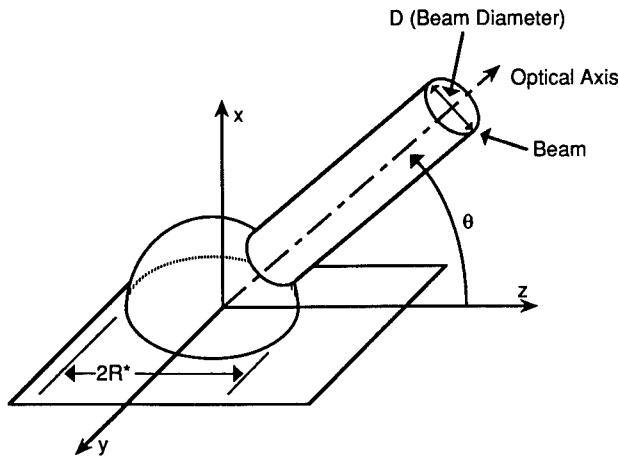


Fig. 3.7 The inviscid flow field established by an airborne-platform optical turret typically yields low-order optical aberrations. This example shows a beam diameter D emerging from a hemispheric bubble of radius R^* .

where $K = 2\pi/\lambda$ (wave number), λ is the optical wavelength, and L is the path length through the disturbance. The phase map is developed by calculating ϕ' for a grid of (x, y) values within the optical aperture. In general, the inviscid aberration field results in low-order aberrations (e.g., focus, tilt, astigmatism).

Simple geometries yield analytical solutions. For example, consider a hemispherical turret having radius R^* and beam diameter D (Fig. 3.7). Then for a Mach number less than the critical value ($M < 0.59$), the magnitude of the inviscid-field-induced focal length F is approximately⁴

$$F = \frac{D^2}{4\lambda\phi'} , \quad (3.8)$$

where λ is the wavelength and ϕ' is the number of waves of distortion across the aperture. In general, if the beam exits at the windward side of the aperture, the air is compressed and ϕ' is positive (beam focus). If the beam is on the leeward side, the flow expands and ϕ' is negative (beam defocus). For a fixed wavelength, scaling follows the general relationship $\phi' \propto \rho'D$. The optical beam must compensate for this aerodynamic lensing; otherwise, beam quality at the focal plane will be degraded.

More complex optical turret geometries require computational fluid dynamics to estimate inviscid field effects. Reference 4 details further analytical and experimental investigations of inviscid flow fields.

Finally, actual aircraft optical turrets have separated flows in the aft zone, for example, azimuthal look angles exceeding about 100 deg. The above equations do not apply in these separated regimes.

3.3.2 Shock Waves

Shock waves develop and intensify as the vehicle accelerates across the transonic into the supersonic regime. Shocks have widths on the order of several kinetic mean free paths, generally many optical wavelengths. Thus, this flow field both refracts and reflects the transmitted beam. Strong shocks can also

cause thermally induced ionization, resulting in additional optical reflection, refraction, and absorption effects. Shocks usually cause low-order aberrations similar to inviscid flows. The strength of the shock (i.e., the density difference across the shock) increases with Mach number. Both shock and inviscid flow fields are dependent on vehicle angle of attack as well as Mach number and the geometry of the body. Blunt bodies have shocks standing some distance ahead of the body; other bodies for moderate angles of attack can have these shock waves attached to the leading edge. In the case of a rapidly maneuvering vehicle these flow-field-induced aberrations can vary markedly with time.

The relationship between the densities ahead (ρ_0) and behind (ρ) the shock is⁵

$$\frac{\rho}{\rho_0} = \frac{(\gamma + 1)M_0^2 \sin^2\theta}{(\gamma - 1)M_0^2 \sin^2\theta + 2}, \quad (3.9)$$

where θ is the shock angle at the optical axis. In general, θ is a complex function of body shape, angle of attack, and Mach number. No analytical scaling relationships have been developed for estimating this shock angle; however, computational fluid dynamics can yield useful approximations. Figure 3.8 shows representative curves for both conical and wedge flow.⁶ Note that in air at the strong shock limit (i.e., large Mach number), $\rho/\rho_0 \rightarrow 6$.

Tracking Error. A shock wave is usually nonorthogonal with respect to the optical axis and so causes both reflection and refraction. Figure 3.9(a) shows an incoming light ray interacting with a shock wave. From Snell's law, the refractive effects can be described by

$$\sin\beta = \sin\beta_0 \left(\frac{1 + G\rho_0}{1 + G\rho} \right), \quad (3.10)$$

where ρ/ρ_0 follows from Eq. (3.9) and $\beta - \beta_0$ is the (apparent) angular shift in target position. Figure 3.9(b) shows this angular offset for various density ratios and two altitudes. Note that for a given condition, the angular deviation magnitude scales with ambient density (altitude).

This refractive effect is a particularly serious problem for a centroid tracking optical system on a supersonic platform. The refraction resulting from the shock effects discussed above, if not sensed by the control system, can cause appreciable tracking offset! A possible approach is incorporation of a predictive offset algorithm.

Focal Length Variations. We next estimate the change in focal length due to optical wave-front refraction by a conical shock. This curved shock acts as an aerodynamic lens and tends to focus light in one plane. The effective focal

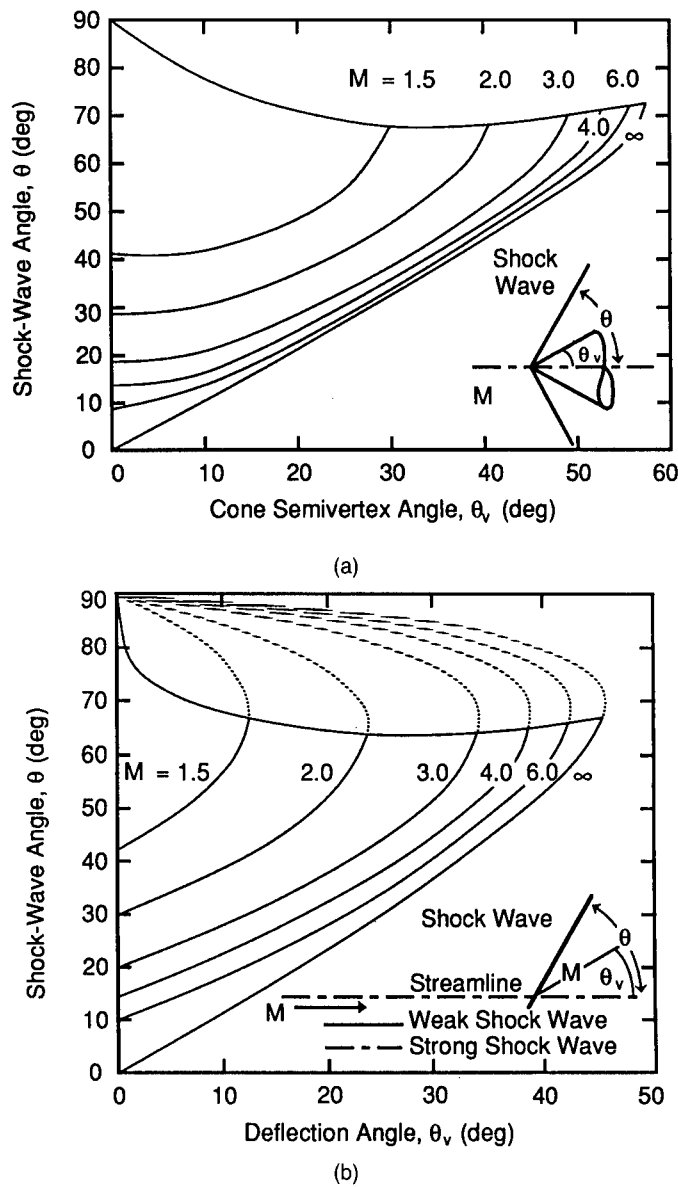


Fig. 3.8 (a) Shock-wave angle for conical flow. (b) Shock-wave angle for wedge flow.

length F of this shock in the plane perpendicular to the airframe longitudinal axis is⁶

$$\frac{F}{X} = \frac{n \tan \theta}{n - n_0}, \quad (3.11)$$

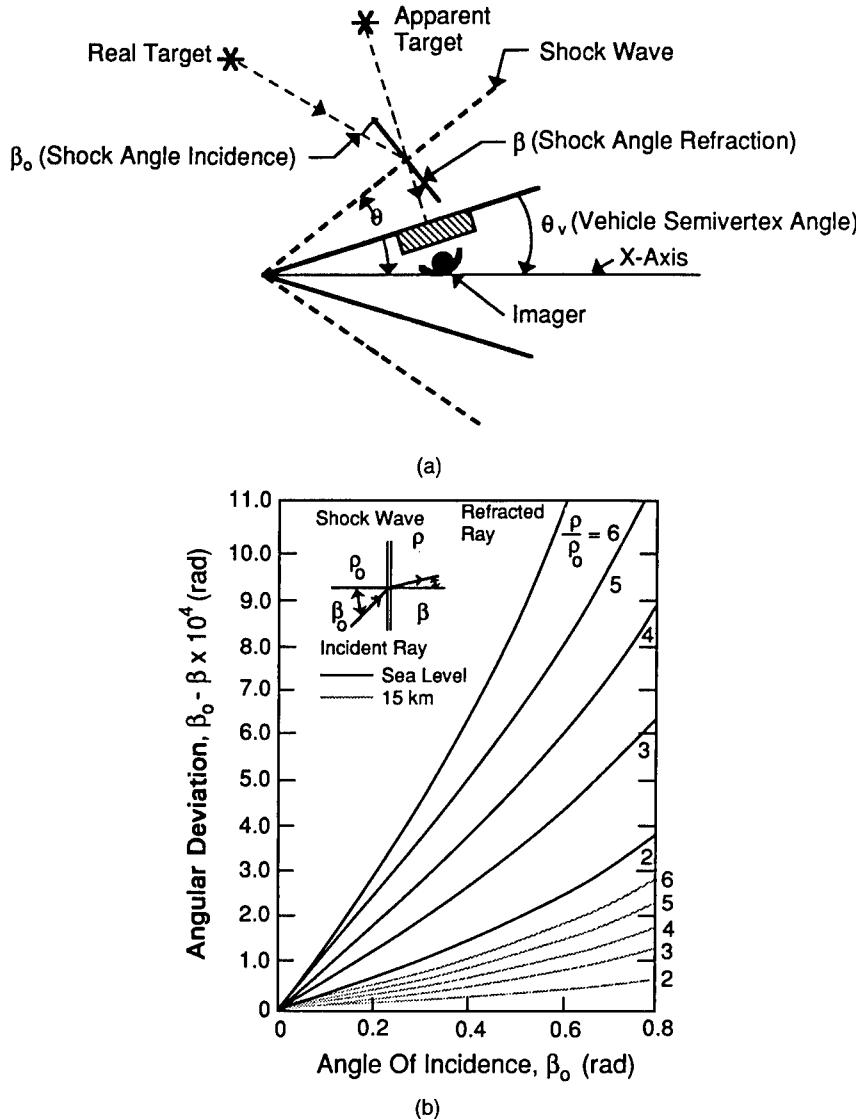


Fig. 3.9 (a) An airborne-platform shock wave causes both reflection and refraction of a transmitting wave front. In general, the reflected component is negligible ($R < 10^{-6}$); however, the refracted component can cause significant (centroid) tracking and focus errors. (b) Angular deviation of optical radiation passing through plane shock waves. Results are approximately invariant with wavelength for $\lambda > 0.5 \mu\text{m}$.

where X is the axial distance from the cone tip to the axis and θ is the shock angle. Substituting the Gladstone-Dale relation [Eq. (3.5)] and using Eq. (3.9) (assume $\gamma = 1.4$ for air) yields ($n_0 = 1$)

$$\frac{F}{X} = \left[\frac{M_0^2 \sin^2 \theta (1 + 6Gp_0) + 5}{6Gp_0 M_0^2 \sin^2 \theta} \right] \tan \theta . \quad (3.12)$$

Optical Reflections at Shock Interface. Finally, it is important to bound the reflected component of a wave front from a shock. In general, suppose light

with an angle of incidence β_0 passes from a medium of index n_0 to a medium n , where β is the refracted angle in that medium. Then the reflecting components for incident light with electric vectors parallel to (R_p) and perpendicular to (R_s) the plane of incidence are¹⁷

$$R_p = \left[\frac{(n/\cos\beta) - (n_0/\cos\beta_0)}{(n/\cos\beta) + (n_0/\cos\beta_0)} \right]^2, \quad R_s = \left(\frac{n \cos\beta - n_0 \cos\beta_0}{n \cos\beta + n_0 \cos\beta_0} \right)^2. \quad (3.13)$$

For normal incidence ($\beta_0 = \beta = 0$ deg) and unpolarized light,

$$R \equiv \frac{1}{2}(R_p + R_s) = \left(\frac{n - n_0}{n + n_0} \right)^2. \quad (3.14)$$

Substituting for density via the Gladstone-Dale relation into Eq. (3.14) (assuming $n_0 = 1$), we find

$$R = \left(\frac{G\rho}{G\rho + 2} \right)^2, \quad (3.15)$$

where ρ follows from Eq. (3.9). A maximum reflectivity is obtained for the case of a strong shock ($\rho/\rho_0 = 6$) at sea level ($\rho_0 = 1.22 \times 10^{-3}$ g/cm³). Substituting in Eq. (3.15) yields $R_{\max} \approx 0.64 \times 10^{-6}$. Thus, the optical reflection from a shock wave in air is less than one part per million. This can be a significant source of optical noise for an active (pulsed) illumination system if this shock-reflected component is comparable to that returned from the illuminated object. However, system signal-to-noise can be markedly improved in this case by range gating the pulsed illuminator return. Example 7 (Sec. 3.4.7) will examine the optical propagation effects of a local shock on a platform imaging system.

3.3.3 Random Flows

Two components of the platform random flow field are turbulent boundary layers (TBLs) and shear layers (SLs). These flows generally form if the local Reynolds number exceeds about 3×10^6 per meter. TBLs usually form within 10 to 20 cm of the platform leading edge and grow aftward as $\sim X^{0.8}$, with X being the distance from the leading edge. A shear layer is formed at a surface of discontinuity (e.g., the recessed window in Fig. 3.5) or when the flow is no longer attached to an aerodynamic surface. Open ports and flow protuberances are other structures that can initiate shear-layer formation. Shear layers generally expand in the downstream direction at a more rapid rate than boundary layers.

Artificial shear layers can be introduced via coolant flow over optical windows. High-speed flight results in fuselage stagnation temperatures many degrees above ambient. This thermal field can induce severe window thermo-optical distortions or melt. Flowing a coolant gas across the window can indeed mollify this distortion; however, the resultant mixing layer becomes an additional optical aberrator.

The fluctuating index of refraction n' of air is primarily determined by the fluctuating density ρ' ($\rho' \equiv \langle \rho'^2 \rangle^{1/2}$). For transparent gaseous media, the Gladstone-Dale relation is $n' = G\rho'$. Figure 3.10 shows the wavelength de-

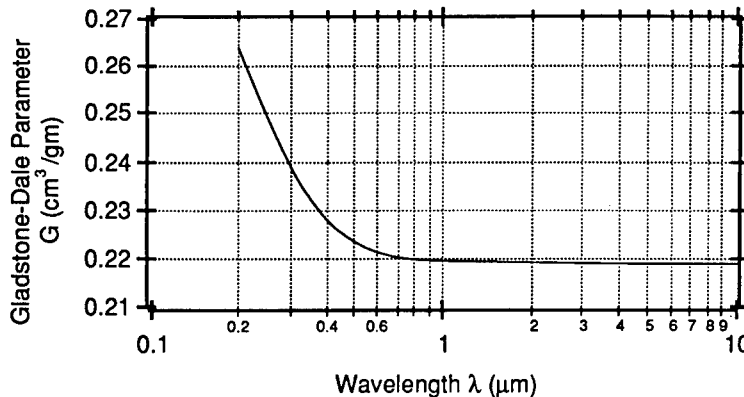


Fig. 3.10 The Gladstone-Dale parameter as a function of wavelength. Note that for $\lambda > 0.5 \mu\text{m}$, this parameter is nearly invariant ($0.22 \text{ cm}^3/\text{g}$).

pendence of G . Note that beyond the mid-visible ($\lambda > 0.5 \mu\text{m}$), this parameter is nearly invariant with wavelength.

The strength of a random flow-induced optical aberration depends on three flow parameters: the magnitude of the density fluctuations ρ' , the line-of-sight phase-correlation length ℓ_z , and the path length L through the flow field. The corresponding optical effect can be estimated by the phase variance from Eq. (3.1).

Correlation lengths of TBLs along the line of sight are typically 10% of the flow thickness. Shear-layer correlation lengths are generally larger, being about 20% of flow thickness. Correlation lengths normal to the optical axis are anisotropic for both random flows; scale lengths in the flow direction (ℓ_x) are generally 2 to 3 times larger than both ℓ_y and ℓ_z . Shear layers tend to be more isotropic.

Next, we turn to a discussion of the effects of random flow fields on airborne optical systems. We first assume all flow correlation lengths to be small compared to our limiting aperture diameter D (i.e., $\ell \ll D$). This is known as the infinite-aperture assumption, and represents a "worst case" for random flow-induced optical aberrations.

Weak Aberrations ($\sigma < \lambda/\pi$). The principal effect is a scattering of photons out of the central lobe [Fig. 3.11(a)]. The resulting Strehl loss, defined as the ratio of the observed (aberrated) peak intensity I to that of a diffraction-limited optical train (I_0), can be approximated by¹

$$S \approx I/I_0 \approx \exp[-(K\sigma)^2] \equiv \exp(-\phi^2) , \quad (3.16)$$

where $K = 2\pi/\lambda$ (wave number), σ^2 is the wave-front variance, and ϕ is the wave-front phase error. The scattered energy from a turbule has a characteristic scattering angle $\theta_s \approx \lambda/\ell_z$. Figure 3.11(a) compares the resulting far field with that of a diffraction-limited system. While this figure depicts an (circular aperture) Airy pattern, results are generally valid. The net result in this weak-aberration case is a loss of system contrast and resolution; however, a central core exists that is essentially diffraction limited.¹ The fact that beam quality can be related to aerodynamically driven system wave-front error is a potent result, and is the cornerstone of aero-optics.

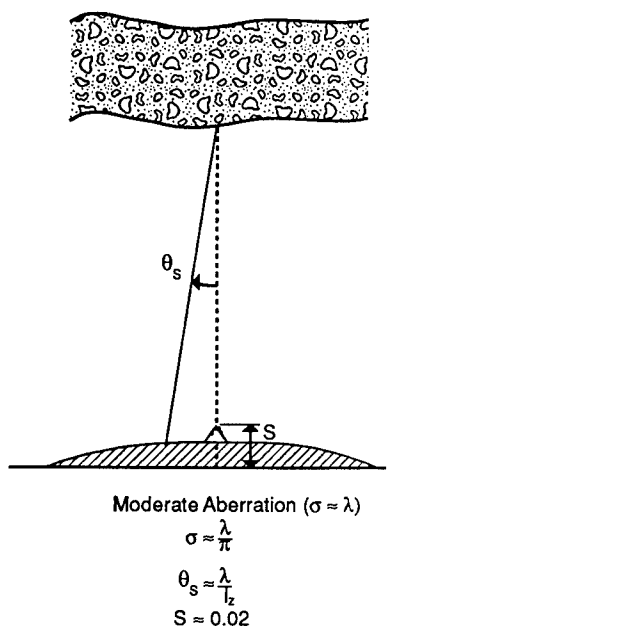
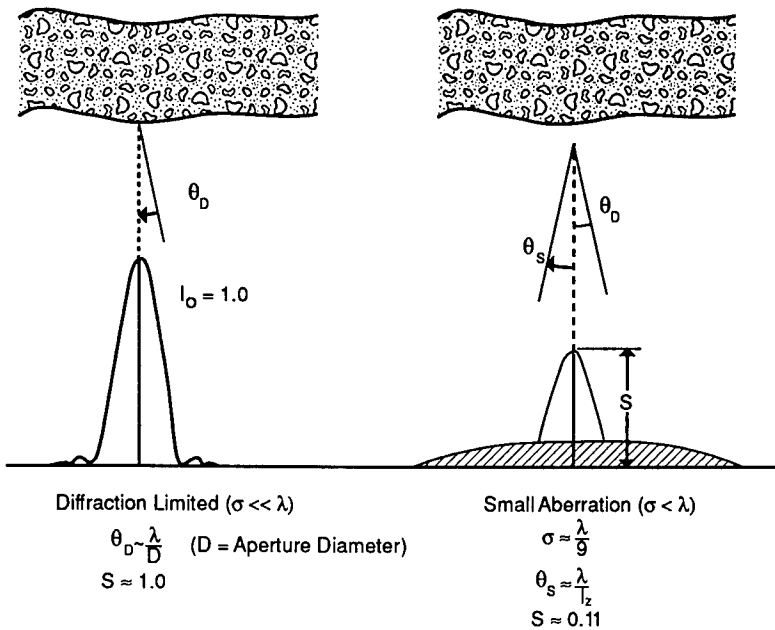


Fig. 3.11(a) Weak-aberration effects on an optical system result principally in a reduction of the Strehl ratio. Note as the degradation increases, the central core maintains approximately intrinsic resolution while suffering a loss in contrast. The corresponding Strehl ratio is estimated from Eq. (3.16). When $\sigma > \lambda/\pi$, the core blends into the background of scattered energy. The central spot in this limit can be approximated by a Gaussian having a width defined by the characteristic flow scattering angle θ_s .

Beam spread is a second measure of system performance. If one assumes a Gaussian beam propagating through a weak aero-optical aberration to a focal plane (energy conserved), then the resulting blur angle is¹⁸

$$\theta_B = \frac{\theta_D}{S^{1/2}}, \quad (3.17)$$

where θ_D is the diffraction-limited angle for the optics. For a uniformly illuminated, unobscured circular aperture, $\theta_D = 2.4 \lambda/D$, where D is the aperture diameter. Thus, θ_B is a measure of the linear growth of the diffraction spot resulting from this aberration. The actual diameter s of the Gaussian focal-plane spot (one standard deviation) is $s = F\theta_B$, where F is the system focal length.

In general, if the optical train has other (independent) aberration sources θ_i (optics, internal beam path, natural turbulence, etc.), then the total blur angle θ is

$$\theta = \left(\sum_{i=1}^N \theta_i^2 \right)^{1/2}. \quad (3.18)$$

The corresponding approximate Strehl ratio is

$$S' = \left(\frac{\theta_D}{\theta} \right)^2. \quad (3.19)$$

As the aberration strength grows, the Strehl ratio continues to drop at the expense of (wide-angle) scattered energy [Fig. 3.11(a)]. When $\sigma \geq \lambda/\pi$, the central core becomes obscure. The Strehl in this case [Eq. (3.16)] is ≤ 0.02 ; the core signal is now less than the combined scattered energy and systems noise levels.

In this weak-aberration regime, there is a wavelength that yields the best performance, be it Strehl or image quality. A general expression for on-axis far-field intensity I_p^* is given by¹⁸

$$I_p^* = \frac{I_0 \tau \exp(-\phi^2)}{1 + (1.57\theta_j D/\lambda)^2}, \quad (3.20)$$

where τ is the optics transmission, D is the aperture diameter, and θ_j is the uncorrected two-axis rms jitter. The diffraction-limited intensity is

$$I_0 = \frac{\pi D^2 P}{(2\lambda F)^2}, \quad (3.21)$$

where F is the system focal length and P is the uniform input power to our (circular) aperture.

We next define a figure of merit for this weak-aberration regime:

$$F_M = \frac{\exp(-\phi^2)}{(n^* \lambda / D)^2 + (1.57\theta_j)^2}, \quad (3.22)$$

where n^* is an overall measure of platform optics fidelity (e.g., $n^* = 1$ for a diffraction-limited system). System capability generally scales with F_M (e.g., on-axis intensity or image quality).

Note that F_M is essentially the ratio of system contrast to resolution. Figure 3.11(b) presents a notional view of this function. For long wavelengths, diffraction dominates ($F_M \propto 1/\lambda^2$), while in the short-wavelength limit the aberrations prevail [$F_M \propto \exp(-\phi_j^2)$]. The optimal wavelength follows by setting $\partial F_M / \partial \lambda = 0$, yielding

$$\lambda^* = \sqrt{2}\pi\sigma \left[1 + \sqrt{1 + \left(\frac{1.57\theta_j D}{n^*\pi\sigma} \right)^2} \right]^{1/2}. \quad (3.23)$$

This optimal wavelength λ^* is a function only of system wave-front error σ , rms jitter θ_j , and limiting telescope diameter D . Note that wavelength-dependent atmospheric transmission losses are neglected here.

Two limiting cases of Eq. (3.23) are of interest:

1. $\theta_j = 0$. Then $\lambda^* = 2\pi\sigma$.

This represents the situation in which the total system mechanical and atmosphere-induced wave-front tilt angle θ_j is small compared to $n^*\pi\sigma/D$.

2. $\theta_j \gg n^*\pi\sigma/D$. Then $\lambda^* \propto \pi(n^*\sigma\theta_j D)^{1/2}$.

In this case, jitter dominates system performance. In general, wave-front tilt must be controlled to $\theta_j \lesssim n^*\pi\sigma/D$; otherwise, the intrinsic advantages of short-wavelength systems are lost.

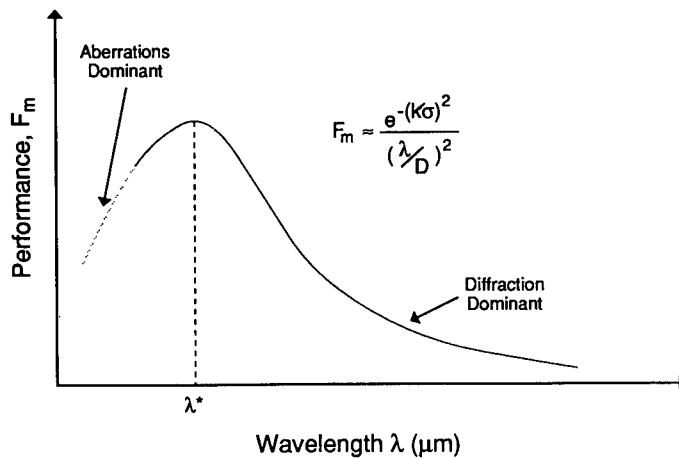


Fig. 3.11(b) An optical imaging or projection system in the weak-aberration regime ($\sigma < \lambda/\pi$) exhibits maximum performance at a wavelength λ^* . In general λ^* is a function of system beam jitter, wave-front variance σ , and optical-aperture size. In the limit of negligible jitter ($\theta_j \approx 0$), $\lambda^* \approx 2\pi\sigma$. At longer wavelengths, diffraction limits performance, while at shorter wavelengths, system aberrations dominate. Wavelength selection in this region can yield a significant performance enhancement for a particular AO aberration.

Note the jitter-free ($\theta_j = 0$) optimal Strehl ratio is $S^* = \exp[-(2\pi\sigma/\lambda^*)^2] = \exp(-1)$. Recall that image resolution in this weak-aberration domain can be approximated by $\theta_B \approx \theta_D/S^{1/2}$. This assumes energy is conserved in the spreading process and the image plane point spread function (PSF) can be approximated by a Gaussian.

Finally, the performance optimization algorithm developed above [Eq. (3.23)] is to be considered a guideline for wavelength selection. Several mission constraints may preclude implementation of the "best" wavelength λ^* , including

1. no operational laser in desired wavelength regime
2. no available detector with adequate response at λ^*
3. strong atmospheric extinction, i.e., absorption or scatter, at λ^*
4. poor transmission by platform optics (e.g., material window)
5. low target absorption or reflection for laser systems in which these are important characteristics.

In all cases, however, optimal system performance will be realized by selecting a wavelength as close to λ^* as possible that fulfills the particular mission requirements.

Strong Aberrations ($\sigma \gg \lambda/\pi$). In this regime the far field or blur spot assumes a Gaussian character. We assume the phase-correlation function C_ϕ is Gaussian,¹ even though empirical evidence suggests this function is not precisely Gaussian:

$$C_\phi = \exp \left[- \left(\frac{R}{\ell_z} \right)^2 \right], \quad (3.24)$$

where R is an aperture-related dimension. The system MTF is

$$M^* = M_o^* \exp \left[- \left(\frac{K\sigma R}{\ell_z} \right)^2 \right], \quad (3.25)$$

where the exponential is the MTF of the turbulent medium and M_o^* is our optics MTF. We assume in this case the random flow field MTF dominates system performance. This is usually the case when the limiting aperture is large compared to the correlation length ($D \gg \ell_z$), and when $(K\sigma)^2 \gg 1$. Taking the Fourier transform of the turbulence MTF yields the normalized PSF²⁰:

$$\text{PSF} = \frac{1}{2\pi\zeta^2} \exp \left[- \left(\frac{r}{\sqrt{2}\zeta} \right)^2 \right], \quad \zeta \equiv \frac{\sqrt{2}\sigma F}{\ell_z}, \quad (3.26)$$

where r is the focal-plane radial dimension and F is the optical system focal length.

Several properties of this strong-aberration (Gaussian) blur spot are of interest. First, integrating the PSF yields the blur-circle full angle θ_B containing p percentage of the energy $\theta_B = 4\sigma/\ell_z[-\ln(1-p)]^{1/2}$. For example, the blur angle corresponding to 84% contained energy is

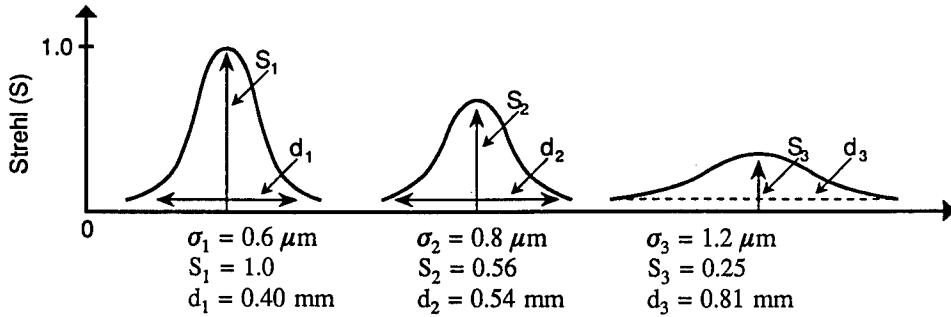


Fig. 3.12 Strehl and blur spot estimates for the random flow-field strong-aberration case ($\sigma \gg \lambda/\pi$). Here, Strehl $S \propto (\ell_z/\sigma)^2$, blur angle $\theta_B \propto \sigma/\ell_z$, and blur spot (84%) diameter $d = F\theta_B$, with F the imager focal length. This example reflects several σ values, with $\ell_z = 2 \text{ cm}$ and $F = 2.5 \text{ m}$. The Strehl calculations are normalized to our weakest aberration case ($\sigma_1 = 0.64 \mu\text{m}$).

$$\theta_{84\%} = 5.41 \frac{\sigma}{\ell_z} . \quad (3.27)$$

This is equivalent to the energy contained in the first minimum for diffraction at a uniformly illuminated circular aperture. Similar energy calculations result in the diameter of any arbitrary blur circle. Note the spot diameter at the sensor is $s = F\theta_B$.

Second, although there is no well-defined central core, the contrast, or Strehl ratio, scales [Eq. (3.26)] as $(\ell_z/\sigma)^2$. Figure 3.12 depicts focal-plane blur circles resulting from several aberrations in the strong regime ($\sigma \gg \lambda/\pi$). Note that focal-plane effects are essentially wavelength independent in this strong-aberration regime (except via the Gladstone-Dale parameter). This represents the geometric-optics limit obtained when radiation propagates through very severe optical aberrations.

Combining System Aberrations. In general, an airborne optical system has several sources of wave-front error. It is useful to combine these individual degradations such that the resulting total wave-front variance σ^2 approximates end-to-end system optical performance. We partition these sources into these three groups:

1. platform optical elements (σ_o^2): mirrors, lasers, windows, cabin turbulence, etc.
2. platform-induced external turbulence (σ_p^2): boundary layers, shear layers, cavity flow, etc.
3. atmospheric effects (σ_a^2): natural turbulence, thermal blooming, etc.

If these sources are independent, then the total wave-front variance is the sum of contributors:

$$\sigma_T^2 = \sigma_o^2 + \sigma_p^2 + \sigma_a^2 . \quad (3.28)$$

Quantitative appraisals of system performance are then obtained by methods described above, depending on whether the net aberration is weak or strong.

Individual elementary-aberration sources can also be combined (e.g., shear layer and cavity flow) as above if independent. If correlations exist among the

several sources, the analysis of net system performance is more detailed. Even in this case, however, the methodology presented above yields a useful bound of projected system performance.

Effects of Finite Optical Apertures. The previous discussions assumed apertures D that are much larger than platform turbulence correlation lengths ℓ_z (i.e., $D \gg \ell_z$). It is important to understand system performance scaling with aperture diameter. This analysis is applicable to both beam projection and imaging applications. We will suppose that the random flow-field aberrations are in the weak regime ($\sigma < \lambda/\pi$) and system wavelength λ is fixed.

In general, the jitter-insensitive MTF for a random flow field is given by²¹

$$M^*\left(f, \frac{D}{\ell_z}\right) = M_o^* \exp(-\phi^2) \left\{ 1 - \exp\left[-\left(\frac{Df}{2\ell_z}\right)^2\right]\right\}, \quad (3.29)$$

where M_o^* is the optics MTF (assume diffraction limited), ϕ is the wave-front phase error, D is the aperture diameter, ℓ_z is the turbulence correlation length along the optical axis, and f is the shear frequency ($0 \leq f \leq 2$). We Fourier transform this to obtain a jitter-free Strehl family of curves for several values of ϕ and D/ℓ_z . Results appear in Fig. 3.13.

Note that for small apertures ($D \ll \ell_z$), the beam suffers little AO-induced aberration. However, diffraction now limits system performance. For large beam diameters ($D \gg \ell_z$), the Strehl ratio approaches [Eq. (3.16)] $S = \exp[-(K\sigma)^2]$. For a given system aberration and wavelength one can (sometimes) achieve better performance with a finite aperture! We will continue this point in Example 3.4.5.

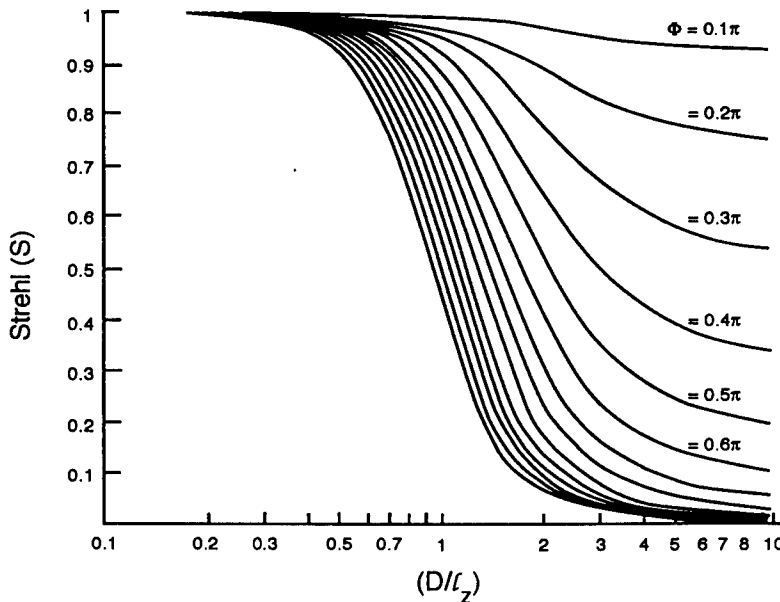


Fig. 3.13 Strehl S family of curves for a jitter-free system. For a given AO phase aberration $\phi = 2\pi\sigma/\lambda$, the resulting Strehl ratio is a strong function of D/ℓ_z , where D is the limiting optics aperture diameter and ℓ_z is the random flow correlation length along the optical axis. For $D/\ell_z \ll 1$, $S \rightarrow 1$; for $D/\ell_z \geq 10$, $S \rightarrow \exp(-\phi^2)$ (this is the so-called “infinite-aperture” limit). This family of curves is generally valid for $\phi \leq 0.7\pi$.

Effects of Flow-Field-Induced Heating. Stagnation heating of windows and shock waves are two primary platform-induced sources of sensor thermal noise. We first examine the detector irradiance resulting from such a source.⁶

We assume the optical system field to be small, with the isothermal (emissivity ϵ) source filling the entire field. Then the spectral radiance is

$$L^* = \frac{1}{\pi} \int_{\Delta\lambda} M_\lambda \epsilon \, d\lambda , \quad (3.30)$$

where spectral exitance M_λ is

$$M_\lambda = \frac{C_1[\exp(C_2/\lambda T) - 1]^{-1}}{\lambda^5} \text{ W cm}^{-2} \mu\text{m}^{-1} , \quad (3.31)$$

where

$$\begin{aligned} C_1 &= 1.19 \times 10^4 \text{ W } \mu\text{m}^4 \text{ cm}^{-2} \\ C_2 &= 1.44 \times 10^3 \mu\text{m K}. \end{aligned}$$

The integral in Eq. (3.30) cannot be evaluated in closed form; however, this integrand can be replaced by an infinite series and integrated term by term.²² The result is (assuming a constant emissivity over the wavelength band $\Delta\lambda$)

$$\begin{aligned} L^* = \frac{C_1}{\pi} \left(\frac{T}{C_2} \right)^4 \epsilon \sum_{n=1}^{\infty} n^{-4} \left\{ \exp(-nx_1)[(nx_1)^3 \right. \\ \left. + 3(nx_1)^2 + 6(nx_1) + 6] \right. \\ \left. - \exp(-nx_2)[(nx_2)^3 + 3(nx_2)^2 + 6(nx_2) + 6] \right\} , \quad (3.32) \end{aligned}$$

where

$$x_1 \equiv \frac{C_2}{\lambda^1 T} , \quad x_2 \equiv \frac{C_2}{\lambda^2 T} . \quad (3.33)$$

In general, this series converges very quickly. For example, only 10 terms are required if one's requirement is

$$\frac{N^{\text{th}} \text{ term in sum}}{\text{Sum of first } N \text{ terms}} < 10^{-10} .$$

(Note that an approximation can be obtained via a radiation slide rule, e.g., General Electric GEN/I5C). The power at the sensor's collector entrance is approximately

$$P^* \cong L^* \pi \Omega^2 A_c , \quad (3.34)$$

where Ω is the sensor FOV half-angle and A_c is the entrance aperture area. The irradiance at the detector is then

$$I = \pi\Omega^2 L^* \tau \frac{A_c}{A_d} , \quad (3.35)$$

where A_d is the detector area and τ is the throughput efficiency of the telescope (we neglect atmospheric losses). Note from geometry that

$$\frac{A_c}{A_d} \simeq \frac{1}{4} \left(\frac{D}{F} \right)^2 \frac{1}{\Omega^2} , \quad (3.36)$$

where D and F are the effective aperture diameter and focal length of the collector, respectively.

Then the irradiance at the detector depends only on telescope parameters and source radiation:

$$I = \frac{\pi}{4} L^* \tau \left(\frac{D}{F} \right)^2 . \quad (3.37)$$

Figure 3.14(a) shows the detector spectral irradiance for MgF₂ at several temperatures.⁶ Figure 3.14(b) depicts the wavelength-dependent emissivity of synthetic sapphire (0.4 cm thick) for several germane temperatures.⁶

Next we consider aerothermal effects on the platform windows.⁶ The primary function of such a window is to protect optical equipment from aerodynamic loading and heating encountered in high-speed flight. This window must meet several additional requirements:

1. Thermo-optical (TO) aberrations within tolerance: In general, curved surfaces yield significant TO aberrations unless the window is thin; however, some minimum thickness is required to support (expected) structural loads.
2. Adequate transmission within the sensor bandpass: Some IR materials suffer increased transmission losses at elevated temperatures (e.g., germanium and silicon).
3. The window thermal noise must be sufficiently small: Window radiation at the sensor is determined by this optic's temperature and emissivity, as well as proximity to the detector. This radiation can saturate the sensor; furthermore, nonuniform radiation can cause ghosts in an imaging system.
4. The window must survive thermomechanical loads induced by flight dynamics.

The rate of aerodynamic heat transfer q to a window per unit area is

$$q = h(T_w - T) , \quad (3.38)$$

where h is the aerodynamic heat-transfer coefficient, T is the window surface temperature, and T_w is the adiabatic wall temperature.

In general, h is a function of wall geometry and flight conditions. For altitudes below 12 km and $1 \leq M \leq 8$, this parameter ranges from 0.01 to 0.05. The adiabatic wall temperature follows from Eq. (3.2).

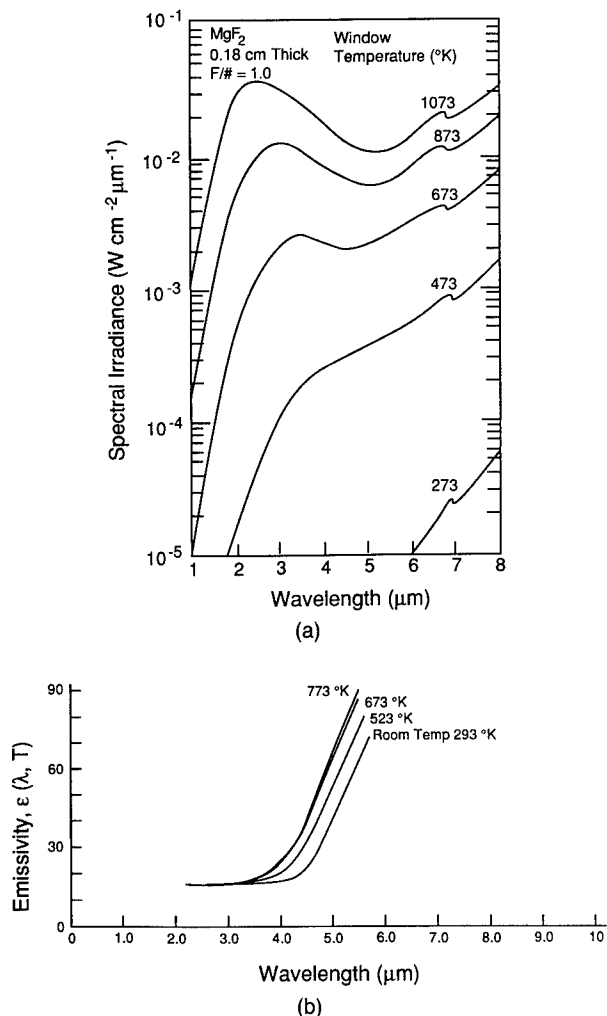


Fig. 3.14 (a) Effective spectral irradiance at a detector. This is shown with a MgF_2 window versus wavelength for several temperatures. (b) Spectral emissivity of synthetic sapphire (0.4 cm thick) for several temperatures.

We assume the window to be thermodynamically thin; i.e., $h\Delta z/K \ll 1$, where Δz is the window thickness, K is the thermal-conductivity window, and radiation and conduction losses are negligible; then

$$h(T_w - T) = \rho C \Delta z \frac{dT}{dt} , \quad (3.39)$$

where ρ is the window density and C is the window heat capacity. The solution is

$$\frac{T_w - T}{T_w - T_i} = \exp\left(-\frac{t}{\tau}\right) , \quad (3.40)$$

where T_i is the initial temperature and τ is the window heating time constant:

$$\tau = \frac{\rho C \Delta z}{h} . \quad (3.41)$$

Consider, for example, a 0.5-cm-thick fused-quartz window at ~ 350 K. Taking $h = 0.03$, $\rho = 2.2$ g/cm³, and $C = 0.8$ J g⁻¹ K⁻¹ results in a window time constant $\tau \approx 29$ s. This is the time required for the temperature ratio [Eq. (3.40)] of this thermodynamically thin window to achieve $1/e$ percent of its final value.

For many applications, the time of operation is short enough to neglect window-heating effects. Also, several approaches can increase the effective window time constant, including

1. Window precool: However, H₂O condensation effects can be important.
2. Increasing window thickness: Here, factors such as increased absorption, optical distortion, and window weight must be considered.
3. Recessing window: This separates the flow boundary layer from the window surface, thus reducing the heat-transfer coefficient. However, this action may also reduce the system field of view as well as induce additional optical aberrations.
4. Window active cooling: This may also result in enhanced AO aberrations.

Recall that the above discussion neglects aerodynamic-induced radiation. At higher Mach numbers, radiation heat transfer becomes significant. In this case, the heat-balance equation becomes

$$h(T_w - T) = \rho C \Delta z \frac{dT}{dt} + \sigma_{SB} \epsilon T^4 , \quad (3.42)$$

where ϵ = equivalent total wall emissivity; σ_{SB} = Stefan-Boltzmann constant.

The above treatment of the interaction of an optical wave front with airborne-platform-induced flow fields gives a flavor for the types of problems encountered in flight. We have not broached the hypersonic regime ($M \geq 8$), where dissociation, ionization (plasma) effects, and acoustical radiation can be important. Neither have we discussed high-power laser (nonlinear) airflow interactions such as thermal blooming and Raman or Brillouin scattering. However, we have developed the tools that allow the optical designer to quantitatively investigate and bound optical-system performance for a broad spectrum of germane airborne-platform scenarios. We turn now to examples of how this information can be applied to practical AO situations.

3.4 AERO-OPTICAL DESIGN AND ANALYSIS EXAMPLES

3.4.1 Example 1—Subsonic Imaging Platform: Boundary-Layer Aberrations

An optical designer has been asked to investigate the quality of images that can be expected to occur on a large transport aircraft flying at various Mach

numbers and altitudes. The camera operates in the mid-visible ($\lambda \sim 0.5 \mu\text{m}$). There are two possible aircraft locations for this instrument. The first site is approximately 10 m aft of the nose, while the second site is located 25 m aft. Both positions are expected to have attached turbulent boundary layers since those location sites are on nominally smooth, nonexpanding or contracting sections of the fuselage. Images are to be collected by a 30-cm-diameter telescope primary mirror; this is taken to be the system limiting aperture. Because of the short-wavelength requirements for this imaging system, a flush material window of high quality is used. The window is conformal with the existing mold lines of the aircraft at both proposed installation sites (Fig. 3.1).

Note that large F-number imaging systems are frequently "detector limited." That is, intrinsic resolution is set by the imager pixel size and spacing rather than the limiting optics (θ_D). For this example we assume an unobscured circular aperture having diameter D ; its full diffraction angle θ_D is $\theta_D = 2.4 \lambda/D = 4 \mu\text{rad}$ at $\lambda = 0.5 \mu\text{m}$. If the detector limit is, say, 20 μrad , then AO aberrations will not be important to system resolution unless they are on the order of 20 μrad or greater.

For attached turbulent boundary layers, one may assume that the total turbulent boundary-layer thickness is between 1 and 1.5% of the distance from the origin of the boundary layer. For the purpose of example here, we take the conservative value and estimate the boundary-layer thicknesses to be 1.5% of the total boundary-layer length (flow direction). The turbulent scale sizes in an attached boundary layer are known to be approximately 10% of the total thickness of the layers. The density fluctuations, on the other hand, are driven by the difference between the wall density and the density that exists external to the boundary layer. The external density is chosen to be the ambient density. The wall density can be computed from the recovery temperature of the vehicle's surface, with the assumption that the static pressure at the surface has a value equal to the atmospheric pressure at the operating altitude [Eq. (3.4)]. The wave-front errors can then be estimated from the square of the fluctuating density values and the product of the scale length and total path length through the turbulent boundary layers according to Eq. (3.1).

Case I (Baseline). For this case, the aircraft's operating altitude is expected to be about 12 km, with a flight Mach number of 0.6. The surface density ρ is about 94% of the free-stream value, with fluctuations of about 10% of the difference, or about 0.006 times the free-stream density. For a station located 10 m downstream of the leading edge, the boundary-layer thickness is approximately 15 cm, with the scale sizes being estimated at 1.5 cm; i.e.,

$$X = 10 \text{ m}, \quad L = 15 \text{ cm}, \quad \ell_z = 1.5 \text{ cm}, \\ \rho_0 = 3.1 \times 10^{-4} \text{ g/cm}^3, \quad \rho' = 1.9 \times 10^{-6} \text{ g/cm}^3.$$

From Eq. (3.1), we have the approximate wave-front error σ as

$$\sigma \cong G(\rho'^2)^{1/2}(2\ell_z L)^{1/2}, \quad (3.43)$$

or

$$\sigma \cong (0.22)(1.9 \times 10^{-6})(2 \times 1.5 \times 15)^{1/2} = 2.8 \times 10^{-6} \text{ cm} = 0.028 \mu\text{m}.$$

For visible wavelengths ($\lambda = 0.5 \mu\text{m}$), the diffraction limit of the system is $2.4\lambda/D = 4 \mu\text{rad}$. The nondimensional wave-front error is $\sigma/\lambda = 0.056$ at $\lambda = 0.5 \mu\text{m}$.

This case represents a weak aberration. From Eq. (3.16), we find the Strehl ratio has a value of 0.88, and the blur angle [Eq. (3.17)] $\theta_B \approx \theta_D/S^{1/2}$ is approximately 1.07 times the diffraction-limited value. This is an approximation for the increase in the diameter of a point source imaged through the boundary layer. For this imaging system, little loss of resolution occurs and negligible contrast loss is experienced.

This optimistic view can be changed significantly by variations in the flight parameters, location on the aircraft, and imager wavelength. The following cases discuss some of these variations.

Case II (Mach Number Excursion). For this case, conditions remain similar to that for Case I, except that the flight Mach number is increased to 0.9. Here we ignore local shock wave effects. Such aero-optical phenomena are broached in Example 7. Now the surface density is only 87% of the atmospheric density, with attendant larger density fluctuations. The TBL thickness and scale sizes are nearly invariant with this increase in Mach number, and the wave-front error is 2.1 times that of Case I. The Strehl ratio drops to 0.57, while the focal-plane spot size becomes 1.33 times the diffraction-limited value; i.e.,

$$\rho'_H = 2.1\rho'_I = 4 \times 10^{-6} \text{ g/cm}^3 .$$

The resulting wave-front error is

$$\sigma_H = 2.1 \sigma_I \quad \text{and} \quad \frac{\sigma_H}{\lambda} \approx 0.12 \text{ at } \lambda = 0.5 \mu\text{m} .$$

The point of Case II is that although this is still a relatively weak aberration ($\sim \lambda/10$), the Mach number does have a strong effect on the contrast because the Strehl ratio has dropped by 30%. If the sensor has sufficient dynamic range, the effect of this contrast loss is minimal. However, a resolution loss will result from image blurring owing to light rays being scattered by the TBL to adjacent sensor (pixel) elements. The resulting blur spot in this case has a diameter that is 33% larger than a diffraction-limited spot diameter.

Case III (Turbulent Boundary-Layer Thickness Excursion). For this case, we examine aero-optical effects 25 m downstream of the origin of the turbulent boundary layer, and assume Case I flight conditions. The boundary-layer thickness is now increased by a factor of 2.5 over the Case I value, while the scale sizes are also 2.5 times that for Case I. (Note our conservative assumption that the TBL thickness L and scale size ℓ_z scale linearly with distance X downstream, rather than the more traditional $L = X^{0.8}$ scaling.) Thus, the wave-front error becomes 2.5 times as large as that for Case I; i.e.,

$$X = 25 \text{ m}, \quad L_{III} \approx 2.5L_I, \quad \text{and} \quad \ell_{III} \approx 2.5\ell_I ,$$

$$\sigma_{III} = 2.5\sigma_I \quad \text{and} \quad \sigma/\lambda = 0.14 \text{ at } \lambda = 0.5 \mu\text{m} .$$

The image contrast loss (Strehl) is now 0.46, with a corresponding blur angle $\theta_B \sim 1.47\theta_D$, or about 6 μrad .

The message from Case III is that the wave-front errors scale linearly with distance downstream of the origin of the turbulent boundary layer; thus, it is highly advantageous to move imaging equipment as far forward on the vehicle as possible. It should be noted that even though the wave-front error scales linearly, the focal-plane effect has a highly nonlinear scaling in this domain according to Eqs. (3.16) and (3.17).

Case IV (Effect of Boundary-Layer Thickness and Increased Mach Number). This is similar to Case II (Mach 0.9), except our optical system is located at the 25 m station. Again, the ratio of surface to atmospheric density is 0.87. The wave-front error is $\sigma/\lambda \sim 0.3$ at $\lambda = 0.5 \mu\text{m}$. This aberration level is between the weak and strong regimes; the far-field Strehl ratio has been reduced such that it is comparable to the (scattered) background. The estimated Strehl is 0.03, with a (weak-aberration) image blur angle $\theta_\beta \sim 5.9 \theta_D$, or approximately 24 μrad . Note that approaching this as a strong aberration yields a predicted blur circle (84% energy) of $\theta_\beta = 5.41 \sigma/\ell_z = 22 \mu\text{rad}$.

A substantial loss of both contrast and resolution exists for this visible imaging system. For example, effective resolution is between five and six times the optics-limited resolution. This condition is similar to those measured on operational platforms.

Case V (Effect of Wavelength). We assume the same flight conditions and position on the vehicle as that in Case IV, but now the imaging-system wavelength is taken to be 2 μm . We suppose an IR window exists that is conformal with the fuselage. Now, the relative wave-front error is reduced fourfold from the higher Mach number case at the aft installation location, so that $\sigma/\lambda = 0.075$ at $\lambda = 2 \mu\text{m}$. This yields a corresponding Strehl ratio and blur angle of $S = 0.8$, $\theta_\beta \sim 1.1\theta_D$, respectively. Note, however, in this case, that the (optics-limited) diffraction angle is four times that of the visible case. Assuming diffraction-limited optics, this $\lambda = 2 \mu\text{m}$ system ($\theta_\beta = 18 \mu\text{rad}$, $S = 0.8$) may outperform its visible-wavelength counterpart ($\theta_\beta = 24 \mu\text{rad}$, $S = 0.03$). This example demonstrates the highly nonlinear nature of system Strehl (contrast) with σ and λ [Eq. (3.16)]. Whether or not selecting a longer wavelength is a useful approach to ameliorate airborne-platform random flow effects obviously depends on the designer's application.

One means of reducing aero-optical platform aberrations is to fly higher or slower. To demonstrate the effects of altitude on system performance, the following case is given.

Case VI (Altitude Effects). Consider the example of Case III with the flight Mach number maintained at 0.6 but the altitude reduced to 1 km. Again, the ratio of surface density to that of the atmosphere remains at 0.94; however, the atmospheric density has increased considerably. This causes a 3.5-fold increase in the wave-front error over that for Case III; i.e., $\rho_0 = 1.1 \times 10^{-3} \text{ g/cm}^3$, $\rho' = 6.6 \times 10^{-6} \text{ g/cm}^3$, and $\sigma_{VI} = 3.5 \times \sigma_{III} = 0.24 \mu\text{m}$. Thus, $\sigma/\lambda = 0.48$. This example represents a situation that is well into the strong-aberration regime. An upper bound for the resulting full blur angle (84% energy) follows from Eq. (3.27):

$$\theta_\beta \approx 5.41 \frac{\sigma}{\ell_z} = 35 \mu\text{rad} .$$

Note that the aberration strength in this strong domain has a weak wavelength dependence (via the Gladstone-Dale parameter). The blur angle θ_β is essentially determined solely by flow aerodynamic parameters. This situation represents the geometric-optics limit.

This case demonstrates that the magnitude of the ambient density has a strong effect on the strength of the aberrations caused by an attached turbulent boundary layer. In general, flying as high and as slowly as possible, while having the optical axis as far forward as feasible, minimizes AO aberrations.

3.4.2 Example 2—Supersonic Imaging Platform: Boundary-Layer Aberrations

Our optical designer had no sooner completed the calculations for the subsonic aircraft when a second mission required the placement of a similar visible imager on a high-speed, high-altitude supersonic aircraft.

Case I (Baseline). Here we consider only optical aberrations due to the supersonic turbulent boundary layer. Associated shock-wave refractive and reflective optical effects will be examined in Example 7. The expected flight Mach number is about 3.0, with an operating altitude of about 20 km. We now assume a 15-cm imaging-aperture diameter. For this situation, the outside atmospheric density is about $\rho_0 \sim 0.9 \times 10^{-4}$ g/cm³; however, because of the aircraft's high Mach number, the surface density is now about 38% of the atmospheric value. If the camera location were limited to a single position approximately 10 m downstream, one estimates a 15-cm-thick boundary layer with 1.5-cm scale sizes. The fluctuating density magnitudes are now substantially larger than those from Example 1 because of the increased difference in the densities at the surface and in the natural atmosphere. Now the fluctuating density is about 6×10^{-6} g/cm³. For this case, the wave-front error is $\sigma \sim 8.9 \times 10^{-6}$ cm, or about 0.18 waves ($\lambda = 0.5 \mu\text{m}$). The Strehl ratio for this weak aberration is approximately 0.28, and the blur angle is 1.9 times that of a diffraction-limited system. The diffraction angle θ_D is about 8 μrad for a system with a 15-cm effective aperture diameter, so that $\theta_\beta \approx 15 \mu\text{rad}$. This example shows that good optical fidelity can be achieved from a supersonic airborne platform.

Case II (Altitude Excursion). This is like Case I except the platform altitude is reduced to 10 km. The outside atmospheric density is now 4.1×10^{-4} g/cm³, with $\rho' \sim 4.6$ times that of Case I. Hence, $\sigma/\lambda \sim 0.83$ at $\lambda = 0.5 \mu\text{m}$, which is a strong aberration. Our corresponding 84% blur angle $\theta_\beta \sim 5.41 \sigma/\ell_z \sim 148 \mu\text{rad}$.

The system Strehl ratio at this altitude relative to Case I can be estimated [Eq. (3.19)] by

$$S \approx \left(\frac{\theta_{\beta I}}{\theta_{\beta II}} \right)^2 \approx 10^{-2}.$$

Again, we note that selection of a longer wavelength could markedly improve system performance. For example, a $\lambda = 3 \mu\text{m}$ system returns the system to the weak-aberration domain ($\sigma/\lambda \approx 0.14$), with $S = 0.46$. The system diffraction angle θ_D is now 48 μrad , with a corresponding blur angle $\theta_\beta \approx \theta_D/S^{1/2}$

$\sim 71 \mu\text{rad}$. This longer-wavelength system offers our designer a potential factor of two resolution improvement. Note, however, that other radiometric factors must be considered, for example, reduced detector signal-to-noise ratio at the longer wavelength.

3.4.3 Example 3—Optical Degradation Resulting from Open Cavity

Other people in the optical designer's group interested in longer wavelengths now ask what the effect might be in a subsonic installation if open-cavity flows were present and the same 15-cm aperture-receiving optics were used for a 2- μm wavelength sensor. A windowless configuration may be selected to afford low-loss transmission for multiple or long wavelengths or to minimize IR thermal noise due to material windows. For these cases, the field between the sensor and the atmosphere consists of a turbulent shear layer and cavity flow (see, for example, Fig. 3.3), rather than the attached turbulent boundary layers of Examples 1 and 2. The thickness and scale sizes characterizing this shear layer depend principally on the cavity length (in the flow direction) and, to a lesser extent, on properties of the upstream fuselage boundary layer. We suppose the 15-cm aperture requires a full one-meter square opening to achieve the desired field of regard. The cavity depth H is taken to be 15 cm. The porous fence located upstream (Fig. 3.3) is assumed to extend beyond the edge of the attached turbulent boundary layer. In this example, we consider optional aberrations resulting from both shear layer and cavity flow fields.

Recall that the thickness L of the shear layer can be estimated by $L \approx 0.25X$, where X is the downstream distance. We suppose the average thickness across this open cavity to be 15 cm. Moreover, we assume for a conservative optical design that the scale sizes (with respect to Case I, baseline) have increased by approximately a factor of two (i.e., $\ell_z \approx 0.2L$), and the rms density fluctuation ρ' has also increased by a factor of two. Thus, the values of the wave-front variance will increase by a factor of 8 [Eq. (3.1)]. Note that the difference between the outside and inside densities has not changed from those in Example 1 (baseline case), since the cavity gas temperature is at the aerodynamic recovery temperature. With these considerations in mind, we see that σ has increased by $\sqrt{8}$, but the wavelength has increased by a factor of 4. This results in a value of σ/λ that has decreased to about 71% of the Example 1 baseline example. The corresponding Strehl ratio and blur angles are 0.94 and $1.03 \theta_D$, respectively. For this 2- μm imaging system, AO effects of this shear flow are negligible.

Next, suppose the 2- μm imager is replaced by a visible sensor ($\lambda \approx 0.5 \mu\text{m}$). Now σ/λ is $\sqrt{8}$ times larger than the Example 1 baseline case ($\sigma/\lambda \approx 0.16$). The corresponding Strehl ratio S and blur angle θ_B are 0.36 and $1.66 \theta_D$, respectively.

A second source of aberration is flow within the cavity itself. Although cavity scale sizes are large compared to the shear layer, the low-velocity flow results in small values of fluctuating density. Thus, the resulting optical aberrations are usually negligible with respect to the external flow fields unless a marked thermal mismatch exists between the cavity gas temperature and the recovery temperature. We now treat this case.

Let ΔT be the temperature differential between the air in the upper and lower parts of the cavity and suppose the fluctuating component T' is 10% of this difference; i.e., $T' = 0.1\Delta T$. Neglecting cavity velocity fluctuations,

$$\frac{\rho'}{\rho} = \frac{T'}{T}, \quad \text{where } \rho \text{ and } T \text{ are the cavity mean values .} \quad (3.44)$$

Substitution yields

$$\rho' = 0.1\rho \left(\frac{\Delta T}{T} \right) . \quad (3.45)$$

We choose as our parameters the Example 1 baseline case: aircraft Mach number = 0.6, aircraft altitude = 12 km, mean cavity density $\rho = 2.9 \times 10^{-4}$ g/cm³, and mean cavity temperature $T = 230$ K. Here, the mean cavity density and temperature are taken to be the recovery parameters [Eqs. (3.3) and (3.4)].

In addition, the cavity correlation length is taken to be $\ell_z \approx 0.2H$, with $H \approx 15$ cm (cavity depth). Finally, a temperature differential $\Delta T \approx 30$ K yields a cavity wave-front error of $\sigma/\lambda = 0.16$ at $\lambda = 0.5$ μm.

In general, the cavity and external random flows are independent. Thus, the net wave-front variance σ_T^2 follows from $\sigma_T^2 = \sigma_{\text{shear layer}}^2 + \sigma_{\text{cavity}}^2$. Substituting the above values yields a total wave-front error $\sigma_T/\lambda \approx 0.23$ at $\lambda = 0.5$ μm. This is a weak aberration, with Strehl ratio S and blur angle θ_B of 0.13 and $2.70D$, respectively.

An interesting limiting case is that of a shallow cavity. This may occur, for example, if a material window is recessed into the fuselage to optimize the field of regard of a platform optical instrument. Such a cavity is defined to be shallow if the expanding shear layer formed at the leading edge intersects the cavity bottom (e.g., window).

Recall that the thickness of a freely expanding shear layer is $L \approx 0.25X$, where X is the downstream distance. This corresponds to a divergence half-angle of about 7 deg. At the window reattachment point, the incipient flow adopts characteristics more akin to a boundary layer. Thus, in the general situation, one can have the remnants of the original shear layer sandwiched between the nascent window boundary layer and the fuselage boundary layer. Though the precise magnitude of the composite wave-front variance is difficult to calculate in this situation, the net optical aberration will probably be somewhat less than that of a deeper cavity. The most desirable aero-optical approach with a window is to mount it conformally with the fuselage, thus avoiding shear-layer formation.

The message here is that open-cavity AO mixing-layer aberration levels can be comparable to shear-layer or boundary-layer effects, particularly if significant thermal differences exist. If the cavity is shallow, shear layer impingement can occur on the bottom surface (e.g., window). The designer is now in a good position to assess the impact of an open cavity on system optical performance.

3.4.4 Example 4—Visible Imager: Selecting the Optimal Wavelength

Imaging tests are being planned using a 30-cm-diameter high-resolution camera system on board a wide-body aircraft. The camera has a rotatable filter wheel that provides selectable imaging bandwidths in steps of 0.1 μm from

0.35 to 1.15 μm (filter bandpass full width at half maximum is $\sim 0.04 \mu\text{m}$). The lead experimenter selects the shortest available wavelength (0.35 μm) wheel position because good resolution is important. The mission is flown at 5-km altitude and Mach 0.8. Postmission analysis reveals unexpectedly poor target resolution. The aircraft boundary layer is suspected to be the culprit. Effective in-flight image resolutions of order 35 to 45 μrad are inferred. Ground calibrations show a system resolution of about 20 μrad limited by the detector. The intrinsic optics resolution limit θ_D at this wavelength is approximately 10 μrad . The test director decides to probe the aircraft boundary layer via a series of aerodynamic measurements. Results reveal a boundary-layer thickness of 20 cm and correlation length ℓ_z of 2 cm at the mission Mach number. The inferred fluctuating density for this random flow is $0.8 \times 10^{-5} \text{ g/cm}^3$. Using Eq. (3.1), he estimates an rms phase error $\sigma = 0.16 \mu\text{m}$. The resulting aberration $\sigma/\lambda \sim 0.46$ borders on the strong regime. The approximate 84% blur angle θ_β is [Eq. (3.27)] 43 μrad , with a corresponding Strehl ratio of $S = (\theta_D/\theta_\beta)^2 \approx 5.3 \times 10^{-2}$, in good agreement with observations. This loss of image contrast can be a constraint unless the detector has adequate sensitivity.

Recall [Fig. 3.11(b)] that there is a wavelength that offers optimal performance for an airborne (infinite aperture) optical system. This wavelength yields the best focal-plane quality for a given array of optics diffraction, platform jitter, and system (weak) aberrations arising from optical elements, aerooptics, and natural turbulence. Here we assume the platform optics are diffraction limited and neglect atmospheric turbulence effects. For this situation, $\sigma = 0.16 \mu\text{m}$, and $D = 30 \text{ cm}$; the two-axis rms jitter is taken to be 1.0 μrad . Substituting in Eq. (3.23) reveals an optimal wavelength $\lambda^* \approx 1.1 \mu\text{m}$. The resulting optical aberration is now weak ($\sigma/\lambda^* \approx 0.15$), with a corresponding estimated Strehl ratio S and blur angle θ_β of 0.43 and 15 μrad , respectively.

Note we have not considered wave-front aberrations due to natural atmospheric turbulence. Since these are independent aero-optical aberrations, the residual atmospheric phase error ϕ_a can be RSS'D with platform error to yield $\phi = (\phi_a^2 + \phi_p^2)^{1/2}$. If this composite aberration ϕ is weak ($\phi = 2\pi\sigma/\lambda \leq 2$), then a new "best" performance wavelength λ^* follows from Eq. (3.23).

The message here is that for a given AO aberration strength, there is a wavelength that yields best system performance. If our optical designer is able to select this optimal wavelength, or one close to it, significant enhancements can result.

3.4.5 Example 5—Aperture Optimization

The experimental team in Example 4 has garnered a considerable imaging database with its 30-cm-diameter high-resolution camera system. Excellent performance has indeed been confirmed at the optimal wavelength ($\lambda^* \approx 1.1 \mu\text{m}$). Now a crucial mission looms that requires propagating a laser beam (wavelength $\lambda = 0.53 \mu\text{m}$) from the platform to the far field. (Flight parameters are unchanged: Mach 0.8, altitude 5 km.) The leader challenges the optical designer: can better overall performance be obtained via a smaller aperture?

Recall that the estimated boundary-layer phase error is $\sigma = 0.16 \mu\text{m}$, with a corresponding correlation length $\ell_z = 2 \text{ cm}$. From Fig. 3.13, we note that the proper Strehl curve is $\phi = 0.60\pi$. As the aperture diameter D is reduced,

Table 3.3 Aperture Optimization of an Airborne Optical System in the Presence of a Random Flow Field Having Strength $\phi = K\sigma \sim 0.60\pi^*$

D (cm)	D/ℓ_z	$S (\times 10^3)$	$F_M (\times 10^3)$
30	15	29	5.0
20	10	100	10.6
16	8	120	8.9
12	6	150	6.8
6	3	250	3.1

*Column 1 is the system limiting aperture diameter D . The second column depicts the ratio of D to the TBL correlation length ($\ell_z = 2$ cm). The resulting AO Strehl ratio, derived from the Fig. 3.13 Strehl family of curves, appears in Column 3. The figure of merit F_M [Eq. (3.46)] tabulated in Column 4 suggests an aperture of about 20 cm in diameter yields the best far-field performance for these platform conditions. Platform two-axis rms jitter is taken to be 1 μ rad.

the Strehl (contrast) increases while resolution decreases via diffraction losses. Correspondingly, as D increases, AO aberrations grow while system diffraction performance improves.

We neglect the effects of natural turbulence and suppose our platform optical-element aberrations (including jitter) are independent of the limiting diameter D . We write our far-field performance figure of merit [Eq. (3.22)] in the form

$$F_M = \frac{S}{(\lambda/D)^2 + (1.57\theta^j)^2}, \quad (3.46)$$

where the Strehl ratio $S = \exp(-\phi^2)$ for an “infinite” aperture (i.e., $D/\ell_z \gg 1$). S follows from the Fig. 3.13 Strehl family of curves for finite apertures. Note that peak laser intensity at the focal plane scales with F_M .

Table 3.3 summarizes F_M values for several aperture diameters. A platform two-axis rms jitter of 1 μ rad is assumed, with remaining parameters defined above. An aperture diameter D of 30 cm defines the limiting case (infinite aperture) in Table 3.3, with a resulting $D/\ell_z = 15$ and a corresponding Strehl ratio of approximately 0.029 (recall this is near the upper bound for a weak aberration). Note that for these platform conditions, the optimal system performance is achieved with an aperture diameter of about 20 cm.

The message conveyed by this example is that for a fixed wavelength and platform AO aberration level, optimal system performance (i.e., resolution or far-field intensity) may be achieved with a finite-aperture diameter D , where an infinite aperture is generally defined by $D/\ell_z > 10$. Note that signal-to-noise-limited applications may lead to selection of the largest feasible aperture.

3.4.6 Example 6—Thermal Noise Resulting from an IR Window

Window thermal effects are an important aspect of an airborne IR optical imager. Heating of the airborne platform windows by fuselage random flow fields can result in IR detector noise and reduced optical transmission through the window. The latter effect reduces the sensor signal; the former can act as a noise source in two ways. First, the overall radiation from the window into the sensor field of view decreases its sensitivity. Second, thermal gradients may appear as false targets to the IR sensor.

A dual-wavelength IR imager has traditionally been flown at an altitude and Mach number of 8 km and 0.45, respectively. Sensor bandwidths are $\Delta\lambda_1 = 3$ to $5 \mu\text{m}$ and $\Delta\lambda_2 = 8$ to $11.5 \mu\text{m}$. The nominal signal-to-noise ratio (S/N) has been estimated to be about 10 for each wavelength band, with the dominant "thermal-noise" source being the germanium (Ge) IR window. (We assume a minimum acceptable S/N of 5 has been established for both wavelength bands.) This inner window surface is convectively heated by cabin air only when its temperature approaches the dew point.

A candidate mission is proposed against a fast, highly dynamic target. The test director concludes that getting an acceptable IR imaging data collection window will require an aircraft Mach number of 0.9 at 8-km altitude. What S/N is expected for the experiment, and what can one do to enhance this?

Assuming a standard atmospheric temperature of 236 K, we find the wall (window) temperature for these two conditions to be [Eq. (3.3)]

$$T_1 = T(M = 0.45) = 244 \text{ K} ,$$

$$T_2 = T(M = 0.90) = 270 \text{ K} .$$

We assume the following characteristics for our IR imaging system:

1. The imager field of view (FOV) is small.
2. The IR window is the dominant source of thermal noise.
3. The IR window fills the entire sensor FOV.
4. The emissivities of germanium are constant across each of the two wavelength bands, with $\epsilon_{\Delta\lambda_1} = 0.45$, $\epsilon_{\Delta\lambda_2} = 0.30$.
5. The IR window is thermodynamically thin; e.g., see Eq. (3.39).

We next examine the ratio R_0 of the window-induced intensities at the detectors. We use Eq. (3.32) to estimate the spectral radiances of the IR window at the two temperatures T_1 and T_2 . We find

$$L_{\Delta\lambda_1}^*(244 \text{ K}) = 0.72 \times 10^{-5} \text{ W cm}^{-2} \Omega^{-1} ,$$

$$L_{\Delta\lambda_1}^*(270 \text{ K}) = 0.25 \times 10^{-4} \text{ W cm}^{-2} \Omega^{-1} ,$$

$$L_{\Delta\lambda_2}^*(244 \text{ K}) = 0.33 \times 10^{-3} \text{ W cm}^{-2} \Omega^{-1} ,$$

$$L_{\Delta\lambda_2}^*(270 \text{ K}) = 0.57 \times 10^{-3} \text{ W cm}^{-2} \Omega^{-1} ,$$

with the thermal noise ratio at the detector being

$$R_{\Delta\lambda_1} \equiv \frac{L_{\Delta\lambda_1}^*(270 \text{ K})}{L_{\Delta\lambda_1}^*(244 \text{ K})} = 3.5 ,$$

$$R_{\Delta\lambda_2} \equiv \frac{L_{\Delta\lambda_2}^*(270 \text{ K})}{L_{\Delta\lambda_1}^*(244 \text{ K})} = 1.7 .$$

Assuming a window-dominated detector S/N at the lower temperature ($T_1 = 244 \text{ K}$) of 10 for each wavelength band, the effective S/N at the candidate mission (Mach 0.9) will be $(\text{S/N})_{\Delta\lambda_1} = 2.9$, $(\text{S/N})_{\Delta\lambda_2} = 5.9$. Note that the 3 to

$5 \mu\text{m}$ band S/N is substantially below the minimum acceptable threshold, while the longer-wavelength S/N value is marginal.

One can perhaps improve this by cooling the inner surface of our IR window (e.g., with a convective flow of gaseous nitrogen). However, the cabin dew point must be monitored to preclude window condensation or frost formation. Either can dramatically alter effective window transmission properties in the IR. An alternative is to fly this mission at higher altitude or lower Mach number. Either approach will lower the effective window temperature, thus reducing detector thermal noise.

A second concern associated with IR windows is thermal-optical aberrations. In general, these depend on several complex factors, including the external and internal surface temperatures, window material properties, and window-mounting techniques. However, the causes of such thermally induced optical distortions are local strains e due to temperature gradients ΔT , which have the relationship $e = \alpha \Delta T$, where α is the coefficient of linear thermal expansion in the optical element. These AO-induced optical distortions are of concern for both outgoing wave-front and imaging systems. Although such effects are generally ameliorated at the longer IR wavelengths, the optical designer must be aware of these aberration sources and include estimates as part of the overall system error budget.

3.4.7 Example 7—Supersonic Vehicle Optical Aberrations

Case I (Nose-Mounted System). Our next challenge is to estimate the AO effects for a nose-mounted optical system on a Mach 6 endoatmospheric vehicle. Figure 3.15 shows a conceptual configuration. When the leading edge of the body is blunt, the shock, or bow, wave does not touch the body. Rather, a subsonic flow field exists behind the shock; the velocity field normal to the surface must be zero at the leading edge. This region in which our optical window is located is known as the flow stagnation zone.

There are three principal sources of optical aberrations: (1) bow shock curvature; (2) stagnation pressure, steady and unsteady at the optical window; and (3) thermo-optical effects.

First consider the strength of the (normal) shock at the optical axis. For a Mach 6.0 vehicle at 8-km altitude, Eq. (3.9) yields $\rho/\rho_0 \approx 5.3$, with $\rho_0 = 5.3 \times 10^{-4} \text{ g/cm}^3$. This is close to the strong shock limit ($\rho/\rho_0 \rightarrow 6$). The corresponding shock reflectivity [Eq. (3.15)] is $R \approx 9 \times 10^{-8}$. Although radiation transmission losses are negligible, the shock-reflected component for an outgoing wave front could be a noise source for the detector unless gated out of the return signal.

The pressure at the nose for incident supersonic flow is given by⁵

$$P = P_0 \frac{\left(\frac{\gamma + 1}{2}\right)^{[(\gamma + 1)/(\gamma - 1)]} M_0^2}{\left[\gamma - \frac{(\gamma - 1)}{2M_0^2}\right]^{1/(\gamma - 1)}} \quad (3.47)$$

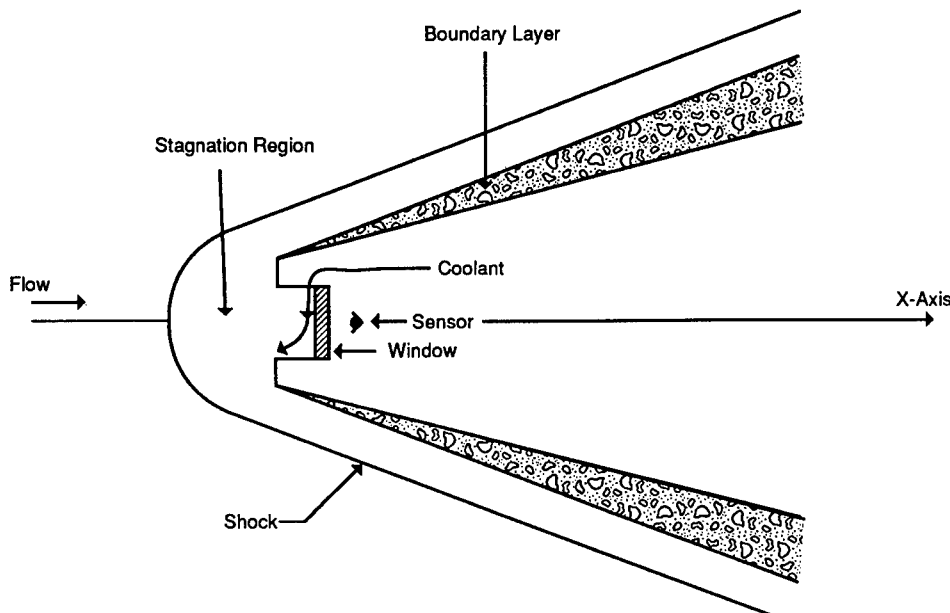


Fig. 3.15 A nose-mounted optical system on a Mach 6 endoatmospheric airborne platform can experience severe window heating due to flow-field stagnation-temperature effects. Careful design to include a window-cooling system is generally required. Note that such stagnation-zone thermal effects can cause strong AO optical aberrations as well as contributing to sensor noise.

For example, $M_0 = 6.0$, altitude 8 km yields a pressure at the window of about 16.5 standard (sea level) atmospheres. Obviously, this mean pressure field must be considered in designing the window for this nose-mounted system. Moreover, window buffeting due to the pressure fluctuations within this nosetip cavity may be an important issue. A useful figure of merit is the ratio of cavity rms unsteady pressure P_{rms} to the free-stream dynamic pressure q . Typical P_{rms} values in this supersonic regime can be 10 to 20% of mean cavity pressure values.

Next, we examine aerothermal effects at the nose-mounted window. We assume a free-stream temperature $T_0 = 236$ K, a Mach number of 6.0, and $\gamma = 1.4$. The approximate nose stagnation temperature [Eq. (3.3)] is 1748 K. A window coolant will probably be required if the missile is in this hypersonic environment for more than a few seconds. Moreover, the resulting cavity turbulence can induce severe optical aberrations. We will consider window-coolant AO effects in our final example.

Case II (Fuselage-Mounted System). An alternative location for a supersonic-platform optical system is along the fuselage, as shown in Fig. 3.5. We again assume an axially symmetric body. Advantages of locating our optical system along the fuselage are reduced drag and less pressure-induced window stress. However, there are two primary disadvantages. First, the optical system field-of-regard is generally restricted with respect to its nose-mounted counterpart. Second, if the optical system is required to perform a tracking function, the

Table 3.4 Look Angle Errors Resulting from an $M = 6.0$ with a 30-deg Shock Angle and the Vehicle at an Altitude of 8 km*

β_0	$\Delta\beta$	$\Delta\beta_{\text{max}}$
20 deg	0.12 (mrad)	0.21 (mrad)
30	0.19	0.34
40	0.27	0.49
50	0.39	0.69
60	0.56	1.01

* β_0 is the incident angle of the optical axis with the normal to the shock. The parameter $\Delta\beta$ is the difference between the incident and refracted wave fronts. Note $\Delta\beta = 0.5$ mrad would result in a 5-m miss distance for a target range of 10 km. The final column shows errors resulting for limiting cases $M \gg 1$ ($\rho/\rho_0 \rightarrow 6$). Note these results have only a weak wavelength dependence via index of refraction.

target image can be shifted in position owing to shock refractive effects. This boresite shift acts as a direct error source for a centroid tracker.

Consider the magnitude of this shock-induced beam steering. Suppose our Mach 6.0, 8-km-altitude vehicle has a shock angle $\theta = 30$ deg. Equation (3.9) yields a density ratio behind this shock $\rho/\rho_0 = 3.9$. The tracker look angle error follows from Eq. (3.10). Table 3.4 summarizes these estimates. Such errors can strongly affect optical tracker performance.

One approach to solving this problem is to have an onboard algorithm that provides a tracking-angle offset by continually calculating the error as a function of vehicle Mach number, angle of attack, look angle, and altitude. However, even if these parameters are well known, errors may result because the vehicle angle of attack is changing rapidly as it tracks a moving target. Figure 3.9(b) summarizes angular deviations due to shock refractive effects as a function of incident angle for a range of platform altitudes.

A second source of optical aberration—primarily defocus and astigmatism—results from vehicle shock curvature effects. Consider again our conical-nosed airframe traveling at Mach 6.0. The focal length of the shock wave in the plane perpendicular to the airframe longitudinal axis is given by Eq. (3.12). Substituting the parameters from our example above yields $F/X = 1.28 \times 10^3$. For example, if our optical axis is 3 m from the nose tip, then $F = 3.84$ km along the cone axis. Suppose our platform imaging system is focused on an object at an actual range $F_0 = 10$ km. If we treat the aerodynamic (shock) lens and the optical-system imager as two thin lenses having a separation that is small compared to either focal length, then the effective system focal length F^* is approximately

$$\frac{1}{F^*} = \frac{1}{F} + \frac{1}{F_0} . \quad (3.48)$$

Substitution yields an effective focal length along one plane of about 2.8 km! The shock surface in the plane parallel to the vehicle axis has markedly less

curvature; thus, this supersonic flow field also causes astigmatic optical effects. If the platform beam-control system does not sense and correct for this shock aero-optical aberration, the transmitted beam will suffer significant loss of far-field performance. Note also that the above results are only weakly wavelength dependent via the Gladstone-Dale parameter.

This example conveys two important messages. First, supersonic vehicle windows will be exposed to extremely hostile environments. Second, fuselage-mounted optical imagers/trackers can experience mission-threatening aberrations from platform shocks and inviscid effects even before random flow effects are considered. All factors must be carefully weighed by an optical designer.

3.4.8 Example 8—Supersonic Vehicle Flow-Field-Induced Thermal-Radiation Effects

Shock waves, random flows, and windows can introduce thermal noise into the platform sensors. We next examine the radiation strengths of these several sources. Consider a Mach 8 vehicle at altitude 10 km ($T_0 = 223$ K) having a wedge-shaped nose with deflection angle $\theta_v = 30$ deg. From Fig. 8(b), the corresponding shock angle θ is approximately 40 deg. The platform near-IR imaging system (sensor bandpass 1 to 2 μm) is located 1 m aft of the vehicle nosetip. We suppose the window coolant system maintains an average window temperature of 300 K. Radiation from flow ionization and plasmas can be important above this Mach number regime; however, these effects are neglected here.

There are, in general, three major vehicle flow-field contributors to sensor thermal noise: the shock layer, the fuselage boundary layer, and the window (adiabatic) temperature.

First, the ratio of static temperatures across a shock wave follows from the perfect gas law and Eq. (3.9):

$$\frac{T}{T_0} = \frac{[2\gamma M_0^2 \sin^2 \theta - (\gamma - 1)][(\gamma - 1)M_0^2 \sin^2 \theta + 2]}{(\gamma + 1)^2 M_0^2 \sin^2 \theta}. \quad (3.49)$$

Substitution of the above values into Eq. (3.49) reveals a temperature T within the shock layer of approximately 1356 K.

Next, the boundary-layer temperature is estimated by taking the temperature behind the shock T as our effective static temperature, with a Mach number in this region following from⁴

$$M^2 = \frac{2 + (\gamma - 1)M_0^2 \sin^2 \theta}{2\gamma M_0^2 \sin^2 \theta - (\gamma - 1)} \frac{1}{(\sin^2 \Delta\theta)}. \quad (3.50)$$

Here, $\Delta\theta$ is the difference between our shock angle θ and the wedge angle θ_v ($\Delta\theta \approx 10$ deg). From Eq. (3.50), the Mach number behind the vehicle shock is $M = 2.38$, with a corresponding adiabatic wall temperature [Eq. (3.3)] $T_w = 2723$ K. Note that Eq. (3.50), with $\Delta\theta$ defined as above, is valid for all two-

dimensional flows, e.g., wedge. However, in the case of three-dimensional fields (e.g., conical flow), this $\Delta\theta$ is valid only at the nosetip. In general, for aft locations the effective $\Delta\theta$ can only be estimated via detailed computational fluid-mechanics methods.

It is instructive to compare the total energy radiated onto the platform sensor by the flow fields to that of the window for the $\theta = 40$ -deg shock-angle case. We assume all three sources fill the detector FOV. Note that the shock radiant contribution is negligible compared to the 2723 K fuselage boundary-layer temperature. We take the total emission rate of air for our flight conditions to be²³ $\approx 0.01 \text{ W/cm}^3$. The corresponding radiant emittance for our 1.5-cm-thick boundary layer is about $1.5 \times 10^{-2} \text{ W/cm}^2$. Assuming a total emissivity of 0.2 for our uniformly cooled (300 K), 1-cm-thick window yields an approximate emittance of $9.2 \times 10^{-3} \text{ W/cm}^2$. In this instance the total radiant emittance of the vehicle flow field exceeds that of the window as a source of detector thermal noise.

In general, the system sensor will have a wavelength bandwidth $\Delta\lambda$. The radiant strength of each component is estimated via Eq. (3.32), using the appropriate temperature and spectral emissivity of each element.

This example illustrates that supersonic airflow effects can be an important source of sensor thermal noise, with radiant strengths comparable to or greater than that of the (cooled) exit window. The optical designer must evaluate these several noise sources and include estimates of the effect of each in the overall sensor signal-to-noise budget.

3.5 AERO-OPTICS: VISIONS AND OPPORTUNITIES

Earlier sections of this chapter discussed the theory and analysis tools available to solve aero-optics problems and the techniques available to access the influence on specific optical propagation problems. The present state of the art offers several opportunities to tailor the flow fields that introduce aero-optical aberrations. Splitter plates can be employed to tailor and control a fuselage turbulent flow field (Fig. 3.16). Injection of a supplemental flow⁴ or its reverse, selective flow removal, can also be used to alter the character of a disturbance.

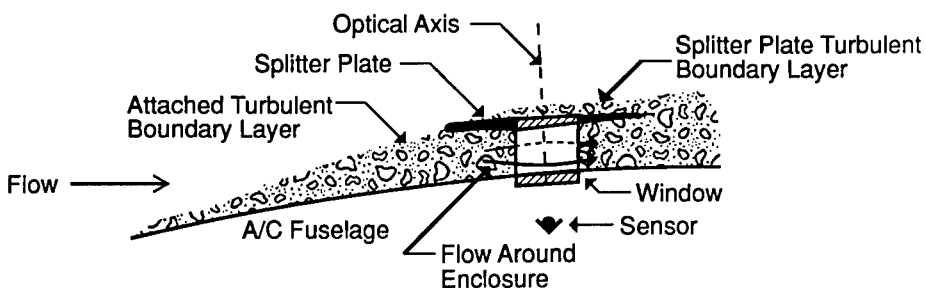


Fig. 3.16 A splitter plate/diverter is a (wind-tunnel) proven technique. The natural TBL is diverted around the enclosed optical train. The splitter plate is positioned in the free stream; the resulting "new" TBL on the plate is considerably weaker than the natural TBL. Although system optical performance generally is improved, the effects of this on platform flight characteristics must be carefully evaluated via computational analyses and/or wind-tunnel simulations.

For open-port applications, techniques for quieting a cavity are available that reduce the mechanical disturbances that cause system jitter, while introducing minimum optical loss (Fig. 3.4). Forward and aft body shapes also have been successfully employed to tailor the flow around an exit aperture or a protuberance extending into the free stream. While all of these techniques can, if properly employed, have a positive effect, total success is unlikely. As long as there is a flow field, residual optical aberration will remain.

Emerging technologies in nonlinear optics (NLO), conventional adaptive optics, and atmospheric compensation offer the promise of correcting not only local aerodynamically induced optical distortions, but compensation of the aberrations in the entire optical system as well.

A nonlinear process known as four-wave mixing has been shown to cancel path optical distortions when a reference source is available.²⁴⁻²⁷ This process actually leads to the dynamic cancellation of the wave-front aberrations within a nonlinear crystal. The technology is fundamentally different from an optical correction system that has to sense the wave-front aberrations and then rapidly compensate for them, such as with a deformable mirror. In the experiments shown in Fig. 3.17, the nonlinear optical material had a very slow response time, on the order of a second or so. The aberration source was a heat gun, and the temporal bandwidth of the aberrations was perhaps several hundred hertz, yet the system worked very well. Because there is rapid cancellation of the phase aberrations, the long time constant of the nonlinear material averages the distortions of the aberrator to zero, yielding a high-quality object image. Thus, while the nonlinear material has a very slow response time, this particular compensation scheme actually is most effective for application with high-frequency bandwidth optical distortions. A limitation inherent with this compensation scheme is that the object and reference sources must be coherent.

Pulsed compensation systems have been proposed to demonstrate the image-compensation phenomenon with less restrictive requirements on the coherence of the object and reference radiation. The process is different in that the aberrations are first imprinted in the nonlinear material, and then subsequently

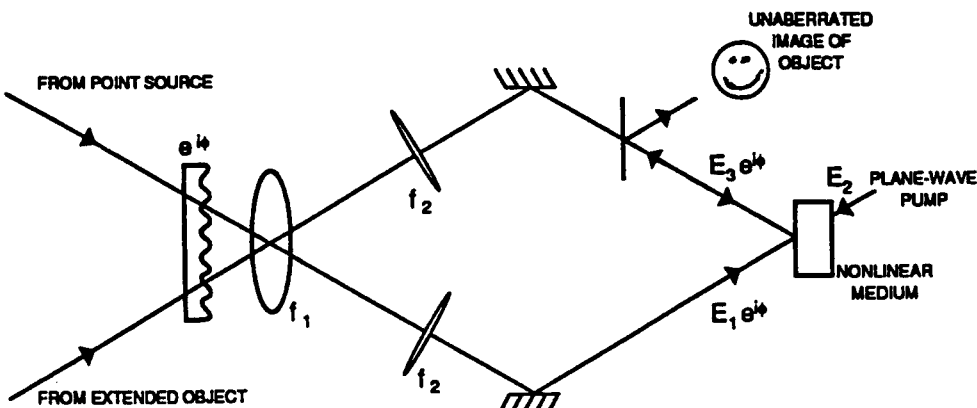


Fig. 3.17 Correction of random flow-field-induced optical aberrations has recently been demonstrated via a nonlinear technique known as four-wave mixing (FWM). Shown is the experimental setup. A limitation of this particular FWM approach is that the object and reference sources must both be coherent.

read out by the object radiation, which is also distorted by the aberration. While some nonlinear materials can be very fast, this rapid response comes at the expense of needing higher peak powers to stimulate the process. But, in this instance, the requirement for the coherence properties of the reference and object radiation is substantially reduced. "Real-time" holograms are an example of such an approach. Generally, such techniques employ a spatial light modulator, a very special nonlinear optical device that operates much like a real-time hologram. While these devices are not of extremely high frequency and spatial bandwidth, they are able to demonstrate good correction of aberrations of 50 to 100 Hz. This approach is well suited for compensating lower temporal frequencies.

Nonlinear optical techniques for correction aberrations may revolutionize optical imaging. Figure 3.18 shows several possible applications; Fig. 3.19 depicts two optical layouts germane to an airborne configuration.

Conventional adaptive optics can provide effective adjunct solutions to aero-optical aberrations. This technology is ideally suited for low spatial and temporal aberration corrections; such aberrations are generated in aero-optical environments by a variety of sources, including thermal, mechanical, and pressure gradients induced by the flow field.

Conventional adaptive optics approaches generally include deformable mirrors and optical wave-front sensors (see Fig. 3.20). Here, the wave-front sensor dissects the entrance aperture of the imaging telescope into small sections, or subapertures. The signal collected by each of these subapertures is sensed to determine its wave-front tilt. The first step is to determine the phase of the aberration; this information is then used to close a correction loop with the deformable mirror. The closed-loop system drives the measured wave-front errors to zero, yielding a compensated image. Applications of adaptive optics to turbulence compensation are described in the literature.^{18,28}

In this general class of compensation systems, there must be a reference source of radiation, and, while this is also true with the nonlinear compensation schemes, there is a major difference. In the conventional adaptive-optics schemes, this radiation can be essentially incoherent. As a consequence, the sensed radiation could be sunlight reflected from the object of interest, or some adaptation of the Guidestar technique,²⁸ in which laser atmospheric Rayleigh scatter is used as a beacon. Alternative reference sources include thermal self-emissions of an object as well as reflected laser radiation.

There are limitations imposed by conventional systems, e.g., the deformable mirror. These mirrors are usually operated with mechanical actuators made of piezoelectric material. Packing these elements together more closely than about 1 cm is difficult. In addition, the mechanical complexity of these systems grows rapidly with aperture size. In general, the number of mechanical actuators required increases as $(D/\ell)^2$, where D is the aperture diameter and ℓ is the flow-field correlation length.

Because these mechanical systems require electronic sensing of the wave-front tilts, computational calculations of the wave-fronts, and mechanical deflection of the deformable mirrors, they tend to have a more limited temporal bandwidth response. However, for many types of aero-optical disturbances of practical interest, the temporal and spatial response of the conventional adaptive-optics systems may suffice. Deformable mirror systems have been

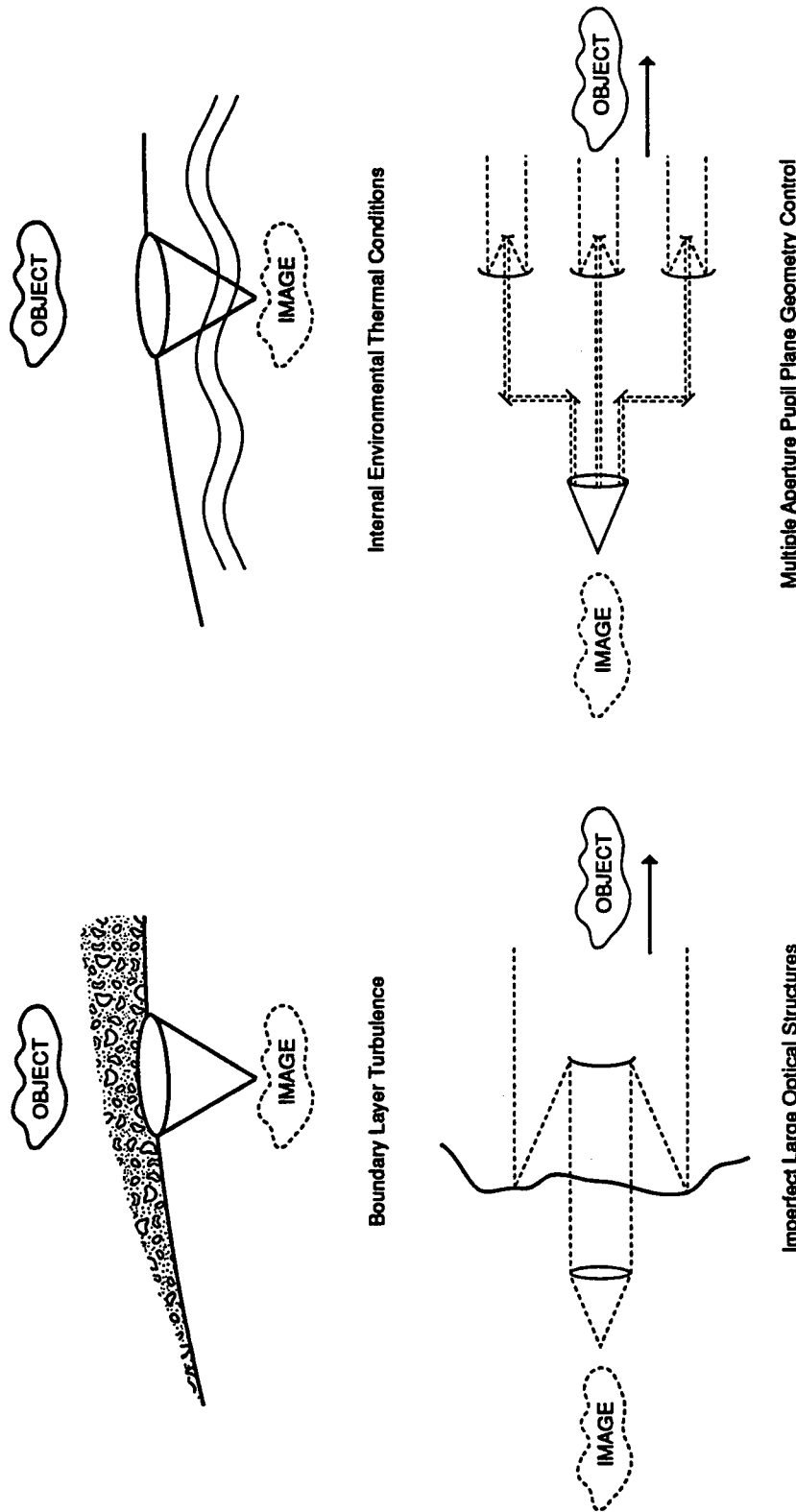
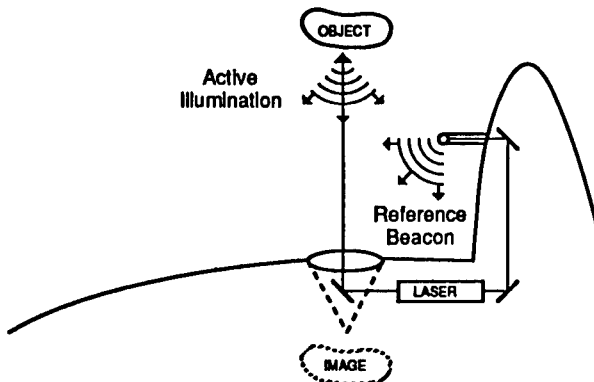
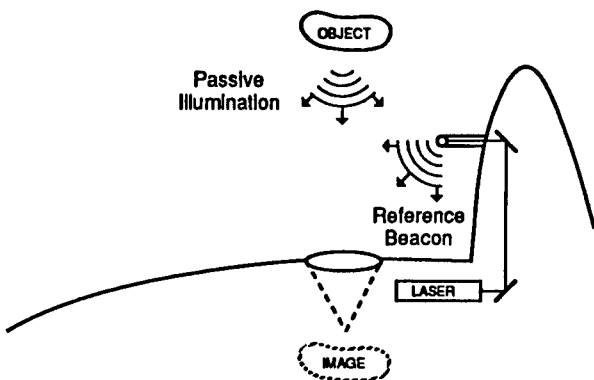


Fig. 3.18 Shown are several classes of optical-train aberrations that can be addressed via nonlinear-optics (NLO) techniques. Correction fidelity depends on the spatial and temporal responses of the NLO material. In principle, NLO beam control can yield almost perfect correction of system optical aberrations, thus allowing nearly diffraction-limited imaging performance.



Active Object Illumination and Coherent Beacon



Passive Object Illumination and Coherent Beacon

Fig. 3.19 Several NLO beam-control implementation techniques are feasible for an airborne platform. Sources of radiation can be obtained from the object (active or passive illumination) or via reference beacons attached to the platform.

demonstrated to operate with bandwidths of several hundred hertz, adequate for many optical-system aberrations. For example, a recent analysis¹⁰ of subsonic-platform aero-optical aberrations indicates that a 100-Hz bandwidth deformable mirror can provide a marked improvement in optical performance. With a wave-front sensor, signal-processing electronics, and the deformable mirror and its drive electronics, significant resource investments are required to implement conventional adaptive optics. However, conventional adaptive optics is a proven technology; its ability to mitigate low-order, low-temporal-bandwidth flow-field aberrations can yield a significant net improvement in overall system contrast, resolution, and brightness.

Airborne-platform visible imaging is a particularly promising application of advanced adaptive-optical beam-control technique (Fig. 3.21). Such an imaging platform has a number of intrinsic advantages, including mobility, speed, and independence from weather strictures. In general, one first locates the imager as far forward on the platform as practical in order to minimize aero-

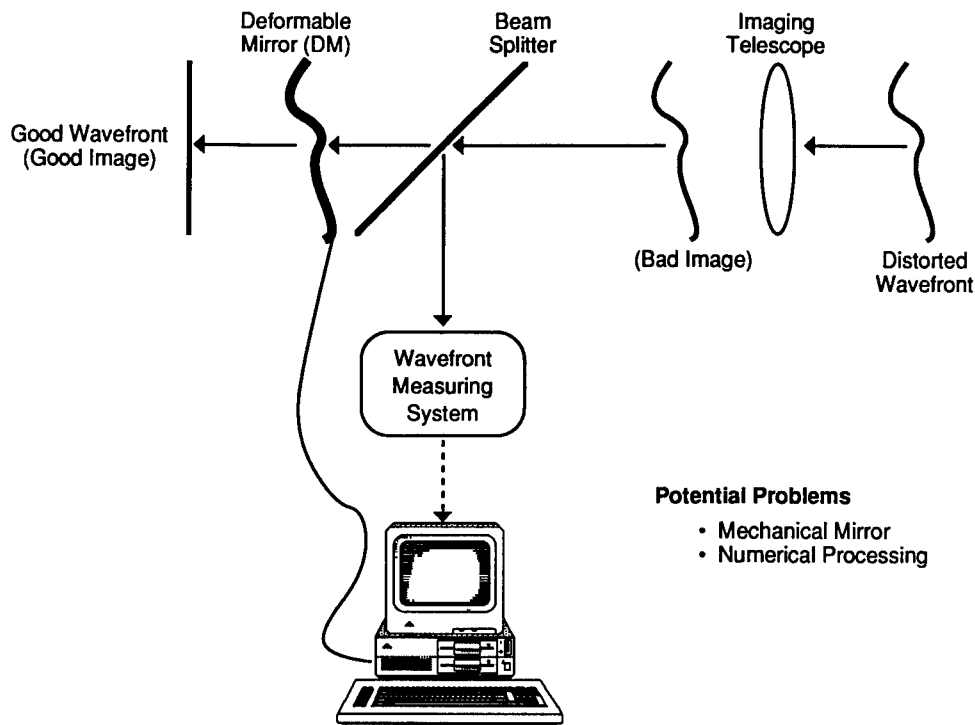


Fig. 3.20 Conventional adaptive-optics compensation systems use deformable mirrors (DMs) and wave-front sensors. Each subaperture phase is measured; phase-conjugate signals are sent to the corresponding zone of the DM. These optomechanical systems are limited in spatial/temporal bandwidth, particularly as the system aperture diameter D increases.

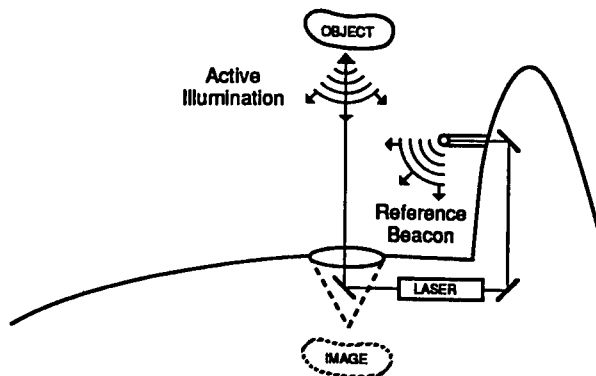


Fig. 3.21 Shown is a promising airborne-platform nonlinear optics (NLO) beam-control technique recently demonstrated in the laboratory. An onboard laser actively illuminates the object and provides a local reference source. Image correction is achieved via four-wave mixing. Heated air was passed across the aperture to simulate airborne-platform AO effects. In principle, NLO techniques can yield nearly diffraction-limited images in the presence of platform-induced optical aberrations.

optical effects. Even so, aircraft-fuselage boundary layers can sometimes severely constrain the performance of large-aperture, visible imaging systems. Nonlinear optical beam-control methods, perhaps in concert with conventional techniques, hold the potential of effecting almost total correction of both ac-induced and natural atmospheric optical aberrations. The exciting result could be image quality from airborne platforms limited only by intrinsic optical-system performance. Such is indeed a noble goal!

References

1. G. W. Sutton, "Effect of turbulent fluctuations in an optically active fluid medium," *AIAA Journal* **7**(9), 1737–1743 (Sep. 1969).
2. J. H. Gladstone and J. Dale, "On the influence of temperature on the refraction of light," *Phil. Trans.* **148**, 887 (1858).
3. G. Havener, "Optical wave front variance: a study of analytical models in use today," AIAA Paper 92-0654 (January 1992).
4. K. G. Gilbert and L. J. Otten, *Aero-Optical Phenomena*, Program in Astronautics and Aero-nautics (Volume 80), American Institute of Aeronautics and Astronautics, New York (1982).
5. L. D. Landau and E. M. Lifshitz, *Fluid Mechanics*, 2nd ed., p. 319, Pergamon Press, Elmsford, NY (1987).
6. L. D. Lorah and E. Rubin, "Aerodynamic influences on infrared system design," in *The Infrared Handbook*, W. L. Wolfe and G. J. Zissis, Eds., The Environmental Research Institute of Michigan, Ann Arbor, MI (Revised 1985).
7. J. E. Craig and W. C. Rose, "Wavelength effects on images formed through turbulence," AIAA Paper 87-1398 (June 1987).
8. J. E. Craig and W. C. Rose, "The optics of aircraft shear flows," AIAA Paper 85-0557 (March 1985).
9. W. C. Rose and J. M. Cooley, "Aerodynamics of the Kuiper Airborne Observatory cavity flow-field," REAR-TR-84-1, Rose Engineering and Research, Inc. (October 1984).
10. J. E. Craig and C. Allen, "Aero-optical turbulent boundary layer/shear layer experiment on the KC-135 aircraft revisited," *Opt. Eng.* **24**(3), 446–454 (1985).
11. J. L. Elliot, E. W. Dunham, R. L. Baron, A. W. Watts, S. E. Kruse, W. C. Rose, and C. M. Gillespie, Jr., "Image quality on the Kuiper Airborne Observatory. I. Results of the first flight series," *Astronomical Soc. Pacific* **101**, 737–764 (1989).
12. H. Schlichting, *Boundary Layer Theory*, 4th ed., McGraw-Hill Book Company, New York (1968).
13. W. C. Rose and J. M. Cooley, "Analysis of the aerodynamic data from the AOA wind tunnel test and implications for the AOA platform," Final Report Contract DAAH01-85-C-0312 (October 1985).
14. W. C. Rose and J. M. Cooley, "Feasibility of the contoured-aft-ramp concept for the KAO. Results from the Phase A and B studies," prepared for Northrop Services, Inc., NASA/Ames Research Center under Prime Contract NAS2-12235 (1987).
15. D. A. Buell, "Airloads near the open port of a one-meter airborne telescope," AIAA Paper 75-71, presented at the 13th Aerospace Sciences Meeting (January 1975).
16. W. C. Rose, "Aerodynamics of seeing on large transport aircraft—Progress report 1 December 1985–31 May 1986," prepared for NASA/Ames Research Center under Contract NCC2-382.
17. W. T. Welford, *Optics*, 3rd ed., p. 61, Oxford University Press, Oxford, UK (1988).
18. R. K. Tyson, *Principles of Adaptive Optics*, p. 15, Academic Press, Orlando, FL (1991).
19. J. B. Shellan, "Phased-array performance degradation due to mirror misfigures, piston error, jitter, and polarization errors," *Journal of the Optical Society of America A* **2**, 4 (1985).
20. M. R. Banish, R. L. Clark, and A. D. Kathman, "Wavelength dependence of blur circle size through turbulent flow," Teledyne Brown Engineering Report No. 1326-25 (1990).
21. D. L. Fried, "Optical resolution through a randomly inhomogeneous medium for very long and very short exposures," *J. Opt. Soc. Am.* **56**, 1372 (1966).

22. M. S. Scholl, "Simulation of spectral radiance of a dynamic infrared source," dissertation, University of Arizona (1980).
23. S. S. Penner, *Quantitative Molecular Spectroscopy and Gas Emissivities*, Addison-Wesley Publishing Company, Reading, MA (1959).
24. K. R. MacDonald, W. R. Tompkin, and R. W. Boyd, "Passive one way aberration correction using four wave mixing," *Opt. Lett.* **13**, 485 (1988).
25. T. G. Alley, M. A. Kramer, D. R. Martinez, and L. P. Schelonka, "Single-pass imaging through a thick dynamic distorter using four wave mixing," *Opt. Lett.* **15**, 81 (1990).
26. M. A. Kramer, T. G. Alley, D. R. Martinez, and L. P. Schelonka, "Effects of thick aberrations on a polarization dependent one-way imaging scheme," *Appl. Opt.* **29**, 2576 (1990).
27. M. A. Kramer, C. J. Wetterer, and T. Martinez, "One way imaging through an aberrator with spatially incoherent light using an optically addressed spatial light modulator," *Appl. Opt.* **30**, 3319 (1991).
28. R. Q. Fugate, D. L. Fried, G. A. Ameer, B. R. Boeke, S. L. Browne, P. H. Roberts, R. E. Ruane, G. A. Tyler, and L. M. Wopat, "Measurement of atmospheric wavefront distortion using scattered light from a laser guide-star," *Nature* **353**, 144–146 (1991).

CHAPTER 4

Nonlinear Propagation: Thermal Blooming

Frederick G. Gebhardt
*Science Applications International Corporation
Lexington, Massachusetts*

CONTENTS

4.1	Introduction	289
4.2	Historical Overview	289
4.2.1	The Early Years: 1964–1969	290
4.2.2	The Middle Years: 1969–1979	290
4.2.3	The Later Years: 1979–Present	290
4.3	Blooming Basics	291
4.3.1	Governing Equations	291
4.3.2	Isobaric Heating	292
4.3.3	Nonisobaric Heating	293
4.4	Steady-State Blooming with Wind/Beam Motion	294
4.4.1	Collimated Beam—Homogeneous Path	294
4.4.2	Focused Beams—Inhomogeneous Paths	299
4.4.3	Up-link Thermal Blooming	304
4.5	Conclusions	311
	References	311

4.1 INTRODUCTION

When a high-energy laser (HEL) beam propagates through the atmosphere, a small portion of the energy is absorbed by certain molecules and particulate matter in the air. The absorbed energy heats the air, causing it to expand and form a distributed thermal lens along the atmospheric path that, in turn, spreads, bends, and distorts the laser beam. This self-induced effect is called thermal blooming and, since it can limit the maximum power that can be efficiently transmitted through the atmosphere, is one of the most serious nonlinear problems encountered in the propagation of high-energy laser radiation in the atmosphere. A variety of thermal blooming effects are relevant for high-energy laser beams in the atmosphere. Many of these effects have been studied extensively and a number of detailed review articles have been written that describe most of the work prior to about 1980.¹⁻⁶

Because of the recent intense interest in small-scale thermal-blooming instabilities,⁷ it has become customary to refer to the large-scale thermal-blooming effects that spread, bend, and distort the entire beam as "whole-beam" thermal blooming. We restrict our attention here primarily to the problem of whole-beam thermal-blooming effects, which represents the bulk of the work prior to 1985. It is interesting to note, however, that the initial interest in and studies of thermal-blooming amplification of small-scale intensity perturbations, or stimulated thermal Rayleigh scattering (STRS),^{8,9} occurred prior to most of the work on whole-beam blooming effects in the atmosphere.

In this chapter we begin with an overview of the work that has been done on thermal blooming during the past twenty-five years. The emphasis here is to try to connect the extensive earlier results for whole-beam blooming effects with the more recent work on up-link thermal-blooming compensation and related small-scale instabilities. Section 2 gives a brief historical overview outlining the particular types of blooming problems that have been studied during each of the major periods of work on blooming since the first observations of "thermal-lens" effects in liquids were reported.^{10,11} The fundamental thermal-blooming equations for continuous-wave (cw) and single-pulse laser beams are presented in Sec. 3. In Sec. 4 some of the basic results and scaling parameters for steady-state whole-beam thermal-blooming effects in the atmosphere are reviewed. Here the blooming is characterized by isobaric heating with convection-dominated heat transfer, due to the combined effects of wind and beam motion. The cases considered include both collimated and focused beams propagating within the absorbing atmosphere as well as that of a ground-based laser beam propagating through the atmosphere to a target in space. Conclusions are presented in Sec. 5.

4.2 HISTORICAL OVERVIEW

If one looks at the work on thermal blooming over the past twenty-five years, one finds that it can be roughly divided into the following three periods based on the types and applications of the blooming problems being studied: (1) the early years (1964–1969), (2) the middle years (1969–1979), and (3) the late years (1979 to the present). The nature and emphasis of the thermal blooming work in these three periods is summarized below.

4.2.1 The Early Years: 1964–1969

Work on whole-beam thermal blooming began with the first reported observation of a new “thermal-lens effect” when transparent absorbing liquids (and some solids) were placed in a laser cavity.^{10,11} The major emphasis initially was on the thermal blooming of stationary cw laser beams in liquids. With thermal conduction as the dominant heat-transfer mechanism, the dominant effect on the laser beam was the spreading produced by the negative-lens-like refractive-index gradient, which naturally led to the use of terms like “thermal defocusing,” “self-defocusing,” “nonlinear defocusing,” “self-induced divergence,” etc.^{12–16} Early interest in the thermal-lens effect was in its practical application for low-absorption measurements.^{17–19} Another early application reported for the thermal-lens effect was for its use as a power-limiting device.²⁰ Interest in high-energy laser-beam propagation in the atmosphere led to the earliest studies of both small-scale^{8,9} and whole-beam^{21–24} convection-dominated thermal-blooming effects in gases.^{15–18}

4.2.2 The Middle Years: 1969–1979

For the next five years or so extensive experimental and theoretical efforts were devoted to developing a basic understanding of atmospheric thermal-blooming effects and their limits for cw, pulsed, and repetitively pulsed high-energy laser-beam propagation.^{1–5} The emphasis in these earlier studies was to develop a basic understanding of the physics of thermal-blooming process using simple and, more-or-less, idealized conditions to represent the characteristics of the laser beam and the atmosphere. A number of detailed wave-optics propagation codes were also developed to treat a variety of atmospheric thermal-blooming problems.^{1,2,4,5,25} Good agreement was obtained from comparisons of the results from the codes and laboratory simulation experiments.⁴ Some of the special blooming problems studied, in addition to the important case of convection-dominated blooming with wind and beam slewing, included the effects of beam jitter, optical turbulence, turbulent mixing, kinetic cooling, stagnation zones, noncoplanar wind and beam slewing, transonic slewing, aerosol blooming, and imaging through blooming. The use of focusing/defocusing, different beam profiles and aperture shapes, and phase compensation were all considered as possible ways for correcting or reducing thermal-blooming effects.⁴ During the later years of this period the emphasis shifted toward (1) the development of both detailed wave-optics codes and systems-level scaling laws for treating the combined effects of thermal blooming together with all relevant linear effects (e.g., nonideal beam quality, beam jitter, turbulence-induced beam spreading and wander) and (2) the consideration of more realistic conditions for the laser beam, scenario, and electro-optical and meteorological (EO-MET) properties of the atmosphere.

4.2.3 The Later Years: 1979–Present

During this most recent period the major emphasis has been on the problems of blooming and its compensation for ground-to-space HEL beam propagation. Interest also shifted from the longer infrared wavelengths of the 10.6- μm CO₂ and 3.8- μm DF lasers of greatest interest in the 1970s to the much shorter

near-UV, visible, and near-infrared wavelengths to obtain the reduced diffraction losses/improved propagation efficiency required for the much longer ranges involved. The requirements for propagating large laser power densities at short wavelengths through the atmosphere for potential strategic missions resulted in significant renewed interest and research in the modeling of HEL beam propagation with adaptive phase correction of thermal blooming and turbulence. There has been an intense effort recently to understand and model the physics of both open- and closed-loop small-scale thermal-blooming instabilities. The instabilities are strongly seeded at short wavelengths by optical-turbulence-induced scintillation effects. Atmospheric velocity turbulence, on the other hand, is expected to be important in damping or reducing the small-scale growth. Small-scale blooming effects are of greater concern than whole-beam blooming for large phase-compensated beams since their limits on the critical/largest correctable power are lower than those due to whole-beam effects.

4.3 BLOOMING BASICS

Thermal blooming refers to the general effects of self-induced phase distortion and the resulting distortion of the laser-beam irradiance that occur when a laser beam propagates through an absorbing medium. The absorbed laser-beam energy, which typically is only a very small fraction of the total laser-beam energy, heats the medium, causing localized gradients in the density and, hence, also the refractive index of the medium, which, in effect, act as a distributed or thick nonlinear lens on the laser-beam propagation. Since the laser-beam heating of the absorbing medium usually results in the expansion and a decrease in refractive index of the medium in the region of the beam where the heating is greatest, the beam is usually defocused and spread, as suggested by the term "blooming." The exact nature of the thermal-blooming effects on the laser beam generally depends, however, on a number of factors. These include (1) the laser beam characteristics [i.e., wavelength, phase and irradiance distributions, and the temporal mode, e.g., cw, single pulse (SP), or repetitively pulsed (RP)]; (2) the kinetics of the absorption process, which determine the time required for the absorbed energy to heat (or, under certain special conditions with CO₂ laser beams, to cool⁴) the atmosphere; (3) the mode(s) of heat transfer that balance(s) the absorbed energy (e.g., thermal conduction, natural or free convection, forced convection, or the generation of sound waves); (4) the time scale of interest (e.g., transient versus steady-state conditions); and (5) the propagation medium and scenario characteristics (e.g., the path length, optical properties, platform speed, slewing, etc.).

4.3.1 Governing Equations

The basic governing equations for the thermal-blooming effects on the laser-beam complex field $u(R)$ are (1) the time-independent paraxial scalar wave equation

$$\left[2ikn(R)\left(\frac{\partial}{\partial z} + \frac{\kappa_e}{2}\right) + \nabla^2 + k^2n^2(R) \right]u(R) = 0 \quad (4.1)$$

and (2) the equation for the refractive index of the absorbing medium

$$n(R) = n_0 + n_B[\alpha I(R)] . \quad (4.2)$$

The envelope of the wave function u is assumed to change slowly compared to the propagation time, and the phase gradients are assumed to be small owing to the heating effects. We have suppressed the harmonic time factor $\exp(-i\omega t)$ for the function u ; $k = \omega/c = 2\pi/\lambda$ is the free-space propagation constant where c and λ are the speed of light and wavelength in vacuum, respectively; and $\kappa_e = \alpha + \sigma$ is the extinction coefficient of the medium where α and σ are the absorption and scattering coefficients, respectively. The refractive index n consists of a constant background value n_0 and the blooming contribution n_B , which is a function of the absorbed laser-beam power density $\alpha I = \alpha|uu^*|$.

4.3.2 Isobaric Heating

For cw laser beams (and also RP beams with negligible SP blooming) in the atmosphere, it is customary to assume that the heating occurs instantaneously and that the heating rate is sufficiently small that pressure disturbances are negligible. Thus, with the heating assumed to be isobaric, i.e., at constant pressure, the blooming contribution to the refractive index is given by $n_B = n_T T_B$, where $n_T = dn/dT = -(n_0 - T_0)/T_0$ is the refractive-index change with respect to temperature of the gas at constant pressure and T_B , the temperature rise due to laser heating, is given by the energy-balance equation

$$\rho C_p \left(\frac{\partial}{\partial t} + \mathbf{v} \cdot \nabla - \frac{K}{\rho C_p} \nabla^2 \right) T_B = \alpha I . \quad (4.3)$$

Equations (4.1) to (4.3) are used to describe the transient development and steady-state solutions for the thermal blooming of a cw or RP laser beam when both thermal conduction and convection heat transfer are present.

Thermal-conduction-dominated blooming, described by the third term in Eq. (4.3), occurs when the beam is stationary (i.e., $v = 0$) and for early enough times or small enough heating that natural convection is still negligible. The basic requirement is that the natural convection velocity v must be much less than χ/a , where $\chi = K/\rho C_p$ is the thermal diffusivity of the medium, with K , ρ , and C_p being, respectively, the thermal conductivity, density, and specific heat at constant pressure; and a is either the beam radius (for the case of whole-beam blooming) or the smallest scale size of interest in the case where small-scale blooming effects on very large uniform intensity beams are of concern. Estimates for the natural convection velocities for liquids and gases with a horizontal beam are given by Smith.⁴

A dimensionless scaling parameter for the magnitude of the steady-state conduction-dominated blooming effect on the laser-beam intensity is given by⁴

$$D_C = - \frac{n_T \alpha P z^2}{2\pi n_0 K a^2} . \quad (4.4)$$

The on-axis intensity decrease in the beam due to blooming after propagating a distance z through the absorbing medium is given approximately by $\exp(-D_C)$.

This expression is based on a perturbation solution and applies for a Gaussian beam with $1/e$ intensity radius a when $\alpha z \ll 1$ and diffraction effects are negligible, i.e., the Fresnel number $N_F = ka^2/z \gg 1$. Conduction-dominated blooming using Eq. (4.4) has also been used as a convenient and direct method for measuring the eddy diffusion coefficient K_h for a turbulent medium in a study of velocity turbulence effects on blooming.²⁶ Early studies of conduction-dominated blooming are described in Refs. 10–20 and 23.

The heat transfer and associated thermal blooming is convection dominated according to Eq. (4.3) when the velocity $v \gg \chi/a$. This condition is virtually always met for laser-beam propagation in the atmosphere since $\chi \approx 0.2 \text{ cm}^2/\text{s}$ for air and χ/a for any beam or scale sizes a of practical interest is negligible compared to almost any except absolutely calm wind conditions. Because of the importance of the convection-dominated blooming problem for atmospheric propagation, it has been studied the most extensively. The dominant features of this type of blooming are for an initially symmetrical circular beam to form a nonsymmetrical crescent-shaped pattern that is spread or bloomed symmetrically transverse to the wind direction and with the peak intensity along the wind direction being shifted into the wind. Some of the key scaling parameters and models and laboratory simulation experiment and wave-optics propagation code results for convection-dominated whole-beam blooming effects in the atmosphere are reviewed in Sec. 4.

4.3.3 Nonisobaric Heating

For very short HEL beam pulses, the isobaric heating assumption does not apply since the heating results in significant pressure and density disturbances that propagate across the beam at the acoustic velocity C_s . To determine the transient blooming contribution to the refractive index for intense short laser pulses, the density change ρ_B due to the nonisobaric laser-beam heating must be found. Combining the hydrodynamic equations of mass, momentum, and energy conservation gives the following equation for the transient, or single-pulse, density change ρ_B ⁴:

$$\left(\frac{\partial^2}{\partial t^2} - C_s^2 \nabla^2 \right) \frac{\partial \rho_B}{\partial t} = (\gamma - 1) \alpha \nabla^2 I . \quad (4.5)$$

Here, $\gamma = C_p/C_v$ is the ratio of specific heats for the medium. With ρ_B given by Eq. (4.5) and the refractive index by $n_B = -n_T (T_0/\rho_0) \rho_B$, where T_0 and ρ_0 are the ambient temperature and density, Eqs. (4.1) and (4.2) are used to calculate the transient, or single-pulse, thermal-blooming effects.⁴ Simple scaling parameters have been found for the two limits of (1) the pulse length t_p being either very short or (2) very long compared to the acoustic transit time $t_a = a/C_s$ across the beam. For the short-time regime $t_p \ll t_a$, the density disturbance grows as t^3 . The thermal blooming in this case is called t -cubed blooming and, for a fixed absorbed energy, can be made negligible by reducing the pulse length. In the long-pulse regime where $t_p \gg t_a$, the density disturbance is proportional to the absorbed energy, which grows linearly with time. Clearly, to avoid or minimize single-pulse blooming effects the pulse length should always be very short compared to the acoustic transit time.^{2–4,6}

With the propagation of repetitively pulsed beams we must consider both the single-pulse blooming effects just mentioned as well as the steady-state isobaric blooming that results from the overlap of density disturbances in the beam path due to the heat deposited into the air by previous pulses. Steady-state repetitively pulsed blooming effects can be avoided if the pulse repetition frequency (PRF) is low enough to allow the heated air from previous pulses to be cleared from the beam path by the wind or beam motion. As the PRF increases, the pulse overlap blooming effects increase until, in the limit of many pulses-per-flow-time (PPFT) of the air across the beam (e.g., PPFT > 10 to 20 for a beam without slewing), the blooming approaches that for the steady-state cw beam case. Propagation limits due to blooming for cw and RP beams are compared in Ref. 3.

4.4 STEADY-STATE BLOOMING WITH WIND/BEAM MOTION

In this section we review the important problem of steady-state whole-beam blooming effects with wind or beam motion. We consider first the simplest case of a collimated beam in a homogeneous absorbing and moving medium. Next, the more general case of a focused beam in a medium with inhomogeneous heating and relative motion of the beam and medium is considered. The thermal blooming for ground-to-space propagation is addressed in the last section.

4.4.1 Collimated Beam—Homogeneous Path

Figure 4.1 shows a qualitative diagram of a cw laser beam propagating in an absorbing medium, such as a horizontal path in the atmosphere, where the absorption α and cross-wind speed v are uniform. As the air moves across the beam the temperature increases due to the absorbed energy from the laser beam. This causes the density of the air and also the refractive index, which is proportional to the density, to decrease as the air moves across the beam. The temperature and refractive-index variations across the beam center along the wind direction are shown in Fig. 1. Since light rays bend in the direction of increasing refractive index, the central ray is shown in the sketch to be bending into the wind. The net result is that the irradiance profile becomes distorted with its peak shifted into the wind.

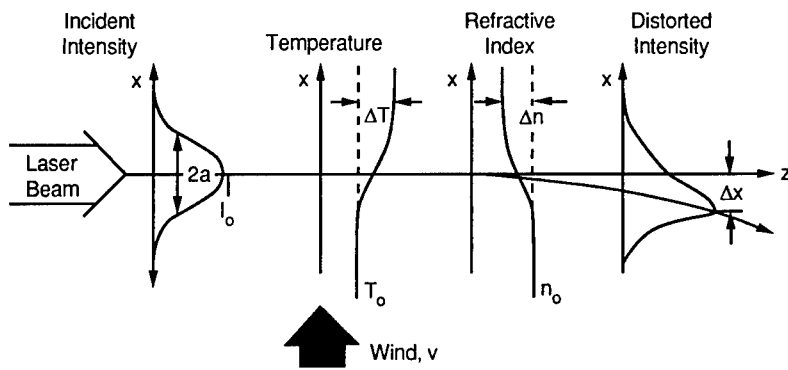


Fig. 4.1 Diagram of the steady-state thermal-blooming problem with wind.

A convenient and useful measure of the strength and overall characteristics of the thermal-blooming effect is given by the optical phase distortion produced by a small section of the thermal lens. The steady-state phase shift due to blooming for the path length z , which we assume to be short enough that the beam irradiance distribution is undisturbed by the blooming and the attenuation due to absorption and scattering is negligible (i.e., the extinction number $N_E = \kappa_e z \ll 1$), is given by

$$\varphi_B(x,y) = kn_T \left(\frac{\alpha z}{\rho C_p v} \right) \int_{-\infty}^x I(x',y) dx' . \quad (4.6)$$

Here we have assumed isobaric heating where the refractive-index distortion due to blooming is $n_B = n_T T_B$ and that T_B is given by Eq. (4.3) in the steady-state limit for the convection-dominated case. Assuming in Eq. (4.6) the irradiance distribution for a Gaussian beam, $I = (P/\pi a^2) \exp(-r^2/a^2)$, where P is the laser-beam power and $D = 2\sqrt{2}a$ is the $1/e^2$ intensity beam diameter, the blooming phase is

$$\begin{aligned} \varphi_{BG}(x,y,z) &= -\frac{\Delta\varphi_G}{2} \exp \left[-\left(\frac{y}{a}\right)^2 \right] \left[1 + \operatorname{erf} \left(\frac{x}{a} \right) \right] \\ &\approx -\frac{\Delta\varphi_G}{2} \left\{ 1 + \frac{2}{\sqrt{\pi}} \left(\frac{x}{a} \right) - \left(\frac{y}{a} \right)^2 \right. \\ &\quad \left. - \frac{2}{\sqrt{\pi}} \left[\frac{1}{3} \left(\frac{x}{a} \right)^3 + \left(\frac{x}{a} \right) \left(\frac{y}{a} \right)^2 \right] + \frac{1}{2} \left(\frac{y}{a} \right)^4 \dots \right\} . \end{aligned} \quad (4.7)$$

The maximum phase shift in radians across the beam along the wind direction is

$$\Delta\varphi_G = \frac{1}{2\sqrt{\pi}} N_D , \quad (4.8)$$

where

$$N_D = \frac{4\sqrt{2}(-n_T)k\alpha Pz}{\rho C_p v D} \quad (4.9)$$

is the Bradley-Herrmann²⁷ distortion number commonly used as a measure for the strength of the thermal blooming. The number of waves N_λ of blooming phase across the beam is now also often used as a measure of the amount of blooming and, from Eq. (4.8), we have that $N_\lambda = \Delta\varphi_G/2\pi = (1/4\pi^{3/2})N_D$.

Referring to the series expansion of the blooming phase in Eq. (4.7), we see the leading linear term in x and the quadratic term in y that produce, respectively, the prism, or beam bending, effect along the wind direction and the negative lens, or defocusing, effect perpendicular to the wind. These dom-

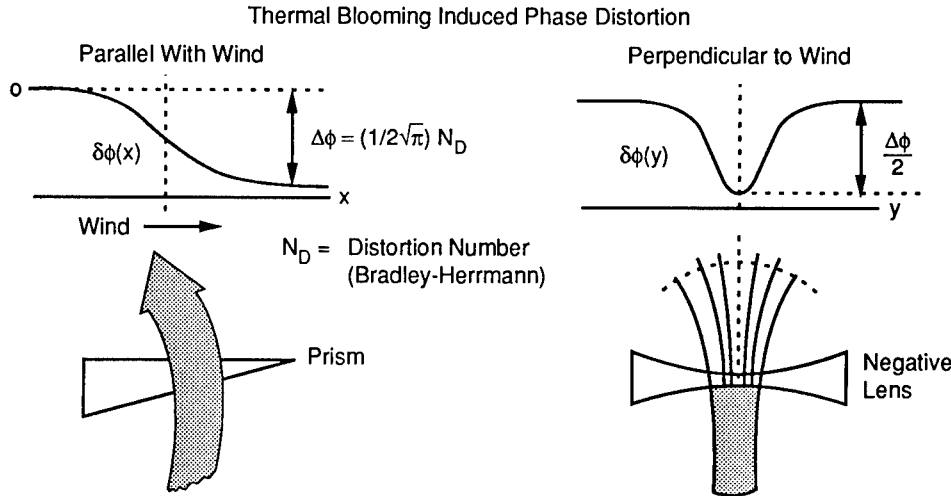


Fig. 4.2 Dominant blooming effects in a wind.

inant blooming effects on the beam are shown in Fig. 4.2 along with the phase distributions along and perpendicular to the wind direction.

The leading terms in the series expansion in Eq. (4.7) of the blooming phase can also be identified with the primary or Seidel aberrations of classical aberration theory.²⁸ In particular, the linear term, which bends the beam, is referred to as distortion and, in this case, is of the pincushion type.^a The quadratic term in y responsible for beam spreading is called astigmatism. The third-order term is coma and the fourth-order term corresponds to spherical aberration for a cylindrical element.

The blooming phase for a uniform irradiance circular beam is also frequently of interest and, using Eq. (4.6), is given by

$$\begin{aligned} \varphi_{BU}(x,y,z) &= -\frac{\Delta\varphi_U}{2} \left[\frac{x}{R_M} + \left(1 - \frac{y^2}{R_M^2} \right)^{1/2} \right] \\ &\approx -\frac{\Delta\varphi_U}{2} \left[1 + \frac{x}{R_M} - \frac{y^2}{2R_M^2} - \frac{y^4}{8R_M^4} \dots \right], \end{aligned} \quad (4.10)$$

where R_M is the beam radius ($D/2$) and the total phase shift across the beam is

$$\Delta\varphi_U = \frac{1}{\sqrt{2\pi}} N_D. \quad (4.11)$$

It is interesting to note that there is no third-order coma term in the blooming phase for the uniform beam. The beam distortion in this case tends to be more elliptical rather than crescent shaped as for the Gaussian beam.

^aThe pincushion distortion is readily identified in experimental measurements of blooming effects on target image quality (e.g., see Ref. 29). An example of pincushion distortion is also shown in Fig. 4.7 of Ref. 28.

Table 4.1 Blooming Phase Characteristics for Several Beam Shapes

		Uniform	Infinite Gaussian	Truncated Gaussian
Total	$\Delta\phi/N_D$	0.225	0.28	0.31
Tilt	$\theta_t/(N_D\lambda/D)$	1/28	1/13.8	1/12.6
Focal length	$f_B/(kD^2/N_D)$	2.22	0.44	0.40
Gradient	$\max\phi'/(N_D/D)$	0.69*	0.65	0.75

*Uniform beam gradient at $x/D = 0.43$, $y/D = 0.475$.

Some of the important characteristics of the blooming phase are compared in Table 4.1 for the uniform, infinite Gaussian, and truncated Gaussian beam shapes. These include (1) the total blooming phase $\Delta\phi$ in radians across the beam; (2) the effective tilt angle θ_t in radians for the beam bending into the wind; (3) the negative-lens focal length f_B for the beam defocusing transverse to the wind; and (4) the maximum phase gradient $\max\phi'$, which occurs near the hotter, downwind edge of the beam. Comparison of the tilt angles and negative-lens focal lengths for the different beam shapes readily shows these blooming effects to be much smaller for the uniform beam than for the two Gaussian beam shapes.

To determine the change in the laser-beam irradiance pattern as a result of thermal blooming requires the solution of the scalar wave equation (4.1) with the irradiance-dependent refractive-index expression n_B as given in Eq. (4.6). Although a number of detailed wave-optics propagation codes have been developed to accurately solve this complex nonlinear propagation problem, much useful insight, including a nondimensional scaling parameter for the thermal-blooming-induced irradiance changes, can be obtained from a perturbation solution of Eq. (4.1) with diffraction effects neglected.³⁰

The general perturbation solution, valid in the ray-optics limit, for the laser-beam irradiance after propagation through a medium with arbitrary refractive inhomogeneities $n(R)$ is³⁰

$$I(x,y,z) = I_0(x,y,z) \exp\left[-\int_0^z \left(\nabla + \frac{\nabla I}{I}\right) \int_0^{z'} \frac{\nabla n}{n_0} dz'' dz'\right], \quad (4.12)$$

where I_0 is the unperturbed irradiance. Assuming the unperturbed Gaussian irradiance $I_0 = (P/\pi a^2) \exp[-(x^2 + y^2)/a^2]$ and weak absorption ($\alpha z \ll 1$), for which the blooming index n_B is given by ϕ_{BG}/k in Eq. (4.7), using Eq. (4.12) for the thermally bloomed irradiance pattern yields³⁰

$$\begin{aligned} \frac{I(x,y,z)}{I_0} = & \exp\left(-N_C\left\{2\left(\frac{x}{a}\right) \exp\left[-\frac{(x^2 + y^2)}{a^2}\right]\right.\right. \\ & \left.\left.+ \frac{\sqrt{\pi}}{2} \exp\left(-\frac{y^2}{a^2}\right) \left(1 - \frac{4y^2}{a^2}\right) \left[1 + \operatorname{erf}\left(\frac{x}{a}\right)\right]\right\}\right). \end{aligned} \quad (4.13)$$

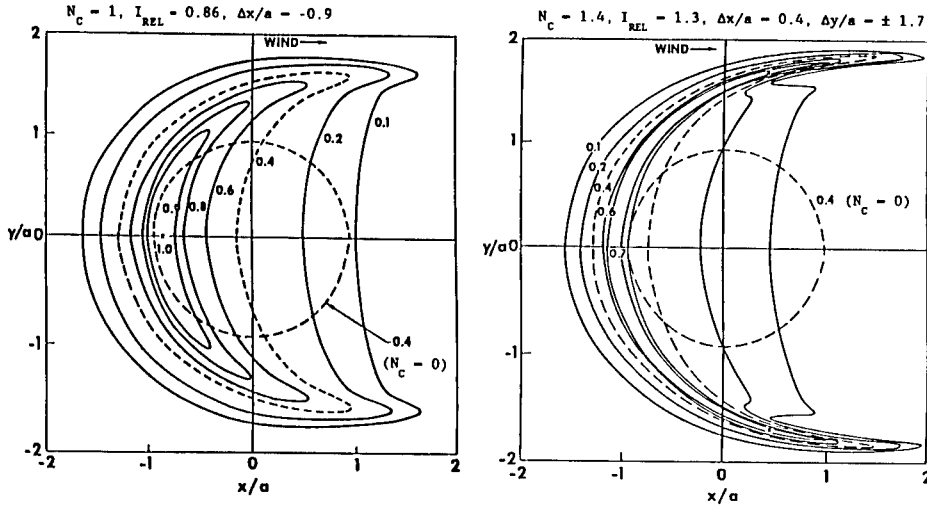


Fig. 4.3 Calculated bloomed irradiance contours for $N_C = 1$ and 1.4 , in the ray-optics limit.³⁰

Here, N_C is the collimated beam irradiance distortion parameter for blooming with a wind, given by

$$N_C = \frac{16\sqrt{2}(-n_T)\alpha P z^2}{\pi n_0 \rho C_p V D^3} . \quad (4.14)$$

The beam distortion parameter N_C can also be written as

$$N_C = \frac{1}{2\pi} \frac{N_D}{N_F} , \quad (4.15)$$

where $N_F = kn_0 D^2/8z$ is the Fresnel number. According to Eq. (4.15) the magnitude of the blooming phase distortion, i.e., N_D , must increase with the Fresnel number N_F to obtain the same amount of beam distortion, as measured by N_C . For small values of N_C the peak intensity, normalized by the undistorted value, decreases as $1 - (\sqrt{\pi}/2)N_C$ and its position is shifted into the wind direction by the amount $\Delta x/a \approx (3/2)N_C$.

The distorted beam irradiance patterns in Fig. 4.3, which apply in the ray-optics limit ($N_F \gg 1$), have been calculated numerically by iterative application of the above perturbation solution.³⁰

The bloomed intensity patterns show the characteristic crescent shape with beam spreading transverse to the wind, the peak intensity shifted into the wind, and, also, a significant focusing effect along the wind direction. For the $N_C = 1$ case, the peak intensity is about 0.86 times the undistorted value and the peak has shifted almost one beam radius into the wind. For the $N_C = 1.4$ case, however, the peak intensity point has shifted from the beam axis along the flow to the wings of the crescent and the thermal focusing has increased it to ~ 1.3 times the unperturbed value. The intensification effect due to the blooming with wind/beam motion was first observed in liquid-cell experiments,³¹ which were conducted with an argon-ion laser at $\lambda = 0.5145 \mu\text{m}$. In

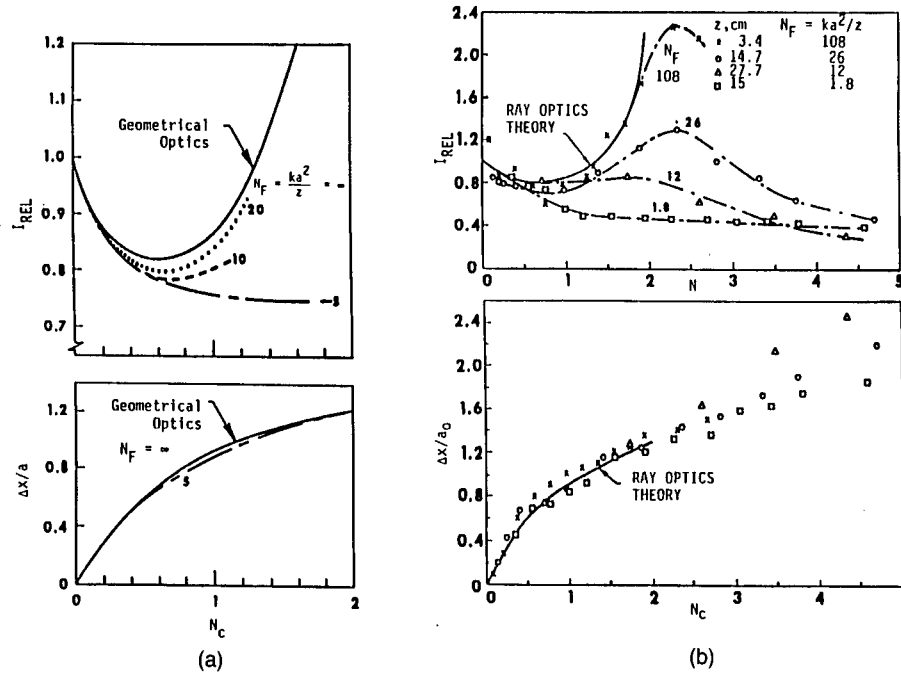


Fig. 4.4 Peak intensity and deflection for collimated beam blooming³³: (a) numerical results for collimated Gaussian beam, $\alpha z \ll 1$, and (b) experimental results for liquid CS_2 .

the first experiments^{22,32} to observe and study the blooming effects due to a wind, which were done in gas (i.e., a small recirculating wind tunnel) with a 10.6- μm CO_2 laser beam, the intensification effect was not observed. The bloomed intensity was found to only decrease, even for very large distortion conditions.

Subsequent computer calculations, with diffraction effects included, and further experiments at 10.6 μm with moving liquid cells, confirmed what had been suspected earlier; i.e., the reason the intensification wasn't observed in the earlier gas experiments was due to the much stronger influence of diffraction, which tended to counteract or limit the thermal self-focusing tendency at the small Fresnel numbers (~ 2.5) of those experiments.³³ Figure 4.4 shows calculated and experimental results for the effects of diffraction on the relative intensity change with blooming, as functions of the beam distortion number N_C and the Fresnel number N_F .³³ Based on these results, intensification with blooming requires a Fresnel number of ~ 20 or more. It is interesting to note that the shift of the peak intensity into the wind does not show any significant dependence on the Fresnel number.

Figure 4.5 compares the distorted and undistorted beam profiles at the same beam distortion number of $N_C \approx 2$ for the Fresnel numbers of 108, 26, 12, and 1.8. From the results in Figs. 4.4 and 4.5 it is clear that diffraction effects strongly compete with and limit the self-focusing tendency of the thermal lens as the Fresnel number decreases.

4.4.2 Focused Beams—Inhomogeneous Paths

The effects of convection-dominated thermal blooming for focused beams, including the effects of beam slewing and finite attenuation, have been studied

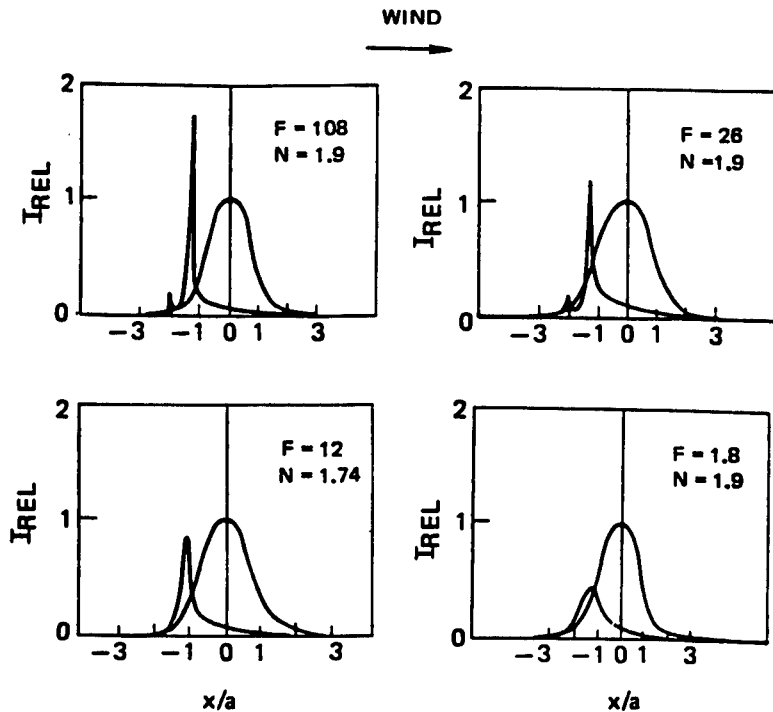


Fig. 4.5 Measured Fresnel number dependence of bloomed intensity for $N_C \approx 2$ (Ref. 33).

extensively using laboratory simulation experiments, ray-optics perturbation theories, and detailed wave-optics propagation codes.¹⁻⁶ Although the wave-optics codes can provide a comprehensive and accurate treatment of this problem as well as a variety of other more complicated blooming problems (e.g., for stagnation zones, transonic slewing, optical turbulence, and phase compensation), simple analytical scaling relations are more convenient and often adequate for providing useful approximations for the blooming effects on the peak irradiance. Such a scaling parameter has been found by using the integral expression in Eq. (4.12) to obtain a generalized beam distortion parameter that accounts for beam focusing and nonuniform winds and beam heating effects.³ The generalized beam distortion parameter³ is

$$N = N_C f(N_E) q(N_F) s(N_\omega) , \quad (4.16)$$

where $N_C = N_D / 2\pi N_F$ is the distortion parameter defined earlier [Eq. (4.14)] for a collimated beam and the functions f , q , and s , which represent correction factors for the effects of finite attenuation (i.e., when the extinction number N_E is not small), the focusing or divergence of the laser beam, and the non-uniform velocity profile with beam slewing, respectively, are given by

$$f(N_E) = \frac{2}{N_E^2} [N_E - 1 + \exp(-N_E)] , \quad (4.17)$$

$$q(N_F) = \frac{2N_F^2}{(N_F - 1)} \left\{ 1 - \ln \left[\frac{N_F}{(N_F - 1)} \right] \right\} , \quad (4.18)$$

$$s(N_\omega) = \frac{2}{N_\omega^2} [(N_\omega + 1) \ln(N_\omega + 1) - N_\omega] . \quad (4.19)$$

The Fresnel number N_F , defined earlier, gives the degree of focusing a_0/a for a focused diffraction-limited beam, where a_0 and a are the beam sizes at the source and focal range z , respectively. The slewing number $N_\omega = \omega z/v_0$, where ω is the slew rate (assumed to be in the direction opposite to the wind), is the ratio of the beam slewing speed at z to the uniform wind speed v_0 . The general beam distortion parameter N thus depends on the four dimensionless parameters N_C , N_F , N_E , and N_ω . Bradley and Herrmann²⁷ have shown that these four parameters completely characterize the thermal-blooming problem for this case. It is interesting to note that when the beam is strongly focused (i.e., $N_F \gg 1$) without slewing ($N_\omega = 0$) and with $N_E \ll 1$, the beam distortion number reduces to $N \approx N_D/\pi$. This means that the peak intensity of the focused beam, relative to the unbloomed value I_{REL} , or, equivalently, the Strehl ratio, in the small perturbation limit, depends on the "phase" distortion number according to $1 - (\sqrt{\pi}/2)N_D$. This is in contrast to the collimated beam case where I_{REL} decreases as $1 - (\sqrt{\pi}/4)N_D/N_F$.

The general beam distortion parameter N has proven useful as a simple empirical correlation or scaling parameter for approximating thermal-blooming effects in terms of the four parameters N_D , N_F , N_E , and N_ω . For example, Fig. 4.6 shows that the experimental and wave-optics code results are reasonably well correlated by the beam distortion parameter N with the simple empirical expression³

$$I_{REL}(N) = (1 + 0.0625N^2)^{-1} . \quad (4.20)$$

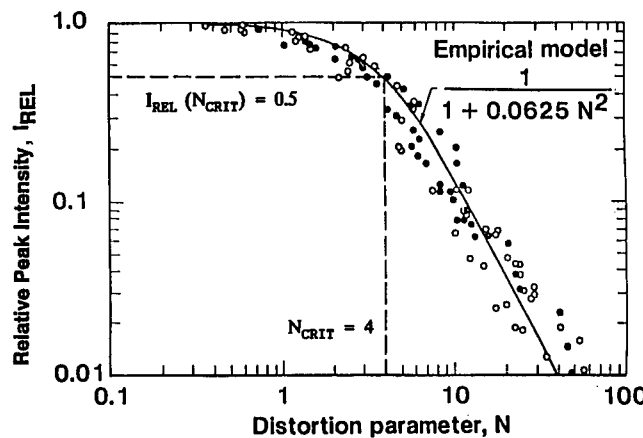


Fig. 4.6 Blooming I_{REL} dependence on the parameter N for experimental and wave-optics code results.³

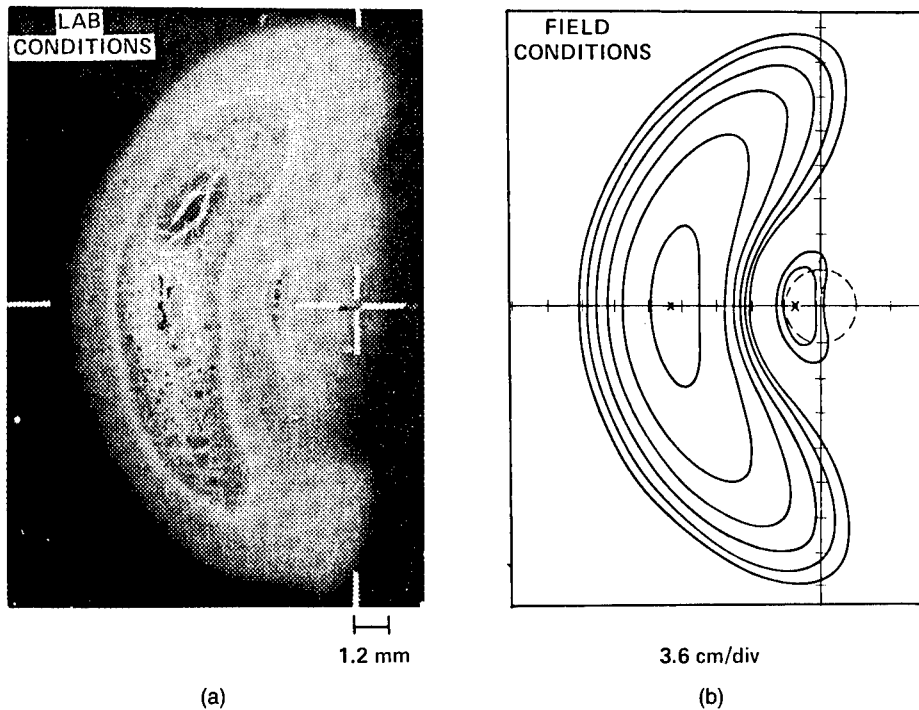


Fig. 4.7 Thermal-blooming patterns from laboratory experiment ($N = 13$) and code calculation ($N = 16$) (Ref. 3): (a) experiment and (b) theory.

The experimental results include data from several different measurements for focused beams with $N_F = 7$, $N_E = 0.4$, and without slewing ($N_\omega = 0$). The code results were obtained for Gaussian focused beams for the following wide range of conditions: $N_F = 3, 6, 10, 18, 28$, and 66 ; $N_E = 0.1, 0.4$, and 0.6 ; and $N_\omega = 0, 3.8$, and 8 .

Figure 4.7 shows a comparison of results from a laboratory experiment and a wave-optics code calculation for the bloomed irradiance pattern of a focused Gaussian beam for very different conditions but with comparable beam distortion numbers N of 13 and 16, respectively.³ The measured and calculated beam patterns are very similar in appearance and have comparable values of I_{REL} of 0.05 and 0.07 and for the normalized shift in peak intensity of 6 and 4.4, respectively.

The conditions for the laboratory blooming experiment and for the code calculation of a field-scale propagation scenario are compared in Table 4.2.³

An important characteristic of the thermal-blooming process is its effect in limiting the peak irradiance that can be propagated to a maximum, or critical, value I_c , independent of the available power at the transmitter. The power at which the critical intensity is achieved is called the critical power P_c ; and since $P \sim N$, P_c corresponds to the value of $N = N_{CRIT}$, where the $I_{REL}(N)$ versus N curve (see Fig. 4.6) has a slope of -1 . This follows since the peak intensity, given by the product of the unbloomed peak I_{PO} and I_{REL} , no longer increases with I_{PO} , which increases linearly with the power, when I_{REL} begins to decrease inversely with power, or, equivalently, N . Figure 4.8 shows the peak intensity versus power curve for thermal blooming, based on the empirical

Table 4.2 Conditions for Simulation Experiment and Wave-Optics Code Results in Fig. 4.7 (from Ref. 3)

	Simulation Experiment	Wave-Optics Code Results
	Lab Conditions	Field Conditions
Medium	CO ₂ at 10 atm	Atmospheric air
Absorption coefficient (cm ⁻¹)	4 × 10 ⁻³	7 × 10 ⁻⁷
Wind velocity (cm/s)	1	200
Wavelength (μm)	10.6	10.6
Power (W)	9	10 ⁵
Beam diameter (cm)	0.9	28.3
Range (m)	1	2 × 10 ³
Beam distortion, <i>N</i>	13	16
Extinction, <i>N_E</i>	0.41	0.134
Fresnel number, <i>N_F</i>	2.6	2.8
Relative irradiance, <i>I_{REL}</i>	0.05	0.07
Peak deflection, Δ <i>x/a</i>	6	4.4

model [Eq. (4.20)] for $I_{\text{REL}}(N)$ shown in Fig. 4.6, where $N_{\text{CRIT}} = 4$ and $I_{\text{REL}}(N_{\text{CRIT}}) = 0.5$. The critical, or optimum, power effect with blooming is clearly shown in Fig. 4.8, where, although the peak intensity initially increases linearly with power ($P \ll P_c$), the maximum is reached when $P = P_c$ and any further increase in power causes the intensity to decrease.

A similar empirical scaling law $I_{\text{REL}}(N)$ has been found to apply for a uniform irradiance beam and is given with the constant factor and exponent in Eq. (4.20) replaced with 0.09 and 1.22, respectively.⁴ In this case $N_{\text{CRIT}} = 25$ and $I_{\text{REL}} = 0.18$, indicating the significantly reduced blooming effects that occur for the uniform versus the Gaussian beam shape.

An example of a direct comparison of a detailed 4-D wave-optics blooming code calculation made with a laboratory simulation experiment is shown in Fig. 4.9.³⁴

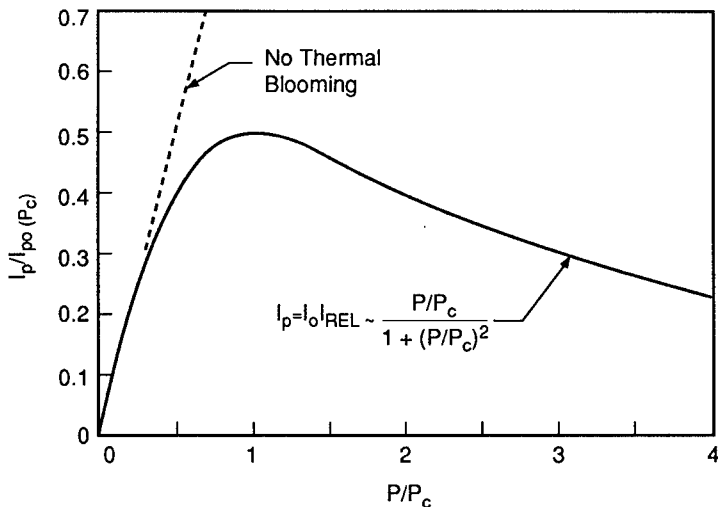


Fig. 4.8 Peak irradiance versus power with thermal blooming.³

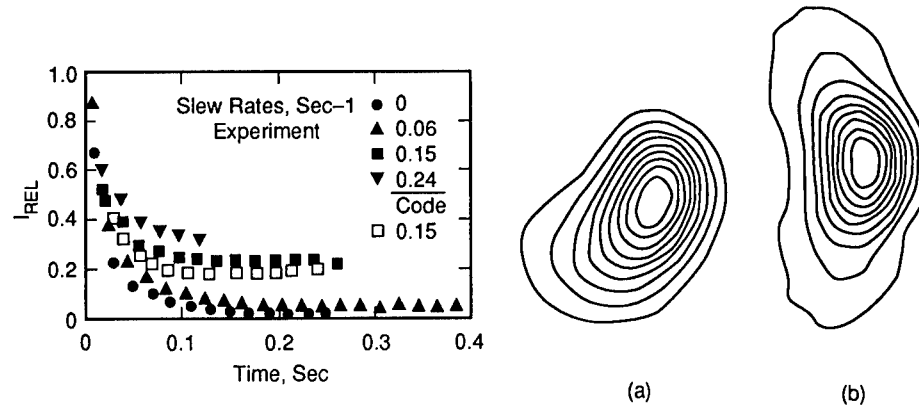


Fig. 4.9 Relative intensity versus time results for 4-D code and experiment for stagnation zone blooming. Calculated blooming patterns are at 0.1 s with (a) and without (b) natural convection.³⁴

The blooming problem studied here is complicated considerably by the combined effects of a focused beam with slewing horizontally, a stagnation region (i.e., with zero flow or beam motion) midway along the propagation path, and with natural-convection vertical flow effects also included. The code results are in good agreement with the experiment for the 0.15 rad/s case compared in Fig. 4.9. The calculated bloomed beam patterns shown in Fig. 4.9 are for the time of 0.1 s with significant natural-convection effects evident, which is the case compared to the experiment [Fig. 4.9(a)], and with natural convection neglected [Fig. 4.9(b)]. These results as well as a number of other detailed comparisons of the propagation codes with laboratory blooming experiments have shown the code calculations of whole-beam thermal-blooming effects to be in good agreement with the experiments.⁴

4.4.3 Up-link Thermal Blooming

In this section we consider thermal blooming for an up-link, or ground-to-space propagation path. A simple ray-optics model is shown to provide a good approximation for the peak far-field Strehl ratio for uncorrected up-link blooming. The ray-optics model for the phase-conjugate-corrected up-link blooming Strehl ratio is then used to obtain the whole-beam instability limit for up-link phase compensation.

Figure 4.10 shows the geometry for the up-link blooming problem. We assume a uniform irradiance beam with power P and diameter D propagating from the laser altitude H_L to the range R in space where it is focused. The laser beam can be considered to be well collimated, with the same uniform irradiance as at the source, within the sensible atmosphere (i.e., $H_L \leq z \leq H_A$) since (1) the focal range R is much larger than the range $H_A - H_L$ through the atmosphere, and (2) both diffraction and blooming effects on the beam irradiance within the atmosphere are small for the large Fresnel numbers (i.e., short wavelengths, large aperture sizes, and short atmospheric heating paths) that are typically of interest. The thermal-blooming effect on the far-field Strehl ratio is thus determined by the blooming phase for the uniform colli-

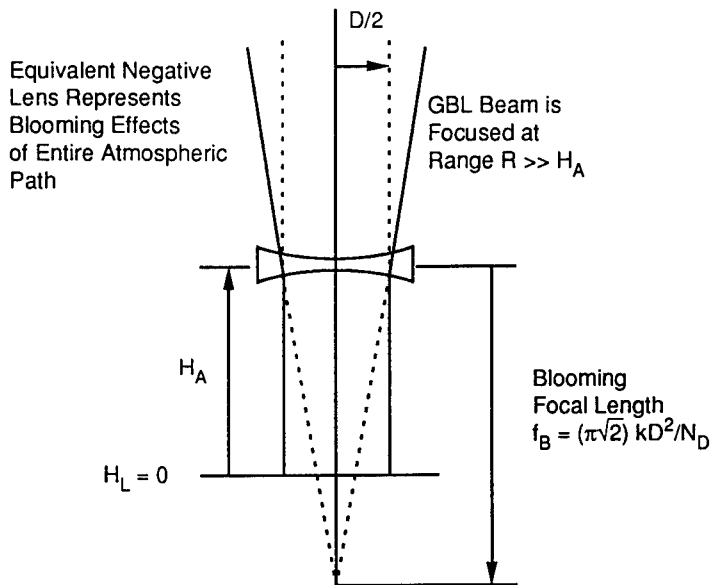


Fig. 4.10 Geometry for up-link blooming.

mated beam at the top of the atmosphere. From Sec. 4.4.1 the blooming phase can be approximated by that for a cylindrical negative lens with focal length

$$f_B = \frac{\pi}{\sqrt{2}} \frac{kD^2}{N_D} . \quad (4.21)$$

Here, $N_D = N_D(H_A)$ is the total of the cumulative distortion number $N_D(H)$ for the entire up-link path. $N_D(H)$ is a generalization by Herrmann of the original Bradley-Herrmann N_D [Eq. (4.9)],²⁷ which describes the distribution of the thermal blooming, as a function of altitude, for up-link propagation. It is defined by

$$N_D(H, \theta_z) = \frac{C_A k P \sec \theta_z}{D} \int_{H_L}^H \frac{\alpha_T(h) T_0 t(h)}{V_E(h) T(h)} dh , \quad (4.22)$$

where

$$C_A = \frac{5.66(-n_T)}{\rho_0 C_p} = 4.72 \times 10^{-9} \text{ m}^3/\text{J} \quad (4.23)$$

is the atmospheric refractivity constant for air at temperature $T_0 = 273$ K. The other parameters in Eq. (4.22) not previously defined are

θ_z = path zenith angle

$\alpha_T(h) = k_m(h) + k_a(h)$ (total absorption coefficient)

$k_m(h)$ = molecular absorption coefficient

$k_a(h)$ = aerosol absorption coefficient

$\sigma_T(h) = \sigma_m(h) + \sigma_a(h)$ (total scattering coefficient)

$\sigma_m(h)$ = molecular scattering coefficient
 $\sigma_a(h)$ = aerosol scattering coefficient
 $V_E(h)$ = effective cross-wind speed including slewing
 $T(h)$ = air temperature
 $t(h)$ = cumulative transmittance

$$= \exp \left\{ -\sec \theta_z \int_{H_L}^h [\alpha_T(h') + \sigma_T(h')] dh' \right\}. \quad (4.24)$$

The peak far-field Strehl ratio at the target range R due to the uncorrected blooming is then found by forming the ratio of the area of the diffraction-limited spot with radius $a_D \sim R\lambda/D$ to the root-sum-squared spot area due to diffraction and blooming combined, where the blooming radius, from Fig. 4.10, is $a_B \sim RD/2f_B$. The Strehl ratio for uncorrected blooming is then

$$SR_{BU} = \left(1 + \frac{N_D^2}{8\pi^4} \right)^{-1/2} \quad (4.25)$$

and depends only on the total phase distortion parameter N_D .

Figure 4.11 shows the uncorrected-blooming Strehl-ratio dependence on the distortion number N_D , which is proportional to the laser-beam power, for a particular case of up-link propagation at zenith for a 1-m diameter excimer laser beam at $\lambda = 0.35 \mu\text{m}$. The distortion number N_D in this case is ~ 70 at the critical power where the Strehl has dropped to about 0.35. Also shown for comparison with the ray-optics model results in Fig. 4.11 are wave-optics code results for the same case. The agreement between the ray-optics model and the wave-optics code results is very good except at the larger distortion values

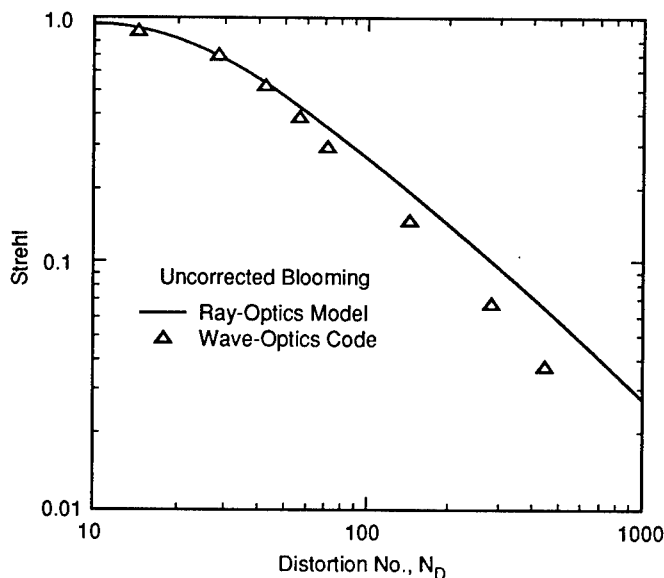


Fig. 4.11 Comparison of ray-optics model and wave-optics code results for up-link blooming.

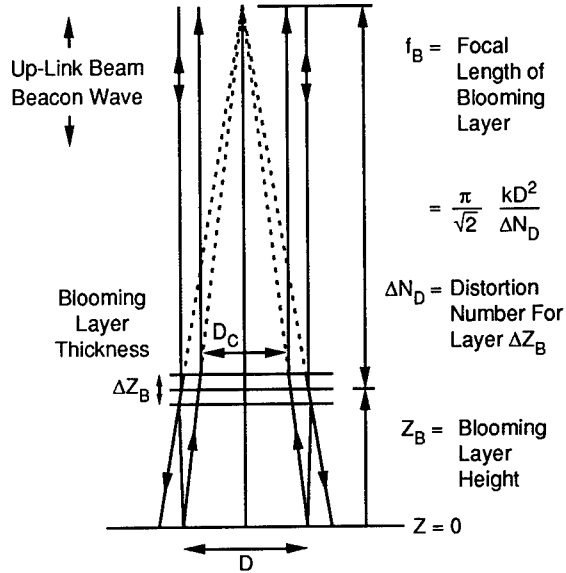


Fig. 4.12 Geometry for phase-compensated up-link blooming.

where the effects of the fourth- and higher-order terms in the blooming phase, which are not included in the ray-optics model, become important.

For phase-compensated up-link blooming we consider the situation shown in Fig. 4.12 where the blooming is limited to a discrete thin layer of thickness ΔZ_B , centered at the altitude Z_B above the transmitter. Following the same procedure as before, the effect of the blooming layer of thickness ΔZ_B is represented by the equivalent negative cylindrical lens of focal length $f_B(Z_B)$. Here, $f_B(Z_B)$ is given by Eq. (4.21) but with $N_D(H_A)$ replaced with the value of the cumulative distortion parameter $N_D(\Delta Z_B, Z_B)$ appropriate for the thickness and position for the particular blooming layer in question.

As shown in Fig. 4.12, the effect of the negative cylindrical lens associated with the blooming layer at height Z_B is to spread the beacon return wave intercepted by the negative lens of diameter D such that it overfills the transmitter aperture at ground level. Perfect phase-conjugate compensation consists simply of focusing the up-link beam to the range $Z_B + f_B$. The focusing correction results in the slightly smaller beam diameter D_C at the altitude Z_B of the blooming layer, as shown in Fig. 4.12. Above the blooming layer the up-link beam emerges perfectly collimated, however, since the original negative cylindrical thermal lens due to the blooming layer exactly cancels the focusing correction applied to the up-link beam.

From Fig. 4.12, the reduced beam diameter D_C at the height of the blooming slab Z_B is given by

$$\frac{D_C}{D} = \frac{f_B}{f_B + Z_B}. \quad (4.26)$$

The reduced beam size D_C at the blooming layer has two effects. First, the irradiance is increased, which increases the strength of the blooming layer at

Z_B . From Eqs. (4.21) and (4.22) the focal length of the blooming layer, as a result of the phase correction, is decreased to the following value:

$$f_{BC} = \left(\frac{D_C}{D}\right)^3 f_B . \quad (4.27)$$

Now, according to Eq. (4.26), correction of the new blooming phase associated with f_{BC} results in a further reduction in the beam diameter D_C .

The phase-conjugate correction process proceeds in an iterative fashion until a stable, self-consistent solution is obtained for Eqs. (4.26) and (4.27), with f_B replaced with f_{BC} in Eq. (4.26). Combining Eqs. (4.26) and (4.27) gives the following cubic equation for $x = D_C/D$:

$$x^3 - x^2 + \frac{Z_B}{f^B} = 0 , \quad (4.28)$$

which must be satisfied when the phase-conjugate correction process has converged.

The second effect of the reduced beam size D_C , which results from the phase-conjugate correction of blooming for the layer at altitude Z_B , is the reduction in the far-field Strehl ratio and is given by

$$SR_{BC} = \frac{D_C}{D} = \left[1 + \left(\frac{D}{D_C} \right)^3 \frac{Z_B}{f_B} \right]^{-1} . \quad (4.29)$$

This reduction in the far-field Strehl ratio occurs because the beam-spreading angle after phase correction increases from λ/D (without correction) to the value λ/D_C . (Note that this occurs only in the plane transverse to the wind where the blooming spreads the beam.)

The solution to Eqs. (4.28) or (4.29), which are equivalent, is given by

$$SR_{BC} = \frac{1}{3} + \frac{2}{3} \cos \left[\frac{1}{3} \cos^{-1} \left(1 - \frac{13.5 Z_B}{f_B} \right) \right] . \quad (4.30)$$

Equation (4.30) provides a physically meaningful (i.e., real) solution for the Strehl ratio only if $Z_B/f_B \leq 4/27$. This means that stable phase-conjugate correction of the blooming layer of strength $\sim 1/f_B$ at the range Z_B is limited to the conditions where

$$0 \leq \frac{Z_B}{f^B} \leq \frac{4}{27} \approx 0.148 . \quad (4.31)$$

Thus, when Z_B/f_B is small, corresponding either with weak blooming (i.e., large f_B) or, equivalently, with stronger blooming, which occurs very close to the transmitter aperture (i.e., small Z_B), phase correction is very effective with the Strehl ratio SR_{BC} approaching unity. As Z_B/f_B increases, phase correction becomes less effective until $Z_B/f_B = 4/27$, where the minimum stable corrected Strehl ratio $SR_{BC} = 2/3$ occurs. For $Z_B/f_B > 4/27$, the phase-conjugate cor-

rection does not converge to a stable improvement over the uncorrected value but, rather, drives the Strehl ratio SR_{BC} to zero. This clearly shows the limit imposed on the phase compensation of whole-beam thermal blooming due to the finite range Z_B of the blooming region from the aperture; i.e., $Z_B \leq 0.148f_B$ for stable phase correction. Similar results showing that stable phase-conjugate correction of thermal blooming can only be obtained for a limited range of the strength of the blooming were first reported by Herrmann³⁵ for the case of laser beams focused within the blooming region.

The phase-correction model for the single thin blooming layer can be extended to the more interesting case of a distributed blooming region by using the value of f_B given in Eq. (4.21) for the entire atmospheric path and by using, for the effective blooming layer range Z_B , the appropriately normalized first moment, with respect to range, of the atmospheric heating distribution function

$$f_H(h) = \frac{\alpha_t(h)T_0t(h)}{V_E(h)T(h)} . \quad (4.32)$$

Recognizing that f_H is the integrand in Eq. (4.22) for the distortion parameter N_D , the effective blooming range Z_B is given by

$$Z_B = \frac{C_A k P \sec^2 \theta_z}{N_D D} \int_{H_L}^{H_A} (h - H_L) f_H(h) dh . \quad (4.33)$$

The corrected blooming Strehl ratio given by Eq. (4.30) is shown in Fig. 4.13 for the same laser beam and atmospheric conditions used earlier for the

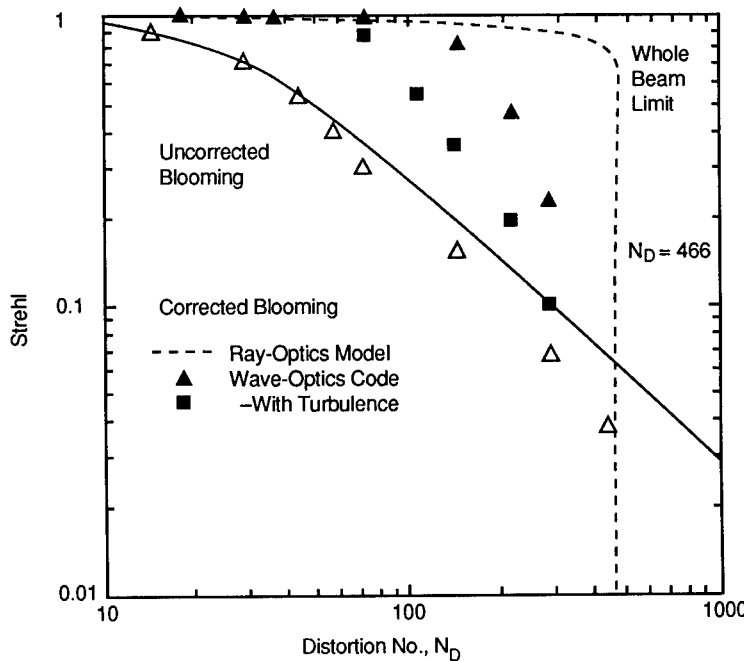


Fig. 4.13 Comparison of ray-optics model and wave-optics code results for phase-compensated up-link blooming.

excimer laser case in Fig. 4.11. For this case, where the effective blooming range Z_B is 12.7 km and the whole-beam Fresnel number N_F is 177, we have that $Z_B/f_B = (1/\pi 2^{1/2})N_D/N_F \approx 3.18 \times 10^{-4} N_D$. The vertical dashed line shows the whole-beam limit for stable blooming phase correction, which for this case occurs at $N_D = 466$. At larger blooming distortion values the phase-conjugate correction leads to unstable conditions with reduced Strehl due to the increased atmospheric heating and beam distortion at high altitudes caused by the runaway focusing correction.

The condition $Z_B/f_B \leq 0.148$ for the whole-beam limit for phase-corrected blooming can also be expressed as $N_D/N_F \leq 2.6$, or $N_C \leq 0.42$, where we have used Eq. (4.21) for f_B for the uniform beam and the Fresnel number is given by $N_F = kD^2/8Z_B$. For the infinite Gaussian beam shape the whole-beam correction limits are $N_D/N_F \leq 0.53$ and $N_C \leq 0.086$, which are about a factor of five smaller than for the uniform beam. From these small values of N_C it is clear that stable phase correction can be achieved only if the whole-beam blooming distortion without correction is kept very small within the effective range Z_B of the up-link blooming layer. Since $N_D \sim P/D$ and $N_F \sim D^2$, the whole-beam limit for the up-link correctable power is seen to scale as D^3 .

The wave-optics code results for phase-corrected blooming alone shown in Fig. 4.13 do not achieve the high Strehl ratios predicted by the ray-optics model [Eq. (4.30)] for distortion conditions well below the whole-beam limit for phase correction. With turbulence (with the coherence length $r_0 = 3.3$ cm) and blooming together, the code results for the corrected Strehl fall off even more rapidly with distortion number. The calculated Strehls are being limited by the effects of small-scale blooming instabilities, which, for the uniform wind direction case, appear as striations parallel to the wind in the beam irradiance and phase. Figure 4.14 shows an example, obtained with Science Application International Corporation's APAC code, of the small-scale blooming distortions in the beacon wave intensity and phase at the ground with phase-compensated turbulence and blooming for a Gaussian beam with the conditions $\lambda = 1.06$

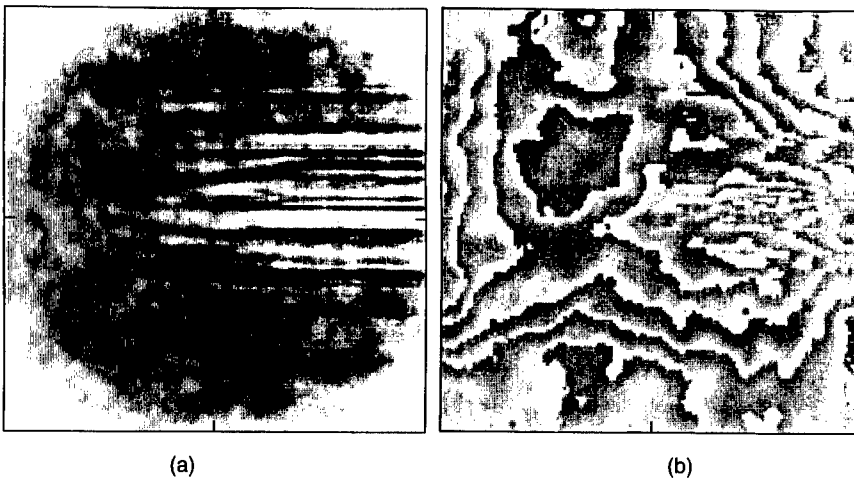


Fig. 4.14 Beacon intensity (a) and beacon phase (b) at the ground with phase-compensated turbulence and blooming for the conditions $\lambda = 1.06 \mu\text{m}$, $N_D = 60$, $N_F = 237$, $r_0 = 7.6 \text{ cm}$, and actuator spacing $d_A = 5 \text{ cm}$.

μm , $N_D = 60$, $N_F = 237$, turbulence coherence length $r_0 = 7.6 \text{ cm}$, and a deformable mirror actuator spacing d_A of 5 cm. Here, $N_D/N_F \sim 0.25$, which is only about one-half the whole-beam correction limit. The Strehl of the high-energy up-link beam has decreased to about 0.6 for this case compared to the values of about 0.9 obtained at lower power without blooming or about 0.96 with blooming alone.

4.5 CONCLUSIONS

An overview has been presented of the work performed on thermal blooming since the first observations were reported. A brief historical overview and a review of the governing equations and basic characteristics of the different types of blooming problems for cw, SP, and RP laser beams were given. The remaining discussion concentrated on the problem of convection-dominated thermal blooming, which is the most important blooming problem for cw or RP HEL beam propagation in the atmosphere. The important results and scaling parameters for describing steady-state convection-dominated whole-beam thermal-blooming effects were reviewed for (1) a collimated beam in a homogeneous atmosphere, (2) focused-beam propagation including the combined effects of wind and beam slewing and finite attenuation, and (3) ground-to-space propagation both with and without phase compensation. In addition to causing severe beam spreading, bending, and distortion, the most serious problem that occurs with all types of thermal blooming is the limit it imposes on the maximum useful power that can be propagated through the atmosphere and concentrated within a small spot, of the order of the diffraction-limited beam size, at the target. Dimensionless parameters and simple scaling laws were presented that can be used to determine the maximum or critical power limits due to whole-beam thermal blooming. A simple ray-optics model for phase-conjugate correction of up-link thermal blooming was presented and used to show that stable correction is limited by whole-beam blooming effects to conditions where the beam distortion within the blooming region is small; i.e., the beam distortion parameter $N_C = (\frac{1}{2}\pi)N_D/N_F$ must be less than ~ 0.09 and 0.4 for Gaussian and uniform beams, respectively. This requirement implies a corrected critical power scaling with D^3 . Propagation code results for phase-compensated up-link blooming alone, and also combined with turbulence, were shown with small-scale blooming instabilities limiting the effectiveness of phase correction to distortion numbers well below the whole-beam critical distortion limit. Current studies of thermal blooming are concentrating on developing a comprehensive understanding of and modeling and analysis capability for the small-scale blooming instability effects and limits on phase-compensated HEL beam propagation in the atmosphere.

References

1. C. B. Hogge, "Propagation of high energy laser beams in the atmosphere," in *Physics of Quantum Electronics, Vol. 1, High Energy Lasers and Their Applications*, S. Jacobs, M. Sargent III, and M. O. Scully, Eds., pp. 177–246, Addison-Wesley, Reading, MA (1974).

2. J. N. Hayes, "Propagation of high energy laser beams through the atmosphere: An overview," AGARD Conf. Proc. No. 183, *Optical Propagation in the Atmosphere*, Sec. 27 (May 1976).
3. F. G. Gebhardt, "High power laser propagation," *Appl. Opt.* **15**(6), 1479–1493 (1976).
4. D. C. Smith, "High-power laser propagation: Thermal blooming," *Proc. IEEE* **65**(12), 1679–1714 (1977).
5. J. L. Walsh and P. B. Ulrich, "Thermal blooming in the atmosphere," in *Laser Beam Propagation in the Atmosphere*, J. W. Strohbehn, Ed., Springer-Verlag, New York (1978).
6. F. G. Gebhardt, "Overview of atmospheric effects on propagation of high energy laser radiation," in *Atmospheric Effects on Radiative Transfer*, C. B. Ludwig, Ed., *Proc. SPIE* **195**, 162–170 (1979).
7. T. J. Karr, "Thermal blooming compensation instabilities," *J. Opt. Soc. Am. A* **6**(7), 1038–1048 (1989).
8. K. A. Breuckner and S. Jorna, "Linearized theory of laser induced instabilities in liquids and gases," *Phys. Rev.* **164**, 182–193 (1967).
9. N. M. Kroll and P. L. Kelley, "Temporal and spatial gain in stimulated light scattering," *Phys. Rev. A* **4**, 763–776 (1971).
10. J. P. Gordon, R. C. C. Leite, R. S. Moore, S. P. S. Porto, and J. R. Whinnery, *Bull. Am. Phys. Soc. Ser. II* **9**, 501 (1964).
11. J. P. Gordon, R. C. C. Leite, R. S. Moore, S. P. S. Porto, and J. R. Whinnery, "Long transient effects in lasers with inserted liquid samples," *J. Appl. Phys.* **36**, 3–7 (1965).
12. K. E. Rieckhoff, "Self-induced divergence of CW laser beams in liquids—A new nonlinear effect in the propagation of light," *Appl. Phys. Lett.* **9**, 87 (1966).
13. W. R. Callen, B. G. Huth, and R. H. Pantell, "Optical patterns of thermally self-defocused light," *Appl. Phys. Lett.* **11**, 103 (1967).
14. J. R. Whinnery, D. T. Miller, and F. Dabby, "Thermal convection and spherical aberration distortion of laser beams in low-loss liquids," *IEEE J. Quantum Electron.* **QE-3**, 382 (1967).
15. H. Inaba and H. Ito, "Observation of power-dependent distortion of an IR beam at 10.6 μ from a CO₂ laser," *IEEE J. Quantum Electron.* **QE-4**, 45 (1968).
16. R. L. Carman and P. L. Kelley, "Time dependence in the thermal blooming of laser beams," *Appl. Phys. Lett.* **12**, 241 (1968).
17. R. C. C. Leite, R. S. Moore, and J. R. Whinnery, "Low absorption measurements by means of the thermal lens effect using an He-Ne laser," *Appl. Phys. Lett.* **5**, 141 (1964).
18. D. Solimini, "Loss measurements of organic materials at 6328 Å," *J. Appl. Phys.* **37**, 3314 (1966).
19. D. Solimini, "Accuracy and sensitivity of the thermal lens method for measuring absorption," *Appl. Opt.* **5**, 1931 (1966).
20. R. C. C. Leite, S. P. S. Porto, and T. C. Damen, "The thermal lens effect as a power-limiting device," *Appl. Phys. Lett.* **10**, 100 (1967).
21. S. A. Akhmanov, D. P. Krindach, A. V. Migulin, A. P. Sukhorukov, and R. V. Khokhlov, "Thermal self-actions of laser beams," *IEEE J. Quantum Electron.* **QE-4**(10), 568–575 (1968).
22. F. G. Gebhardt and D. C. Smith, "Effects of wind on thermal defocusing of CO₂ laser radiation," *Appl. Phys. Lett.* **14**(2), 52–54 (1969).
23. D. C. Smith, "Thermal defocusing of CO₂ laser radiation in gases," *IEEE J. Quantum Electron.* **QE-5**, 600–607 (1969).
24. A. J. Glass, "Thermal blooming in gases," *Opto-Electronics* **1**, 174–178 (1969).
25. D. M. Cordray and P. B. Ulrich, "Computer techniques for solution of the high-energy laser propagation problem," in *Atmospheric Effects on Radiative Transfer*, C. B. Ludwig, Ed., *Proc. SPIE* **195**, 182–191 (1979).
26. F. G. Gebhardt, D. C. Smith, R. G. Buser, and R. S. Rohde, "Turbulence effects on thermal blooming," *Appl. Opt.* **12**(8), 1794–1805 (1973).
27. L. C. Bradley and J. Herrmann, "Phase compensation for thermal blooming," *Appl. Opt.* **13**(2), 331–334 (1974).
28. E. L. O'Neill, *Introduction to Statistical Optics*, Chap. 4, Addison-Wesley, Reading, MA (1964).
29. F. G. Gebhardt, "Self-induced thermal distortion effects on target image quality," *Appl. Opt.* **11**(6), 1419–1423 (1972).

30. F. G. Gebhardt and D. C. Smith, "Self-induced thermal distortion in the near field for a laser beam in a moving medium," *IEEE J. Quant. Electron.* **QE-7**(2) 63–73 (1971).
31. R. J. Hull, P. L. Kelley, and R. L. Carman, "Self-induced thermal lens effect in CCl_4 in the presence of beam motion," *Appl. Phys. Lett.* **17**, 539–541 (1970).
32. D. C. Smith and F. G. Gebhardt, "Saturation of the self-induced thermal distortion of laser radiation in a wind," *Appl. Phys. Lett.* **16**(7), 275–278 (1970).
33. F. G. Gebhardt and D. C. Smith, "Effects of diffraction on the self-induced thermal distortion of a laser beam in a crosswind," *Appl. Opt.* **11**(2), 244–248 (1972).
34. P. J. Berger, P. B. Ulrich, J. T. Ulrich, and F. G. Gebhardt, "Transient blooming of a slewed laser beam containing a region of stagnant absorber," *Appl. Opt.* **16**(2), 345–354 (1977).
35. J. Herrmann, "Properties of phase conjugate adaptive optical systems," *J. Opt. Soc. Am.* **67**(3), 290–295 (1977).

Index

- 1.7- to 1.5- μm window
water-vapor absorption in, 53
- 1976 U.S. Standard Atmosphere, 13
- 2.0- to 2.5- μm window
water-vapor absorption in, 53
- 3- to 5- μm window
water-vapor absorption in, 49–52
- 8- to 12- μm window
water vapor absorption in, 46–50
- Aberrations, optical, 235–237, 246–284, 296
beam spread, 246, 248, 256
beam tilt, 246
boundary-layer aberrations, 264–269
heat-induced, 261–264
inviscid aberration field, 249
jitter, 248, 257
low-order aberrations, 249
open cavity optical degradation, 269–270
scaled to aperture diameter, 260
Strehl loss, 246, 248, 254–256
strong aberrations, 258–259
supersonic vehicle optical aberrations, 274–278
look angle errors, 276
shock curvature effects, 276
from thermal blooming, 296
astigmatism, 296
coma, 296
pincushion distortion, 296
Seidel, 296
spherical, 296
total wave-front variance, 259
wave-front error, 254
weak aberrations, 254–258
- Absolute humidity, 11
- Absorbance, 69–71, 81–82
closed-form expressions for, 82
- Absorber amount, 70
- Absorptance, 6, 81
- Absorption, atmospheric, 13–86, 291
aerosols, 130
carbon monoxide, 62–63
collision-induced, 9, 17, 36–38
continuum absorption, 17, 39–56, 58–59, 130
1.7- to 1.5- μm window, 53–54
2.0- to 2.5- μm window, 53
3- to 5- μm window, 49–52
8- to 12- μm window, 46–50
effects of scattering on, 55–56
far-wing absorption, 54–56
- millimeter-wave window, 44–47
models, 54–55
temperature dependence, 54–55
water-vapor dimers, 54
- line-by-line models, 17
- local-line absorption, 39–40, 42, 58, 130
- methane, 59–60
- molecular, 13
- nitrogen, 63–65
- nitrous oxide, 60–61
- oxygen, 60–65
- ozone, 59–61
- total absorption, 15
- trace gases, 63
- water vapor, 41–56
- Absorption band models, 17, 69–87
absorbance, 69–71, 81–82
absorber amount, 70–71
absorptance, 81
- Elsasser (regular) band model, 69, 71–75
nonoverlapping approximation, 74–75
strong-line approximation, 73–74
weak-line approximation, 71–73
- quasi-random model, 69, 80–81
- random-Elsasser model, 69, 80
- statistical (random) band model, 69, 75–80
equal intensity lines, 76
exponential-tail S⁻¹ random-band model, 79–80
Goody band model, 77
line strength with exponential probability distribution, 76–77
strong-line, weak-line, and
nonoverlapping line approximations, 77–79
- strong-line absorption, 70, 77–79
- temperature and frequency dependence, 81–83
- transmittance, 69, 75, 80
transmittance calculations, 83–87
weak-line absorption, 71, 77–79
- Absorption coefficient
collision-broadened absorption coefficient, 41
continuum absorption coefficient, 41, 50
of carbon dioxide, 59
dimensionless broadening coefficient, 41, 52
foreign broadening coefficient, 41
gas self-broadening coefficient, 41
of mixed gases, 86
nitrogen-broadening water-vapor coefficient, 46, 48, 50
of ozone, 85

- of a spectral line, 14–15, 24
 of water vapor, 41–56, 86
 water-vapor self-broadening coefficient, 46–52
 up-link propagation equation, 305
- Acoustic sounders, 206
- Acoustic transit time, 293
- Actuators, 280, 311
- Adaptive optics, 201, 279–284
 actuators, 280
 deformable mirrors, 279–280, 283
 Guidestar technique, 280
 wave-front sensors, 280, 283
- Adaptive phase correction, 291, 307–308
- Advection, 175, 193
- Aero-optical design examples, 264–284
 aperture optimization, 271–272
 boundary-layer aberrations, 264–269
 IR window thermal noise, 272–274
 open cavity, 269–270
 optimal wavelength, 270–271
 subsonic imaging platforms, 264–268
 supersonic imaging platforms, 268–269
 supersonic vehicle aberrations, 274–277
 supersonic vehicle thermal radiation effects, 277–278
 visible imagers, 270–271
- Aero-optical design solutions, 278–284
 adaptive optics, 279–284
 atmospheric compensation, 279
 deformable mirrors, 279–280, 283
 flow removal, 278
 four-wave mixing, 280–283
 Guidestar technique, 280
 holography, 280
 nonlinear optics, 279–284
 pulsed compensation systems, 279–280
 spatial light modulators, 280
 splitter plates, 278
 supplemental flow, 278
 wave-front sensors, 280, 283
- Aerodynamic effects on optical systems, 235–285
 flow-field-induced heating, 261–264
 inviscid flows, 247–249
 random flow fields, 253–264
 infinite-aperture assumption, 254, 260
 strong aberrations, 258–260
 weak aberrations, 254–258
 shock waves, 249–253
 optical reflections, 252–253
- Aerodynamic flow fields, 235, 237–246
 boundary layers, 241–243, 247
 compressibility effects, 240
 free-stream velocity, 240
 heating, 240–241
 inviscid flows, 247
 Mach number, 237–239
 Newtonian flow, 237
 open cavities, 243–246
 plasmas, 241
 Reynolds number, 237–238
 shear layers, 243–247
 stagnation temperature, 241
- Aerodynamic lensing, 249
- Aerodynamic parameters
 density fluctuations, 236, 254
 correlation length, 236, 254
 path length, 236, 254
 symbols, nomenclature, and units, 239–240
 wave-front variance, 236–237
- Aeromechanical mechanical effects on optical systems, 235–285
- Aerosol blooming, 290
- Aerosol scatter, 12, 92–109, 123–127
 mutual coherence function, 123–127
 polydispersions, 99–100
 particle size distribution function, 99
 phase function, 99–101, 110
 single scatter (Mie theory), 92–96
 absorption efficiency, 98
 backscatter cross section, 96
 backscatter efficiency, 96, 98
 backscatter intensity, 96
 electric dipole scattering, 97
 extinction cross section, 96, 99
 extinction efficiency, 95–98
 $m\text{-}x$ domain, 97–99
 polarization effects, 94–95
 Rayleigh scattering, 97
 scatter cross section, 96
 scatter efficiency, 95–98
 single-scatter albedo, 96, 99
- Aerosols, 11–12
 absorption, 130
 aerosol size distribution models, 105–109
 Junge (power law) model, 107–108
 log-normal distribution, 108
 modified gamma distribution, 105–108
 zero-order logarithmic distribution, 108
 obscurants, 109
 permittivity, 104
 refractive index of, 104–105
 terrestrial aerosols, 100–109
 vertical density variations, 102–104
- AFGL. *See* Phillips Laboratory
- AFGL AMOS turbulence model, 218–219
- Air density, 209, 247, 250, 254, 291, 293–294
- Aircraft, 235–285
- Airy pattern, 254
- Ammonium sulfate refractive index, 104
- Amplitude, 179–183
- Angle of arrival, 194–195, 197
- Anisoplanatism, 201
- Aperture diameter, 193–194, 199
- Aperture filter function, 195
- Aperture plane, 190
- Apertures, 191, 200–201
 circular (Airy), 254, 259
 finite, 260, 272
 infinite-aperture limit, 254, 260
 optimization of, 271–272
 transmitter, 195, 307–308
- Atmosphere, 7–13. *See also* Earth-atmosphere
 geometry
 gas composition, 9–11
 particle composition, 11–13
 structure, 7–8

- Atmospheric boundary layer, 168, 201–206
 interfacial layer, 202
 inversion layer, 202–204
 mixed layer, 202
 surface layer, 202, 204
- Atmospheric heating distribution function, 309
- Atmospheric phenomena
 absorption, 13–86
 aerodynamic effects, 233–285
 refraction, 86–91
 scattering, 92–127
 spectral characteristics, 13–39
 thermal blooming, 287–313
 transmission, 3–156
 turbulence, 157–232
- Atmospheric propagation. *See* Absorption; Atmospheric transmission; Laser beam propagation; Propagation; Scattering; Turbulence; Thermal blooming
- Atmospheric refractivity constant, 305
- Atmospheric spectroscopy. *See* Spectroscopy, atmospheric
- Atmospheric transfer function, 190
- Atmospheric transmission, 1–156. *See also* Absorption; Atmosphere; Index of refraction; Propagation; Refraction, atmospheric; Scattering; Spectroscopy, atmospheric; Thermal blooming
 symbols, nomenclature, and units, 4–5
- Atmospheric transmission codes, 127–147. *See also* FASCODE, HITRAN database; LOWTRAN; MODTRAN
- Attenuation, 299
- Backscattering, 92, 96, 98
- Balloon-borne instruments, 207, 209–211
- Beacon wave intensity, 310
- Beam distortion parameter, 295–296, 299–302, 305–306, 309–311
- Beam focus/defocus, 249
- Beam jitter, 290. *See also* Jitter
- Beam profiles, 299
- Beam radius, 196
- Beam slewing, 290, 294, 299–300, 304
 slewing number, 301
- Beam spreading (broadening), 196–197, 227–229, 235, 246, 248, 256, 290, 298, 308
- Beam tilt, 182, 197, 246
- Beam wander, 159, 182, 196–197, 227–229, 235, 290
- Beams. *See also* Laser beam propagation
 coherence of, 200–201
 collimated, 195, 198–199
 diverging, 195
 focused, 195–199
 Gaussian, 196, 293–297, 299, 302, 305, 310–311
- BHMIE subroutine, 133, 136–138
- Blooming phase, 295–297, 305, 307–308. *See also* Thermal blooming
 negative-lens focal length, 297
 phase gradient, 297
- tilt angle, 297
- Blur angle, 256, 258–259
- Blur spot, 258–259
- Born approximation, 178–180
- Bouguer's law (Beer-Lambert's law), 112
- Boundary layers, 241–243. *See also* Random flows
 laminar boundary layers, 241
 inviscid lensing effects, 241
 static pressure, 241
 and optical aberrations, 264–268
 turbulent boundary layers, 241–243, 247, 253–254, 265
 free-stream density, 242
 optical phase variance, 242
 scale length, 242
 scaling relations, 241–242
 shock waves, 243, 247
 turbines, 242
- Boundary-layer turbulence models, 212–217
 boundary-layer inversion, 215
 convective boundary layer, 216
 Kaimal model, 212–215
 Kukharets-Tsvang model, 215–216
 Kunkel-Walters model, 213–215
 Monin-Obhukov length, 212–213
 similarity theory, 212–214
- Broadening coefficients, 41, 46–56
- Brunt-Vaisala frequency, 170, 173, 213, 223
- C_n^2 . *See* Index of refraction structure parameter
- Carbon dioxide, 9
 absorption, 32, 39, 44, 56–59
 continuum absorption, 58–59
 integrated intensities, 57
 local-line absorption, 58
 vibrational bands, 57
 concentration of, 11
- Carbon monoxide, absorption, 62–63
- Cavities, open, 235–236, 243–246
 acoustical effects, 243
 aft ramp, 245–246
 Airborne Optical Adjunct aircraft, 245
 entrainment requirement, 244
 porous fence, 244–245
 resonance, 243–246
 sound pressure level, 246
- Cavity flow field, 236
- Central limit theorem, 180
- Chapman function, 113–115
- CLEAR I turbulence model, 220, 228
- Clouds, 108–109, 203
- Coherence length, 191–193, 197, 200, 210–211, 216, 219, 222, 228, 311
- Computer codes for atmospheric propagation, 127–147
- Computers, personal, 96
- Contrast. *See* Image contrast
- Convection, 167, 203, 205, 210, 214–216, 289, 291–292, 304
- Covariance, 180–181, 184–190, 198
- Covariance function, 161–167

- C_T^2 instruments, 202, 206
 Cutoff frequency, 192
- Deformable mirrors, 279–280, 283, 311
 Density, air. *See* Air density
 Deserts, 205, 210–211, 220
 Detectors, 187, 246. *See also* Imagers
 Detectors, airborne. *See also* Imaging systems, airborne
 - emissivity, 263
 - power, 261
 - spectral exitance, 261
 - spectral irradiance, 261–263
 - spectral radiance, 261
 - transmission, 262
 Diffraction, 197, 257, 259–260, 299, 306
 Distortion, 195
 Dust, 100
 - refractive index, 104
 Earth-atmosphere geometry, 89–91
 - effects of refraction, 90
 - optical horizon, 89
 Eddies, 193
 Effective blooming range, 309
 Electric field, 177
 Electro-optic sensors, scattering effects, 111–112
 Energy, conservation of, 200
 Exosphere, 8
 Extinctance, 6
 Extinction coefficient, 3, 6–7, 112, 292
 Extinction cross section, 95
 Extinction number, 295, 300
- Far-infrared, 18
 FASCODE, 25, 32, 55, 128, 133–135
 Fata Morgana, 91
 Figure of merit, 256
 Filter functions, 181, 183, 188–189
 Finite optical apertures, 260
 Focal plane, 195
 Focusing, beam, 300–301
 Focusing correction, 307
 Fog, 103, 109
 Free atmosphere, 206–209
 - stratification, 206–207, 212
 - stratosphere, 207, 209
 - tropopause, 207
 - troposphere, 206–207, 209
 Free-stream density, 242, 244
 Fresnel approximation, 179, 185–186
 Fresnel length, 187, 210
 Fresnel number, 293, 298–301, 304
 Frozen turbulence hypothesis, 175–176, 186, 206, 209
 Fused quartz, 264
 Fused silica optical mode constants, 106
- Gases, atmospheric. *See also* Absorption; Carbon dioxide; Carbon monoxide; Methane; Nitrogen; Nitrous oxide; Oxygen; Ozone; Trace gases; Water vapor
 - absorption by, 39–65
 - amount in atmosphere, 9
 - density in atmosphere, 12–13
 - fundamental vibrational frequencies, 21
 - isotopic abundance, 67
 - mixing ratio, 10
 - rotational constants of, 19
 Gaussian focal-plane spot, 256
 Gaussian laser beams. *See* Laser beam propagation
 Geometric-optics limit, 259
 Geometrical optics, 299
 Germanium, 262, 273
 Gladstone-Dale parameter, 236, 247, 252–254
 Green flash, 91
 Green spot, 90
 Greenhouse effect, 39, 57
- Haze, 12, 100, 108
 Heat transfer, 262, 289, 291–293
 Heat-balance equation, 264
 HITRAN database, 19, 21, 26, 35, 39, 42, 58, 65–69, 85
 Holography, 237, 280
 Homogeneous fluctuations, 165
 Hufnagel turbulence model, 221–223
 Hufnagel-Valley turbulence model, 222, 225
 Humidity. *See also* Absolute humidity; Relative humidity
 - effects on C_n^2 , 172–173
 - specific, 170–171
 Huygens-Fresnel theory, 179, 200
 Hydrometers, 11–12
 Hygroscopic particles, 100, 102
- Ideal gas law, 11, 13
 Image blurring, 190, 193–195, 235
 Image contrast, 123, 235, 246, 254–258
 Image dancing, 182, 190, 193–195
 Image displacement, 195
 Image quality, 256–257. *See also* Aberrations, optical; Aerodynamic effects on optical systems; Image contrast; Image resolution
 Image resolution, 192–193, 226–227, 235, 246, 254–258
 Imagers, visible, 269–271, 282–284
 Imaging, effects of turbulence, 190–195, 226–227
 - image blurring, 190, 193–195
 - image dancing, 190, 193–195
 Imaging systems, airborne, 236, 248–284. *See also* Detectors, airborne
 - aero-optical design considerations, 264–284
 Imaging through a scattering medium, 123–127
 - contrast, 123
 - mutual coherence function, 123–127

- optical transfer function, 123–127
 point spread function, 123, 127
 polarization, 125
 visibility range, 123
- I**Index of extinction, 6–7
IIndex of refraction, 21, 86–89, 159, 169, 171–174, 177, 180, 247, 253, 291–294
 aerosols, 104–105
 Brunt-Vaisala frequency, 171, 173
 complex, 25, 93, 104
 ducting effects, 91
 Fata Morgana, 91
 green flash, 91
 green spot effect, 90
 inferior mirages, 91
 at infrared wavelengths, 88
 mirages, 91
 potential refractivity, 173
 at radar frequencies, 88
 refraction correction angle, 89–91
 Sellmeier model, 88–89
 subrefractive conditions, 90–91
 superior mirages, 91
 superrefractive conditions, 90–91
 water-vapor contribution, 88
- I**Index of refraction structure parameter (C^2), 159, 172–174, 185–186, 189, 191, 202–228
- I**nertial range, 167
- Infrared windows, 235, 243, 262–263, 272–274
- I**ntensification effect, 298
- I**ntensity, 184, 186–187, 200–201, 225–225
- I**ntensity, far-field, 256–257
- I**ntensity variance, 184, 225
- I**nterferometric calorimeter measuring technique, 53–54
- I**nterferometry, 237
- I**nterferometry, speckle, 195
- INTRP subroutine, 139–142
- Inviscid flows, 247–249
- I**onization, 247, 250, 277
- I**onosphere, 7–8
- I**rradiance distortion parameter, 298
- I**sobaric heating, 289, 292–293, 295
 energy-balance equation, 292
- I**soplanatic angle, 201, 210–211, 219, 222
- I**isoplanatism, 201
- Jet stream, 207–209, 222
- Jitter, 235, 248, 257, 279, 290
- Kaimal turbulence model, 212–215
- K**inetic cooling, 290
- Kolmogorov theory, 161, 167–169, 175, 180–181, 183, 185, 209
- Kukharets-Tsvang turbulence model, 215–216
- Kunkel-Walters turbulence model, 213–215
- Laboratory simulation experiments, 300, 302–303
- Laser beam power density, 292
- Laser beam propagation, 157–232, 287–313. *See also* Aberrations, optical; Absorption; Scattering; Thermal blooming; Turbulence, optical
 atmospheric scattering, 111
 beam intensity, 292–293, 298–304
 critical intensity, 302
 critical power, 302–303
 cw beams, 292–294
 empirical scaling law, 303
 Gaussian beams, 293–297, 299, 302, 305, 310–311
 laboratory propagation simulation experiments, 300–303
 peak irradiance, 302–303, 307
 ray-optics thermal propagation model, 300, 306, 309, 311
 repetitively pulsed beams, 292–294
 thermal blooming effects, 289–311
 uniform beams, 297, 311
 very-short-pulse HEL beams, 293–294
 wave-optics propagation codes, 297, 301, 303–304, 306, 309–310
- Lidar, 197, 206
- Localized gradients, 291
- Log amplitude, 182–190, 198–199, 225
- LOWTRAN, 25, 55, 83, 85–87, 127–132
- Mach number, 237–239, 266–267
- Magnesium fluoride, 263
- Maxwell's equations, 177
- Mesosphere, 7
- Meteorology, synoptic, 202, 207, 209
- Methane, absorption, 59–60
- Microwave spectral region
 absorption bands, 39
- Mid-infrared, 18
- Mie scatter, 92–98. *See also* Aerosols, scatter
- MIEGEN subroutine, 143–147
- Millimeter-wave spectral region
 absorption bands, 39
 propagation model, 32
 water-vapor absorption in, 44–47
- Mirages, 91
- Modified von Karman spectrum, 174–175, 182
- MODTRAN, 25, 86, 128, 132
 Curtis-Godson approximation, 86
- Modulation transfer function, 191–194, 200–201, 258, 260
- Molecular Rayleigh scattering. *See* Rayleigh scattering
- Molecule classification, 18
- Moments, measurement of, 210–211
- Monin-Obhukov length, 212–213
- Mountains, 205, 210–211, 218–220
- Mutual coherence function, 123–127, 187–188, 190–191, 193
- Mutual intensity function, 190
- Navier-Stokes equations, 161
- Near-infrared, 18

- Negative lens (defocusing) effect, 295, 305
- Nitrogen, 9, 17, 21, 32, 41
absorption continuum, 63–65
broadening, 43, 46, 48, 50, 52
- Nitrous oxide, absorption, 60–61
- NOAA (VanZandt) turbulence model, 223–224
- Nonisobaric heating, 293–294
- Nonlinear optics, 279–284
coherent beacon, 282–283
four-wave mixing, 279, 283
holography, 280
spatial light modulators, 280
- Nonlinear propagation. *See* Thermal blooming
- Nonuniform velocity profile, 300
- Number density, 3
- Obscurants. *See* Aerosols; Dust; Haze
- Optical aberrations. *See* Aberrations, optical
- Optical depth, 6
- Optical design. *See* Aero-optical design examples; Aero-optical design solutions
- Optical mode constants, 105–107
 $\alpha\text{-Fe}_2\text{O}_3$, 107
fused silica, 106
quartz, 107
sodium chloride, 105
- Optical phase, 247
- Optical phase distortion, 295
- Optical phase variance, 242
- Optical transfer function, 123–127, 181, 191, 201
- Optical turbulence. *See* Turbulence, optical
- Optical turbulence profiles, 217–221
- Optimal wavelength, 257, 270–271
- Oxygen, 9, 17, 21–22, 41
absorption, 32, 60–65
broadening, 48
- Ozone, 7, 22
absorption, 59–61
- Paraxial scalar wave equation, 291–292
- Particle scattering. *See* Aerosol scatter
- Particles, atmospheric, 11–13
aerosols, 11–12
hydrometers, 11–12
radius range, 12
- Permittivity, 104
- Perturbation series, 177–178
- Perturbations, 179, 293
- Phase, 179–183, 190
- Phase compensation, 300, 304, 307–311
- Phase covariance, 182
- Phase distortions, 159, 190, 195, 201
- Phase function approximation, 121–22
Henyey-Greenstein phase functions, 121–122
- Phase shift, 295–296
- Phase-correlation function, 258
- Phillips Laboratory (formerly AFGL), 19, 21, 25, 39, 66
- Photoacoustic laser measurement, 44, 46, 49–50
- Photon absorption, 14
- Photon scattering, 254
- Pixel field of view, 236
- Plane waves, 181, 183–185, 188–192, 195, 198–200
- Plasmas, 247, 277
- Point spread function, 123, 127, 190, 258
- Polarization, 94–95, 177
- Polydispersions, 99–100. *See also* Aerosol scatter
- Power in the bucket, 246
- Power spectrum, 162–163
- Prandtl number, 171
- Prism (beam-bending) effect, 295
- Propagation, 115–147, 157–232, 287–313. *See also* Atmospheric transmission; Laser beam propagation; Scattering; Thermal blooming; Turbulence
computer codes, 127–147
far-field, 194
FASCODE examples, 134–135
LOWTRAN examples, 130–132
near-field, 194
optical, 7–8
phase function approximation, 121–122
pulse stretching, 122–123
radio-wave, 7–8
symbols, nomenclature, and units, 160
transport theory, 115–119
through turbulence, 176–201
amplitude and phase statistics, 179–183
beam effects, 195–201
imaging effects, 190–195
isoplanatism, 201
polarization effects, 177
scintillation, 184–190
wave equation solutions, 177–179
- Pulse length, 293
- Pulse stretching, 122–123
- Quartz
optical mode constants, 107
refractive index, 104
- Radar, 177, 207, 223
Doppler, 210
Sousy, 208
- Radiation slide rule, 261
- Radiative transfer, atmospheric, 3–7
- Radiative transfer equation, 6–7
- Radiosonde, 223
- Raman scattering, 17
- Random flow fields, 253–264. *See also* Aerodynamic effects on optical systems
shear layers, 253–254
turbulent boundary layers, 253
- Range gating, 253
- Ray-optics model, 297–300, 304, 306, 309–311
- Rayleigh (molecular) scattering, 12, 17, 55–56, 97, 109–110. *See also* Aerosol scatter
- Receivers, 185
- Reflections, at shock-wave interface, 252–253

- Refraction, atmospheric, 86–91
 Refractive index. *See* Index of refraction
 Relative humidity, 10, 103, 203–205, 207
 Resolution. *See* Image resolution
 Reynolds number, 237–238, 242, 253
 Riccati equation, 178
 Rytov approximation, 178–180, 184, 186–187, 190, 199, 225
- Sapphire, 263
 Saturation vapor pressure of H_2O , 10, 12
 Scatterance, 6
 Scattering, 177–179
 backscattering, 177
 forward scattering, 177
 laser, 195
 multiple scattering, 177, 186
 Scattering angle, 254
 Scattering, atmospheric, 92–127. *See also*
 Aerosol scatter; Mie scatter; Rayleigh scattering; Propagation
 aerosol scatter, 92–109, 123–127
 algorithms, 133, 136–147
 BHMIE subroutine, 133, 136–138
 INTRP subroutine, 139–142
 MIEGEN subroutine, 143–147
 SPHERE scattering program, 139
 example applications, 110–115
 molecular Rayleigh scattering, 12, 17, 55–56, 109–110
 multiple scattering, 115–119
 mutual coherence function, 123–127
 by particles, 9, 12
 Raman scattering, 17
- Scattering coefficient, 305
 Scintillation, 159, 183–195, 198–200, 210, 224–226, 291
 Scintillometers, 186, 219
 horizontal, 186
 stellar, 186, 210, 224
 Sea salt, 102
 Sellmeier's equation, 25
 Shear layers, 236, 243–247, 253–254
 Bernoulli effect, 244
 Shock waves, 243, 249–253
 Signal-to-noise ratio, 237, 253, 273
 Silicon, 262
 Similarity theory, 212–214
 Single scatter. *See* Mie scatter
 Single-scatter approximation, 7
 SLC turbulence models, 217–219
 Sodium chloride
 optical mode constants, 105
 refractive index, 104, 106
 Solar flux, 213
 Source term for path emission or scattering, 3, 6
 Spatial coherence, 191
 Spatial frequency, 192
 Specific intensity, 115–119
 Speckle, 195
 Speckle interferometry, 195
 Spectral extinction cross section, 3
 Spectral radiance, 3
 Spectral scattering cross section, 3
 Spectrometers, 43–44
 Spectroscopy, atmospheric, 13–39
 Birnbaum's line shape, 59
 classical oscillator model, 22–25
 absorption coefficient, 24
 electric susceptibility, 23
 free-space permittivity, 23–25
 Lorentz line shape, 24, 30, 32, 36
 relative permittivity, 23–25
 Sellmeier's equation, 25
 time harmonic behavior, 23
 Van Vleck–Weisskopf line-shape function, 25
 collision-broadened line shape, 30–38
 autocorrelation function, 30–31, 33–34
 collision-broadened half-width at half-intensity, 31
 exponential wing, 34
 far-wing, 33–34
 line-mixing effects, 32
 self-broadening coefficient, 31–32
 definitions, 14–15
 absorption coefficient, 14–15
 line-shape function, 14
 spectral line half-width, 14
 spectral line strength, 14
 Doppler line shape, 35–36
 Doppler equation, 35
 Maxwell–Boltzmann distribution, 35
 Doppler spectral density function, 36
 dipole moments, 15–17, 23
 electron polarizability, 17
 electronic spectra, 18, 21–22
 Heisenberg uncertainty principle, 29
 homogeneous line shapes, 28–35
 infrared-active rotational spectra, 16
 inhomogeneous line shapes, 28, 35–37
 intramolecular potentials, 15–17
 light-matter interaction, 22–26
 line position, 18, 66
 line-shape profiles, 28–37
 line strength, 26, 66
 molecule classification, 18
 asymmetric top, 18–19
 linear, 18
 spherical top, 18
 natural line shapes, 30
 Einstein spontaneous emission coefficient, 30
 half-width at half-intensity, 30
 line-profile function, 30
 nonpolar molecules, 16
 partition functions, 26–28
 for diatomic molecules, 27
 Maxwell–Boltzmann distribution function, 26
 for polyatomic molecules, 27–28
 polar molecules, 16
 quadrupole moments, 16
 quantum mechanical model, 25–26
 autocorrelation function, 25
 dipole matrix element, 26

- line strength, 26
 line-profile function, 25
 partition function, 26
 power spectral density function, 25
 refractivity model, 37–39
 anomalous dispersion, 38
 Hilbert transform, 37–38
 index of absorption, 37
 index of refraction, 37–38
 Sellmeier equation, 38
 rotation bands, 20–21
 rotational quantum numbers, 16
 rotational selection rules, 16–17
 anti-Stokes vibrational band, 17
 O-branch, 17
 P-branch, 17, 21
 Q-branch, 17, 21
 R-branch, 17, 21
 S-branch, 17
 Stokes vibrational band, 17
 rotational spectra, 18–20
 rotational constants, 18–19
 rotational term values, 18–19
 rotational-vibrational spectra, 21–22
 vibration bands, 20–21
 combination bands, 20
 fundamental transitions, 20
 hot bands, 20
 overtone bands, 20
 vibrational term value function, 20
 vibrational frequencies of atmospheric molecules, 21
 vibrational quantum numbers, 16
 vibrational spectra, 16
 Voigt line shape, 36–37
- Spectrum, 180–181, 185
 SPHERE scattering program, 139
 Spherical waves, 183–185, 188–192, 195, 198–200
 Stagnation zones, 290, 300, 304
 Stars
 scintillation, 186, 224–225
 Stimulated thermal Rayleigh scattering, 289
 Stokes vector, 94
 Stratification, 206–207, 212
 Stratosphere, 7, 207, 209, 219, 221
 Strehl ratio, 246, 248, 255–256, 258–260, 301, 304, 306, 308–309, 311
 Structure functions, 165–173, 180–181, 198
 structure coefficient, 172
 Surface boundary layers, 235
 Symbols, nomenclature and units, 3–5, 160, 239–240
- Tatarski equation, 173
 Temperature, 203–207
 adiabatic wall, 262, 277
 inversions, 174, 203–204
 lapse rate, 209
 potential temperature, 169–170, 223
 relation to C_n^2 , 209
 temperature spectrum, 174
- Thermal blooming, 287–313. *See also* Laser
 beam propagation; Propagation
 blooming phase, 295–297
 collimated beam—homogeneous path, 294–299
 convection-dominated blooming, 293, 299, 311
 focused beams—inhomogeneous path, 299
 isobaric heating, 292–293
 nonisobaric heating, 293–294
 paraxial scalar wave equation, 291–292, 297
 pulse overlap blooming effects, 294
 single-pulse thermal-blooming effects, 293–294
 small-scale thermal-blooming instabilities, 289–291, 310
 stagnation zone blooming, 290, 304
 steady-state blooming, 294–311
 t -cubed blooming, 293
 thermal blooming intensification effect, 298
 thermal-blooming phase distortion, 296, 298
 thermal-conduction-dominated blooming, 292–293
 thermally bloomed irradiance pattern, 297–298
 up-link (ground-to-space) thermal blooming, 304–311
 up-link thermal-blooming compensation, 289
 wave-optics propagation codes, 297
 whole-beam thermal blooming, 289–290
- Thermal blooming phase distortion, 296, 298
 Thermal conductivity, 292
 Thermal diffusivity, 292
 Thermal focusing, 298
 Thermal lens, 289–290, 295
 Thermal noise, 261–262, 272–274, 277
 Thermal plumes, 173, 206
 Thermo-optical aberrations, 253, 261–264, 274
 Thermomechanical loads, 262
 Thermosonde, 203–205, 207–208, 223
 Thermosphere, 8
 Trace gases, absorption, 63
 Transmission. *See* Atmospheric transmission
 Transmission along a slant path, 112–115, 131
 Transmittance, 6, 69, 75, 80, 83–87, 306
 calculation methods, 83–87
 aggregate method, 83–84
 LOWTRAN method, 83, 85–87
 MODTRAN method, 86
 Transonic slewing, 290, 300
 Transport theory, 115–119
 discrete ordinates method, 120–121
 four-flux theory, 120
 transport equation parameters, 115–119
 diffuse intensity, 120
 field intensity, 116–117
 flux density, 117
 incident flux, 120
 irradiance, 117
 optical distance, 118
 radiant emittance, 117
 source function, 118
 specific intensity, 116–119
 surface intensity, 116
 two-flux theory (Kubelka-Munk), 119–120

- Transverse coherence length, 191
 Tropopause, 207, 219
 Troposphere, 7, 39, 206–207, 209, 219–221
 Turbulence, atmospheric, 159, 235–237, 290, 310. *See also* Turbulence, optical
 Turbulence, mechanical, 173–174, 203
 Turbulence, optical, 159–232, 300. *See also*
 Laser beam propagation; Propagation
 atmospheric temporal statistics, 174–176
 conservative passive scalars, 169–171
 adiabatic lapse rate, 170
 Brunt-Väisälä frequency, 170, 173
 one-dimensional spectrum, 170–172
 potential temperature, 169–170
 potential temperature structure constant, 170–171
 three-dimensional spectrum, 170–172
 velocity fluctuations, 169
 definition, 161
 index of refraction, 171–174
 index of refraction structure parameter (C_2^2), 172–174
 modified von Karman spectrum, 174–175, 182
 von Karman spectrum, 174, 182
 Kolmogorov theory, 167–169, 175
 measurement of, 201–211
 atmospheric boundary layer, 201–206
 free atmosphere, 206–209
 intermittency, 209
 measurement of moments, 210–211
 stationarity, 209
 volume averaging, 209
 models of, 211–224
 AFGL AMOS model, 218–219
 boundary-layer turbulence, 212–217
 CLEAR I model, 220
 Hufnagel model, 221–223
 Hufnagel-Valley model, 222
 Kaimal model, 212–215
 Kukharets-Tsvang model, 215–216
 Kunkel-Walters model, 213–215
 NOAA (VanZandt) model, 223–224
 optical turbulence profiles, 217–221
 similarity theory, 212–214
 SLC models, 217–219
 propagation through, 176–201
 statistical concepts, 161–164
 covariance function, 161–167
 ergodicity, 162
 homogeneity, 163, 165
 isotropism, 163
 power spectrum, 162–163
 Wiener-Khinchine theorem, 162, 165–166
 structure functions, 165–173
 inverse relation, 166
 isotropic property, 166
 theory, 161–176
 Turbulence, strong, 187, 197
 Turbulence, weak, 197
 Turbulent boundary layers, 236, 247, 253–254
 Turbulent mixing, 290
 Turret, hemispherical, 249
 Ultraviolet, 18, 21
 Up-link (ground-to-space) thermal blooming, 304–311
 Velocity turbulence, 161
 Visibility, 123
 Visible spectral region, 18
 Volcanoes, 100
 von Karman spectrum, 174, 182
 Water
 in the atmosphere, 7, 10
 phase function, 101
 refractive index, 104
 Water vapor, 9–12, 16, 169, 171
 absolute humidity, 11
 absorption, 39–56
 absorption coefficient, 86
 continuum absorption, 42–56, 130
 1.7- to 1.5- μm window, 53–54
 2.0- to 2.5- μm window, 53
 3- to 5- μm window, 49–52
 8- to 12- μm window, 46–50
 effects of scattering on, 55–56
 far-wing absorption, 54–56
 millimeter-wave window, 44–47
 models, 54–55
 temperature dependence, 54–55
 water-vapor dimers, 54
 integrated intensities, 41, 43
 local-line absorption, 42, 130
 partial pressure, 10
 relative humidity, 10
 rotational constants, 19
 saturation vapor pressure, 10, 12
 transmittance, 85
 vibrational frequency, 20
 water-vapor partial pressure, 45–46, 49, 54
 Wave equation, 177–179
 Wave-front distortion, 247
 Wave-front sensors, 280, 283
 Wave-front tilt angle, 257
 Wave-optics propagation codes, 297, 303–304, 306, 309–310
 Wave-structure function, 181, 190
 Wiener-Khinchine theorem, 162, 165–166
 Wind, 165, 175–176, 186, 203, 206–207, 216–217, 222–223
 effects on laser beam propagation, 289, 294–299, 301
 speed, 186, 193, 203, 208, 213, 221, 306
 structure function, 167
 velocity structure function, 167
 Wind shear, 167, 223
 Wind tunnels, 237
 Windows. *See* Infrared windows
 Zenith angle, 190